Ultra Wideband Communications: Novel Trends
Antennas and Propagation

Edited by Mohammad Matin

ULTRA WIDEBAND COMMUNICATIONS: NOVEL TRENDS – ANTENNAS AND PROPAGATION

Edited by **Mohammad A. Matin**

Ultra Wideband Communications: Novel Trends - Antennas and Propagation
Edited by Mohammad Matin

Contributors

Avi Zadok, Yair Peled, Xiaoxia Wu, Moshe Tur, Alan E. Willner, Daniel Grodensky, Daniel Kravitz, Karlo Queiroz Costa, Victor Dmitriev, Mohamed Nabil Srifi, Fei Yu, Chunhua Wang, Duje Čoko, Zoran Blazevic, Ivan Marinović, Qiubo Ye, Zhi Ning Chen, Terence See, Salman Naeem Khan, Muhammad Ashfaq Ahmed, El Gibari Mohammed, Averty Dominique, Li Hongwu, Lupi Cyril, Toutain Serge, Mahe Yann, Gonzalo Llano Ramirez, Andres Navarro Cadavid, Juan Carlos Cuellar, Woon Geun Yang, Woo Chan Kim, Abdelhalim Mohamed, Lotfollah Shafai, Dinh Tran, Qingsheng Zeng, Javad Ahmadi-Shokouh, Robert C. Qiu, Francisco Saez de Adana, Paolo Baldonero, Antonio Manna, Fabrizio Trotta, Roberto Flamini, Baptiste Cadilhon, Bruno Cassany, Jean Christophe Diot, Modin Patrick, Laurent Pécastaing, Valérie Bertrand, Chin-Lung Yang, Chieh-Sen Li

Notice

Statements and opinions expressed in the chapters are these of the individual contributors and not necessarily those of the editors or publisher. No responsibility is accepted for the accuracy of information contained in the published chapters. The publisher assumes no responsibility for any damage or injury to persons or property arising out of the use of any materials, instructions, methods or ideas contained in the book.

We are IntechOpen,
the world's leading publisher of
Open Access books
Built by scientists, for scientists

4,000+
Open access books available

116,000+
International authors and editors

120M+
Downloads

151
Countries delivered to

Our authors are among the

Top 1%
most cited scientists

12.2%
Contributors from top 500 universities

Interested in publishing with us?
Contact book.department@intechopen.com

Numbers displayed above are based on latest data collected.
For more information visit www.intechopen.com

Meet the editor

Dr. Mohammad A. Matin is currently working at the Department of Electrical Engineering and Computer Science, North South University as an Assistant Professor. He obtained his Ph.D. degree in wireless communications from Newcastle University, UK and M.Sc. degree in digital communications from Loughborough University, UK. Dr. Matin was the visiting lecturer at the National University of Malaysia. He has published over 40 refereed journal and conference papers. He has presented invited talks in Bangladesh, China and Malaysia and has served as a referee of a few renowned journals. He also served as a technical session chair of few international conferences like MIC-CPE 2008, ICCIT 2008, ICCIT 2010, ICMMT 2010 etc. He is currently serving as an editorial board member of IET-WSS, JECE, etc. He has received a number of prizes and scholarships including the Best Student Prize (Loughborough University), Commonwealth Scholarship and Overseas Research Scholarship (ORS). His current research interests include UWB communications, wireless sensor networks, cognitive radio, EM modeling, and antenna engineering.

Contents

Preface

Ultra wideband (UWB) has advanced and merged as a technology, and many more people are aware of the potential for this exciting technology. The current UWB field is extremely dynamic, with new techniques and ideas where several issues are involved in developing the systems, such as antenna design, channel model, and interference. However, the antenna design for UWB signal is one of the main challenges, especially when low cost, geometrically small and radio efficient structures are required for typical applications. It is expected that an appropriate antenna configuration should be part of a UWB chipset with a full reference design. It requires a theoretical basis for computation and estimation of antenna design parameters and performance prediction that determine the performance of precision range and direction measurements.

This book offers basic as well as advanced research materials for antennas and propagation. It has taken a theoretical and experimental approach to some extent, which is more useful to the reader in the long run. The book highlights the unique design issues which put the reader in a good pace to be able to understand more advanced research and make a contribution in this field themselves. It is believed that this book serves as a comprehensive reference for graduate students in UWB antenna technologies.

Chapter 1 explains the generation of UWB impulse radio using self-phase modulation in optical fibers. Two different nonlinear mechanisms had been employed: self-phase modulation (SPM) and Stimulated Brillouin scattering (SBS) for the generation of UWB waveforms.

Chapter 2 presents a comprehensive overview of UWB measurements of all empirical data available on various fading properties of indoor radio wave communication channels. The analytic summaries lead to insights on UWB fading channel characterization and modeling.

The propagation of the UWB signals in indoor environments is an important task for the implementation of WPANs which is explained in chapter 3.

Chapter 4 provides a detailed description of the UWB channel in the frequency domain, using the models defined by IEEE 802.2.15.3a and 802.2.15.4a for High Data

Rate Wireless Personal Area Network (HDR-WPAN), Body Area Networks (BAN) and Sensors Networks, among other applications. A theoretical model for the fade depth and fading margin of the channel energy is presented in accordance to the parameters of the IEEE 802.15.4a UWB channel model.

Chapter 5 is about the estimations of the channel parameters which have certain dependency on the system bandwidth.

Accurate modeling and improved physical understanding of pulse reflection from dispersive media is crucial in a number of applications, including optical waveguides, UWB radar, ground penetrating radar, UWB biological effects, stealth technology and remote sensing which is explained in chapter 6. The time domain technique based on the numerical inversion of Laplace transform is also developed and extended to the modeling of ultra wideband pulse reflection from Lorentz, Debye and Cole–Cole media.

Chapter 7 explores planar antennas which are widely used in UWB systems because of their low cost of fabrication, low size, and simple structure. In this chapter, four planar UWB antennas with cuts at the edges and parasitic loops have been analyzed. The investigated antennas are: a rectangular monopole with two loops, a rectangular monopole with four loops, a rectangular monopole with cuts at the edges, and a rectangular monopole with cuts at the edges and two parasitic loops. Here, to enlarge the matching bandwidth, the dimensions of the antennas were optimized with cut-and try method.

Chapter 8 presents butterfly-shaped monopole antenna that has demonstrated good impedance and radiation performance across the UWB band.

Monopole disc antennas, with circular, elliptical and trapezoidal shapes, have simpler two-dimensional geometries and are easier to fabricate compared to the traditional UWB monopole antennas with three-dimensional geometries such as spheroidal, conical and teardrop antennas. In chapter 9, different square, circular and elliptical disc monopole antenna geometries are designed and analyzed for both omnidirectional and directional applications. The feeding structure is optimized to have a maximum impedance bandwidth starting at 3 GHz.

Printed disc monopole antennas are designed in chapter 10 which could be treated as a good candidate for current and future ultra wideband applications, due to their attractive features (i.e. small size, low profile, low cost, impedance bandwidth, gain, nearly omnidirectional radiation).

In chapter 11, rectangular and diamond shaped sleeve UWB antennas are presented for UWB performance. The analysis of sleeve UWB antenna is also be explained on the basis of transmission line model of antenna and characteristic modes to get insight details of the sleeves behavior and their effect on the impedance bandwidth.

In chapter 12, an ultra-wideband coplanar waveguide (CPW)-fed planar monopole antenna with dual band rejection characteristics is presented. The main problem of the frequency band rejection design is the difficulty of controlling the bandwidth of the notch band in a limited space. Furthermore, strong couplings between two adjacent notch bands design are obstacles to achieve efficient dual band-notched UWB antennas. Therefore, an efficient frequency bands rejection of the WLAN band and WiMAX band is difficult to implement for UWB applications.

In chapter 13, a CPW-fed novel planar ultra-wideband antenna with dual band-notched characteristics is introduced.

Chapter 14 present an ultra-wide bandwidth back-to-back coplanar-microstrip grounded coplanar waveguide (GCPW-MS-GCPW) transition without making via-hole in the substrate or patterning the bottom ground plane which simplifies the manufacturing and facilitates the on-wafer characterization with Ground-Signal-Ground (GSG) probe station.

The choice and the design of the radiating components of a high power microwave source are vital as they determine the choice of all or part of the complete system. It has been explained in chapter 15 that 3D simulations coupled with experimental tests on prototypes made it possible to refine the various geometrical parameters of the components to obtain the best possible levels of electromagnetic performance in small volumes.

Chapter 16 provides an introduction about UWB multifunctional antennas, pointing out all the main features, advantages and drawbacks, in a quick and easy-to-understand way before going into the details. The chapter starts with presenting a brief history of UWB radiating elements, and continues explaining the theory behind the frequency independent antennas and the feeding techniques, and finally, suggests a complete design of UWB multifunctional phased array.

In chapter 17, a novel design method is presented for reconfigurable antennas that are independent of the geometries and the dimensions of the antennas, providing wide tuning ranges and controllable selectivity.

The design methodology and conceptual approach of the super wideband (SWB)-prototype has been discussed in chapter 18.

I hope that students will find this book useful as a learning tool for research in this exciting field.

Mohammad A. Matin
North South University
Bangladesh

Part 1

UWB Waveform Generation

1

Ultra-Wideband Waveform Generation Using Nonlinear Propagation in Optical Fibers

Avi Zadok[1], Daniel Grodensky[1], Daniel Kravitz[1], Yair Peled[2],
Moshe Tur[2], Xiaoxia Wu[3] and Alan E. Willner[3]

[1]Bar-Ilan University
[2]Tel-Aviv University
[3]University of Southern California
[1,2]Israel
[3]USA

1. Introduction

Ultra-wideband (UWB) radio is a transmission technology that is based on short pulses, whose spectral width is on the order of several GHz. UWB signals are free of sine-wave carriers, and their duty cycle and power spectral density are low. These characteristics provide UWB radio with unique advantages: improved immunity to multi-path fading, increased ranging resolution, large tolerance to interfering legacy systems, enhanced ability for penetrating obstacles, and low electronic processing complexity at the receiver. UWB technology is considered attractive for a myriad of applications, including high-speed internet access, sensor networks, high accuracy localization, precision navigation, covert communication links, ground-penetrating radar, and through-the-wall imaging (Yang & Giannakis, 2004).

Of the various potential UWB radio applications, much attention has turned to wireless personal area networks, which address short-range, ad-hoc, and high-rate connectivity among portable electronic devices. UWB radio is among the standards that are being considered to replace cables in such networks, due to its multi-path and interference tolerance, low power, and high efficiency. Research efforts in this area have intensified since 2002 when the United States Federal Communication Commission (FCC) allocated the frequency range of 3.6-10.1 GHz for unlicensed, UWB indoor wireless communication (Federal Communications Commission [FCC], 2002). Interest is not limited to indoor wireless communication only: the FCC report relates to imaging systems and vehicular radar systems as well (FCC, 2002). The vehicular radar standard, in particular, specifies a high central frequency of 24 GHz or higher (FCC, 2002). The electronic generation of complex UWB waveforms at such high frequencies is increasingly challenging.

The FCC standard imposes several limitations on the transmitted signals. First, the power spectral density must comply with complicated spectral masks (FCC, 2002). In addition, the total signal power is severely restricted, limiting the range of UWB indoor wireless transmission, for example, to only 10-15 m. In many scenarios, UWB radio-based systems would need to extend their wireless transmission range by other distribution means. As the

frequencies of UWB signals continue to increase, with 100 GHz transmission already reported (Chow et al., 2010), optical fibers become the preferable distribution medium. With radio-over-fiber integration on the horizon, the generation of the UWB pulses by photonic methods becomes attractive. Microwave-photonic generation techniques can offer flexible tuning of high-frequency pulse shapes, inherent immunity to electromagnetic interference, and parallel processing via wavelength division multiplexing (Capmany et al., 2005). Driven by the promises of integration and flexibility, much research effort has been dedicated to photonic generation of UWB waveforms in recent years.

Most microwave-photonic UWB generation schemes thus far target *impulse radio* implementations: the transmission of tailored short pulses and their subsequent coherent detection. One category of photonic UWB generation techniques relied on the conversion of phase to intensity modulation (Yao et al., 2007; Zeng & Yao, 2006; Zeng et al., 2007). This method is simple to implement, however it offers few degrees of freedom for pulse shaping and minimal reconfiguration. Waveforms generated using this method are restricted to a Gaussian mono-cycle or a Gaussian doublet shape. Higher-order pulse shapes were generated based on microwave-photonic tapped delay line filters, with both positive and negative coefficients (Bolea et al., 2009; Bolea et al., 2010). Pulse generation based on four-coefficient filters had been demonstrated (Bolea et al., 2009), however each additional coefficient required an extra laser source.

Another interesting approach is based on nonlinear dynamics in semiconductor optical amplifiers (SOAs) and laser diodes. Cross-gain modulation (XGM) effects in SOAs and cross-absorption effects in electro-absorption modulators had been used in Gaussian monocycle and doublet waveform generation (Ben-Ezra et al., 2009; Wu, et al., 2010; Xu et al., 2007a, 2007b). Relaxation oscillations in directly-modulated or externally-injected distributed feedback lasers were recently demonstrated as well (Gibbon et al., 2010; Pham et al., 2011; Yu et al., 2009). The technique is well suited to the FCC spectral mask for indoor wireless communication: wireless transmission of 3.125 Gbits/s, employing high-order waveforms, had been experimentally demonstrated (Gibbon et al., 2010; Pham et al., 2011). On the other hand, waveform generation based on relaxation oscillations is restricted to the order of 10 GHz by the laser diode dynamics.

The most elaborate waveform tailoring was provided by optical spectrum shaping and subsequent frequency-to-time mapping (Abtahi et al., 2008a, 2008b, 2008c; McKinney et al., 2006; McKinney, 2010). These techniques relied on careful spectral shaping of the transmitted waveforms in order to maximize the transmitted power within the constraints of the FCC mask. However, the demonstrations required mode-locked laser sources, and either bulky free-space optics (McKinney et al., 2006; McKinney, 2010) or highly complex fiber gratings with limited tuning (Abtahi et al., 2008a, 2008b, 2008c). Major progress had been recently achieved, with the pulse-shaping optics successfully replaced by a programmable, integrated silicon-photonic waveguide circuit (Khan et al., 2010).

Nonlinear propagation effects in optical fibers are powerful tools for optical signal processing. However, they have been seldom used in UWB pulse generation research. Li and coauthors used cross-gain modulation in an optical parametric amplifier to generate monocycle and doublet pulse shapes (Li et al., 2009). Velanas and coauthors used a cross-phase-modulation (XPM) based technique to obtain monocycle shapes (Valenas et al., 2008). Both schemes required two input laser sources.

In the first section of this work, we use nonlinear propagation of a pulse train from a single laser source for the generation of high-order UWB impulse radio waveforms (Zadok et al.,

2009; Zadok et al., 2010a, 2010b, ©2010 IEEE). All-optical edge detectors of the input pulses intensity are used to generate two temporally-narrowed replicas of the input pulse train. The edge detection relies on the time-varying chirp introduced by self-phase modulation (SPM), and judiciously tuned optical filters. SPM accumulates through propagation along sections of fiber, which can also serve for the distribution of pulses from a network terminal to a remote antenna element. The shapes of the narrowed replicas are subtracted from that of the original pulse train in a broadband, balanced differential detector. The resulting waveforms are highly reconfigurable through adjustments of the input power and tuning of the optical filters. High-order UWB waveforms, having a center frequency of 34 GHz and a fractional bandwidth of 70% are generated.

UWB architectures that are based on impulse radio require elaborate pulse shaping and a detailed knowledge of the communication channel properties (Qiu et al., 2005; Yang & Giannakis 2004). A possible alternative is the transmission of modulated, broadband noise waveforms. One such implementation relies on direct energy detection (Sahin et al., 2005). Incoherent detection, however, compromises the immunity to interference of UWB technology. Coherent detection can be restored using transmit-reference (TR) schemes, in which the modulated noise is accompanied by a delayed, unmodulated replica of itself (Narayanan & Chuang, 2007). Data is recovered by a matched delay at the receiver end (Narayanan & Chuang, 2007), and knowledge of the channel response is not required (Sahin et al., 2005). Photonic generation of UWB noise has been demonstrated recently, based on the chaotic dynamics of a laser diode in a feedback loop (Zheng et al., 2010).

In the second part of this work we propose, analyze and demonstrate the photonic generation of UWB noise, based on the amplified spontaneous emission associated with stimulated Brillouin scattering in optical fibers (SBS-ASE) (Peled et al., 2010, ©2010 IEEE). The noise bandwidth is extended to 1.1 GHz, using a recently proposed method for broadening of the SBS process (Zadok et al., 2007). Gaussian noise of such bandwidth can be readily generated electrically, however photonic generation techniques are appealing from a radio-over-fiber integration standpoint (Yao et al., 2007). Both direct detection and TR-assisted coherent detection are demonstrated. The performance is in agreement with the theoretical analysis.

Finally, as noted above, UWB waveforms find applications in various radar systems. Noise-based waveforms, in particular, provide better immunity to interception and jamming (Chuang et al., 2008; Narayanan, 2008). Similarly to UWB communication, photonic techniques could provide flexible and reconfigurable generation of broadband, high-carrier frequency noise waveforms, integrated with simple long-reach distribution. In the last section of this work, we show preliminary ranging measurements of metal objects based on SBS-ASE noise waveforms.

2. UWB impulse radio generation using self-phase modulation in optical fibers

2.1 Self-phase modulation based edge detection

Consider the optical field $E_{in}(t)$ of an input train of super-Gaussian pulses (Zadok et al., 2010b, ©2010 IEEE):

$$E_{in}(t) = \sum_n \sqrt{P_{in}} \exp\left[-\left[\left. |t - nT_0| \right/ 2\tau_0 \right]^m \right] \exp(j\omega_0 t), \qquad (1)$$

with a peak power level P_{in}, central optical frequency ω_0, width parameter τ_0 and pulse separation T_0. The parameter m determines the exact shape of the input pulses, and t denotes time. In propagating along a highly nonlinear fiber (HNLF) of length L [km] and negligible dispersion, the optical field undergoes SPM:

$$E_{HNLF}(t) = E_{in}(t)\exp\left[j\varphi(t) \right] = E_{in}(t)\exp\left[j\gamma L \left| E_{in}(t) \right|^2 \right] \tag{2}$$

where γ [W · km] $^{-1}$ is the nonlinear coefficient of the fiber. The nonlinearly induced phase modulation $\varphi(t)$ represents an effective temporally-varying shift of the optical frequency (chirp):

$$\Delta f_{pulse}(t) = \frac{1}{2\pi}\frac{\mathrm{d}\varphi(t)}{\mathrm{d}t} = \frac{\gamma L}{2\pi}\frac{\mathrm{d}\left| E_{in}(t) \right|^2}{\mathrm{d}t} \tag{3}$$

Figure 1 shows the instantaneous power $\left| E_{in}(t) \right|^2$ of a single input super-Gaussian pulse with m = 5 (top panel), and the corresponding $\Delta f_{pulse}(t)$ for a 1 km-long HNLF with γ = 11.3 [W · km] $^{-1}$ (bottom panel). The leading (trailing) edge of the pulse is associated with a positive (negative) frequency shift. Edge detection of $E_{HNLF}(t)$ is implemented by an optical bandpass filter (BPF) of spectral width 2δ, detuned from ω_0 by a frequency offset $\Delta\omega > \delta > 0$. The BPF would block most of the waveform, except for a segment of sufficient SPM: $2\pi \cdot \Delta f_{pulse}(t) > \Delta\omega - \delta$. As seen in equation (3), this segment corresponds to the leading edge of the pulse. The BPF therefore represents an all-optical intensity edge detector. The details of the narrowed replica of the pulse at the BPF output are determined by its spectral width and detuning as well as the input power P_{in}. The endpoints of the filtered waveform $t_{1,2}$ are approximately given by: $\mathrm{d}\left| E_{in}(t_{1,2}) \right|^2 / \mathrm{d}t = (\Delta\omega - \delta)/\gamma L$. The trailing edge can be filtered in a similar manner, with $\Delta\omega < 0$, $|\Delta\omega| > \delta > 0$. Figure 2 shows the instantaneous power $\left| E_{\pm}(t) \right|^2$ at the output of two 75 GHz-wide BPFs, whose central frequencies are detuned from ω_0 by $\Delta\omega_{\pm}/2\pi$ = ± 135 GHz, respectively. As expected, the filtered waveforms emphasize the pulse edges, and both are narrower than the original input pulse. The shape of the two narrowed replicas can be subtracted from that of the original pulse to generate an UWB waveform, as described next.

2.2 UWB waveform generation using all-optical edge detectors

Figure 3 shows a schematic drawing of a setup for UWB waveform generation, based on all-optical edge detection (Zadok et al., 2010b, ©2010 IEEE). The input super-Gaussian pulse train is split in two branches. The upper branch includes a high-power erbium-doped fiber amplifier (EDFA) and an HNLF section. At the HNLF output, the spectrally broadened pulses are split into two paths once again, and the light in each path is filtered by an individually tunable BPF: one is tuned to detect the pulse leading edge as discussed above, whereas the other is adjusted as a trailing edge detector. The power level of each of the two pulse train replicas is individually adjusted by a variable optical attenuator (VOA). In addition, the relative delay between the two pulse trains can be modified by a tunable delay line (TDL). The two pulse trains are then joined together and directed to the negative port of a balanced, differential detector. Since the difference between the central frequencies of the two replicas is outside the detector bandwidth, beating between the two is largely avoided.

A reference pulse train, arriving from the lower branch of the setup, is detected at the positive port of the balanced detector. The relative delay and magnitude of the reference pulse train are controlled by a second EDFA and TDL.
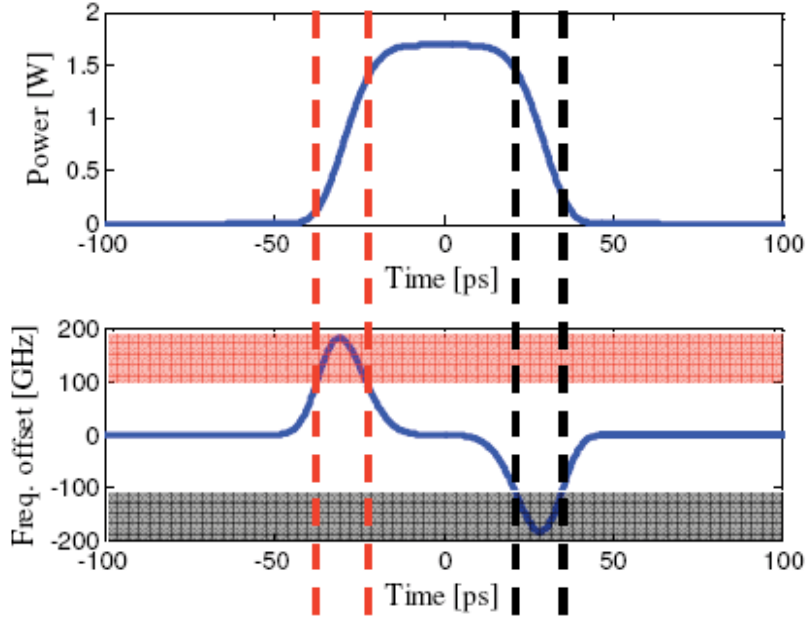
Fig. 1. Top - instantaneous power of an input super-Gaussian pulse: m = 5, τ_0 = 27 ps, P_{in} = 1.7 W. Bottom – simulated SPM-induced instantaneous frequency shift $\Delta f_{pulse}(t)$: L = 1 km, γ = 11.3 [W·km]$^{-1}$. Horizontal shaded regions in the bottom panel schematically denote the passbands of two detuned optical filters. Vertical dashed lines schematically illustrate the temporal edges of the corresponding waveforms at the filters output. ©2010 IEEE.
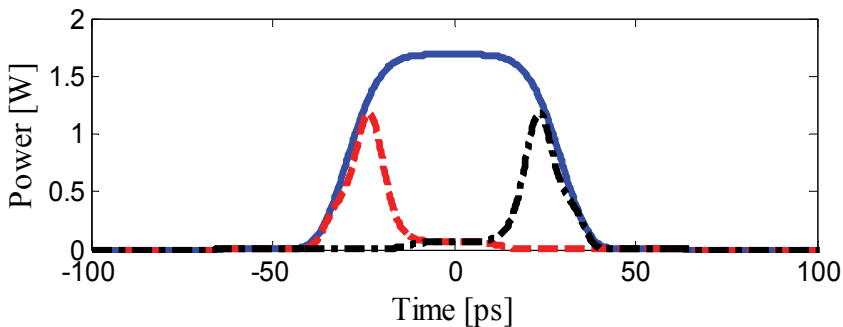
Fig. 2. Solid - instantaneous power of an input super-Gaussian pulse (same as top panel of Fig. 1). Dashed – simulated instantaneous pulse power following propagation in a HNLF and filtering by a 75 GHz-wide BPF, detuned from ω_0 by $\Delta\omega_+/2\pi$ = 135 GHz. HNLF parameters are the as those in the bottom panel of Fig. 1. Dashed-dotted – same as dashed curve, with the BPF detuned from ω_0 by $\Delta\omega_-/2\pi$ = -135 GHz. ©2010 IEEE.
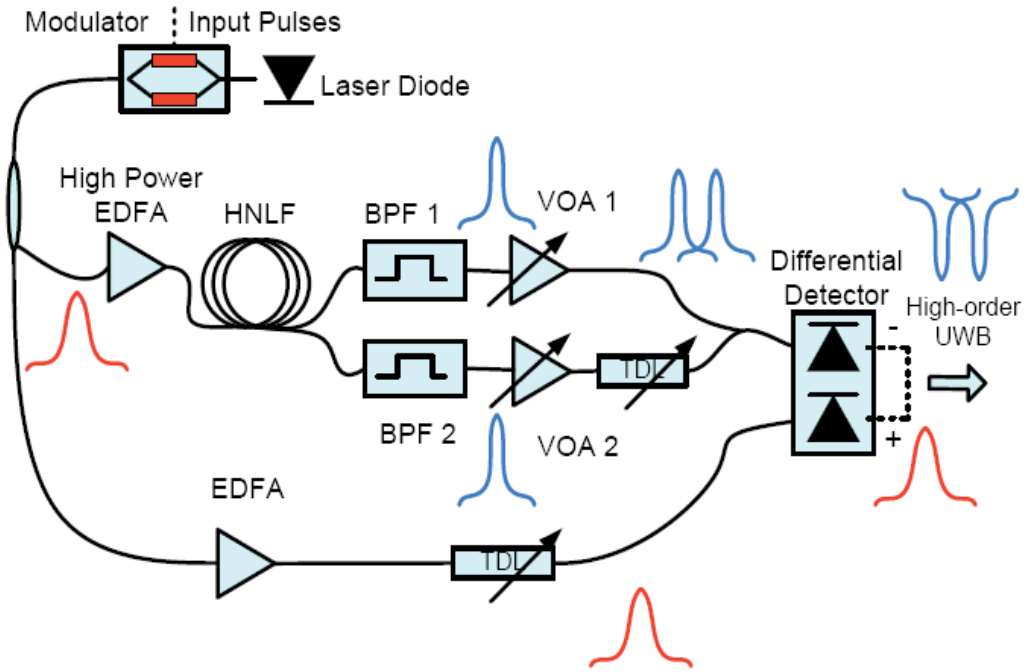
Fig. 3. A schematic diagram of the UWB pulse generation scheme. EDFA: erbium-doped fiber amplifier; HNLF: highly nonlinear fiber; BPF: bandpass filter; VOA: variable optical attenuator; TDL: tunable delay line. ©2010 IEEE.

The electrical waveform at the balanced detector output can be expressed as:

$$V(t) \propto \left|E_{in}(t)\right|^2 - a_+\left|E_+(t-t_+)\right|^2 - a_-\left|E_-(t-t_-)\right|^2 \qquad (4)$$

where $a_\pm$ and $t_\pm$ are the relative power levels and delays of the leading and trailing edge waveforms, respectively. Unless corrected by the TDLs, the relative delays $t_\pm$ correspond to max (min) of the input intensity derivative. The complete waveform design requires a numeric calculation. Nonetheless, the following relations may serve as useful starting points: $t_+ = -t_- \approx \frac{1}{2}\tau_0$, $a_\pm \approx \frac{1}{2}\int\left|E_{in}(t)\right|^2 dt \Big/ \int\left|E_+(t)\right|^2 dt$. The central frequency f_c of $V(t)$ is on the order of $1/\left|t_2 - t_1\right|$, where $\left|t_2 - t_1\right|$ is the temporal width of the narrowed replica at the output of the edge detectors (see previous section).

Figure 4 shows a simulated example of the normalized shape of $V(t)$ (top panel) and its corresponding power spectral density $\left|\tilde{V}(\Omega)\right|^2$ (bottom), where Ω represents a radio frequency (RF) variable. The calculation parameters were the same as those of the previous section, with $a_\pm = 1.85$ and $t_\pm = \pm 10$ ps. The central frequency f_c of the high-order, UWB output waveform is 34 GHz. The high and low -10 dB cutoff frequencies $f_{H,L}$ are 47 GHz and 23 GHz, respectively, providing a fractional bandwidth $B_{fr} \equiv \left(f_H - f_L\right)/f_c$ of 70%. $V(t)$ can be simply modified through changing the peak power, width and shape of the incoming pulse train, the detuning of the BPFs, and the relative magnitude and delay of the replica trains of narrowed pulses. Experimental generation of UWB waveform is described next.
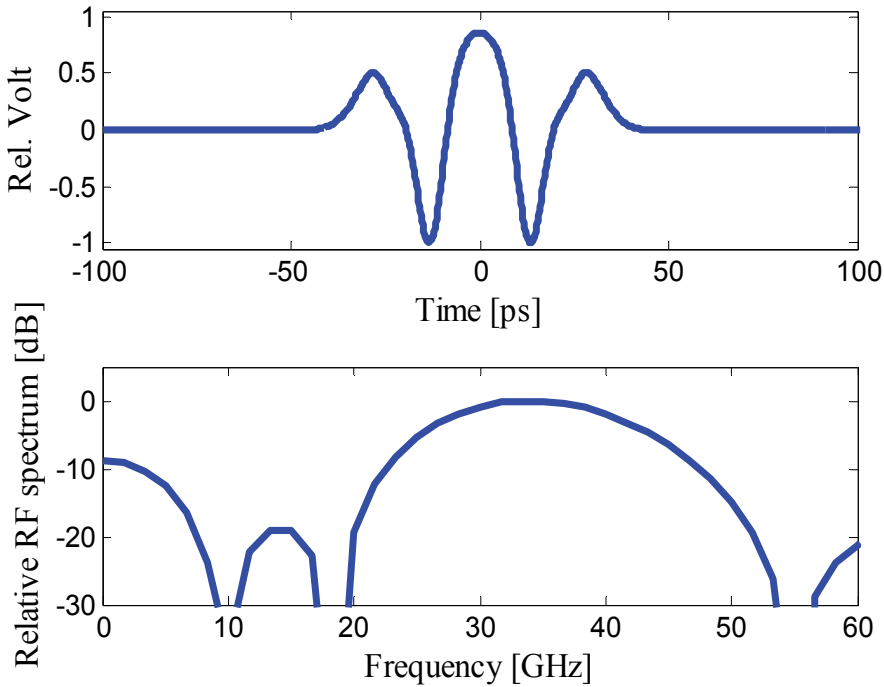
Fig. 4. Top – Simulated output waveform $V(t)$. The input pulse, HNLF and BPFs parameters are the same as those of Figs. 1 and 2, $a_\pm = 1.85$ and $t_\pm = \pm 10$ ps. Bottom – the corresponding RF spectrum $\left| \tilde{V}(\Omega) \right|^2$. ©2010 IEEE.

2.3 Experimental results

The generation of UWB pulses was demonstrated experimentally, using the setup of Fig. 3 (Zadok et al., 2010b, ©2010 IEEE). The parameters of the input pulse train and HNLF, and the settings of the BPFs, VOAs and TDLs were the same as those of the previous sections. The separation T_0 between neighboring pulses was 600 ps, corresponding to a data rate of 1.67 Gb/s. The average power of the amplified, input pulse train was 160 mW. Figure 5 shows the measured optical spectra $\left| \tilde{E}_{in}(\lambda) \right|^2$, $\left| \tilde{E}_{HNLF}(\lambda) \right|^2$ and $\left| \tilde{E}_\pm(\lambda) \right|^2$, corresponding to $E_{in}(t)$, $E_{HNLF}(t)$ and $E_\pm(t)$ respectively, as a function of wavelength λ.

Figure 6 (top) shows the measured $V(t)$ alongside the corresponding simulation. The experimental RF spectrum $\left| \tilde{V}(\Omega) \right|^2$, calculated by taking the Fourier transform of the measured $V(t)$, is shown at the bottom of Fig. 6 alongside the simulated results. The experimental waveform generally agrees with the simulation.

The flexibility of the waveform generation method is illustrated in Fig. 7 (Zadok et al., 2009; Zadok et al., 2010a), in which the setup parameters were adjusted to approximate the FCC mask for unlicensed indoor wireless UWB communication (FCC, 2002). In this experiment, Gaussian pulses (m = 2) of width τ_0 = 100 ps, peak power P_{in} = 1 W and spacing T_0 = 800 ps were used. Only a single edge detection BPF was used in the experiment, with a spectral width of 40 GHz and detuning $\Delta\omega/2\pi$ of 30 GHz. The normalized output waveform $V(t)$ approximates a Gaussian doublet pulse shape (top panel). The calculated $\left| \tilde{V}(\Omega) \right|^2$ is drawn

on the lower panel, alongside the FCC mask. The measurement generally complies with the mask requirements, although infringements can be seen at the lower frequency range.
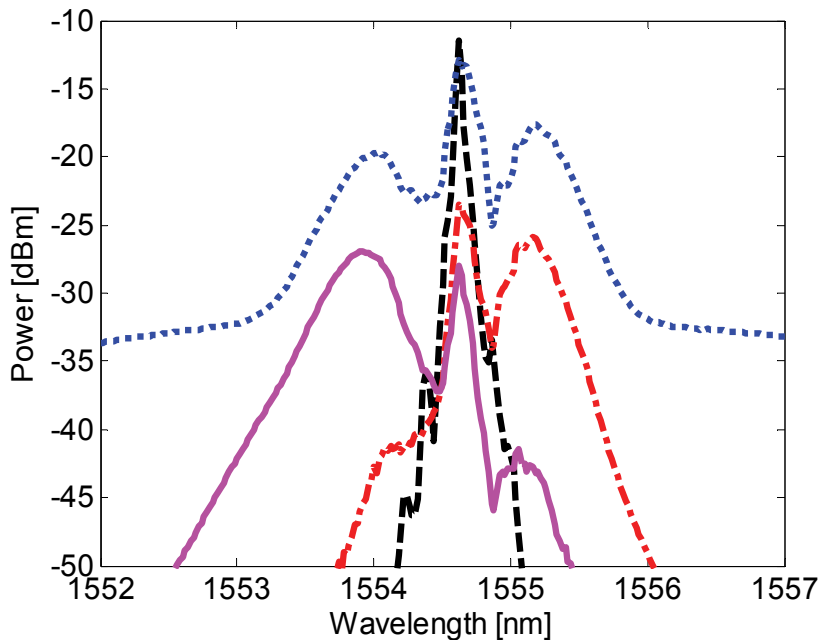
Fig. 5. Measured optical power spectra corresponding to $E_{in}(t)$ (dashed, black), $E_{HNLF}(t)$ (dotted, blue), $E_{+}(t)$ (solid, magenta) and $E_{-}(t)$ (dashed-dotted, red). The experimental parameters were the same as those of the simulations in Fig. 4. ©2010 IEEE.

The FCC mask infringements of the experimental Fig. 7 can be considerably reduced with the use of a narrower BPF: Figure 8 shows an example of simulated $V(t)$ and $\left|\tilde{V}(\Omega)\right|^{2}$ obtained with a single 10-GHz wide BPF. Results may be further improved by using two BPFs, as in Fig. 6.

2.4 Discussion and future work

The proposed technique for the photonic generation of UWB relies on all-optical detection of intensity edges of incoming super-Gaussian pulses. The technique could be particularly suitable for high-frequency waveforms, such as those intended for high-resolution vehicular radar systems. The edge detectors were implemented based on SPM in a section of HNLF, and using two BPFs in parallel. However, both edges might be detected simultaneously with the application of just one band-stop optical filter centered at ω_{0}, which would remove the center of the pulse (see Fig. 1). Data can be transmitted through simple on-off keying of the input pulses. On the other hand, pulse polarity modulation is not simply supported by the proposed approach.

The waveform generation setup includes multiple optical paths, the lengths of which were not matched in the experiment. The integrity of the UWB shape in a data-carrying, operational system could require path length equalization on mm scale. The problem might

be alleviated by using short fiber spans and high peak power levels, environmental isolation of fiber sections or active compensation. Alternatively, the relative delays $t_{\pm}$ could be controlled using dispersion rather than TDLs along different paths. The stability of the experimental setup was thus far validated over a couple of hours. Long term stability was not tested. The transmission of actual data using the proposed approach is the subject of further work.
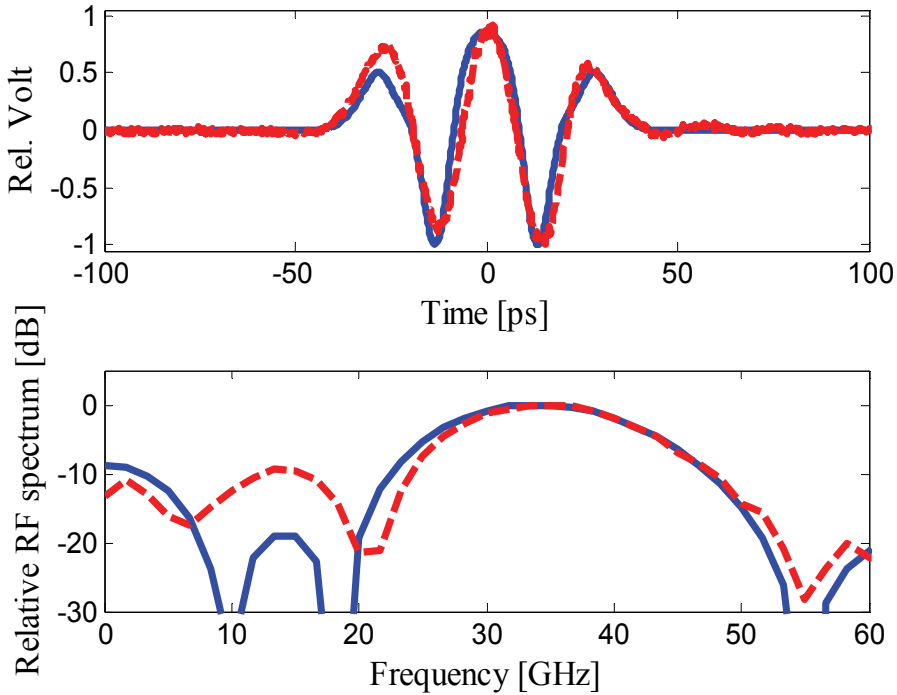
Fig. 6. Top – Simulated (solid, blue) and measured (dashed, red) output waveform $V(t)$. The experimental parameters were the same as those of the simulations in Fig. 4. Bottom – the corresponding simulated (solid, blue) and calculated experimental (dashed, red) RF spectra $|V(\Omega)|^2$. ©2010 IEEE.

The shaping and distribution scheme of the UWB pulses requires a two-fiber connection between a transmitter and a remote antenna element. Single-fiber transmission would be possible if a reference pulse shape $|E_{in}(t)|^2$ could be extracted from the SPM-broadened $E_{HNLF}(t)$ at the receiver. Ideally $|E_{HNLF}(t)|^2 = |E_{in}(t)|^2$, however residual dispersion and EDFA noise might distort the reference pulse shape. A potential solution might be narrow-band optical filtering centered at ω_0.

The comparison of the technique proposed in this work to previous approaches draws interesting analogies. Here, SPM introduces a time-to-frequency mapping, in which different temporal sections of the input pulses acquire different frequency shifts. This process is somewhat analogous to frequency-to-time mapping-based techniques (Abtahi et al., 2008a; McKinney et al., 2006; Wang et al., 2007), in which dispersion is used to assign a different delay to different spectral components of an input waveform. The subtraction of

the intensity profile of delayed replicas from the original pulse shape might be viewed as a tapped-delay line filtering method. It should be noted, though, that the subtracted waveforms are obtained through nonlinear processing and are not scaled copies of the input. The nonlinear propagation enables the generation of higher-order waveforms while using only two replicas, and also allows for simple reconfiguration through input power adjustments.
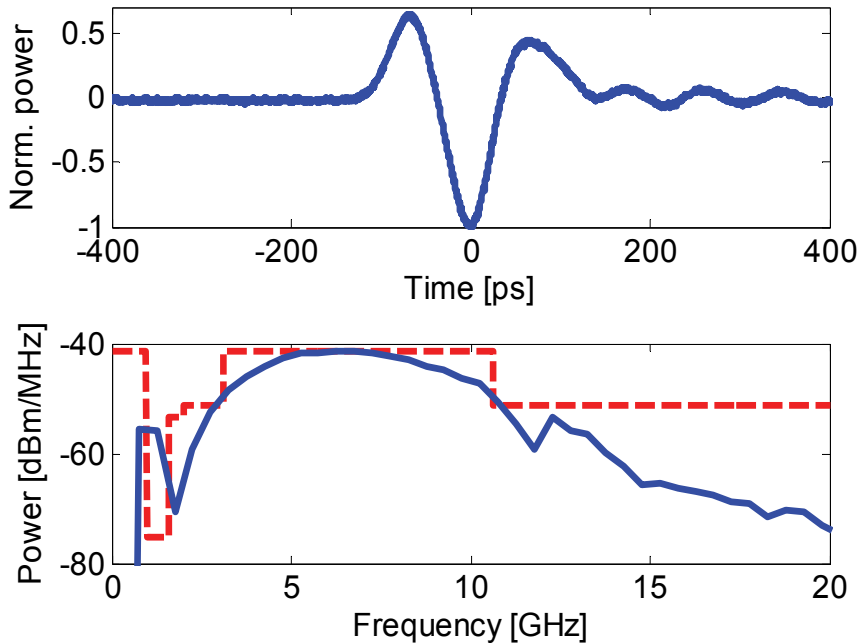
Fig. 7. Top– measured $V(t)$. Bottom– calculated experimental RF power spectrum $\left|V(\Omega)\right|^2$ (solid), alongside the FCC mask for indoor UWB communication (FCC, 2002) (dashed). Input parameters: P_{in} = 1 W, τ_0 = 100 ps , m = 2, T_0 = 800 ps. HNLF parameters: L = 1 km, γ = 11.3 [W·km]$^{-1}$. A single 40-GHz wide BPF was used, detuned by $\Delta\omega/2\pi$ = 30 GHz. ©2010 IEEE.

3. UWB noise waveforms generation using stimulated Brillouin scattering amplified spontaneous emission

As discussed above, impulse radio UWB communication requires elaborate pulse shaping, using either electrical or optical means. Alternatively, the criteria of UWB transmission may be met based on modulated noise waveforms, which could be simpler to generate. UWB noise communication had been previously proposed and demonstrated in several works (Haartsen et al., 2004; Haartsen et al., 2005; Narayanan & Chuang, 2007; Sahin et al., 2005). However, only few studies examined the use of optical techniques for noise generation. In one such recent example (Zheng et al., 2010), UWB noise was generated based on the chaotic dynamics of a laser diode within a fiber-optic feedback loop. UWB noise can be readily generated using electrical techniques (Upadhyaya, 1999), however optical methods are nonetheless appealing as part of a radio-over-fiber integrated system.
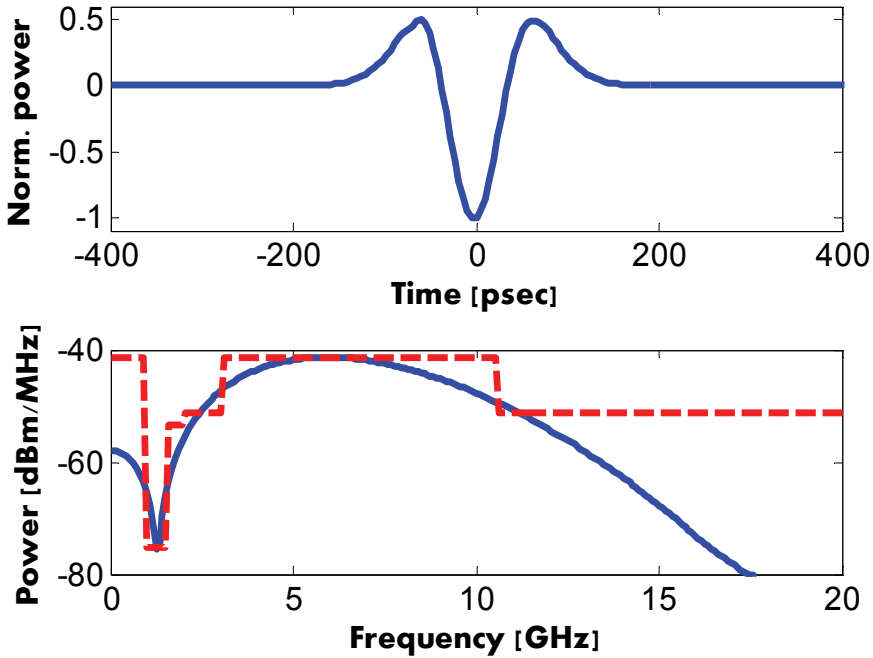
Fig. 8. Top– simulated $V(t)$. Bottom– corresponding simulated RF power spectrum $\left|V(\Omega)\right|^2$ (solid), alongside the FCC mask for indoor UWB communication (FCC, 2002) (dashed). Input pulses parameters: P_{in} = 1 W, τ_0 = 70 ps , m = 2. HNLF parameters: L = 1 km, γ = 11.3 [W·km]$^{-1}$. A single 10-GHz wide BPF was detuned from ω_0 by $\Delta\omega/2\pi$ = 20 GHz. ©2010 IEEE.

The rejection of interfering signals in UWB receivers relies on a proper matched filtering of incoming waveforms. The matched filter, in turn, requires precise knowledge of the transmitted pulse shapes and the transfer properties of the communication channel. In noise-based UWB schemes, a reference waveform must be provided to the receiver separately. In such transmit-reference (TR) techniques, an unmodulated replica of the data-carrying noise waveform is transmitted in parallel. Data and reference can by time-multiplexed, or launched at different intermediate frequencies or over two orthogonal polarizations (Narayanan and Chuang, 2007). TR UWB communication based on optically generated waveforms is demonstrated below.

3.1 Broadband noise generation

Stimulated Brillouin scattering (SBS) requires the lowest activation power of all non-linear effects in silica optical fibers. In SBS, a strong pump wave and a typically weak, counter-propagating signal wave optically interfere to generate, through electrostriction, a traveling longitudinal acoustic wave. The acoustic wave, in turn, couples these optical waves to each other (Boyd, 2008). The SBS interaction is efficient only when the difference between the optical frequencies of the pump and signal waves is very close (within a few tens of MHz) to a fiber-dependent parameter, the Brillouin shift Ω_B, which is of the order of $2\pi \cdot 11$ GHz in silica fibers at room temperature and at 1550 nm wavelength (Boyd, 2008). An input signal

whose frequency is Ω_B lower than that of the pump, ('Stokes wave'), experiences SBS amplification. Among its numerous applications, SBS is used in optical processing of high frequency microwave signals (Loayssa et al., 2000; Loayssa & Lahoz, 2006; Loayssa et al., 2006; Shen et al., 2005; Zadok et al., 2007).

In the absence of a seed input signal wave, SBS could still be initiated by thermally-excited acoustic vibrations (Boyd, 2008). The naturally occurring vibrations scatter a fraction of the incident pump into a preliminary signal, which is then further amplified. In this scenario, SBS acts as a *generator* of amplified spontaneous emission (ASE) at the signal frequency. This SBS-ASE is the underlying mechanism of the UWB noise waveform generation described below. UWB generation requires a substantial spectral broadening of the inherently narrowband SBS process. Bandwidths of several GHz are routinely achieved through pump wave modulation (Zadok et al., 2007; Zhu et al., 2007).

A schematic drawing of a TR-assisted, SBS-ASE UWB noise transmitter is shown in Fig. 9 (Peled et al., 2010, ©2010 IEEE). Light from a distributed feedback (DFB) laser source is directly modulated and amplified. The spectrally broadened light is launched into a section of HNLF of length L and loss coefficient α as an SBS pump. Let us denote the generated, counter-propagating SBS-ASE noise field as $E_s(t)$. The power spectral density (PSD) of $E_s(t)$ is given by (Wang et al., 1996):

$$P(\omega_s) \propto \hbar\omega_s \left(\exp\left[g(\omega_s) L_{\text{eff}} - \alpha L \right] - 1 + \right.$$
$$\left. \left[1 - \exp(-\alpha L) \right] \left\{ \exp\left[g(\omega_s) L_{\text{eff}} \right] - 1 \right\} \middle/ \left[g(\omega_s) L_{\text{eff}} \right] \right) \tag{5}$$

In (5) L_{eff} is the effective length of the fiber, and ω_s is the optical frequency of the generated Stokes wave. For a broadened pump, the SBS power gain coefficient $g(\omega_s)$, in units of m⁻¹, can be approximated as (Zadok et al., 2007; Zhu et al., 2007):

$$g(\omega_s) \propto P_p(\omega_s + \Omega_B) \tag{6}$$

where P_p denotes the pump PSD.

Careful synthesis of the pump laser direct modulation could provide a uniform P_p, and hence a uniform $P(\omega_s)$, within a range of several GHz (Zadok et al., 2007). The optical noise can be down-converted to the radio frequency (RF) domain through heterodyne beating with a local oscillator of frequency ω_{LO} on a broadband detector. The real-valued beating term $V(t)$ is proportional to a single ASE quadrature component, and is therefore of Gaussian statistics. Its PSD $\tilde{V}(\Omega)$ scales with $P(\omega_s = \Omega + \omega_{\text{LO}})$. The spectral width of $\tilde{V}(\Omega)$ is bounded by that of the pump.

3.2 Performance of transmit-reference UWB communication using SBS-ASE noise waveforms

In a TR-based implementation, the SBS-ASE noise field passes through an imbalanced Mach-Zehnder interferometer (MZI), with a differential delay of τ (see Fig. 9) (Peled et al., 2010, ©2010 IEEE). Light in the upper arm of the MZI is on/off modulated by information pulses of duration T_0. Following heterodyne down conversion, the electric signal to be transmitted can be expressed as:

$$V_{\mathrm{TR}}(t) = \sum_n a_n \mathrm{win}\big[(t-nT_0)/T_0\big]V(t)+V(t-\tau)\,, \tag{7}$$

where $\mathrm{win}(\xi)=1$ for $0<\xi\le 1$ and equals zero elsewhere, n is an integer and a_n is a binary data value. Data is recovered at the receiver by electrically mixing the incoming signal with a replica that is delayed by τ, and integrating over T_0:

$$Y[n] = \int_{nT_0}^{(n+1)T_0} V_{\mathrm{TR}}(t)V_{\mathrm{TR}}(t+\tau)\mathrm{d}t\,. \tag{8}$$

We require that $\tau \ll T_0$, in which case the decision variables for '1' and '0' are expressed as:

$$Y^{(1)}[n] = C_{V,T_0,n}(0)+C_{V,T_0,n}(\tau)+C_{V,T_0,n}(-\tau)+C_{V,T_0,n}(2\tau)\,. \tag{9}$$

$$Y^{(0)}[n] = C_{V,T_0,n}(\tau) \tag{10}$$

where $C_{V,T_0,n}(\xi)\equiv\int_{nT_0}^{(n+1)T_0}V(t)V(t+\xi)\mathrm{d}t$. Note that for $\tau\ll T_0$, $C_{V,T_0,n}(\tau)\approx C_{V,T_0,n}(-\tau)$. The ensemble averages of (9)-(10) are given by (Goodman, 2000):

$$I_1 = \big\langle Y^{(1)}[n]\big\rangle_n = T_0\big[\Gamma_V(0)+2\Gamma_V(\tau)+\Gamma_V(2\tau)\big]\approx T_0\Gamma_V(0)\,. \tag{11}$$

$$I_0 = \big\langle Y^{(0)}[n]\big\rangle_n = T_0\Gamma_V(\tau)\ll I_1 \tag{12}$$

where $\Gamma_V(\xi)$ denotes the autocorrelation $\langle V(t)V(t+\xi)\rangle$. Equation (12) requires that τ is much longer than the coherence time τ_c of $V(t)$. Next the standard deviations $\sigma_{1,0}$ of equations (9)-(10) are estimated. Using the high-order moment theorem for real variables of Gaussian statistics (Goodman, 2000):

$$\begin{aligned}\sigma_{V,T_0}^2(\xi)&\equiv\big\langle C_{V,T_0,n}^2(\xi)\big\rangle_n-\big\langle C_{V,T_0,n}(\xi)\big\rangle_n^2\\ &=\iint_{T_0}\big[\Gamma_V(t-t')\big]^2\mathrm{d}t\mathrm{d}t'+\iint_{T_0}\Gamma_V(t-t'-\xi)\Gamma_V(t-t'+\xi)\mathrm{d}t\mathrm{d}t'\end{aligned}. \tag{13}$$

For $T_0\gg\tau_c$, the first term of (13) equals $T_0\tau_c\big[\Gamma_V(0)\big]^2$ (Goodman, 2000). The second term reduces to the first for $\xi\approx 0$, and vanishes for $\xi\gg\tau_c$. Using equations (9), (10) and (13):

$$\sigma_1^2 = \sigma_{V,T_0}^2(0)+4\sigma_{V,T_0}^2(\tau)+\sigma_{V,T_0}^2(2\tau)=7\tau_c T_0\big[\Gamma_V(0)\big]^2\,, \tag{14}$$

$$\sigma_0^2 = \tau_c T_0\big[\Gamma_V(0)\big]^2\,. \tag{15}$$

The Q parameter for UWB communication based on Gaussian noise with TR is given by:

$$Q_{\mathrm{TR}} = (I_1-I_0)/(\sigma_1+\sigma_0) = \sqrt{T_0/\tau_c}\Big/\big(\sqrt{7}+1\big)=0.27\sqrt{T_0/\tau_c}\,. \tag{16}$$

The corresponding value for direct detection equals:

$$Q_{\mathrm{dir}} = \tfrac{1}{\sqrt{2}}\sqrt{T_0/\tau_c} = 2.58Q_{\mathrm{TR}}\,. \tag{17}$$
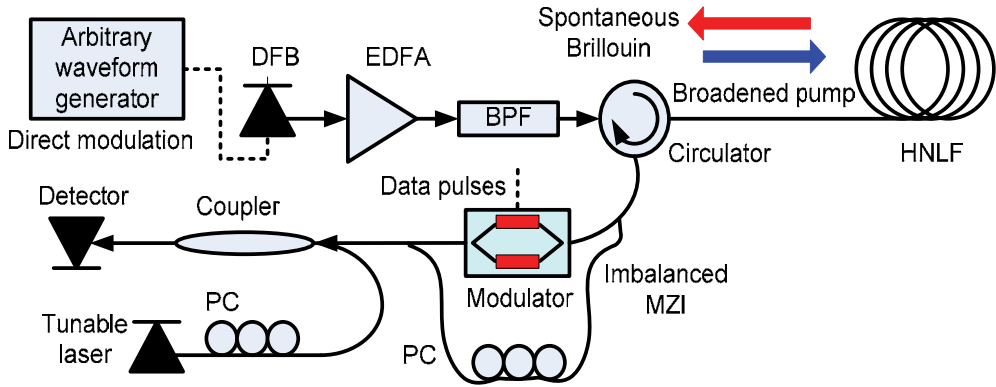
Fig. 9. Setup for a transmit-reference, ultra-wideband noise transmitter based on the amplified spontaneous emission of Brillouin scattering. DFB: distributed feedback laser; EDFA: erbium-doped fiber amplifier; BPF: band-pass filter; HNLF: highly nonlinear fiber; PC: polarization controller; MZI: Mach-Zehnder Interferometer. ©2010 IEEE.

3.3 Experimental demonstration of UWB communication

UWB noise generation based on SBS-ASE and its coherent detection were demonstrated experimentally. Light from a DFB laser was directly modulated by an arbitrary waveform generator (see Fig. 9) (Peled et al., 2010, ©2010 IEEE). The modulating waveform was (Zadok et al., 2007):

$$i(t) = i_0 - \Delta i \left(t \bmod T_{\mathrm{p}} / T_{\mathrm{p}} \right)^{2.1} , \qquad (18)$$

where T_{p} = 500 ns is the modulation period, i_0 = 80 mA is the DFB bias current and $\Delta i \sim 7.5$ mA is the modulation magnitude. A heterodyne measurement of the modulated DFB PSD is shown in Fig. 10 (top). The DFB output was amplified to 250 mW by an EDFA, and launched into 3.5 km of HNLF (α = 1 dB/km) as an SBS pump wave. Fig. 10 (center) shows the PSD $\tilde{V}(\Omega)$ of the down-converted SBS-ASE noise. $\tilde{V}(\Omega)$ is uniform within a range of 1.1 GHz. The arbitrary central frequency of 2.4 GHz was chosen due to equipment limitations. $\tilde{V}(\Omega)$ can be broadened beyond 10 GHz with stronger pump amplification (Zhu et al., 2007), hence no fundamental limitations prevent the compliance of the noise waveform with the FCC standard. Fig. 10 (bottom) shows a histogram of $V(t)$, alongside a Gaussian distribution of equal variance. The SBS-ASE noise is well described by Gaussian statistics. $\tau_{\mathrm{c}} \equiv \int_{-\infty}^{\infty} \left[\Gamma_V(\xi) \right]^2 d\xi \big/ \left[\Gamma_V(0) \right]^2$ of 0.45 ns was directly calculated from samples of $V(t)$ (Goodman, 2000).

The SBS-ASE optical field was modulated by square waves using an electro-optic modulator. First, the lower arm of the MZI was disconnected, and the modulated noise was directly detected. Fig. 11 (top) shows an example of the detected waveform with T_0 = 112 ns. Q_{dir} was estimated by sampling $V(t)$ over several hundred periods, and calculating equation (8) with τ = 0. The results for T_0 = 112 and 225 ns were Q_{dir} = 10 and 14.7, respectively. The results agree with the predicted values of 11.1 and 15.8. The differences could be due to the finite extinction ratio of the modulator and additive detector noise.
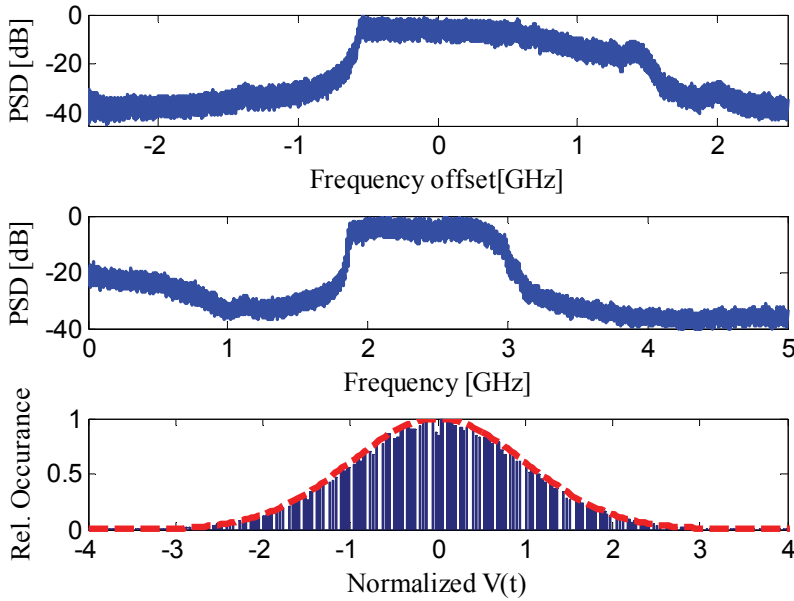
Fig. 10. Top – Power spectral density (PSD) of the directly modulated stimulated Brillouin scattering (SBS) pump wave. Center – PSD of the down-converted SBS amplified spontaneous emission (SBS-ASE) $\tilde{V}(\Omega)$. Bottom - Histogram of the down-converted SBS-ASE noise $V(t)$ (bar), alongside a zero-mean Gaussian distribution of equal variance (line). ©2010 IEEE.

TR-assisted coherent detection of UWB noise communication was demonstrated by reconnecting the lower arm of the MZI with τ of 12.2 ns. Fig. 11 (center) shows an example of $V_{TR}(t)$ and the bottom panel shows its autocorrelation. A secondary peak corresponding to τ is evident. Fig. 12 shows an example of the calculated experimental histograms of $Y^{(1)}[n]$ and $Y^{(0)}[n]$. The estimated Q_{TR} values for T_0 = 112 and 225 ns were 3.25 and 4.6, respectively. Based on the experimental values of Q_{dir}, equation (17) suggests a Q_{TR} of 3.9 and 5.7 for the two symbol durations. The difference may stem from unequal power splitting in the MZI or residual statistical correlation among the terms of $Y^{(1)}[n]$ (see equation (9)).

3.4 UWB noise radar based on SBS-ASE

The SBS-ASE UWB noise waveforms discussed above were also used in a proof-of-concept radar measurement. To that end, the generated waveform $V(t)$ was split in two branches. The waveform in one branch was amplified to -5 dBm and transmitted by a horn antenna with a gain of 20 dBi. The waveform was reflected from a 40X40 cm² metallic object at different distances. The reflections were collected by a second, identical antenna, amplified and sampled by a real-time digitizing oscilloscope with a bandwidth of 6 GHz. A replica of $V(t)$ in the other arm was sampled by a second oscilloscope channel as a reference. The correlation function between the two sampled waveforms was calculated, and the distance to the target was estimated based on the timing of the observed correlation peak. Figure 13

shows the measured correlation for several target distances. The full width at half-maximum of the correlation peaks suggests an estimated resolution of 20 cm, in good agreement with the expected value of 15 cm for a 1 GHz-wide noise waveform.
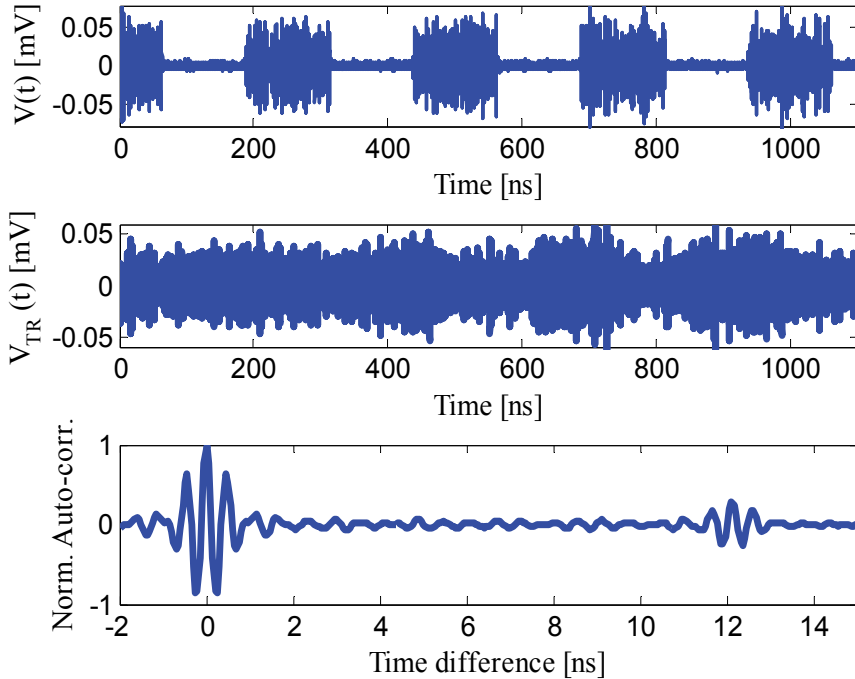
Fig. 11. Top – Measured modulated noise $V(t)$ with no transmitted reference, symbol duration T_0 = 112 ns. Center – Measured $V_{TR}(t)$ with a transmitted reference, T_0 = 112 ns, relative delay τ = 12.2 ns. Bottom- Normalized autocorrelation of $V_{TR}(t)$ (T_0, τ as above). ©2010 IEEE.
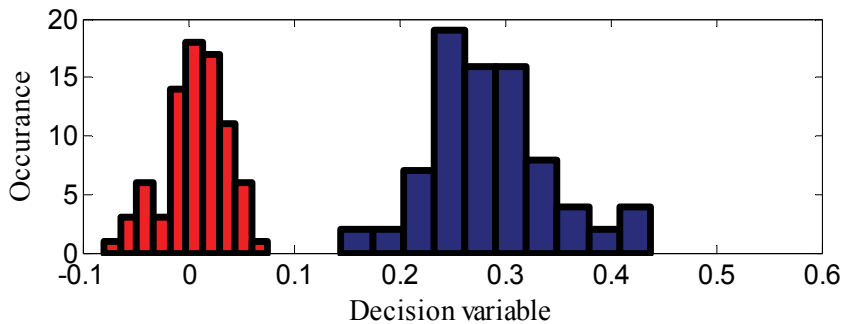
Fig. 12. Experimental histograms of the decision variable $Y[n]$ for ultra-wideband noise communication with a transmitted reference, based on amplified spontaneous emission from Brillouin scattering. T_0 = 112 ns, τ = 12.2 ns Left: logical '0'. Right: logical '1'. Histograms consist of 160 symbols. ©2010 IEEE.
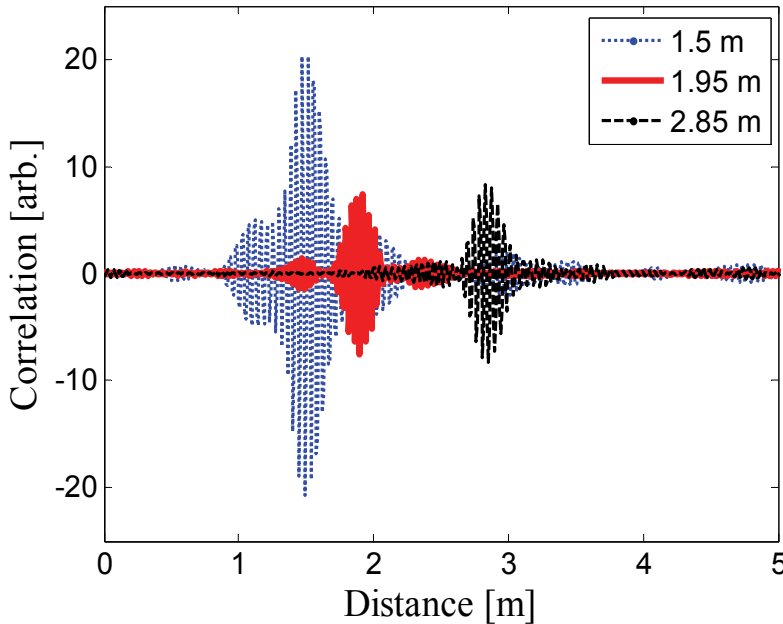
Fig. 13. Measured correlation between a UWB noise waveform reflected from a metal target and a reference replica. The transmitted 1 GHz-wide noise waveforms were optically generated using SBS-ASE. The distances to the target were 1.5 m (blue, dotted); 1.95 m (red, solid) and 2.85 m (black, dahsed).

4. Concluding remarks

In this chapter, nonlinear propagation over optical fibers was used for the generation of UWB waveforms. Two different nonlinear mechanisms had been employed: SPM and SBS. The generation of both UWB impulse radio shapes and UWB noise had been demonstrated. Impulse radio pulse shapes were generated based on SPM. The technique relied on the time-to-frequency mapping that accompanies SPM spectral broadening of pulses, in implementing all-optical edge detectors. The edge detectors provided temporally-narrowed replicas of an input train of standard pulses. The shapes of the narrow replicas were later electrically subtracted from that of the original pulses by a differential detector. The method provides multiple degrees of freedom for shaping high-order UWB waveforms of high central radio frequencies, up to 34 GHz. Noise waveforms were generated based on the ASE that accompanies SBS in fiber. The ASE noise bandwidth was broadened to 1.1 GHz via pump modulation. The method is readily extendable to the generation of waveforms having arbitrary central radio frequencies, and widths approaching 10 GHz. The noise waveforms were used in proof-of-concept demonstrations of transmit-reference UWB communication and UWB noise radar.

The techniques reported rely on off-the-shelf components only. Few of the components included in the experimental setups, such as EDFA, HNLF or differential detector, are currently too expensive for certain applications. Higher cost may be more tolerable in applications in which a single transmitter is broadcasting to a large number of simple receivers, or where waveforms of high-order and high-frequency are required.

A primary motivation which is driving microwave photonics research in general, and UWB-related photonic techniques in particular, is the potential for a radio-over-fiber integrated system which brings together fiber-optic distribution and broadband all-optical processing. In this respect, techniques which employ the fiber itself as the waveform-generating medium stand out. Future work will be dedicated to advance the proposed methods towards applications.

5. References

Abtahi, M.; Mirshafiei, M.; Magne, J.; Rusch, L. A. & LaRochelle, S. (2008a). Ultra-wideband waveform generator based on optical pulse-shaping and FBG tuning. *IEEE Photonics Technology Letters*, Vol. 20, No. 2, (January 2008), pp. 135-137, ISSN 1041-1135.

Abtahi, M.; Magne, J.; Mirshafiei, M.; Rusch, L.A. & LaRochelle, S. (2008b). Generation of Power-Efficient FCC-Compliant UWB Waveforms Using FBGs: Analysis and Experiment. *Journal of Lightwave Technology,* Vol. 26, No. 5, (March 2008), pp. 628-635, ISSN 0733-8724.

Abtahi, M.; Mirshafiei, M.; LaRochelle, S. & Rusch, L.A. All-Optical 500-Mb/s UWB Transceiver:An Experimental Demonstration (2008c). *Journal of Lightwave Technology*, Vol. 26, No. 15, (August 2008), pp. 2795-2802, ISSN 0733-8724.

Ben-Ezra, Y. ; Lembrikov, B. I. & Haridim, M. (2009). Ultrafast All-Optical Processor Based on Quantum-Dot Semiconductor Optical Amplifiers. *IEEE Journal of Quantum Electronics*, Vol. 45, No. 1-2, (January 2009), pp. 34-41, ISSN 0018-9197.

Bolea, M.; Mora, J.; Ortega, B. & Capmany, J. (2009). Optical UWB pulse generator using an N tap microwave photonic filter and phase inversion adaptable to different pulse modulation formats. *Optics Express*, Vol. 17, No. 7, (March 2009), pp. 5021-5032, eISSN 1094-4087.

Bolea, M.; Mora, J.; Ortega, B.; & Capmany, J. (2010). Flexible Monocycle UWB Generation for Reconfigurable Access Networks (2010). *IEEE Photonics Technology Letters*, Vol. 22, No. 12, (May 2010), pp. 878-880, ISSN 1041-1135.

Boyd, R. W. (2008). *Nonlinear optics*, third edition, Academic Press, ISBN 978-0-12-369470-6, San Diego, CA.

Capmany, J.; Ortega, B.; Pastor, D. & Sales, S. (2005). Discrete-time optical processing of microwave signals. *Journal of Lightwave Technology*, Vol. 23, No. 2, (February 2005), pp. 702-723, ISSN 0733-8724.

Chow, C. W.; Kuo, F. M.; Shi, J. W.; Yeh, C. H.; Wu, Y. F.; Wang, C. H.; Li, Y. T. & Pan, C. L. (2010). 100 GHz ultra-wideband (UWB) fiber-to-the antenna (FTTA) system for in-building and inhome networks. *Optics Express*, Vol. 18, No. 2, (January 2010), pp. 473-478, eISSN 1094-4087.

Chuang, J.; DeMay, M. W. & Narayanan, R. M. (2008). Design, Analysis, and Performance of a Noise Modulated Covert Communications System. *EURASIP Journal on Wireless Communications and Networking*, Vol. 2008, (July 2008), Article ID 979813, eISSN 1687-1499.

Gibbon, T.B.; Yu, X; Gamatham, R; Guerrero Gonzalez, N; Rodes, R; Bevensee Jensen, J; Caballero, A & Monroy I. T. (2010). 3.125 Gb/s Impulse Radio Ultra-Wideband

Photonic Generation and Distribution Over a 50 km Fiber With Wireless Transmission. *IEEE Microwave and Wireless Components Letters,* Vol. 20, No. 2, (February 2010), pp. 127-129, ISSN 1531-1309.

Goodman, J. W. (2000). *Statistical Optics*, Wiley Classics Library Edition, ISBN 0-471-39916-7, New York, NY.

Haartsen, J. C.; Meijerink, A.; Bekkaoui, A.; Taban, A. & Tauritz, J. L. (2004). Novel wireless modulation technique based on noise. *Proceedings of IEEE 11th Symposium on Communications and Vehicular Technology in the Benelux (SCVT 2004),* Ghent, Belgium.

Haartsen, J. C.; Shang, X.; Balkema, J. W.; Meijerink, A. & Tauritz, J. L. (2005). A new wireless modulation scheme based on frequency-offset. *Proceedings of IEEE 12th Symposium on Communications and Vehicular Technology in the Benelux (SCVT 2005),* Enschede, the Netherlands.

Hanawa, M.; Mori, K.; Nakamura, K.; Matsui, A. & Nonaka, K. (2010). Experimental demonstration of high-resolution ultra-wideband impulse radar based on electrical-optical hybrid pulse generation. *IET Microwaves, Antennas and Propagation,* Vol. 4, No. 10 (October 2010), pp. 1462-1468, ISSN 1751-8725.

Khan, M.; Shen, H.; Xuan, Y.; Zhao, L.; Xiao, S.-J.; Leaird, D. E.; Weiner, A. M. & Qi, M. H. (2010). Ultrabroad-bandwidth arbitrary radiofrequency waveform generation with silicon photonic chip-based spectral shaper. *Nature Photonics,* Vol. 4, No. 2, (February 2010), pp. 117-U30, ISSN 1749-4885.

Li, J.; Kuo, B. P.-P. & Wong, K. K.-Y. (2009). Ultra-wideband pulse generation based on cross-gain modulation in fiber optical parametric amplifier. *IEEE Photonics Technology Letters,* Vol. 21, No. 4, (February 2009), pp. 212-214, ISSN 1041-1135.

Loayssa, A.; Benito, B. & Grade, M. J. (2000). Optical carrier-suppression technique with a Brillouin-erbium fiber laser. *Optics Letters*, Vol. 25, No. 4, (February 200), pp. 197-199, ISSN 0146-9592.

Loayssa, A. & Lahoz, F. J. (2006). Broadband RF photonic phase shifter based on stimulated Brillouin scattering and single side-band modulation. *IEEE Photonics Technology Letters,* Vol. 18, No. 1, (January 2006), pp. 208-210, ISSN 1041-1135.

Loayssa, A.; Capmany, J.; Sagues, M. & Mora, J. (2006). Demonstration of incoherent microwave photonic filters with all-optical complex coefficients. *IEEE Photonics Technology Letters,* Vol. 18, No. 16, (August 2006), pp. 1744-1746, ISSN 1041-1135.

McKinney, J. D.; Lin, I. S. & Weiner, A. M. (2006). Shaping the power spectrum of ultra-wideband radio-frequency signals. *IEEE Transactions on Microwave Theory and Techniques*, Vol. 54, No. 12 part 1, (December 2006), pp. 4247-4255, ISSN 0018-9480.

McKinney, J. D. (2010). Background-Free Arbitrary Waveform Generation via Polarization Pulse Shaping. *IEEE Photonics Technology Letters,* Vol. 22, No. 16, (August 2010), pp. 1193-1195, ISSN 1041-1135.

Narayanan, R. M. & Chuang, J. (2007). Covert communication using heterodyne correlation random noise signals. *Electronics Letters,* Vol. 43, No. 22, (October 2007), pp. 1211-1212, ISSN 0013-5194.

Narayanan, R. M. (2008). Through-wall radar imaging using UWB noise waveforms. *Journal of the Franklin Institute,* Vol. 345, No. 6, (September 2008), pp. 659-678, ISSN 0016-0032.

Peled, Y.; Tur, M. & Zadok, A. (2010). Generation and Detection of Ultra-Wideband Waveforms Using Stimulated Brillouin Scattering Amplified Spontaneous Emission. *IEEE Photonics Technology Letters,* Vol. 22, No. 22, (November 2010), pp. 1692-1694, ISSN 1041-1135.

Pham, T.-T.; Yu, X.; Dittmann, L. & Monroy, I. T. (2011). Integration of Optically Generated Impulse Radio UWB Signals into Baseband WDM-PON. Accepted for publication in *IEEE Photonics Technology Letters,* Vol. 23, (2011), ISSN 1041-1135.

Qiu. R. C.; Liu, H. & Shen, X. (2005). Ultra-wideband for multiple access communication. *IEEE Communications Magazine*, Vol. 43, No. 2, (February 2005), pp. 80-87, ISSN 0163-6804.

Sahin, M. E.; Guvenc, I. & Arslan, H. (2005). Optimization of energy detector receivers for UWB systems. *Proceedings of the IEEE 61st Vehicular Technology Conference*, Stockholm, Sweden, Vol. 2, (May-June 2005), pp. 1386-1390 ISSN 1550-2252.

Shen, Y.; Zhang, X. & Chen, K. (2005). Optical single side-band modulation of 11 GHz RoF system using stimulated Brillouin scattering. *IEEE Photonics Technology Letters* Vol. 17, No. 6, (June 2005), pp. 1277-1279, ISSN 1041-1135.

United States Federal Communication Commission (FCC). (2002). Technical report ET-Docket 98-153, FCC02-48, (April 2002).

Upadhyaya, S. J. (1999). Noise Generators. *Wiley Encyclopedia Electrical and Electronics Engineering*. Online ISBN: 9780471346081, New York, NY.

Velanas, P.; Bogris, A.; Argyris, A. & Syvridis, D. (2008). High-speed all-optical first- and second-order differentiators based on cross-phase modulation in fibers. *Journal of Lightwave Technology*, Vol. 26, No. 18, (September 2008), pp. 3269-3276, ISSN 0733-8724.

Wang, C.; Zeng, F. & Yao, J. P. (2007). All-fiber ultrawideband pulse generation based on spectral shaping and dispersion-induced frequency-to-time conversion. *IEEE Photonics Technology Letters,* Vol. 22, No. 3, (February 2007), pp. 137-139, ISSN 1041-1135.

Wang, J.; Tang, W. and Zhu, W. (1996). Stimulated Brillouin scattering initiated by thermally excited acoustic waves in absorption media. *Optics Communications*, Vol. 123, No. 4-6, (February 1996), pp. 574-576, ISSN 0030-4018.

Wu, T.-H.; Wu, J.-P. & Chiu, Y.-J. (2010). Novel Ultra-wideband (UWB) photonic generation through photodetection and crossabsorption modulation in a single electroabsorption modulator. *Optics Express*, Vol. 18, No. 4, (February 2010), pp. 3379-3384, eISSN 1094-4087.

Xu, J.; Zhang, X.; Dong, J.; Liu, D. & Huang, D. (2007a). High-speed all-optical differentiator based on a semiconductor optical amplifier and an optical filter. *Optics Letters*, Vol. 32, No. 13, (July 2007), pp. 1872-1874, ISSN 0146-9592.

Xu, J.; Zhang, X.; Dong, J.; Liu, D. & Huang, D. (2007b). All-optical differentiator based on cross-gain modulation in semiconductor optical amplifier. *Optics Letters*, Vol. 32, No. 20, (October 2007), pp. 3029-3031, ISSN 0146-9592.

Yang, L. & Giannakis, G. B. (2004). Ultra-wideband communications: an idea whose time has come. *IEEE Signal Processing Magazine*, Vol. 21, No. 6, (November 2004), pp. 26-54, ISSN 1053-5888.

Yao, J.; Zeng, F. & Wang, Q. (2007). Photonic generation of ultrawideband signals. *Journal of Lightwave Technology*, Vol. 25, No. 11, (November 2007), pp. 3219-3235, ISSN 0733-8724.

Yu, X.; Gibbon, T. B.; Pawlik, M.; Blaaberg, S. & Monroy, I. T. (2009). A photonic ultra-wideband pulse generator based on relaxation oscillations of a semiconductor laser. *Optics Express*, Vol. 17, No. 12, (June 2009), pp. 9680-9687 eISSN 1094-4087.

Zadok, A.; Eyal, A. & Tur, M. (2007). GHz-wide optically reconfigurable filters using stimulated Brillouin scattering. *Journal of Lightwave Technology*, Vol. 25, No. 8, (August 2007), pp. 2168-2174, ISSN 0733-8724.

Zadok, A.; Wu, X.; Sendowski, J.; Yariv, A. & Willner, A. E. (2009). Flexible All-Fiber Generation of Ultra-Wideband Signals via Pulse Compression and Differential Detection. Paper FWK3 in *Proceedings of Frontiers in Optics* San-Jose, CA October 2009.

Zadok, A.; Wu, X.; Sendowski, J.; Yariv, A. & Willner, A. E. (2010a). Photonic generation of ultra-wideband signals via pulse compression in a highly nonlinear fiber. *IEEE Photonics Technology Letters*, Vol. 22, No. 4, (February 2010), pp. 239-241, ISSN 1041-1135.

Zadok, A.; Wu, X.; Sendowski, J.; Yariv, A. & Willner, A. E. (2010b). Reconfigurable generation of high-order ultra-wideband waveforms using edge detection," *Journal of Lightwave Technology*, Vol. 28, No. 16, (August 2010), pp. 2207-2012, ISSN 0733-8724.

Zeng, F. & Yao, J. P. (2006). Ultrawideband signal generation using a high-speed electrooptic phase modulator and an FBG-based frequency discriminator. *IEEE Photonics Technology Letters* Vol. 18, No. 19, (October 2006), pp. 2062–2064, ISSN 1041-1135.

Zeng, F.; Wang, Q. & Yao, J. P. (2007). All-optical UWB impulse generation based on cross phase modulation and frequency discrimination. *Electronics Letters*, Vol. 43, No. 2, (January 2007), pp. 119–121, ISSN 0013-5194.

Zheng, J.-Y.; Zhang, M.-J.; Wang, A.-B. & Wang, Y.-C. (2010). Photonic generation of ultrawideband pulse using semiconductor laser with optical feedback. *Optics Letters*, Vol. 35, No. 11 (June 2010), pp. 1734-1736, ISSN 0146-9592.

Zhu, Z.; Daws, A. M. C.; Gauthier, D. J.; Zhang, L. & Willner, A. E. (2007). Broadband SBS slow light in an optical fiber. *Journal of Lightwave Technology*, Vol. 25, No. 1, (January 2007), pp. 201-206, ISSN 0733-8724.

Part 2

UWB Channel – Theory and Measurements

Ultra-Wideband (UWB) Communications Channel – Theory and Measurements

Javad Ahmadi-Shokouh[1] and Robert Caiming Qiu[2]
[1]*University of Sistan and Baluchestan*
[2]*Tennessee Tech University*
Iran
USA

1. Introduction

The most recent increase in demand within the wireless user community for short-range, very high rate data and video transmission devices has motivated the growth of a new generation of broadband wireless access communication systems, i.e. Ultra-Wideband (UWB) radio (1)-(4). UWB technology has been employed for several decades in military and commercial communications applications like high-speed mobile Local Area Networks (LAN), imaging and surveillance systems, ground penetration radars, automotive sensors, medical monitors and recently Wireless Personal Area Networks (WPAN) (5). Spread-spectrum communication systems using ultra-short impulses have seen a renewed interest because of its fine resolution in delay to the order of a tenth of nanosecond though at the cost of a ultra wide frequency band. Low transmission power and large bandwidth together render the power spectral density of the transmitted signal extremely low, which allows the frequency-underlay of a UWB system with other existing radio systems. Hence, the short range radio UWB will play a critical role in the local/home (*pico-cell*) level of the broadband networks due to its unprecedented, broad bandwidth. Indoor wireless systems operate in the areas where usually there is no Line-of-Sight (LOS) radio path between the terminals, the transmitter, and the receiver, and where due to obstructions (furniture, partitions, walls, etc.), multi-diffraction, multi-reflections, and multi-scattering effects occur. These lead to not only additional losses (with regarding those obtained in LOS), but also multipath fading of the signal strength observed at the receiver. Basically, one of the most important aspects of any radio channel-modeling activity is the investigation of the distribution functions of channel parameters. Typically, these distributions are obtained from measurements or simulations based on almost exact or simplified descriptions of the environment. However, such methods often only yield insights into the statistical behavior of the channel and are not able to give a physical explanation of observed channel characteristics. Due to the extremely broad bandwidth, the channel is highly dispersive, even for an individual path. Physics-based models (2) are usually required to understand the multipath pulses waveforms that are necessary for optimal reception.

There exist very good fundamental investigations on the UWB propagation channel characterization and modeling in the literature (6)-(11). More particularly, the references (9) and (11) give an excellent overview of the UWB channels and the authors in (10)

present a very comprehensive tutorial on the UWB channel modeling. To understand the fundamental limits and potential applications of UWB technology, in this paper we will investigate the empirical measurements on the UWB propagations channels. Our focus in this integrated survey lies on the indoor environments, including office, laboratory, commercial and residential buildings. Moreover, we consider some special applications of the UWB systems which have an indoor-like areas, e.g. inside a Magnetic Resonance Imaging (MRI) system, underground mine and so on. A large number of references, more than 100 and mostly recently published, are used in this investigation. The basic channel characterization parameters are extracted and discussed. We review all the channel characterization procedures in this regard. To characterize a UWB propagation indoor channel, a common method is applying a Radio-Frequency (RF) signal to the channel and making an empirical evaluation of the received signal. Through this type of channel characterization, essential metrics are drawn which are: *Path-Loss (PL)*, *large-scale fading*, *small-scale fading*, *multipath arrival rate*, *Power-Delay-Profile (PDP)*, *Root-Mean-Squared (RMS) delay spread*, *temporal correlation*, *Angle-of-Arrival (AOA)*, *spatial correlation across the receiver's spatial aperture*, *Frequency-Selectivity (FSE)* and *Pulse-Distortion (PD)*.

The rest of this paper organized as follows: in Section II, a general formulation of the UWB Channel Impulse Response (CIR) is presented. Section III provides the employed channel characterization procedures and measurement settings. In section IV, we review the channel fading's power-Loss characteristics. A survey on the channel fading's temporal characterizations is presented in Section V. In section VI, the channel fading's spatial characteristics is being reviewed. We then investigate on the channel fading's frequency-dependent characteristics in Section VII. Finally, Section VIII concludes the paper.

2. Multipath Channel Impulse Response (CIR) and basic definitions

A common and convenient model for characterization of the multiptah channel is the discrete-time impulse response model. In this model, the multipath delay axis τ is discretized into equal time delay segments called *bins* (12), (13). Each bin has a time delay width equal to $\Delta\tau = \tau_{i+1} - \tau_i$. Any number of multipath signals received within the ith bin are represented by a single resolvable *multipath component* having delay τ_i (13). A reasonable bin size is the specific measurement's *time resolution* since two paths arriving within a bin cannot be resolved as distinct path. The relative delay of the ith multipath component as compared to the first arriving component is called *excess delay* and if the total number of possible multipath components is N, the *maximum excess delay* of the propagation channel is given by $N\Delta\tau$ (13).

In a multipath propagation channel, since the received signal consists of a series of attenuated, time delay, phase shifted replicas of the transmitted signal, the impulse response of multipath channel can be expressed as (1) (13).

$$h(\tau, t) = \sum_{i=0}^{N(t)-1} a_i(\tau, t) e^{j\varphi_i(\tau, t)} \delta(\tau - \tau_i(t)) \tag{1}$$

where $a_i(\tau, t)$, $\varphi_i(\tau, t)$ and $\tau_i(t)$ are the real amplitude, the phase shift and excess delay, respectively, of ith multipath component at time t. Generally, the parameters a_i, φ_i and τ_i are random time-variant functions because of the motion of people and equipment in and around of buildings. However, since the rate of their variations is very slow as compared with the measurement time interval, these parameters can be treated as time-invariant

random variables within one snapshot (bin) of measurement. Moreover these parameters are frequency-dependent since they are related to radio signal characteristics such as transmission and reflections.

The time-invariant CIR (2), assuming a stationary environment, was first suggested in (14) to describe multipath-fading channels. This model has been used successfully in mobile radio applications (12) and can be applied to the UWB indoor propagation channels.

$$h\left(\tau\right) = \sum_{i=0}^{N-1} a_i\left(\tau\right) e^{j\varphi_i(\tau)} \delta\left(\tau - \tau_i\right) \tag{2}$$

A discrete space-time separable CIR (3), which is originally proposed by (15) and developed by (16), is employed in (17) to represent the UWB channel's impulse response. In this model, the impulse response for the multipath delay τ, so-called Time-of-Arrival (TOA), and AOA θ is given by

$$h\left(\tau, \theta\right) = \sum_{l=0}^{\infty} \sum_{k=0}^{\infty} \beta_{kl} e^{j\phi_{kl}} \delta\left(\tau - T_l - \tau_{kl}\right) \delta\left(\theta - \Theta_l - \omega_{kl}\right) \tag{3}$$

where β_{kl}, ϕ_{kl}, τ_{kl}, and ω_{kl} are respectively the amplitude, the phase shift, the arrival time and the azimuth AOA of the kth arrival of the lth cluster. T_l and Θ_l represent the lth cluster's first arrival time and the azimuth AOA respectively. In other words, for a particular cluster l the inner sum reveals the rays corresponding to the same cluster, i.e. intra-cluster representation. Accordingly, the intra-cluster rays are said to be from different ls.

3. Measurement settings

3.1 Measurement environments

UWB channel fading depends on detailed aspects of the indoor setting- including not only describing the architectural floor plan but details of the interior door. In an accurate fading study among the measurement campaigns all of these detail must be taken into account. In the present work's survey character on the indoor setting, we however consider an abbreviation but unified of the whole setting used in the measurement campaigns. Although this issue can lead to apparent wide variability in empirical results for nominally comparable setting, as more measurements are carried out new categories may be introduced which may provide a better classification in terms of the variability of the signal statistics. Table 1 represents the proposed categories based on the reviewed literature UWB channel-fading measurements.

3.2 Multipath propagation measurements techniques

Due to the importance of the multipath structure in determining the small-scale fading effects, a number of wideband channel sounding techniques have been developed. Wideband measurement techniques as described in (13) are

- *Direct Pulse (DP):* In the this measurement system, a repetitive wideband pulse is transmitted and a receiver with wide bandpass filter is utilized to receive the pulses. Then, the received signal is amplified using a Low Noise Amplifies (LNA) and detected with an envelope detector before being stored and displayed on a digital oscilloscope. This structure gives an immediate measurement of the square of CIR convolved with the probing pulse. In this measurement, the minimum resolvable delay between multipath

component equals the probing pulse width. To measure impulse response (2), the probing pulse $p(t)$ approximates the delta function. If $p(t)$ has a time duration much smaller than the impulse response of multipath channel $p(t)$ does not need to be deconvolved from the received signal in order to determine the relative multipath signal strength in the impulse response (2) (13).

- *Spread Spectrum Sliding Correlator (SC):* In a spread spectrum channel sounder, a carrier signal by mixing with a binary Pseudo-Noise (PN) sequence becomes spread over a large bandwidth and then is transmitted. The spread spectrum signal is then received, filtered and despread using a PN sequence generator. In this measurement system, the chip rate of the PN sequence generator determines the time resolution. The sliding correlator operation serves to time dilate the measured channel impulse response, thereby compressing the measurement bandwidth and easing hardware requirements. Moreover, a spread spectrum channel sounder has a higher dynamic range compared to the direct pulse system (13).

- *Frequency Sweeping (FS):* In this measurement, a Vector Network Analyzer (VNA) controls a synthesized frequency sweeper. The sweeper scans a particular frequency band by stepping through discrete frequencies. Obviously, the number and spacings of these frequency steps impact the time resolution. This frequency domain representation is then converted to the time domain using Inverse Discrete Fourier Transform (IDFT) processing, giving a band-limited version of the impulse response.

Table 1 shows what type of measurement technique is employed for the reviewed literature of the UWB channel-fading campaigns.

3.3 Space and time resolution

All above utilized measurement approaches use a band-limited probing waveform and thus have limited time resolution. Even with the sub-nanosecond resolution, used in the measurements, the received signal pulse may still contain several multipath components and thus may fade in a small local area. The time resolution can directly affect time of arrival measurements. For instance, increasing the time-domain resolution of the channel response to resolve the direct LOS path improves the performance of location finding systems employing TOA estimation techniques. Various measurement campaign's temporal resolutions are summarized in Table 1. In these measurements, the different spatial grids in size and spacing are utilized to assess the spatial variation (Table 1). The associated grids are located horizontally where the measurements are made at the center of each grid cell. Although the essential spatial fading statistics have been drawn based on the measurements made inside the grid, some campaigns like in (38) move the grid to obtain the extra parameter statistics like multipath cluster phenomenon.

3.4 Frequency range and bandwidth

A UWB signal defined by the Federal Communication Commission (FCC) is a signal with greater than 25% relative (coherent) bandwidth[1], it is also true that UWB signals tend to have large absolute bandwidths (75) which are not less than $500 MHz$.

The relative bandwidth definition of UWB is stated as follows:

$$B_{rel} = 2 \cdot \frac{f_h - f_l}{f_h + f_l} \ = \ \frac{W}{f_c} \tag{4}$$

---

[1] Sometimes termed "fractional bandwidth".

References	Environment	Measur. Tech.	Time Res.* (ns)	Measurement Grid		Frequency-Bandwidth	
				Grid Size	Spacing (cm)	Absolute (GHz)	Relative
(17)-(23)	Office and Laboratory	DP	2	7×7	15	NA	NA
(24)-(25)	Office building and Corridor	FS	400	3×3	3	$1 - 9$	1.6
(26)	Ship Compartments	SC	NA	NA	NA	$0.8 - 2.5$	1.03
(27)-(32)	Residential House	FS	320	5×5	5	$4.375 - 5.625$	0.25
(33)-(34)	Residential and Commercial Building	FS	266.6	5×5	5	$2 - 8$	1.2
(35)	Office and Laboratory	FS	266.6	NA	NA	$2 - 8$	1.2
(36)	Residential House	FS	NA	1×20	1.253	$2 - 8$	1.2
(37)	Laboratory	FS	400	10×10	10	$2 - 6$	1
(38)	Office and Corridor	FS	NA	30×30	1	$1 - 11$	1.66
(39)	Office	FS	NA	30×30	1	$1 - 11$	1.66
(40)	Auditorium and Office	DP/SC/FC	NA	NA	NA	$1 - 3$	1
(41)-(43)	Office	SC	200	NA	NA	$1.25 - 2.75$	0.75
(44)	Office	FS	106	NA	NA	$3.1 - 10.6$	1.1
(45)	Office, Laboratory and Reading room	DP	2	1×61	2	NA	NA
(46)-(47)	Laboratory and Classroom	FS	200	NA	NA	$2 - 6$	1
(48)-(49)	Office and Classroom	DP	0.1	3×3	45	$0.1 - 12$	1.967
(50)-(51)	Office and Classroom	FS	33.6	3×3	45	$0.1 - 12$	1.967
(52)-(53)	Office	FS	500	1×90 (Circle)	2.8	$3.1 - 10.6$	1.094
(54)	Office	FS	NA	1×5	10	$3.1 - 10.6$	1.094
(55)	Office	DP	0.05	1×23	5	$3.1 - 10.6$	1.094
(56)-(58)	Office and Laboratory	SC	0.8	25×25	2	$3.6 - 6$	0.5
(59)	Office and Laboratory	FS	200	5×5	2, 8, 16	$2 - 12$	1.43
(60)	Office and Laboratory	SC	0.83	5×5	2, 8, 16	$3.6 - 6$	0.5
(61)	Residential Apartment	FS	229.6	5×5	15	$3 - 10$	1.077
(62)	Office, Laboratory, and Classroom	FS	33.6	3×3	45	$0.1 - 12$	1.967
(63)	Office, Laboratory, Factory and Residential	FS	1000	NA	100	$3 - 8$	0.91
(64)	Office	FS	100	4×4	30	$3 - 11$	1.14
(65)	MRI	DP	0.8	1×8 (Circle)	15	$3.168 - 4.752$	0.4
(66)	Office	FS	200	21×21	2	$2 - 10$	1.33
(67)-(69)	Underground Mine	FS	533	8×5	7	$2 - 5$	0.857
(70)	Underground Mine	SC	2.25	7×7	15	$2.55 - 3.45$	0.3
(71)	Office	FC	533.3	7×7	5	$3 - 6$	0.66
(72)	Office, residential, Chamber	FC	533.3	1×9	15	$3 - 6$	0.66
(73)	Chamber	FC	NA	NA	NA	$1.5 - 8$	1.368
(74)	Office and Chamber	SC	213.3	1×12 (Circle)	8	$3.1 - 10.6$	10.94

* Pulse-width for DP, twice a chip period for SC and maximum-detectable-delay for FS (13).

Table 1. UWB Channel-Fading Measurement Settings

where f_h and f_l denote frequencies at the upper and lower band edges, respectively. W is the absolute-bandwidth, and f_c is the center frequency. Table 1 shows the absolute- and relative-bandwidth utilized by each reference.

4. Channel fading's power-loss characteristics

4.1 Path-loss
Generally speaking, PL arises from the propagating wavefront's increasing surface area as the wavefront radiates outward from the transmitting antenna and the obstructive effects of objects distributed between transmitter and receiver antennas such as *free space loss*, *refraction*, *reflection*, *diffraction*, *clutter*, *aperture-medium coupling loss*, and *absorption*.

Both non-empirical and empirical propagation models illustrate that average path-loss increases logarithmically as a function of Transmitter-Receiver (TR) separation distance in

indoor radio channels (13):

$$\overline{PL\left(d\right)} = \overline{PL_0} + 10\,n\,\log_{10}\left(\frac{d}{d_0}\right) + F_A \tag{5}$$

where n, PL_0, d and F_A are respectively the path-loss exponent which shows the rate at which the path-loss increases with distance, the intercept point which is the path-loss at d_0 (a reference distance), the transmitter-receiver separation distance, and the Floor Attenuation Factor (FAF). The bars in (5) denote the average values for the same floor measurement and over all transmitter-receiver antennas locations, while maintaining the same transmitter-receiver separation distance. The variations about the average path-loss value (5) are called shadow fading and are discussed later. The path-loss exponent n depends on the propagation environment. In free space, $n = 2$; with obstructions, $n > 2$ (13).

Measurements (21), (22), (24)-(27), (29), (30), (33), (34), (41)-(43), (45)-(58), (60), (63), (65), (68), (70)-(72) and (74) show that (5) is applicable for both Line-of-Sight (LOS) and Non-Line-of-Sight (NLOS), i.e. when there is no LOS path between the transmitter and receiver, UWB channels with the calibrated PL parameters in Table 2. Depending on the UWB receiver architecture, the PL parameters can be obtained by different methods. Basically, the UWB indoor path-loss is calculated by the total received power integrating the power delay profiles (defined in 5.2.1) over all delay bins (21), (22), and (41)-(43). However, if the receiver uses a threshold detection strategy which tracks the peak of the received signal, the calculated PL is based on the peak CIR power metric (41)-(43). Moreover, some of the receiver structures only detect the first path; thus, the first path power is only employed for the PL calculation (63).

The UWB indoor path-loss exponent n measured in different environments behaves as a random variable (24), (25), (27), (29) and (30). In (27), (29), (30), (33) and (34), it is also shown that n follows a normal distribution (see Table 2). From the measurement results:

1) Table 2 shows $1.4 < n < 4.1$ for a regular indoor environment except for the hard-NLOS situation (22), (60) and (63), and a very short-distance path-loss measurements (55) and (65). A hard-NLOS scenario is basically defined for when there is no direct or reflected path between transmitter and receiver e.g. two different rooms (24). However, in (60) this definition corresponds to the situation in which not only the transmitter and receiver are located in different rooms but also the blockage effect of the other obstacles are considered. On the other hand, a soft-NLOS scenario mostly happens when there are reflected paths between the transmitter and the receiver. e.g. in a room. In (22) and (60), the high value path-loss exponent $n = 7.4$ is reported for a multi-wall scenario. Moreover, $n = 4.9$ is reported in (63) for a multi-floor measurement. In (55) and (65), it is shown that for a short distance NLOS scenario the path-loss exponent n is less than 1. This result, however, can be justified using a small scale fading. The path-loss exponent for a

2) It is shown in (22) and (63) that the path-loss exponent n can be dependent on the TR distance. To present this dependence, a *dual-slope* model of the normalized mean PL (5) is proposed in (22) and (63) for different distance regions

$$\overline{PL_D\left(d\right)} = \begin{cases} 10\,n_1\,\log_{10}\left(\frac{d}{d_0}\right) & d \le D \\ \overline{PL_D} + 10\,n_2\,\log_{10}\left(\frac{d}{d_0}\right) & d > D \end{cases} \tag{6}$$

References	Environment		d_0 (m)	$\overline{PL_0}$ (dB)	n^*		σ_χ (dB)		Notes
					μ_n	σ_n	μ_{σ_χ}	σ_{σ_χ}	
(21)	Office/Laboratory	LOS/NLOS	1	NA	2.4	NA	5.9	NA	-
(22)	Office/Laboratory	LOS/NLOS	1	0†	2.04	NA	4.3	NA	$d \leq 11m$
				−56†	7.4	NA		NA	$d > 11m$
(24)-(25)	Office	LOS	0.151	39.82	1.4	0.35	NA		-
		Soft-NLOS	0.082	NA	3.2	0.21			
		Hard-NLOS	0.067	NA	4.1	1.87			
(26)	ship Compartment	NLOS	NA	NA	1.65	NA	NA		-
(27), (29)-(30)	Residential	LOS	1	47	1.7	0.3	1.6	0.5	-
		NLOS	1	51	3.5	0.97	2.7	0.98	
(33)-(34)	Commercial	LOS	1	43.7	2.04	0.30	1.2	0.6	-
		NLOS	1	47.3	2.94	0.61	2.4	1.3	
	Residential	LOS	1	74.2	1.82	0.39	1.5	0.6	
		NLOS	1	50.4	3.34	0.73	2.6	0.9	
(42)-(43)	Office	NLOS	1	0†	3	NA	NA		Peak Power, $d > 1m$
					2	NA			Total Power
(41)	Office	NLOS	NA	NA	2.9	4.75	NA		Peak Power
					2.1	3.55			Total
(45)	Office/Laboratory	LOS/NLOS	1	−10.9†	3.4	NA	3.2	NA	$d > 5m$
	Reading room	LOS	1	1.15†	1.8	NA	0.6	NA	
(46)-(47)	Laboratory/Classroom	LOS	1	NA	1.55	NA	1.98	NA	{RX,TX}={OMNI,OMNI}
					1.65	NA	1.19	NA	{RX,TX}={OMNI,DIR}
					1.72	NA	0.77	NA	{RX,TX}={DIR,DIR}
(48)-(49)	Office/Classroom	LOS	1	NA	1.58	NA	1.91	NA	Biconical Antenna
		NLOS	1	NA	2.41	NA	3.26	NA	
		LOS	1	NA	1.6	NA	1.58	NA	TEM Horn Antenna
		NLOS	1	NA	2.6	NA	6.08	NA	
(50)-(51)	Office/Classroom	LOS	1	NA	1.3	NA	2.6	NA	Biconical Antenna
		NLOS	1	NA	2.3	NA	2.4	NA	
		LOS	1	NA	1.3	NA	2.8	NA	TEM Horn Antenna
		NLOS	1	NA	2.4	NA	5.1	NA	
(52)-(53)	Office	LOS	1	53.7	1.62	NA	1.7	NA	-
		NLOS	1	59.4	3.22	NA	5.7	NA	
(54)	Office	LOS	0.1	4	1.7	NA	NA	NA	-
(55)	Office	LOS	1	20	2.21	NA	NA	NA	RX & TX on a desk
		NLOS	1	20	−1.06	NA	NA	NA	Monitor Blocked
				NA	NA	1	NA	NA	Desk Blocked (on & under)
				7.5	0.17	NA	NA	NA	Body Blocked
(56)-(58)	Office/Laboratory	LOS	1	50.54	1.916	NA	1.42	NA	-
		NLOS	3.73	67.15	3.663	NA	2.18	NA	
(60)	Office/Laboratory	LOS	1	NA	1.8	NA	2.57	NA	-
		NLOS	4.037	NA	11.05	NA	5.17	NA	
		Hard-NLOS²	4.037	NA	7.33	NA	NA	NA	Multi-wall effect
(63)	Office/Laboratory	Hard-NLOS	1	42	3.5	NA	5.1	NA	$d \leq 10m$
				77	2.2	NA		NA	$d > 10m$
	Residential	NLOS	1	42	2.7	NA	3.9	NA	Same floor
					3.6	NA	2.7	NA	Inter-floor
	Factory	LOS		42	1.5	NA	2.4	NA	$d \leq 10m$
				57	2.9	NA		NA	$d > 10m$
(65)	MRI	LOS/NLOS	0.087	28	0.435	NA	NA	NA	Empty barrel
					0.646	NA	NA	NA	Water-filled barrel
(67)-(69)	Underground Mine	LOS	1	66	1.47	NA	1.1	NA	-
		NLOS	5	52.5	2.45	NA	2.94	NA	
(70)	Underground Mine	LOS/NLOS	10	0†	1.8	NA	NA		Peak Power
					1.64	NA			Total Power
(71)	Office	LOS/NLOS	0.1	56.1	5.8	NA	5	NA	-
(72)	Office	NLOS	1	75.8	2.67	NA	NA	NA	-
	Chamber	LOS	1	82	3.29	NA	NA	NA	
(74)	Office and Chamber	LOS/NLOS	1	82	2.6	NA	NA	NA	-

* The same-floor path-loss exponent (see note for some exceptions).

† These intercept values are calculated based on a normalized path-loss.

Table 2. Path-loss Characteristics

where D, $\overline{PL_D}$, n_1 and n_2 are respectively the break point distance in the model, the intercept point, the path-loss exponent for the first slope, i.e. $d \leq D$, and the path-loss exponent for the second slope, i.e. $d > D$. All these values are calculated through the curve-fitting process on the measured data.

3) There is no significant difference between the measured values of n for UWB channels and narrowband indoor channels which are reported in (13).

4) The path-loss in a ship compartment area follows in-building LOS (within one room) cases.

5) The path-loss exponent n slightly increases if directional antennas are employed for the receiver and transmitter (46)-(51) because it reduces some of the obstructive effects of objects distributed between transmitter and receiver like diffraction, reflection and absorption. In other words, the directive antenna does not use the considerable multipath energy while an omni-directional antenna does.

6) The standard deviation of the path-loss exponents for different measurement locations/environments, like rooms and buildings but in the same category like residential (27), (29) and (30), is higher for NLOS cases than for LOS cases.

7) Different types of indoor environment (e.g. office, laboratory, residences) lie in different subranges of $n \in [1.4, 4.1]$. Instead of a deterministic n, it has been modeled as a Gaussian random variable with empirically determined mean and variance, for residential houses in (27), (29) and (30), and commercial areas in (33) and (34).

8) To the best of the authors' knowledge, there is only one published paper on the F_A measurement (63). It is shown in (63) that there is no significant difference in the path loss model between a single and multi-floor measurement. However, the results in (63) show a considerable difference between the aforementioned scenarios when the measurements are performed at the entrance/back of the building.

4.2 Large-scale fading
(5) overlooks shadowing loss (χ), which augments (5) to:

$$PL\left(d\right) = \overline{PL\left(d\right)} + \chi \qquad (7)$$

UWB measurements (21), (22), (24), (27), (29), (30), (33), (34), (41), (43), (45)-(53), (56)-(58), (60), (63) and (68) indicate a zero-mean log-normally distribution for χ with its standard deviation σ_χ dependent on the particular propagation environment (see Table 2). >From large-scale fading measurement results:

1) Shadowing loss is generally greater for residences than for offices. environments.

2) In a LOS scenario, the shadowing loss is less than in a NLOS case.

3) For the LOS scenarios, the shadowing loss decreases if directional antennas are employed for the receiver or transmitter. Indeed, the spatial filtering using a directive antenna results in a more stable average PL.

4) To the authors' knowledge, there are no published paper investigating the relationship between χ and the transmitter-receiver separation distance, there exists only one paper published on the inter-floor shadowing loss (63) which reports an inter-floor shadowing loss less than the same-floor shadowing loss for a residential environment (see Table 2). The same result is also observed for an office/laboratory environment (the inter-floor

References	Environment		Small-Scale Type	distribution(s)**	distribution parameters
(17)	Office/Laboratory	LOS/NLOS	Spatial	Rayleigh(σ)	$\sigma = 0.46$
(21)- (22)	Office/Laboratory	LOS/NLOS	Spatial	Nakagami(m)	$m \sim \mathcal{N}[\mu_m(\tau_k), \sigma_m^2(\tau_k)]$
(24) and (25)	Office/ Laboratory/ Corridor	LOS	Temporal	Weibull(μ, σ, λ)	$\mu = -306, \sigma = 311, \lambda = 45$
		Soft-NLOS			$\mu = -304, \sigma = 320, \lambda = 46$
		Hard-NLOS			$\mu = -304, \sigma = 322, \lambda = 45$
(31)	Residential	LOS/NLOS	Temporal	Gaussian($0, \sigma$)	$\sigma = 4.7$
(35)	Office/Laboratory	LOS	Temporal	Rician(k)	$k \propto \{d^*, \tau_k\}$
(38)	Office/Corridor	LOS/NLOS	Temporal	Rician(k)	$k = -9dB$
(39)	Office	NLOS	space-time†	Gaussian($0, \sigma$) $\times$ Potential(a)	NA
(45)	Office/Laboratory	LOS/NLOS	Spatial	Gaussian($0, \sigma$)	$\sigma_{d^*=5} = 1.13, \sigma_{d=7} = 1.24$ $\sigma_{d=10} = 1.16, \sigma_{d=14} = 1.41$
	Reading room	LOS			$\sigma_{d=5} = 0.13, \sigma_{d=7} = 0.26$ $\sigma_{d=10} = 0.22, \sigma_{d=14} = 0.31$
(52)	Office	LOS/NLOS	Spatial	Rician(k)	NA
(57)	Office/Laboratory	LOS/NLOS	Spatial	Nakagami(m)	$\mu_m = 1.5, \sigma_m = 0.5$
(71)	Office	LOS/NLOS	Spatial	Nakagami(m)	Corresponding αGamma=2

* d is the transmitter/receiver separation distance.
** All distributions are on amplitude except Weibull(μ, σ, λ) which is for received power.
†The Gaussian distribution corresponds to the spatial small-scale amplitude
and the Potential distribution corresponds to the temporal small-scale amplitude.

Table 3. Small-scale statistics

shadowing loss $\sigma_\chi = 1.8$ and the same-floor shadowing loss $\sigma_\chi = 3.4$) (63). However, in such an environment when we move from the inter-floor scenario to the multi-floor one the inter-floor shadowing loss increases even more than a same-floor case (the inter-floor shadowing loss $\sigma_\chi = 1.8$ and the multi-floor shadowing loss $\sigma_\chi = 5.1$) (63).

5) As many wireless devices are wearable, the human-antenna interaction could be significant not only in open areas (40) but also in dense scatterer environments (like in an office) (71). A UWB channel measurement for Body Area Networks (BAN) is presented in (72). Significant echoes from the body, e.g. from the arms, and deterministic echoes from the floor are observed in human-body effect measurement (72). In (74), the performance of the UWB impulse radio for BAN employing a monopole antenna. The results in (74) show that the shadowing loss in a WBAN channel does not follow the log-normal distribution. Obayashi and Zander (77) model the body-shadowing deterministically with the existing ray-determination methods for narrow-band channels, but no corresponding study has been done for UWB with UWB's distinctive demands on ray-tracing methods.

4.3 Small-scale fading

Basically, "small-scale fading" describes the received signal amplitude/energy's fluctuations over a short duration or in the spatial neighborhood at the moving antenna's nominal location (13). This definition can be generalized to UWB communications as the constructive and destructive interferences of the multipath components due to a change in the moving antenna location in the order of the sub-spatial width of the transmitted pulse. In the UWB small-scale measurements, the moving antenna is mostly receiver antenna (17), (21), (22), (24), (25), (31), (35), (39), (45), (57) and (71); however, a moving transmitter antenna is used in (38) and (52). In the UWB indoor applications, the transmitter an receiver and scatterer move slowly (if at all) relative to the information symbol duration. The UWB channel's small-scale fading thus depends mostly on the multipath phenomena and the signal bandwidth.

Measurement campaigns (17), (18), (21), (22), (24), (25), (31), (35), (38), (39), (45), (52), (57) and (71) present different results for the small-scale statistics of received signal amplitude/energy due to *measuring time-delay interval*, *measuring data set (grid size and spacing)*, and *environment type*. Table 3 shows the proposed mathematical distributions, associated with the measured

essential parameters (shown in the last column), for the small scale fading reported by different measurement campaigns. >From small-scale fading measurement results:

1. The small-scale distribution's parameters depend on the transmitter-receiver separation distance.

2. Most of the small-scale amplitude measurements show the clustering effect.

3. The more clustered office environment generally has higher standard deviations than open areas like reading rooms, due to the multipath phenomenon.

4. The small-scale distribution strongly depends on environment type (e.g. it is shown in (39) that the small-scale amplitude follows the Gaussian distribution whose parameters are fixed for an European office, and also results from (21) and (22) show that the small-scale amplitude follows the Nakagami distribution whose parameters change with increasing excess delay for an American office).

5. As each temporal bin sums many multipath, the central limit theorem gives the Gaussian distribution for the small-scale magnitude statistics for large delays, but the Gaussian distribution is only approximate at small delays; hence, the Nakagami distribution (21) and (22) whose parameters change with increasing excess delay can fit well the small-scale amplitude while the Gaussian distribution is proposed in (7) for mathematical convenience.

5. Channel fading's temporal characterizations

5.1 Multipath arrival rate
The arrival rate model in (16) is employed in (17), (52) and (57) to measure arrival rate statistics based on the multipath clustering phenomenon used in (3)

$$p\left(T_l|T_{l-1}\right) = \Lambda e^{-\Lambda(T_l - T_{l-1})} \tag{8}$$

$$p\left(\tau_{k,l}|\tau_{(k-1),l}\right) = \lambda e^{-\lambda\left(\tau_{k,l} - \tau_{(k-1),l}\right)} \tag{9}$$

where Λ and λ are respectively the cluster arrival rate and the ray arrival rate. Results in (17), (52) and (57) show a smaller ray-arrival rate but a larger cluster-arrival rate for UWB than in (16) for narrowband (see Table 4). Due to UWB's smaller ray-arrival rate but a larger cluster-arrival rate than narrowband, the reflection mechanism seems to be superior than other mechanisms like diffraction. In (71), a different model is suggested for BAN channels. Indeed, it is shown in (71) that a Weibull distribution provides a better fit to the measured data for the arrival rate statistics.

5.2 Multipath delay spread
5.2.1 Power delay profile
"power delay profile" is the small-scale averaged Instantaneous Power Delay Profile (IPDP) $P(\tau) = |h(\tau)|^2$ (13) where $h(\tau)$ is the multipath CIR defined in (2). The average IPDP is made over a local area (a neighborhood at the moving antenna's nominal location) for spatial small-scale or over a short period of time (mostly a delay resolution *bin*) for temporal small-scale. As shown in (17), (21), (22), (24), (25), (28), (31), (37), (38), (52) and (57), the power delay profile is related to the excess delay as

$$\overline{P(\tau)} = \overline{a_0^2}\, e^{-\frac{\tau}{\gamma}} \tag{10}$$

Parameters	UWB (17)	UWB (52)		UWB (57)		Narrowband (16)	Narrowband (16)
		LOS	NLOS	LOS	NLOS	*(Building 1)*	*(Building 2)*
$\frac{1}{\Lambda}$	45.5	27.4	40.1	39	17	16.8	17.3
$\frac{1}{\lambda}$	2.3	0.168	0.161	NA	NA	5.1	6.6
Γ_C	27.9	15.7	7.5	25.18	13	33.6	78.0
γ_r	84.1	16.5	12	12.2	18	28.6	82.2

Table 4. Narrowband and UWB Propagation Channels' Arrival Rates and Time Constants (ns)

where $\overline{a_0^2}$ denotes the first multipath's average power and γ symbolized power decay-rate. Moreover, the presented data in (17), (52) and (57) verify the double exponential decay law of (15):

$$\overline{P\left(T_l, \tau_{kl}\right)} = \overline{a_0^2} \cdot e^{-\frac{T_l}{\Gamma_C}} \cdot e^{-\frac{\tau_{kl}}{\gamma_r}} \tag{11}$$

where Γ_C and γ_r determine the inter-cluster (i.e. the earliest arrival of each cluster) decay-rate and the intra-cluster (i.e. arrival rays inside the clusters) decay-rate, respectively. The parameters Γ_C and γ_r are measured in (17), (52) and (57) via a manually, so-called visually-inspection, cluster selecting approach. Moreover, it is shown in (71) that a linear-exponential decay law could fit the measurement results better than the double-exponential one. In (71), a dual-slope model is suggested for the cluster arrival time and an exponential model for the ray arrival time. Table 5 summarizes the power delay profile empirical statistics presented in the open literature. From the UWB's power delay profile measurement results:

1. Referring to the double exponential model (11), UWB has smaller inter-cluster decay-rate comparing to narrowband (see Table 4). However, different results provided in (17), (52) and (57) do not show any trend comparing with the narrowband measurement (16). In fact, these parameter highly depend on the particular propagation channel setting. For instance, the inter-cluster decay-rate depends primarily on the building and the floor-plan itself but the intra-cluster decay-rate depends primarily on furnishing.

2. Measurements always have decreasing power decay-rate mean and standard deviation with more obstruction.

3. The delay profile's attenuation is inversely proportionate to the transmitter-receiver separation distance.

4. Reflection gives the strongest paths in power delay profile with a noticeable difference than other multipath mechanisms like diffraction; hence, other mechanisms such diffraction and diffuse scattering are minor and ignorable. Corridors, due to their LOS nature and unlike offices, have two clusters. The minor-cluster is a copy of the main-cluster, reflected off the opposite wall. Hence, the main-cluster's delay is inversely proportional to the transmitter-receiver separation distance.

5.2.2 Time dispersion

Time dispersion phenomenon, mainly due to multipath in an indoor propagation environment, can highly affect the transmitted data rate and reduce the capacity in a multi-user UWB communication system. The time dispersion of the UWB signals is usually presented by the first central moment and the square root of the second central moment of

Reference	Environment		$\overline{a_0^2}$	γ (ns)		τ_{RMS} (ns)		Notes
				Mean*	σ_γ	Mean*	σ_τ	
(17)	Residential	LOS/NLOS	0.2	28	NA	NA	NA	inter-cluster arrivals
			0.3	84	NA	NA	NA	intra-cluster arrivals
(21)-(22)	Office/Laboratory	LOS/NLOS	0.031	39.8	1.34	NA	NA	-
(24)-(25)	Office/Laboratory/ Corridor	LOS	NA	0.010	0.021	NA	NA	$\frac{1}{\gamma}$ statistics
		Soft-NLOS	NA	0.008	0.018	NA	NA	
		Hard-NLOS	NA	0.006	0.023	NA	NA	
(26)	ship compartment	NLOS	NA	NA	NA	82.6	NA	-
(27)	Residential	LOS	NA	NA	NA	4.7	2.3	-
		NLOS	NA	NA	NA	8.2	3.3	
(28)	Residential	LOS	0.23	0.83	1.06	NA	NA	$\frac{1}{\gamma}$ statistics
		NLOS	NA	0.89	1.03	NA	NA	
(31)	Residential	LOS	0.4	1.09	0.14	4.56	2.16	$\frac{1}{\gamma}$ statistics $d^\dagger = 5m$
		NLOS	0.1	1.07	0.12	8.98	4.23	
(37)	Laboratory	LOS	NA	34.36	2.16	12.3	0.5	$d = 5m$
		NLOS	NA	43.77	1.96	14.86	1.65	
(38)	Office	LOS/NLOS	NA	13.6	1.5	NA	NA	-
(41)	Office	NLOS	NA	NA	NA	6	5.22	$d = 5m$
(42)	office	NLOS	NA	NA	NA	20	NA	$d = 5m$
(45)	Office/Laboratory	LOS/NLOS	NA	NA	NA	14.3	2.8	-
	Reading Room	LOS	NA	NA	NA	19.9	1.8	
(46)-(47)	Laboratory/ Reading Room	LOS	NA	NA	NA	17.34	NA	{RX,TX}={OMNI,OMNI}
			NA	NA	NA	11.35	NA	{RX,TX}={OMNI,DIR}
			NA	NA	NA	7.71	NA	{RX,TX}={DIR,DIR}
(48)-(49)	Office/Classroom	LOS	NA	NA	NA	7	5	Biconical Antenna
		NLOS	NA	NA	NA	13	7	
		LOS	NA	NA	NA	3	2	TEM Horn Antenna
		NLOS	NA	NA	NA	10	5	
(50)-(51)	Office/Classroom	LOS	NA	NA	NA	8.5	NA	Biconical Antenna
		NLOS	NA	NA	NA	16.2	NA	
		LOS	NA	NA	NA	1.7	NA	TEM Horn Antenna
		NLOS	NA	NA	NA	7.1	NA	
(52)-(53)	Office	LOS	NA	15.7	NA	4.1	2.7	inter-cluster arrivals
		NLOS	NA	16.5	NA	9.9	5	
		LOS	NA	7.5	NA	4.1	2.7	intra-cluster arrivals
		NLOS	NA	12	NA	9.9	5	
(55)	Office	LOS	NA	NA	NA	6.6	NA	-
		NLOS	NA	NA	NA	9.3	NA	
(61)	Residential	LOS	NA	NA	NA	14	1	-
		NLOS	NA	NA	NA	35	6	
(64)	office	NLOS	NA	NA	NA	22.8	2.61	-
(65)	MRI	LOS/NLOS	NA	NA	NA	12	NA	Empty barrel
			NA	NA	NA	5	NA	Water-filled barrel
(68)	Underground Mine	LOS	NA	NA	NA	11.8	4.4	-
(70)	Underground Mine	LOS	NA	NA	NA	34	NA	-
		NLOS	NA	NA	NA	42	NA	
(72)	Office	NLOS	NA	NA	NA	3.2	NA	-
	Chamber	LOS	NA	NA	NA	1.5	NA	
(73)	Chamber	LOS	NA	NA	NA	1.5	NA	-
(74)	Office and Chamber	LOS/NLOS	NA	NA	NA	< 12	NA	-

* over all measurement
$\dagger$ d is the transmitter/receiver separation distance

Table 5. Multipath Delay Spread Statistics

PDP, i.e. the mean excess delay τ_m and the root mean square delay spread τ_{RMS}, defined as follows

$$\tau_{RMS} = \sqrt{\frac{\sum_i \overline{P(\tau_i)}(\tau_i - \tau_m)^2}{\sum_i \overline{P(\tau_i)}}}, \quad \tau_m = \frac{\sum_i \overline{P(\tau_i)}\tau_i}{\sum_i \overline{P(\tau_i)}} \tag{12}$$

Strong echoes with long delays contribute disproportionately to τ_{RMS} which is provided to communications performance. Most of the measurement campaigns employs the delay spread τ_{RMS} to evaluate the time dispersion of the UWB pulses. However, the ratio τ_m / τ_{RMS} is also suggested in (48), (49) and (58) as an effective criterion of the time dispersion. The delay spread τ_{RMS} is empirically found to depend on the environment structure such as the size and type of building and existence or absence of a clear LOS path (Table 5). UWB measurements (27), (37), (41)-(43), (46), (47) and (65) show that τ_{RMS} increases with increasing the transmitter-receiver separation distance. A Normal distribution is suggested by (27), (28), (31) and (45) to approximately fit the τ_{RMS} variations. Since both path-loss and τ_{RMS} increase with transmitter-receiver separation, a correlation between them can be investigated. It is shown in (27), (41) and (65) that the path-loss increases linearly as τ_{RMS} goes up. Moreover, the delay spread τ_{RMS} is more correlated with path-loss than with the transmitter-receiver separation, for offices. To summarize, the delay spread τ_{RMS}

1) is directly related to the transmitter-receiver separation.

2) has a higher mean and standard deviation for LOS than for NLOS.

3) is log-normal for office, laboratory, reading room and residential areas where office/laboratory and reading room have the same standard deviation as residence NLOS and LOS cases respectively.

4) is decreased when the antenna becomes more directive.

5) is more correlated with path-loss than with the transmitter-receiver separation for offices.

5.3 Temporal correlation
The temporal correlation coefficient is computed by spatially averaging the correlation between the power of the multipath components arriving to the same room at different excess delays.

$$\rho_{i,i+l} = \frac{E\left\{\left(P(\tau_i) - \overline{P(\tau_i)}\right)\left(P(\tau_{i+l}) - \overline{P(\tau_{i+l})}\right)\right\}}{\sqrt{E\left\{\left(P(\tau_i) - \overline{P(\tau_i)}\right)^2\right\}E\left\{\left(P(\tau_{i+l}) - \overline{P(\tau_{i+l})}\right)^2\right\}}} \tag{13}$$

where $E\{.\}$ denotes the spatial averaging over the local area. The temporal correlation coefficient $\rho_{i,i+l}$ is useful metric to reveal the resolvability of the CIR components in the impulse radio channels, i.e. UWB. It is enough to calculate the correlation coefficient between adjunct bins as this coefficient obviously decreases when the bins are in distance on the time axes.

Measurements (21), (22) and (45) show that the temporal correlation coefficient is below 0.2 and negligible for indoor UWB. This results in a resolvable fading for the UWB channels and benefits of using RAKE receivers for this kind of channels.

Parameters		UWB (36)	UWB (17)	NB (16) (*Building 1*)	NB (16) (*Building 2*)
σ		22.5°	38°	25.5°	21.5°

Table 6. Azimuth AOA Standard Deviation

6. Channel fading's spatial characteristics

6.1 The fading multipath angle of arrival

Obstacles like walls, floor, furniture and human-body throughout a building, causes AOA to spread over a wide range and frequency-dependent due to frequency-dependent reflection, scattering and/or diffraction (87). Welch *et al.* (40) present measurements that for open-areas (like auditorium) antenna-human intracts to create a very sharp null, but little effects for highly clustered environments (like office). Prettie *et al.* (36) show the signal's AOA is frequency-independent for LOS, but frequency-dependent for NLOS case. (36) gives a smaller range of the signal's AOA for residence than in (17) for offices (Table 6).

Cramer *et al.* (17) assume CIR (3) to be separable function of delay and azimuth: $h(\tau, \theta) = h_1(\tau) h_2(\theta)$ where $h_2(\theta) = \sum_{l=0}^{\infty} \sum_{k=0}^{\infty} \beta_{k,l} \delta(\theta - \Theta_l - \omega_{k,l})$ due to the angular deviation of the signal arrivals within a cluster from the cluster mean, over all AOA's within the cluster, does not increase as a function of delay. In (17), Θ_l is found using the above mathematical form to be approximately uniform over all angles and ω_{kl} is zero-mean Laplacian:

$$p(\omega_{kl}) = \frac{1}{\sqrt{2}\sigma} e^{-\left| \frac{\sqrt{2}\omega_{kl}}{\sigma} \right|} \tag{14}$$

with a standard deviation (σ) of 38° which is larger than for narrowband channels (Table 6). Moreover, the received signal magnitude $\beta_{k,l}$ is a Rayleigh-distributed random variable with a mean-square value which follows the double exponential (11) as $\overline{\beta_{k,l}^2} = \overline{P(T_l, \tau_{kl})}$ (17). To summarize:

1) The inter-cluster and intra-cluster azimuth AOA is uniform and Laplacian, respectively similar to narrowband (80). However, UWB has a wider ($\sigma = 38°$) Laplacian distribution for the intra-cluster azimuth AOA than narrowband.

2) AOA is frequency-independent for the LOS case but frequency-dependent for the NLOS case. Offices have wider ($\sigma = 38°$) AOA spread than household ($\sigma = 22.5°$).

3) The human-body has a little effect on AOA spread in dense environments but can create a very sharp nulls in open areas.

6.2 Received data's spatial correlation across the receiver's spatial aperture

The spatial dependence of the UWB channels is analytically demonstrated via a space-frequency correlation function between the received signals S_1 and S_2 (36)

$$R(\xi, \omega) = E\{S_1 S_2\} = J_0\left(\omega \frac{\xi}{c}\right) + \frac{2}{\beta} \sum_{\substack{n=-\infty \\ n \neq 0}}^{\infty} \frac{j^n}{n} J_n\left(\omega \frac{\xi}{c}\right) e^{jn\alpha_0} \sin\left(\frac{n\beta}{2}\right) \tag{15}$$

where $J_n(.)$, ξ, c, ω, β and α_0 represent respectively the nth-order Bessel function, the inter-antennas spacing distance, the speed of light, the wireless frequency, the angular range in which AOA is assumed to be uniformly distributed and the AOA mean. As (15) implies, the correlation length is less at higher frequency. To evaluate this result, Prettie *et al.* (36) have made a set of measurements along baselines of the antenna positions at several locations in

a residential environment. Although the measurement results (36) for NLOS case obey the space-frequency correlation function (15), they contradicts (15) for LOS case. Another set of spatial correlation measurements has been reported in (45). Li and Wong (45) show that

1. The average spatial correlation coefficient to depend on the excess delay. This averaging is made over all antenna separations and over all antenna locations for each environment. The correlation reaches the highest values for $\tau = 0$, but then decreases for larger excess delay ($\tau = 10ns$).

2. For the same excess delay, the open areas like high ceiling reading room present a higher correlation coefficient than office/laboratory environments.

3. The correlation coefficients for $\tau = 0$ are insensitive to the transmitter-receiver separation in offices/laboratories.

7. Channel fading's frequency-dependent characteristics

Due to a large bandwidth in UWB systems, the *frequency-dependent* aspects of the channels should be taken into account when we characterize and model the channel. There exist many frequency-relative components of the UWB communication channel which affect the traveling signal like the antenna pattern, materials in the propagation environment etc. In such a channel, not only the frequency selectivity of the environment, which is mainly due to the propagation effects e.g. multipath phenomenon, disperses the transmitted signal but also the transmit/receive antenna does. Hence, in an impulse radio channel these aspects must be evaluated separately as are done in this section.

7.1 Frequency selectivity
7.1.1 Transfer function characterization
Obstructions situated between the transmitter-receiver behave differently as different frequencies. To account for frequency-dependent electromagnetic behavior of scatterers, (1) is generalized in (8) to:

$$h\left(\tau, t, f_n\right) = \sum_{i=0}^{N(t,f_n)-1} a_n\left(\tau, t, f_n\right) e^{\theta(\tau,t,f_n)} \delta\left(\tau - \tau_n\left(t, f_n\right)\right)$$

where f_n is the nth operating frequency. In this model, the total bandwidth is divided into several sub-bands. The center frequency of the sub-bands is called operating frequency. Moreover, a distinct wideband model, considering the bandwidth, for each sub-band in UWB is proposed in (8). The above-mentioned frequency-dependency has been verified by the measurements in different ways. Measurements (24), (25), (36), (38), (43) and (79) show that the power gain decreases with increasing frequency; as for free-space propagation, the received power is proportional to f^{-2} (38), (42), (43), (79). Alvarez *et al.* (24), (25) show that the mean level, averaged spatially on the assigned local area (see Table 1), of channel transfer-function (in dB) is approximately :

$$10\log_{10}\overline{|H(f)|^2} = k_p\, e^{-\delta f} \tag{16}$$

where k_p and δ are respectively a constant and the frequency decaying factor which is highly dependent on the antenna specifications (24) and (25). In (24) and (25), it is indicated that the obstruction leads to faster power-decay per unit frequency (see Table 7). Kunisch and

Cases	δ (nS)	
	$E[\delta]^*$	$\sigma[\delta]^*$
LOS	1.01	0.18
Hard-NLOS	1.16	0.21
Soft-NLOS	1.36	0.24

* over all measurements in each case

Table 7. Frequency Decaying Factor δ Statistics

Pamp (38) have also investigated the frequency-dependent power-decay in offices, for both LOS and NLOS, which includes inside office NLOS and through-wall, i.e. hard-NLOS (24), cases. This frequency dependency is first studied in 1990s by using a physics-based approach (88)-(90). The NLOS case has a slightly steeper decay than LOS case for higher frequencies. The mean transfer-function magnitude, averaged spatially on the assigned local area (see Table 1), decays with increasing frequency:

$$\overline{|H(f)|} = k_a \left(\frac{f}{F} \right)^{-m} \tag{17}$$

where $|H(f)|$, $F = \sqrt{f_h f_l}$, k_a and m, are respectively the transfer-function magnitude, the center frequency with bandwidth $BW = f_h - f_l$ (see Table 1), the amplitude factor, and the power law exponent. For the LOS case $m \sim 2$ with little variance because of the strong paths' coherent summation. However, moving from LOS to NLOS results in a a large decrease in m, i.e. a slower decay with f. For the NLOS and between-offices cases, m has larger variance as the multipath become more obstructed, but has mean equal 1.2 for the between-offices cases 1 and 2, and 1.1 for NLOS case. For both LOS and NLOS cases, $\log_{10} k_a$ is almost linear dependent on m, i.e. one can write $m = \alpha \log_{10} k_a$ where α is real positive value. Substituting this linear function into (17) yields

$$\overline{|H(f)|} = k_a \left(\frac{f}{F} \right)^{-\alpha \log_{10} k_a} \tag{18}$$

As seen $\overline{|H(f)|}$ is no longer a linear function of k_a and therefore deviates from the simple power law. Lao *et al.* (44) show how the transmission coefficients with amplitude and phase information change for different building materials. According to their investigation, the amplitude decreases slightly with increased frequency for chip-wood material whereas for other materials: plaster board, calcium-silicate board and tempered-glass, the amplitude changes randomly. Meanwhile, it is shown in (44) that the variations in the transmission coefficient amplitude for tempered-glass are significant in the measured band. Moreover, the frequency behavior of the channel based on both vertical and horizontal polarization is measured in (44). For different polarizations, measurement results indicate that variation is not significant for plaster-board and Ca-Si board. For tempered glass, the variation is large than the other material in the most of the band. To summarize:

1. $\overline{|H(f)|^2}$ decays exponentially versus frequency. More clustered obstruction increases this decay rate.

2. $\overline{|H(f)|^2}$ deviates from the power law, with m having a larger variance with more obstruction. $\log_{10} k_\beta$ is approximately linearly related to m.

3. As expected, there is a strong relationship between the frequency-dependent parameters of channel and the materials used in the propagation environments.

7.2 Pulse-distortion
7.2.1 Physical description
As shown in Section 7.1, the UWB channel is seen to be frequency-selective. The phenomenon can be apparently explained by the Geometric Theory of Diffraction (GTD) in the frequency domain. However, from the electromagnetics point of view this frequency dependence is not surprising in the high-frequency radio propagation. This frequency dependency accordingly causes the pulse distortion in the time domain.

Investigations in (81)-(89) show a true picture for the UWB radio propagation which says if a pulse propagates along multiple rays or paths, the received pulses will experience different pulse distortion for different paths. In other words, the pulse waveforms of these received pulses are different. These different pulse-distortions are basically difficult to model by the state of the art statistical measurements. Hence, the physics-based deterministic behavior of the UWB pulse transmission needs to be considered to parameterize the pulse-distortion. In particular, recently the IEEE 802.15.4a channel model (90) adopted a special form of the channel model suggested in (87), (88) and (89). It cited two papers (88) and (89) for first introducing the frequency dependence in the channel model.

Although the pulse-distortion is not so severe for indoor applications such as those targeted by IEEE 802.15.3a, it could cause serious problems for IEEE 802.15.4a systems. To address these problems, (91) and (92) give a tutorial review of physics-based ultra-wideband signals and their optimum and sub-optimum detection. Moreover, in (91) a physics-based deterministic model, which captures a lot of properties that are not available in the existing statistical models such as the IEEE 802.15.4a model, is proposed for urban environments consisting of high-rise buildings.

7.2.2 Physic-based channel model
As discussed earlier in Section 2, the conventional multiptah channel model 2 is used to characterize the UWB channels. One reason for this use is that the wireless communications community is so accustomed to Turin's multipath model (14) which is designed for narrowband systems and where no pulse distortion is implicitly assumed for each individual path. To mathematically model the pulse-distortion phenomenon, a generalized version of the channel model (2) is proposed in (2):

$$h\left(\tau\right) = \sum_{l=1}^{L} A_l\left(\tau\right) h_l(\tau) * \delta\left(\tau - \tau_i\right) \tag{19}$$

where $h_l(\tau)$ represents an arbitrary function that has finite energy and $*$ symbolizes the convolution. Although, the statistical parameterization of $h_l(\tau)$ is a challenging task, it can be obtained through exact, experimental, numerical or/and asymptotic methods. For instance, $h_l(\tau)$ is obtained in (91) and (92) by asymptotic solutions of MaxwellŠs equations using GTD and Uniform Theory of Diffraction (UTD).

When the bandwidth of the employed transmission waveform goes infinite, the empirical channel models become invalid, since no measurement system has infinite bandwidth. The physics-based model of (19), however, is still valid. For practical applications, it is often sufficient to consider a special form (104)

$$H_l(j\omega) = (j\omega)^{-\alpha_l} \tag{20}$$

$$h_l(\tau) = \frac{1}{\Gamma(\alpha_l)} \tau^{-(1-\alpha_l)} U(\tau) \tag{21}$$

where α_l assumes a positive real value, e.g., $\alpha_l = 1/2$. The $U(\tau)$ is Heaviside's function. The Gamma function is defined as $\Gamma(z) = \int_0^\infty t^{z-1} e^{-t} dt$ where the real part of z is positive, i.e., $\Re(z) > 0$. The function $\tau^{-(1-\alpha_l)} U(\tau)$ has a singularity at $t = 0$, and must be treated as a generalized function. It is also regarded as an unbounded linear operator. In fact, it is the behavior of this operator at $t = 0$ that determines its singular value distribution. Note Eq.(20) is valid for infinite bandwidth or $\omega \to \infty$.

The total channel response for L paths is (104)

$$y(t) = \sum_{l=1}^{L} A_l (I^{\alpha_l} x(t)) * \delta(\tau - \tau_l) \tag{22}$$

where I^{α_l} can be treated as linear fractional integral operators. The fractional integral of the order α is defined as (108)

$$I^\alpha f(x) \equiv \frac{1}{\Gamma(\alpha)} \int_a^x \frac{f(t)}{(x-t)^{1-\alpha}} dt, \quad x > a \tag{23}$$

where $\alpha > 0$ is a real value. This integral is also called Riemann-Liouville fractional integral. The singular value decomposition (SVD) for I^{α_l} has given in (104). Based on its SVD, the capacity of the channel can be thus derived (104). A comprehensive theory is given in (104).

7.2.3 A time-reversal based system paradigm

Often it is more convenient to design a system, based on the channel cross-correlation

$$R_{hh}(t) = h_{forward}(-t; \mathbf{r}_0, \mathbf{r}_1) * h_{reverse}(t; \mathbf{r}_1, \mathbf{r}_0) \tag{24}$$

where $*$ denotes linear convolution, and $\mathbf{r}_0$ and $\mathbf{r}_1$ are the positions of the transceiver. If the channel is reciprocal (99), i.e.,

$$h_{forward}(t; \mathbf{r}_0, \mathbf{r}_1) = h_{reverse}(t; \mathbf{r}_1, \mathbf{r}_0), \tag{25}$$

then, $R_{hh}(t) = h(-t) * h(t)$ reduces to the auto-correlation of the channel impulse response, where the spatial positions are dropped for brevity. The use of auto-correlation simplifies the system design based on the channel impulse response only. One good analogy is the spread-spectrum system that uses the auto-correlation of the spreading codes. The channel impulse response can be viewed as a spatial code.

A so-called generalized RAKE is proposed to compensate for pulse distortion in (81) and (82). This approach however is complex to implement. A time-reversal based system paradigm that exploits the rich multipath and also mitigates pulse distortion is recently used (1), (81), (92)-(96).

The principle of time-reversal is based on the reciprocity of a time division duplexing (TDD) channel. The objective of the proposed research is to achieve (cost-effective and energy-efficient) time-reversal non-coherent reception as an alternative to coherent communications so that the rich multipath of a UWB channel can be fully exploited as a RAKE receiver does. The new system paradigm exploits the hostile, rich-multipath channel (time-reversed CIR) to achieve simplicity. Combining time-reversal with Multiple-Input

Multiple-Output (MIMO) that is the most promising approach to use spectrum and transmission power will further take advantage of spatial-temporal focusing (99)-(104). As a result, time-reversal trades the extremely huge bandwidth of impulse radio and the high power efficiency of MIMO for range extension, while retaining the low-power and low-cost of noncoherent energy-detection (97). This proposed new system paradigm will, through time-reversal, take advantage of the unique impulsive nature of the UWB signals (100; 101), a new dimension of a communication channel. The new frontier of impulsive time-reversal adds more degrees of freedom in exploiting the spatio-temporal dimensions of signals. Finally, the experimental demonstration of time reversal using a UWB system test-bed is carried out over the air recently (103).

7.2.4 Antenna impact

Different from a narrowband system, a UWB system must include antennas as pulse shaping filters. In addition, antennas act as different pulse shaping filters for different angles. Due to unpredictable arriving angles of multi-path, antennas *distort* or *shape* the transmitted pulses differently for different paths, as experimentally observed. Thus, both antennas and propagation environments suggest channel models of (19). The antenna impact on the pulse deformation is studied in (92) and (105). In particular, the antenna as the source of possible distortions on the matching and the radiation pattern is introduced in (105) and also a model for the input impedance and a model to have a representation of the radiation pattern is proposed in (105). The result in (106) show both pulse distortion in the time domain and frequency filtering in the frequency domain. Moreover, a procedure is proposed in (106) how to design a UWB antenna with minimum pulse distortion. The frequency-dependent delay of UWB antennas is investigated in (107). A strong agreement with the delay extracted via time-domain impulse response measurements is shown in (107).

8. Conclusions

In this paper, a comprehensive investigation on the UWB propagation channels measurements is presented. We have reviewed the essential parameters of the channel, like those used in physics-based models, based on a large number of measurement campaigns. These parameters include the important propagation effects in UWB communication channels: 1) Power-loss characteristics including *Path-Loss (PL)*, *large-scale fading* and *small-scale fading*. 2) Temporal characteristics including *multipath arrival rate*, *multipath delay spread (Power Delay Profile (PDP) and Root-Mean-Squared (RMS) delay spread)* and *temporal correlation*. 3) Spatial characteristics including *multipath Angle-of-Arrival (AOA)* and *spatial correlation across the receiver's spatial aperture*. 4) Frequency characteristics including *Frequency-Selectivity (FSE)* and *Pulse-Distortion (PD)*. We have supported this tutorial overview by a integrated summary on measurement results giving insights on UWB fading channel characterization and modeling.

9. Acknowledgment

10. References

[1] R. C. Qiu, X. Shen, M. Guizani and T. Le-Ngoc "Introduction," in *UWB Wireless Communications*, Editors: X. Shen, M. Guizani, R.C. Qiu, T. Le-Ngoc, John Wiley, 2006.

[2] R. C. Qiu, H. P. Liu and X. Shen, "Ultra-Wideband for Multiple Access," *IEEE Commun. Mag.*, pp. 2-9, Feb. 2005.

[3] R. C. Qiu, R. Scholtz and X. Shen," Ultra-Wideband Communications-A New Horizon," *IEEE Trans. Vehi. Tech.*, special issue editorial, Vol. 54, No. 5, pp. 1-3, Sept. 2005.

[4] X. Shen, M. Guizani, H. H. Chen, R. C. Qiu, and A. F. Molisch, "Ultrawideband Wireless Communications-Theory and Applications," *IEEE Jour. Selected Areas in Commun.*, special issue editorial, Second Quarter 2006.

[5] J. D. Taylor, *Ultra-Wideband Radar Technology*, Baco Raton, Florida, USA: CRC Press, 2001.

[6] W. Zhuang, X. Shen and Q. Bi, "Ultra-wideband wireless communications," *Wireless Commun. and Mobile Computing*, vol. 3, no. 6, pp. 663-685, 2003.

[7] A. F. Molisch, J. R. Foerster and M. Pendergrass, "Channel Models for Ultra wideband Personal Area Networks," *IEEEWireless Commun. Mag.*, vol. 10, no. 6, pp. 14-21, December 2003.

[8] Z. Irahhauten, H. Nikookar and G. Janssen, "An Overview of Ultra Wide Band Indoor Channel Measurements and Modeling," *IEEE Microwave and Wireless Components Letters*, vol. 14, no. 8, pp. 386-388, August 2004.

[9] A. F. Molisch, "Ultrawideband Propagation Channels-Theory, Measurement, and Modeling," *IEEE Trans. Vehi. Tech.*, vol. 54, no. 5, pp. 1528-1545, Sep. 2005.

[10] A. F. Molisch, D. Cassioli, C.-C. Chong, S. Emami, A. Fort, B.n Kannan, J. Karedal, J. Kunisch, H. G. Schantz, K. Siwiak and M. Z.Win, "A Comprehensive Standardized Model for Ultrawideband Propagation Channels," *IEEE Trans. Ant. Propag.*, vol. 54, no. 11, pp. 3151-3166, Nov. 2006.

[11] A. F. Molisch, "Ultrawideband propagation channels," Submitted to *Proceeding IEEE*, 2008.

[12] H. Hashemi, "The indoor radio propagation channel," *IEEE Proceedings*, vol. 3, no. 7, pp. 943-968, July 1993.

[13] T. S. Rappaport, *Wireless Communications: Principles and Practice*, Upper Saddle River, New Jersey, USA: Prentice Hall PTR, 1996.

[14] G. L. Turin, "Communication Through Noisy, Random-Multipath Channels," *IRE Convention Record*, part 4, pp. 154-166, 1956.

[15] A. A. M. Saleh and R. A. Valenzuela, "A statistical model for indoor multipath propagation," *IEEE Journal on Selected Areas in Commun.*, vol. 5, no. 2, pp. 128U˝ 137, Feb. 1987.

[16] Q. Spencer, B. Jeffs, M. Jensen and A. Swindlehurst, "Modeling the Statistical Time and Angle of Arrival Characteristics of an Indoor Multipath Channel," *IEEE Jour. on Selected Areas in Commun.*, Vol. 18, pp. 347-360, March 2000.

[17] R. J.-M. Cramer, R. A. Scholtz and M. Z. Win, " Evaluation of an Ultra-Wide-Band Propagation Channel ," *IEEE Trans. Ante. and Propag.*, vol. 50 , no. 5 , pp. 561-570, May 2002.

[18] M. Z. Win, R. A. Scholtz and M. A. Barnes, "Ultra-wide Bandwidth Signal Propagation for Indoor Wireless Communications," *IEEE Int. Conf. on Commun.*, pp. 56-60, 1997.

[19] R. J. Cramer, M. Z. Win and R. A. Scholtz, "Impulse radio multipath characteristics and diversity reception," *IEEE Int. Conf. on Commun.*, pp. 21-26, 1998.

[20] R. A. Scholtz, R. J. Cramer and M. Z. Win, "Evaluation of the Propagation Characteristics of Ultra-Wideband Communication Channels," *IEEE Ant. and Propag. Soc. Int. Symp.*, pp. 1650-1654, 1998.

[21] D. Cassioli, M. Z. Win and A. F. Molisch, "A Statistical Model for the UWB Indoor Channel," *IEEE Vehi. Technology Conf.*, pp. 1159-1163, Spring 2001.

[22] D. Cassioli, M. Z. Win and A. F. Molisch, "The Ultra-Wide Bandwidth Indoor Channel: From Statistical Model to Simulations," *IEEE Jour. on Selected Areas in Commun.*, vol. 20, no. 6, pp. 1247-1257, August 2002.

[23] M. Z. Win and R. A. Scholtz, "Characterization of Ultra-Wide Bandwidth Wireless Indoor Channels: a Communication-Theoretic View," *IEEE Jour. on Selected Areas in Commun.*, vol. 20, no. 9, pp. 1613-1627, December 2002.

[24] A. Alvarez, G. Valera, M. Lobeira, R. P. Torres and J. L. Garcia, "Ultra Wideband Channel Model for Indoor Environments," *IEEE Jour. of Commun. and Net.*, vol. 5, no. 4, pp. 1-10, December 2003.

[25] A. Alvarez, G. Valera, M. Lobeira, R. Torres and J. L. Garcia, "New Channel Impulse Response Model for UWB Indoor System Simulations," *IEEE Vehi. Tech. Conf.*, pp. 1-5, Spring 2003.

[26] D. R. J. Estes, T. B. Welch, A. A. Sarkady and H. Whitesel, "Shipboard Radio Frequency Propagation Measurements for Wireless Networks," *IEEE Military Commun. Conf.*, pp. 247-251, 2001.

[27] S. S. Ghassemzadeh, R. Jana, C. W. Rice, W. Turin and V. Tarokh, "A Statistical Path Loss Model for in-home UWB Channels," *IEEE Ultra Wideband Sys. and Tech. Conf.*, pp. 59-64, 2002.

[28] S. S. Ghassemzadeh, L. J. Greenstein, T. Sveinsson and V. Tarokh, " A Multipath Intensity Profile Model for Residential Environments," *IEEE Wireless Commun. and Net. Conf.*, pp. 150-155, 2003.

[29] S. S. Ghassemzadeh and V. Tarokh, "UWB Path Loss Characterization in Residential Environments," *IEEE Int. Microwave Symp. Digest* pp. 365-368, 2003.

[30] S. S. Ghassemzadeh and V. Tarokh, "UWB Path Loss Characterization in Residential Environments," *IEEE Radio Freq. Integ. Circuits Symp.*, pp. 501-504, 2003.

[31] S. S. Ghassemzadeh, L. J. Greenstein, T. Sveinsson and V. Tarokh, "An Impulse Response Model For Residential Wireless Channels," *IEEE Global Telecommun. Conf.*, pp. 1-5, 2003.

[32] S. S. Ghassemzadeh, R. Jana, C. W. Rice, W. Turin, and V. Tarokh, "Measurement and Modeling of an Ultra-Wide Bandwidth Indoor Channel," *IEEE Trans. Commun.*, vol. 52, no. 10, pp. 1786-1796, Oct. 2004.

[33] S. S. Ghassemzadeh, L. J. Greenstein, A. Kavcic, T. Sveinsson and V. Tarokh, " UWB Indoor Path Loss Model for Residential and Commercial Buildings.," *IEEE Vehi. Tech. Conf.*, pp. 3115-3119, Fall 2003.

[34] L. J. Greenstein, S. S. Ghassemzadeh, S.-C. Hong and V. Tarokh, "Comparison Study of UWB Indoor Channel Models," *IEEE Trans. Wireless Commun.*, vol. 6, no. 1, pp. 128-135, Jan. 2007.

[35] V. Hovinen, M. Hamalainen, and T. Patsi, "Ultra Wideband Indoor Radio Channel Models: Preliminary Results," *IEEE Ultra Wideband Sys. and Tech. Conf.*, pp. 75-79, 2002.

[36] C. Prettie, D. Cheung, L. Rusch and M. Ho, "Spatial Correlation of UWB Signals in a Home Environment ," *IEEE Ultra Wideband Sys. and Tech. Conf.*, pp. 65-69, 2002.

[37] J. Keignart and N. Daniele, "Subnanosecond UWB Channel Sounding in Frequency and Temporal Domain," *IEEE Ultra Wideband Sys. and Tech. Conf.*, pp. 25-30, 2002.

[38] J. Kunisch and J. Pamp, "Measurement Results and Modeling Aspects for the UWB Radio Channel," *IEEE Ultra Wideband Sys. and Tech. Conf.*, pp. 19-23, 2002.

[39] H. Luediger, B. Kull, S. Zeisberg and A. Finger, "An Ultra-Wideband Indoor NLOS Radio Channel Amplitude Probability Density Distribution," *IEEE Int. Symp. on Spread Spect. Tech. and Applic.*, pp. 68-72, 2002.

[40] T. B. Welch, R. L. Musselman, B. A. Emessiene, P. D. Gift and D. K. Choudhury, "The Effects of the Human Body on UWB Signal Propagation in an Indoor Environment," *IEEE Jour. Selected Areas in Commun.*, vol. 20, no. 9, pp. 1778-1782, Dec. 2002.

[41] S. M. Yano, "Investigating the Ultra-Wideband Indoor Wireless Channel," *IEEE Vehi. Tech. Conf.*, pp. 1200-1204, Spring 2002.

[42] K. Siwiak, H. Bertoni and S. M. Yano, "Relation Between Multipath and Wave Propagation Attenuation," *IEE Elect. Letters*, vol. 39, no. 1, pp. 142-143, Jan. 2003.

[43] K. Siwiak and D. Mckeown, *Ultra-Wideband Radio Technology*, West Sussex, England: John Wiley and Sons, 2004.

[44] R.-R. Lao, J.-H. Tarng and C. Hsiao, "Transmission coefficients measurement of building materials for UWB systems in 3 -10 GHz," *IEEE Vehi. Tech. Conf.*, pp. 11-14, Spring 2003.

[45] Q. Li and W. S. Wong, "Measurement and Analysis of the Indoor UWB Channel," *IEEE Vehi. Tech. Conf.*, pp. 1-15, Fall 2003.

[46] J. A. Dabin, Ni Nan, A. M. Haimovich, E. Niver, H. Grebel, "The Effects of Antenna Directivity on Path Loss and Multipath Propagation in UWB Indoor Wireless Channels," *IEEE Ultra Wideband Sys. and Tech.*, pp. 305-309, 2003.

[47] J. A. Dabin, A. M. Haimovich and H. Grebel, "A Statistical Ultra-Wideband Indoor Channel Model and the Effects of Antenna Directivity on Path Loss and Multipath Propagation," *IEEE Jour. Selected Areas in Commun.*, vol. 24, no. 4, pp. 752-758, April 2006.

[48] A. H. Muqaibel, A. Safaai-Jazi, A. M. Attiya, A. Bayram and S. M. Riad, "Measurement and Characterization of Indoor Ultra-Wideband Propagation," *IEEE Ultra Wideband Sys. and Tech. Conf.*, pp. 295-299, 2003.

[49] A. Muqaibel, A. Safaai-Jazi, A. Attiya, B. Woerner and S. Riad, "Path-Loss and Time Dispersion Parameters for Indoor UWB Propagation," *IEEE Trans. Wireless Commun.*, vol. 5, no. 3, pp. 550-559, March 2006.

[50] R. M. Buehrer, W. A. Davis, A. Safaai-Jazi and D. Sweeney, "Characterization of the Ultra-wideband Channel," *IEEE Ultra Wideband Sys. and Tech. Conf.*, pp. 26-31, 2003.

[51] B. M. Donlan, D. R. McKinstry and R. M. Buehrer, "The UWB Indoor Channel: Large and Small Scale Modeling," *IEEE Trans. Wireless Commun.*, vol. 5, no. 10, pp. 2863-2873, Oct. 2006.

[52] P. Pagani and P. Pajusco, "Experimental Analysis of the Ultra Wideband Propagation Channel Over the 3.1 GHz - 10 GHz Frequency Band," *IEEE Int. Symp. on Personal, Indoor and Mobile Radio Commun.*, pp. 1-5, 2006.

[53] P. Pajusco and P. Pagani, "Frequency Dependence of the UWB Indoor Propagation Channel," *Second Euopean Conf. Ant. Propag.*, pp. 1-7, 2007.

[54] Y. Suzuki and T. Kobayashi, "Ultra Wideband Signal Propagation in Desktop Environments," *IEEE Ultra Wideband Sys. and Tech. Conf.*, pp. 493-497, 2003.

[55] Z. Irahhauten, J. Dacuna, G. J. M. Janssen and H. Nikookar, "UWB Channel Measurements and Results for Wireless Personal Area Networks Applications," *European Conf. on Wireless Tech.*, pp. 189-192, 2005.

[56] A. Durantini, W. Ciccognani and D. Cassioli, "UWB Propagation Measurements by PN-Sequence Channel Sounding," *IEEE Int. Conf. on Commun.*, pp. 3414-3418, 2004.

[57] D. Cassioli and A. Durantini, "A Time-domain Propagation Model of the UWB Indoor Channel in the FCC-compliant Band 3.6 - 6 GHz based on PN-sequence Channel Measurements," *IEEE Vehic. Tech. Conf.*, pp. 213-217, Spring 2004.

[58] W. Ciccognani, A. Durantini and D. Cassioli, "Time Domain Propagation Measurements of the UWB Indoor Channel Using PN-Sequence in the FCC-Compliant Band 3.6U˝ 6 GHz," *IEEE Trans. Ant. Propag.*, vol. 53, no. 4, pp. 1542-1549, April 2005.

[59] D. Cassioli, A. Durantini and W. Ciccognani, "The role of path loss on the selection of the operating bands of UWB systems," *IEEE Int. Symp. on Personal, Indoor and Mobile Radio Commun.*, pp. 2787-2791, 2004.

[60] A. Durantini and D. Cassioli, "A Multi-Wall Path Loss Model for Indoor UWB Propagation," *IEEE Vehic. Tech. Conf.*, pp. 30-34, Spring 2005.

[61] C.-C. Chong, Y. Kim and S.-S. Lee, "UWB Indoor Propagation Channel Measurements and Data Analysis in Various Types of High-Rise Apartments," *IEEE Vehic. Tech. Conf.*, pp. 150-154, Fall 2004.

[62] A. Bayram, A. M. Attiya, A. Safaai-Jazi and S. M. Riad, "Frequency-Domain Measurement of Indoor UWB Propagation," *IEEE Ant. and Propag. Soc. Symp.*, pp. 1303-1306, 2004.

[63] B. Alavi, N. Alsindi and Kaveh Pahlavan, "UWB Channel Measurements for Accurate Indoor Localization," *IEEE Military Commun. Conf.*, pp. 1-7, 2006.

[64] K. Leechaikitjaroen, S. Promwong, P. Supanakoon, S. Chensirikul and S. Kaewmechai, "Indoor Measurement Results of UWB Impulse Radio for Shot-Range Wireless Systems with RMS Delay Spread and Path Loss," *IEEE Int. Symp. on Commun. and Info. Tech.*, pp. 684-688, 2005.

[65] N. A. Alsindi, D. Birru and D. Wang, "Ultra-Wideband Channel Measurement Characterization for Wireless Magnetic Resonance Imaging Applications," *41th Annual Conf. on Info. Scien. and Sys.*, pp. 135-140, 2007.

[66] S. Bories, A. Sibille and C. Roblin, "UWB Indoor Channel Measurement Study," *IEEE Int. Workshop Ant. tech., Small Ant. and Novel Metamaterials*, pp. 466-469, 2005.

[67] A. Chehri, O. Fortier, H. Aniss and P.-M. Tardif, "UWB Spatial fading and Small Scale Characterization in Underground Mines," *IEEE 23th Biennial Symp. Commun.*, pp. 213-218, 2006.

[68] A. Chehri, O. Fortier and P.-M. Tardif, "Measurement and Modeling of Line-of-Sight UWB Channel in Underground Mines," *IEEE Global Telecommun. Conf.*, pp. 1-5, 2006.

[69] A. Chehri, O. Fortier and P.-M. Tardif, "Large Scale Fading and Time Dispersion Parameters of UWB Channel in Underground Mines," Accepted for publication in *Iint. Jour. Ant. Propag.*, 2008.

[70] H. I. Volos, C. R. Anderson, W. C. Headley, R. M. Buehrer, C. R. C. M. da Silva and A. Nieto, "Preliminary UWB Propagation Measurements in an Underground Limestone Mine," *IEEE Global Telecommun. Conf.*, pp. 3770-3774, 2007.

[71] A. Fort, J. Ryckaert, C. Desset, P. De Doncker, P. Wambacq and L. Van Biesen, "Ultra-Wideband Channel Model for Communication Around the Human Body," *IEEE Jou. Selec. Area Commun.*, vol. 24, no. 4, pp. 927-933, Apr. 2006.

[72] T. Zasowski, F. Althaus, M. Stager, A. Wittneben, G. Troster, "UWB for Noninvasive Wireless Body Area Networks: Channel Measurements and Results," *IEEE Conf. Ultra Wideband Sys. Tech.*, pp. 285-289, 2003.

[73] T. Zasowski, G. Meyer, F. Althaus and A. Wittneben, "UWB Signal Propagation at the Human Head," *IEEE Trans. Microwave Theory Tech.*, vol. 54, no. 4, pp. 1836-1845, Apr. 2006.

[74] Y. P. Zhang and Q. Li, "Performance of UWB Impulse Radio With Planar Monopoles Over On-Human-Body Propagation Channel for Wireless Body Area Networks," *IEEE Trans. Ant. Propag.*, vol. 55, no. 10, pp. 2907-2914, Oct. 2007.

[75] FCC document 00-163, "Revision of part 15 commission rules ET Docket No. 98-153 regarding UWB transmission systems", adopted 5-10-200

[76] M. Lott and I. Forkel, "A Multi-Wall-and-Floor Model for Indoor Radio Propagation," *IEEE Vehi. Tech. Conf.*, pp. 464-468, Spring 2001.

[77] S. Obayashi and J. Zander, "A Body-Shadowing Model for Indoor Radio Communication Environments," *IEEE Trans. Ant. Propag.*, vol. 46, no. 6, pp. 920-927, June 1998.

[78] A. Abdi and M. Kaveh, "Level Crossing Rate in Terms of the Characteristic Function: A New Approach for Calculating the Fading Rate in Diversity Systems," *IEEE Trans. Commun.*, vol. 50, no. 9, pp. 1397-1400, Sep. 2002.

[79] M. Ghavami, L. B. Michael and R. Kohno, *Ultra Wideband Signals and Systems in Communications Engineering*, West Sussex, England: John Wiley and Sons, 2004.

[80] Q. Spencer, M. Rice, B. Jeffs and M. Jensen, "A statistical model for angle of arrival in indoor multipath propagation," *IEEE Vehi. Tech. Conf.*, pp. 1415-1419, Spring 1997.

[81] R. C. Qiu, Q. Zhang and N. Guo, "A Generalized RAKE Receiver for UWB Communications," *IEEE Jour. on Selected Areas in Commun.*, to appear, 2006.

[82] R. C. Qiu, "Pulse Propagation and Detection," *UWB Wireless Communications*, Editors: X. Shen, M. Guizani, R.C. Qiu, T. Le-Ngoc, John Wiley, 2006.

[83] R. C. Qiu, "UWB Wireless Communications," *Design and Analysis of Wireless Networks*, edited by Yi Pan and Yang Xiao, Nova Science Publishers, 2004.

[84] R. C. Qiu, Chapter "UWB Pulse Propagation Processes," *UWB Wireless Communications - A Comprehensive Overview*, Editor: Thomas Kaiser (Germany), Eurasip, 2005.

[85] R. C. Qiu, "A Generalized Time Domain Multipath Channel and Its Application in Ultra Wideband (UWB) Wireless Optimal Receiver Design: Part III System Performance Analysis," *IEEE Trans. Wireless Commun.*, to appear.

[86] R. C. Qiu, "A Generalized Time Domain Multipath Channel and its Application in Ultra Wideband (UWB) Wireless Optimal Receiver Design: Part II Wave- Based System Analysis," *IEEE Trans. Wireless Commun.*, vol. 3, no. 11, pp. 2312-2324, Nov. 2004.

[87] R. C. Qiu, "A Study of the Ultra-Wideband Wireless Propagation Channel and Optimum UWB Receiver Design," *IEEE Jour. on Selected Areas in Commun.s*, vol. 20, no. 9, pp. 1628-1637, December 2002.

[88] R. C. Qiu and I.T. Lu, "Multipath Resolving with Frequency Dependence for Broadband Wireless Channel Modeling," *IEEE Trans. Vehi. Tech.*, vol. 48, no. 1, pp. 273-285, Jan. 1999.

[89] R. C. Qiu and I-Tai Lu, "Wideband Wireless Multipath Channel Modeling with Path Frequency Dependence," *IEEE Int. Conf. on Commun.*, pp. 277 - 281, 1996.

[90] Channel Model Subcommittee, "Status of models for UWB propagation channel," *IEEE 802.15.4a Channel Model (Final Report)*, http://www.ieee802.org/15/pub/TG4a.html, August 2004.

[91] R. C. Qiu, C. Zhou and Q. Liu, "Physics-Based Pulse Distortion for Ultra-Wideband Signals," *IEEE Trans. Vehi. Tech.*, vol. 54, no. 5, September 2005.

[92] R. C. Qiu, "Optimum and Sub-Optimum Detection of Physics-Based Ultra-Wideband SignalsU° A Tutorial Review," *Dynamics of Continuous, Discrete and Impulsive Systems – An International Journal for Theory and Applications (Series B): Special Issue on UWB Wireless Communications*, vol. 12, no. 3, June 2005.

[93] R. C. Qiu, C. M. Zhou, N. Guo, and J. Q. Zhang, "Time Reversal with MISO for Ultra-Wideband Communications: Experimental Results," *IEEE Ant. and Wireless Propag. Letters*, Vol. 5, pp. 269-273, 2006.

[94] N. Guo, R. C. Qiu, and B. M. Sadler, "Reduced-Complexity Time Reversal Enhanced Autocorrelation Receivers Considering Experiment-Based UWB Channels", *IEEE Trans. Wireless Commun.*, vol. 6, no. 12, December 2007.

[95] N. Guo, R. C. Qiu, and B. M. Sadler, "An Ultra-Wideband Autocorrelation Demodulation Scheme with Low-Complexity Time Reversal Enhancement," *IEEE Military Commun. Conf.*, Atlantic City, NJ, Oct. 17-20, 2005.

[96] R. C. Qiu, C. Zhou, N. Guo, and J. Q. Zhang, "Time Reversal with MISO for Ultra-Wideband Communications: Experimental Results," Invited Paper, *IEEE Radio and Wireless Symp.*, San Diego, CA, 2006.

[97] R. C. Qiu, "Time Reversed MIMO for UWB Communications," *2006 Workshop on Short Range UWB Radio Systems*, Santa Monica, CA, April 12, 2006.

[98] C. Zhou and R. C. Qiu, "Spatial Focusing of Time-Reversed UWB Electromagnetic Waves in a Hallway Environment," *IEEE 38th Southeastern Symp. on Sys. Theory*, Cookeville, TN, March 2006.

[99] R. C. Qiu, C. Zhou, J. Q. Zhang, and N. Guo. "Channel Reciprocity and Time-Reversed Propagation for Ultra-Wideband Communications". In *IEEE AP-S International Symposium on Antennas and Propagation, Honolulu, Hawaii*, vol. 1 (June, 2007).

[100] C. Zhou, N. Guo, and R. C. Qiu. "Experimental Results on Multiple-Input Single-Output (MISO) Time Reversal for UWB Systems in an Office Environment". In

IEEE Military Communications Conference (MILCOM07), Orlando, Florida (October, 2007).

[101] C. M. Zhou, B. M. Sadler, and R. C. Qiu. "Performance Study on Time Reversed Impulse MIMO for UWB Communications Based on Realistic Channels". In *IEEE Conf. Military Comm., MILCOM'07*, Orlando, FL (October, 2007).

[102] C. M. Zhou, N. Guo, and R. C. Qiu, "A Study on Time Reversed Impulse UWB with Multiple Antennas Based on Measured Spatial UWB Channels", *IEEE Trans. Vehicular Tech.* (submitted for publication, 2008).

[103] R. C. Qiu and et al. "Time-Reversal Based Range Extension Technique for Ultra-Wideband (UWB) Sensors and Applications in Tactical Communications and Networking". (Quarterly) Technical Report to Office of Naval Research (ONR) Contract No. N00014-07-1-0529,, Tennessee Tech University, Cookeville, TN (April, 2008). 69 pages.

[104] R. C. Qiu, "Physics-Based Channel Models and Fundamental Limits", Book Chapter, "Underwater Acoustic Sensor Networks", Edited by Prof. Yang Xiao, to be published by Auerbach Publications, Taylor & Francis Group, ISBN-10: 1420067117, ISBN-13:978-1420067118, 2008

[105] I. Pele, A. Chousseaud and S. Toutain, "Simultaneous Modeling of Impedance and Radiation Pattern Antenna for UWB Pulse Modulation," *IEEE Ant. and Propag. Soc. Symp.*, pp. 1871-1874, 2004.

[106] W. Lauber and S. Palaninathan, "Ultra-Wideband Antenna Characteristics and Pulse Distortion Measurements," *IEEE Int. Conf. on Ultra-Wideband*, pp. 617-622, 2006.

[107] J. D. McKinney, D. Peroulis and A. M. Weiner, "Time-Domain Measurement of the Frequency-Dependent Delay of Broadband Antennas," *IEEE Trans. Ant. Propag.*, vol. 56, no. 1, pp. 39-47, Jan. 2008.

[108] K. S. Miller and B. Ross, *An Introduction to the Fractional Calculus and Fractional Differential Equations.* (Wiley, NY, 1993).

Propagation Models for the Characterization of the Indoor UWB Channel

Francisco Saez de Adana
Universidad de Alcala
Spain

1. Introduction

Ultra-wideband (UWB) technology has developed rapidly over the past several years. This technology is especially attractive in high-data-rate and short-range wireless communications. These applications make UWB technology suitable for indoor mobile communication applications, such as wireless personal-area networks (WPAN). This interest has motivated the study of the propagation of the UWB signals in indoor environments as an important task for the implementation of WPANs.

In the last decades, significant effort has been focused on the characterization of the indoor channel for narrowband systems. Statistical (Motley & Keenan, 1990; Saleh & Valenzuela, 1987; Seidel & Rappaport, 1992; Tornevik et al., 1993) and deterministic (Lauer et al., 1984; Saez de Adana et al., 2000; Tarng et al., 1997; Whitman et al., 1995) models have been used most frequently in these studies. The statistical models are based on the obtention of closed formulas to characterize the propagation channel. These formulas are derived from the data obtained from measurement campaigns in different environments. Alternatively, the deterministic models are based mostly on the use of ray-tracing techniques (Saez de Adana et al., 2000; Tarng et al., 1997; Whitman et al., 1995) to predict the multipath phenomena and the Uniform Theory of Diffraction (UTD) technique (Kouyoumjian & Pathak, 1974) to calculate the received power or the propagation losses. However, the features of the UWB systems (with bandwidth in the range of GHz) render the conventional narrowband propagation models, both statistical and deterministic, inapplicable. These models are based primarily on frequency-domain analysis, while UWB requires a time-domain analysis due to its wide bandwidth. Therefore, special models must be used to predict the signal propagation in UWB systems. Although the number of statistical models developed for UWB systems is not as extensive as that for narrowband systems, some recent examples can be found in the literature (Cassioli et al., 2001, 2002, Dabin et al., 2006; Molisch et al., 2006). These models have been obtained, as in the case of narrowband systems, by obtaining closed expressions that fit the behavior of the received signal measured in several locations in a measurement campaign.

Regarding the deterministic models, frequency-domain UTD can be applied, performing an analysis at several frequencies and obtaining the time response using an Inverse Fourier Transform. However, this procedure is computationally inefficient in comparison to direct analysis in the time domain. Instead, the Time-Domain Uniform Theory of Diffraction (TD-UTD) was developed to obtain a solution in the time domain for the reflection and the

diffraction of a transient electromagnetic wave. The inclusion of the multipath phenomena in this theory and the analysis in the TD makes this technique suitable for UWB applications. TD-UTD was first developed by Veruttipong and Kouyoumjian (Veruttipong & Kouyoumjian, 1979), who applied the inverse Laplace transform to the frequency-domain UTD formulation. Later, Rousseau and Pathak (Rousseau & Pathak, 1995) presented closed-form solutions for the diffraction by an edge by modifying the formulation presented in (Veruttipong & Kouyoumjian, 1979). The results obtained in (Rousseau & Pathak, 1995) can be directly applied to develop a method for the calculation of the indoor propagation in UWB systems.

In this chapter, the formulation of both a statistical approach and a deterministic approach are presented. The statistical approach has been selected from the available literature because it seems very suitable for the case of UWB systems. The deterministic formulation was developed by the author of this chapter and consists of modifying the formulation presented in (Rousseau & Pathak, 1995) to introduce the contribution of lossy materials present in the indoor environment to reflection, transmission and diffraction. The goal is to obtain the reflection, transmission or diffraction coefficients using an Analytical Time Transform (ATT) from their expressions in the frequency domain. In addition, multiple interactions are also considered in this approach. These interactions include multiple reflections and transmissions and the interactions between reflected and diffracted rays. Thus, both reflection-diffraction and diffraction-reflection interactions are included. These interactions, which are obtained in the frequency domain from the product of the coefficients involved in the propagation mechanisms, can also be computed in the time domain by convolving those coefficients instead.

The deterministic approach is completed, including the analysis of a real site, which proves the validity of the model and its ability to analyze realistic environments. Some experimental measurements and comparisons with the predictions of the proposed model are presented in this chapter.

2. Statistical approach

The statistical models are obtained based on the statistical analysis of the experimental data. Some measurements are performed for a given scenario and a propagation model is obtained based on these results after the statistical analysis. In this chapter, one of these statistical models is presented. This model was obtained from measurements performed in a typical modern office building (Cassioli et al., 2002).

This propagation model provides all the parameters and distributions necessary to obtain the power delay profile. First, the attenuation of the received power satisfies the following expression, dependent on the distance:

$$L(dB) = \begin{cases} 20.4 \log\left(\dfrac{d}{d_0}\right) & d \leq 11 \text{ m} \\[2mm] -56 + 74 \log\left(\dfrac{d}{d_0}\right) & d > 11 \text{ m} \end{cases} \tag{1}$$

The small-scale average-power delay profile (SSA-PDP) accomplishes the following expression:

$$g(\tau) = \sum_{k=1}^{N_{bins}} G_k \delta(\tau - \tau_k) \tag{2}$$

where $g(\tau)$ is the average energy received with delay τ, normalized to the total energy at one meter, and N_{bins} is the number of bins selected in the observation window. The idea of quantizing the delay axis into bins comes from (Rappaport et al., 1991). In that way, the local PDP is obtained by integrating the received power within each bin. This local PDP is expressed in terms of the pairs $\{G_k, \tau_k\}$, where G_k is the ratio between the energy received at a distance d and the total energy received at one meter. This value is called the energy gain and is obtained over a bin with size $\Delta\tau$ beginning with a delay $\tau_k = (k-1)\Delta\tau$. In the model proposed in (Cassioli et al., 2002), $\Delta\tau = 2$ ns.

An exponential decay from the second bin can be assumed. Therefore,

$$g(\tau) = G_1 \delta(\tau - \tau_1) + \sum_{k=2}^{N_{bins}} G_2 \delta(\tau - \tau_k) e^{\frac{-(\tau_k - \tau_2)}{\varepsilon}} \tag{3}$$

where ε is the decay constant of the SSA-PDP.

The total average energy received in the observation interval T is

$$G_{tot} = \int_0^T g(\tau) d\tau = G_1 + \sum_{k=2}^{N_{bins}} G_2 e^{\frac{-(\tau_k - \tau_2)}{\varepsilon}} \tag{4}$$

Because the second term of expression (4) is a geometric series,

$$G_{tot} = G_1 \left[1 + rF(\varepsilon) \right] \tag{5}$$

where $r = \dfrac{G_2}{G_1}$ is the power ratio and

$$F(\varepsilon) = \frac{1 - e^{\frac{-(N_{bins} - 1)\Delta\tau}{\varepsilon}}}{1 - e^{\frac{-\Delta\tau}{\varepsilon}}} \tag{6}$$

A lognormal distribution around the mean value of the path loss can be considered:

$$G_{tot} = LN(-L; 4.3) \tag{7}$$

The average energy gains are obtained by inverting (5)

$$G_k = \begin{cases} \dfrac{G_{tot}}{1 + rF(\varepsilon)} & \text{for } k = 1 \\[4mm] \dfrac{G_{tot}}{1 + rF(\varepsilon)} re^{\frac{-(\tau_k - \tau_2)}{\varepsilon}} & \text{for } k = 2, \ldots, N_{bins} \end{cases} \tag{8}$$

and therefore

$$g(\tau) = \frac{G_{tot}}{1 + rF(\varepsilon)} \left\{ \delta(\tau - \tau_1) + \sum_{k=2}^{N_{bins}} \left[re^{\frac{-(\tau_k - \tau_2)}{\varepsilon}} \right] \delta(\tau - \tau_k) \right\} \tag{9}$$

This model characterizes the local PDP by the pairs $\{G_k, \tau_k\}$, as mentioned above, with $\tau_k = (k-1)\Delta\tau$ and G_k generated by a superposition of large- and small-scale statistics.

The first step is to obtain G_{tot} from (12). Next, the power ratio r and the decay factor ε are generated. These two values are treated as stochastic variables, modeled as lognormal variables according to the experience for narrowband systems shown in (Hashemi, 1979). The shape of the distribution is obtained from the measured data. Therefore,

$$\varepsilon = LN(16.1; 1.27) \qquad (10)$$

$$\varepsilon = LN(16.1; 1.27) \qquad (11)$$

and the width of the observation window is T=5.

With these parameters, SSA-PDP is completely specified by (9) and the local PDP can be obtained by obtaining the normalized energy gains $G_k^{(i)}$ of every bin k and every location i. $G_k^{(i)}$ are considered to be gamma-distributed independent variables with an average given by (8) and values m_k generated as independent truncated Gaussian variables

$$m_k = TN(\mu_m(\tau_k); \sigma_m^2(\tau_k)) \qquad (12)$$

with

$$\mu_m(\tau_k) = 3.5 - \frac{\tau_k}{73} \qquad (13)$$

$$\sigma_m^2(\tau_k) = 1.84 - \frac{\tau_k}{160} \qquad (14)$$

3. Deterministic approach

The classical UTD in the frequency domain obtains the field at an observation point inside an indoor environment as the sum of the contribution of different rays. These rays that started from the source reached that observation point either directly or after one or several reflections, diffractions, transmissions or combinations of these effects. Accordingly, the TD-UTD analytical impulse response in that environment can be obtained from an ATT, which consists of a one-sided Inverse Fourier Transform (IFT) of the frequency response, as can be seen in (Rousseau & Pathak, 1995; Veruttipong & Kouyoumjian, 1979), and can be written as

$$\overset{+}{f_I}(t) = \overset{+}{f_I^i}(t) + \overset{+}{f_I^r}(t) + \overset{+}{f_I^t}(t) + \overset{+}{f_I^d}(t) + \overset{+}{f_I^{mr}}(t) + \overset{+}{f_I^{mt}}(t) + \overset{+}{f_I^{rd}}(t) + \overset{+}{f_I^{dr}}(t) \qquad (15)$$

where $\overset{+}{f_I^i}(t)$, $\overset{+}{f_I^r}(t)$, $\overset{+}{f_I^t}(t)$, $\overset{+}{f_I^d}(t)$, $\overset{+}{f_I^{mr}}(t)$, $\overset{+}{f_I^{mt}}(t)$, $\overset{+}{f_I^{rd}}(t)$ and $\overset{+}{f_I^{dr}}(t)$ are the analytical signal representations for the direct field $\overset{+}{f_I^i}(t)$, reflected field $\overset{+}{f_I^r}(t)$, transmitted field $\overset{+}{f_I^t}(t)$, diffracted field $\overset{+}{f_I^d}(t)$, multiply reflected field $\overset{+}{f_I^{mr}}(t)$, multiply transmitted $\overset{+}{f_I^{mt}}(t)$, reflected-diffracted-field $\overset{+}{f_I^{rd}}(t)$ and diffracted-reflected field $\overset{+}{f_I^{dr}}(t)$, respectively. Therefore, the impulse response shown in equation (15) includes all multipath phenomena, as mentioned previously. Each term in equation (15) will be described in the following sections.

3.1 Direct field

The contribution of the direct field to the impulse response is obtained as the ATT of the usual Geometrical Optics (GO) incident field and can be expressed by the following equation (Rousseau & Pathak, 1995):

$$\overset{+}{f_I^i}(t) = E_0^i \left| A_i(s_i) \right| \overset{+}{\delta}(t - s_i / c) \tag{16}$$

where E_0^i is the initial field value, which is constant with time and frequency, $A_i(s_i)$ is the spreading (or spatial divergence) factor for the direct ray, and s_i is the distance between the source and the observation point. The spreading factor for the direct ray is given by (Rousseau & Pathak, 1995):

$$A_i(s_i) = \sqrt{\frac{\rho_1^i \rho_2^i}{(\rho_1^i + s_i)(\rho_2^i + s_i)}} \tag{17}$$

where ρ_1^i and ρ_2^i are the principal radii of curvature of the incident wavefront at the observation point (see Figure 1).
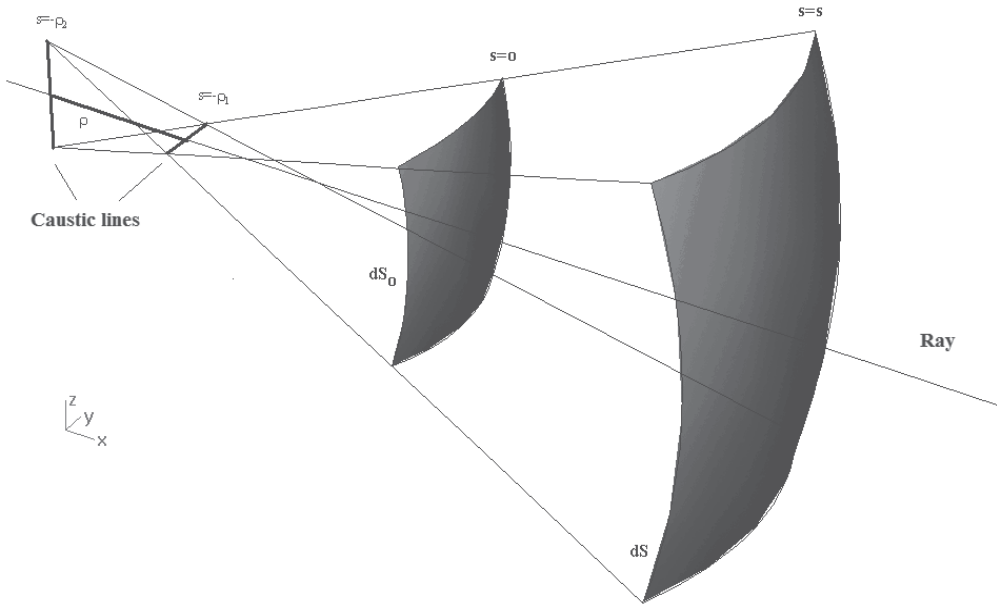
Fig. 1. Incident-ray wavefront

3.2 Reflected field

Similar to the case of the direct field, the contribution of the reflected field to the impulse response is obtained from the ATT of the classical GO expression in the frequency domain by the following equation:

$$\overset{+}{f_I^r}(t) = E_0^i \overset{+}{\bar{R}}(t - s_i / c - s_r / c) \left| A_i(s_i) A_r(s_r) \right| \tag{18}$$

where s_i is, in this case, the distance between the source and the reflection point and s_r is the distance between the reflection point and the observation point. $A_r(s_r)$ is the spreading (or spatial divergence) factor for the reflected ray, which is expressed as (Rousseau & Pathak, 1995)

$$A_r(s_r) = \sqrt{\frac{\rho_1^r \rho_2^r}{(\rho_1^r + s_r)(\rho_2^r + s_r)}}$$

(19)

where ρ_1^r and ρ_2^r are the principal radii of curvature of the reflected wavefront at the observation point.

In equation (18), $\overset{+}{\overline{\overline{R}}}(t)$ is the TD dyadic reflection coefficient, which must be expressed in terms of its vertical and parallel components. These coefficients are obtained as the ATT of the classical Fresnel reflection coefficients (Yao et al., 2003) for a reflected surface composed of a lossy material. By performing this ATT, the parallel component can be expressed as

$$\overset{+}{R}_{||}(t) = K\overset{+}{\delta}(t) + \frac{4\kappa}{1-\kappa^2}\frac{e^{-at}}{t}\sum_{n=1}^{\infty}(-1)^{n+1}nK^n I_n(at)$$

(20)

where I_n is the modified Bessel function of order n and

$$K = \frac{1-\kappa}{1+\kappa} \qquad \kappa = \frac{\sqrt{\varepsilon_r - \cos^2\phi}}{\varepsilon_r \sin\phi} \qquad a = \frac{120\pi\sigma c}{2\varepsilon_r}$$

The perpendicular component is as follows:

$$\overset{+}{R}_{\perp}(t) = -\left[K\overset{+}{\delta}(t) + \frac{4\kappa}{1-\kappa^2}\frac{e^{-at}}{t}\sum_{n=1}^{\infty}(-1)^{n+1}nK^n I_n(at)\right]$$

(21)

where, in this case,

$$\kappa = \frac{\sin\phi}{\sqrt{\varepsilon_r - \cos^2\phi}} \qquad a = \frac{120\pi\sigma c}{2\varepsilon_r\left(1 - \dfrac{\cos^2\phi}{\varepsilon_r}\right)}$$

and the rest of parameters are the same.

3.3 Transmitted field

The impulse response for the transmitted field is analogous to that response for the reflected field and can be written as

$$\overset{+}{f_I^r}(t) = E_0^i \overset{+}{\overline{\overline{T}}}(t - s_i/c - s_t/c)\left|A_i(s_i)A_t(s_t)\right|$$

(22)

where s_i is, in this case, the distance between the source and the transmission point, s_t is the distance between the transmission point and the observation point, $A_t(s_t)$ is the spreading (or spatial divergence) factor for the transmitted ray, which can be obtained using expression (19) by replacing the radii of curvature of the reflected wavefront by those of the transmitted wavefront, and $\overset{+}{\overline{\overline{T}}}(t)$ is the TD dyadic transmission coefficient, which must also be expressed

in terms of its vertical and parallel components. The transmission coefficient can be obtained easily by considering that the relationship between the reflection and the transmission coefficients are the same in the time domain as in the frequency domain and is given by

$$\overset{+}{\overline{T}}(t) = I + \overset{+}{\overline{R}}(t) \tag{23}$$

where I is the identity matrix.

3.4 Diffracted field

In the case of diffraction, its contribution to the impulse response is given by the ATT of the UTD expression for the frequency domain as follows:

$$\overset{+}{f_I^d}(t) = E_0^i \overset{+}{\overline{D}}(t - s_i / c - s_d / c) |A_i(s_i)A_d(s_d)| \tag{24}$$

where s_i is, in this case, the distance between the source and the diffraction point, s_d is the distance between the diffraction point and the observation point, $A_d(s^d)$ is the spreading (or spatial divergence) factor for the reflected ray given by (Rousseau & Pathak, 1995)

$$A_d(s_d) = \sqrt{\frac{\rho^s}{(\rho^s + s_d) \cdot s_d}} \tag{25}$$

where ρ^s is the principal radius of curvature of the diffracted wavefront at the observation point.

On the other hand, $\overset{+}{\overline{D}}(t)$ is the TD dyadic diffraction coefficient, which must be expressed in terms of its components with respect to the edge-fixed system. The diffraction coefficients for a PEC wedge are obtained as the sum of four terms, as in (Rousseau & Pathak, 1995). If the lossy materials are included in the formulation, the last two terms corresponding to the contribution of the reflected shadow boundary must include the effect of the lossy reflection coefficient. In the frequency domain, this inclusion is performed by a product. Therefore, the convolution between the reflection coefficient and these two terms of the diffraction coefficient must instead be performed in the time domain. Performing this convolution results in the following expression for the diffraction coefficients:

$$\overset{+}{\overline{D}}_{\beta,\varphi}(t) = \overset{+}{D_1}(t) + \overset{+}{D_2}(t) + \overset{+}{\overline{R}}_{\perp,||} |*\left[\overset{+}{D_3}(t) + \overset{+}{D_4}(t) \right] \tag{26}$$

The expressions for $\overset{+}{D_1}(t)$, $\overset{+}{D_2}(t)$, $\overset{+}{D_3}(t)$ and $\overset{+}{D_4}(t)$ are given as follows (Rousseau & Pathak, 1995):

$$\overset{+}{D_1}(t) = A_0 \cot\left[\frac{\pi + (\phi - \phi')}{2n} \right] \overset{+}{F}\left[L^i a^+(\phi - \phi') \right] \tag{27}$$

$$\overset{+}{D_2}(t) = A_0 \cot\left[\frac{\pi - (\phi - \phi')}{2n} \right] \overset{+}{F}\left[L^i a^-(\phi - \phi') \right] \tag{28}$$

$$\overset{+}{D}_3(t) = A_0 \cot\left[\frac{\pi + (\phi + \phi')}{2n}\right]\overset{+}{F}\left[L^{rn}a^+(\phi + \phi')\right] \tag{29}$$

$$\overset{+}{D}_4(t) = A_0 \cot\left[\frac{\pi - (\phi + \phi')}{2n}\right]\overset{+}{F}\left[L^{ro}a^-(\phi + \phi')\right] \tag{30}$$

with $A_0 = \dfrac{-1}{2n\sqrt{2\pi}\sin\beta_0^i}$, where β_0^i is the angle between the direction of incidence and the

vector of the edge and $\overset{+}{F}(x,t) = \dfrac{\sqrt{x/\pi}\left(j\sqrt{t} + \sqrt{x/c}\right)}{\sqrt{t}\left(t + x/c\right)}$.

The L^i are distance parameters associated with the incident shadow boundaries and are the same as in the frequency domain. These parameters are given by

$$L^i = \frac{s_d\left(\rho_e^i + s_d\right)\rho_1^i\rho_2^i}{\rho_e^i\left(\rho_1^i + s_d\right)\left(\rho_2^i + s_d\right)}\sin^2\beta_0^i \tag{31}$$

$$L^{ro,n} = \frac{s_d\left(\rho_e^{ro,n} + s_d\right)\rho_1^{ro,n}\rho_2^{ro,n}}{\rho_e^{ro,n}\left(\rho_1^{ro,n} + s_d\right)\left(\rho_2^{ro,n} + s_d\right)}\sin^2\beta_0^i \tag{32}$$

where ρ_1^i is the radius of curvature 1 of the incident wavefront at the edge, ρ_2^i is the radius of curvature 2 of the incident wavefront at the edge, ρ_e^i is the radius of curvature of the incident wavefront at edge-fixed plane of incidence, $\rho_1^{ro,m}$ is the radius of curvature 1 of the reflected wavefront from the o and n faces, respectively, $\rho_2^{ro,m}$ is the radius of curvature 2 of the reflected wavefront from the o and n faces, respectively, and $\rho_e^{ro,m}$ is the radius of curvature of the reflected wavefront from the plane containing the reflected ray and the edge.

The function $a^\pm$ in the expressions (27)-(30) is given by

$$a^\pm(\beta^\pm) = 2\cos^2\left(\frac{2n\pi N^\pm - \beta^\pm}{2}\right)$$
$$\beta^\pm = \phi^d \pm \phi^i \tag{33}$$
$$2\pi n N^+ - \left(\phi^d \pm \phi^i\right) = \pi$$
$$2\pi n N^- - \left(\phi^d \pm \phi^i\right) = -\pi$$

The geometrical parameters involved in the calculation of the diffraction coefficients are the same as in the frequency domain as shown in Figure 2 and are explained in (Kouyoumjian & Pathak, 1974).

3.5 Multiple reflected and multiple transmitted fields

The expressions for the m-order reflections and transmissions are easily derived recursively from the first-order effects. For instance, the second-order reflection is a single reflection where the source is set as the first reflection point and the incident field is the simple reflected field. Using this recursion, an m-order reflection that reaches the observation point would contribute the following term to the impulse response:

$$f_I^{\overset{+}{mr}}(t) = E_0^i \overset{\overset{+}{=}}{R}_M \left| A_t(s_t) \right| \tag{34}$$

where

$$s_t = s_i + \sum_{j=1}^{m} s_r^j$$

$$A_t(s_t) = A_i(s_i) \prod_{j=1}^{m} A_r(s_r^j)$$

$$\overset{\overset{+}{=}}{R}_M = \overset{\overset{+}{=}}{R}_1(t - s_i \, / \, c - s_r^1 \, / \, c) * \dots * \overset{\overset{+}{=}}{R}_m(t - s_i \, / \, c - \sum_{i=1}^{m} s_r^j \, / \, c)$$

s_r^j is the distance between the jth the (j+1)th reflection points (or between the mth reflection point and the observation point in the case of the last reflection).
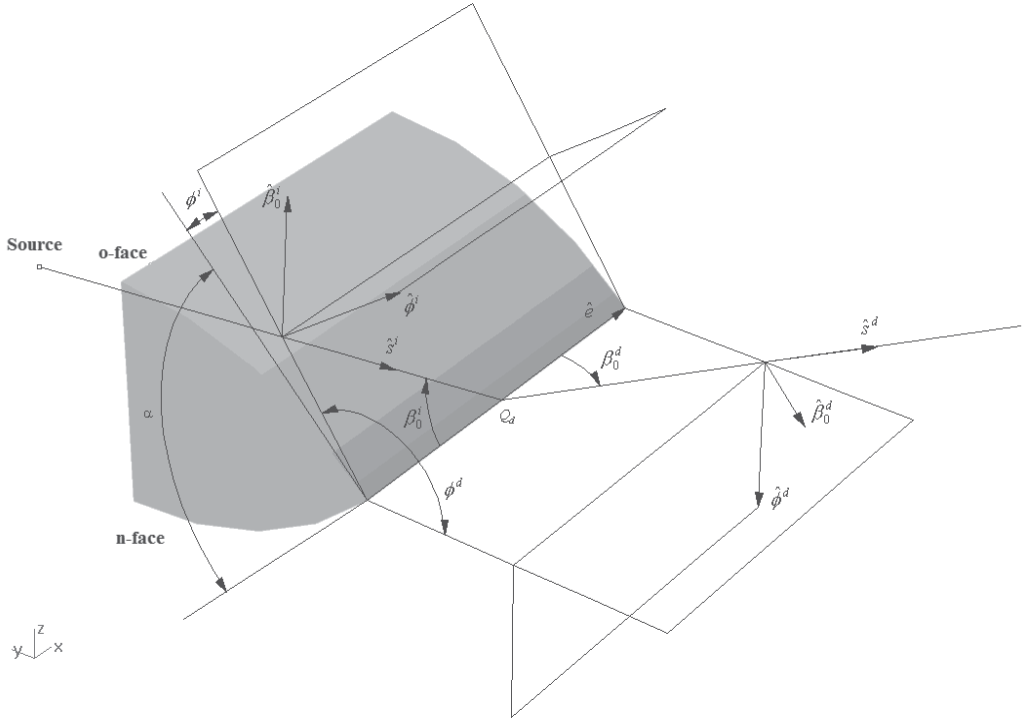
Fig. 2. Geometrical parameters and an edge-fixed system for the diffracted ray. In the figure, $\hat{e}$ is the vector of the edge, Q_d is the diffraction point, $\hat{s}^i$ and $\hat{s}^d$ are the incident and diffraction directions, respectively, β_0^i, β_0^d, ϕ^i and ϕ^d ($\beta_0^i = \beta_0^d = \beta_0$) are the diffraction angles, and $\hat{\beta}_0^i, \hat{\phi}^i$ and $\hat{\beta}_0^d, \hat{\phi}^d$ are the vectors of the edge-fixed system necessary to apply the diffraction coefficients. All parameters are explained in (Kouyoumjian & Pathak, 1974) because they are identical to those in the frequency domain case

Analogously, the m-order transmitted field is

$$\overset{+}{f_I^{mt}}(t) = E_0^i \overset{+}{\overline{T}}_M \left| A_t(s_t) \right| \tag{35}$$

where $\overset{+}{\overline{T}}_M(t) = I + \overset{+}{\overline{R}}_M(t)$.

3.6 Reflected-diffracted and diffracted-reflected fields

Following the same procedure as for multiple reflections, the contribution of the interaction between an edge and a reflecting surface to the impulse response can be written as

$$\overset{+}{f_I^{rd}}(t) = E_0^i \left[\overset{+}{\overline{R}}(t - s_i / c - s_r / c) * \overset{+}{\overline{D}}(t - s_i / c - s_r / c - s_d / c) \right] \cdot \left| A_i(s_i) A_r(s_r) A_d(s_d) \right| \tag{36}$$

for the case of reflection-diffraction interactions and

$$\overset{+}{f_I^{dr}}(t) = E_0^i \left[\overset{+}{\overline{D}}(t - s_i / c - s_d / c) * \overset{+}{\overline{R}}(t - s_i / c - s_r / c - s_d / c) \right] \cdot \left| A_i(s_i) A_d(s_d) A_r(s_r) \right| \tag{37}$$

for the case of diffraction-reflection interaction.

The meaning of these parameters is analogous to the previous effects.

4. Deterministic analysis of a realistic environment

The results of the deterministic approach presented in this chapter compared with measurements are shown in this section. The measurements were performed in a complex realistic site to investigate the validity of the approach. The measurements were done in the corridor of the second floor of the Polytechnic Building of the University of Alcala. Figure 3 shows the plan schematic of the measurement site. The dimensions of the scenario are 7.9x20.7 m. A 3D plane-facets model has been designed to represent the realistic environment composed of 77 facets. The material composition of the elements of the site was concrete for the walls, wood for the doors and glass for the windows. Table I lists the electrical properties of these three materials considered in our model.

Material	ε_r	σ (S/m)
Concrete	4.5	0.01
Wood	2	10^{-5}
Glass	6.5	10^{-12}

Table 1. Electrical characteristics of the materials for the measurement scenario

Several measurements were performed on the site. Examples of one Line-of-Sight (LOS) and one Non-Line-of-Sight (NLOS) case will be shown in this section. Figure 3 illustrates the position of the transmitter and the receiver in both cases. The coordinates of the transmitter were (1.60, 5.55, 1.10). The coordinates of the receivers were (5.0, 1.78, 1.10) for the LOS case and (9.55, 1.3, 1.10) for the NLOS case. All the coordinates are given in meters.

Measurements were conducted in the frequency domain using the network analyzer (VNA) Agilent E8362B. A linearly polarized double-ridged waveguide antenna was used as the
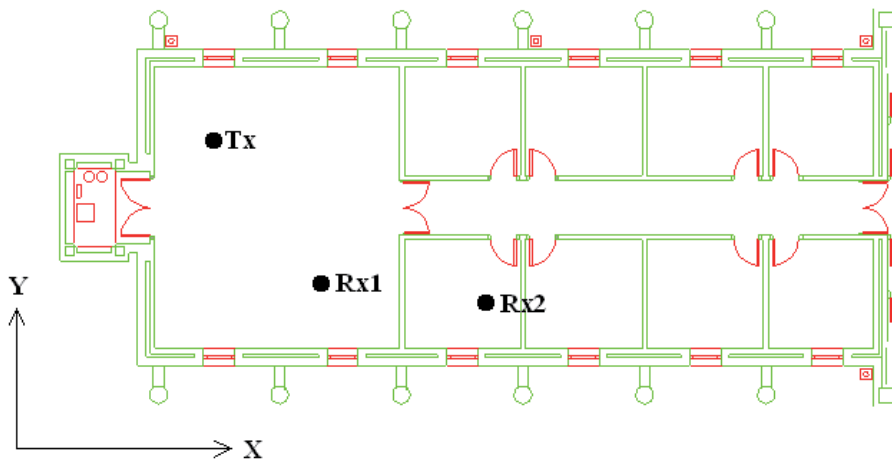
Fig. 3. Plan of the Polytechnic Building corridor of Alcala University and TX and RX placements for the measurement antennas

transmitter (TX) and as the receiver (RX). The frequency range of these antennas was 1 to 18 GHz. In this range, the average VSWR ratio was lower than 1.5.

Figure 4 shows an overview of the measurement setup. The VNA was set to transmit 3201 tones uniformly distributed over the 1-18 GHz frequency range. This transmission gave an excess delay of 188 ns and a maximum distance of 56.4 m. The temporal resolution for the 17 GHz frequency was 59 ps.
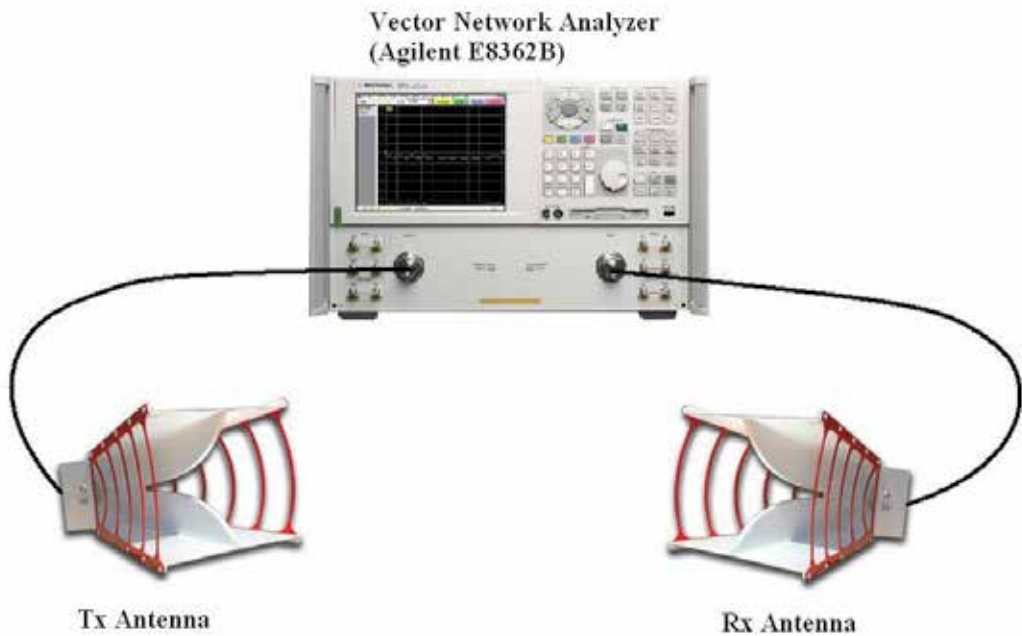
Fig. 4. Overview of the measurement setup

The input signal is expressed as a sum of a small number of simple expansion functions for a more efficient convolution with the TD-UTD impulse response. In this approach, the input signal is represented as the sum of waveforms with analytical signal representations that are simple poles in the complex time plane. This representation allows the convolution to be expressed in a closed form, thus speeding up computation. Moreover, the antenna transfer function is included in this representation. Equations (38) and (39) show the representation of the input signal and the closed form for the convolution, respectively.

$$\overset{+}{i}(t) = \frac{j}{\pi} \sum_{n=1}^{n} \frac{A_n}{t + j\tau_n} \tag{38}$$

$$\overset{+}{o}(t) = \frac{1}{2} \overset{+}{i}(t) * \overset{+}{f}(t) = \sum_{n=1}^{N} A_n \overset{+}{f}(t + j\tau_n) \tag{39}$$

The comparisons between the measurements and our approach for the normalized PDP in the LOS and the NLOS cases are shown in Figures 5 and 6, respectively. As can be seen, a good agreement between calculation and measurement is obtained in both cases. The mean errors were 3.5 dB for the LOS case and 4.6 dB for the NLOS case, which are very good for UWB applications.
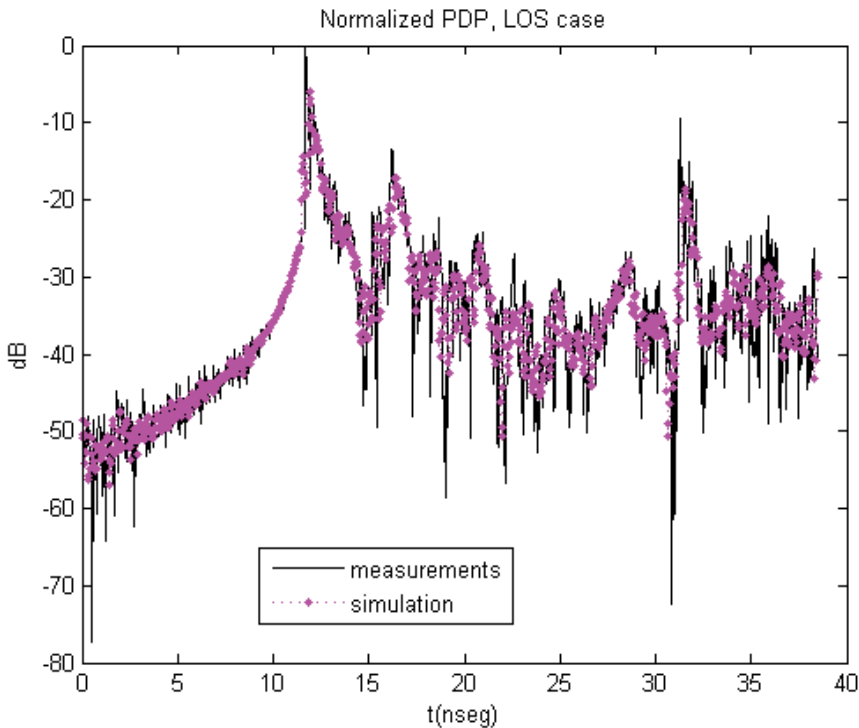
Fig. 5. Comparison between measurements and simulation for the LOS case
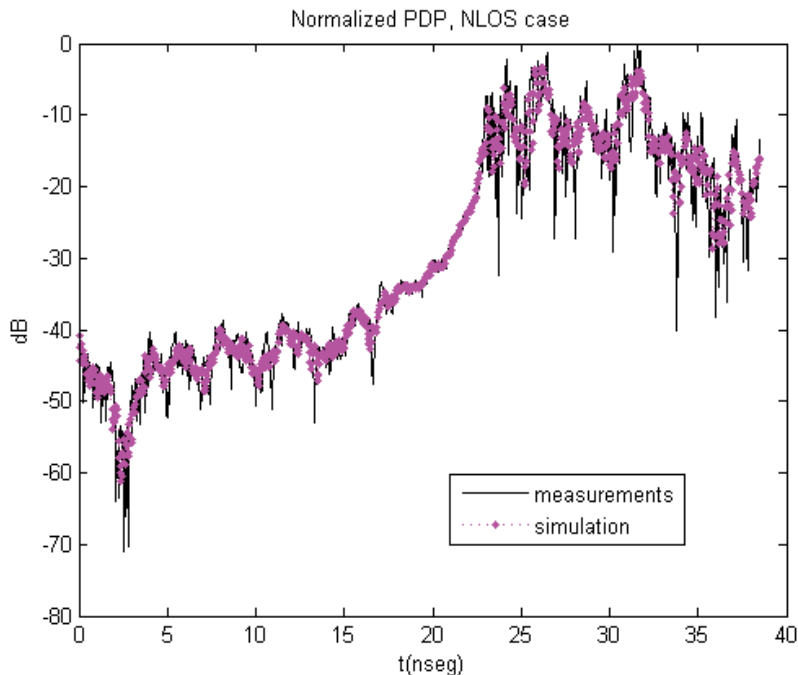
Fig. 6. Comparison between measurements and simulation for the NLOS case.

5. Acknowledgment

6. References

Cassioli, D.; Win, M. & Molisch, A. (2001). A Statistical Model for the UWB Indoor Channel, *Proceedings of 20015 53rd Vehicular Technology Conference,* pp. 1159, ISBN 0-7803-6728-6, Rhodes, Greece, May 6-9 2001.

Cassioli, D.; Win, M. & Molisch, A. (2002). The Ultra-Wide Band Indoor Channel: from Statistical Model to Simulations, *IEEE Journal on Selected Areas in Telecommunications,* Vol.20, No.6, (August 2002), pp. 1247-1257, ISSN 0733-8716.

Dabin, J.A.; Haimovich, A.M. & Grebel, H. (2006). A Statistical Ultra-Wide Band Indoor Channel Model and the Effects of Antenna Directivity on Path Loss and Multipath Propagation, *IEEE Journal on Selected Areas in Telecommunications* Vol.24, No.4, (April 2006), pp. 752-758, ISSN 0733-8716.

Hashemi, H. (1979). Simulation of the Urban Radio Propagation Channel. *IEEE Transactions on Vehicular Technology,* Vol. 28, No. 3 (March 1979), pp. 213-225, ISSN 0018-9545.

Kouyoumjian, R.G. & Pathak, P.H. (1974). A Uniform Geometrical Theory of Diffraction for an Edge in a Perfectly Conducting Surface, *Proceedings of the IEEE,* Vol.62, No.11 (November 1974), pp. 1448-1461, ISSN 0018-9219.

Lauer, A.; Bahr, A. & Wolff, I. (1984). FDTD Simulations of Indoor Propagation, *Proceedings of 1994 44th Vehicular Technology Conference,* pp. 883, ISBN 0-7803-1927-3, Stockholm, Sweden, June 8-10, 1994.

Molisch, A.; Cassioli, D.; Chong, C.; Emami, S.; Fort, A.; Kannan, B.; Karedal, J.; Kunisch, J.; Schantz, H.G.; Siwiak, K. & Win, M.Z. (2006). A Comprenhensive Standardized Model for Ultrawideband Propagation Channels, *IEEE Transactions on Antennas and Propagation,* Vol.54, No.11, (November 2006), pp. 3151-3166 ISSN 0018-926X.

Motley, A.J. & Keenan, J.M.P (1990). Radio Coverage in Buildings, *British Telecom Technological Journal, Special Issue Mobile Communications,* Vol.8, No. 1 (January 1990), pp. 19-24, ISSN 1358-3948.

Rappaport, T.S.; Siedel, S.Y. & Takamizawa, K. (1991). Statistical Channel Impulse Response Models for Factory and Open Plan Building Radio Communication System Design. *IEEE Transactions on Communications,* Vol.39, No.5, (May 1991), pp. 794-807, ISSN 0090-6778.

Rousseau, P.R. & Pathak, P.H. (1975). Time-Domain Uniform Theory of Diffraction for a Curved Wedge, *IEEE Transactions on Antennas and Propagation,* Vol.43, No.12, (December 1995), pp. 1375-1382, ISSN 0018-926X.

Saez de Adana, F.; Gutiérrez, O.; González, I.; Pérez, J. & Cátedra, M.F. (2000). Propagation Model Based on Ray-Tracing for the Design of Personal Communications, *IEEE Transactions on Vehicular Technology,* Vol.49, No.6, (November 2000), pp. 2105-2112, ISSN 0018-9545.

Saleh, A.A. & Valenzuela, R.A. (1987). A Statistical Model for Indoor Multipath Propagation, *IEEE Journal on Selected Areas on Communication,* Vol.5, No.2, (February 1987), pp. 128-137, ISSN 0733-8716.

Seidel, S.Y. & Rappaport, T.S. (1992). 914 MHz Path Loss Prediction Models for Indoor Wireless Communications in Multifloored Buildings, *IEEE Transactions on Antennas and Propagation,* Vol.40, No.2, (February 1992), pp. 207-217, ISSN 0018-926X.

Tarng, J.H.; Chang, W.R. & Hsu, B.J. (1997). Three-Dimensional Modelling of 900 MHz and 2.44 GHz Radio Propagation in Corridors, *IEEE Transactions on Vehicular Technology,* Vol.46, No.2, (May 1997), pp. 519-526 ISSN 0018-9545.

Tornevik, C.; Berg, J.E., Lotse, F. & Madfors, M. (1993). Propagation Models, Cell Planning and Channel Allocation for Indoor Applications of Cellular Systems, *Proceedings of 1993 43rd Vehicular Technology Conference,* pp. 867-870, ISBN 0-7803-1267-8, Secaucus, New Jersey, USA, May 18-20 1993.

Veruttipong, T. & Kouyoumjian, R.G. (1979). Early-Time Responses of Currents and Charges on Wedges and Strips, *Proceedings of the 1979 Antennas and Propagation Society International Symposium*, pp. 590-593, Seattle, Washington, USA, June 18-22 1979.

Whitman, G.M.; Kim, K.S. & Niver, E. (1995). A Theoretical Model for Radio Signal Attenuation inside Buildings, *IEEE Transactions on Vehicular Technology,* Vol.44, No.3, (August 1995), pp. 621-629, ISSN 0018-9545.

Yao, R.; Chen, Z. & Zhu, W. (2003). An Efficient Time-Domain Ray Model for UWB Indoor Multipath Propagation Channel, *Proceedings of 2003 58th Vehicular Technology Conference,* pp. 1293, ISBN 0-7803-7954-3, Orlando, Florida, USA, October 6-9, 2003.

Frequency UWB Channel

Gonzalo Llano, Juan C. Cuellar
and Andres Navarro
Universidad Icesi
Colombia

1. Introduction

Ultra wideband (UWB) transmission systems are characterized with either a fractional bandwidth of more that 20%, or a large absolute bandwidth (>500 MHz) in the 3.1 GHz to 10.6 GHz band, and for a very low power spectral density (-41.25 dBm/MHz, equivalent to 75nW/MHz), which allows to share the spectrum with other narrowband and wideband systems without causing interference (FCC, 2002), this spectral allocation has initiated an extremely productive activity for industry and academia.

Wireless communications experts now consider UWB as available spectrum to be utilized with a variety of techniques and not specifically related to the generation and detection of short RF pulses as in the past (Batra, 2004). For this reason, UWB systems are emerging as the best solution for high speed short range indoor wireless communication and sensor networks, with applications in home networking, high-quality multimedia content delivery, radars systems of high accuracy, etc. UWB has many attractive properties, including low interference to and from other wireless systems, easier wall and floor penetration, and inherent security due to its Low Probability Interception/Detection (LPI/D). Two of the most promising applications of UWB are High Data Rate Wireless Personal Area Network (HDR-WPAN), and Sensor Networks, where the good ranging and geo-location capabilities of UWB are particularly useful and of interest for military applications (Molisch, 2005).

Three types of UWB systems are defined by the Federal Communications Commission in United States: imaging systems, communication, measurement and vehicular radar systems. Currently the United States permits operation of UWB devices. In Europe a standardization mandate was forwarded to CEN/CENELEC/ETSI for harmonized standards covering UWB equipment (ECS, 2007), and regulatory efforts are studied by Japan (Molisch, 2005). In order to deploy UWB systems which carry out all those potentials, we need to analyze UWB propagation and the channel properties arising from this propagation, especially in the frequency domain. Given the large bandwidth (7.5 GHz) authorized for UWB and hence its low time resolution (133 ps), the conventional channel models developed to model the received envelope as a Rayleigh random variable in narrowband and wideband transmissions are inadequate in UWB signaling. Multipath fading resistance and high data rate transmission capacity, are the main characteristics of the UWB technology (Batra, 2004), render such UWB technology an excellent candidate for many indoor and short-range applications as compared to other wireless technologies. Applications of UWB can be found in high data rate wireless personal area networks, positioning, location and home network communications related to multimedia applications (Liuqing, 2007).

2. Statistical characterization of UWB channel

All wireless systems must be able to deal with the challenges of operating over a environment hostile, as the mobile wireless channel with multipath propagation channel, where objects in the environment cause multiple reflections to arrive at the receiver. As a result, the wireless systems will experience multipath fading, or amplitude fluctuations, resulting from the constructive or destructive combining of the reflected paths. Therefore an accurate channel model is needed to design a wireless system and to predict maximum ranges, power transmission, modulation schemes, rate coding, and transmission rates.

There are several ways to characterize a wireless channel: Deterministic and Statistical methods. When the channel is influenced by some unknown factor, exact prediction with deterministic models is not possible; in this case, statistical models are used. These statistical models are based on extensive measurements campaigns and they give us the channel behavior, especially, the received envelope and the path arrival time distribution.

To characterize the UWB channel using statistical methods, the IEEE 802.15 standardization group responsible for HDR-WPAN and Low Rate WPAN (LR-WPAN) organized two working groups: Task Group 3a (TG3a) and 4a (TG4a) to development an alternative physical layer based on UWB signaling (Molisch, 2005). IEE 802.15.3a TG3a proposed a channel model for HDR-WPAN applications (Foerster et al., 2003) and the TG4a a channel model for evaluation low rate applications proposed by the IEEE 802.15.4a standard (Mol05 et al., 2005)]. The TG4a model can be used in indoor and outdoor environments with longer operating range (i.e.,>10 m in indoor and up to few hundred meters for outdoor) and lower data rate transmission (between 1 kb/s and several Mb/s). There are two techniques signaling for this standard: a multiband orthogonal frequency division multiplexing (MB-OFDM) and a code-division multiple access (CDMA).

2.1 IEEE 802.15.3a channel model

To characterize the UWB channel for applications HDR-WPAN three indoor channel models have been proposed: the Rayleigh tap delay line model (same as the one used in 802.11 standard), Saleh-Valenzuela (S-V) (Saleh, 1987) and the Δ-K (Hashemi, 1993) models. The S-V and Δ-K models use a Poisson statistical process in order to model the arrival time of clusters (multipath components –MPC- which arrive from a same scatter). Nevertheless, the S-V model is unique in its approach of modeling the arrival time in cluster as well as MPC within a cluster. The S-V model defines that the multipath arrival times are random process based in Poisson distributions. Therefore the inter-arrival time of MPC are exponentially distributed, and defines four parameters to describe the channel: The cluster arrival rate (Λ), the path arrival rate (λ) within a cluster, the cluster decay time constant (η), path time constant (γ).

The principle of S-V channel is shown in the Fig.1. In this model, the small scale amplitude fading statistics follow a Rayleigh distribution and the power an exponential distribution, is defined by the cluster and ray decay factors.

However, measurements in UWB channels indicated that the small scale amplitude statistics denoted by α_{k1}, follow a lognormal or Nakagami-m distribution. The IEEE TG3a recommended using a lognormal distribution for the multipath gain magnitude. In this temporal model the power of the clusters and ray decays over time, this effect was modeled as an exponentially decaying power profile with increasing delay from the first path. Fig. 2

shows the temporal model of the 802.15.3a UWB channel. Based on these results, the SV model was modified for IEEE TG3a.
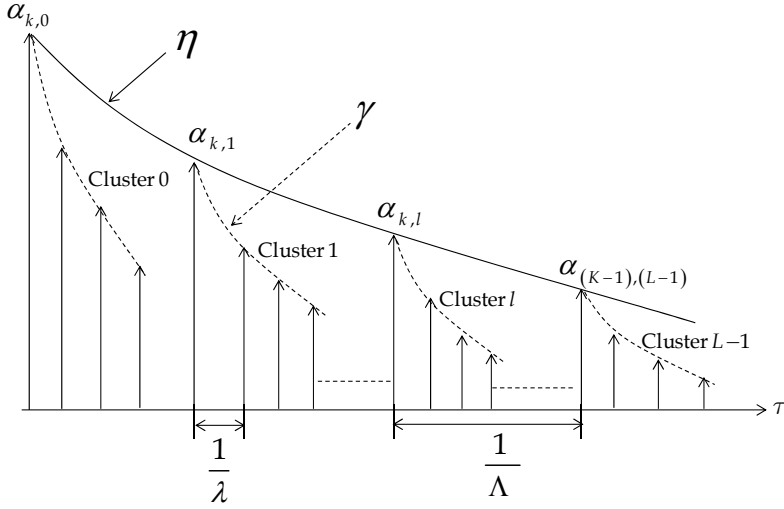
Fig. 1. Principle of the Saleh-Valenzuela Channel model
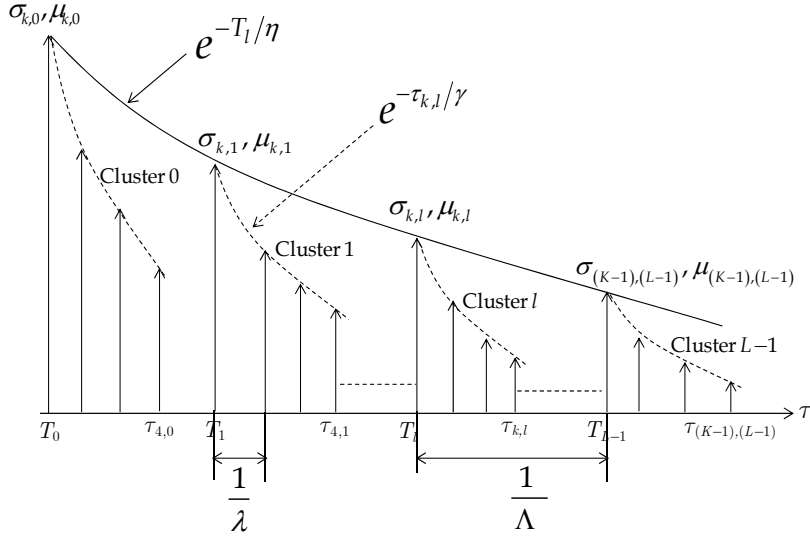
Fig. 2. Temporal model of IEEE 802.15.3a UWB Channel

The channel impulse response (CIR) time-variant for 802.15.3a UWB channel and denoted by $h(t;\tau)$, is given by (Foerster et al., 2003) as

$$h(t;\tau) = X(t)\sum_{l=1}^{L_C}\sum_{\substack{k=1 \\ l \neq k}}^{L_T}\xi_l(t)\beta_{k,l}(t)e^{j\varphi k, l(t)}\delta\left[\tau - T_l(t) - \tau_{k,l}(t)\right], \tag{1}$$

where, t represents the temporal variation of the channel due to motion of the receiver and τ the channel multipath delay. In addition, l represents the cluster index and k the MPC index within a lth cluster; L_c is the cluster numbers and L_r the rays numbers within the cluster (Multipath Components –MPC-), T_l is the arrival time of the lth cluster; and $\tau_{k,l}$ is the arrival time of the kth component inside the lth cluster. ξ_l is the amplitude of the lth cluster, $\beta_{k,l}$ is the amplitude of the kth path inside the lth cluster, $\varphi_{k,l} = 2\pi f_c \tau_{k,l}$, the phase of the path and $\delta(\bullet)$ the Kronecker delta function. $X(t)$ is a stochastic process that define the variations in the path gain amplitude due to non-line-of-sight (NLOS) propagation and characterize the slow fading (shadowing) and $\alpha_{k,l}(t) = \xi_l(t)\beta_{k,l}(t)$ is a stochastic processes that characterize the fast fading of the 802.15.3a UWB channel.

Let $\Delta\tau_{k,l} = \tau_{k,l} - \tau_{(k-1)l} = 1/W$, the width of the resolvable timebin, W the channel bandwidth, $N = \lceil L_c \times L_r \rceil = \lceil \tau_{\max}/\Delta\tau_{k,l} \rceil$ the number of timebins for the CIR of $h(t;\tau)$ defined in (1), $\tau_{\max}$ is the maximum excess delay of the channel and $\lceil \bullet \rceil$ is the ceiling function. If the nth timebin does not contain any MPC, then $\alpha_{k,l}(t) = \xi_l(t)\beta_{k,l}(t)=0$. Note, that in the Equation (1) the variation of the magnitude of the complex envelope due to slow fading or shadowing appears as a multiplier effect through the random variable (RV) $X = 10^{x/20}$, where x is a independent normal RV with zero mean and standard deviations $\sigma_x(\text{dB})=3$ dB [Foe03], i.e., $x \sim \mathcal{N}(0,\sigma_x)$. Therefore, X is a independent lognormal RV with zero mean and standard deviation in nepers $\sigma_X(\text{Np})$, i.e., $X \sim \mathcal{L}(0,\sigma_X)$, where $\sigma_X\ (\text{Np})=[\ln(10)/20]\sigma_x(\text{dB})$. The amplitude of the envelope of the 802.15.3a UWB channel considering the slow fading and fast fading is calculated as

$$\Upsilon(t) = |h(t;\tau)| = X(t)\sum_{l=1}^{L_c}\sum_{\substack{k=1 \\ l \neq k}}^{L_r}\xi_l(t)\beta_{k,l}(t) \tag{2}$$

Since the two stochastic processes that characterize the fast fading and slow fading (shadowing) are independent, uncorrelated and static. The mean power of 802.15.3a UWB channel is given by

$$\Omega_\Upsilon \triangleq E\{\Upsilon^2\} = E\{X\}\sum_{l=0}^{L_c-1}\sum_{k=0}^{L_r-1}E\left\{|\xi_l\beta_{k,l}|^2\right\} = \bar{X}\sum_{l=0}^{L_c-1}\sum_{\substack{k=0 \\ l \neq k}}^{L_r-1}\Omega_{k,l}\ , \tag{3}$$

where, $E\{\cdot\}$ denote statistical expectation, $\Omega_{k,l}$ is the mean power of the kth MPC or path due to fast fading, $\bar{X}$ is the mean power due to shadowing and is given by

$$E\{X\} = \exp\left(\frac{\sigma_X^2}{2}\right) = \exp\left[\left(\frac{\ln(10)}{20}\right)^2\frac{\sigma_x^2(\text{dB})}{2}\right], \tag{4}$$

Since $\sigma_x(\text{dB}) = 3$ dB, the average power variation due to shadowing is $\bar{X} = 1.04$ dB. Applications using UWB systems are designed for indoor or outdoor environments, where the mobility of the TX/RX is very low. Therefore, the effect of temporal selectivity caused by either relative motion between the mobile and base station or by movement of objects in the channel which causes frequency shift by Doppler spread of the signal MB-OFDM in an UWB system, is very small compared with the bandwidth of UWB channel (1.584 GHz in

mode 1). Consequently 802.15.3a UWB channel is assumed time-invariant or static during the transmission of an OFDM symbol (Malik, 2008), i.e., $h(t;\tau) = h(\tau)$. Similarly, the channel is assumed Wide Sense Stationary (WSS), its mean energy remains constant during transmission of an MB-OFDM symbol, i.e., $m_{h(t;\tau)} \triangleq E\{h(t;\tau)\} = \text{Kte}$, and its autocorrelation function does not depend on the absolute momentos t_1 and t_2, depends on the difference between the two time points $\tau = t_1 - t_2$, i.e., $R_{h(t;\tau)}(t_1,\tau_1;t_2,\tau_2) \triangleq E\{h^*(t_1,\tau_1)h(t_2,\tau_2)\}$.

Hence, that we can assume the channel impulse response (CIR) of the indoor 802.15.3a UWB channel given by Eq. (1) as time-invariant, and only consider the dispersive effect of the channel denoted by variable, τ, therefore, the CIR of the UWB channel time-invariant is given by (Foerster at et., 2003) as

$$h(\tau) = \sum_{l=1}^{L_C} \sum_{\substack{k=1 \\ l \neq k}}^{L_r} \alpha_{k,l} e^{j\varphi k,l} \delta(\tau - T_l - \tau_{k,l})$$ (5)

The module $h(\tau)$ denoted by $\alpha_{k,l} = |h(\tau)|$, represent the gain magnitude due to the fast fading in UWB channel and is defined as a random variable (RV) that follow a lognormal distribution with mean $\mu_{k,l}$ and standard deviation $\sigma_{k,l}$, i.e., $\alpha_{k,l} \sim \mathcal{L}(\mu_{k,l},\sigma_{k,l})$. In the temporal model of 802.15.3a UWB channel, the mean power of the kth MPC or path is given by

$$\Omega_{k,l} = E\{\alpha_{k,l}^2\} = E\{|\xi_l \beta_{k,l}|^2\} = \Omega_0 \exp(-T_l/\eta)\exp(-\tau_{k,l}/\gamma),$$ (6)

where Ω_0 is the mean power of the first path inside the first cluster. The amplitudes of the contributions $|\xi_l \beta_{k,l}|$ are mutually independent RV and their phases $\varphi_{k,l}$ are uniformly distributed from 0 to 2π. The module of the amplitude of the paths follows a lognormal distribution, given by

$$|\xi_l \beta_{k,l}| = 10^{(\mu_k,l+n1+n2)/20} \rightarrow 20\log(\xi_l \beta_{k,l}) \sim \mathcal{N}(\mu_{k,l},\sigma_c^2 + \sigma_r^2),$$ (7)

where n_1 and n_2 are independent normal RV with zero mean and standard deviations σ_c and σ_r, given by $n_1 \sim \mathcal{N}(0,\sigma_c)$ and $n_2 \sim \mathcal{N}(0,\sigma_r)$ and correspond to the fading on each cluster and path respectively; $\mathcal{N}(a,b)$ represents a Gaussian distribution with mean a and standard deviation b. The mean denoted by $\mu_{k,l}$, for the lognormal distribution of $|\xi_l \beta_{k,l}|$ is obtained from Eq. (6) and Eq. (7) as

$$\mu_{k,l} = \frac{10\ln(\Omega_0) - 10T_l/\eta - 10\tau_{k,l}/\gamma}{\ln(10)} - \frac{(\sigma_c^2 + \sigma_r^2)\ln(10)}{20}.$$ (8)

The distribution of the cluster arrival time and ray arrival time is exponential whose probability density function (PDF) is given by

$$p_T(T_l|T_{l-1}) = \Lambda \exp[-\Lambda(T_l - T_{l-1})], l > 0, \quad p_\tau(\tau_{k,l}|\tau_{(k-1),l}) = \lambda \exp[-\lambda(\tau_{k,l} - \tau_{(k-1),l})], k > 0$$ (9)

Average arrival time between clusters and rays inside a cluster is obtained from Eq. (9) according to (Llano, et al., 2009) as

$$E\{T_l\} = \Lambda \int\limits_0^\infty T_l \exp\left[-\Lambda(T_l)\right] dT_l = \frac{1}{\Lambda}; \quad E\{\tau_{k,l}\} = \lambda \int\limits_0^\infty \tau_{k,l} \exp\left[-\lambda(\tau_{k,l})\right] d\tau_{k,l} = \frac{1}{\lambda}. \tag{10}$$

More details of the channel model parameters IEEE TG3a can be found in (Foerster, 2003).

2.2 IEEE 802.15.4a channel model

This model was developed by the IEEE 802.15.4a standardization group for UWB systems ranging with low rates transmission (Molisch et al., 2005). Such as in the 802.15.3a channel model, the impulse response (in complex baseband) is modeled for the IEEE 802.15.4a by a generalized SV model, denoted by $h(\tau)$, is given by (Molisch et al., 2005).

$$h(\tau) = \sum_{l=1}^{L_c} \sum_{\substack{k=1 \\ l \neq k}}^{L_r} \alpha_{k,l} e^{j\varphi_{k,l}} \delta\left(\tau - T_l - \tau_{k,l}\right), \tag{11}$$

where l and k represent the cluster and ray indexes within the lth cluster, respectively; $\alpha_{k,l}$ and $\varphi_{k,l}$ correspond to the multipath gain coefficient and phases of the kth ray in the lth cluster, respectively; T_l is the arrival time of the lth cluster; and $\tau_{k,l}$ is the arrival time (in relation to T_l) of the kth ray in the lth cluster. The cluster arrival time and the ray arrival time within each cluster are modeled as a Poisson distribution with arrival rates Λ and λ, respectively, with $\lambda > \Lambda$. The MPCs amplitudes, $\alpha_{k,l}$, follow a Nakagami-m distribution and they are mutually independent RV. The phase terms $\varphi_{k,l}$ are uniformly distributed between 0 and 2π. In the channel model, the number of clusters, L_c, is a Poisson distributed RV with probability density function (PDF) given by (Molisch et al., 2005)

$$p_{L_c}(L_c) = \frac{\overline{(L_c)}^{L_c}}{L_c!} \exp\left(-\overline{L_c}\right), \, L_c > 0, \tag{12}$$

where $\overline{L_c}$ is the mean number of clusters. According to this model, the statistics of the cluster inter-arrival times are described by a negative exponential RV whose PDF can be written as (Molisch et al., 2005)

$$p_T\left(T_l | T_{l-1}\right) = \Lambda \exp\left[-\Lambda\left(T_l - T_{l-1}\right)\right], l > 0. \tag{13}$$

Due to the discrepancy in the fitting for the indoor residential, and indoor and outdoor office environments the IEEE TG4a proposes to model ray arrival times with mixtures of two Poisson processes as follows

$$p_\tau\left(\tau_{k,l} | \tau_{(k-1),l}\right) = \nu\lambda_1 \exp\left[-\lambda_1\left(\tau_{k,l} - \tau_{(k-1),l}\right)\right] + (1-\nu)\lambda_2 \exp\left[-\lambda_2\left(\tau_{k,l} - \tau_{(k-1),l}\right)\right], \, k > 0, \tag{14}$$

where ν is the mixture probability, λ_1 and λ_2 are the ray arrival rates. The mean time between rays arrives inside a cluster is obtained from Eq. (14) according to (Llano 2009) as

$$E\{\tau_{k,l}\} = \nu\lambda_1 \int\limits_0^\infty \tau_{k,l} \exp\left[-\lambda_1(\tau_{k,l})\right] d\tau_{k,l} + (1-\nu)\lambda_2 \int\limits_0^\infty \tau_{k,l} \exp\left[-\lambda_2(\tau_{k,l})\right] d\tau_{k,l} = \frac{\nu(\lambda_2 - \lambda_1) + \lambda_1}{\lambda_2 \lambda_1} \tag{15}$$

Power delay profile (PDP) in the 802.15.4a UWB channel is exponentially distributed within each cluster and the power of each MPC denoted by $\Omega_{k,l}$, can be calculated as

$$\Omega_{k,l} = E\{\alpha_{k,l}^2\} = \Omega_l \frac{1}{\gamma_l\big[(1-\beta)\lambda_1 + \beta\lambda_2 + 1\big]}\exp(-\tau_{k,l}/\gamma_l), \tag{16}$$

where Ω_l is the integrated mean power of the lth cluster, and γ_l is the intra-cluster decay time constant. The mean power Ω_l of the lth cluster follows an exponential decay, and in agreement (Molisch et al., 2005) can be calculated as

$$10\log(\Omega_l) = 10\log\left[\exp\left(-\frac{T_l}{\eta}\right)\right] + M_{cluster}, \tag{17}$$

where T_l is the arrival time of the cluster given by Eq. (13). $M_{cluster}$ is a RV Gaussian distributed with standard deviation $\sigma_{cluster}$. The cluster decay rates γ_l depend linearly on the arrival time of the cluster and is expressed as $\gamma_l = k_l + \gamma_0$, where k and γ_0 are parameters of the model. Fig. 3 shows the 802.15.4a UWB channel model used in simulations to evaluate the response frequency.
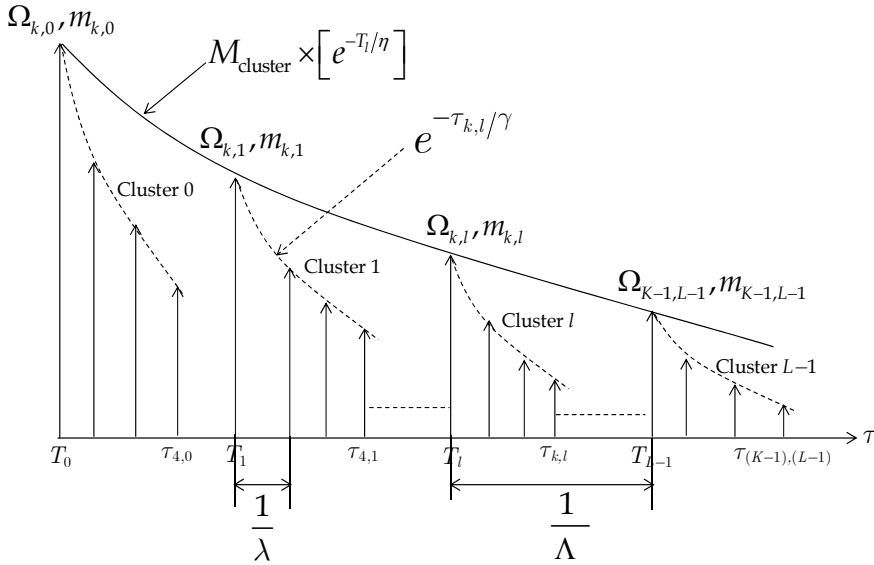
Fig. 3. Temporal model of IEEE 802.15.4a UWB Channel

In the 802.15.4a UWB channel model, the small scale fading for the multipath gain magnitude $\alpha_{k,l}$, is modeled as a Nakagami-m distribution whose probability density function (PDF) is given by (Nakagami, 1960)

$$f_{\alpha k,l}(\alpha_{k,l}) = \frac{2}{\Gamma(m_{k,l})}\left(\frac{m_{k,l}}{\Omega_{k,l}}\right)^{mk,l}\alpha_{k,l}^{2mk,l-1}\exp\left(-\frac{m_{k,l}}{\Omega_{k,l}}\alpha_{k,l}^2\right), \quad m_{k,l} \geq 0.5, \tag{18}$$

where $m_{k,l}$ is the fading parameter of the kth path inside the lth cluster, $\Gamma(\bullet)$ is the gamma function and $\Omega_{k,l}$ is mean power of the kth path within the lth cluster given by Eq. (16). The $m_{k,l}$ parameter is modeled as a lognormal distributed RV, whose logarithm has a mean μ_m and standard deviation σ_m given by (Molisch et al., 2005)

$$\mu_m(\tau) = m_0 - k_m(\tau); \quad \sigma_m(\tau) = \hat{m}_0 - \hat{k}_m(\tau), \tag{19}$$

where $m_0, k_m, \hat{m}_0, \hat{k}_m$, are parameters of the model. More details of the channel model parameters IEEE TG4a can be found in (Molisch et al., 2005).

2.3 Frequency UWB channel

The studio of the UWB channel in frequency is of great interest to analyze the performance of the MB-OFDM UWB system concerning to the channel estimation, channel equalization, adaptive coding, bit and symbol error performance. Moreover, an accurate model in frequency of the UWB channel is required to design adaptive modulation and estimation channel techniques which increase the channel capacity. Frequency analysis of UWB channel and MB-OFDM signaling, with channel impulse response given by Eq. (5) and Eq. (11) shows that the amplitude of each subcarriers can be approximated by a Nakagami-m distribution and therefore its power is a Gamma distribution (Nakagami-m squared). In addition, this analysis enables to calculate the power correlation coefficient between a couple of subcarriers, important for the calculating the fade depth and fading margin due to small-scale fading. This analytical approach in frequency domain enables a proper evaluation of the link budget in terms of the bandwidth channel and it can be used to design and implement UWB communications systems.

2.3.1 Channel Transfer Function of the UWB channel

Hence, we will calculate the Channel Transform Function (CTF) through Fourier transform (FT) of the CIR given by Eq. (5). We will show that if the magnitude denoted by $|\xi_l \beta_{k,l}|$ in time of each of the 802.15.3a UWB channel contributions is modeled as a lognormal or Nakagami-m as the 802.15.4a, random variable (RV) and the number of MPC is high, the magnitude of the ith subcarrier denoted by $|H(f_i)| = r_i$, can be approximated by a Nakagami-m RV with equivalent fading parameter m_{eq}^i, and equivalent average power Ω_{eq}^i, (Llano, 2009) expressed as a function of the average time of arrival of the clusters, $1/\Lambda$, of the rays within a cluster, $1/\lambda$, decay rate of the cluster $1/\eta$, and rays $1/\gamma$. i.e., $r_i \sim \mathcal{M}\left(m_{eq}^i, \Omega_{eq}^i\right)$, where, $i = 0,1,\cdots,N_f$, and N_f defines the number of subcarriers in MB-OFDM UWB signaling. The Fourier transform of the CIR given by Eq. (5) and Eq. (11), denoted by $H(f_i)$, is expressed according to (Llano et al., 2009) as

$$H(f_i) = \mathcal{F}\{h(\tau)\} = \int_{-\infty}^{\infty} h(\tau)\exp(-j2\pi f\tau)d\tau$$
$$= \sum_{l=1}^{L_C}\sum_{\substack{k=1 \\ l \neq k}}^{L_r} \alpha_{k,l}\exp\left\{-j\left[2\pi f_i\left(T_l + \tau_{k,l}\right) - \varphi_{k,l}\right]\right\} = \sum_{l=1}^{L_C}\sum_{\substack{k=1 \\ l \neq k}}^{L_r} \alpha_{k,l}\exp\left[-j\left(\theta_{k,l}\right)\right]' \tag{20}$$

where, $\alpha_{k,l}$ and $\theta_{k,l} = 2\pi f_i(T_l + \tau_{k,l}) - \varphi_{k,l}$, are the magnitude and phase respectively, at the ith subcarrier of the channel, and $\mathcal{F}\{\cdot\}$ Fourier transform operation. Let N_f be the number of

subcarriers or frequency points in the CTF, then $\Delta f = W/(N_f - 1) = 4.125$ MHz, is the frequency separation between subcarriers in a MB-OFDM UWB system. The magnitude $|H(f_i)| = r_i$, of the ith subcarrier in the frequency domain it is modeled as a Nakagami-m RV with probability density function (PDF) given by (Nakagami, 1960)

$$f_{|H(f_i)|}(r_i) = \frac{2}{\Gamma\left(m^i_{eq}\right)}\left(\frac{m^i_{eq}}{\Omega^i_{eq}}\right)^{m^i_{eq}} r_i^{2m^i_{eq}-1} \exp\left(-\frac{m^i_{eq}}{\Omega^i_{eq}}r_i^2\right), \quad m^i_{eq} \geq 0.5, \tag{21}$$

where Ω^i_{eq}, is the average power and m^i_{eq}, the fading parameter of the UWB channel.

2.3.2 Average power and fading parameter in frequency

The average power Ω^i_{eq}, and the fading parameter m^i_{eq}, of the ith subcarrier in UWB channel can be expressed according to (Nakagami, 1960) as

$$\Omega^i_{eq} \triangleq E\{r_i^2\} = E\{|H(f_i)|^2\} = E\{|H_R(f_i)|^2 + |H_I(f_i)|^2\}, \tag{22}$$

$$m^i_{eq} \triangleq \frac{\left(E\{|H(f_i)|^2\}\right)^2}{E\{|H(f_i)|^4\} - \left(E\{|H(f_i)|^2\}\right)^2}. \tag{23}$$

where, $|H_R(f_i)|$ and $|H_I(f_i)|$ are the real and imaginary part of the module $|H(f_i)|$ of the channel transfer function of the channel. The average power for the 802.15.4a UWB channel is obtained from Eq. (20) and Eq. (22) according to (Llano et al., 2009) as

$$\Omega^i_{eq} = \sum_{l=1}^{L_C}\sum_{\substack{k=1\\l\neq k}}^{L_r} E\{r_i^2\} = \sum_{l=1}^{L_C}\sum_{\substack{k=1\\l\neq k}}^{L_r}\Omega_{k,l} = \Omega_0\sum_{l=1}^{L_C}\sum_{\substack{k=1\\l\neq k}}^{L_r}\exp\left[-\left(\frac{T_l}{\eta} + \frac{\tau_{k,l}}{\gamma}\right)\right] \times \frac{M_{\text{cluster}}}{\gamma\left[(1-\beta)\lambda_1 + \beta\lambda_2 + 1\right]}. \tag{24}$$

The fading parameter m^i_{eq}, in frequency of the ith subcarrier of the 802.15.4a UWB channel, can be expressed according to (Llano at al., 2009) as

$$m^i_{eq} = \frac{\left(\sum_{l=1}^{L_C}\sum_{k=1}^{L_r}\Omega_{k,l}\right)^2}{\sum_{l=1}^{L_C}\sum_{k=1}^{L_r}\left(\frac{\Omega^2_{k,l}}{m_{k,l}}\right) + \sum_{l=1}^{L_C}\sum_{\substack{n=1\\(l,k)\neq(n,m)}}^{L_C}\sum_{k=1}^{L_r}\sum_{m=1}^{L_r}\Omega_{k,l}\Omega_{m,n}}. \tag{25}$$

where, $\Omega_{k,l}$ is the mean power of the kth MPC or path given by Eq. (16) and $m_{k,l}$ is the fading parameter defined as a lognormal distributed RV, whit mean μ_m and standard deviation σ_m given by Eq. (19), i.e., $m_{k,l} \sim \mathcal{L}(\mu_m, \sigma_m)$. Fig. 4 shows the comparison of the amplitude $|H(f_i)|$ PDF of the 802.15.4a UWB channel, between the simulated data and the Nakagami-m analytical approximation, where Ω^i_{eq}, and m^i_{eq}, are calculated from Eq. (24) and Eq. (25). 8 clusters and 12 rays by cluster were assumed in simulations. The rest of parameters used in the Fig. 4 were: $\sigma_c = \sigma_r = 3.4$ dB, $\eta = 24$, $\gamma = 12$ and $\Omega_0 = 1$.
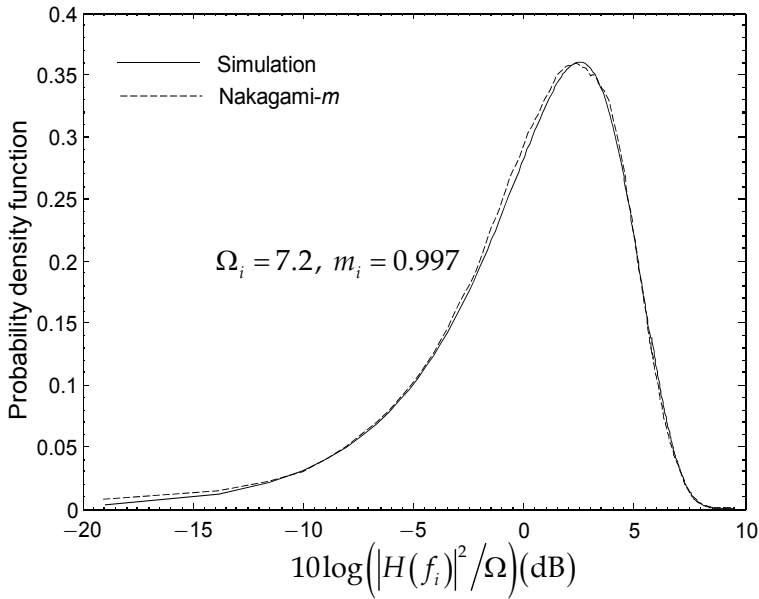
Fig. 4. Probability density function of the 802.15.4a UWB channel frequency amplitude $|H(f_i)|$ using the Nakagami-*m* analytical approximation

From Fig. 4, it can be observed that the Nakagami-*m* approximation and simulation curves are very similar and these results show that for a UWB channel with Nakagami-*m* fading and independents MPCs: a) the magnitude of the channel response frequency at each frequency bin is approximately Nakagami-*m* distributed with the mean power (Eq. (24)) and the fading parameter (Eq. (25)); and b) these results also show that if the MPC number is higher that 96 (number of rays multiplied by number of clusters) then the relative error in the m_{eq}^{i}, is less than 0.1% with respect to $m_{eq}^{i}=1$ (Rayleigh fading). The Mean Squared Error (MSE) between the data simulated and Nakagami-*m* PDF analytical expression given by Eq. (21) in Fig. 4 is de 0.16%. MSE is calculated as

$$\text{MSE} = E\left\{\frac{1}{N}\sum_{n=1}^{N}\left(r_n - \hat{r}_n\right)^2\right\}, \tag{26}$$

where, r_n represent the analytical value obtained in the Eq. (21), $\hat{r}_n$ the value simulated and *N* the samples number. Fig. 5 shows the cumulative distribution function (CDF) for the amplitude $|H(f_i)|$ of channel response frequency normalized by the mean power Ω_{eq}^{i}. Note that $|H(f_i)|$ becomes Rayleigh distributed for a sufficiently high number of MPC (typical environment in UWB channels). For instance, if the MPC number is higher than 63 contributions then the difference of the CDF for 10⁻³ between the simulated distribution and the Rayleigh distribution is less than 2 dB.

2.3.3 Power correlation coefficient
As mentioned above, calculating the power correlation coefficient is important for evaluation of the fade depth and fade margin due to small-scale fading and allows a proper
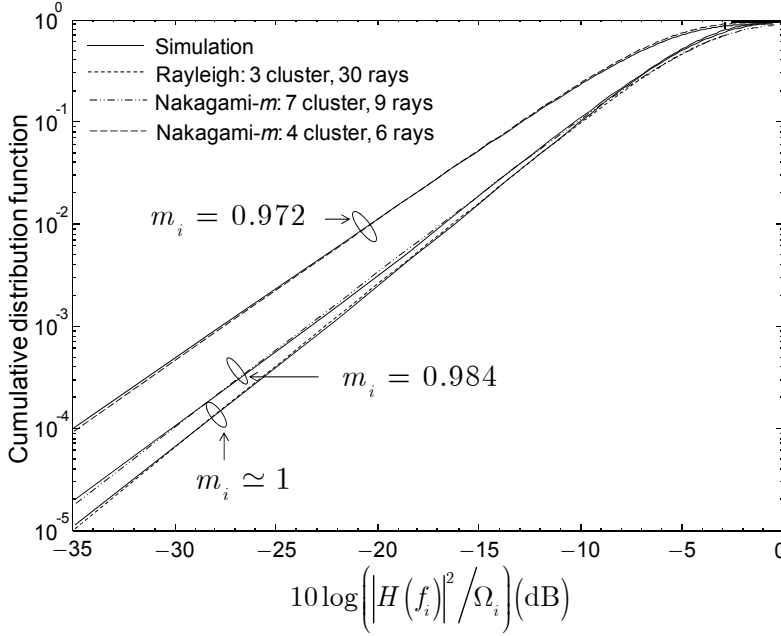
Fig. 5. Cumulative distribution function of the normalized channel frequency amplitude
$|H(f_i)|$, using the Nakagami-m analytical approximation, for several MPC contributions.

evaluation of the link budget in terms of the bandwidth channel. In addition, as shown later, this analysis enable to calculate and validate through simulation the coherence bandwidth and coherence time of the MB-OFDM UWB channel. The power correlation coefficient $\rho_{i,j}$ in frequency of the UWB channel between the ith and jth subcarrier is defined according to (Papoulis, 2002) as

$$\rho_{ij} \triangleq \frac{\text{cov}\left\{r_i^2 r_j^2\right\}}{\sqrt{\text{var}\left\{r_i^2\right\}\text{var}\left\{r_j^2\right\}}} = \frac{E\left\{r_i^2 r_j^2\right\} - E\left\{r_i^2\right\}E\left\{r_j^2\right\}}{\sqrt{\text{var}\left\{r_i^2\right\}\text{var}\left\{r_j^2\right\}}}, \tag{27}$$

where, $r_i = |H(f_i)|$, defines the amplitude of the ith subcarrier in frequency, and is approximated by a Nakagami-m distribution, therefore its power denoted by $r_i^2 = \left|H(f_i)\right|^2$ is a Gamma distribution and var($\cdot$) is the variance of the RV. The variance of the power $r_i^2 = \left|H(f_i)\right|^2$, of the ith subcarrier is given according to (Papoulis, 2002) as

$$\text{var}\left\{r_i^2\right\} \triangleq \text{var}\left\{\left|H(f_i)\right|^2\right\} = E\left\{\left|H(f_i)\right|^4\right\} - E^2\left\{\left|H(f_i)\right|^2\right\}. \tag{28}$$

The nth moment of the Nakagami-m distribution is given by (Nakagami, 1960)

$$E\left\{r^n\right\} = \frac{2}{\Gamma(m)}\left(\frac{m}{\Omega}\right)^m \int_0^\infty r^{2m+n-1}\exp\left(-\frac{mr^2}{\Omega}\right)dr = \frac{\Gamma\left(m+\frac{n}{2}\right)}{\Gamma(m)}\left(\frac{\Omega}{m}\right)^{\frac{n}{2}}, \tag{29}$$

where, n is a natural number. Evaluating Eq. (28) considering Eq. (29) is obtained

$$\text{var}\{r_i^2\} = E\left\{|H(f_i)|^4\right\} - E^2\left\{|H(f_i)|^2\right\} = \frac{\Gamma\left(m_{eq}^i + 2\right)}{\Gamma\left(m_{eq}^i\right)}\left(\frac{\Omega_{eq}^i}{m_{eq}^i}\right)^2 - \left[\frac{\Gamma\left(m_i + 1\right)}{\Gamma\left(m_{eq}^i\right)}\left(\frac{\Omega_{eq}^i}{m_{eq}^i}\right)\right]^2 = \frac{\left(\Omega_{eq}^i\right)^2}{m_{eq}^i} \, . \quad (30)$$

Since the indoor UWB channel is assumed static during the transmission of an OFDM symbol, then the equivalent average power $\Omega_{eq}^i(i=1,\cdots,N_f)=\Omega$ and the equivalent fading parameter, $m_{eq}^i(i=1,\cdots,N_f)=m$. Substituting Eq. (30) in Eq. (27) is obtained $\rho_{i,j}$ as

$$\rho_{ij} \triangleq \frac{E\left\{r_i^2 r_j^2\right\} - \Omega_{eq}^i \Omega_{eq}^i}{\sqrt{\frac{\left(\Omega_{eq}^i\right)^2}{m_{eq}^i} \times \frac{\left(\Omega_{eq}^j\right)^2}{m_{eq}^j}}} = \left(\frac{E\left\{r_i^2 r_j^2\right\} - \Omega^2}{\Omega^2}\right) m \, . \quad (31)$$

Solving from Eq. (31) $E\left\{r_i^2 r_j^2\right\}$ in the numerator, is obtained according to (Llano et al., 2009)

$$E\left\{r_i^2 r_j^2\right\} = \sum_{l=1}^{L_C}\sum_{k=1}^{L_r}\left(\frac{m_{k,l}+1}{m_{k,l}}\right)\Omega_{k,l}^2 + \sum_{l=1}^{L_C}\sum_{\substack{k=1 \\ l \neq k}}^{L_r}\sum_{n=1}^{L_C}\sum_{\substack{m=1 \\ n \neq m}}^{L_r}\Omega_{m,n}\Omega_{k,l}\left[1 + \cos\left(B_{l,n}^{k,m}\right)\right] \, , \quad (32)$$

where, $B_{l,n}^{k,m} = 2\pi f\left[\left(T_l + \tau_{k,l}\right) - \left(T_n + \tau_{m,n}\right)\right](i-j)$. Substituting Eq. (32) in Eq. (31) considering Eq. (24) and Eq. (25), one can be obtain a closed-form general expression of the power correlation coefficient for MB-OFDM UWB channel in frequency according to (Llano et al., 2009) as

$$\rho_{ij} = \frac{\displaystyle\sum_{l=1}^{L_C}\sum_{k=1}^{L_r}\left(\frac{\Omega_{k,l}^2}{m_{k,l}}\right) + \sum_{l=1}^{L_C}\sum_{\substack{k=1 \\ l \neq k}}^{L_r}\sum_{n=1}^{L_C}\sum_{\substack{m=1 \\ n \neq m}}^{L_r}\Omega_{m,n}\Omega_{k,l}\cos B_{l,n}^{k,m}}{\displaystyle\sum_{l=1}^{L_C}\sum_{k=1}^{L_r}\left(\frac{\Omega_{k,l}^2}{m_{k,l}}\right) + \sum_{l=1}^{L_C}\sum_{\substack{k=1 \\ (l,k)\neq(n,m)}}^{L_r}\sum_{n=1}^{L_C}\sum_{m=1}^{L_r}\Omega_{m,n}\Omega_{k,l}} \, . \quad (33)$$

Note, that the power correlation coefficient given by the equation (33) is function of frequency separation between subcarriers, $\Delta f = f_1 - f_2 = W/(N_f - 1) = 4.125$ MHz, where W is the channel bandwidth in UWB system ($W = 7.5$ GHz), $N_f = 128$, is the number subcarriers in MB-OFDM UWB, and $\Delta_\tau = \left(T_l + \tau_{k,l}\right) - \left(T_n + \tau_{m,n}\right)$ the time delay of all multipath components (MPC) in the receiver. Particularizing Eq. (33) for the 802.15.3a MB-OFDM UWB channel is obtained to according (Llano et al., 2009)

$$\rho_{ij} = \frac{\displaystyle K\sum_{l=1}^{L_C}\sum_{k=1}^{L_r}\Omega_{k,l}^2 + \sum_{l=1}^{L_C}\sum_{\substack{k=1 \\ l \neq k}}^{L_r}\sum_{n=1}^{L_C}\sum_{\substack{m=1 \\ n \neq m}}^{L_r}\Omega_{m,n}\Omega_{k,l}\cos B_{l,n}^{k,m}}{\displaystyle K\sum_{l=1}^{L_C}\sum_{k=1}^{L_r}\Omega_{k,l}^2 + \sum_{l=1}^{L_C}\sum_{\substack{k=1 \\ (l,k)\neq(n,m)}}^{L_r}\sum_{n=1}^{L_C}\sum_{m=1}^{L_r}\Omega_{m,n}\Omega_{k,l}} \, . \quad (34)$$

with, $A = \exp\left(4\sigma_{np}^2\right) - 2$ and σ_{np} the standard deviation of the lognormal fading in nepers units, given by

$$\sigma_{np} = \frac{\ln(10)}{20}\sqrt{\sigma_c^2 + \sigma_r^2} \, , \quad (35)$$

where, σ_c and σ_r are the standard deviations in dB units of clusters and rays, respectively. Fig. 6 shows the comparison of the correlation coefficient between simulated data and the analytical expression given by Eq. (34) for the following parameters: $\sigma_c = \sigma_r = 3.4$ dB, $\eta = 24$, $\gamma = 12$, $\Omega_0 = 1$, $L_c = 8$ and $L_r = 12$.
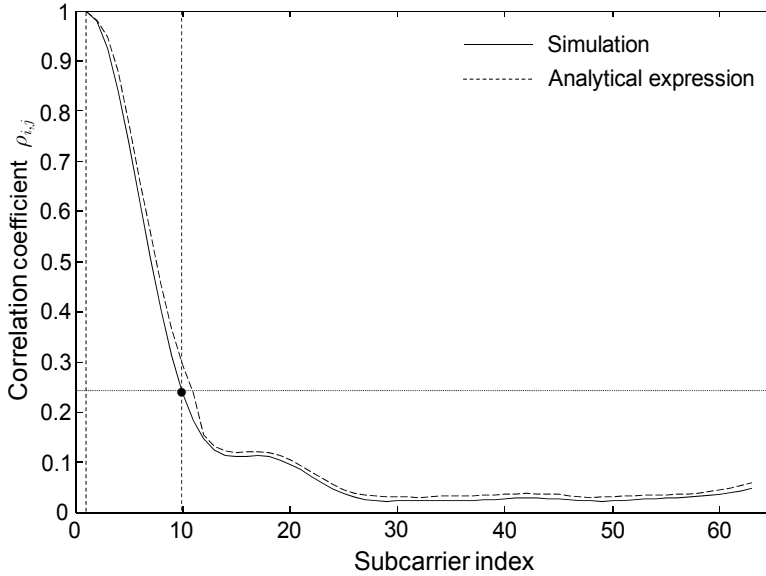
Fig. 6. Correlation coefficient as a function of the subcarrier order with respect to the first subcarrier position in the IEEE 802.15.3a MB-OFDM UWB channel type CM4.
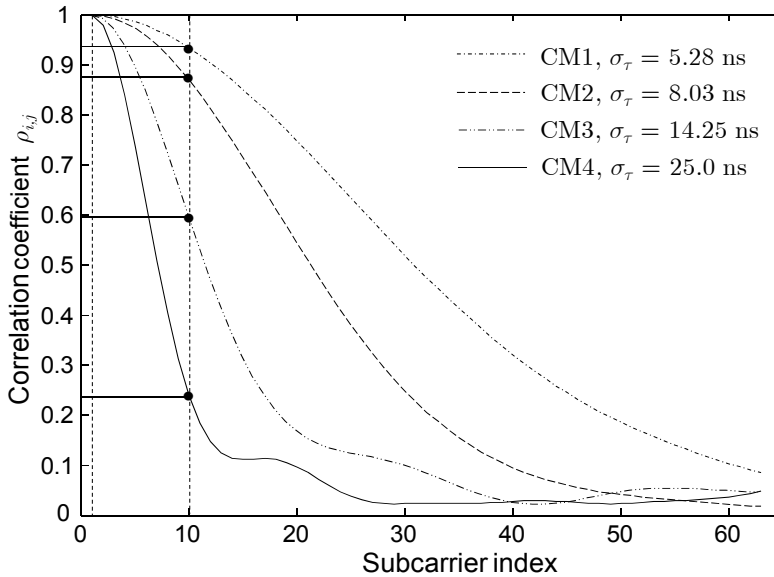
Fig. 7. Correlation coefficient as a function of the subcarrier order and delay spread in the 802.15.3a MB-OFDM UWB channel.

Note that for the maximum frequency separation between two pilot tones in MB-OFDM UWB channel defined as 9×4.125 MHz = 37.125 MHz, the correlation coefficient $\rho_{i,j}$ between the first (pilot) and tenth subcarrier is in a range from 0.25 to 0.98 for UWB channel CM4. Fig. 7 shows the correlation coefficient as a function of the UWB channel delay spread σ_τ, for four channel scenarios: CM1(σ_τ = 5.28 ns), CM2(σ_τ =8.03 ns), CM3(σ_τ =14.25 ns), and CM4(σ_τ = 25 ns). From this figure, we can observe a high dependence of the correlation coefficient between a couple of subcarriers on the delay spread. The parameters used in the simulations are given by (Foerster, 2003).

2.3.4 Coherence bandwidth of the MB-OFDM UWB channel

In this section we calculate the coherence bandwidth of UWB channel from the correlation coefficient $\rho_{i,j}$. The coherence bandwidth B_C is a parameter used to characterize the wireless channel in frequency domain, and can be defined as the range of frequencies over which the channel equally affects all spectral components of the transmitted signal, In other words, its transfer function $H(f,t)$ remains constant during transmission of an MB-OFDM symbol. Hence, the channel can be considered flat in frequency, i.e., passes all spectral components with approximately equal gain and linear phase. When the bandwidth of the transmitted signal B_S, is higher than the coherence bandwidth B_C, then the channel is frequency selective, which means that some spectral components of the signal B_S, will be modified quite differently by the channel, producing distortion in the received signal.

From Eq. (33) we find an expression to calculate the coherence bandwidth B_C. Let $A = \sum_{l=1}^{L_C} \sum_{k=1}^{L_r} \left(\frac{\Omega_{k,l}^2}{m_{k,l}} \right)$ and, $B = \sum_{l=1}^{L_C} \sum_{k=1}^{L_r} \sum_{n=1}^{L_C} \sum_{m=1}^{L_r} \Omega_{k,l} \Omega_{m,n}$. After simple algebraic operations, an

expression is defined for frequency separation Δf of UWB channel in function of $\rho_{i,j}$ according to (Llano et al., 2009) as

$$B_C = \Delta f = \frac{\arccos\left[\dfrac{A(\rho_{ij}-1)}{B} + \rho_{ij} \right]}{2\pi\Delta\tau}. \tag{36}$$

Note which Eq. (36) aggress with [Fle96, Eq. (5)]. When $\rho_{i,j} = 1$, corresponds to the highest correlation in frequency, in this case the coherence bandwidth $B_C = \Delta f = 0$ (represents the same frequency bin, $f_i = f_j$). When $\rho_{i,j} \to 0$, the temporal bins are widely separated and $\Delta\tau \to \sigma_\tau$ Then

$$B_C = \Delta f \simeq \frac{1}{4\sigma_\tau}. \tag{37}$$

Fig. 8 shows the simulation of the coherence bandwidth B_C defined in (36) as a function of delay spread for UWB channel. Note, that for $\rho_{i,j} = 0.75$, $B_C = 4.7$ MHz, this value agrees with coherence bandwidth obtained in the measurement campaign for the indoor UWB channel carried out in the iTEAM of the Polytechnic University of Valencia (Spain) (Diaz 2007).
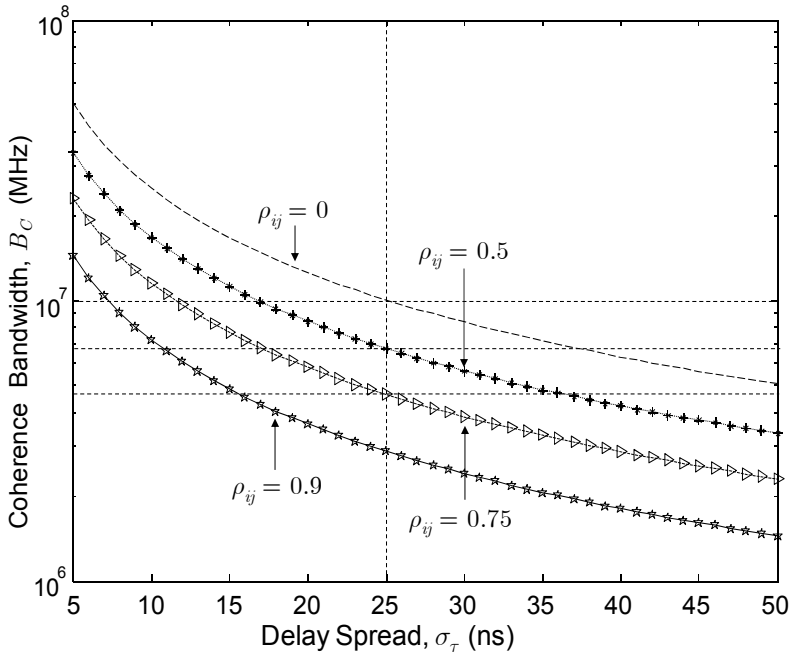
Fig. 8. Coherence bandwidth of the UWB channel as a function of delay spread

2.3.5 Coherence time of the MB-OFDM UWB channel

Delay spread, σ_τ, and *coherence bandwidth B_C*, are parameters which describe the time dispersive of the wireless channel in a local area, sufficient to characterize a static wireless channel. However, they do not offer information about the time varying of the channel in a small-scale region, caused by either relative motion between the mobile and base station or by movement of objects in the channel (Rappaport, 1996). To model the dynamic characteristic of the wireless channel, two parameters are defined: *Doppler spread* denoted by f_D and *coherence time* by T_C.

Doppler spread f_D is a measure of the spectral broadening caused by the time rate of change of the mobile radio channel. Coherence time T_C is the time domain dual of Doppler spread and are inversely proportional to one another.

Coherence time T_C for the UWB channel can be derived from Eq. (33). Defining $\Delta f = f_D$ and $\Delta \tau \to \sigma_\tau$, resulting

$$T_C = \frac{\arccos\left[\dfrac{A\left(\rho_{ij}-1\right)}{B} + \rho_{ij}\right]}{2\pi f_D}. \tag{37}$$

According to Eq. (37) when $f_D \to 0$, the wireless channel can be assumed static, because T_C, is high compared with the time transmission of a data frame in MB-OFDM UWB. Fig. 9 shows the simulation of the coherence time T_C derived in Eq. (37) as a function of Doppler spread for UWB channel. Note that for f_D = 13.2 Hz, T_C = 13 ms. The time transmission of a data

frame in MB-OFDM UWB is 0.63 ms (ECM, 2008). That is, it can transmit up to 22 data frames in the coherence time T_C = 13 ms.
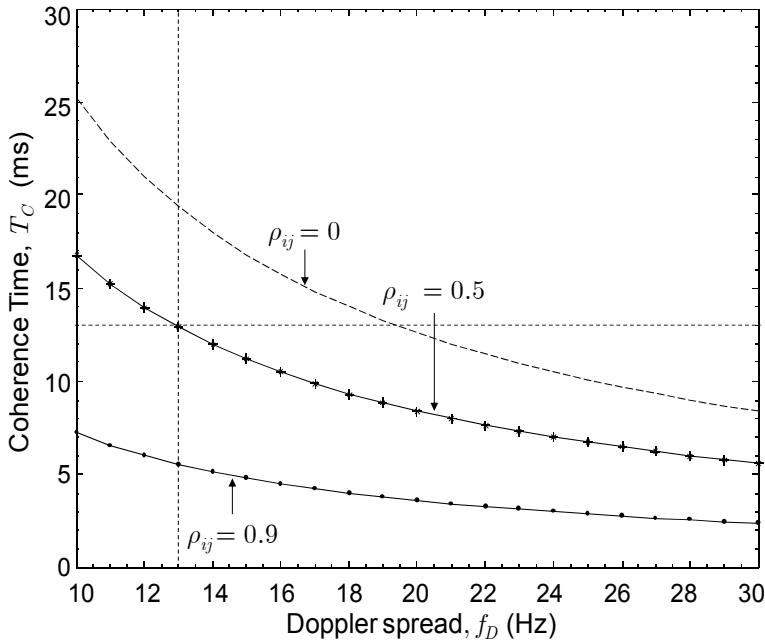
Fig. 9. Coherence time of the UWB channel as a function of Doppler spread

2.4 UWB channel power variation

The development of UWB communications systems requires a proper channel power characterization related to the propagation environment. Given the wideband nature of the UWB signal (bandwidth of 7.5 GHz), it is of paramount importance to characterize the channel power variations in terms of the channel bandwidth in order to evaluate the performance of UWB applications. It is well known that in wireless channels the multipath propagation causes destructive signal interference leading to small-scale fading. In an unresolved multipath components (MPCs) channel, the received signal can suffer severe fading increasing the system outage probability and degrading its performance (Jakes, 1974). In view of the fact that multipath propagation can produce received signal fade, it is necessary to provide additional power in the link budget to enhance the system quality. This additional power is known as fade margin (Cardoso, 2003). Other parameter to understand the small-scale fading concept is the fade depth that is referred to the received signal power variations about its local mean (Yang, 1999).

In order to have a complete description of the link budget and to define accurately the receiver sensitivity, a proper characterization of the channel power behavior is necessary. In this sense, the fade depth, the fade margin and the average power are important parameters to obtain an adequate description of the link budget, because they condition the final outage probability, and their knowledge is very useful to the radio network planning [Jak74]. It is well known that the fade depth and the fade margin depend on the channel bandwidth, the transmitted-received distance (Bastidas, 2005), and the small-scale fading conditions.

Therefore, their dependence is closely related to the environment where the propagation occurs. Due to the importance of these parameters in the radio network planning, they have been extensively analyzed in the literature, especially in narrowband channels. In (Cardoso, 2003), the fade depth and fade margin are evaluated for a Rician channel as a function of the equivalent received bandwidth, showing that the fade margin variation is related to the channel bandwidth and that it falls monotonically when the channel bandwidth increases. In (Yanng, 1999), the dependence of the received signal level distribution on the channel bandwidth is studied by computer simulations, showing that the fade depth has a strong dependence on the equivalent channel bandwidth. In (Malik, 2008), a relationship between the fade depth and the channel bandwidth is derived from a measurements campaign carried out in an indoor scenario. Therefore, the study of the average signal level, the fade depth and the fade margin in wideband transmission systems is a key issue for the development of wireless systems. Since UWB systems employ a bandwidth higher than 500 MHz (FCC, 2002), an adequate characterization of the channel power variations is necessary to deploy such systems. In this section, we propose as a novel contribution an analytical approach to derive the fade depth and fade margin under the assumption that the received power is Gamma distributed. In our investigation, we have considered the IEEE 802.15.4a UWB channel model developed for indoor and outdoor environments in low data rate WPAN applications (Molisch, 2005), where the wireless channel is assumed quasi-static during the symbol transmission (Hashemi, 1993), the module of the channel impulse response of the UWB channel denoted by $|h(\tau)| = \alpha$, which describe the small scale fading in the time follow a Nakagami-m distribution, and the module of the channel transfer function $|H(f_i)| = r_i$ also follow a Nakagami-m distribution.

Since the module $|H(f_i)|$ of each of the frequency bins in a UWB channel can be approximated by a Nakagami-m distribution, then the instantaneous power in frequency follows a Gamma distribution (Nakagami-m squared). Therefore, it is possible to assume that the UWB channel power in a bandwidth $\Delta f = f_1 - f_2$, denoted by Ψ_f can be approximated by a Gamma distribution.

In the words, $r_i = |H(f_i)|$ represents the magnitude of the CTF and follows a Nakagami-m distribution, i.e., $r \sim \mathcal{M}(m_{eq}, \Omega_{eq})$, where m_{eq} is the fading parameter and Ω_{eq} the mean power in the frequency bin. $\Psi_f = r^2 = |H(f)|^2$ represents the power in a bandwidth $\Delta f = f_1 - f_2$, and follows a Gamma distribution, i.e. $\Psi_f \sim \mathcal{G}(m_{\Delta f}, \Omega_f)$. We have checked the results derived from this analytical approach with Monte Carlo simulation results for several environments described in the UWB IEEE 802.15.4a channel model.

2.4.1 Analytical approach of the power distribution in UWB channel: the Fade depth and the fade margin

In this section, we propose an analytical approach to evaluate the power distribution, the *fade depth* and the *fade margin* as a function of the channel bandwidth. This approach is based on the IEEE 802.15.4a channel model described previously. Asymptotic values for the *fade depth* and the *fade margin* are derived and compared with simulation results for indoor residential and outdoor environments in both line-of-sight (LOS) and non-line-of-sight (NLOS) conditions. Simulation results have been performed using the Monte Carlo method. For each environment considered, 1000 realizations of a small local area have been simulated, modeling the number of clusters, rays, cluster arrival and ray arrival times. The

small local area corresponds to a small region around the receiver, in which the number of clusters and rays are constant, and only the phase and amplitude of rays change for short displacements. In addition, for each realization, 60000 simulations of the MPCs phase and amplitude have been performed to model the power channel variations. Our analytical approach starts with the calculation of the channel transfer function (CTF) of the IEEE 802.15.4a UWB channel, this result was already found previously and is given by the Eq. (20) which is repeated here for convenience.

$$H(f_i) = \mathcal{F}\{h(\tau)\} = \sum_{l=1}^{L_C}\sum_{\substack{k=1\\l\neq k}}^{L_r}\alpha_{k,l}\exp\left\{-j\left[2\pi f_i\left(T_l+\tau_{k,l}\right)-\varphi_{k,l}\right]\right\} = \sum_{l=1}^{L_C}\sum_{\substack{k=1\\l\neq k}}^{L_r}\alpha_{k,l}\exp\left[-j\left(\theta_{k,l}\right)\right].$$

From the Parseval relation (Proakis, 1995), the UWB channel power in linear units (mW) inside the bandwidth, $\Delta f = f_2 - f_1$, denoted by $\Psi_{\Delta f}$, is calculated in frequency as

$$\Psi_{\Delta f} = \int_{f1}^{f2}\left|H(f)\right|^2 df\,,\tag{38}$$

where $|H(f)|$ is the magnitude of the CTF, f_1 and f_2 are the lower and upper frequencies, respectively. The squared module $|H(f)|^2$ is given according to (Llano et al., 2009) as

$$\left|H(f)\right|^2 = \left(\sum_{l=1}^{L_C}\sum_{k=1}^{L_r}\alpha_{k,l}^2 + \sum_{l=1}^{L_C}\sum_{\substack{n=1\\(l,k)\neq(n,m)}}^{L_C}\sum_{k=1}^{L_r}\sum_{m=1}^{L_r}\alpha_{k,l}\alpha_{m,n}\cos\left\{2\pi f\left[\left(T_l+\tau_{k,l}\right)-\left(T_n+\tau_{m,n}\right)+\left(\varphi_{k,l}-\varphi_{m,n}\right)\right]\right\}\right),\tag{39}$$

where $(l,k)\neq(n,m)$, represents the condition to evaluate the quadruple summation, i.e., $l\neq n$ OR $k\neq m$.

A. Channel power: We have assumed total independence between a pair of MPCs amplitude coefficients, in accordance with (Casioli et al., 2002), (Chong, 05) where the correlation coefficients between the amplitude of two MPCs measured remains below 0.2 (Casioli et al., 2002), and 0.35 (Chong, 2005). The UWB channel power inside the bandwidth Δf(Hz) according to Eq. (38) is given by

$$\begin{aligned}\Psi_{\Delta f}(\mathrm{mW}) = \int_{f1}^{f2}\left|H(f)\right|^2 df = \sum_{l=1}^{L_C}\sum_{k=1}^{L_r}\alpha_{k,l}^2\int_{f1}^{f2}df + \\ \sum_{l=1}^{L_C}\sum_{\substack{n=1\\(l,k)\neq(n,m)}}^{L_C}\sum_{k=1}^{L_r}\sum_{m=1}^{L_r}\alpha_{k,l}\alpha_{m,n}\int_{f1}^{f2}\cos\left\{2\pi f\left[\left(T_l+\tau_{k,l}\right)-\left(T_n+\tau_{m,n}\right)+\left(\varphi_{k,l}-\varphi_{m,n}\right)\right]\right\}df\end{aligned}.\tag{40}$$

Solving the two integrals in Eq. (40), UWB channel power inside the bandwidth Δf(Hz), according to (Llano et al., 2010) is given by

$$\begin{aligned}\Psi_{\Delta f}(\mathrm{mW}) = \Delta f\sum_{l=1}^{L_C}\sum_{k=1}^{L_r}\alpha_{k,l}^2 + \\ \frac{1}{2\pi}\sum_{l=1}^{L_C}\sum_{\substack{n=1\\(l,k)\neq(n,m)}}^{L_C}\sum_{k=1}^{L_r}\sum_{m=1}^{L_r}\frac{\alpha_{k,l}\alpha_{m,n}}{\left(T_l+\tau_{k,l}\right)-\left(T_n+\tau_{m,n}\right)}\left[\sin\left(2\pi f_2 C_{l,n}^{k,m}\right)-\sin\left(2\pi f_1 C_{l,n}^{k,m}\right)\right]\end{aligned},\tag{41}$$

where $C_{l,n}^{k,m} = \left[\left(T_l + \tau_{k,l}\right) - \left(T_n + \tau_{m,n}\right)\right] + \left(\varphi_{k,l} - \varphi_{m,n}\right)$. Note that in Eq. (40) the first term represents the average power inside the bandwidth Δf(Hz), and the second term the fluctuation of the instantaneous power as a function of the limits frequencies f_1 and f_2 and the delay of each multipath component. A comparison of the channel power PDF between simulated data and the Gamma approximation calculated using Eq. (41) for an indoor residential environment is shown in Fig. 10. The PDFs curves plotted correspond to a single realization (one small local area) of the indoor residential environment with LOS condition for different channel bandwidths (Δf = 2 GHz, 5 GHz, and 7 GHz).
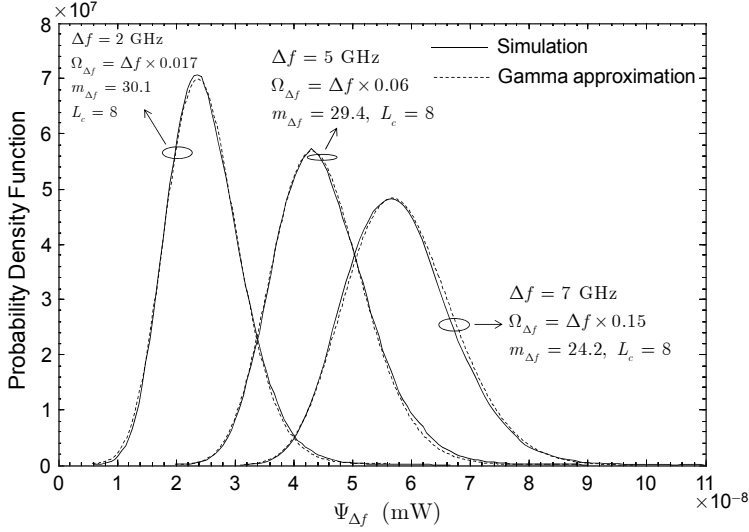
Fig. 10. Probability density function of the power, Ψ_f, in the indoor residential 802.15.4a UWB channel model with LOS condition and several values of channel bandwidth.

Other comparison that support the assumption that the Gamma distribution can be able to provide a good approximation to the channel power variations due to fast fading are shown in Fig. 11, where indoor residential and outdoor environments are considered in LOS and NLOS conditions with a channel bandwidth equal to 1 GHz. It is worth to note that the results show a higher fading parameter in LOS compared to the NLOS condition for the same channel bandwidth and environment. The parameters used in the simulation results are summarized in Table I. The goodness-of-fit of the Gamma distribution to the simulated data in Fig. 10 and Fig. 11 has been assessed through the Kolmogorov-Smirnov (KS) test for a 5% significant degree (Massey, 1951).

B. Mean power: The mean power denoted by Ω_f expressed in linear units (mW) in UWB channel inside of the bandwidth Δf can be calculated from Eq. (41) as

$$E\left\{\Psi_{\Delta f}\right\} = E\left\{\int_{f1}^{f2} \left|H(f)\right|^2 df\right\} = \Delta f \sum_{l=1}^{L_C}\sum_{k=1}^{L_r} E\left\{\alpha_{k,l}^2\right\} + \frac{1}{2\pi}$$

$$\times \sum_{\substack{l=1 \\ (l,k)\neq(n,m)}}^{L_C}\sum_{n=1}^{L_C}\sum_{k=1}^{L_r}\sum_{m=1}^{L_r} E\left\{\frac{\alpha_{k,l}\alpha_{m,n}}{\left[\left(T_l + \tau_{k,l}\right) - \left(T_n + \tau_{m,n}\right)\right]}\left[\sin\left(2\pi f_2 C_{l,n}^{k,m}\right) - \sin\left(2\pi f_1 C_{l,n}^{k,m}\right)\right]\right\}. \quad (42)$$

Assuming the random variables $\alpha_{k,l}$, $\alpha_{m,n}$, $\varphi_{k,l}$, independents and the phase $\varphi_{k,l}$, uniformly distributed between 0 and 2π. Then, mean power for the IEEE 802.15.4a result to solve the Eq. (42) according to (Llano et al., 2010) as

$$E\left\{\Psi_{\Delta f}\right\} = \Delta f \sum_{l=1}^{L_C} \sum_{k=1}^{L_r} E\left\{\alpha_{k,l}^2\right\} = \Delta f \sum_{l=1}^{L_C} \sum_{k=1}^{L_r} \Omega_{k,l}$$
$$= \Delta f \sum_{l=1}^{L_C} \sum_{k=1}^{L_r} \exp\left[-\left(\frac{T_l}{\eta} + \frac{\tau_{k,l}}{\gamma}\right)\right] \times \frac{M_{\text{cluster}}}{\gamma\left[(1-\beta)\lambda_1 + \beta\lambda_2 + 1\right]}.$$

(43)

where $\Omega_{k,l}$ is the average power of each contribution in the 802.15.4a UWB channel calculated from the Eq. (16). Now, we investigate the channel power dependence on the channel bandwidth, deriving an analytical expression for the *fade depth* and the *fade margin*. Before performing these calculations is necessary to express the power of the UWB channel in logarithmic units (dBm) as $\Phi_{\Delta f}(\text{dBm})=10\log[\Psi_{\Delta f}(\text{mW})]$.
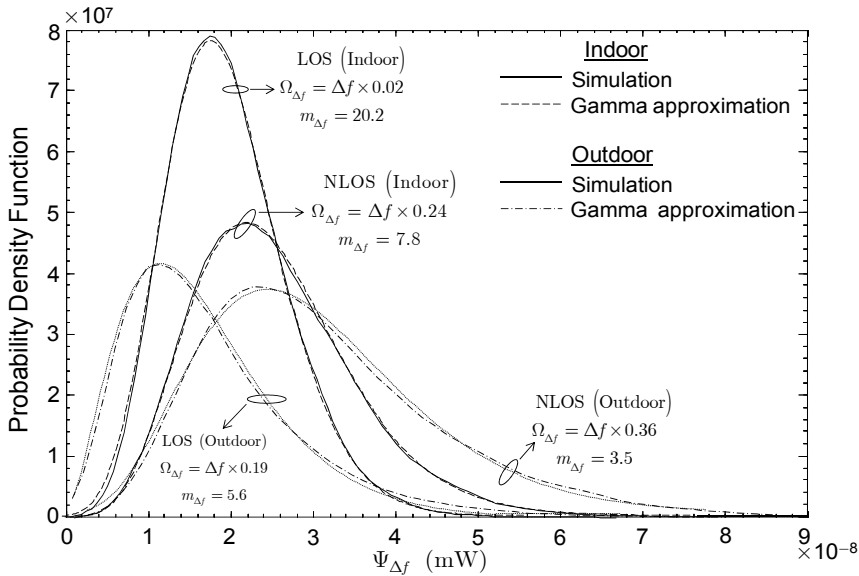
Fig. 11. Probability density function of the channel power, $\Psi\Delta f$, for indoor residential and outdoor environments with LOS and NLOS with a channel bandwidth $\Delta f = 1$ GHz.

C. Fade depth: The fade depth, denoted by $F_{n\sigma}$, can be defined as a measure of the channel power variation due to the small-scale fading (Malik, 2008). In a statistically sense, the fade depth is calculated as n times the standard deviation σ, of the channel power variations expressed in logarithmic units, i.e., $F_{n\sigma} = n \times \sigma$, with $n = 1, 2, 3,…,$. Therefore we calculated the standard deviation, σ, of channel power variation. Due to each MPC amplitude, $\alpha_{k,l}$, is modeled as a Nakagami-m random variable and the magnitude of the each frequency bin of the UWB channel $r=|H(f_i)|$ also is modeled as Nakagami-m distribution, according to the results show in Fig. 10 and Fig. 11, we have assumed that in a small local area around the receiver, the channel power variation $\Psi_f = r^2 = |H(f)|^2$ in linear units (mW) given by Eq. (41)

can be modeled as a Gamma distribution. As defined above the power of the UWB channel in logarithmic units (dBm) is expressed as $\Phi_{\Delta f}(dBm)=10\log[\Psi_{\Delta f}(mW)]$, the variance and standard deviation of the channel power in dBm is calculated as

$$\text{var}\left\{\Phi_{\Delta f}\left(dBm\right)\right\} \triangleq \sigma_{\Phi}^{2} = E\left\{\Phi_{\Delta f}^{2}\left(dBm\right)\right\} - E^{2}\left\{\Phi_{\Delta f}\left(dBm\right)\right\}. \tag{44}$$

Model parameters	Indoor residential		Outdoor	
	LOS	NLOS	LOS	NLOS
$\overline{L_c}$	3.0	3.5	13.6	10.5
Λ (1/ns)	0.047	0.12	0.0048	0.0243
λ_1 / λ_2 (1/ns)	1.54/0.15	1.77/0.15	0.13/2.41	0.15/1.13
β	0.095	0.045	0.0078	0.062
η (ns)	22.61	26.27	31.7	104.7
γ_0 (ns)	12.53	17.5	3.7	9.3
σ_{cluster} (dB)	2.75	2.93	3.0	3.0
k_{γ}	0	0	0	0
m_0 (dB)	0.67	0.69	0.77	0.56
k_m	0	0	0	0
$\hat{m}_0$ (dB)	0.28	0.32	0,78	0,25
$\hat{k}_m$	0	0	0	0

Table I. IEEE 802.15.4a UWB channel model parameters

The Gamma distribution in linear units can be derived easily from Nakagami-m distribution as, $r = \sqrt{\Psi}$, where Ψ and r are the RV Gamma and Nakagami-m respectively. Since cumulative distribution function (CDF) of RV Ψ (power) and r (amplitude) can be equal, i.e., $F_r(r) = F_\Psi(\Psi)$, then according to (Papoulis, 2002), (Peebles, 2001)

$$\int_{-\infty}^{r} f_X\left(x\right)dx = \int_{-\infty}^{\Psi} f_Y\left(y\right)dy. \tag{45}$$

Differentiating Eq. (45) and using transformation of variables, results

$$f_\Psi\left(\Psi\right) = f_r\left(r\right)\frac{dr}{d\Psi}. \tag{46}$$

The PDF of the Gamma distribution in linear units is obtained from Eq. (21) and Eq. (46) as

$$f_{\Psi_{\Delta f}}\left(\Psi_{\Delta f}\right) = \frac{1}{\Gamma\left(m_{\Delta f}\right)}\left(\frac{m_{\Delta f}}{\Omega_{\Delta f}}\right)^{m\Delta f} \Psi_{\Delta f}^{\;m\Delta f-1} \exp\left(-\frac{m_{\Delta f}\Psi}{\Omega_{\Delta f}}\right), \; \Psi_{\Delta f} \geq 0, \; m_{\Delta f} \geq 0,5, \tag{47}$$

where, $\Psi_{\Delta f}$ (mW) is the power in the bandwidth Δf, $\Omega_{\Delta f} = E\{\Psi_{\Delta f}\}$ the average power, and $m_{\Delta f} = \Omega_{\Delta f}^2 \big/ E\left\{\left(\Psi_{\Delta f} - \Omega_{\Delta f}\right)^2\right\}$ the fading parameter. As mentioned above the channel power in dBm, can be expressed as

$$\Phi_{\Delta f}\left(dBm\right) = 10\log\left(\Psi_{\Delta f}\right) \rightarrow \Psi_{\Delta f} = 10^{\frac{\Phi_{\Delta f}(dBm)}{10}} . \tag{48}$$

From (48) perform the following transformations

$$\Phi_{\Delta f}\left(dBm\right) = \frac{10}{\ln(10)}\ln\left(\Psi_{\Delta f}\right); \quad \frac{\partial \Phi_{\Delta f}\left(dBm\right)}{\partial \Psi_{\Delta f}} = \frac{10}{\Psi_{\Delta f}\ln(10)} . \tag{49}$$

To solve Eq. (44) is necessary to express the Gamma distribution in dBm. From Eq. (46), Eq. (47) and Eq. (49), Gamma distribution in logarithmic units (dBm) is expressed as

$$f_{\Phi_{\Delta f}}\left(\Phi_{\Delta f}\right) = \frac{\ln(10)}{10\Gamma\left(m_{\Delta f}\right)}\left(\frac{m_{\Delta f}}{\Omega_{\Delta f}}\right)^{m\Delta f} 10^{\frac{m\Delta f \Phi_{\Delta f}}{10}} \exp\left(-\frac{m_{\Delta f}}{\Omega_{\Delta f}}10^{\frac{\Phi_{\Delta f}}{10}}\right), \quad -\infty < \Phi_{\Delta f} < \infty . \tag{50}$$

Variance and standard deviation of the power $\Phi_{\Delta f}$ (dBm) is calculated from the central moments of the Gamma random variable in dBm as

$$E\left\{\Phi_{\Delta f}^n\left(dBm\right)\right\} = \frac{\ln(10)}{10\Gamma\left(m_{\Delta f}\right)}\left(\frac{m_{\Delta f}}{\Omega_{\Delta f}}\right)^{m\Delta f} \int_{-\infty}^{\infty} \Phi_{\Delta f}^n 10^{\frac{m\Delta f \Phi_{\Delta f}}{10}} \exp\left(-\frac{m_{\Delta f}}{\Omega_{\Delta f}}10^{\frac{\Phi_{\Delta f}}{10}}\right)d\Phi_{\Delta f} . \tag{51}$$

Particularizing $n = 1$ in Eq. (51) and considering Eq. (48) and Eq. (49), we obtain the first moment of the Gamma RV in dBm as

$$E\left\{\Phi_{\Delta f}\left(dBm\right)\right\} = \frac{10}{\ln(10)\Gamma\left(m_{\Delta f}\right)}\left(\frac{m_{\Delta f}}{\Omega_{\Delta f}}\right)^{m\Delta f} \int_{0}^{\infty} \Psi_{\Delta f}^{m\Delta f-1}\ln\left(\Psi_{\Delta f}\right)\exp\left(-\frac{m_{\Delta f}}{\Omega_{\Delta f}}\Psi_{\Delta f}\right)d\Psi_{\Delta f} . \tag{52}$$

To solve the integral in Eq. (50) we use (Gradshteyn, 2007, (4.352 1))

$$\int_{0}^{\infty} x^{\nu-1}\exp(-\mu x)\ln(x)dx = \frac{\Gamma(\nu)}{\mu^{\nu}}\left[\psi(\nu) - \ln(\mu)\right]; \; \mathrm{Re}(\mu) > 0 \wedge \mathrm{Re}(\nu) > 0 , \tag{53}$$

where, $x = \Psi_{\Delta f}$, $\nu = m_{\Delta f}$, $\mu = m_{\Delta f}/\Omega_{\Delta f}$, $\Gamma(\cdot)$ gamma function and $\psi(\nu) = \frac{\partial}{\partial \nu}\left\{\ln\left[\Gamma(\nu)\right]\right\}$ Psi (digamma) function (Abramowitz, 1972, (6.3.1)). Therefore, the mean or first moment of the Gamma distribution in dBm can be expressed as

$$E\left\{\Phi_{\Delta f}\left(dBm\right)\right\} = \frac{10}{\ln(10)}\left[\psi\left(m_{\Delta f}\right) - \ln\left(\frac{m_{\Delta f}}{\Omega_{\Delta f}}\right)\right] . \tag{54}$$

The second central moment or mean squared value of the Gamma distribution is calculated by substituting in Eq. (51) $n = 2$, and using Eq. (49) is obtained

$$E\left\{\Phi_{\Delta f}^{2}\left(\text{dBm}\right)\right\}=\left[\frac{10}{\ln(10)}\right]^{2}\frac{1}{\Gamma\left(m_{\Delta f}\right)}\left(\frac{m_{\Delta f}}{\Omega_{\Delta f}}\right)^{m\Delta f}\int_{0}^{\infty}\Psi_{\Delta f}^{m\Delta f-1}\left[\ln\left(\Psi_{\Delta f}\right)\right]^{2}\exp\left(-\frac{m_{\Delta f}}{\Omega_{\Delta f}}\Psi_{\Delta f}\right)d\Psi_{\Delta f}.\quad(55)$$

We can solve integral in Eq. (55) using (Gradshteyn, 2007, (4.358 2))

$$\int_{0}^{\infty}x^{\nu-1}\exp\left(-\mu x\right)\left[\ln\left(x\right)\right]^{2}dx=\frac{\Gamma\left(\nu\right)}{\mu^{\nu}}\left\{\left[\psi\left(\nu\right)-\ln\left(\mu\right)\right]^{2}+\zeta\left(2,\nu\right)\right\};\text{Re}\left(\mu\right),\text{Re}\left(\nu\right)>0,\quad(56)$$

where, $\zeta(\cdot,\cdot)$ Zeta Hurwitz function whose integral representation according to (WolframMathworld, 2011) is expressed as

$$\zeta\left(s,a\right)=\frac{1}{\Gamma(s)}\int_{0}^{\infty}\frac{t^{s-1}\exp\left(-at\right)}{1-\exp\left(-t\right)}dt;\ \ \text{Re}\left(s\right)>1\wedge\text{Re}\left(a\right)>0.\quad(57)$$

with $s=2$ and $a=\nu$, according to (WolframMathworld_a, 2011), then $\zeta(a,\nu)$ is given by

$$\zeta\left(2,\nu\right)=\frac{1}{\Gamma(2)}\int_{0}^{\infty}\frac{t\exp\left(-\nu t\right)}{1-\exp\left(-t\right)}dt=\psi'\left(\nu\right),\quad(58)$$

Where $\psi'(\cdot)$ is trigamma function (Abramowitz, 1972 (6.4.1)) define the first derivate of digamma function or second derivate of the natural logarithm of gamma function. This is

$$\psi\left(\nu\right)=\frac{\partial}{\partial\nu}\left\{\ln\left[\Gamma(\nu)\right]\right\};\ \ \psi'\left(\nu\right)=\frac{\partial}{\partial\nu}\left[\psi\left(\nu\right)\right]=\frac{\partial^{2}}{\partial^{2}\nu}\left\{\ln\left[\Gamma(\nu)\right]\right\}.\quad(59)$$

Substituting Eq. (56) and Eq. (58) in Eq. (55) results (Llano et al., 2010)

$$E\left\{\Phi_{\Delta f}^{2}\left(\text{dBm}\right)\right\}=\left[\frac{10}{\ln(10)}\right]^{2}\left\{\left[\psi\left(m_{\Delta f}\right)-\ln\left(\frac{m_{\Delta f}}{\Omega_{\Delta f}}\right)\right]^{2}+\psi'\left(m_{\Delta f}\right)\right\}\quad(60)$$

Finally, variance and standard deviation, σ, of the UWB channel power variation in dBm, is obtained by substituting Eq. (60) and Eq. (54) in Eq. (44), resulting according to (Llano et al., 2010)

$$\text{var}\left\{\Phi_{\Delta f}\left(\text{dBm}\right)\right\}=\left[\frac{10}{\ln(10)}\right]^{2}\psi'\left(m_{\Delta f}\right);\quad\sigma\left\{\Phi_{\Delta f}\left(\text{dBm}\right)\right\}=\frac{10}{\ln(10)}\sqrt{\psi'\left(m_{\Delta f}\right)}\quad(61)$$

Note, that the standard deviation, σ, does not depend on the mean power $\Omega_{\Delta f}$, but depends on the fading parameter $m_{\Delta f}$, defined as

$$m_{\Delta f}=\frac{\left(E\left\{\Psi_{\Delta f}\right\}\right)^{2}}{E\left\{\left(\Psi_{\Delta f}\right)^{2}\right\}-\left(E\left\{\Psi_{\Delta f}\right\}\right)^{2}}\quad(62)$$

The numerator of Eq. (62) correspond to the mean power calculated in Eq. (43) square, i.e.,

$$\left(E\left\{\Psi_{\Delta f}\right\}\right)^2 = \left(\Delta f \sum_{l=1}^{L_C}\sum_{k=1}^{L_r}\Omega_{k,l}\right)^2 \tag{63}$$

Calculating, $E\{(\Psi_{\Delta f})^2\}$ using Eq. (41) results

$$E\left\{\left(\Psi_{\Delta f}\right)^2\right\} = \left(\Delta f\right)^2\left(\sum_{l=1}^{L_C}\sum_{k=1}^{L_r}E\left\{\alpha_{k,l}^4\right\} + \sum_{l=1}^{L_C}\sum_{\substack{k=1\\k\neq l}}^{L_r}\sum_{n=1}^{L_C}\sum_{\substack{m=1\\m\neq n}}^{L_r}E\left\{\alpha_{k,l}^2\right\}E\left\{\alpha_{m,n}^2\right\}\right) +$$
$$+ \quad \frac{1}{2\pi^2}\sum_{l=1}^{L_C}\sum_{\substack{k=1\\k\neq l}}^{L_r}\sum_{n=1}^{L_C}\sum_{\substack{m=1\\m\neq n}}^{L_r}\frac{E\left\{\alpha_{k,l}^2\right\}E\left\{\alpha_{m,n}^2\right\}}{\left[\left(T_l+\tau_{k,l}\right)-\left(T_n+\tau_{m,n}\right)\right]^2}\times D_{l,n}^{k,m} \tag{64}$$

where $D_{l,n}^{k,m} = \sin^2\left\{\pi\Delta f\left[\left(T_l+\tau_{k,l}\right)-\left(T_n+\tau_{m,n}\right)\right]\right\}$, $(l,k)\neq(n,m)$ represents the condition to evaluate the quadruple summation, i.e., $l\neq n$ OR $k\neq m$. Substituting Eq. (63) and Eq. (64) in Eq. (62) and after some mathematical operations, results

$$m_{\Delta f} = \frac{\left(\Delta f\sum_{l=1}^{L_C}\sum_{k=1}^{L_r}\Omega_{k,l}\right)^2}{\left(\Delta f\right)^2\sum_{l=1}^{L_C}\sum_{k=1}^{L_r}\frac{\Omega_{k,l}^2}{m_{k,l}} + \frac{1}{2\pi^2}\sum_{l=1}^{L_C}\sum_{n=1}^{L_C}\sum_{\substack{k=1\\(l,k)\neq(n,m)}}^{L_r}\sum_{m=1}^{L_r}\frac{\Omega_{k,l}\Omega_{m,n}}{\left[\left(T_l+\tau_{k,l}\right)-\left(T_n+\tau_{m,n}\right)\right]^2}\times D_{l,n}^{k,m}}, \tag{65}$$

where $\Omega_{k,l}$, $m_{k,l}$, T_l and $\tau_{k,l}$, are defined according to UWB channel model. As defined above the fade depth can be calculated as n times the standard deviation, σ, of the channel power variations in dBm, i.e., $F_{n\sigma} = n\times\sigma$, with $n = 1, 2, 3,\ldots,$. Thus, the fade depth is analytically calculated as

$$F_{n\sigma}\left(\text{dB}\right) = \frac{10n}{\ln\left(10\right)}\sqrt{\psi'\left(m_{\Delta f}\right)}. \tag{66}$$

Trigamma function $\psi'(\cdot)$ can be evaluated numerically using Mathematica®, or Matlab®. However, this function can also be expressed using an equivalent function. For values of $m_{\Delta f}\geq 1$, the trigamma function, according to (Abramowitz, 1972, (6.4.12)) is approximated by an asymptotic series expansion. Therefore, the fade dept is expressed as

$$F_{n\sigma}\left(\text{dB}\right) = \frac{10n}{\ln\left(10\right)}\sqrt{\psi'\left(m_{\Delta f}\right)} \cong \frac{10n}{\ln\left(10\right)}\sqrt{\frac{1}{m_{\Delta f}}+\frac{1}{2m_{\Delta f}^2}+\frac{1}{6m_{\Delta f}^3}} \tag{67}$$

The relative error of Eq. (67) series expansion is less than 6.6×10^3 for $m_{\Delta f}\geq 1$, which corresponds to the values used in simulations. A comparison between the analytical approximation of the fade depth given by Eq. (67) and simulation results is shown in Fig. 12 for an indoor residential environment with NLOS condition. The channel parameters used in the simulation results are summarized in Table I. It can be observed that simulation and analytical results are very similar, which is in agreement with the assumption that the power in a channel bandwidth Δf can be modeled by a Gamma distribution.

The results also show that in channel bandwidths less than 1 MHz (Narrowband channel), the fade depth $F_{n\sigma}$ is approximately constant: 5.6 dB for $n = 1$, 11.0 dB for $n = 2$, 16.5 dB for

n = 3 and 27.8 dB for n = 5, as corresponds to the behavior of a narrowband channel without frequency diversity gain. From Fig. 12 we can also observe that $F_{n\sigma}$ converges asymptotically from approximately 2 GHz. Note that the fade depth is lower in UWB channels (0.8 dB for n = 1) which narrowband channels (5.6 dB for n = 1), this mean the UWB systems are more resistant to multipath. The floor level of the fade depth is a consequence of the amplitude variations of the MPCs for short displacements of the receiver within a small local area. The maximum error between simulation and analytical results is approximately 0.45 dB for n = 1, corresponding to Δf = 8 MHz.
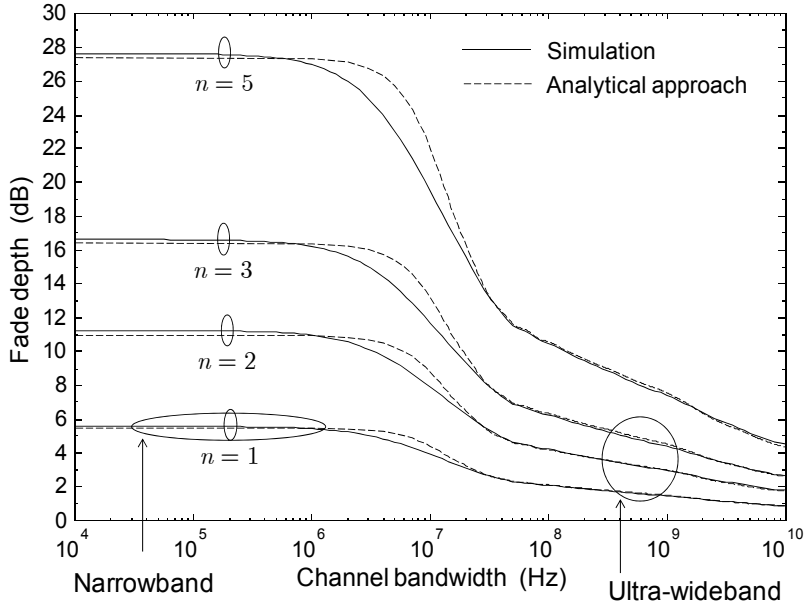
Fig. 12. Fade depth, $F_{n\sigma}$, for the indoor residential IEEE 802.15.4a UWB channel model derived from the analytical approach and simulation results under NLOS condition.

C. Fade margin: The fade margin can be defined as the difference in channel power corresponding to a probability P and the 50% of the cumulative distribution function (CDF) of the received channel power (Fig. 13). The fade margin associated to a probability P and denoted by FM_{P}, is related to the channel power by

$$P = \mathrm{Pr}\left\{E\left\{\Phi_{\Delta f}\left(\mathrm{dBm}\right)\right\} - FM_{P\%}\left(\mathrm{dB}\right) \leq \Phi_{P\%}\left(\mathrm{dBm}\right)\right\}, \tag{68}$$

where, $\Phi_{\Delta f}(\mathrm{dBm})$ is the channel power in dBm calculated from Eq. (41) in a bandwidth Δf, as $\Phi_{\Delta f}(\mathrm{dBm})$=10log[$\Psi_{\Delta f}(\mathrm{mW})$], and $\Phi_{P\%}(\mathrm{dBm})$ is the channel power not exceeded with a probability $P\%$.

Average channel power in dBm denoted by $E\{\Phi_{\Delta f}(\mathrm{dBm})\}$ was calculated in Eq. (54). The value not exceeded with a probability $P\%$ of a Gamma RV in logarithmic units, $\Phi_{P\%}$ (dBm) whose PDF given by Eq. (50), is expressed as $P = \mathrm{Prob}\left\{\Phi_{\Delta f} \leq \Phi_{P}\right\}$. For convenience, we calculate this probability using the PDF of the corresponding Gamma distribution as

$$P = \text{Prob}\left\{\Phi_{\Delta f} \leq \Phi_P\right\} = \text{Prob}\left\{\Psi_{\Delta f} \leq \Psi_P\right\} = \int_0^{\Psi_P} f_{\Psi_{\Delta f}}\left(\Psi_{\Delta f}\right) d\Psi_{\Delta f}, \tag{69}$$

where, $f_{\Psi_{\Delta f}}\left(\Psi_{\Delta f}\right)$ is the PDF of the Gamma RV in linear units given by Eq. (47). Substituting Eq. (47) in Eq. (69) results

$$P = \frac{1}{\Gamma\left(m_{\Delta f}\right)}\left(\frac{m_{\Delta f}}{\Omega_{\Delta f}}\right)^{m\Delta f} \int_0^{\Psi_P} \Psi_{\Delta f}^{m\Delta f - 1} \exp\left(-\frac{m_{\Delta f}\Psi_{\Delta f}}{\Omega_{\Delta f}}\right) d\Psi_{\Delta f}, \ \Psi_{\Delta f} \geq 0, \ m_{\Delta f} \geq 0,5. \tag{70}$$

Solving the integral in Eq. (70) is obtained

$$P = 1 - \frac{1}{\Gamma\left(m_{\Delta f}\right)}\Gamma\left(m_{\Delta f}, \frac{m_{\Delta f}}{\Omega_{\Delta f}}\Psi_P\right), \tag{71}$$

where $\Gamma(\cdot,\cdot)$ is the incomplete function gamma (Abramowitz, 1972, (6.5.3)). Since our objective is to calculate Ψ_P, which is inside argument of incomplete function gamma, we use the regularized incomplete function gamma $Q(\cdot,\cdot)$ defined according to (WolframMathworld_b, 2011) as

$$z = Q(a,s) = \frac{\Gamma(a,s)}{\Gamma(a)}, \tag{72}$$

where $a = m_{\Delta f}$, $s = m_{\Delta f}\Psi_P/\Omega_{\Delta f}$, and $z = 1-P$. Operating on Eq. (72) according to Eq. (71) and using the inverse of the regularized incomplete function gamma $Q^{-1}(\cdot,\cdot)$ defined in (WolframMathworld_c, 2011) as

$$z = Q(a,s)/; \rightarrow s = Q^{-1}(a,z) \tag{73}$$

After carry out simple mathematical operation in Eq. (73), power $\Psi_{P\%}$ in linear units (mW) not exceeded with a probability $P\%$ is given according to (Llano et al., 2010) as

$$\Psi_P(\text{mW}) = \frac{\Omega_{\Delta f}}{m_{\Delta f}}Q^{-1}\left(m_{\Delta f}, 1-P\right) \tag{74}$$

Expressing Eq. (74) in logarithmic units (dBm), results

$$\Phi_P(\text{dBm}) = 10\log\left[\Psi_P(\text{mW})\right] = 10\log\left(\frac{\Omega_{\Delta f}}{m_{\Delta f}}\right) + 10\log\left[Q^{-1}\left(m_{\Delta f}, 1-P\right)\right], \tag{75}$$

Finally we can obtain a closed form expression of the fade margin $FM_P(\text{dB})$ for UWB channel substituting Eq. (54) and Eq. (75) in Eq. (68), resulting

$$FM_P(\text{dB}) = \frac{10}{\ln(10)}\psi\left(m_{\Delta f}\right) - 10\log\left[Q^{-1}\left(m_{\Delta f}, 1-P\right)\right]. \tag{76}$$

where $m_{\Delta f}$ is given by Eq. (65). Note that the fade margin is independent of the mean channel power $\Omega_{\Delta f}$. For P approximating to 0, the regularized incomplete Gamma function

Q^{-1} can be asymptotically extended according to (WolframMathworld_d, 2011). Therefore, the fade margin given by Eq. (76) can be written as

$$FM_P\left(\text{dB}\right)_{P\to 0} \cong \frac{10\psi\left(m_{\Delta f}\right)}{\ln\left(10\right)} - 10\log\left\{\omega^1 + \frac{\omega^2}{\left(m_{\Delta f}+1\right)} + \frac{\left(3m_{\Delta f}+5\right)\omega^3}{2\left(m_{\Delta f}+1\right)^2\left(m_{\Delta f}+2\right)}\right.$$
$$\left. + \frac{\left[m_{\Delta f}\left(8m_{\Delta f}+33\right)+31\right]\omega^4}{3\left(m_{\Delta f}+1\right)^3\left(m_{\Delta f}+2\right)\left(m_{\Delta f}+3\right)} + \cdots\right\}, \tag{77}$$

where $\omega = \left[\Gamma\left(m_{\Delta f}+1\right)P\right]^{\frac{1}{m\Delta f}}$. We have found that the error using Eq. (77) increases as $m_{\Delta f}$. For a relative error between the closed form expression given by Eq. (76) and the approximation given by Eq. (77) equal to 1%, for 6 terms of the summation, the maximum value of $m_{\Delta f}$ is 9.9 for a probability $P = 1\%$ and 15.6 for a probability $P = 0.1\%$.
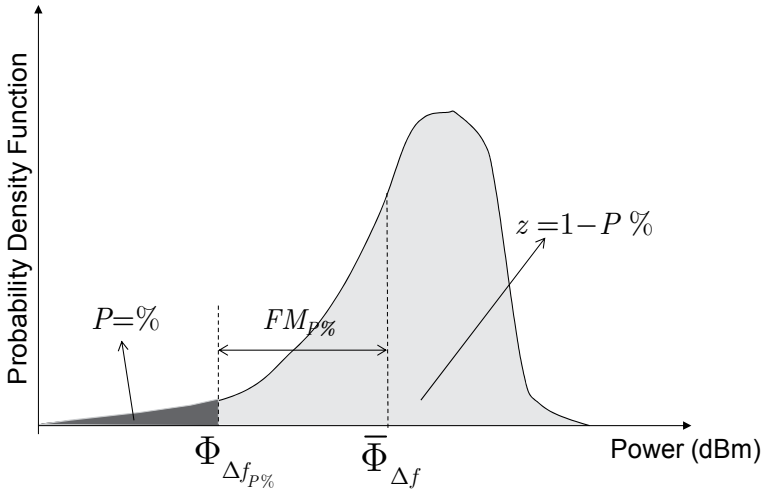
Fig. 13. Fade margin in UWB channel

Fig. 14 shows the fade margin FM_p given by Eq. (76) for the indoor residential NLOS 802.15.4a channel model as a function of the channel bandwidth for three different probabilities: $P = 5\%$, 10% and 20%. Note that the fade margin in a channel bandwidth less than 1 MHz is approximately constant, and the difference between the Gamma approximation and the simulation for these bandwidth values is around 0.05 dB for $P = 20\%$, 0.05 dB for $P = 10\%$, and 0.25 dB for $P = 5\%$. Moreover, a maximum difference of 1 dB and 0.5 dB between the Gamma approximation and simulation results is found at $\Delta f = 8$ MHz, for $P = 5\%$ and $P = 10\%$, respectively.

The difference between analytical and simulation results in Fig. 14 can be explained analyzing the second term of the channel power given by Eq. (41). For high channel bandwidths, the second term in Eq. (41) is negligible compared to the first term. Thus, the channel power in linear units (mW) can be approximated as a Gamma distribution. For low channel bandwidths, the second term in Eq. (41) corresponds to the finite sum of $\alpha_{k,l}\alpha_{m,n}$,

where $\alpha_{k,l}$ and $\alpha_{m,n}$ are Nakagami-*m* distributed and mutually independent RVs. It can be demonstrated that the sum of the product of Nakagami-*m* RVs can be approximated as a Gamma distribution (Nakagami, 1960). Therefore, the channel power is well approximated as a Gamma distribution. Nevertheless, for medium channel bandwidths, between 2 MHz and around 50 MHz for the results shown in Figure 14, the channel power in linear units is not approximated so well to a Gamma distribution due to the second term in Eq. (41).
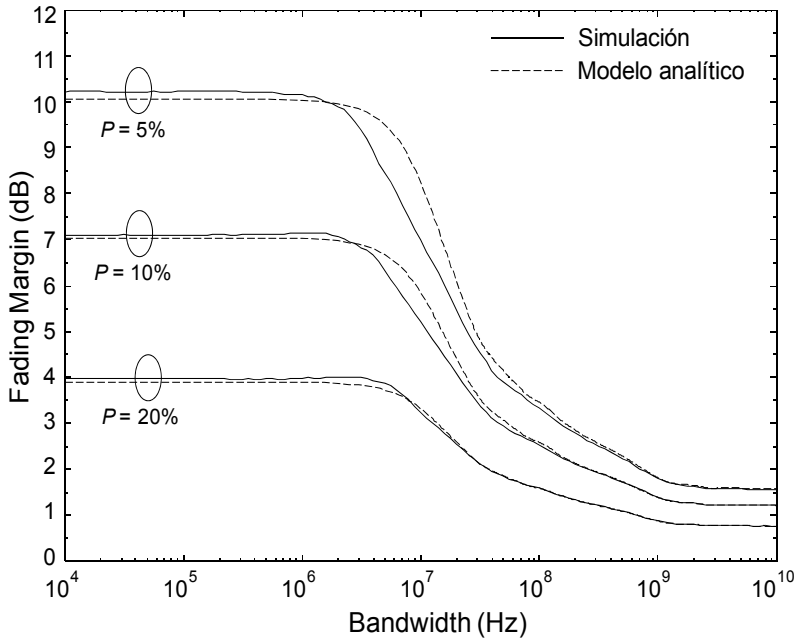
Fig. 14. Fade margin, FM_p , in the indoor residential IEEE 802.15.4a UWB channel model derived from the analytical approach and simulation results in NLOS condition.

3. Conclusions

In this chapter, we showed that UWB channel with small-scale fading statistics modeled as lognormal or Nakagami-*m* RV can be approximated in the frequency domain by a Nakagami-*m* distribution, whose fading and mean power parameters are explicit functions of the delay parameters and decay time constants of the UWB channel. Moreover the subcarrier frequency distribution can be approximated by a Rayleigh distribution if the number of MPC is high. Additionally, we found an exact expression for the correlation coefficient between a couple of subcarriers amplitudes in the frequency for the IEEE 802.15.3a and IEEE 802.15.4a UWB channel.

Also, we investigate the variations of the received power as a function of the bandwidth channel, taking the IEEE 802.15.4a channel model as our point of reference. The results show that the channel power can be modeled by a Gamma distribution. Under the assumption that the channel power is Gamma distributed, an analytical approach to characterize the *fade depth* and the *fade margin* for indoor and outdoor environments is proposed. Also, asymptotic expressions for the fading parameter of the Gamma distribution as a function of

the channel rms delay spread are proposed and discussed. The performance of the analytical approach has been checked by comparison with simulation results considering different propagation conditions for indoor residential and outdoor environments. The results show that the fade depth is approximately constant for channel bandwidths below 1 MHz (just about 5.5 dB for n=1), i.e, the fade depth is bandwidth independent for narrowband channels, and adopts an asymptotic convergence for channel bandwidths beyond 2 GHz (just about 0.8 dB for n=1). A similar behavior of the fade margin occurs in terms of the channel bandwidth. This analytical approach enables a proper evaluation of the link budget in terms of the bandwidth channel and it can be used to design and implement UWB communications systems.

4. References

Abramowitz M, I.A., Stegun. (1972). Handbook of Mathematical Functions; with Formulas, Graphs and Mathematical Tables.

Batra A, J. Balakrishnan, G. R. Aiello, J, R, Foerster, & A. Dabak. (2004). Design of a multiband OFDM system for realistic UWB channel environments. *IEEE Trans. Microwave Theory Tech.*, vol. 52, no. 9, pp. 2123-2138.

Bastidas-Puga E.R, F. Ramírez-Mireles, & D. Muñoz-Rodríguez. (2005). On fading margin in ultra wideband communications over multipath channels. *IEEE Transactions on Broadcasting*, vol. 51, pp. 366-370, Sep. 2005.

Cardoso F. & L. Correia. (2003). Fading depth dependence on system bandwidth in mobile communications – an analytical approximation. *IEEE Trans. Veh. Technol.*, vol. 52, pp. 587-593, May 2003.

Cassioli D, M. Z. Win, & A.F. Molisch. (2002). The ultra-wideband indoor channel: from statistical model to simulations. *IEEE J. Select. Areas Commun.*, vol. 20, pp. 1247-1252.

Chong C.C, & S. K. Yong. (2005). A generic statistical-based UWB channel model for high-rise apartments. *IEEE Trans. Antennas Propag.*, vol. 53, no. 8, pp. 2389–2399.

Díaz A, A.P. García, L. Rubio. (2007). Time dispersion characterization for UWB mobile radio channels between 3.1 and 10.6 GHz. *IEEE Proc. Int. Symp. Antennas and Propagation Society*, Hawaii, USA, June, 2007.

European Committee for Standardization. (2007). Standardization mandate forwarded to cen/cenelec/etsi for harmonised standards covering ultra-wideband equipment. [Online]. Available: http://www.etsi.org/WebSite/document/aboutETSI/EC_Mandates/m407_EN_Adonis_13099.pdf

Fleury B.H. (1996). An uncertainty relation for WSS processes and its application to WSSUS systems. *IEEE Trans. Commun.*, vol. 44, no. 12, pp. 1632-1634.

Federal Communications Commission. (2002). Revision of part 15 of the commission´s rules regarding ultra-wideband transmission systems: first report and order. Federal Communications Commission, USA, Washington, DC, USA, Tech. Rep. FCC 02-48, February 2002

Foerster J.R *et al*. (2002). Channel modeling subcommittee final report. IEEE, Document IEEE 02490r0P802-15 SG3a, 2003.

Gradshteyn I.S & I.M. Ryzhik. (2007). Tables of Integrals, Series and Products. Nueva York: Academic, 2007.

Hashemi H. (1993). Impulse response modeling of indoor radio propagation channels. *IEEE J. Select. Areas Commun.*, vol. 11, pp. 967–978.

Jakes W.C. (1974), *Microwave Mobile Communications*. Wiley, New York, 1974.

Liuqing Y, & G.B. Giannakis. (2004). Ultra-wideband communications: an idea whose time has come. *IEEE Signal Processing Mag.*, vol. 21, pp. 26-54, Nov. 2004.

Llano G. J. Reig, & L. Rubio. (2009). The UWB-OFDM channel analysis in frequency. *IEEE 69th Vehicular Technology Conference*: VTC2009-Spring 26–29-. Barcelona, Spain.

Llano G. Reig, J. Rubio, L. (2010). Analytical Approach to Model the Fade Depth and the Fade Margin in UWB Channels. *IEEE Trans. Veh. Technol.*, vol. 48, no. 9, pp. 4214-4221.

Massey F.J. (1951). The Kolmogorov-Smirnov test for goodness of fit. *Journal of the American Statistical Association*, vol. 46, no. 253, pp. 68-78, 1951.

Molish A. F. *et al*,. (2005). IEEE 802.15.4a channel model final report. Tech. Rep., Document IEEE 802.1504-0062-02-004a.

Molisch A.F. (2005). Ultra wideband propagation channels theory, measurement, and modeling. *IEEE Trans. on Veh. Technol.*, vol. 54, pp. 1528-1545, Sep. 2005.

Malik W.Q. B. Allen, & D.J. Edwards (2008). Bandwidth dependent modeling of small scale fade depth in wireless channels. *IET Microw. Antenn. Propag.*, vol. 2, no. 6, pp. 519-528.

Nakagami M. (1960). The *m*-distribution, a general formula of intensity distribution of rapid fading," *in Statistical Methods of Radio Wave Propagation*, W. G. Hoffman, Ed. Oxford, England.

Papoulis A. & Unnikrishna S. (2002). *Probability, Random Variables and Stochastic Processes*. 4th ed. New York: McGraw-Hill.

Proakis J. G. (1995). *Digital Communications*. Third Edition, McGraw-Hill Book Company, New York.

Peebles P.Z, Jr. (2001). *Probability, Random Variables and Random Signal Principles*. 4th ed. New York: McGraw-Hill.

Rappaport T.S. (1996). Wireless Communications Principles and Practice, Prentice Hall, Inc, New Jersey.

Saleh A.M. & R. Valenzuela. (1987). A statistical model for indoor multipath propagation. *IEEE J. Select. Areas Commun*, vol 2, pp. 128-137.

WolframMathworld. (2011, Feb). [Online]. Available:
http://functions.wolfram.com/10.02.07.0001.01 (Last access, 15/02/2011)

WolframMathworld. (2011, Feb). [Online]. Available:
http://functions.wolfram.com/10.02.03.0029.01 (Last access, 15/02/2011)

WolframMathworld. (2011, Feb). [Online]. Available:
http://functions.wolfram.com/06.08.02.0001.01 (Last access, 15/02/2011)

WolframMathworld. (2011, Feb). [Online]. Available:
http://functions.wolfram.com/06.12.02.0001.01 (Last access, 15/02/2011)

WolframMathworld. (2011, Feb). [Online]. Available:
http://functions.wolfram.com/06.12.06.0007.01 (Last access, 15/02/2011)

Yang J. & S. Kozono. (1999). A study of received signal-level distribution in wideband transmissions in mobile communications. *IEEE Trans. Veh. Technol.*, vol. 48, pp. 1718-1725.

Effects of Bandwidth on Estimation of UWB Channel Parameters

Duje Čoko, Zoran Blažević and Ivan Marinović
University of Split
Faculty of Electrical Engineering, Mechanical Engineering
and Naval Architecture
Croatia

1. Introduction

The subject of this chapter is to investigate the effect of bandwidth on a short range indoor UWB channel performance. This research is based on a measurement campaign performed on a wooden desk surface placed in an office room at our faculty building. A vector network analyzer (VNA) is used to sweep the 1 GHz, 2 GHz, 5 GHz and 7.5 GHz bandwidths centered at 6.85 GHz, obtaining the frequency response of the channel. Using the VNA time domain capability the channel impulse response is obtained. This is equivalent to sounding the channel with frequency chirp pulses equal in duration to the inverse of the frequency bandwidth. In other words, a narrower bandwidth results in a wider pulse in time domain.

Although the measurements are performed in same environment for all bandwidths, it is expected that an UWB channel itself would not be equally perceived by different pulse widths. A wider system bandwidth results in shorter pulses, which in turn account for finer temporal and spatial resolution. In this way more multipath components can be resolved as the pulses overlap in a lesser extent.

The fundamental differences between an UWB channel and a narrowband channel arise from the frequency selectivity of the propagation process (Molisch, 2005). As the UWB signal has a wide frequency spectrum which may extend to several gigahertz, the frequency dependence of diffraction/reflection coefficients and dielectric constants can be significant (Di Benedetto et al., 2006). A number of papers report on the effect of carrier frequency on channel parameters. One such investigation (Cassioli et al., 2004) finds a strong dependence between the path loss model exponent and the carrier frequency, yet states that there is no correlation with the bandwidth. (Ghassemzadeh et al., 2005) presented an extensive measurement campaign at two different bandwidths (1.25 GHz and 6 GHz) centered at 5 GHz, reporting mostly minor differences in parameter values between the two bandwidths. Another paper (Choi et al., 2009) models the path loss exponent variation as a function of frequency. A research project (Chang & Tarng, 2007) investigates the effects of bandwidth on observable multipath clustering and Δ-*K* model parameters for an indoor UWB wireless channel with signal bandwidths of 0.5, 1 and 2 GHz. However, to authors' knowledge, so far there have been no attempts to investigate the effects of bandwidth on estimating the path loss, shadowing, mean excess delay and RMS delay spread in short range UWB scenarios,

which are the key parameters for assessing the link budget, signal-to-noise ratio and intersymbol interference of the system.

The next section of the chapter explains the measurement procedure and equipment and describes the measurement environment. The subsequent sections present the path loss, shadowing, mean excess delay and RMS delay spread parameter values estimated from the measured power delay profiles, respectively. The obtained results are discussed in the seventh section. The chapter is concluded in the eighth section, briefly summarizing all the key findings of this research.

2. Experimental setup

The measurement campaign took place on an empty desk in one of the offices at our faculty building. The surface of the desk is cleared to ensure the line of sight (LOS) between the transmitter and the receiver. The desk used in measurements is made of wood, chipboard and MDF. Inner walls that separate offices and laboratories are mainly made of plasterboard constructed with a thin wire grid composition, while the external wall and floors are made of reinforced concrete. The floor is entirely covered with wooden parquetry. The doors are made of plywood, while the office furniture is made of various wooden materials and glass. In the vicinity of the desk on which the measurements are conducted is another desk with the measurement equipment and two cabinets in the bottom left corner of the office, as shown on the office plan on Fig. 1. This additional furniture in the office is introduced as an intentional scattering system to approximate a real-life scenario.
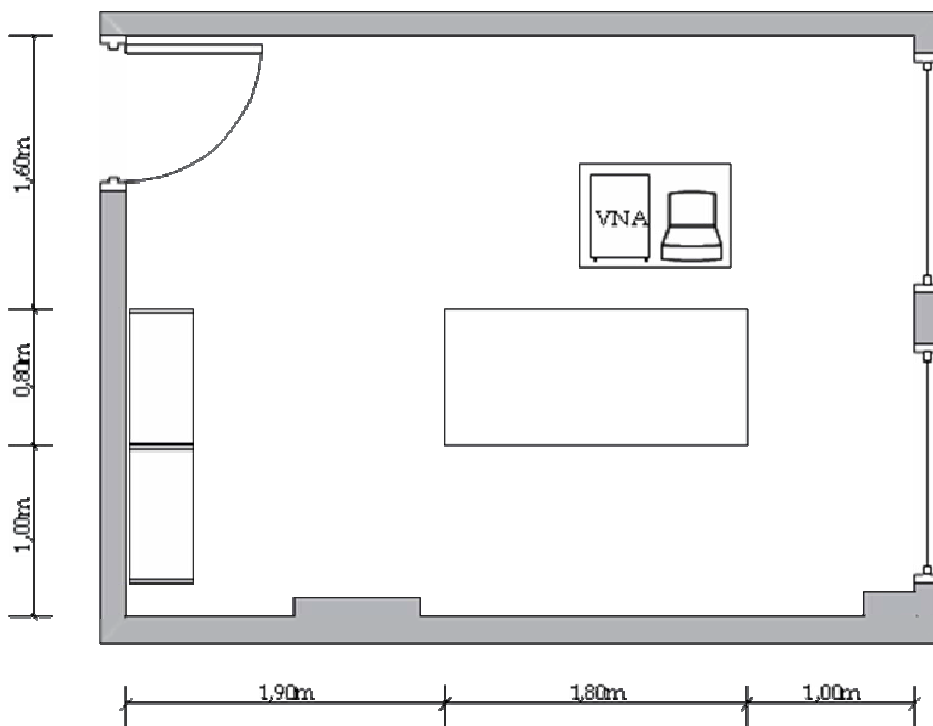
Fig. 1. Office plan

A 1.6 m x 0.7 m grid with 0.1 m spacing is drawn on a sheet of paper (Fig. 2) which is fixed on a surface of a plain office desk. This forms a matrix of 17 x 8 measurement points across the desktop. The transmitting antenna (presented by a red disk in Fig. 2) is placed on the top of the 9th column in a fixed position. The receiving antenna (presented by a blue disk in Fig. 2) is moved along the remaining 135 points for each measurement. Both antennas are erected on styrofoam blocks at the same height of 4.5 cm with their azimuth planes being parallel to the desk surface ($\Theta = 0°$).
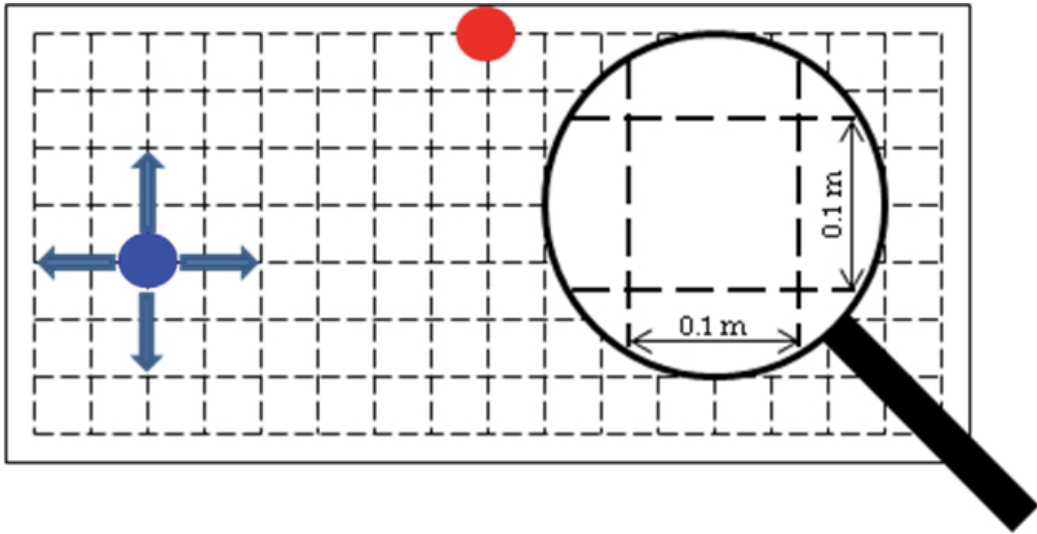
Fig. 2. Measurement grid and antenna positioning method. The red and blue disks present the transmitting antenna and the receiving antenna, respectively.

2.1 Measurement setup

The measurement setup is presented on Fig. 3. The transmitting antenna (Tx) is connected to the port 1 of the HP 8720A vector network analyzer (VNA) by a semi-rigid coaxial cable. The receiving antenna (Rx) is connected to the port 2 of the VNA by a flexible coaxial cable. The attenuation of the cables is compensated by the calibration procedure. The measured data from the VNA is transferred by the HP interface bus (HP-IB) to the data acquisition PC (PC-DAQ), where the data is stored for further processing.
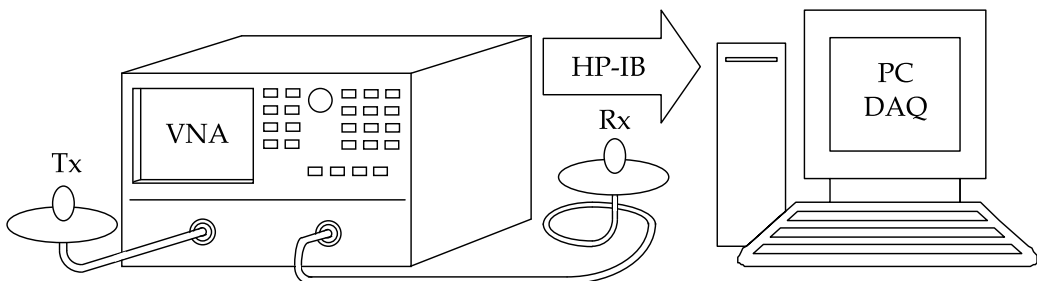
Fig. 3. Measurement setup

2.1.1 Vector network analyzer

A vector network analyzer (VNA) is used to measure the system's forward complex transmission coefficients $S_{21}(f_i)$ at 801 discrete evenly spaced frequencies within a given frequency span. In this way the band-limited transfer function of the system H is obtained:

$$H_{meas}(f) = W(f)H(f),\tag{1}$$

where H_{meas} is the measured transfer function and W is the selected transformation window of the VNA.

Using an inverse Fourier transform $\mathfrak{I}^{-1}$, the measurement results can be observed in the time delay domain, presenting the power delay profile (PDP) which gives the time distribution of the received signal power from a transmitted pulse:

$$\mathfrak{I}^{-1}\{H_{meas}(f)\} = h(\tau).\tag{2}$$

The measured data acquired from the VNA thus presents the frequency averaged power delay profiles.

The excess delay t is obtained by subtracting the time of arrival τ_0 of the first multipath component of the power delay profile from the time delay τ relative to the time instant of transmitting the pulse:

$$t = \tau - \tau_0.\tag{3}$$

By activating the VNA's averaging function, the last 16 measurements are averaged to reduce the temporal variations in the system. This results in a time averaged power delay profile:

$$P_h(t) = \frac{1}{N}\sum_{i=1}^{N}|h_i(t)|^2,\tag{4}$$

where $N = 16$.

Prior to each measurement the VNA is calibrated using a specific calibration standard. The measured data is acquired via HP-IB interface to a PC for further analysis and correction. Before the parameter extraction procedure each measured PDP is corrected with respect to the predefined threshold, which was set to 5 dB above the noise level for all measured points. This correction sets all the delay bins with energies below this threshold to zero-energy bins.

2.1.2 Antennas

A pair of omnidirectional UWB antennas used in this measurement campaign was built according to the design proposed in (Taniguchi et al., 2006). To verify the omnidirectionality of the built antennas, their radiation patterns were measured in a TESEQ 750 GTEM cell at different frequencies generated by a HP 8340A synthesized sweeper. This method is based on measuring the power received by antenna under test (AUT) which is placed inside the cell. The received power was measured using a Rohde&Schwarz NRP-Z21 universal power sensor. Electric field in the vicinity of the AUT is measured by an isotropic electric field probe HI-4455 positioned next to the AUT. The antenna gain G in dBi is calculated using the following expression (Živković & Šarolić, 2010):

$$G = -162.8 + 20\log(f) + P_{rec} - E_i, \tag{5}$$

where f is the signal frequency in Hz, P_{rec} is the power received by AUT expressed in dBm, and E_i is the incident electric field in dBV/m. The radiation patterns measured at 4 GHz, 7 GHz and 10 GHz are presented on Fig. 4.
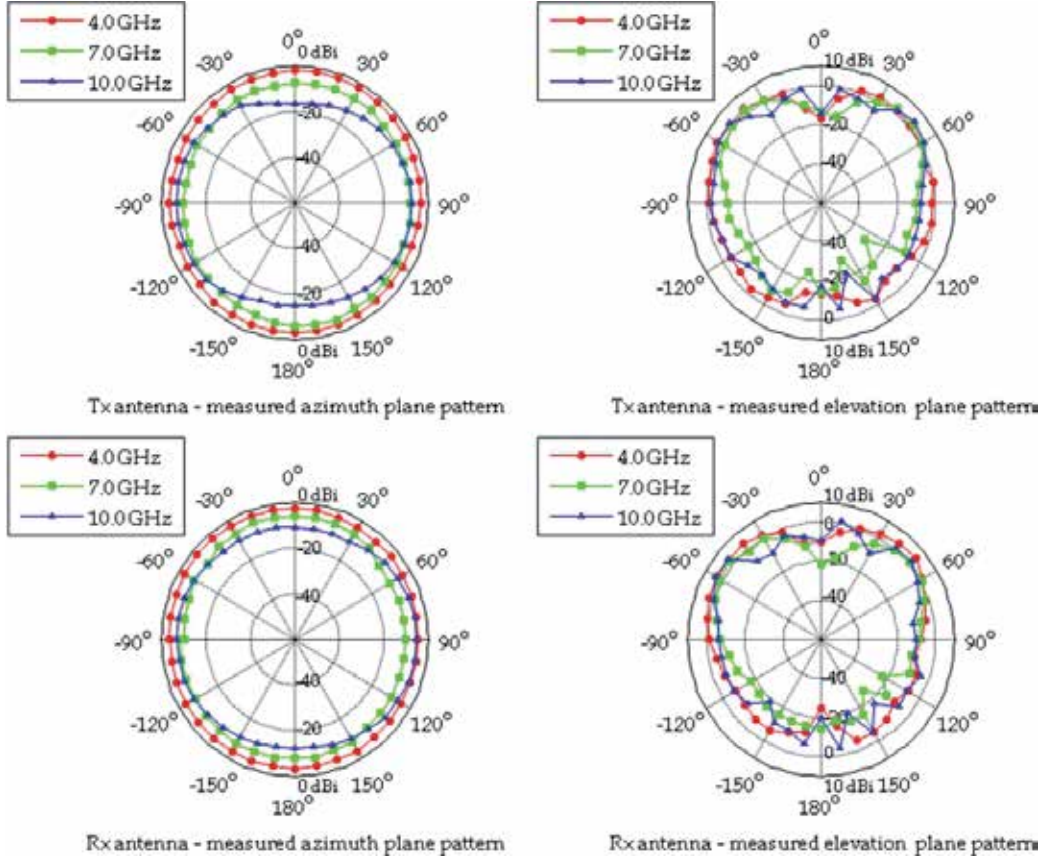
Fig. 4. Measured radiation patterns for both antennas at 4 GHz, 7 GHz and 10 GHz.

In addition, the VNA was used to measure the VSWR throughout the widest frequency bandwidth of 7.5 GHz, centered at 6.85 GHz. A full port calibration was performed before each measurement. The results, presented on Fig. 5, show that the VSWR is less than 2.5 throughout the entire frequency span.

Finally, the power delay profiles for different bandwidths were measured at a reference distance d_0 (= 0.1 m) at 0°, 45°, 90°, 135° and 180° in azimuth plane, while keeping both antennas at same height h (= 4.5 cm). Averaging the measured results and calculating the path loss from the power delay profile (Section 3) the total path loss at 0.1 m was estimated:

$$PL(d_0) = PL_{FS}(d_0) - G_r - G_t, \tag{6}$$

where PL_{FS} is the free space path loss, G_r and G_t are receiving and transmitting antenna gains, respectively, all expressed in dB.
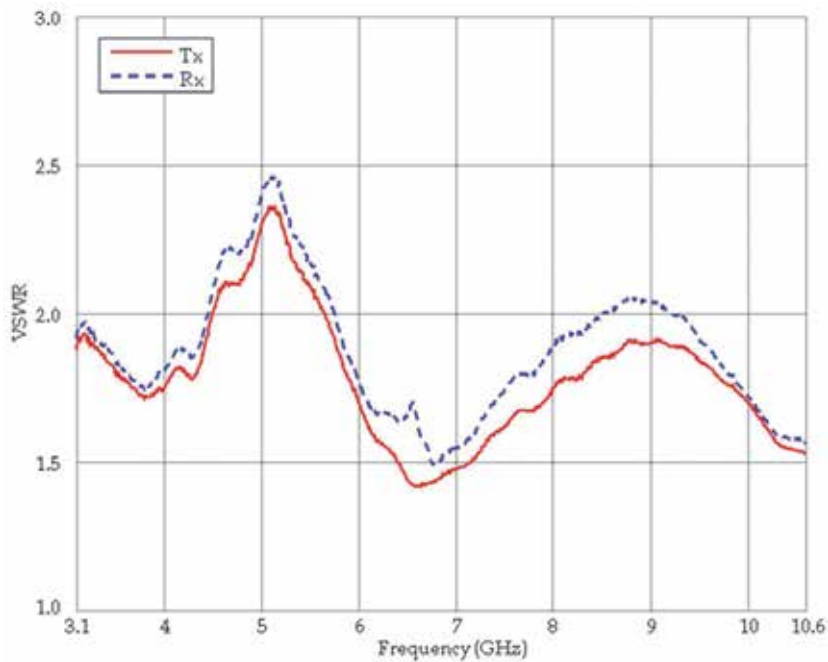
Fig. 5. Measured VSWR for both antennas vs. frequency.

Applying the Friis equation with f_c (= 6.85 GHz) as the center frequency, c (= 3*10^8 m/s) as the velocity of light and d_0 (= 0.1 m) as a referent antenna separation, the free space path loss is obtained:

$$PL_{FS}(d_0)[\text{dB}] = 20\log\left(\frac{4\pi f_c d_0}{c}\right) = 29.16 \text{ dB}. \tag{7}$$

Under the assumption that antenna gains are equal ($G_r = G_t = G_a$) we estimate the antenna gain within a given bandwidth:

$$G_a[\text{dB}] = \frac{PL_{FS}(d_0)[\text{dB}] - PL(d_0)[\text{dB}]}{2}. \tag{8}$$

The results are shown in Table 1.

Bandwidth	1 GHz	2 GHz	5 GHz	7.5 GHz
Antenna gain	-0.475 dB	-0.54 dB	-0.035dB	0.26 dB

Table 1. Estimated antenna gains at 0.1 m separation for different bandwidths.

The measurement results show that the antenna gain may be approximated to 0 dBi, implying a ±1 dB tolerance.

2.1.3 System resolution and dynamic range
After a preliminary observation of the power delay profiles on various measurement points at different bandwidths, it is noticed that the noise threshold is constant (slightly below -90

dB). Besides that, as the power in the profile decays with delay, there are no observable multipath components above the noise threshold approximately 60 ns after the time instant of transmitting the pulse for each bandwidth. According to this fact the display window from 0 ns to 80 ns is chosen for all considered bandwidths and measurement points. Since this window is sampled at 801 points, the display resolution for all measurements is 0.1 ns.

The temporal resolution of the measurement system is equal to the inverse of the bandwidth and has a value greater than the display resolution. Otherwise, the display window would exceed the maximum observable delay (Hovinen et al., 2002).

Once the VNA was calibrated, the pulse shape was observed it the time delay domain for each different bandwidth (Fig. 6). All pulses have a different peak value at $\tau = 0$, which is caused by normalizing the measurement results to the total energy of the pulse.
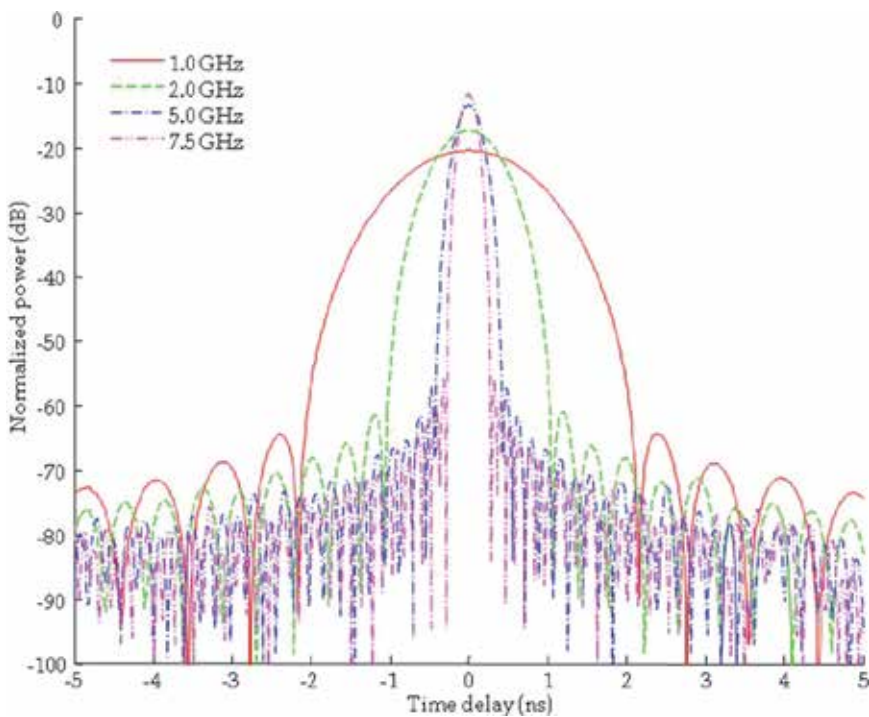
Fig. 6. The shape of the calibrated pulse for different bandwidths.

The VNA provides a windowing feature which is needed because of the abrupt transitions at the start and stop frequencies of the measured frequency span. The band limiting of a frequency domain response causes overshoot and ringing in a time domain response. This limits the usefulness of the time domain measurement in terms of the sidelobes and a pulse wider than the system resolution. The window used in the presented measurements is the normal window, which has a sidelobe level 44 dB below the pulse peak value and extends the pulse width to value of 3.84 times the system resolution for a bandpass mode (Hewlett-Packard Company, 1989). This has a direct consequence in spreading the pulse spatially, so that the spatial resolution of the system is degraded and the system can no longer resolve the multipath components with the precision expected from the system resolution. Another

consequence is that when observing the delays in relation to the time instant of the peak of the transmitted pulse, one can observe a certain amount of energy received in negative delay times. To eliminate this, several power delay profiles where the total energy was not captured are removed from the final set of measured data. Hence, the minimum measurement distance is half of the spatial width of the pulse at a given bandwidth.

Furthermore, the RMS delay spread is estimated for each pulse, as this value is to be subtracted from the measured RMS delay spread of each power delay profile (Section 6). The results are presented in Table 2.

Bandwidth	1 GHz	2 GHz	5 GHz	7.5 GHz
System resolution	1 ns	0.5 ns	0.2 ns	0.133 ns
Display resolution	0.1 ns	0.1 ns	0.1 ns	0.1 ns
Pulse width	3.84 ns	1.92 ns	0.768 ns	0.512 ns
Spatial width	1.152 m	0.576 m	0.23 m	0.154 m
Estimated pulse power	1.66 dB	1.66 dB	1.66 dB	1.66 dB
Pulse RMS delay spread	567 ps	283.4 ps	113.4 ps	75.6 ps

Table 2. System and pulse parameters for different bandwidths.

Fig. 7 shows a detail of normalized power profiles for different bandwidths. All the profiles are measured at 0.78 m antenna separation. It is evident that the measurement system with a narrow bandwidth cannot resolve as much multipath components as the same measurement system with wider bandwidth.
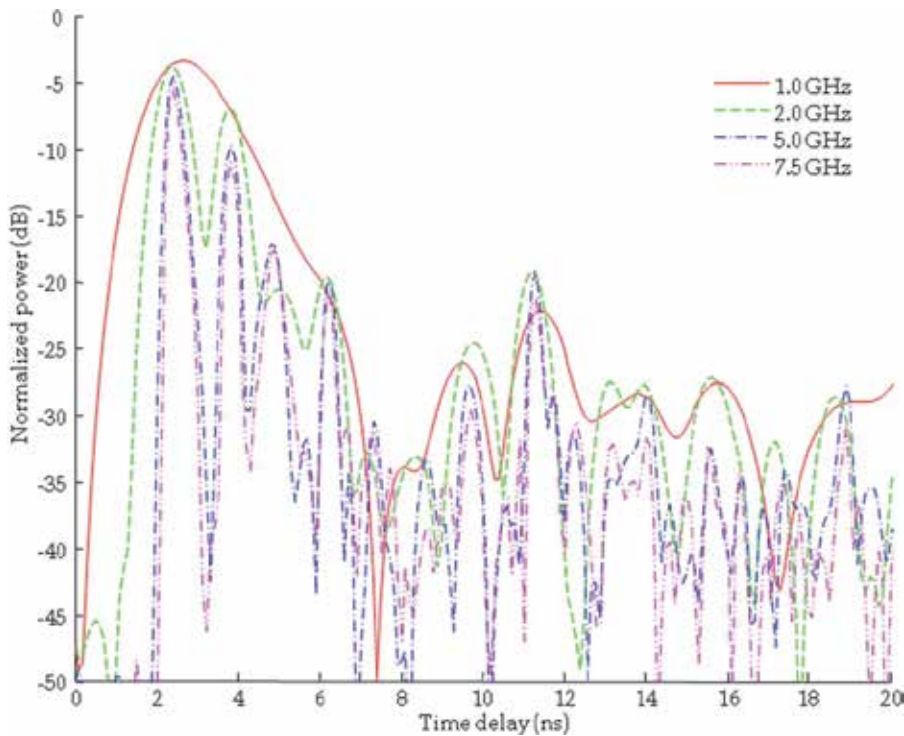
Fig. 7. A detail of normalized power delay profiles at d = 0.78 m for different bandwidths.

3. Path loss

The total path loss is defined as attenuation in the energy of pulse while propagating from the transmitting antenna to the receiving antenna. This can be expressed as a ratio of total energy of the transmitted pulse vs. total energy of the received power delay profile:

$$PL = \frac{\int w^2(t)dt}{\int P_h(t)dt}. \tag{9}$$

The path loss model (Ghassemzadeh at al., 2003) defines the path loss exponent n which characterizes the log-distance dependence and equals 2 for the free space propagation:

$$PL(d) = PL(d_0) + 10 \cdot n \cdot \log(d/d_0) + S, \quad d > d_0, \tag{10}$$

where d is the separation between the transmitter and the receiver, $PL(d_0)$ is the path loss at the reference distance d_0, and S denotes the shadowing term (Section 4).

The total energy received at the Rx antenna is estimated by summing the energy in the entire corrected power delay profile. By subtracting the measured total path loss at a reference distance from this value, we estimate the relative path loss:

$$\overline{PL}[\text{dB}] = PL(d) - PL(d_0)[\text{dB}], \tag{11}$$

where $PL(d)$ presents the path loss estimated from the power delay profile measured at distance d, and $PL(d_0)$ is the measured total path loss at a reference distance, which is selected as $d_0 = 0.1$ m (see Table 1).

The relative path loss values estimated from the measured power delay profiles are presented on Fig. 8 at different system bandwidths as a function of antenna separation in a logarithmic scale. In this manner the linear regression lines can be fitted into the measurement data using the least square method. The calculated free space path loss line (7) is added for comparison. Note that the correlation coefficient increases while the path loss exponent slightly decreases with increasing bandwidth.

The path loss exponent values estimated in this measurement campaign are comparable to the values found in literature up to date.

A indoor LOS measurement campaign which took place inside an anechoic chamber on a 1.2 m x 0.8 m rectangular aluminum conductive plate simulating a heavy-duty office desk (Suzuki & Kobayashi, 2005) found a path loss exponent value of $n = 1.6$ using a vertically polarized transmission. This value is lower than the free space path loss exponent ($n = 2$) and the authors attribute this discrepancy to the effects of the diffracted waves from the finite plate edges. The frequency of the UWB signal spanned from 3.1 GHz to 10.6 GHz.

Short range indoor LOS measurements have also been performed in a 6 GHz to 8 GHz frequency band, with a transmitter-receiver distance ranging from 1 m to 5 m (Bose, 2006). A path loss analysis yields a path loss exponent of $n = 1.85$.

A 3.6 GHz – 6 GHz measurements in 1 m – 11 m range (Cassioli & Durantini, 2004) report a path loss exponent of $n = 1.916$ for indoor LOS scenarios.

An UWB indoor LOS channel measurement campaign was evaluated in (Cassioli et al, 2001), finding a path loss exponent of $n = 2.4$.

An extensive research based on analysis of over 300000 power delay profiles measured in 4.375 GHz – 5.625 GHz in various indoor LOS scenarios presented in (Ghassemzadeh et al., 2002) finds the average path loss exponent to have a value of $n = 1.7$.

Although the frequency dependence analysis of the channel parameters investigated in (Cassioli et al., 2004) resulted in a wide range of path loss exponent values between 0.6 and 2.2 for indoor LOS scenarios, there is no marked dependence on the system bandwidth.
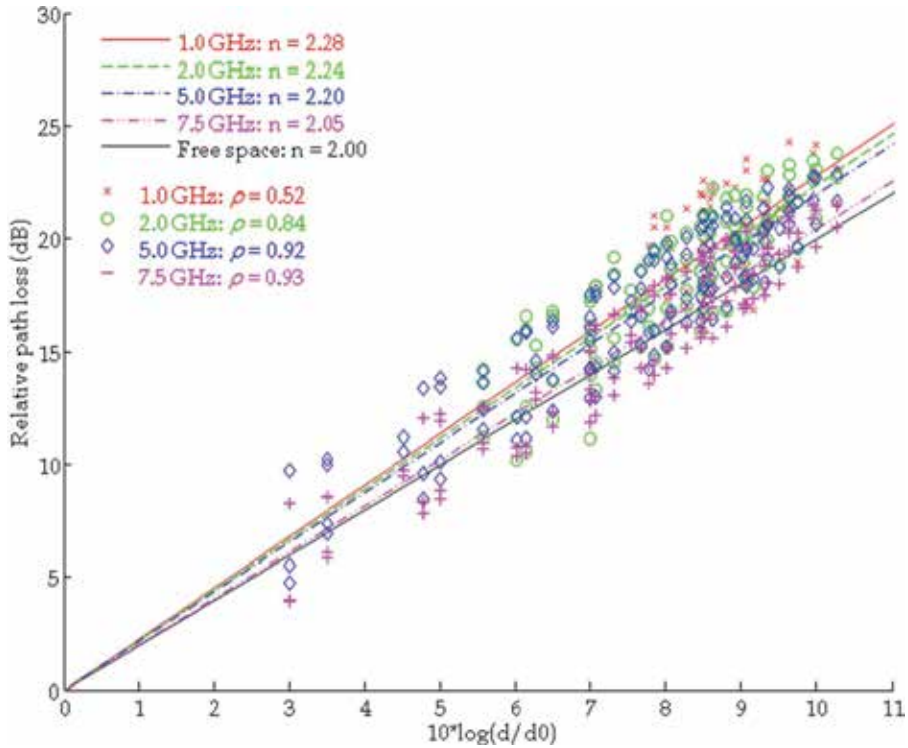
Fig. 8. Scatter plots of the estimated relative path loss vs. logarithm of the normalized distance for different bandwidths. The regression lines represent the path loss power laws.

4. Shadowing

The shadowing term S denotes a zero-mean Gaussian random variable with standard deviation σ, which is estimated from the experimental data:

$$S \sim N(0,\sigma). \tag{12}$$

The shadowing term captures the path loss deviations from its median value.

Fig. 9 presents a comparison of empirical cumulative distribution functions (CDF) of the estimated shadowing term S and theoretical lognormal CDFs with respective standard deviations for different bandwidths, shown in Table 3. For comparison, a far-right column showing the calculated parameter values in free space at central frequency of 6.85 GHz (7) is added.

In a 3.6 GHz – 6 GHz indoor LOS measurements (Cassioli & Durantini, 2004) shadowing is modeled as lognormal, with standard deviation of 1.42 dB for indoor LOS scenarios.
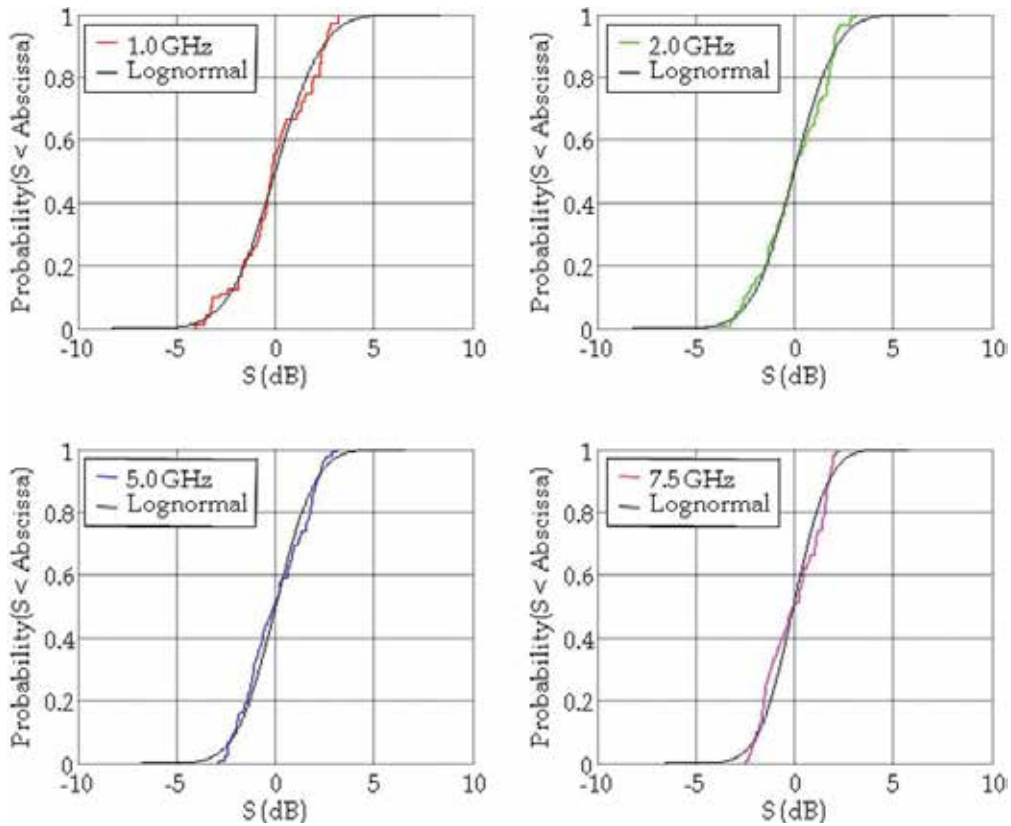
Fig. 9. Empirical CDF of the shadowing term S obtained from the experimental path loss values for different bandwidths. The black line on each CDF represents the theoretical lognormal CDF with the respective calculated standard deviation.

System BW	1 GHz	2 GHz	5 GHz	7.5 GHz	Free space (7)
PL_0	30.12 dB	30.24 dB	29.23 dB	28.63 dB	29.16 dB
n	2.28	2.24	2.2	2.05	2
σ	1.87 dB	1.67 dB	1.57 dB	1.39 dB	0 dB

Table 3. Measured path loss at a reference distance d = 0.1 m, path loss exponents n and standard deviations of the shadowing term S for different bandwidths. Note that the standard deviation of the shadowing term S decreases as the bandwidth increases.

An UWB indoor LOS channel measurement campaign was evaluated in (Cassioli et al, 2001), finding standard deviation of shadowing term of 5.9 dB.
An extensive research based on analysis of over 300000 power delay profiles measured in 4.375 GHz – 5.625 GHz for indoor LOS scenarios presented in (Ghassemzadeh et al., 2002) reports on the standard deviation of the shadowing term of 1.6 dB.

5. Mean excess delay

Mean excess delay is commonly used to describe the time dispersion characteristics of a transmission channel. It is defined as the first moment of the power delay profile:

$$\bar{\tau} = \frac{\int\limits_{0}^{\infty} t P_h(t)\,dt}{\int\limits_{0}^{\infty} P_h(t)\,dt}. \qquad (13)$$

The scatter plot of the mean excess delay values, estimated according to (13) from the measured power delay profiles, is presented on Fig. 10 in dependence on the antenna separation for different bandwidths.

Fig. 11 presents a scatter plot of the estimated mean excess delay in function of the estimated total path loss for different bandwidths. We find a significant correlation between these two parameters, which is slightly increasing with the bandwidth.
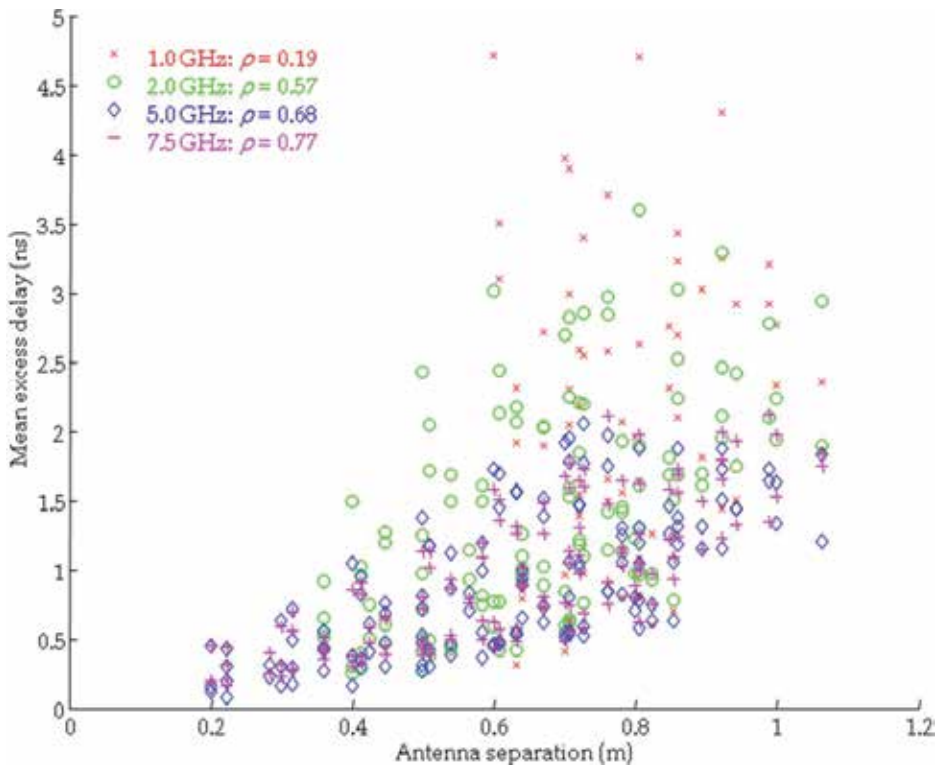
Fig. 10. Scatter plot of estimated mean excess delay vs. antenna separation for different bandwidths. Note that the correlation between these two estimated parameters increases with bandwidth.
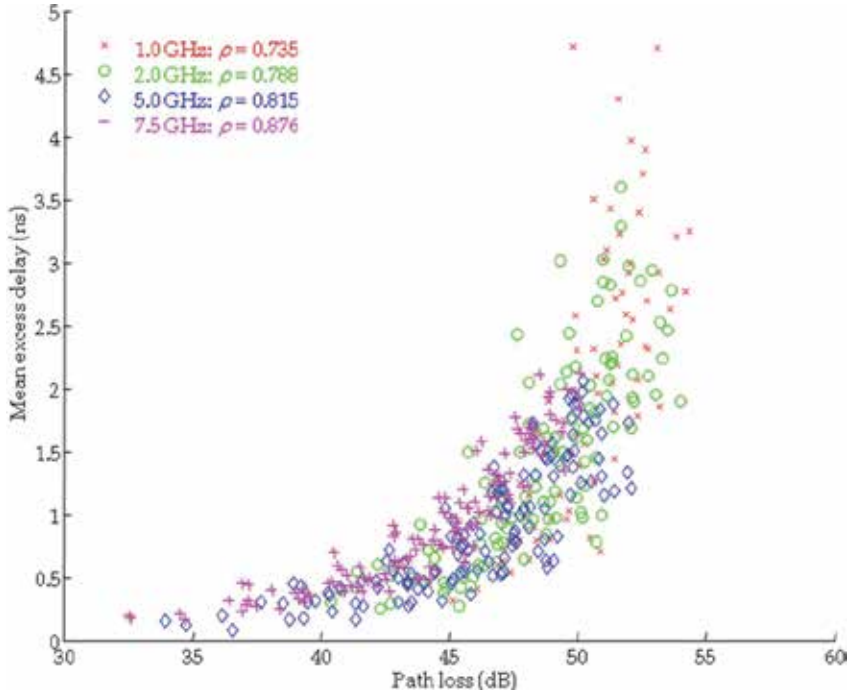
Fig. 11. Scatter plot of estimated mean excess delay vs. estimated total path loss for different bandwidths. Note the slight increase in correlation for larger bandwidths.

6. RMS delay spread

RMS delay spread is another parameter that characterizes the time dispersion of the channel. It is defined as a square root of the second central moment of the power delay profile:

$$\tau_{RMS} = \sqrt{\frac{\int_0^\infty \left(t - \bar{\tau}\right)^2 P_h(t)\, dt}{\int_0^\infty P_h(t)\, dt}}. \tag{14}$$

As omitting the subtraction of the RMS delay spread of the calibrated pulse would yield overestimated results (Varela & Sánchez, 2001), in order to estimate the RMS delay spread it is necessary to subtract the RMS delay spread of the calibrated pulse from the RMS delay spread of each measured PDPs (Saleh & Valenzuela, 1987):

$$\tau_{RMSest} = \tau_{RMSmeas} - \tau_{RMSpulse}, \tag{15}$$

where $\tau_{RMSmeas}$ is the RMS delay spread estimaed from the measured power delay profile (14) and $t_{RMSpulse}$ is the estimated RMS delay spread value of the calibrated pulse at a given bandwidth (Table 2). The results show a certain dependence on the antenna separation, where the correlation coefficient rises as the bandwidth increases (Fig. 12).

Fig. 13 presents a comparison of empirical cumulative distribution functions (CDF) of the estimated RMS delay spread values and theoretical normal CDFs with respective standard deviations for different bandwidths, shown in Table 4. Note that the mean value of the estimated RMS delay spread values decreases with increasing bandwidth.

System BW	1 GHz	2 GHz	5 GHz	7.5 GHz
Mean	5.93 ns	4.85 ns	3.85 ns	3.9 ns
Std. dev.	1.37 ns	1.37 ns	1.25 ns	1.36 ns

Table 4. Mean values and standard deviations of estimated RMS delay spread values for different bandwidths.
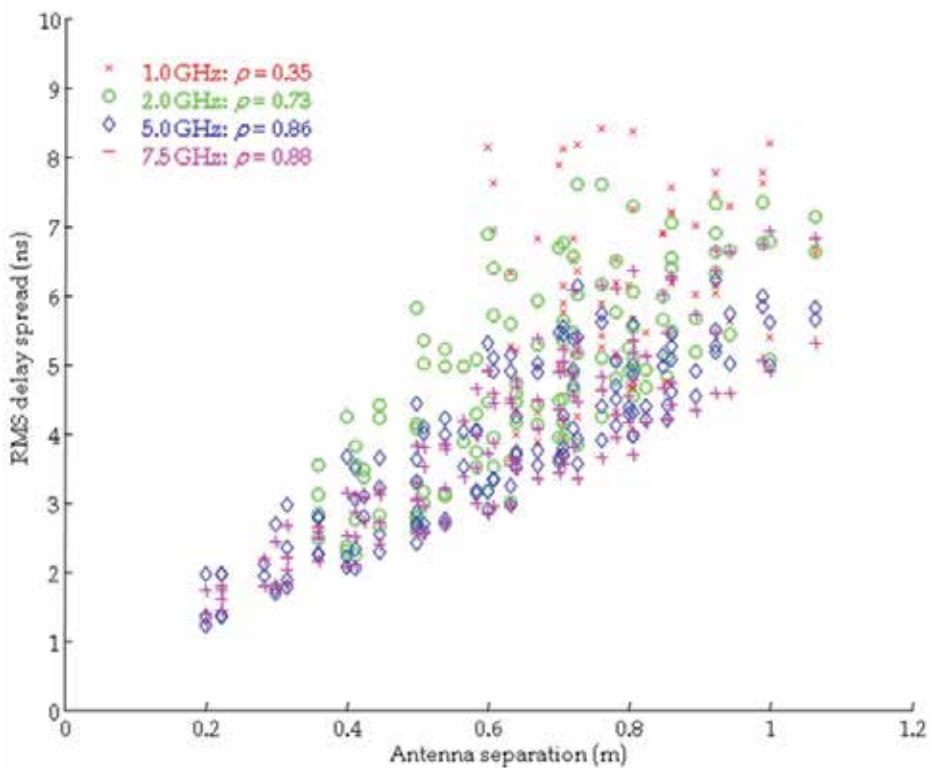
Fig. 12. Scatter plot of estimated RMS delay spread vs. antenna separation for different bandwidths. Note that the correlation coefficient increases with the bandwidth.

An extensive research based on analysis of over 300000 power delay profiles measured in 4.375 GHz – 5.625 GHz presented in (Ghassemzadeh et al., 2002) reports on normally distributed mean excess delay and RMS delay spread with mean value of 4.7 ns and standard deviation of 2.3 ns for indoor LOS scenarios. This increase is explained to be largely due to paths with longer delays having larger path loss values associated with them. Fig. 14 presents a scatter plot of estimated RMS delay spread in dependence of the total path loss. It is evident that these two parameters are strongly correlated.
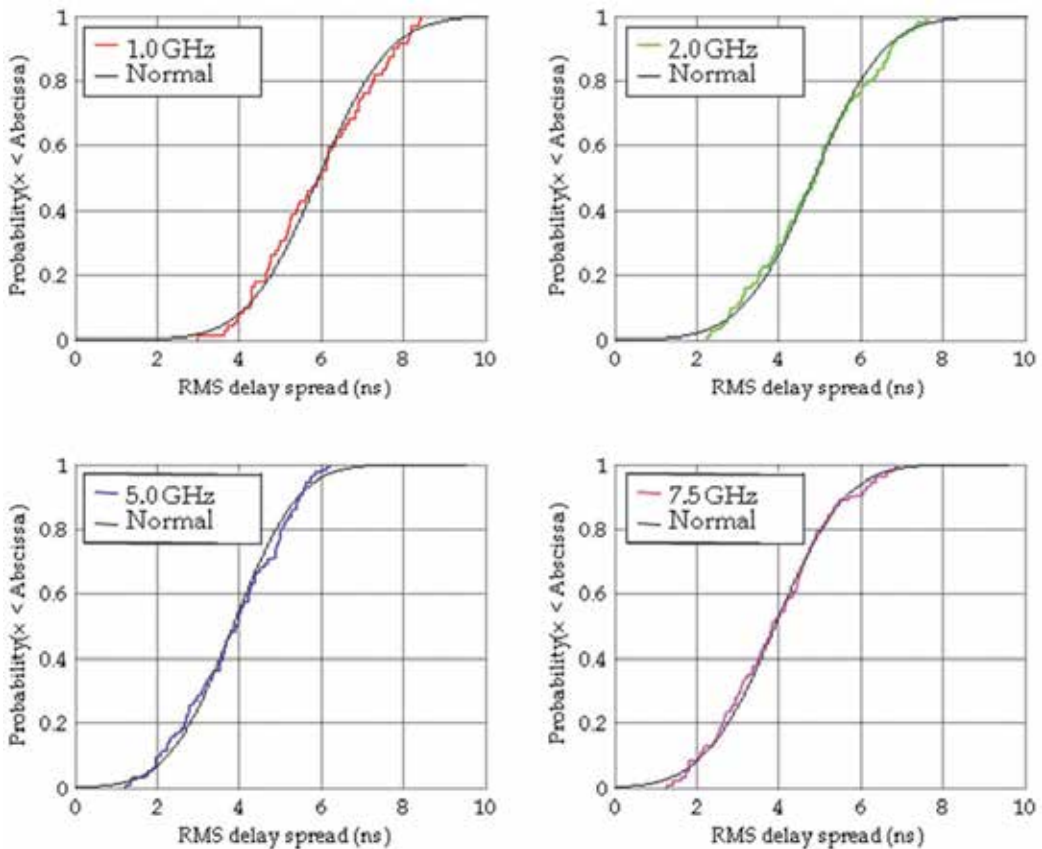
Fig. 13. Empirical CDF of estimated RMS delay spread obtained for different bandwidths. The black line on each CDF represents the theoretical normal CDF with the respective calculated mean and standard deviation.
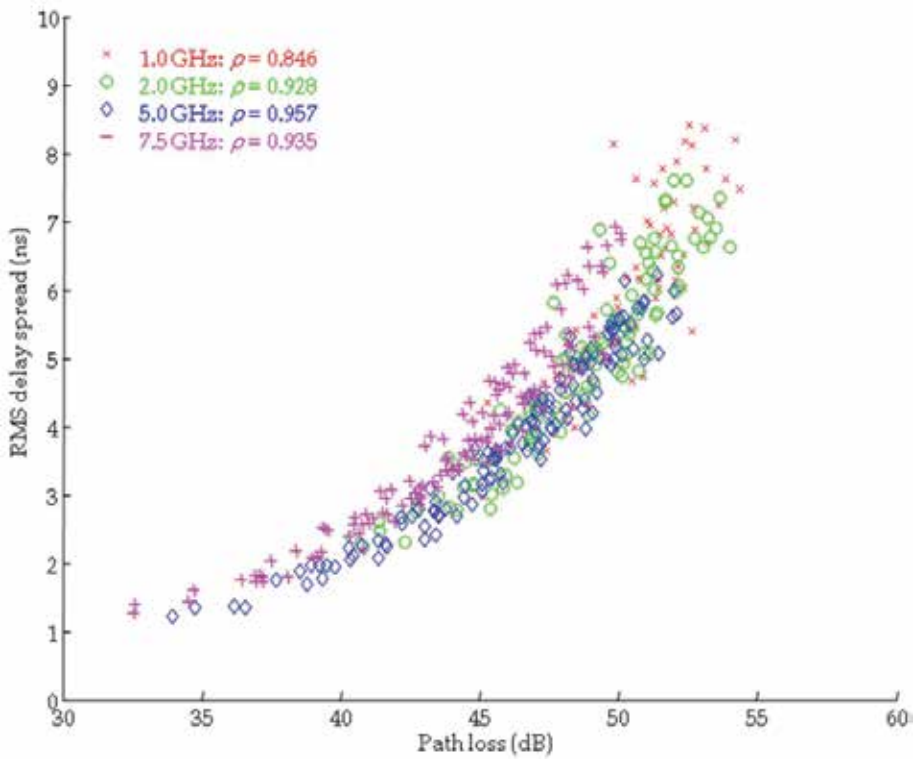
Fig. 14. Scatter plot of estimated RMS delay spread vs. estimated total path loss for different bandwidths.
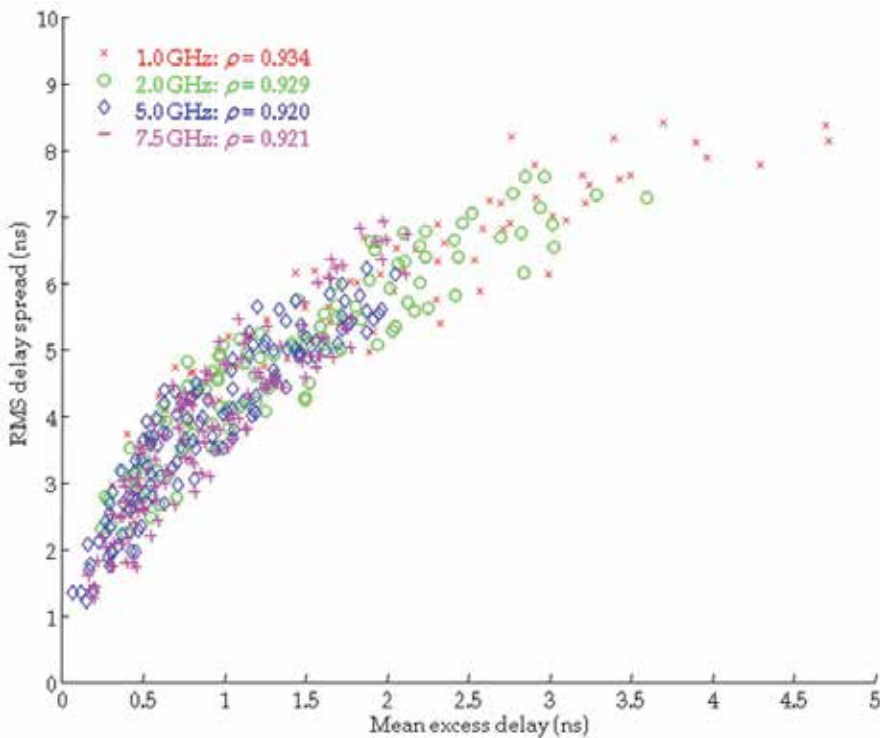
Fig. 15. Scatter plot of estimated RMS delay spread vs. estimated mean excess delay for different bandwidths.

A scatter plot of estimated RMS delay spread in function of the estimated mean excess delay is presented on Fig. 15. A strong correlation is observed for all bandwidths.

7. Discussion

The research presented in this chapter showed a certain dependence of the estimation of channel parameters on the system bandwidth.

First, the estimated path loss exponent slightly decreases with increasing the system bandwidth. An explanation can be found in the frequency selective propagation mechanisms, since different frequency components experience different impact of diffraction, reflection and transmission, where the coefficients that define these processes are dependent on the frequency of the transmitted signal. The estimated path loss exponent is slightly higher than the free space path loss exponent (between 2.05 and 2.28 for different bandwidths). Considering that the path loss exponent estimates for UWB indoor scenarios found in the literature are regularly below 2, the additional loss in the presented measurement campaign might be explained by the influence of the used desk, made of wood, chipboard and MDF.

Second, the estimated standard deviation of the shadowing term evidently decreases with increasing the system bandwidth, which in turn causes the increase in correlation between the estimated total path loss and antenna separation. This can also be explained as a direct consequence of the frequency selective propagation mechanisms. At larger bandwidths,

more frequency components will be immune to reflections and diffraction, so that the received signal will be more consistent.

Third, the estimated RMS delay spread decreases with increasing the system bandwidth, because the system with wider spectrum is able to resolve more multipath components.

It is shown that estimated correlations between the various channel parameters investigated in this research are greater as the system bandwidth increases. This is obviously another consequence of better temporal resolution in due to shorter pulses at wider bandwidths.

8. Conclusion

The main scope of this chapter was to explore the validity of well established empirical methods used for UWB channel modeling and to propose the estimated values of the model parameters for a specific propagation environment.

An indoor UWB measurement campaign presented in this chapter was performed on an empty surface of a desk placed in a typical office room. The channel impulse responses were measured on the surface of the desk at different system bandwidths using a VNA method. The channel parameter values were estimated from the measurement results for each different bandwidth. The estimated values are comparable with the ones found in literature. Analyzing the estimated values we have found that the estimations of the channel parameters show a certain dependence on the system bandwidth. The estimated path loss exponent values, standard deviations of the shadowing term, RMS delay spread mean values and mean excess delay values are all decreasing with increasing bandwidth for this indoor LOS scenario.

The analysis of correlation between the estimated values showed that the correlation coefficients tend to be higher at wider bandwidths.

9. Acknowledgment

10. References

Bose, R. (2006). Ultra Wideband Channel Modeling for Personal Area Network, *Proceedings of First European Conference on Antennas and Propagation (EuCAP 2006)*, pp. 1-4, ISBN 978-92-9092-937-6, Nice, France, 6-10 November 2006

Cassioli, D. & Durantini, A. (2004). A time-domain Propagation Model of the UWB Indoor Channel in the FCC-compliant Band 3.6 – 6 GHz based on PN-sequence Channel Measurements, *Proceedings of IEEE 59th Semiannual Vehicular Technology Conference (VTC '04)*, Vol. 1, pp. 213-217, ISBN 0-7803-8255-2, Milan, Italy, 17-19 May 2004

Cassioli, D., Durantini, A. & Ciccognani, W. (2004). The Role of Path Loss on the Selection of the Operating Bands of UWB Systems, *Proceedings of IEEE 15th International Symposium on Personal, Indoor and Mobile Radio Communications (PIMRC 2004)*, Vol. 4, pp. 2787-2791, ISBN 0-7803-8523-3, Barcelona, Spain, 5-8 September 2004

Cassioli, D., Win, M.Z. & Molisch, A.F. (2001). A Statistical Model for the UWB Indoor Channel, *Proceedings of IEEE 53rd Vehicular Technology Conference (VTC '01)*, Vol. 2, pp. 1159-1163, ISBN 0-7803-6728-6, Rhodes, Greece, 6-9 May 2001

Chang, W.-J. & Tarng, J.-H. (2007). Effects of Bandwidth on Observable Multipath Clustering in Outdoor/Indoor Environments for Broadband and Ultrawideband Wireless Systems, *IEEE Transactions on Vehicular Technology*, Vol. 56, No. 4, (July 2007), pp. 1913-1923, ISSN 0018-9545

Choi, J., Kang, N.-G., Sung, Y.-S., Kang, J.-S. & Kim, S.-C. (2009). Frequency-Dependent UWB Channel Characteristics in Office Environments, *IEEE Transactions on Vehicular Technology*, Vol. 58, No. 7, (September 2009), pp. 3102-3111, ISSN 0018-9545

Ghassemzadeh, S.S., Greenstein, L.J., Kavcic, A., Sveinsson, T. & Tarokh, V. (2003). An Empirical Indoor Path Loss Model For Ultra-Wideband Channels, *Journal of communication and networks*, Vol. 5, No. 4, (December 2003), pp. 303-308, ISSN 1229-2370

Ghassemzadeh, S.S., Greenstein, L.J., Sveinsson, T., Kavcic, A. & Tarokh, V. (2005). UWB Delay Profile Models for Residential and Commercial Indoor Environment, *IEEE Transactions on Vehicular Technology*, Vol. 54, No. 4, (July 2005), pp. 1235-1244, ISSN 0018-9545

Ghassemzadeh, S.S., Jana, R., Tarokh, V., Rice, C.W. & Turin, W. (2002). A Statistical Path Loss Model for In-home UWB Channels, *Proceedings of IEEE Conference in Ultra Wideband Systems and Technologies (UWBST '02)*, pp. 59-64, ISBN 0-7803-7496-7, Baltimore, Maryland, USA, 21-23 May 2002

Hewlett-Packard Company (1989). Time and Frequency Domain Transforms, In: *HP 8719A, HP 8720B Microwave Network Analyzer Operating Manual*, Hewlett-Packard Company, Santa Rosa, California, USA

Hovinen, V., Hämäläinen, M., & Pätsi, T. (2002). Ultra Wideband Indoor Radio Channel Models: Preliminary Results, *Proceedings of IEEE Conference in Ultra Wideband Systems and Technologies (UWBST '02)*, pp. 75-79, ISBN 0-7803-7496-7, Baltimore, Maryland, USA, 21-23 May 2002

Molisch, A.F. (2005). Ultrawideband Propagation Channels-Theory, Measurement and Modeling, *IEEE Transactions on Vehicular Technology*, Vol. 54, No. 5, (September 2005), pp. 1528-1545, ISSN 0018-9545

Molisch, A.F. (May 31, 2006). UWB Propagation Channels, In: *UWB Communication Systems: A Comprehensive Overview*, Di Benedetto, M.-G., Kaiser, T., Molisch, A.F., Opperman, I., Politano, C. & Porcino, D., pp. 21-118, Hindawi Publishing Corporation, ISBN 977-5945-10-0, New York, USA

Saleh, A.A.M., & Valenzuela, R.A. (1987). A Statistical Model for Indoor Multipath Propagation. *IEEE Journal on Selected Areas in Communications*, Vol. 5, No.2, (February 1987), pp. 128-137, ISSN 0733-8716

Suzuki, Y. & Kobayashi, T. (2005). Ultra Wideband Signal Propagation in Desktop Environments, *IEICE Transactions on Fundamentals of Electronics, Communications and Computer Sciences*, Vol. E88-A, No. 9, (September 2005), pp. 2272-2278, ISSN: 0916-8508

Taniguchi, T., Maeda, A. & Kobayashi, T. (2006). Development of an Omnidirectional and Low-VSWR Ultra Wideband Antenna, *International Journal on Wireless & Optical Communications*, Vol. 3, No. 2, (August 2006), pp. 145-157, ISSN 0219-7995

Varela, M.S. & Sánchez, M.G. (2001). RMS Delay and Coherence Bandwidth Measurements in Indoor Radio Channels in the UHF Band, *IEEE Transactions on Vehicular Technology*, Vol. 50, No. 2, (March 2001), pp. 515-525, ISSN 0018-9545

Živković, Z. & Šarolić, A. (2010). Measurements of Antenna Parameters in GTEM cell. *Journal of Communications Software and Systems*, Vol. 6, No. 4, (December 2010), pp. 125-132, ISSN 1845-6421

Part 3

UWB Pulse Reflection

Ultra Wideband (UWB) Pulse Reflection from a Dispersive Medium Half Space

Qingsheng Zeng[1] and Gilles Y. Delisle[2]
[1]Communications Research Centre
[2]Technology Integration Centre, Technopôle Defense & Security
Canada

1. Introduction

Electromagnetic wave reflection from dispersive media has been a subject of interest to researchers for many years. The advent of ultra wideband (UWB) short pulse sources has recently attracted renewed interest in this aspect. Accurate modeling and improved physical understanding of pulse reflection from dispersive media is crucial in a number of applications, including optical waveguides, UWB radar, ground penetrating radar, UWB biological effects, stealth technology and remote sensing. Numerous researchers have demonstrated that Lorentz, Debye and Cole-Cole models can be used to accurately predict dispersive properties of many media.

In the seminal work of Sommerfeld (Sommerfeld, 1914) and in the subsequent refinements of Oughstun and Sherman (Oughstun & Sherman, 1988) (Oughstun & Sherman, 1989) (Oughstun & Sherman, 1990), the investigations have focused on the Lorentz material, which is a good model for many materials encountered in optics and engineering. The reflection of a short pulse by a Lorentz medium has been considered for TE (transverse electric) polarization by Gray (Gray, 1980) and for TM (transverse magnetic) polarization by Stanic et al (Stanic et al., 1991). In each of these studies, the authors find the impulse response of the reflected field by calculating the inverse transform of the frequency domain reflection coefficient as an infinite series of fractional order Bessel functions. Although this gives a convenient analytical result, the series form provides little insight into the behavior of the reflected field waveform. Cossman et al have presented a compact form for both TE (Cossman et al., 2006) and TM (Cossman et al., 2007) reflection coefficients, which provide useful intuition about the response of a Lorentz medium half space. However, the mathematical derivations are lengthy and the solutions involve exponential and modified Bessel functions and require convolution operation to evaluate. Particularly, because of the greater complexity of the TM frequency domain reflection coefficient, a more involved process is needed, including the introduction of a term that does not appear in the TE case. Under some conditions this term is noncausal, although the final expression for the impulse response is causal. Moreover, when the incident angle is equal to 45[0], the general expressions cannot be used directly due to singularities, and a special form of TM time domain reflection coefficient is separately achieved.

The use of short pulses to probe materials has prompted the study of the reflection of transient waves from material half space of other types. The Debye model (Debye, 1945) is

utilized to describe the frequency behavior of the permittivity of many type materials, especially polar liquids. This model has been extended to include conductivity (Kosmas et al., 2004) and several relaxation components (Oswald et al., 1998), and has been used to describe the behavior of such diverse materials as biological tissues (Ong et al., 2003), building materials (Ogunsola et al., 2006), circuit boards (Zhang et al., 2003) and ceramics (Guerra & Eiras, 2004). A standard technique for the measurement of material parameters is to interrogate the material, either in free space (Piesiewicz et al., 2005) or in a waveguide system (Jones et al., 2005) with an electromagnetic pulse. It is therefore important to have an efficient method analyzing the time-domain reflection properties of a Debye material. Rothwell (Rothwell, 2007) worked out the time domain reflection coefficients of a Debye half space for both horizontal and vertical polarizations that involve exponential and modified Bessel functions and require convolution operations to evaluate. Another model commonly used to capture the relaxation-based dispersive properties is the Cole–Cole model (Cole & Cole, 1941) that is more general than the Debye model. For many types of materials including biological tissues, the Cole–Cole models provided an excellent fit to experimental data over the entire measurement frequency range. However, to our knowledge, the time-domain reflection coefficient of a Cole–Cole half space for any polarization has been not available so far, perhaps due to the computational complexity of embedding a Cole–Cole dispersion model into numerical methods.

All materials are to some extent dispersive. If a field applied to a material undergoes a sufficient rapid change, there is a time lag in the response of the polarization or magnetization of the atoms. It has been found that such materials have complex, frequency dependent constitutive parameters. On the one hand, the lossy material is dispersive since it has a complex, frequency dependent permittivity. On the other hand, the Kronig−Kramers relations imply that if the constitutive parameters of a material are frequency dependent, they must have both real and imaginary parts (Rothwell & Cloud, 2001). Such a material, if isotropic, must be lossy. So dispersive materials are general lossy and must have both dissipative and energy storage characteristics. However, many materials have frequency range called transparency ranges over which the imaginary parts are smaller compared to real parts of constitutive parameters. If we restrict our interest to these ranges, we may approximate the material as lossless.

In this chapter, the time domain technique based on the numerical inversion of Laplace transform is developed and extended to the modeling of ultra wideband pulse reflection from Lorentz, Debye and Cole−Cole media. All these three dispersive models satisfy the Kronig−Kramers relations required for a causal material (Rothwell & Cloud, 2001). Firstly, for readers' convenience, the numerical inversion of Laplace transform is presented. Next, the time domain reflection coefficients, viz impulse responses, of Lorentz, Debye and Cole−Cole half spaces are achieved for both TE and TM cases. Then, the transient reflections of an arbitray pulse from these media are determined by convolving the incident pulse with the impulse responses of these media, instead of using Prony's method to decompose the incident pulse into a series of finite attenuating exponential signals as in our previous work (Zeng & Delisle, 2006). Based on the time domain analysis of reflected pulses from these dispersive half spaces, some waveform parameters are estimated and the material diagnosis is carried out. Lastly, the work on transient wave reflection from dispersive media is summarized with some meaningful conclusions. Our results show excellent agreement with those in the literature, validating the correctness and effectiveness of our technique.

2. Numerical inversion of Laplace transform

The Laplace transform (image function in the complex frequency domain) $F(s)$ and the inverse Laplace transform (original function in the time domain) $f(t)$ are related by the forward transformation

$$Lf(t) = F(s) = \int_0^\infty f(t)e^{-st}dt \qquad (1)$$

and the inverse transformation

$$L^{-1}F(s) = f(t) = \frac{1}{2\pi j}\int_{\gamma-j\infty}^{\gamma+j\infty} F(s)e^{st}ds \,. \qquad (2)$$

In general, it is straightforward to take the Laplace transform of a function. However, the inverse transformation is often difficult. In many cases, the method using simple rules and a table of transforms, and the method using the Bromwich integral and Cauchy integral theorem do not work well, hence some numerical technique must be utilized. To implement the numerical inversion method, the following conditions must be satisfied (Zeng, 2010). Based on the properties of $F(s)$, such a number γ_0 can always be found that in the region of convergence, $0 < \gamma_0 < \mathrm{Re}(s)$, 1) $F(s)$ converges absolutely, 2) $\lim_{s\to\infty} F(s) = 0$, 3) $F(s)$ does not have any singularity and branch point, and 4) $F(s^*) = F^*(s)$ where the asterisk denotes complex conjugate.

The most distinctive feature of this method lies in the approximation for e^{st}. Its main points are:

i)
$$e^{st} = \lim_{\rho\to\infty} \frac{e^\rho}{2\cosh(\rho-st)} = e^{st} - e^{-2\rho}e^{3st} + e^{-4\rho}e^{5st} - \cdots \qquad (3)$$

ii)
$$e^{st} \approx E_{ec}(st,\rho) = \frac{e^\rho}{2\cosh(\rho-st)} = \frac{e^\rho}{2}\sum_{n=-\infty}^{\infty}\frac{(-1)^n j}{st-\left[\rho+j(n-0.5)\pi\right]} \qquad (4)$$

iii) The Bromwich integral is transformed to the integral around the poles of $E_{ec}(st,\rho)$.

Then $f(t)$ is approximated by $f_{ec}(t,\rho)$, which is expressed by

$$f_{ec}(t,\rho) = \frac{1}{2\pi j}\int_{\gamma-j\infty}^{\gamma+j\infty} F(s)E_{ec}(st,\rho)\,ds = f(t) - e^{-2\rho}f(3t) + e^{-4\rho}f(5t) - \cdots = \left(e^\rho/t\right)\sum_{n=1}^{\infty}F_n \qquad (5)$$

where $t > 0$, and

$$F_n = (-1)^n \mathrm{Im}\, F\left\{\left[\rho+j(n-0.5)\pi\right]/t\right\} \qquad (6)$$

Equation (5) shows that the function $f_{ec}(t,\rho)$ gives a good approximation to $f(t)$ when $\rho \gg 1$, and can be used for error estimation. Equations (5) and (6) are derived by substituting $E_{ec}(st,\rho)$ from (4), and can be applied to the numerical inversion of the Laplace transform. In practice, the infinite series in (5) has to be truncated after a proper number of

terms. Since the infinite series is a slowly convergent alternating series, truncating to a small number of terms leads to a significant error. An effective approach using the Euler transformation has been developed, which works under the following conditions (Hosono, 1981): a) There exists an integer $k \geq 1$ such that the signs of F_n alternate for $n \geq k$; b) For $n \geq k$, $\frac{1}{2} < |F_{n+1}/F_n| \leq 1$. With conditions a) and b), (5) can be truncated with $f_{ec}^{lm}(t,a)$, which has $N = l + m$ terms and is given by

$$f_{ec}^{lm}(t,\rho) = \left(e^\rho/t\right)\left(\sum_{n=1}^{l-1} F_n + 2^{-m-1}\sum_{n=0}^{m} A_{mn}F_{l+n}\right) \tag{7}$$

where A_{mn} are defined recursively by

$$A_{mm} = 1, \quad A_{mn-1} = A_{mn} + \binom{m+1}{n}. \tag{8}$$

In this method, the upper bound for the truncation errors is given by

$$R^{lm} = \left|f_{ec}^{l+1,m}(t,\rho) - f_{ec}^{l,m}(t,\rho)\right| \tag{9}$$

while the upper bound for the approximation errors is given by

$$\left|f_{ec}(t,\rho) - f(t)\right| \approx M e^{-2\rho}, \tag{10}$$

If

$$\left|f(t)\right| \leq M \qquad \text{for all} \quad t > 0.$$

As indicated in (10), the relative approximation errors are less than $e^{-2\rho}$, while the truncation errors increase with t and decrease with N. For a typical value of t, the calculation is repeated by increasing N to determine a proper number of terms in (5), which makes the truncation errors small enough.

3. Pulse reflection from a Lorentz medium half space

Consider a sinusoidal stead-state plane wave of frequency ω incident on an interface separating free space (region 1) from a homogeneous Lorentz medium (region 2). The angle of incidence measured from the normal to the interface is θ, and the electric field is polarized perpendicular to the plane of incidence (TE polarization). Region 1 is described by the permittivity ε_0 and permeability μ_0, while region 2 is described by the permittivity $\varepsilon(\omega) = \varepsilon_0 \varepsilon_r(\omega)$ and permeability μ_0. The reflection coefficient, defined as the ratio of the tangential incident field to reflected electric field, is given by (Cossman et al., 2006)

$$\Gamma(\omega) = \frac{Z(\omega) - Z_0}{Z(\omega) + Z_0}, \tag{11}$$

where the wave impedance of the incident wave is $Z_0 = \eta_0/\cos\theta$ and the wave impedance of the transmitted wave is

$$Z(\omega) = \frac{\eta(\omega)\, k(\omega)}{k_z(\omega)} \,. \tag{12}$$

Here $\eta_0 = (\mu_0/\varepsilon_0)^{1/2}$, $\eta = (\mu_0/\varepsilon)^{1/2}$, $k_z = (k^2 - k_0^2 \sin^2\theta)^{1/2}$, $k_0 = \omega(\mu_0 \varepsilon_0)^{1/2}$ and $k = \omega(\mu_0 \varepsilon)^{1/2}$. The relative permittivity of a single resonance Lorentz medium has the form

$$\varepsilon_r(\omega) = 1 + \frac{b^2}{\omega_0^2 - \omega^2 + 2j\omega\delta} \,. \tag{13}$$

Here ω_0 is the resonance frequency, δ is the damping coefficient, and b is the plasma frequency of the medium. Letting the Laplace transform variable be $s = j\omega$ and substituting Equation (13), then the Laplace domain reflection coefficient may be written in the form

$$\Gamma(s) = \frac{\left(s^2 + 2\delta s + \omega_0^2\right)^{1/2} - \left(s^2 + 2\delta s + \omega_0^2 + B^2\right)^{1/2}}{\left(s^2 + 2\delta s + \omega_0^2\right)^{1/2} + \left(s^2 + 2\delta s + \omega_0^2 + B^2\right)^{1/2}} \tag{14}$$

where $B = b/\cos\theta$. Factoring the quadratic forms under the radicals gives the alternative form

$$\Gamma(s) = \frac{\left((s-s_1)(s-s_2)\right)^{1/2} - \left((s-s_3)(s-s_4)\right)^{1/2}}{\left((s-s_1)(s-s_2)\right)^{1/2} + \left((s-s_3)(s-s_4)\right)^{1/2}} \tag{15}$$

where

$$s_{1,2} = -\delta \pm \lambda_1 \qquad\qquad \lambda_1 = \left(\delta^2 - \omega_0^2\right)^{1/2}, \tag{16}$$

$$s_{3,4} = -\delta \pm \lambda_3 \qquad\qquad \lambda_3 = \left(\delta^2 - \omega_0^2 - B^2\right)^{1/2}, \tag{17}$$

λ_1 and λ_3 may be either real or imaginary, depending on the values of ω_0, δ and B. The image function $\Gamma(s)$ given in (15) clearly satisfies four conditions 1) – 4) listed in Section 2 under which $f(t)$ can be approximated by $f_{ec}(t,\rho)$. It can be proved that, for $s = [\rho + j(n-0.5)\pi]/t$, $\Gamma(s)$ meets both two conditions a) and b) described in Section 2 under which $f_{ec}^{lm}(t,\rho)$ can be used to approximate $f_{ec}(t,\rho)$ (Zeng, 2010). The proof would not be given here due to the limited space. So the transient reflection coefficient $\Gamma(t)$, the original function of $\Gamma(s)$, can be calculated using Equation (7).

To compare our results with those in (Cossman et al, 2006), the same incident angle, $\theta = 30^0$, and the same three sets of parameters are chosen as in (Cossman et al., 2006), with each set of parameters corresponding to each of the three possible cases. The first set of parameters is chosen as $\omega_0 = 4.0 \times 10^{16} s^{-1}$, $\delta = 0.28 \times 10^{16} s^{-1}$, $b^2 = 20.0 \times 10^{32} s^{-2}$, corresponding to case 1 for $\delta << \omega_0$. In this case, the waveform highly oscillates and only slightly damps, as plotted in Figure 1 (a).

The next set of parameters is $\omega_0 = 2.0 \times 10^{15} s^{-1}$, $\delta = 0.28 \times 10^{16} s^{-1}$, $b^2 = 20.0 \times 10^{29} s^{-2}$. This choice of parameter corresponds to case 2 for $\delta^2 > \omega_0^2 + B^2$, where the resulting waveform is overdamped and has only one single negative peak without any oscillation, as shown in Figure 1 (b).
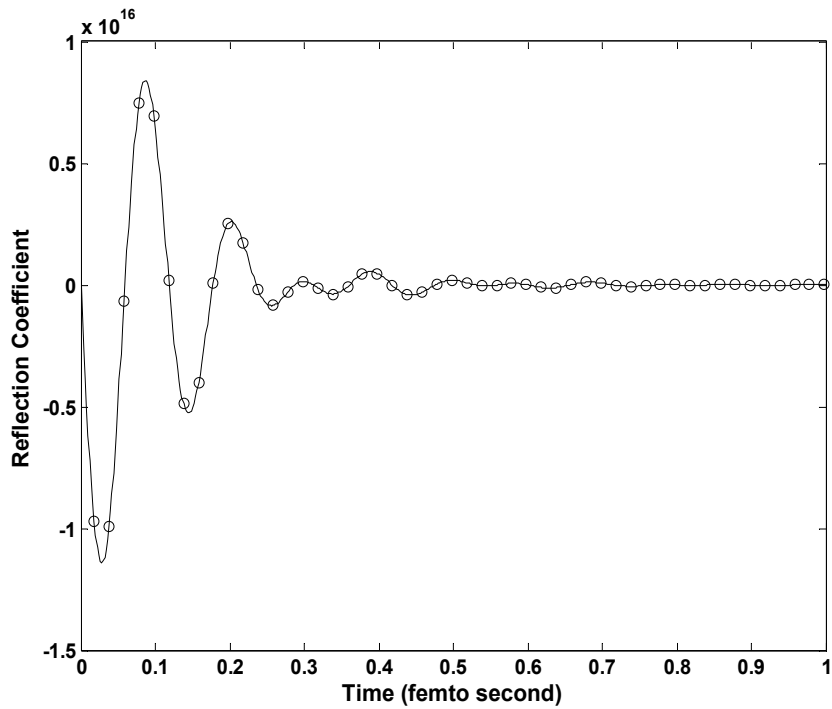
(a) $\omega_0 = 4.0 \times 10^{16} s^{-1}$, $\delta = 0.28 \times 10^{16} s^{-1}$, $b^2 = 20.0 \times 10^{32} s^{-2}$, $\delta << \omega_0$.
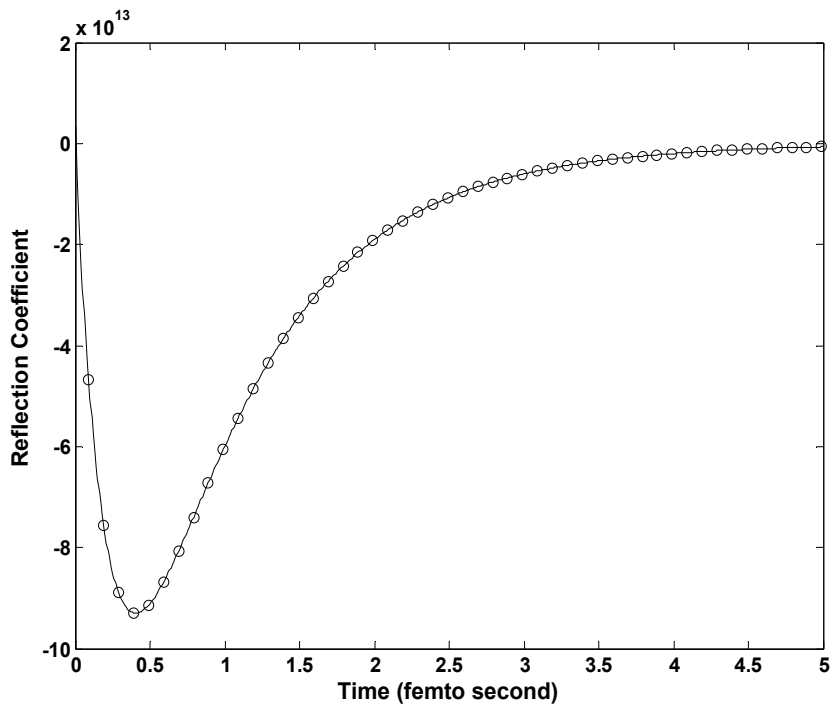
(b) $\omega_0 = 2.0 \times 10^{15} s^{-1}$, $\delta = 0.28 \times 10^{16} s^{-1}$, $b^2 = 20.0 \times 10^{29} s^{-2}$, $\delta^2 > \omega_0^2 + B^2$
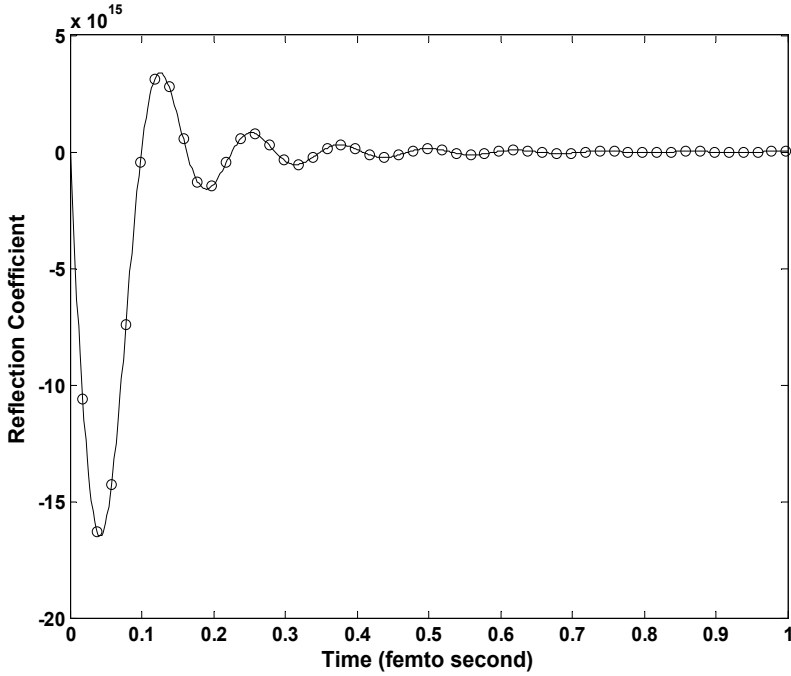
(c) $\omega_0 = 2.0 \times 10^{15} s^{-1}$, $\delta = 0.28 \times 10^{16} s^{-1}$, $b^2 = 20.0 \times 10^{32} s^{-2}$, $\delta > \omega_0$ but $\delta^2 < \omega_0^2 + B^2$.

Fig. 1. Transient reflection coefficient for TE polarization with incident angle $\theta = 30^0$ and three sets of material parameters. Solid line – our result; Small circle – result in (Cossman et al., 2006).

The third choice of parameters is $\omega_0 = 2.0 \times 10^{15} s^{-1}$, $\delta = 0.28 \times 10^{16} s^{-1}$, $b^2 = 20.0 \times 10^{32} s^{-2}$, which corresponds to case 3 for $\delta > \omega_0$ but $\delta^2 < \omega_0^2 + B^2$. In this case, the waveform has more damping and less oscillation than that in case 1, but has more oscillation than that in case 2, as illustrated in Figure 1 (c).

For the case of TM polarization (magnetic field perpendicular to the plane of incidence), the originally defined reflection coefficient is still given by (11), the impedance of a plane wave in the free space (ratio of tangential electric field to tangential magnetic field at the interface) is $Z_0 = \eta_0 \cos\theta$, the impedance of a wave in the Lorentz medium is

$$Z(\omega) = \frac{\eta(\omega) k_z(\omega)}{k(\omega)}.$$ (18)

The incident angle θ is measured in the same way as in TE case, η_0, η, k_z, k_0, and k are the same as those for TE polarization, respectively. Letting the Laplace transform variable be $s = j\omega$ and substituting (13) and (18) into (11), the Laplace domain reflection coefficient may be written in the form

$$\Gamma(s) = \frac{\left((s-s_1)(s-s_2)(s-s_5)(s-s_6)\right)^{1/2} - \left((s-s_3)(s-s_4)\right)^{1/2}}{\left((s-s_1)(s-s_2)(s-s_5)(s-s_6)\right)^{1/2} + \left((s-s_3)(s-s_4)\right)^{1/2}} = \frac{N(s)}{D(s)},$$ (19)

where

$$s_{1,2} = -\delta \pm \lambda_1 \qquad\qquad \lambda_1 = \left(\delta^2 - \omega_0^2\right)^{1/2}, \qquad\qquad (20)$$

$$s_{3,4} = -\delta \pm \lambda_3 \qquad\qquad \lambda_3 = \left(\delta^2 - \omega_0^2 - b^2\right)^{1/2}, \qquad\qquad (21)$$

$$s_{5,6} = -\delta \pm \lambda_5 \qquad\qquad \lambda_5 = \left(\delta^2 - \omega_0^2 - B^2\right)^{1/2}. \qquad\qquad (22)$$

Here ω_0, δ, b and B are the same as those for TE polarization, and λ_1, λ_3 and λ_5 may be either real or imaginary, depending on the values of ω_0, δ, b and B.

As indicated in the introduction, the solution of transient reflection coefficient in TM case is more complicated and involved than that in TE case. In (Cossman et al., 2007), a term that does not appear in the TE case needs to be introduced and a special form of the time domain reflection coefficient needs to be separately solved when the incident angle is equal to 45^0, which is however not needed with numerical Laplace transform. The image function $\Gamma(s)$ given in (19) obviously satisfies four conditions 1) – 4) listed in Section 2. Furthermore, it can also be proved that $\Gamma(s)$ given in (19) meets both two conditions a) and b) in Section 2 (Zeng, 2010).

To compare our results with those in (Cossman et al, 2007), the same incident angles and the same sets of material parameters are chosen as in (Cossman et al., 2007). The first case uses $\theta = 30^0$ along with the material parameters, $\omega_0 = 4.0 \times 10^{16} s^{-1}$, $\delta = 0.28 \times 10^{16} s^{-1}$, and $b^2 = 20.0 \times 10^{32} s^{-2}$, corresponding to the case for $\delta << \omega_0$. So the waveform of $\Gamma(t)$ is highly oscillatory and only slightly damped, as plotted in Figure 2 (a).

In the second case, the material parameters are chosen as $\omega_0 = 2.0 \times 10^{15} s^{-1}$, $\delta = 0.28 \times 10^{16} s^{-1}$, and $b^2 = 20.0 \times 10^{29} s^{-2}$, along with $\theta = 30^0$. This corresponds to the case for $\delta^2 > \omega_0^2 + B^2$, and the waveform of $\Gamma(t)$ shows no oscillatory behavior and only a single negative peak, as shown in Figure 2 (b).

In the third case, the choice of parameters is $\omega_0 = 2.0 \times 10^{15} s^{-1}$, $\delta = 0.28 \times 10^{16} s^{-1}$, $b^2 = 20.0 \times 10^{32} s^{-2}$, again with $\theta = 30^0$, which corresponds to the case for $\delta > \omega_0$ but $\delta^2 < \omega_0^2 + B^2$. Thus, $\Gamma(t)$ is more damping and less oscillatory than with the first choice of parameters but more oscillatory than with the second choice of parameters, as illustrated in Figure 2 (c).

In the fourth case, the material parameters are the same as those in the first case, but $\theta = 50^0$ is used. The result is achieved by directly using our approach that does not lead to any noncasual term, and is plotted in Figure 2 (d).

The final case examines the special case of $\theta = 45^0$ with the same choice of material parameters as in the first case. With our approach, this case does not need to be processed separately and can be treated as a general case for any incident angle. This result is illustrated in Figure 2 (e), and is very similar to that shown in Figure 2 (d), since the incident angle in this case differs by only 5^0 from that in the fourth case.

Figure 1 and Figure 2 demonstrate that our results perfectly agree with those in (Cossman et al., 2006) and in (Cossman et al., 2007), respectively, for all the different cases.
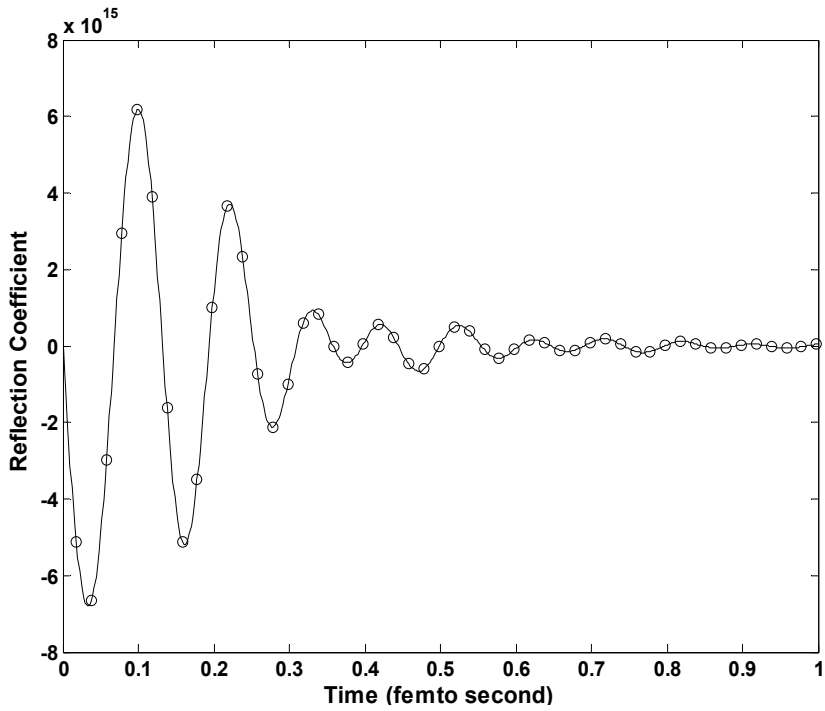
(a) $\theta = 30^0$, $\omega_0 = 4.0 \times 10^{16} s^{-1}$, $\delta = 0.28 \times 10^{16} s^{-1}$, $b^2 = 20.0 \times 10^{32} s^{-2}$, $\delta << \omega_0$.
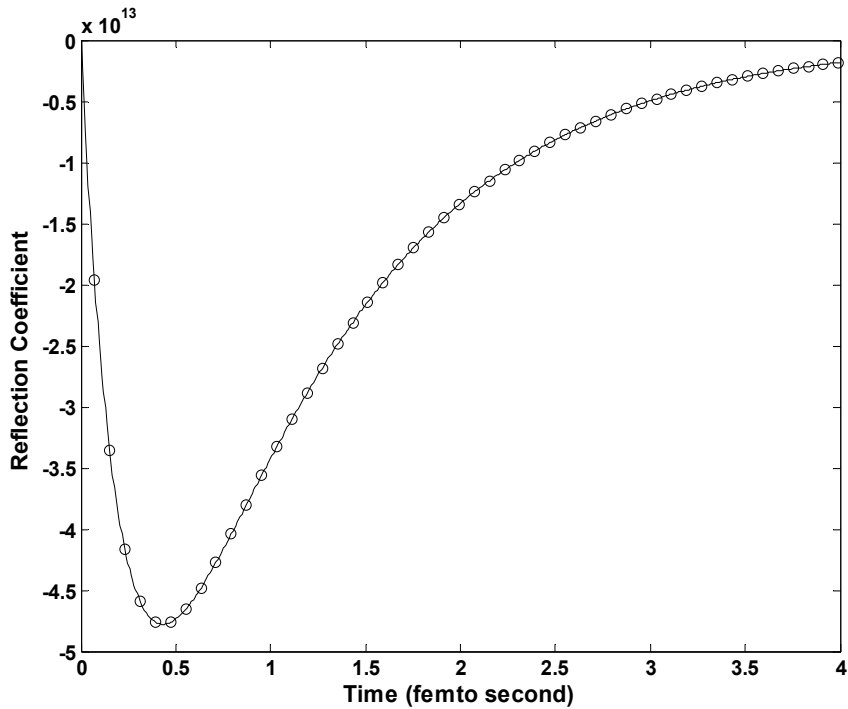
(b) $\theta = 30^0$, $\omega_0 = 2.0 \times 10^{15} s^{-1}$, $\delta = 0.28 \times 10^{16} s^{-1}$, $b^2 = 20.0 \times 10^{29} s^{-2}$, $\delta^2 > \omega_0^2 + B^2$.
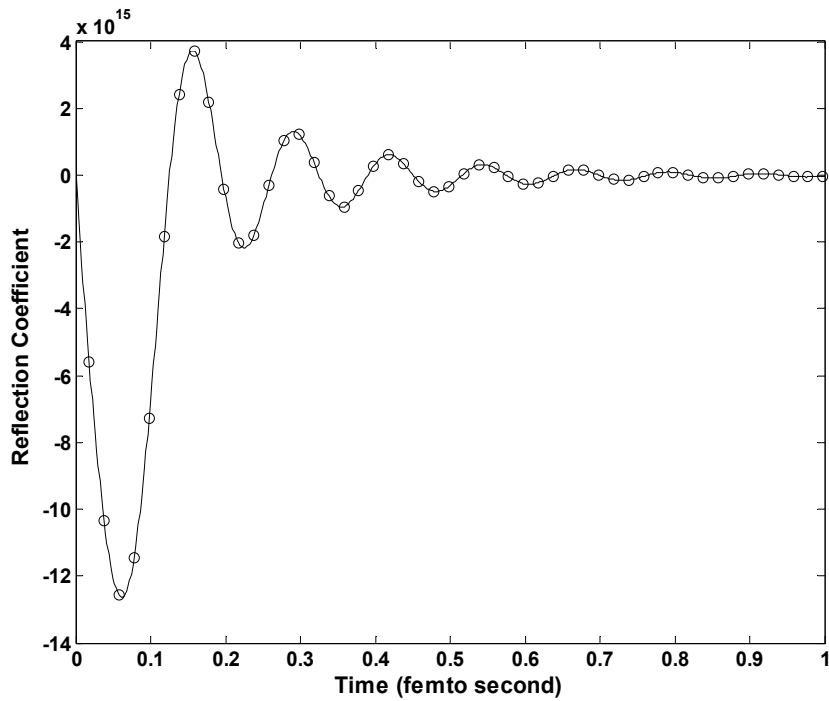
(c) $\theta = 30^0$, $\omega_0 = 2.0 \times 10^{15} s^{-1}$, $\delta = 0.28 \times 10^{16} s^{-1}$, $b^2 = 20.0 \times 10^{32} s^{-2}$, $\delta > \omega_0$ but $\delta^2 < \omega_0^2 + B^2$.
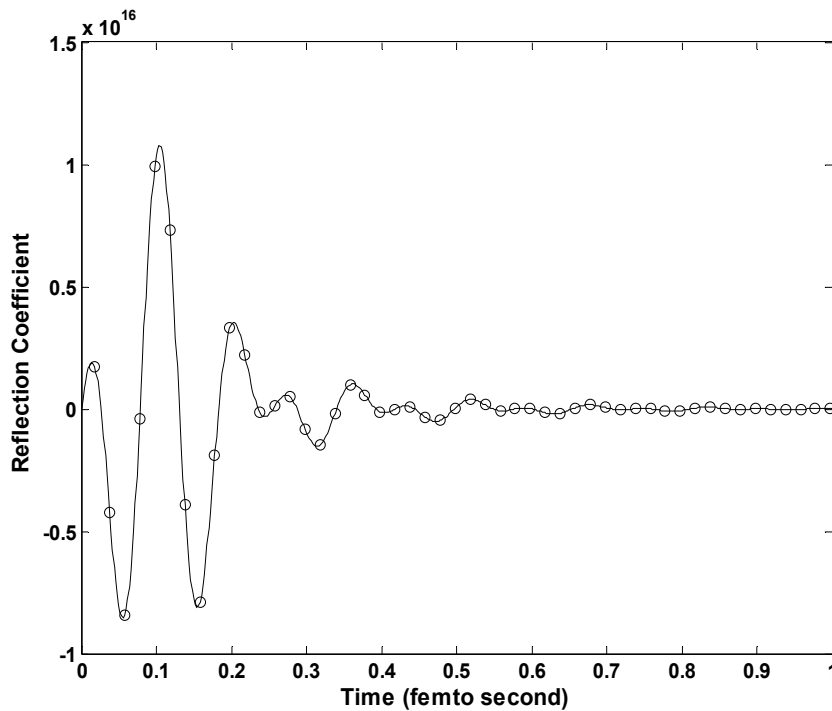
(d) $\theta = 50^0$, $\omega_0 = 4.0 \times 10^{16} s^{-1}$, $\delta = 0.28 \times 10^{16} s^{-1}$, $b^2 = 20.0 \times 10^{32} s^{-2}$, $\delta << \omega_0$.
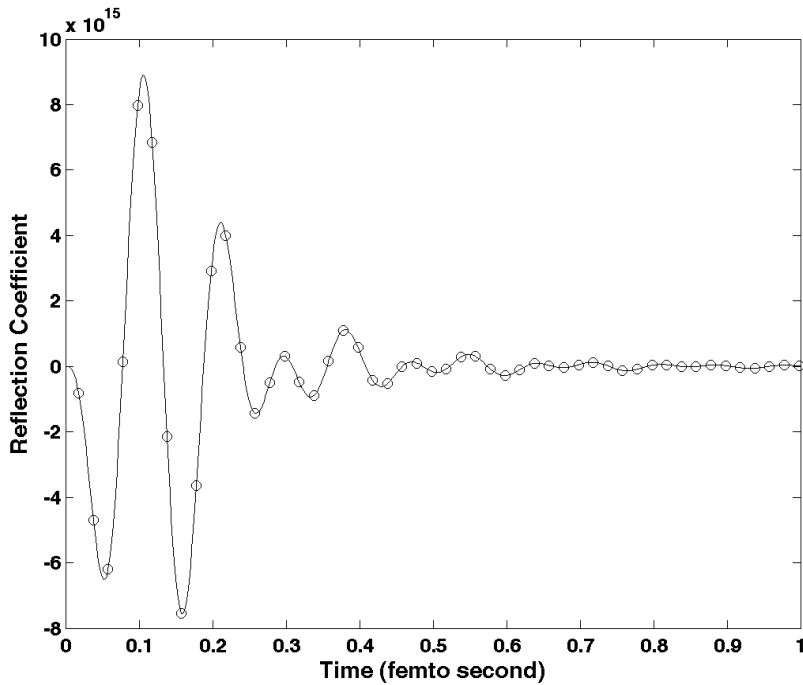
(e) $\theta = 45^0$, $\omega_0 = 4.0 \times 10^{16} s^{-1}$, $\delta = 0.28 \times 10^{16} s^{-1}$, $b^2 = 20.0 \times 10^{32} s^{-2}$, $\delta << \omega_0$.

Fig. 2. Transient reflection coefficient for TM polarization, with incident angle $\theta = 30^0$ and three sets of material parameters (a) (b) (c), and with incident angle $\theta = 50^0$ and $\theta = 45^0$ and one set of material parameters (d) (e) . Solid line – our result; Small circle – result in (Cossman et al., 2007).

4. Pulse reflection from a Debye and Cole–Cole medium half space

The knowledge of material properties is required in various technological fields, such as geophysics, material science and biomedical engineering. The characterization of bulk materials would be the most direct way to acquire this knowledge and greatly helpful to understand the underlying physics at the microscopic level, which is much more complicated in comparison with the existing formulations of the bulk effects. A typical approach to bulk material characterization is to examine reflected electromagnetic pulses from the interface between free space and the investigated material. Many kinds of materials show the relaxation-based dispersive properties that are commonly captured by the Debye (Debye, 1945) and Cole–Cole (Cole & Cole, 1941) models. Rothwell (Rothwell, 2007) worked out the time domain reflection coefficients of a Debye half space for both horizontal and vertical polarizations that involve exponential and modified Bessel functions and require convolution operations to evaluate. To our knowledge, the time domain reflection coefficient of a Cole–Cole half space for any polarization has been not available so far. It is the purpose of this section to develop a new technique for transient analysis of pulse reflection from Debye and Cole–Cole media, and apply this technique to waveform parameter estimation and material characterization.

4.1 Time domain reflection coefficients

Without losing generality and for the comparison with the results in (Rothwell, 2007), the one-order model with zero ionic conductivity is utilized in this work. Introduce the Laplace variable $s = j\omega$, and consider the interface between free space and a dielectric half space with unity permeability and a permittivity $\varepsilon(s) = \varepsilon_0 \varepsilon_r(s)$ described by the following unified equation

$$\varepsilon_r(s) = \varepsilon_\infty + \frac{\varepsilon_s - \varepsilon_\infty}{1 + (s\tau)^{1-\alpha}} , \tag{23}$$

where ε_s and ε_∞ are the static and optical dielectric constants ($\varepsilon_s > \varepsilon_\infty$), respectively, τ is the relaxation time, (23) becomes a one-pole Debye equation when $\alpha = 0$, and is a one-order Cole–Cole equation when $0 < \alpha \leq 1$. A nonzero Cole–Cole parameter α is a measure for broadening dispersion, which tends to broaden the relaxation spectrum and results from a spread of relaxation times centered around τ (Rothwell & Cloud, 2001). A unified formulation for a Cole–Cole or Debye half space is given below.

A plane wave is obliquely incident onto a dispersive half space from free space, at an incidence angle θ relative to the normal to the interface. The reflection coefficients are given by

$$R_H(s) = \frac{\cos\theta - \sqrt{\varepsilon_r(s) - \sin^2\theta}}{\cos\theta + \sqrt{\varepsilon_r(s) - \sin^2\theta}} \tag{24}$$

and

$$R_V(s) = \frac{\sqrt{\varepsilon_r(s) - \sin^2\theta} - \varepsilon_r(s)\cos\theta}{\sqrt{\varepsilon_r(s) - \sin^2\theta} + \varepsilon_r(s)\cos\theta} \tag{25}$$

for horizontal and vertical polarizations, respectively. Substituting $\varepsilon_r(s)$ from (23) leads to

$$R_H(s) = \frac{\sqrt{s^{1-\alpha} + s_0} - K_H\sqrt{s^{1-\alpha} + s_1}}{\sqrt{s^{1-\alpha} + s_0} + K_H\sqrt{s^{1-\alpha} + s_1}} \tag{26}$$

and

$$R_V(s) = \frac{\sqrt{s^{1-\alpha} + s_0}\sqrt{s^{1-\alpha} + s_1} - K_V\left(s^{1-\alpha} + s_2\right)}{\sqrt{s^{1-\alpha} + s_0}\sqrt{s^{1-\alpha} + s_1} + K_V\left(s^{1-\alpha} + s_2\right)} , \tag{27}$$

where

$$s_0 = \left(\frac{1}{\tau}\right)^{1-\alpha} , \quad s_1 = \left(\frac{1}{\tau}\right)^{1-\alpha}\frac{\varepsilon_s - \sin^2\theta}{\varepsilon_\infty - \sin^2\theta} > s_0 , \quad s_2 = \left(\frac{1}{\tau}\right)^{1-\alpha}\frac{\varepsilon_s}{\varepsilon_\infty} , \tag{28}$$

$$K_H = \frac{\sqrt{\varepsilon_\infty - \sin^2\theta}}{\cos\theta} , \tag{29}$$

and

$$K_V = \frac{\varepsilon_\infty \cos\theta}{\sqrt{\varepsilon_\infty - \sin^2\theta}} \ . \tag{30}$$

Either $R_H(s)$ or $R_V(s)$ does not satisfy the second one of the four conditions listed in Section 2, that is, is not asymptotic to zero at high frequency, but instead

$$\lim_{s\to\infty} R_H(s) = R_H^\infty = \frac{1-K_H}{1+K_H} \ , \tag{31}$$

and

$$\lim_{s\to\infty} R_V(s) = R_V^\infty = \frac{1-K_V}{1+K_V} \ . \tag{32}$$

So $R_H(t)$ and $R_V(t)$ have the impulsive components, $R_H^\infty(t)$ and $R_V^\infty(t)$, with the amplitudes of R_H^∞ and R_V^∞, respectively. Subtracting the terms R_H^∞ and R_V^∞ from $R_H(s)$ and $R_V(s)$ respectively gives the "reduced" reflection coefficients,

$$\bar{R}_H(s) = R_H(s) - R_H^\infty = \frac{2K_H}{1+K_H} \frac{\sqrt{s^{1-\alpha}+s_0} - \sqrt{s^{1-\alpha}+s_1}}{\sqrt{s^{1-\alpha}+s_0} + K_H\sqrt{s^{1-\alpha}+s_1}} \ , \tag{33}$$

and

$$\bar{R}_V(s) = R_V(s) - R_V^\infty = \frac{2K_V}{1+K_V} \frac{\sqrt{s^{1-\alpha}+s_0}\sqrt{s^{1-\alpha}+s_1} - (s^{1-\alpha}+s_2)}{\sqrt{s^{1-\alpha}+s_0}\sqrt{s^{1-\alpha}+s_1} + K_V(s^{1-\alpha}+s_2)} \ . \tag{34}$$

Both $\bar{R}_H(s)$ and $\bar{R}_V(s)$ satisfy the four conditions in Section 2, under which $f(t)$ can be approximated by $f_{ec}(t,\rho)$. It can be proved that, for $s = [\rho + j(n-0.5)\pi]/t$, both $\bar{R}_H(s)$ and $\bar{R}_V(s)$ also obey the two conditions a) and b) in Section 2, under which $f_{ec}^{lm}(t,\rho)$ can be used to approximate $f_{ec}(t,\rho)$ (Zeng, 2010). Hence, both reduced time domain reflection coefficients $\bar{R}_H(t)$ and $\bar{R}_V(t)$ can be calculated using Equation (7). The required time domain reflection coefficients $R_H(t)$ and $R_V(t)$ are obtained by adding $R_H^\infty(t)$ and $R_V^\infty(t)$ to $\bar{R}_H(t)$ and $\bar{R}_V(t)$, respectively.

Before applying this technique to waveform parameter estimation and material characterization, its correctness and effectiveness are verified by comparing the reduced transient reflection coefficients with those in (Rothwell, 2007). Several different cases are considered, each following the Debye model ($\alpha = 0$) with different values of the parameters ε_s, ε_∞ and τ. In the numerical trials, for each ρ value (ρ = 3, 6, 10 and 20), we set N = 15 (l = 9, m = 6), 20 (l = 14, m = 6), 39 (l = 20, m = 19), 59 (l = 29, m = 30), and 99 (l = 49, m = 50) and achieved almost the same results for $f_{ec}^{lm}(t,\rho)$, indicating that the truncation errors are small enough. In the following examples, ρ = 3 and N = 15 (l = 9, m = 6).

Figure 3 (a) illustrates the reduced reflection coefficients of water (at standard temperature and pressure) calculated using our technique, and compares them to the results in (Rothwell, 2007) with an excellent agreement. The reduced reflection coefficients do not
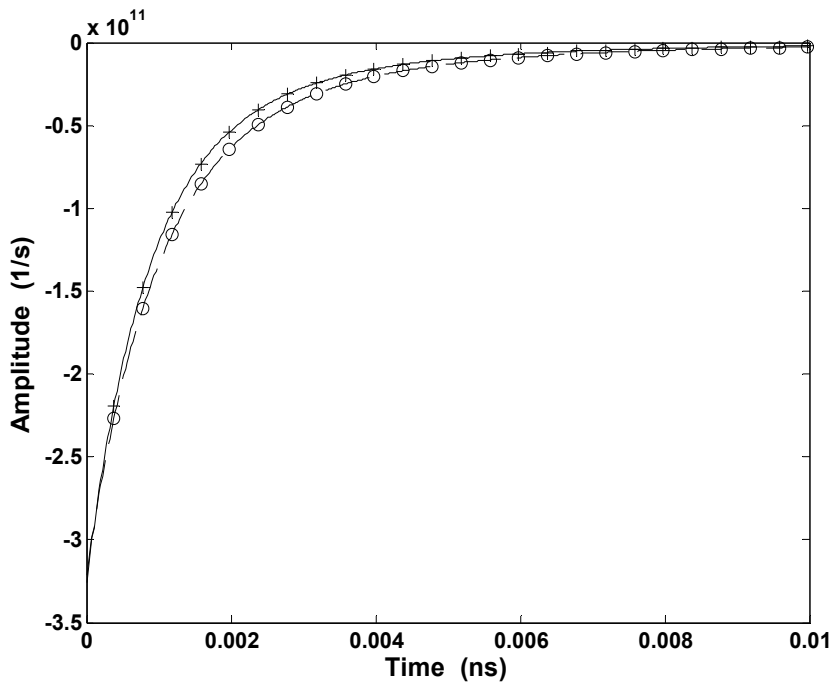
(a) Water, $\alpha = 0$, $\varepsilon_s = 78.3$, $\varepsilon_\infty = 5.0$, $\tau = 9.6 \times 10^{-12}$ s.
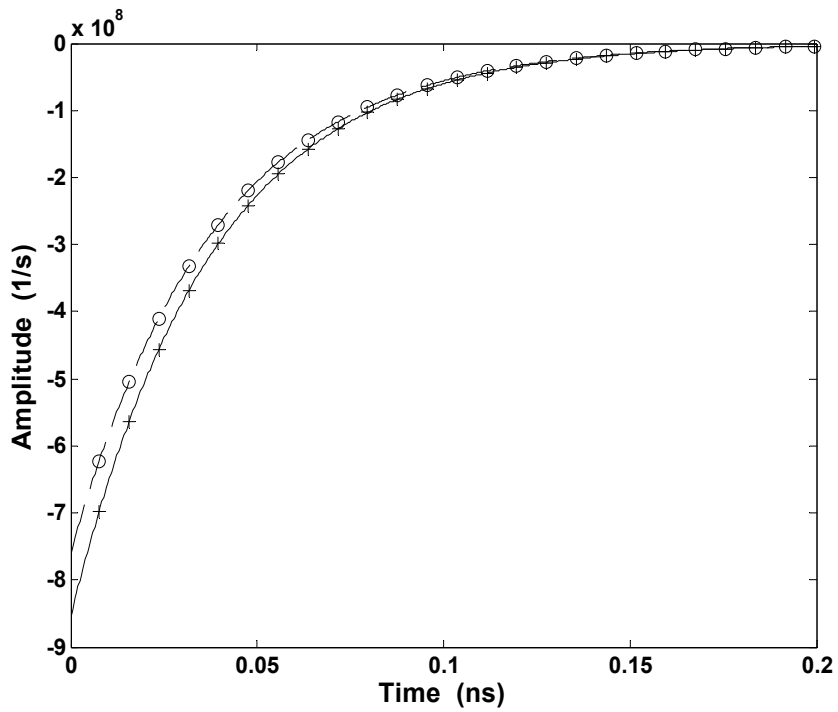
(b) Martian soil simulant, $\alpha = 0$, $\varepsilon_s = 3.57$, $\varepsilon_\infty = 3.12$, $\tau = 0.041 \times 10^{-9}$ s.
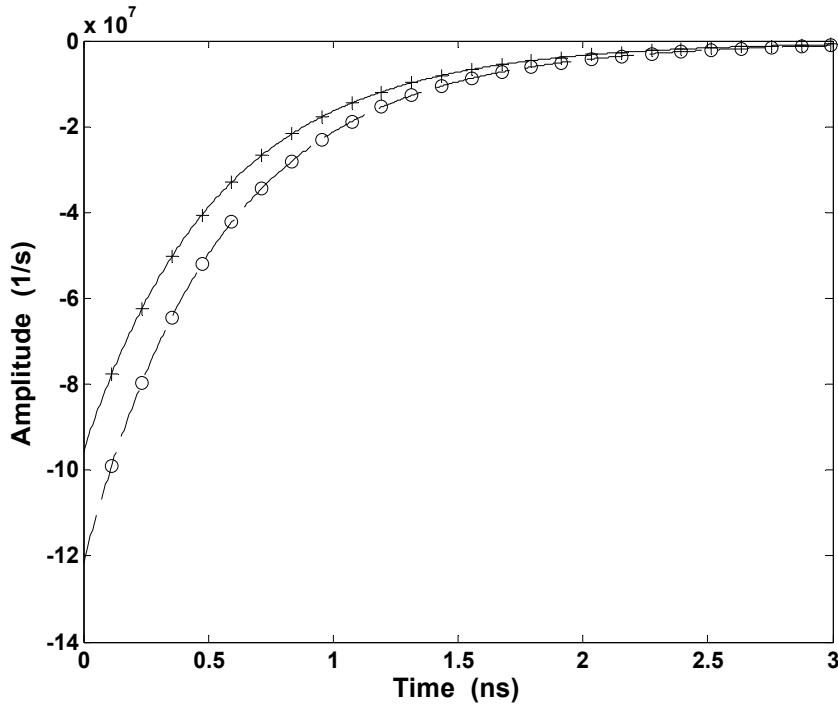
(c) Ceramic, $\alpha = 0$, $\varepsilon_s = 494$, $\varepsilon_\infty = 155$, $\tau = 1.39 \times 10^{-9}$ s.

Fig. 3. Time domain reduced reflection coefficients of Debye half space for $\theta = 30^0$. Solid line: Our results for horizontal polarization; Plus sign: Results for horizontal polarization in (Rothwell, 2007); Dashed line: Our results for vertical polarization; Circle: Results for vertical polarization in (Rothwell, 2007).

include any impulsive component with the amplitude of R_H^∞ or R_V^∞ . The large scale on the vertical axis may be disconcerting at first look, but it should be noted that these reflection coefficients will be convolved with incident pulses with durations on the order of nanoseconds.

Figure 3 (b) compares the reduced reflection coefficients of a Martian soil stimulant found using our technique to the results in (Rothwell, 2007). Our results agree with those in (Rothwell, 2007) very well. Since the static and optical permittivities for the soil are comparable, the relaxation effect is less dramatic than that for water while the durations of transient reflection coefficients are longer than that for water due to the longer relaxation time.

Figure 3 (c) shows the reduced reflection coefficients of a Lanthanum modified $PbTiO_3$ ferroelectric ceramic. There is an excellent agreement between our results and those in (Rothwell, 2007). The static and optical permittivities are much larger than those in the above two cases, but relaxation time is also quite large, making the durations of these reflection coefficients have the order of several nanoseconds.

Consider a Gaussian waveform incident upon a water half-space at $\theta = 30^0$. The incident field is horizontally polarized and has an amplitude of 1 V/m and a pulse width of 1 ps. The reflected waveform can be determined using the convolution,

$$E_H^r(t) = R_H(t) * E^i(t) = \overline{R}_H(t) * E^i(t) + R_H^\infty E^i(t), \tag{35}$$

where $\overline{R}_H(t)$ is shown in Figure 3 and R_H^∞ is given by (31). The reflected waveform is plotted in Figure 4, from which it is seen that the incident Gaussian waveform is maintained, but with a long tail contributed by the waveform of $\overline{R}_H(t)$ due to the relaxation effect.
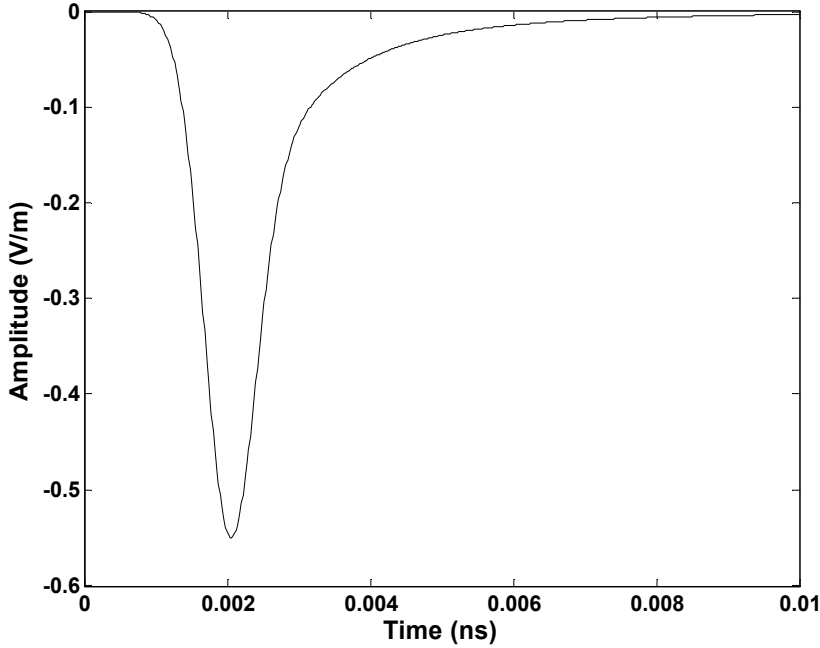
Fig. 4. Reflected waveform for a horizontally polarized Gaussian pulse incident on a water half space at $\theta = 30^0$.

4.2 Waveform parameter estimation and material characterization

Based on the above transient analysis, this technique can be utilized for the estimation of waveform parameters of reflected pulses. As an example, consider a mixture of water and ethanol with a volume fraction v_F. Here, $v_F = 0$ corresponds to pure ethanol while $v_F = 1$ corresponds to pure water. Bao et al. have shown the permittivity of this mixture is described quite well by the Debye model and have measured the Debye parameters for various volume fractions (Bao et al., 1996). The parameters can be approximated by the following expressions:

$$\varepsilon_\infty = -19.1\, v_F^2 + 18.5\, v_F + 4.8, \tag{36}$$

$$\varepsilon_s - \varepsilon_\infty = 53\, v_F + 22, \tag{37}$$

$$\tau = 0.15 \times 10^{-1.27\, v_F}\ \text{ns}. \tag{38}$$

For water the Cole–Cole parameter α is only 0.02, indicating that a Debye description is sufficient. However, not all polar materials have a permittivity that follows the Debye model

as closely as water. Some oil has a Cole–Cole parameter α up to 0.23 (Rothwell & Cloud, 2001). In this work, assuming that the permittivity of the mixture above is described by the Debye and Cole–Cole equations, waveform parameters estimation and material diagnosis are explored, respectively, and the corresponding results in two cases are compared with each other.

One of the most important waveform parameters is the correlation between two waveforms. It indicates the degree to which two waveforms resemble and is defined by

$$C(t) = \left(\frac{\int_0^\infty s_1(t') s_2(t+t') \, dt'}{s_m} \right)^2 , \tag{39}$$

$$s_m = \max\left(\int_0^\infty s_1^2(t') \, dt', \int_0^\infty s_2^2(t') \, dt' \right). \tag{40}$$

Let $s_1(t)$ and $s_2(t)$ be the incident and reflected waveforms, respectively, and consider the Guassian waveform in Section 4.1 incident upon a mixture half space. The maximum value $C_{\max}$ of $C(t)$ is plotted versus the volume fraction v_F for three values of Cole–Cole parameter α and three incident angles in Figure 5 (a), and versus α for two v_F values and three incident angles in Figure 5 (b). It is seen that $C_{\max}$ increases with the increase of v_F, α and θ. Assume that a mixture with $\alpha = 0$ and $v_F = 0.7$ is desired. Whether this fraction has been achieved could be determined by examining the maximum correlation between two reflected or reduced reflected waveforms for the desired volume fraction and for the mixture to be determined Let $s_1(t)$ and $s_2(t)$ be two reflected waveforms for the desired volume fraction and for the mixture, respectively, and also let $s_1(t)$ and $s_2(t)$ be two reduced reflected waveforms for the desired volume fraction and for the mixture, respectively. $C_{\max} = 1$ indicates that the mixture has the desired volume fraction, while $C_{\max} < 1$ means that the mixture has a different volume fraction from the desired one. Using a reduced reflected waveform obtained from $\bar{E}_H^r(t) = \bar{R}_H(t) * E^i(t)$ leads to a much higher detection accuracy than using a reflected waveform calculated by $E_H^r(t) = R_H(t) * E^i(t)$. Figure 6 (a) shows that it is not easy to detect the desired mixture because $C_{\max}$ calculated using reflected waveforms does not decrease quickly in the proximity of the peak. Moreover, increasing the incident angle will significantly deteriorate the detection accuracy. The peak nearly cannot be detected for larger incident angles. In contrast, Figure 6 (b) shows that the desired mixture can be easily identified since $C_{\max}$ calculated using reduced reflected waveforms decreases sharply on two sides of the peak. Furthermore, increasing the incident angle even up to 89^0 (almost grazing incidence) will not deteriorate the detection accuracy.

Assume that a mixture with $\alpha = 0.1495$ and $v_F = 0.6$ is desired. With the range of $C_{\max}$, Figure 7 (a) indicates that it is almost impossible to detect the desired mixture because $C_{\max}$ calculated using reflected waveforms does not significantly decrease on two sides of the peak. In addition, increasing the incident angle will further deteriorate the detection accuracy. Figure 7 (b) demonstrates that the desired mixture can be identified since $C_{\max}$ calculated using reduced reflected waveforms decreases on two sides of the peak. Meanwhile, increasing the incident angle even up to 89^0 will not deteriorate the detection accuracy basically. Comparing Figure 7 (b) with Figure 6 (b), it is seen that detection of a

mixture with a desired α value is much more difficult than detection of a mixture with a desired v_F value.

(a)

(b)
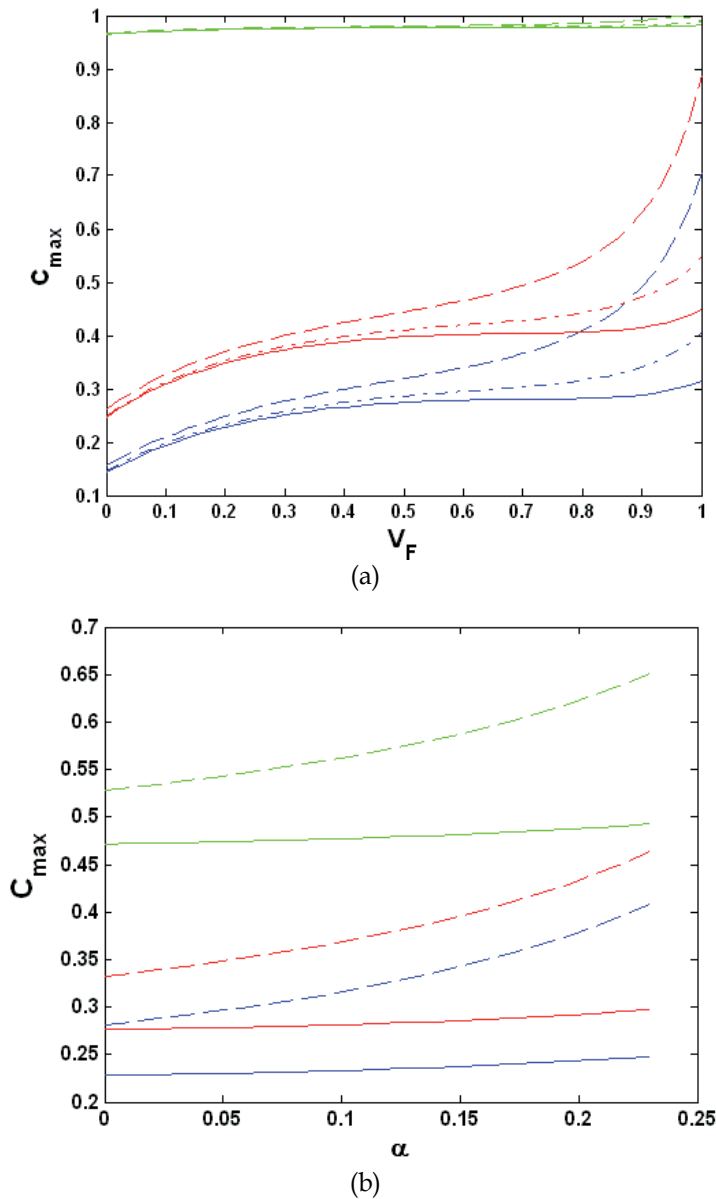
Fig. 5. Maximum correlation between the incident and reflected waveforms for a mixture irradiated by a horizontally polarized Gaussian pulse.

a.   versus v_F for $\alpha = 0$ (solid lines), 0.1 (dash-dot lines) and 0.23 (dashed lines), and for $\theta = 0^0$ (blue lines), 45^0 (red lines) and 89^0 (green lines).

versus α ($0 \le \alpha \le 0.23$) for $v_F = 0.2$ (solid lines) and 0.8 (dashed lines), and for $\theta = 0^0$ (blue lines), 30^0 (red lines) and 60^0 (green lines).
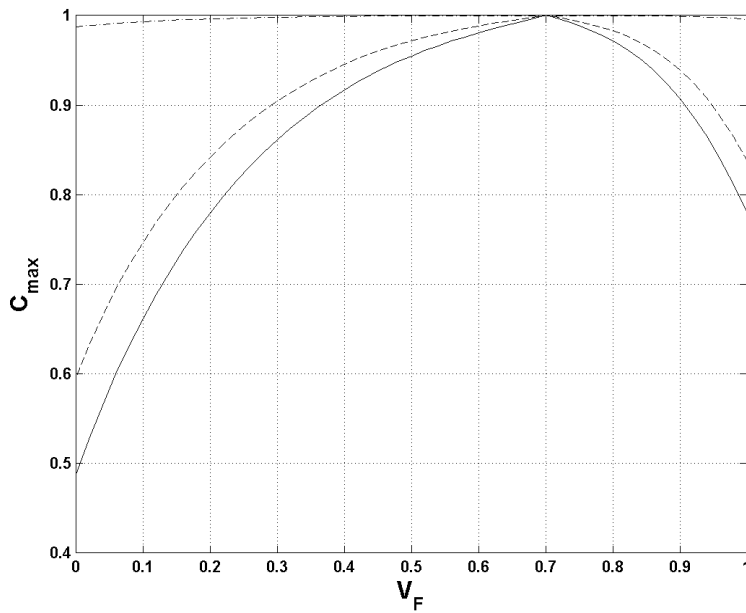
(a)
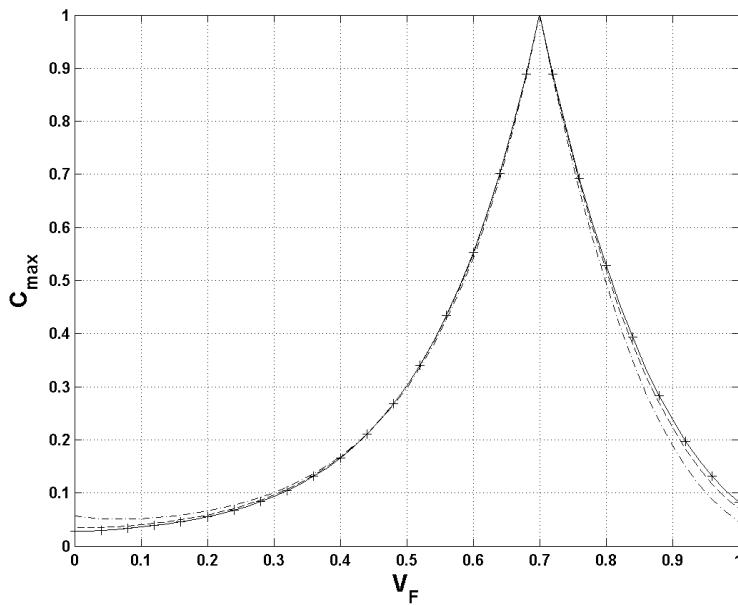
(b)

Fig. 6. Maximum correlation between two reflected waveforms (a) and between two reduced reflected waveforms (b) for the desired volume fraction and for the mixture to be determined, with a horizontally polarized Gaussian pulse incident on the mixture at $\theta = 0^0$ (solid lines), 45^0 (dashed lines) and 89^0 (dash-dot lines), when $\alpha = 0$ and v_F varying. Plus sign: Corresponding results in (Rothwell, 2007).

5. Conclusion

In general, two approaches are employed to analyze transient reflection and propagation. One is to approximate an arbitrary incident signal with a finite number of attenuating exponential signals using Prony's method and to apply numerical inversion of Laplace

(a)

(b)
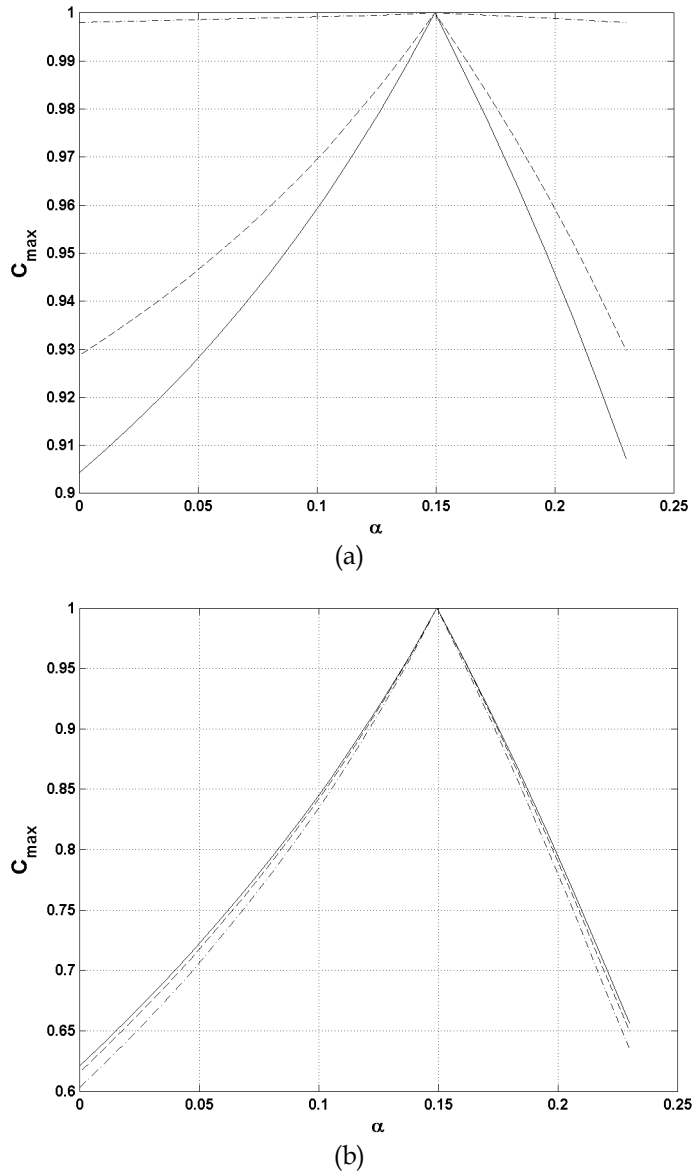
Fig. 7. Maximum correlation between two reflected waveforms (a) or between two reduced reflected waveforms (b) for the desired volume fraction and for the mixture to be determined, with a horizontally polarized Gaussian pulse incident on the mixture at $\theta = 0^0$ (solid lines), 45^0 (dashed lines) and 89^0 (green lines), when $v_F = 6$ and α varying.

transform (NILT) to the final image function, which is the product of the frequency domain reflection or tramsimission coefficient and the image function of the approximating incident signal. The accuracy of this approach is limited by the numerical errors from both NILT and the decomposition of the original incident signal into of a series of finite attenuating exponential signals (Zeng & Delisle, 2006). As shown in sections 4.1 and 4.2, another approach is to use NILT for determinating the transient reflection or transmission coefficient and to convolve the incident signal with the time domain reflection or transmission coefficient. The accuracy of this approach depends on both NILT and numerical convolution, which normally incurs smaller errors than decomposing an arbitrary signal into a series of finite attenuating exponential signals. Section 4.1 presents time domain reflection coefficients for both TE- and TM-polarized plane waves incident on a Lorentz medium half space using NILT. Three possible cases are discussed, each of which is determined by a different relationship between the damping coefficient, oscillation and plasma frequencies. The result is an exponentially damped waveform that oscillates based on the conditions of each case.

In section 4.2, the properties of a half space are described in frequency domain by the Debye and Cole–Cole models, respectively, which are commonly used to capture the relaxation-based dispersive properties. First, transient reflected pulses are analyzed and waveform parameters are estimated. Then, based on the estimation, the relationships between the waveform parameters of reflected pulses and the properties of dispersive material as well as incident angles are discussed. Meanwhile, the results obtained with the Debye model are compared to those obtained with the Cole–Cole model. The application of these results to material characterization and diagnosis is explored. It is shown that using the reduced time domain reflection coefficients often brings more physical insights and leads to an efficient algorithm and a robust scheme for dispersive material diagnosis. There is excellent agreement between our results and those in (Rothwell, 2007), which validates the correctness and effectiveness of this work.

6. References

Bao, J.-Z.; Swicord, M. & Dawes, C. (1996). Microwave dielectric characterization of binary mixtures of water, methanol and ethanol. *J. Chem. Phys.*, Vol. 104, 1996, pp. 4441-4450.

Cole, K. & Cole, R. (1941). Dispersion and absorption in dielectrics. *J. Chemical Phys.*, Vol. 9, No. 4, Apr. 1941, pp.341–351.

Cossmann, S.; Rothwell, E. & Kempel, L. (2006). Transient reflection of TE-polarized plane waves from a Lorentz-medium half-space. *J. Opt. Soc. Am., Series A*, Vol. 23, No. 9, September 2006, pp. 2320-2323.

Cossmann, S.; Rothwell, E. & Kempel, L. (2007). Transient reflection of TM-polarized plane waves from a Lorentz-medium half-space. *J. Opt. Soc. Am., Series A*, Vol. 24, No. 3, March 2007, pp. 882-887.

Debye, P. (1945). *Polar Molecules*. Dover Publications, New York, USA.

Gray, K. (1980). The reflected impulse response of a Lorentz medium. *Proc. IEEE*, Vol. 68, 1980, pp. 408-409.

Guerra J. & Eiras, J. (2004) High frequency dielectric relaxation in Lanthanum modified $PbTiO_3$ ferroelectric ceramics. *Material Res.*, Vol. 7, 2004, pp. 325–328.

Hosono, T. (1981). Numerical inversion of Laplace transform and some applications to wave optics. *Radio Sci.,* Vol. 16, No. 6, Nov.–Dec. 1981, pp. 1015–1019.

Jones, S.; Mace, R. & Or, D. (2005). A time domain reflectometry coaxial cell for manipulation and monitoring of water content and electrical conductivity in variably saturated porous media. *Vadose Zone J.*, Vol. 4, 2005, pp. 977-982.

Kosmas, P.; Rappaport, C. & Bishop, E. (2004). Modeling with the FDTD method for microwave breast cancer detection. *IEEE Trans. Microwave Theory Tech.*, Vol. 52, No. 8, Suppl. 2, August 2004, pp. 1890-1897.

Ogunsola, A.; Reggiani, U. & Sandrolini, L. (2006). Modelling shielding properties of concrete. *Proc. 17th International Symposium on Electromagnetic Compatibility*, Zurich, Switzerland, Feb. 27–March 3, 2006, pp. 34–37.

Ong, K.; Dreschel, W. & Grimes, C. (2003). Detection of human respiration using square-wave modulated electromagnetic impulses. *Microwave Optical Technol. Lett.*, Vol. 36, 2003, pp. 339- 349.

Oswald, B.; Erni, D.; Benedickter, H.; Bächtold, W. & Flühler, H. (1998). Dielectric properties of natural materials. *Proc. IEEE Antennas and Propagation Society International Symposium*, Vol. 4, 1998, pp. 2002-2005.

Oughstun, K. & Sherman, G. (1988). Propagation of electromagnetic pulses in a linear dispersive medium with aborption (the Lorentz medium). *J. Opt. Soc. Am.*, *Series B,* Vol. 5, 1988, pp. 817-849.

Oughstun, K. & Sherman, G. (1989). Uniform asymptotic description of electromagnetic pulse propagation in a linear dispersive medium with aborption (the Lorentz medium). *J. Opt. Soc. Am.*, *Series A,* Vol. 6, 1989, pp. 1394-1420.

Oughstun, K. & Sherman, G. (1990). Uniform asymptotic description of ultrashort rectangular optical pulse propagation in a linear, causally dispersive medium, *Phys. Rev. A*, Vol. 41, 1990, pp. 6090-6113.

Piesiewicz, R. & et al. (2005). Terahertz characterisation of building materials. *Electron. Lett.*, Vol. 41, 2005, pp. 1002-1004.

Rothwell, E. & Cloud, M. (2001). *Electromagnetics,* Chapter 4, pp. 189-348, CRC Press, Boca Raton, FL, USA.

Rothwell, E. (2007). Plane-wave impulse response of a Debye half space. *Electromagnetics*, Vol. 27, No. 4, May 2007, pp. 195–206.

Sommerfeld, A. (1914). Über die Fortpflanzung des Lichtes in dispergierenden Medien. *Ann. Phys.*, Vol. 44, 1914, pp. 177-202.

Stanic, B.; Milanovic, D. & Cvetic, J. (1991). Pulse reflection from a lossy Lorentz medium half-space (TM polarization), *J. Phys. D: Appl. Phys.*, Vol. 24, 1991, pp. 1245-1249.

Zeng, Q. (2010). *Transient Analysis of Electromagnetic Waves Based on Numerical Inversion of Laplace Transform,* Ph.D. dissertation, University of Ottawa, Ottawa, Ontario, Canada, May 2010.

Zeng, Q. & Delisle, G. (2006). Characterization for ultra wideband pulses transmitting through a lossy dielectric slab. *2006 IEEE International Conference on Ultra-Wideband (ICUWB 2006)*, Waltham, Massachusetts, USA, September 24-27, 2006, pp.213-218.

Zhang, J. & et al. (2003). Reconstruction of the parameters of Debye and Lorentzian dispersive media using a genetic algorithm. *Proc. IEEE Electromagnetic Compatibility International Symposium*, Atlanta, Georgia, USA, June 21–26, 2003, pp. 898–903.

Part 4

UWB Antennas and Arrays

Planar Monopole UWB Antennas with Cuts at the Edges and Parasitic Loops

Karlo Costa and Victor Dmitriev
Federal University of Para
Brazil

1. Introduction

In ultra wideband (UWB) systems, extremely short pulses are used. These pulses can provide data with high bit rate. They usually occupy ultra wide band in the frequency domain. The spectrum of frequencies reserved for these systems is 3.1-10.6GHz. Examples of UWB signal applications are communications, radar and imaging systems (Aiello & Batra, 2006; Schantz, 2005).

Planar antennas are widely used in UWB systems because of their low cost of fabrication, low size, and simple structure. Some examples of conventional planar monopoles antennas with rectangular, triangular and circular geometries are presented in (Chen & Chia, 2006). One of the deficiencies of the rectangular monopole is its relatively small matching bandwidth which is about 80% (Ammann, 1999). This value is smaller than the full bandwidth of the UWB systems, which is 110% (the frequency range is 3.1-10.6 GHz).

Some techniques can be used to enlarge the bandwidth of planar monopole antenna. For this purpose, modifications of the ground plane and a T aperture in the geometry of the antenna were made (Hong et al., 2006). In (Valderas et al., 2006), a monopole planar antenna with a folded patch was used, and antennas with elliptical geometries were analyzed in (Abbosh & Bialkowski, 2008).

To improve the impedance bandwidth, a technique of combining microstrip and linear antennas with parasitic loops is used. This technique is based on minimizing the reactive energy stored in the near zone of the radiator. This is achieved because the two elements possess opposite average reactive energy.

In this work, we analyze four planar UWB antennas with cuts at the edges and parasitic loops. The antennas investigated are: a rectangular monopole with two loops, a rectangular monopole with four loops, a rectangular monopole with cuts at the edges, and a rectangular monopole with cuts at the edges and two parasitic loops. To enlarge the matching bandwidth, the dimensions of the antennas were optimized with cut-and try method. For the numerical analysis, some Method of Moments (MoM) codes were developed (Harrington, 1968). For comparison, some calculations were made using the software IE3D.

2. Geometries of the antennas

Fig. 1 shows the geometries of the proposed antennas. In this figure, W is the width of the antenna and $H+L$ is the height of the patch with respect to the ground plane. The parameters

is the width of the feeding transmission line which connects the planar monopole with the inner conductor of the coaxial cable. The dimensions of the rectangular cuts at the edges of the antennas shown in Figs. 1c-d are w_1 - w_6. The dimensions of the loops are W_1 e L_1 and their widths are r_1 e r_2. The distance between the loops and the monopole is d. Notice that the geometries of these antennas are symmetrical with respect to the plane $x=W/2$.

3. Mathematical model

3.1 Integral equation for the electric field

The mathematical model of the antenna on Fig. 1 was realized by the integral equation for electromagnetic potentials in the frequency domain with the temporal dependence $\exp(j\omega t)$ (Balanis, 2005):

$$\bar{E}_r = -j\omega\mu_0 \iint_S \bar{J} \frac{e^{-jkR}}{4\pi R} ds' + \nabla\left[\frac{1}{j\omega\varepsilon_0} \iint_S \nabla\cdot\bar{J} \frac{e^{-jkR}}{4\pi R} ds'\right] \tag{1}$$

where $\bar{E}_r$ (V/m) is the electric field radiated by a current density $\bar{J}$ (A/m) on the conductors of the antenna. This current will appear when the antenna is fed by a coaxial cable connected at the point $x=L/2$ (Fig. 1). The parameter S represents the superficial area of the antenna, j is imaginary unit, $k=\omega(\mu_0\varepsilon_0)^{1/2}$, ω is the angular frequency (rad/s), μ_0 and ε_0 are the magnetic permeability and electrical permittivity, respectively, of the free space and R is the distance between one point on S and an observation point near the antenna.

3.2 Numerical solution by MoM

The numerical MoM solution of (1) presented in this section is explained by using example of the rectangular monopole antenna (Fig. 2). With minor modifications in the geometry, this model is used to analyze the proposed UWB antenna (Fig. 1).

The problem to be solved here is to find the current distribution $\bar{J}$ in (1) when a given external electric field $\bar{E}_i$ is falling on the antenna. This incident field represents the source of the problem. The conductors of the antenna are considered lossless. In this case, the boundary condition on S is $(\bar{E}_r + \bar{E}_i)\cdot\bar{a}_t = 0$, where $\bar{a}_t$ is an tangential unity vector on S. To solve this problem by MoM (Harrington, 1968), the following approximations are firstly established:

$$\bar{J} = \sum_{n=1}^{N_x-1}\sum_{m=1}^{N_z} J_x^{n,m} P_{J_x}^{n,m}\bar{a}_x + \sum_{n=1}^{N_x}\sum_{m=1}^{N_z-1} J_z^{n,m} P_{J_z}^{n,m}\bar{a}_z \tag{2}$$

$$\nabla\cdot\bar{J} = -\frac{1}{j\omega}\sum_{n=1}^{N_x}\sum_{m=1}^{N_z}\left[\frac{J_x^{n,m}-J_x^{n-1,m}}{\Delta x} + \frac{J_z^{n,m}-J_z^{n,m-1}}{\Delta z}\right]P_\sigma^{n,m} \tag{3}$$

where

$$P_{J_x}^{n,m} = \begin{cases} 1 &, & x_{n-1/2} < x < x_{n+1/2} \text{ and } z_{m-1} < z < z_m \\ 0 &, & \text{otherwise} \end{cases} \tag{4}$$

$$P_{J_z}^{n,m} = \begin{cases} 1 & , \quad z_{m-1/2} < z < z_{m+1/2} \text{ and } x_{n-1} < x < x_n \\ 0 & , \quad \text{otherwise} \end{cases} \tag{5}$$

$$P_{\sigma}^{n,m} = \begin{cases} 1 & , \quad x_{n-1} < x < x_n \text{ and } z_{m-1} < z < z_m \\ 0 & , \quad \text{otherwise} \end{cases} \tag{6}$$
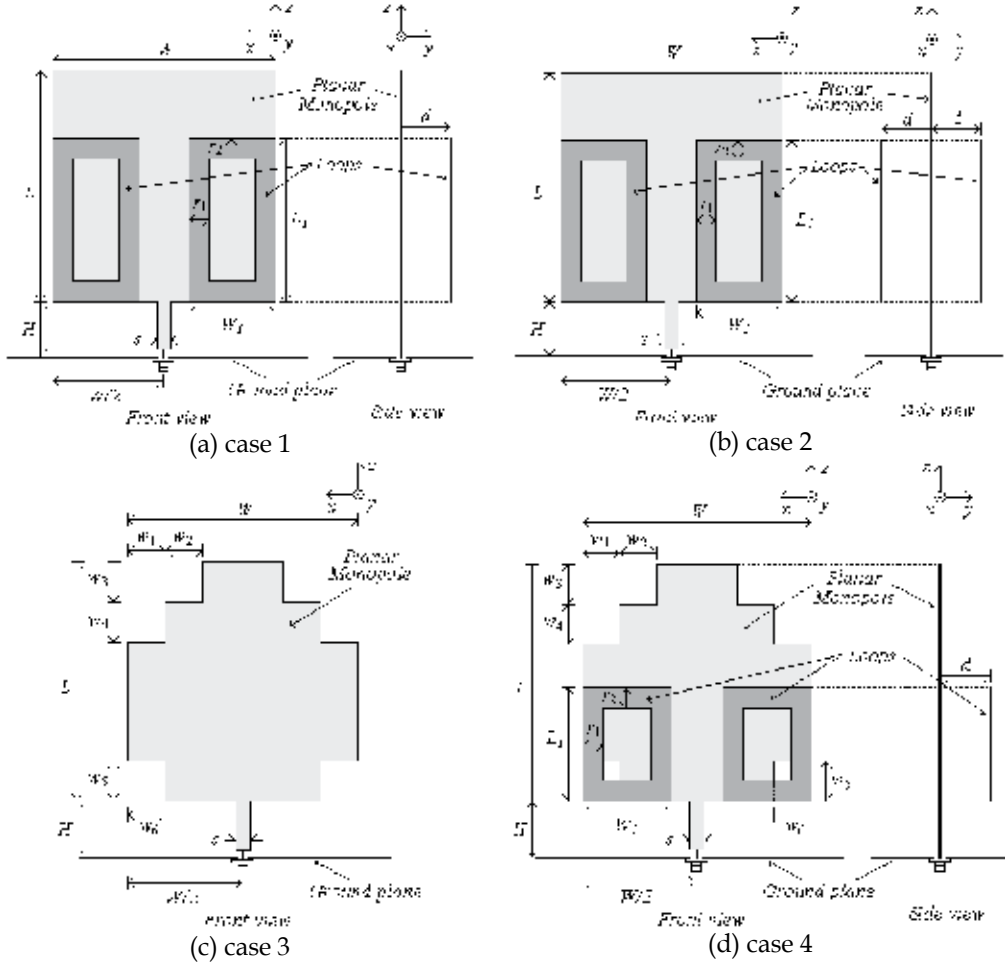
Fig. 1. Geometries of the four proposed UWB planar monopoles with cuts at the edges and parasitic loops. (a) case 1: a rectangular monopole with two loops, (b) case 2: a rectangular monopole with four loops, (c) case 3: a rectangular monopole with cuts at the edges, and (d) case 4: a rectangular monopole with cuts at the edges and two parasitic loops.

Fig. 3 shows geometrical details used in each current element of index I inside the grid in Fig. 2. In Fig. 3, the direction of P_I^- to P_I^+ is parallel to an axis of the coordinate system ($+x$ or $+z$). Inserting (2) and (3) into (1), using the boundary condition and calculating the integral in one segment Δl_J, which connects the points P_J^- and P_J^+, the following equation can be obtained:

$$\int_{\Delta l_J} \overline{E}_i \cdot \overline{dl} = \sum_{I=1}^{N_t} J_I \left[j\omega\mu_0 \Phi \overline{\Delta l_I} \cdot \overline{\Delta l_J} + \frac{1}{j\omega\varepsilon_0} \left(\Phi^{++} - \Phi^{-+} - \Phi^{+-} + \Phi^{--} \right) \right] \tag{7}$$
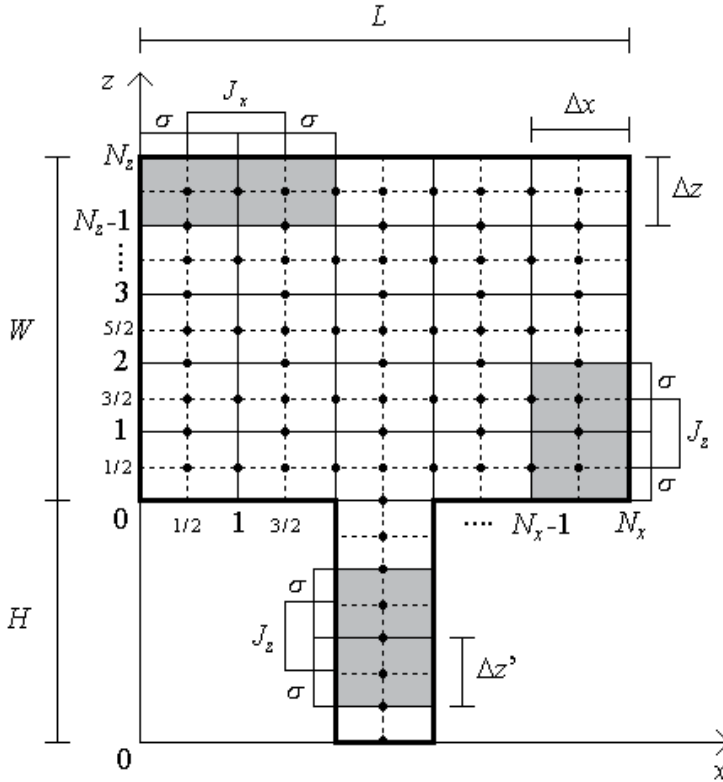
Fig. 2. Details of the MoM discretization for the conventional rectangular antenna.
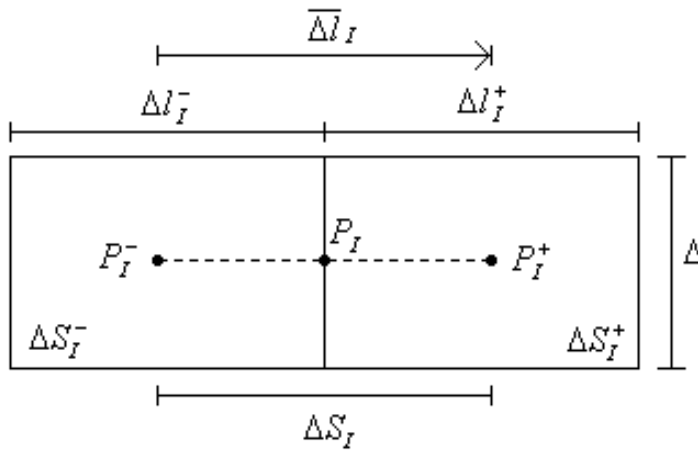
Fig. 3. Geometry of one generic current element of the grid in Fig. 2.

where $N_t=(N_x-1)\times(N_z)+(N_z-1)\times(N_x)+N_h$ is the total number of unknowns J_I, and N_h is the number of segments on the height H. The current density J_I can be $J_x^{n,m}$ or $J_z^{n,m}$ in (2) and (3). The functions Φ are the mutual interactions between the elements I and J. These functions are calculated by the following expressions:

$$\Phi = \frac{1}{\Delta l_I} \iint_{\Delta S_I} \frac{e^{-jkR_{IJ}}}{4\pi R_{IJ}} ds' \Bigg|^{P_J} \tag{8}$$

$$\Phi^{++} = \frac{1}{\Delta l_I^+} \iint_{\Delta S_I^+} \frac{e^{-jkR_{IJ}^{++}}}{4\pi R_{IJ}^{++}} ds' \Bigg|^{P_J^+} \tag{9}$$

$$\Phi^{+-} = \frac{1}{\Delta l_I^+} \iint_{\Delta S_I^+} \frac{e^{-jkR_{IJ}^{+-}}}{4\pi R_{IJ}^{+-}} ds' \Bigg|^{P_J^-} \tag{10}$$

$$\Phi^{-+} = \frac{1}{\Delta l_I^-} \iint_{\Delta S_I^-} \frac{e^{-jkR_{IJ}^{-+}}}{4\pi R_{IJ}^{-+}} ds' \Bigg|^{P_J^+} \tag{11}$$

$$\Phi^{--} = \frac{1}{\Delta l_I^-} \iint_{\Delta S_I^-} \frac{e^{-jkR_{IJ}^{--}}}{4\pi R_{IJ}^{--}} ds' \Bigg|^{P_J^-} \tag{12}$$

The variables R in (8)-(12) are the mutual distances between the points (+ or −) of the current element I to the points (+ or −) of the current element J. If $kR<<1$, the following approximations can be used:

$$\Phi = \frac{1}{4\pi\Delta l}\left[\Delta l \times \ln\frac{(\sqrt{\Delta l^2 + \Delta^2} + \Delta)}{(\sqrt{\Delta l^2 + \Delta^2} - \Delta)} + \Delta \times \ln\frac{(\sqrt{\Delta l^2 + \Delta^2} + \Delta l)}{(\sqrt{\Delta l^2 + \Delta^2} - \Delta l)} - jk\Delta l \times \Delta \right] \quad \text{if } I = J \tag{13}$$

$$\Phi = \frac{1}{4\pi\Delta l}\frac{e^{-jkR}}{R}(\Delta l \times \Delta) \quad \text{if } I \neq J \tag{14}$$

The left side of (7) means a voltage ΔV applied between the points P_J^- and P_J^+. When (7) is desenvolved for $J=1, 2, ..., N_t$, a linear system of order N_t is obtained. For a given excitation field $\overline{E}_i$, the solutions of this system produce the total current density of the antenna $\overline{J}$.

The ground plane is modeled by infinite and perfect conductor, therefore one can use the image theory. The coaxial cable is modelled by a delta gap $\Delta V=1V$ between the ground plane and the antenna. This voltage is applied in the first segment of the dimension H of the antenna, near the ground plane (Fig. 2). With this feeding, the voltages of the other segments are null.

The rectangular loops were described by striplines with one-dimensional current density. This current possesses component J_x for the segments along the direction x and J_z for the segments along the direction z. For thin loops, it is a good approximation. The total number of current elements of the loops is N_e, and the total number of current elements of the antenna is $N_t=(N_x-1)\times(N_z)+(N_z-1)\times(N_x)+N_h+N_e$.

4. Numerical results

Four MoM codes based on the model presented in previous section were developed in this work. With these computational programs, several simulations were made. Some of the geometrical parameters such as (w_i, i=1,2,...6), W_1, L_1, r_1, r_2 and d, were varying, and other dimensions of the antennas such as L=18, W=25, H=1.25 and s=2 were fixed (all dimensions are given in millimeters). From the results of these simulations, it was observed that the dimensions of the cuts and the loops which give better input matching results are presented in Table 1. In this table, all the dimensions are in millimeters, and the fractional bandwidth of each antenna is also presented.

	W_1	L_1	r_1	r_2	d	w_1	w_2	w_3	w_4	w_5	w_6	$B(\%)$
Case 1	8	17	2	2	5	-	-	-	-	-	-	91
Case 2	8	16	2	2	6	-	-	-	-	-	-	95
Case 3	-	-	-	-	-	3	3	4	4	4	3	>110
Case 4	8	14	2	2	6	3	3	4	4	4	3	>110

Table 1. Dimensions and fractional bandwidth (B) of the monopoles presented in Fig. 1. All the antennas have L=18, W=25, H=1.25 and s=2 (all dimensions are in millimetres).

In all simulations with the developed codes, the discretization with square cells $\Delta z=\Delta x$=1mm was used. In the simulations done with the software IE3D, a convergence criteria of $\lambda/20$ in F=15GHz, where λ is the wavelength and F is the operation frequency was used.

4.1 Input impedance and reflection coefficient

Figs. 4-5 show the results of the input impedance ($Z_{in}=R+jX$) and the reflection coefficient of the antennas given in Fig. 1 with the dimensions given in Table 1. The reflection coefficient was calculated by the expression $\Gamma=20\log(\text{abs}((Z_{in}-Z_0)/(Z_{in}+Z_0)))$, where Z_0=50Ω is the characteristic impedance of the feeding transmission line. For comparison, we presented in these figures the results of the conventional rectangular planar monopole with the same dimensions L=18, W=25, H=1.25 and s=2 (all dimensions are in millimetres). These results were obtained with the developed MoM codes and the software IE3D. One can note a good agreement between them.

We see in Fig. 4 the effects of the loops on the resonant response of the input impedance of the antennas. In the cases 1 and 2 of Figs. 4(a) and (b) the resonance of the rectangular patch is near the frequency F=3.5GHz and the resonance of the loops is near the frequency F=6GHz, where for the case 2 (Fig. 4(b)) this resonance is more intense because in this case there are more loops (four) than the case 1 (two). The antennas that have cuts at the edges in the patch (Figs. 4(c) and (d)), the resonances of the patch and loops are similar to the other cases 1 and 2, but the resonance of the patch with cuts is a little bit greater.
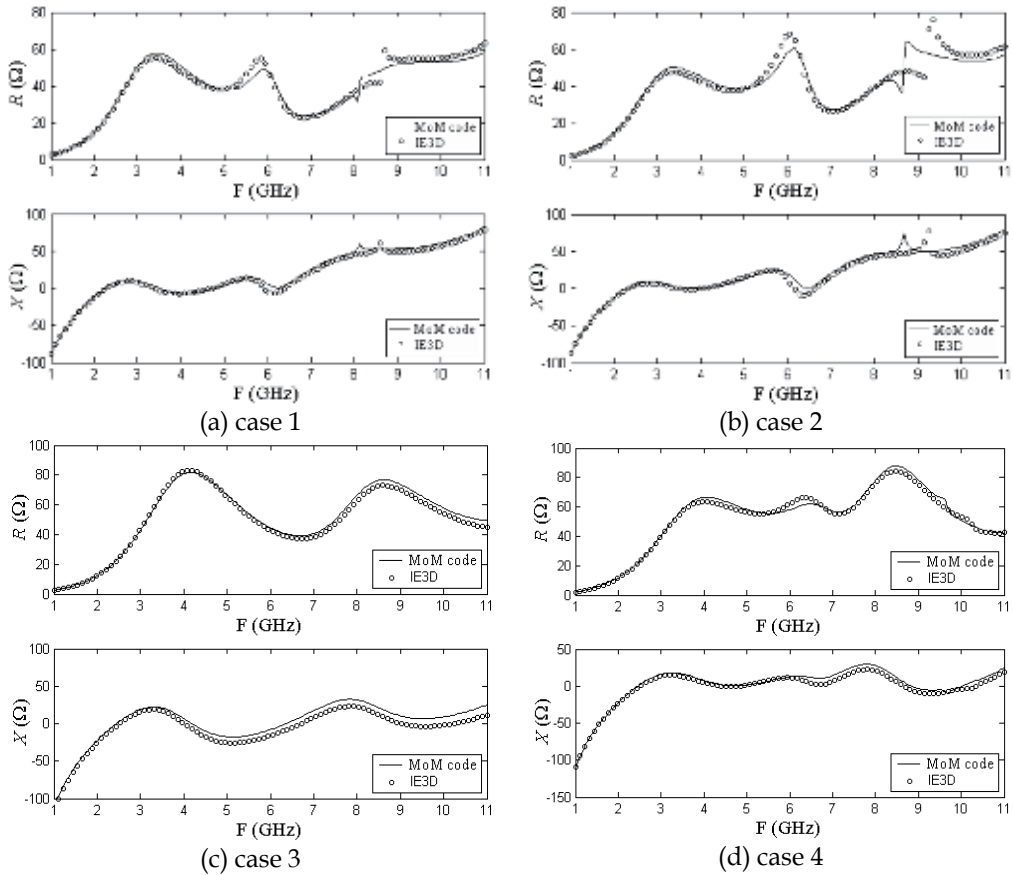
Fig. 4. Input impedance of the four proposed UWB planar monopoles with cuts at the edges and parasitic loops. (a) case 1. (b) case 2. (c) case 3. (d) case 4.

The proximity of the patch and loops resonances in all these antennas produce a coupling of resonances, where the real part of the input impedance R varies less with frequency around the value of 50Ω, and the imaginary part of the input impedance X is closer to zero. This produces a better input matching of these antennas with a transmission line with characteristic impedance 50Ω.

From Fig. 5, one can observe that the conventional rectangular monopole antenna has a bandwidth near the 80%, which does not cover the whole frequencies of UWB systems. The antenna of case 1 possesses impedance matching ($\Gamma<-10$dB) in the bandwidth of 91%, and for the antenna of case 2, the bandwidth is 95%. The antennas of cases 3 and 4 with cuts (with and without loops) possess impedance matching in the range of frequencies of UWB systems (3.1-10.6 GHz). But only the antenna of case 4 with cuts at the edges and two loops has the reflection coefficient $\Gamma<-15$dB in the frequency range 3-7GHz (Fig. 5(d)). Thus, the antenna of case possesses a better impedance matching.

4.2 Current distribution

This section presents the modal current distributions of the proposed antennas in some frequencies, calculated with the developed codes. Fig. 6 shows the distributions of the

superficial currents calculated with the developed MoM codes on the patch of the antenna case 2 (Fig. 1(b)) with four loops at the frequency F=4.7GHz. This figure presents the rectangular components J_x and J_z. Fig. 6(c) showing the current distribution using small arrows. We observe that the mode of this antenna along the axis z is similar to that of the rectangular monopole with $W=\lambda/4$.

(a) case 1

(b) case 2
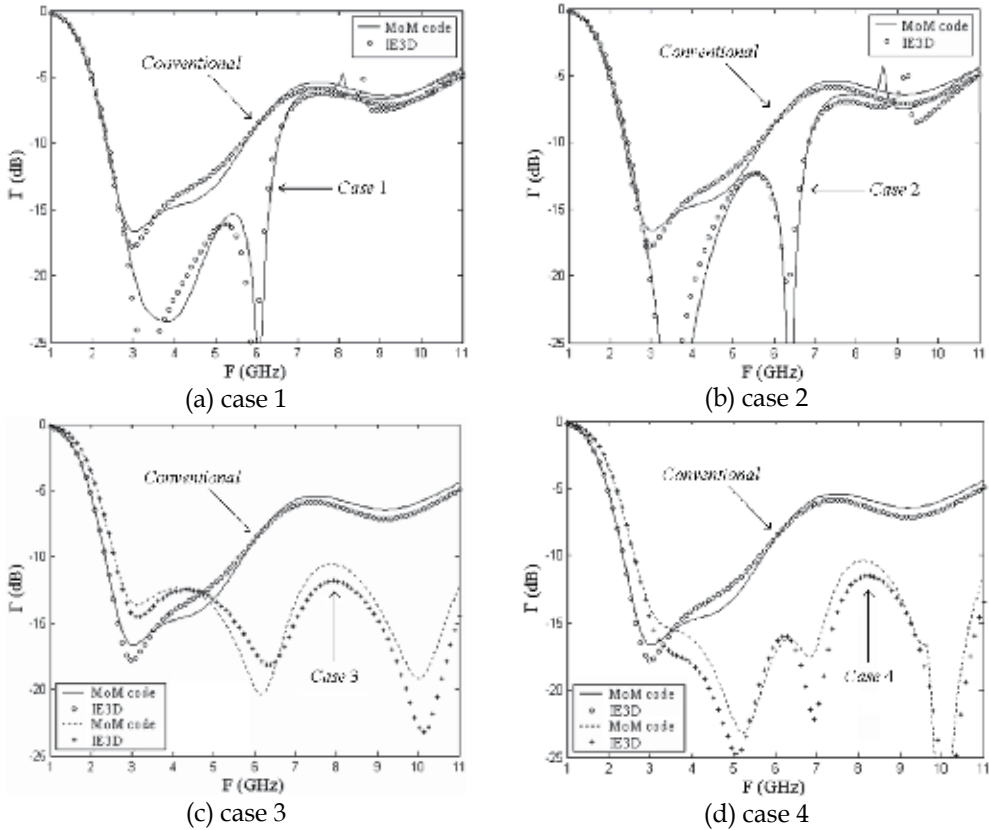
(c) case 3

(d) case 4

Fig. 5. Reflection coefficient of the proposed UWB planar monopoles with cuts at the edges and parasitic loops. (a) case 1. (b) case 2. (c) case 3. (d) case 4.

Fig. 7 presents examples of current distribution on the surface of the antenna in case 4 with cuts and two loops at the frequencies F=4 and 8GHz obtained by the MoM code. These current distributions are similar to that of the resonant modes with $W=\lambda/4$ and $\lambda/2$, which are characteristics of the rectangular planar monopole antenna.

4.3 Radiation diagrams

Figs. 8 and 9 present the radiation diagrams of the antennas for cases 2 and 3 with two and four loops respectively. These diagrams were calculated in the middle frequency of the band. The results showed were calculated with the MoM codes and with the software IE3D. A good agreement of the results is observed.

The vertical diagrams at the planes xz and yz are presented in these figures. The diagrams at the horizontal plane are almost omnidirectional in all the frequency range of the band. We

observe that only the antenna with two loops (Fig. 8) shows asymmetrical characteristics at the plane yz. This is due to the asymmetry of the antenna geometry in this plane.

(a) J_x (b) J_z

(c) J
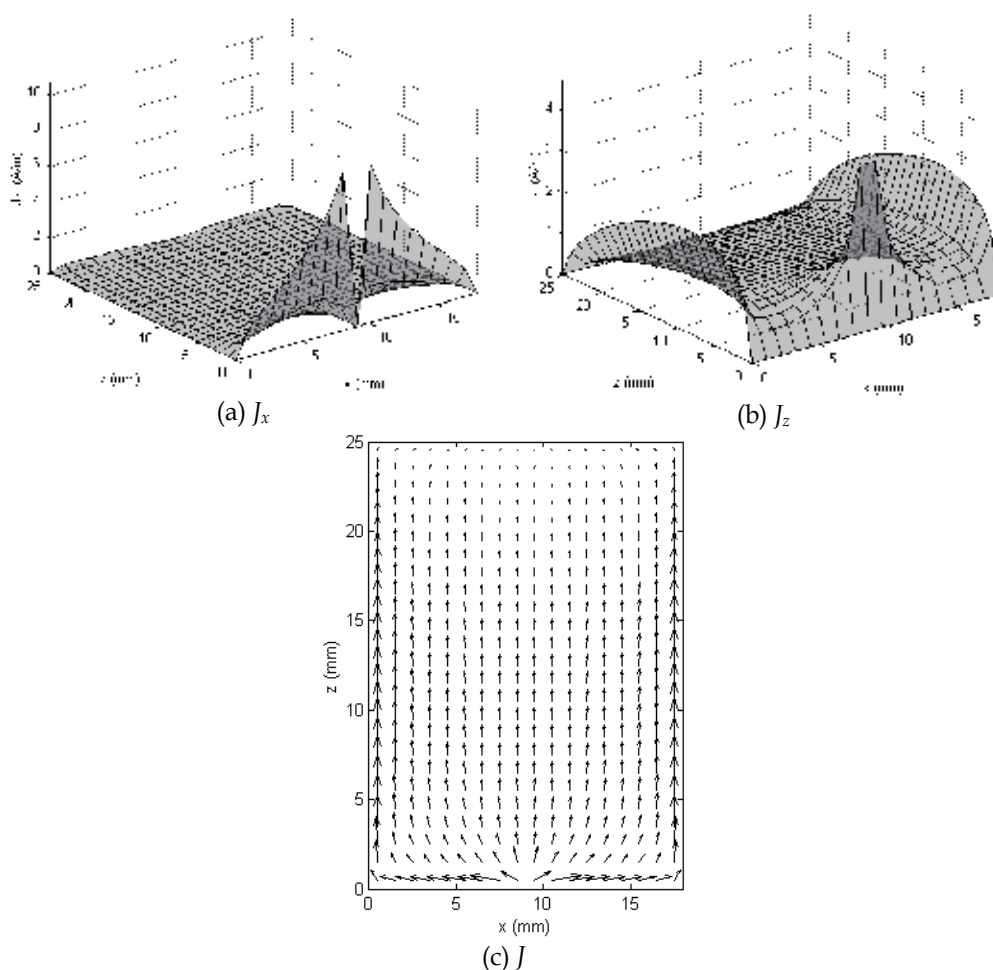
Fig. 6. Current distribution of the antenna for case 2 with four loops at the frequency F=4.7GHz . (a) J_x. (b) J_z. (c) total current J in arrows form.

Fig. 10 shows the radiation diagrams of the antenna case 4 with two loops for the frequencies F=2.5, 5.0, 7.5 and 10.0 GHz. The results were calculated by the MoM code and by the software IE3D. One can see a good agreement between them. These figures present the radiation diagrams in the planes xz and yz. The horizontal diagrams in the plane xy are omnidirectional in the inferior band (3-5GHz), but they have a small directionality in the upper band (5-10GHz). These results are explained by asymmetry of the antenna's geometry in this plane, because there are two loops only in front of the antenna in the plane $y=d$ (Fig. 1(d)). With two loops placed symmetrically at the other side of the antenna in the plane $y=-d$, the diagram could be symmetrical for all frequencies of the band 3-10GHz.

In the vertical plane, the variation of the diagrams with the frequency is a function of the current distribution in the patch of the antenna, where for low frequency the distribution is

near the resonant mode of $W=\lambda/4$, and for higher frequency the distribution is near the resonant mode of $W=\lambda/2$.
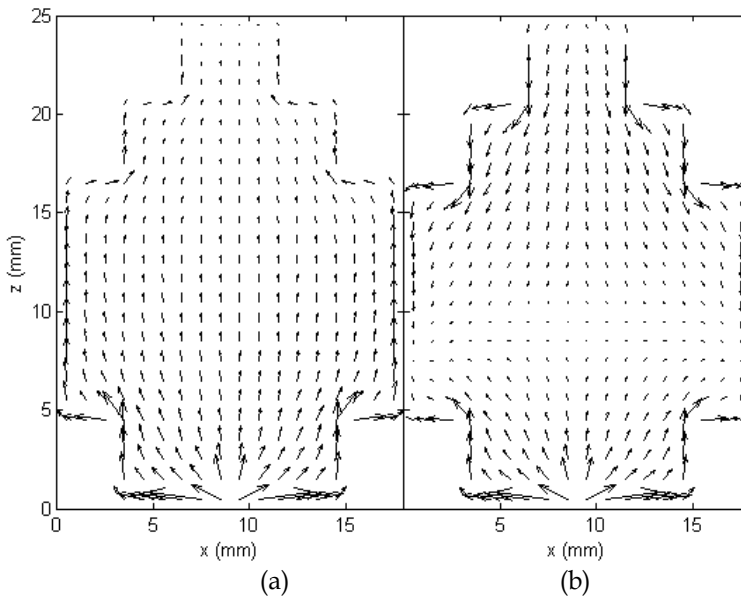
Fig. 7. Current distribution of the antenna in case 4. (a) F=4GHz. (b) F=8 GHz.
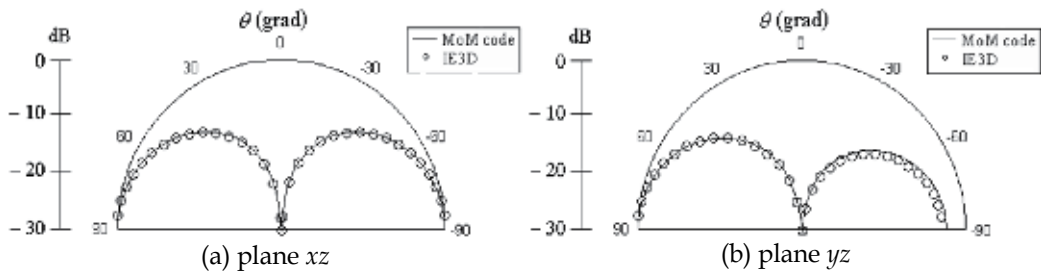
Fig. 8. Radiation diagrams of the antenna case 1 with two loops at the frequency F=4.5GHz. (a) Plane xz. (b) Plane yz.
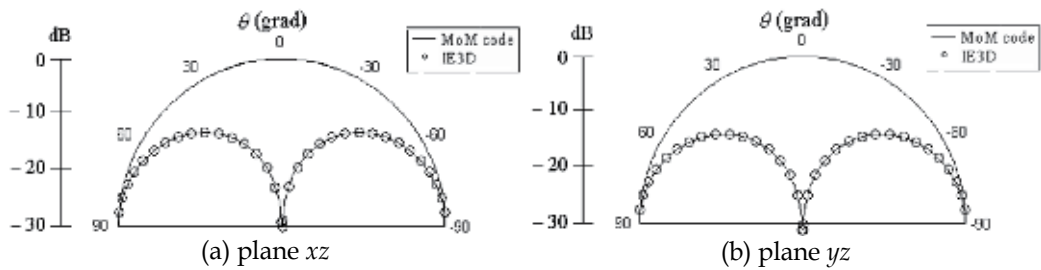
Fig. 9. Radiation diagrams of the antenna case 2 with four loops at the frequency F=4.7GHz. (a) Plane xz. (b) Plane yz.
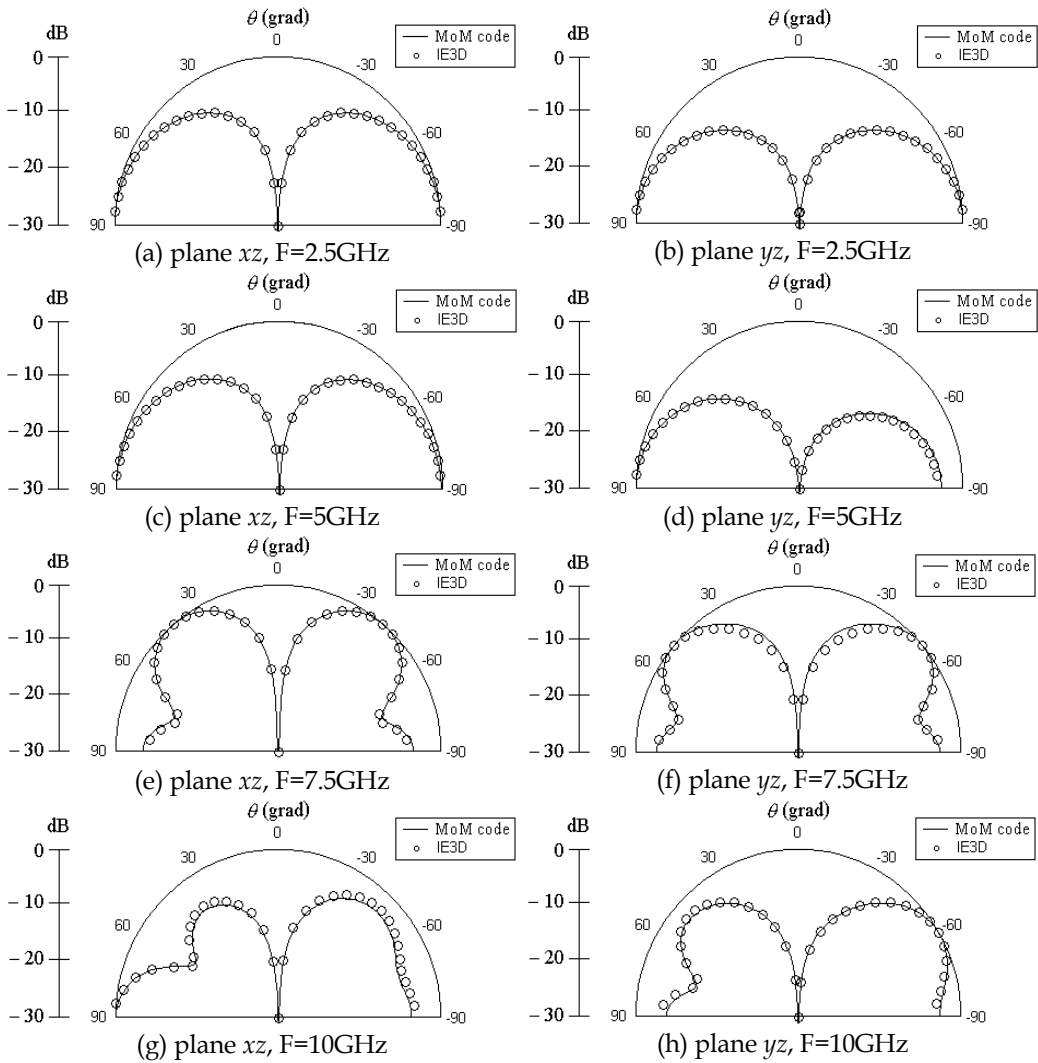
Fig. 10. Radiation diagrams at vertical planes of the antenna case 4. (a) Plane *xz*, F=2.5GHz.
(b) Plane *yz*, F=2.5GHz. (c) Plane *xz*, F=5GHz. (d) Plane *yz*, F=5GHz. (e) Plane *xz*, F=7.5GHz.
(f) Plane *yz*, F=7.5GHz. (g) Plane *xz*, F=10GHz. (h) Plane *yz*, F=10GHz.

5. Conclusion

We presented in this work four antennas with good input matching and radiation diagrams for applications in UWB systems. The antennas are planar monopoles with cuts at the edges and parasitic loops. The analysis of these antennas was made by the developed MoM codes and by the software IE3D. The results obtained by these programs have a good agreement. From the presented results, one can note that the loops improve the input matching, and the cuts at the edges enlarge the bandwidth. The effect of the loops is to introduce a new resonance near the patch's resonance, so that the coupling of these resonances enlarges the input matching of the antenna. The antenna that presented the best input matching was the

one with cuts at the edges and two loops, where the bandwidth covers all the range of frequencies of UWB systems (3.1-10.6 GHz). We also observed that the radiation diagrams of these antennas are a function of the frequency and the antenna's geometry. One proposal for future work is the analysis of antennas with cuts at the edges and four parasitic loops placed symmetrically with respect to the plane *xy* in order to improve the radiation diagram of the antenna.

6. Acknowledgment

7. References

Abbosh, A. & Bialkowski, M. (2008). Design of ultrawideband planar monopole antennas of circular and elliptical shape, *IEEE Trans. Ant. Propag.*, Vol. 56, pp. 17–23.

Aiello, R. & Batra, A. (2006). *Ultra Wideband Systems: Technologies and Applications*, Elsevier, Oxford.

Ammann, M. J. (1999). Square planar monopole antenna, *Proceedings of 1999 IEE Nat. Conf. on Antennas and Propagation*, pp. 37–40.

Balanis, C. A. (2005). *Antenna Theory: Analysis and Design*, JohnWiley, New York.

Chen, Z. N. & Chia, Y. W. M. (2006). *Broadband Planar Antennas: Design and Applications*, J. W. Sons, New York.

Costa, K. Q. & Dmitriev, V. (2006). Combination of electric and magnetic dipoles with single-element feeding for broadband applications, *Microw. Opt. Techn. Lett.*, Vol. 48, No.1, pp. 8–12.

Costa, K. Q., Dmitriev, V., Nascimento, D. C. & da S. Lacava, J. C. (2007). Broadband L-probe fed patch antenna combined with passive loop elements, *IEEE Ant. and Wireless Propag. Lett.*, Vol. 6, pp. 100–102.

Harrington, R. F. (1968). *Field Computation by Moment Method, Macmillan*, New York.

Hong, C. Y., Ling, C. W., Tarn, I. Y. & Chung, S. J. (2006). Design of a planar ultrawideband antenna with a new band-notch structure, *IEEE Trans. Ant. Propag.*, Vol. 55, pp. 3391–3397.

Schantz, H. (2005). *The Art and Science of Ultrawideband Antennas*, Artech House, Boston.

Valderas, D., Legarda, J., GuitiÃl'rres, I. & Sancho, J. I. (2006). Design of uwb folded-plate monopole antennas based on tlm, *IEEE Trans. Ant. Propag.*, Vol. 54, pp. 1676–1687.

Characteristics of an Ultra-Wideband (UWB) Butterfly-Shaped Monopole Antenna

Qiubo Ye[1], Zhi Ning Chen[2] and Terence S. P. See[2]
[1]*Communications Research Centre*
[2]*Institute for Infocomm Research*
[1]*Canada*
[2]*Singapore*

1. Introduction

UWB is a promising wireless technology that can operate at very low power emission levels while communicating high data rates over short distances. It has attracted much attention as a means of expanding capacity from the already heavily utilized wireless bands. The Federal Communications Commission (FCC) has allocated a bandwidth of 7.5 GHz between 3.1 GHz to 10.6 GHz for commercial UWB communication systems.

In this emerging technology, the antenna design is a challenge. Like conventional antenna design, the return loss has to remain higher than 10 dB over the frequency range of operation. For a UWB antenna, the radiation properties should be reasonably satisfactory over the bandwidth. For example, omni-directional radiation patterns are required for indoor and vehicular applications. For a more complete pattern analysis, the total field which includes the co- and cross-polarizations of the radiation should be taken into account. The time domain performance such as the group delay and impulse response should also be examined (Chen et al., 2004).

Recently, several monopoles have been proposed for various UWB applications. These antennas make use of different structures to meet the requirements of return loss and radiation pattern. A monopole comprised of a square planar structure positioned perpendicular to the ground plane has been proposed, where bevelling or a shorting post is used to optimize and achieve a broad impedance bandwidth (Ammann & Chen, 2003). A bi-arm rolled monopole (Chen, 2005) which is constructed by rolling a planar monopole has shown that it is capable of achieving broadband and omni-directional radiation characteristics within the UWB band. The UWB antenna in (Behdad & Sarabandi, 2005) consists of half of a coupled sectorial loop above the ground plane. The optimized design is able to achieve an 8.5 : 1 frequency bandwidth for the voltage standing wave ratio (VSWR) < 2.2. Its radiation patterns are relatively consistent within the frequency band. In another design (Liang et al., 2005), a printed circular disc monopole is fed by microstrip line. Its impedance bandwidth covers the UWB frequency band and the radiation patterns are nearly omni-directional. The antenna geometry in (Qiu et al., 2006) is a circular notched ring with an attached element inside the hole. This antenna has band-notched characteristics, which meet the input impedance requirement of the UWB band while avoiding interference

within the 5.15–5.875 GHz bands occupied by existing wireless systems. A half-bowtie radiating element with a staircase-shape and a modified ground plane has been proposed (Cho et al., 2006). It has a very wide impedance bandwidth and the wireless local area network (WLAN) band is notched in the vicinity of 5 GHz. The time domain performance of these monopoles has been investigated by simulation, measurement or both.

The antenna to be presented in this chapter consists of a butterfly-shaped monopole above a ground plane. The butterfly-shaped radiator comprises two circular or elliptical wings which are connected to the two edges of a conducting plate. The wings may make different angles with the ground plane. This antenna is designed to offer a 10-dB return loss across the entire UWB bandwidth. The radiation patterns and cross-polarization performance will be investigated by simulation and validated by measurement. In addition, the group delay is examined, and the transmitted and received signals are compared with two identical antennas placed at different angles relative to each other at a far-field separation.

This chapter is organized as follows. Section 2 describes the antenna configuration and design. A parametric study of the effect of the angle between the wings of the antenna and ground plane on the return loss $|S_{11}|$ is highlighted. Section 3 presents and analyzes the simulated and measured return losses and radiation patterns in detail. Section 4 examines the effect of the size of the ground plane on the antenna performance in terms of the return loss and radiation patterns. In Section 5, a two-antenna system is constructed to investigate the group delay as well as the characteristics of the transmitted and received signals. Finally, Section 6 concludes the chapter and points out possible future research directions in this area.

2. Antenna configuration and design

The proposed antenna is comprised of two perfectly electrically conducting (PEC) plates that are connected to the two edges of a rectangular PEC plate which is horizontal to the ground plane, as shown in Figure 1. The configuration mimics the shape of a butterfly. In general, the two PEC plates – two wings of the butterfly – can be circular, elliptical, or any shapes for impedance matching purpose. The antenna is implemented at a height h above the ground plane. In order to achieve the good impedance matching and desired radiation patterns, the angle α between the wing and the z-axis can be varied. The feed point of the antenna is located at its rectangular plate by a coaxial probe through a SubMiniature version A (SMA) connector.

In this chapter, the design with elliptical wings has been chosen and the effect of the angle α on the return loss is investigated. The antenna design starts with a conventional elliptical vertical monopole and an identical element is added for optimization. A conducting base is used to connect the two wings and feed cable. The optimized dimensions of the antenna are determined by simulation and shown as follows: The major axis of the elliptical wings $2b$ = 28.8 mm, the minor axis $2a$ = 22.8 mm, w = 3 mm, h = 2 mm, l = 12 mm, and d = 5 mm. Since the wavelength at 3 GHz (close to the lower edge operating frequency of 3.1 GHz) is 100 mm, the sizes of the major and minor axes of the elliptical wings are about a quarter of the wavelength.

Using Mentor Fidelity based on the FDTD method with α = 0°, 15°, 30°, and 45°, the simulated return losses are displayed in Figure 2. It can be observed that when α = 0°, 15°,
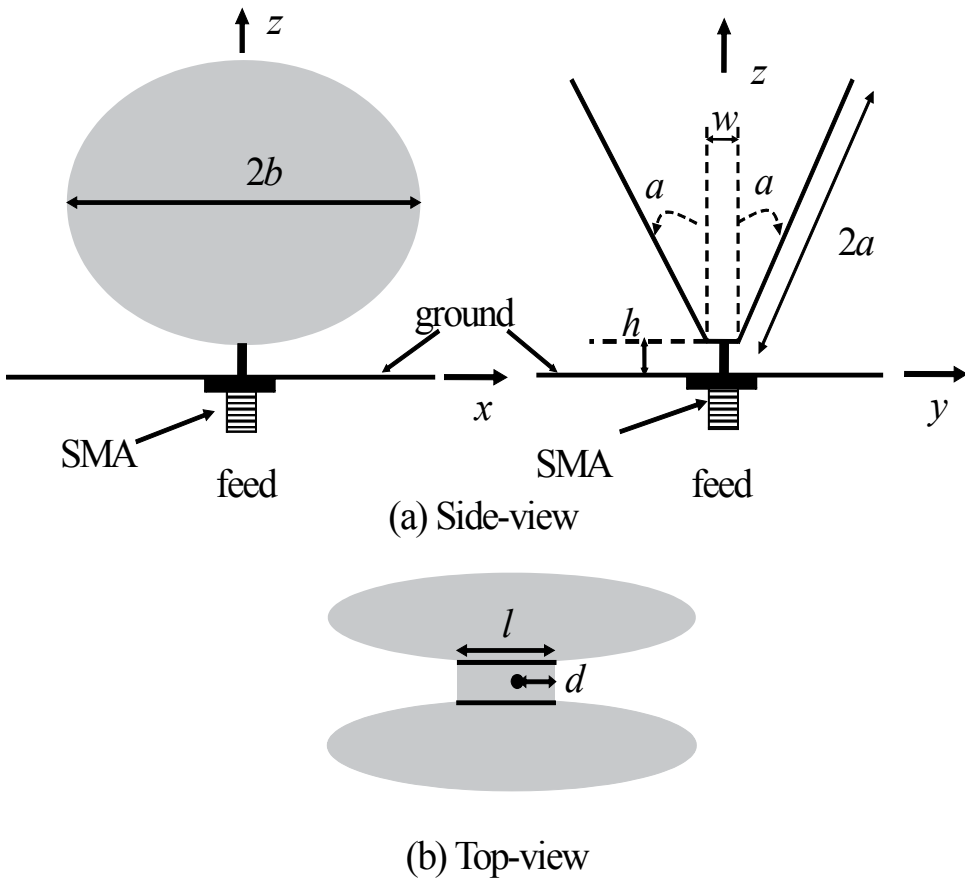
Fig. 1. Geometry of the butterfly-shaped antenna: (a) side-view; (b) top-view.

and 30°, the return loss $|S_{11}|$ is higher than 10 dB across the UWB band. The return loss bandwidth can be made much wider when $\alpha = 15°$ and 30° but the antenna height is lower as compared to the case when $\alpha = 0°$. When $\alpha = 45°$, the return loss $|S_{11}|$ is smaller than 10 dB between 3–4 GHz and 5–6 GHz. It can be concluded that the return loss will not be able to satisfy the UWB requirements when $\alpha > 45°$. Therefore, it can be seen that the EM coupling between the two wings greatly affects the impedance matching of the antenna. With α greater than 45°, the wings get closer to the ground plane and the return loss will deteriorate because of the shorting effect by the ground plane. Compared to a conventional disc monopole, the antenna has one more degree of freedom for impedance matching. Since α can be varied over a certain range, the antenna can be designed with a lower profile in the vertical direction.

3. Analysis and discussion for return loss and radiation patterns

As a design example, the elliptical wings of the butterfly-shaped antenna are chosen to be orthogonal to the ground plane, i.e. $\alpha = 0°$ for ease of fabrication. The dimensions of the

antenna remain unchanged. This antenna was fabricated and verified by measurement. The first part of this section compares the simulated and measured return loss of the antenna. The second part provides the co- and cross-polarized radiation patterns at the two principal planes (*x-z* and *y-z*). The radiation patterns are displayed at three frequencies, 3, 7, and 10 GHz. For comparison, the simulated radiation patterns when $\alpha = 45°$ are added. The simulated co-polarized patterns of the antenna when $\alpha = 0°$ and $\alpha = 45°$ in the *x-y* plane at 3, 7, and 10 GHz are also shown. From the results, it can be concluded that the radiation patterns from 3 GHz to 10 GHz are generally stable and the radiation patterns are omni-directional in the azimuth (horizontal) plane.
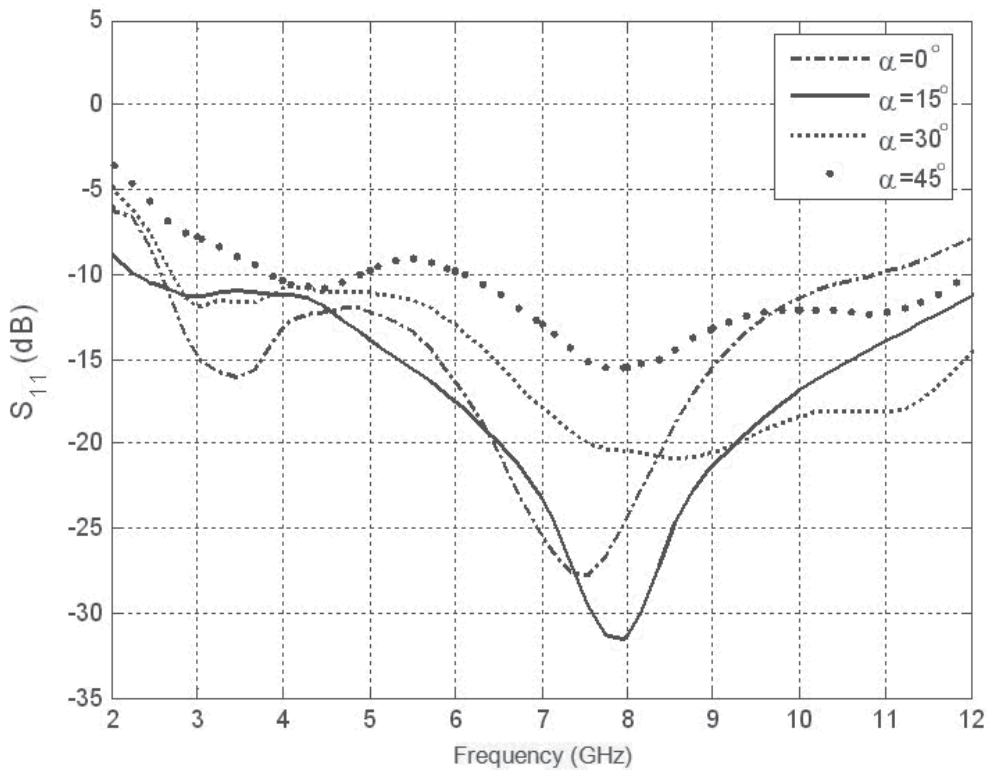
Fig. 2. Simulated return losses of the butterfly-shaped antenna for different angle α.

3.1 Return loss

The simulated and measured return losses $|S_{11}|$ are compared in Figure 3. The simulated return loss $|S_{11}|$ has a frequency range above 10 dB from 2.6–10.6 GHz, which covers the entire UWB band. On the other hand, the measured $|S_{11}|$ has a well-matched frequency range from 2.6–9.3 GHz. The slight discrepancy between the simulated and measured results at the higher frequency range is caused by the fabrication tolerance in that the antenna surfaces are not entirely flat and the two wings are not parallel at $\alpha = 0°$. This illustrates that the impedance matching is sensitive to the angle α.
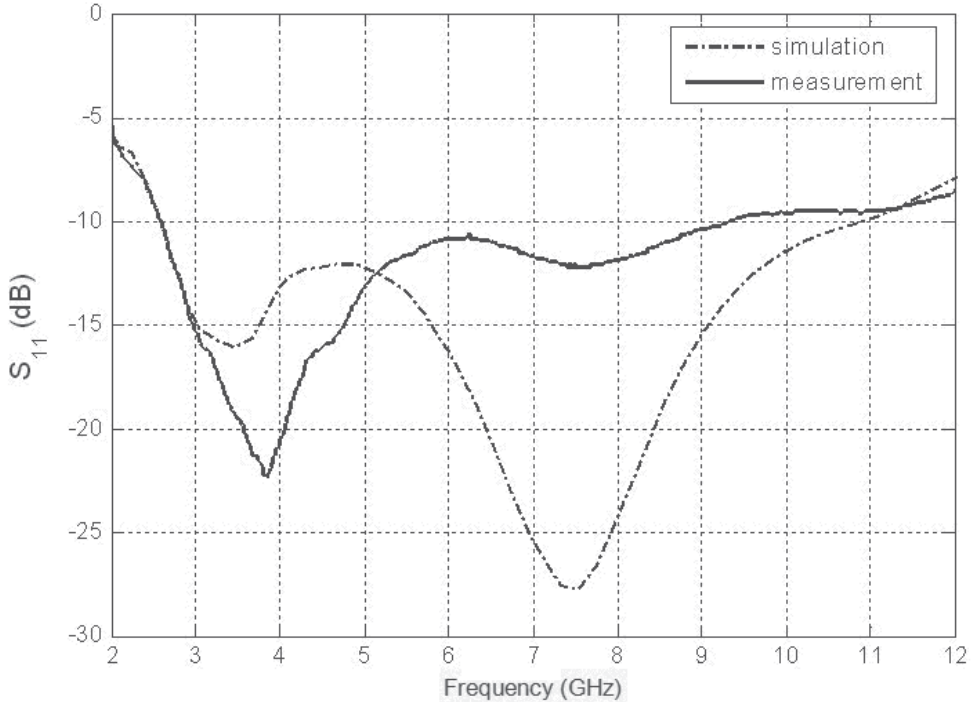
Fig. 3. Simulated and measured return losses.

3.2 Radiation patterns

Figures 4–6 show the co- and cross-polarized radiation patterns in the *x-z* plane at 3, 7, and 10 GHz, respectively. In the case when $\alpha = 0°$, both simulation and measurement results are displayed, and the simulated patterns when $\alpha = 45°$ are also given for comparison. It can be seen that the highest gain is around 5 dBi for the three frequencies. The ripples in the measured co-polarized radiation patterns are caused by the RF cable under the finite-size ground plane. Generally, good agreement between the simulated and measured co-polarized radiation patterns at the three frequencies has been achieved. The simulated cross-polarized radiation is typically below -40 dBi and the measured results are generally between -40 dBi and -15 dBi. This discrepancy is acceptable considering the difference in simulation and measurement setup. In the simulation, the SMA connector of the coaxial cable is not taken into account. Furthermore, it is difficult to get accurate data for levels below -30 dBi in the measurement. The simulated co-polarized patterns when $\alpha = 45°$ agree quite well with those when $\alpha = 0°$. Also, it can be observed that the gain is quite constant around 5 dBi for the three frequencies when $|\theta| = 50°$.
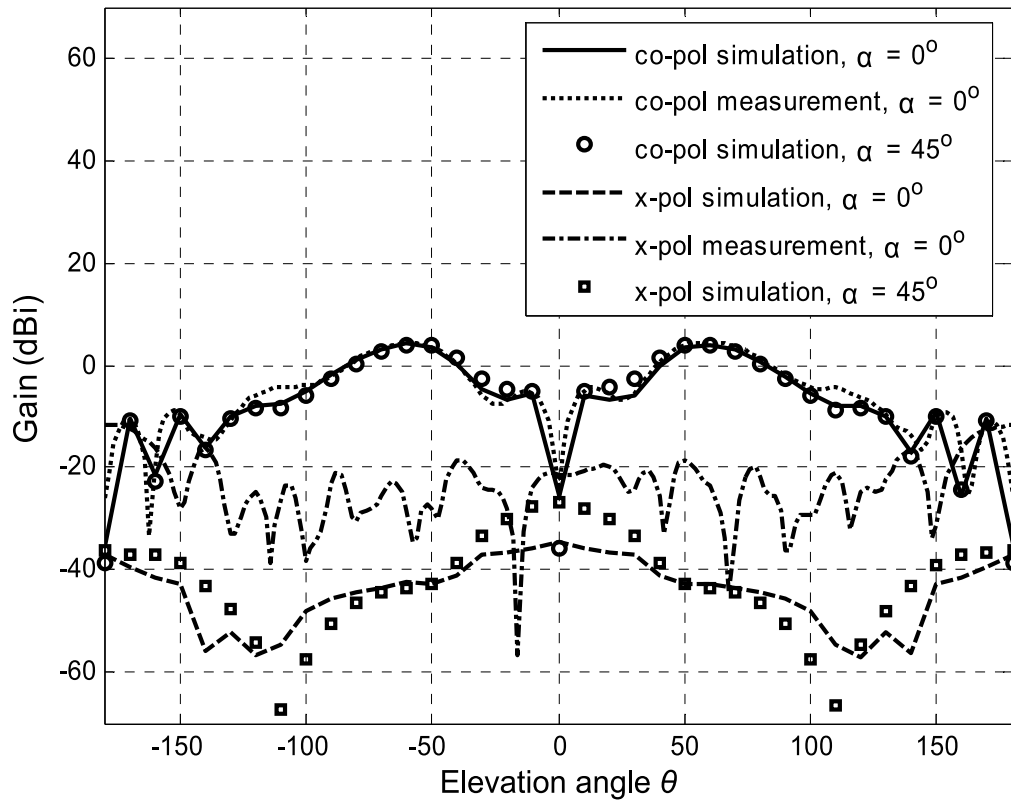
Fig. 4. Radiation patterns in the *x-z* plane at 3 GHz.
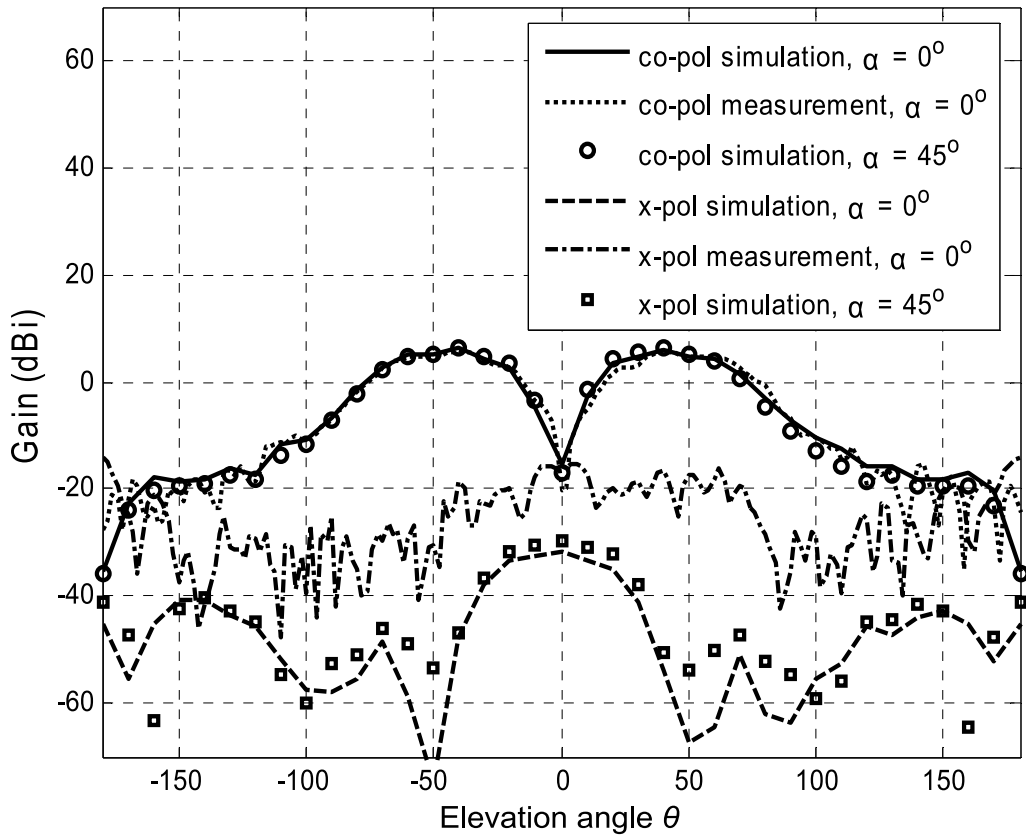
Fig. 5. Radiation patterns in the *x-z* plane at 7 GHz.
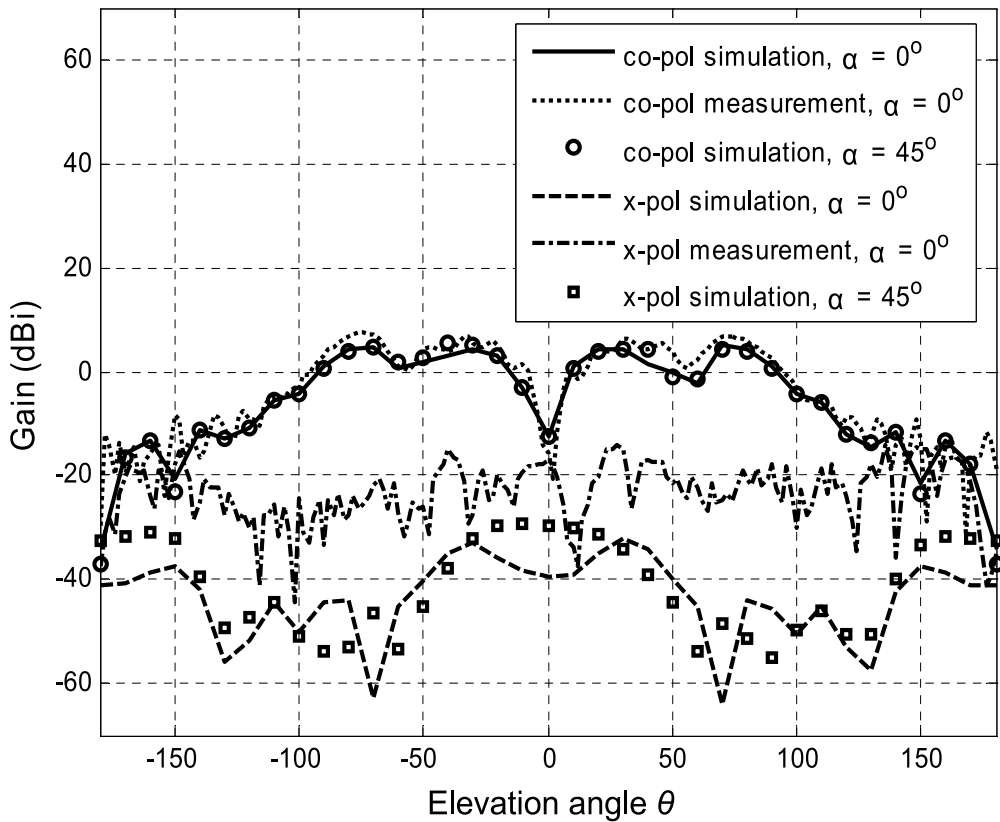
Fig. 6. Radiation patterns in the *x-z* plane at 10 GHz.

Similarly, Figures 7–9 show the co- and cross-polarized radiation patterns in the *y-z* plane at 3, 7, and 10 GHz, respectively. In the case when $\alpha = 0°$, both simulation and measurement results are displayed, and the simulated patterns when $\alpha = 45°$ are also given for comparison. The highest gain is also around 5 dBi. Good agreement between the simulated and measured results for the co-polarized radiation patterns can be observed at 3 GHz and 7 GHz. At 10 GHz, the measured co-polarized gain is about 2 dBi higher than the simulated result. The measured cross-polarized pattern at 3 GHz is between -40 dBi to -20 dBi, while the simulated result is between -60 dBi to -25 dBi. At 7 GHz and 10 GHz, the simulated and measured cross-polarized patterns agree quite well. The simulated co-polarized patterns when $\alpha = 45°$ agree quite well with those when $\alpha = 0°$ at 3 GHz and 7 GHz but poorer agreement is observed in the co-polarized radiation patterns at 10 GHz. This is because the variation in the angle α has changed the radiation properties. The gain is quite constant around 5 dBi at the three frequencies when $|\theta| = 50°$. The small variation in the patterns is one of the factors to ensure that the waveform of the received signal is well-preserved.
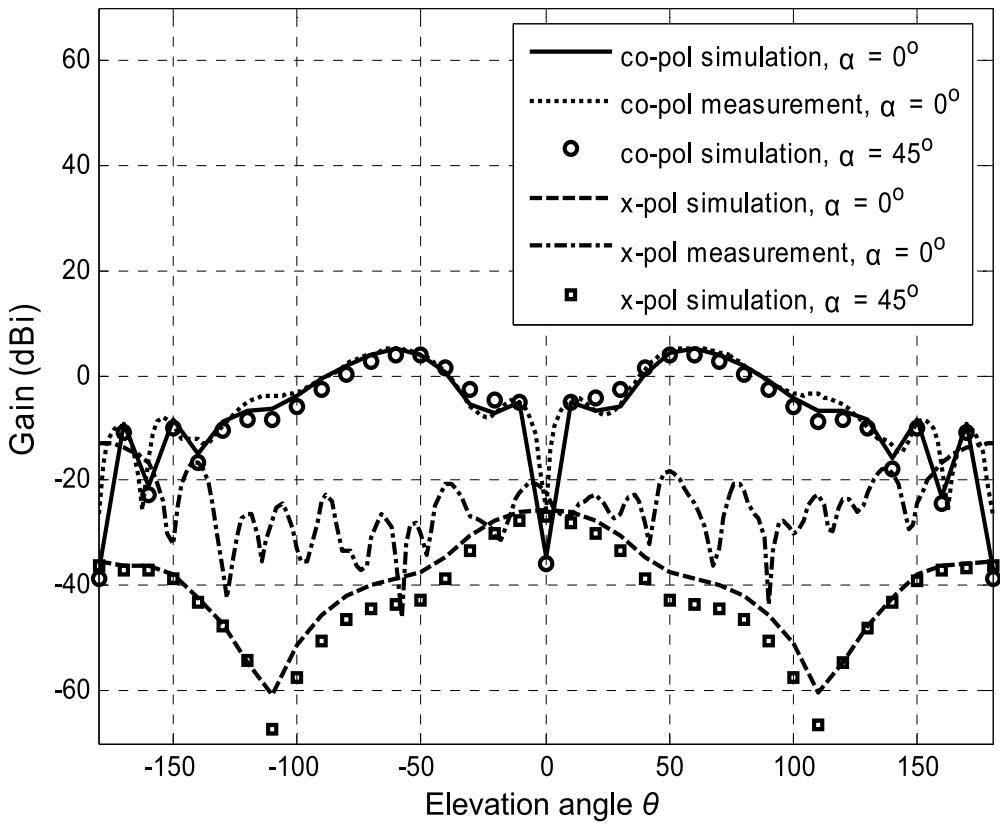
Fig. 7. Radiation patterns in the *y-z* plane at 3 GHz.
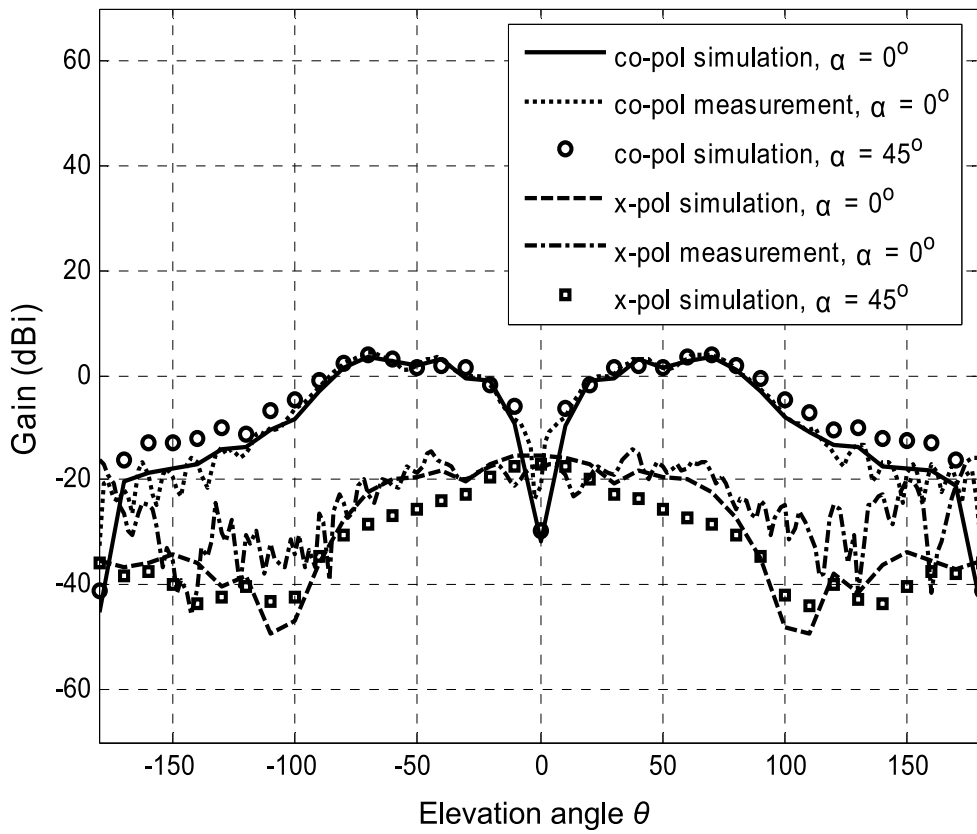
Fig. 8. Radiation patterns in the *y-z* plane at 7 GHz.
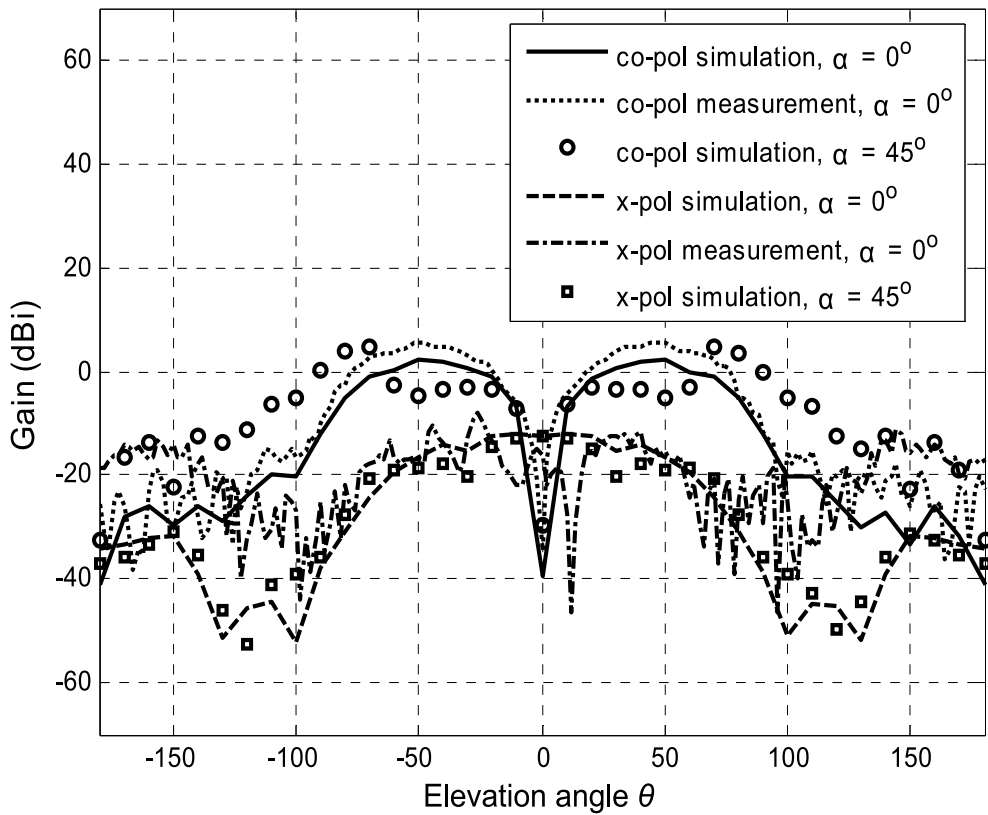
Fig. 9. Radiation patterns in the *y-z* plane at 10 GHz.
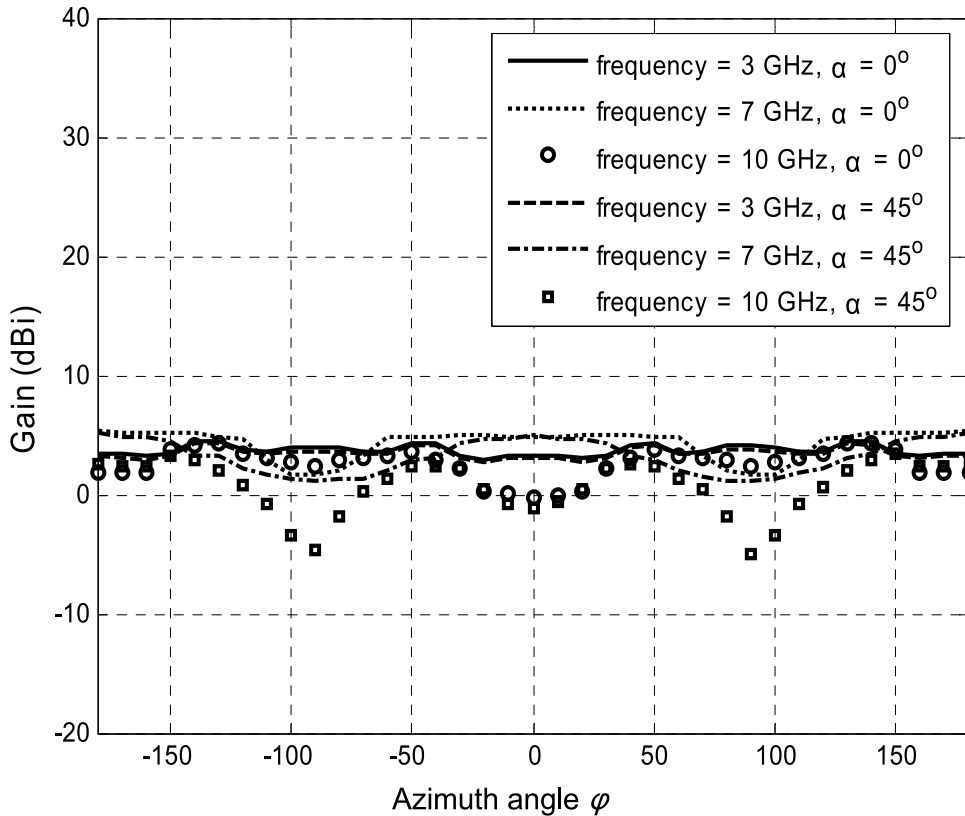
Fig. 10. Co-polarized radiation patterns in the *x-y* plane.

Figure 10 shows the simulated co-polarized patterns when $\alpha = 0°$ and $\alpha = 45°$ in the *x-y* plane at 3, 7, and 10 GHz. The radiation patterns are generally quite stable at the three frequencies, except for the case when $\alpha = 45°$ at 10 GHz.

From the radiation patterns in the *x-z*, *y-z*, and *x-y* planes, it can be concluded that the variation in radiation pattern from 3–10 GHz is small, giving omni-directional patterns in the azimuth plane. The small variation in the co-polarized radiation when α is changed from 0° to 45° is conducive for reducing the distortion in the received waveform (Chen et al., 2004).

4. Ground plane effect on the antenna performance

In the above discussions, the ground plane size for the antenna is 300 mm× 300 mm, which is much larger than the wavelength corresponding to the lower edge frequency of the UWB

band. Furthermore, depending on the requirements of different applications, the ground plane size for this antenna may be varied. From the study conducted in this Section, it will be shown that the size of the ground plane will greatly affect the antenna performance in terms of $|S_{11}|$ as well as the radiation properties such as gain, co- and cross-polarized radiation patterns across the bandwidth.

4.1 Ground plane effect on return loss

The FDTD-based Fidelity software from Mentor was used to investigate the performance of the antenna with different square ground planes of length 25, 50, 100, 200, and 300 mm.

The return loss performance for the antennas with different ground plane sizes is displayed in Figure 11. It can be observed that for ground plane sizes larger than 100 mm × 100 mm, the return loss is quite stable with little variation. When the size is reduced to 50 mm × 50 mm and then to 25 mm × 25 mm, the impedance matching deteriorates at the lower frequencies but remains relatively unchanged at the higher frequencies. Hence, the impedance bandwidth is reduced. This is expected because for the radiating elements of a monopole mounted on a finite-size ground plane, the outer edge of the ground plane diffracts the incident radiation in all directions. This diffraction consequently alters the current distribution on the ground plane. At 3 GHz, the ground plane size of 50 mm × 50 mm corresponds to ½ λ × ½ λ, and 25 mm × 25 mm is equivalent to ¼ λ × ¼ λ. When the ground plane size is reduced from 300 mm × 300 mm to 100 mm × 100 mm, the return loss remain almost unchanged. As the ground plane size is reduced to 50 mm × 50 mm, the return loss at 3 GHz increases by about 3 dB. When the ground plane size is further reduced to 25 mm × 25 mm, the return loss is increased by another 5 dB. Evidently, the outer-edge diffraction becomes increasingly significant as the size of the ground plane is reduced, especially when the size is less than 1 λ × 1 λ. With a small size, the edge diffraction adversely impacts the impedance matching of the antenna. The performance of the return loss at the upper edge of the frequency band is relatively unaffected as the size of the ground plane is still considered to be electrically large at the higher frequencies.

4.2 Ground plane effect on radiation patterns

The effect of the size of the ground plane on the radiation patterns has been investigated across the UWB band. Figures 12–14 show the simulated radiation patterns at 3.1 GHz, 6.85 GHz, and 10.6 GHz in the *x-z* plane. From Figure 12, it can be seen that for the small ground plane sizes of 25 mm × 25 mm and 50 mm × 50 mm, the patterns are quite flat across 40° < $|\theta|$ < 150° and the peak gain is close to 0 dBi. For the larger ground planes, the peak gain is greater than 0 dBi and peaks at around $|\theta|$ = 50°.

Figure 13 shows that the radiation patterns at 6.85 GHz peak at around $|\theta|$ = 50°. The peak gain is slightly higher than at 3.1 GHz. The antenna with a ground plane size of 25 mm × 25 mm experiences an increase in back lobes which can be reduced by increasing the size of the ground plane. From Figure 14, it can be observed that the ground plane size does not have a significant effect on the radiation patterns at 10.6 GHz, except for the higher back lobes when a smaller ground plane is used. In the main radiation directions, the gain varies from -3 dBi to 5 dBi across the bandwidth. Similar observations from the radiation patterns in the *y-z* plane can be made and are therefore not shown for brevity.
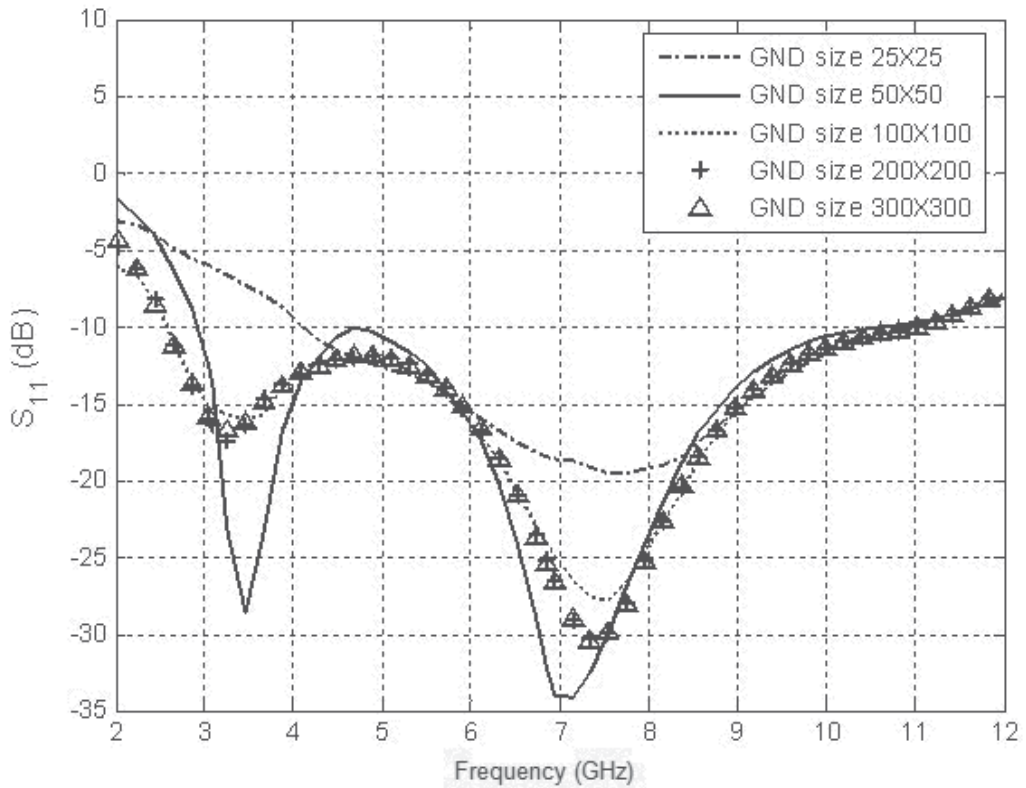
Fig. 11. Simulated return losses for the antennas with different ground plane sizes.

An infinite-size ground plane prevents monopole radiation into the half space beneath the ground plane. In practice, a monopole antenna has to be installed on a ground plane of finite size. It has been observed that the impedance matching will be degraded significantly if the ground plane size is smaller than $1\lambda \times 1\lambda$ as outer edge diffraction will modify the current distribution on the ground plane and the monopole antenna. The radiation characteristics of an antenna in terms of the gain and patterns will also be affected. This has been verified from Figures 12–14. At 3.1 GHz, the peak gain drops by about 5 dBi while the back lobe increases by approximately 5 dBi when the size of the ground plane is 50 mm × 50 mm and 25 mm × 25 mm. At 6.85 GHz, the peak gain drops by about 3 dBi and the back lobe is increased by approximately 5 dBi for the ground plane size of 25 mm × 25 mm as compared to other ground plane sizes. At 10.6 GHz, the back lobe is increased by approximately 6 dBi when the size of the ground plane is reduced to 25 mm × 25 mm. By decreasing the size of the ground plane, the magnitude of the currents along the outer edges of the ground plane is increased. Hence, the outer-edge diffraction effect becomes increasingly significant for antennas with small ground planes, which in turn alters the current distribution and thereby adversely affects the radiation properties by reducing the peak gain and increasing the back lobes.
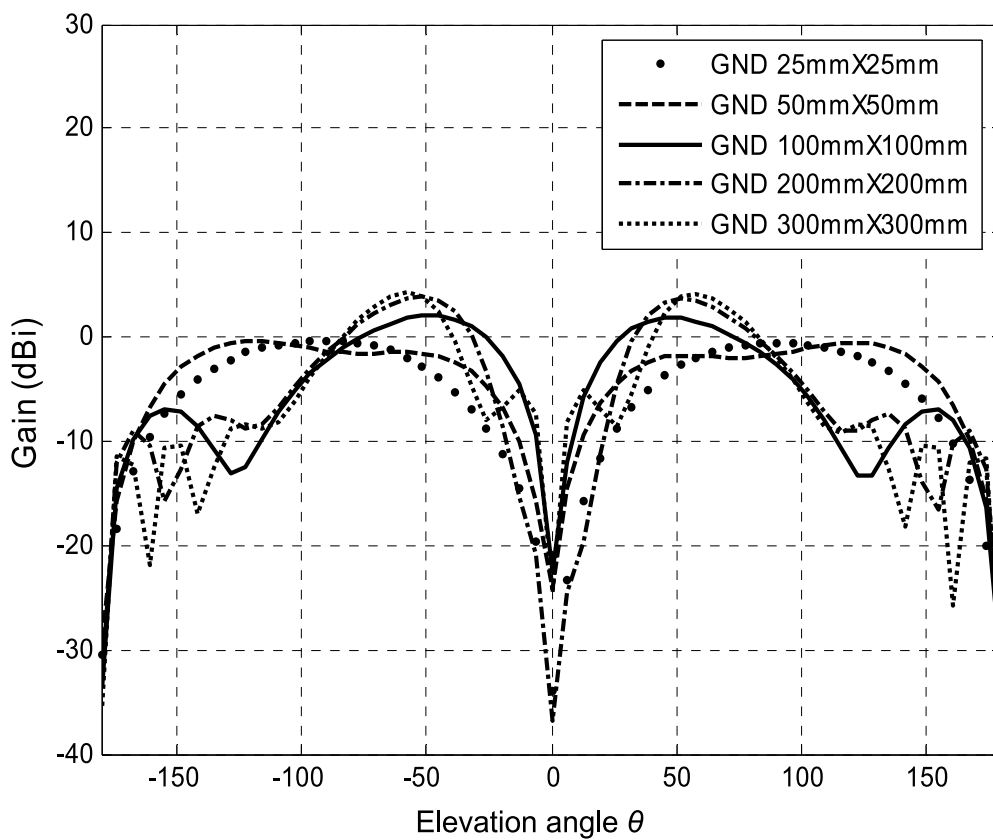
Fig. 12. Simulated radiation patterns in the *x-z* plane at 3.1 GHz.
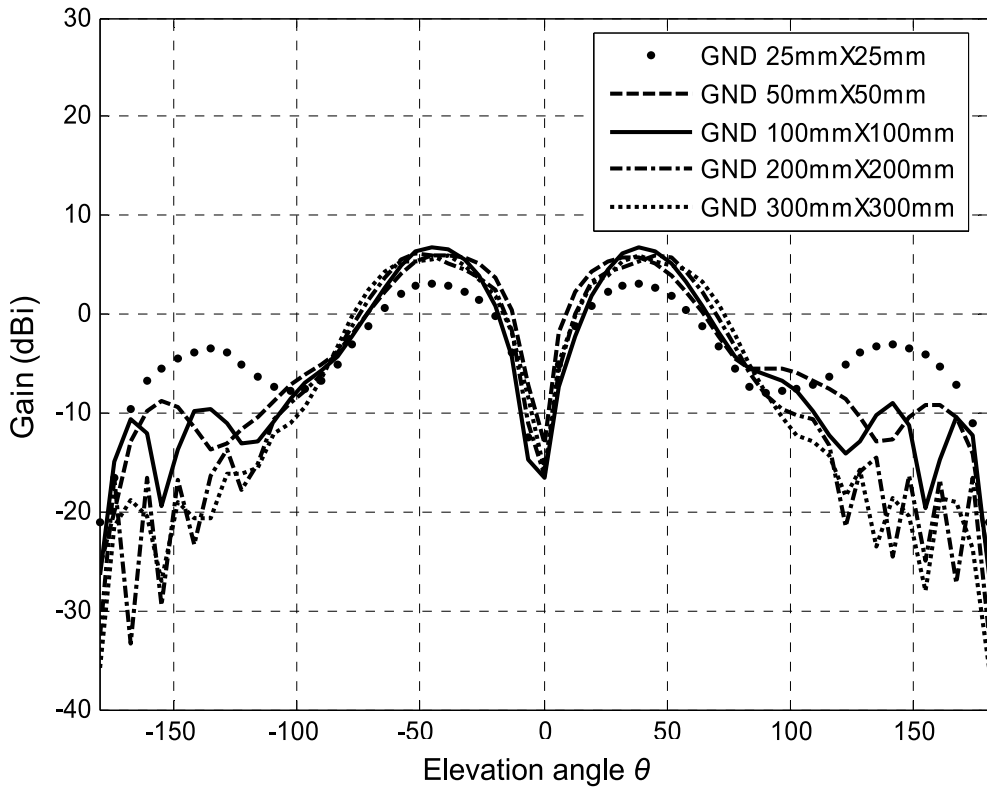
Fig. 13. Simulated radiation patterns in the *x-z* plane at 6.85 GHz.
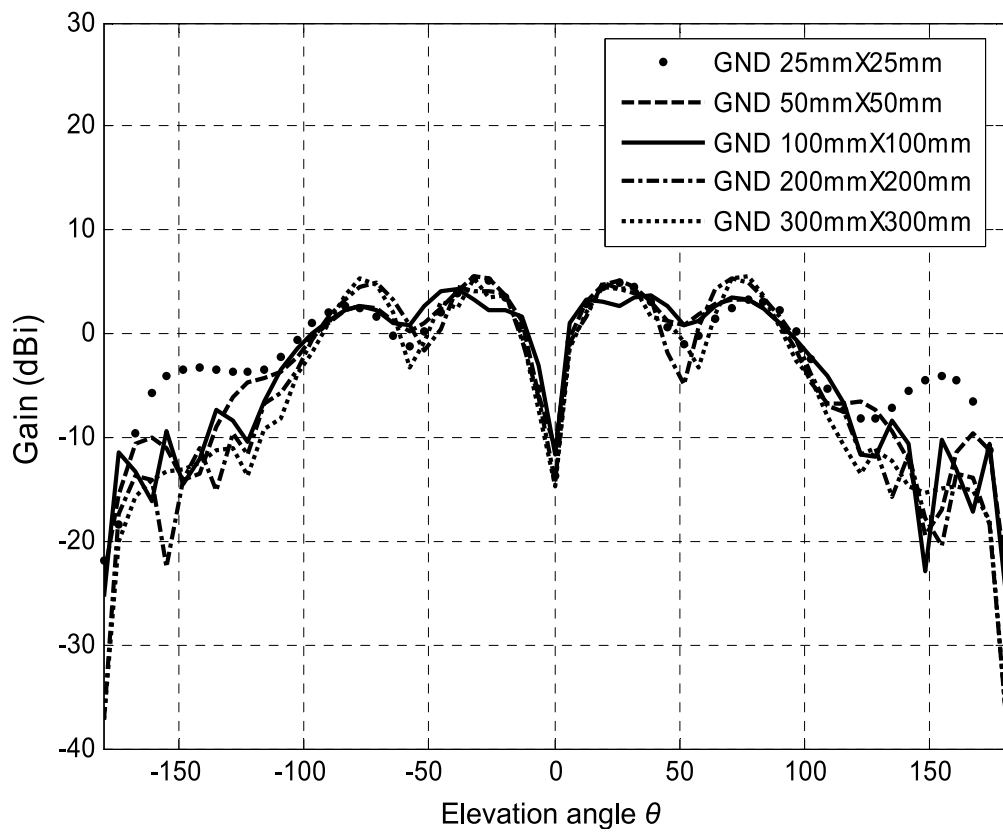
Fig. 14. Simulated radiation patterns in the *x-z* plane at 10.6 GHz.

5. Time domain characteristics

In order to evaluate the antenna performance in the time domain, a transmit-receive antenna system has been built. The antenna system consists of two identical antennas separated by a distance in the far-field region. This system is implemented using an FDTD model and becomes a two-port structure. The source pulse is fed to the input of the transmit antenna. The radiated pulse from the output of the transmit antenna travels in free space before entering the receive antenna. In this study, the antenna with $\alpha = 0°$ will be considered. The receive antenna can be rotated at different angles with respect to the transmit antenna and the received pulse will then be compared with the source and radiated pulses.

The antenna system has been simulated using the FDTD method and the group delay is calculated and shown in Figure 15. The far-field distance between the two antennas is 250 mm. In this case, the two antennas are positioned face-to-face. The group delay is defined as the change in the phase of the transmission response S_{21} with respect to the angular frequency and it provides information about the degree of signal distortion. From Figure 15, it can be seen that the variation in the group delay is within 1 ns within the UWB band. Beyond 11 GHz, the frequency components suffer from time distortion, which results in a reduced fidelity of the received signal.
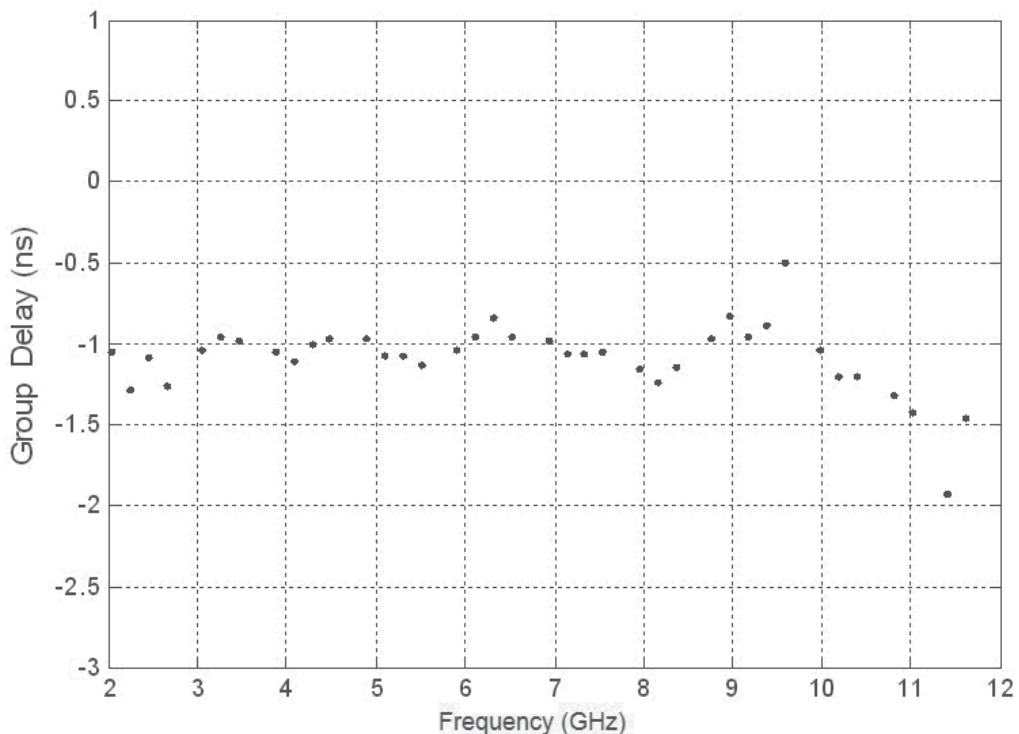
Fig. 15. Group delay of the antenna system.

Figure 16 shows the comparison of the received signals when the receive antenna is oriented at angles of 0°, 45°, and 90° with respect to the transmit antenna. The source and radiated pulses are also included. Rx 0° represents the received signal when the wings of the receive antenna are directly facing the wings of the transmit antenna, while Rx 90° represents the signal when the wings of receive antenna are perpendicular to the wings of the transmit antenna. All the received signals have been normalized with respect to the source pulse for comparison. It can be observed that the shapes of the received signals are similar and the normalized peak amplitude in the main lobe varies from 1 V to around 0.7 V for the different angles. The peak amplitude in the ripple of the received signals changes from around 0.1 V to 0.4 V. The distortion in the received signal may be caused by the larger variation in the group delay of the antenna system, especially at the higher frequencies.
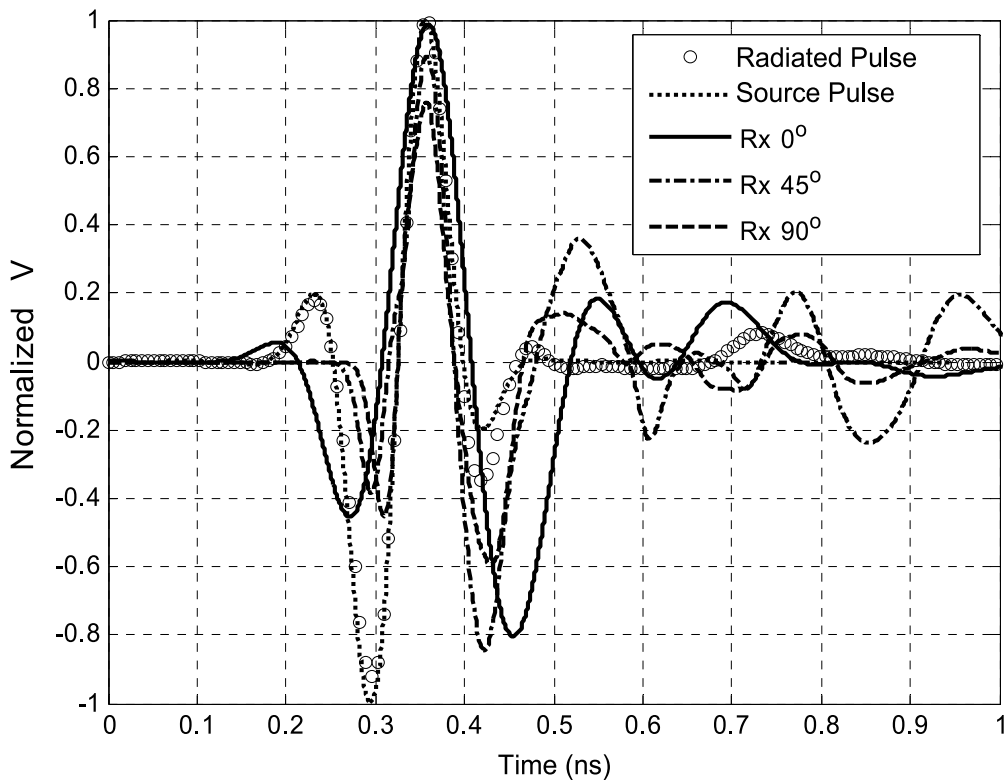
Fig. 16. Comparison of the received pulse with the source and radiated pulses.

6. Conclusion

The proposed butterfly-shaped monopole antenna has demonstrated good impedance and radiation performance across the UWB band. The wings of the antenna can be oriented at an angle of up to 45° with respect to the ground plane and still meet the UWB requirements. The co- and cross-polarized radiation patterns for the proposed antenna have shown stable performance across the entire UWB band in the principal planes. In addition, the radiation is omni-directional in the azimuth plane. However, at 10 GHz, the

patterns are adversely affected when $\alpha = 45°$. The design has been validated by both simulation and measurement.

A study has been conducted to investigate the effect of the size of the ground plane on the antenna performance. It has been shown that when the size of the ground plane is comparable to or smaller than $1\lambda \times 1\lambda$ (wavelength corresponding to the lower edge of the UWB band), the return loss performance deteriorates, especially at the lower edge of the UWB band. At the same time, the small ground plane has resulted in a decrease in the peak gain at 3 GHz and an increase in the back lobe radiation across the entire UWB band.

Based on the phase of the transmission response S_{21} of the antenna system, the variation in the calculated group delay is within 1 ns across the UWB band. The received signals for the different angles of the receive antenna with respect to the transmit antenna are similar in shape and their peak amplitudes vary within a small range. The study has shown that this antenna is capable of providing stable gain and little distortion in the radiated and received pulses, which makes it suitable for pulsed based UWB wireless communication and radar applications.

Future research directions in this area may involve antenna miniaturization as well as the optimization of the current distribution on the antenna so as to reduce signal distortion. In order to avoid interference with other existing communication systems, band notching will be required, which may be achieved in the proposed butterfly-shaped monopole antenna by cutting slots on the radiators.

7. References

Ammann, M. J. & Chen, Z. N. (2005). Wideband Monopole Antennas for Multiband Wireless System, *IEEE Antennas & Propagation Magazine,* Vol. 45, No. 2, (Apr. 2003), pp. , ISSN 1045-9243.

Behdad, N. & Sarabandi, K. (2005). A Compact Antenna for Ultrawide-Band Applications, *IEEE Transactions on Antennas and Propagation,* Vol. 53, No. 7, (Jul. 2005), pp. 2185-2192, ISSN 0018-926X.

Chen, Z. N. (2005). Novel Bi-Arm Rolled Monopole for UWB Applications, *IEEE Transactions on Antennas and Propagation,* Vol. 53, No. 2, (Feb. 2005), pp. 672-677, ISSN 0018-926X.

Chen, Z. N.; Wu, X. H.; Li, H. F.; Yang, N. & Chia, M. Y. W. (2004). Considerations for Source Pulses and Antennas in UWB Radio Systems, *IEEE Transactions on Antennas and Propagation*, Vol. 52, No. 7, (July 2004), pp. 1739-1748, ISSN 0018-926X.

Cho, Y. J.; Kim, K. H.; Choi, D. H.; Lee, S. S. & Park, S.-O. (2006) A Miniature UWB Planar Monopole Antenna with 5-GHz Band-Rejection Filter and the Time-Domain Characteristics, *IEEE Transactions on Antennas and Propagation,* Vol. 54, No. 5, (May 2006), pp. 1453-1460, ISSN 0018-926X.

Liang, J.; Chiau, C. C.; Chen, X. & Parini, C. G. (2005). Study of a Printed Circular Disc Monopole Antenna for UWB Systems, *IEEE Transactions on Antennas and Propagation,* Vol. 53, No. 11, (Nov. 2005), pp. 3500-3504, ISSN 0018-926X.

Qiu, J.; Du, Z.; Lu, J. & Gong, K. (2006). A Planar Monopole Antenna Design with Band-Notched Characteristic, *IEEE Transactions on Antennas and Propagation,* Vol. 54, No. 1, (Jan. 2006), pp. 288-292, ISSN 0018-926X.

Performance Study on Modern Ultra Wideband Monopole Antennas

Abdelhalim Mohamed and Lotfollah Shafai
University of Manitoba
Canada

1. Introduction

The proposed use of ultra wideband (UWB) technology in communication services has motivated the research towards more design and performance studies of modern UWB antennas, (FCC, 2002). Interference of UWB antennas with the existing technologies, phase centre stability of modern UWB antennas, low cross-polarization UWB antennas, high gain directional UWB antennas with stable phase centre, symmetrical E- and H- Plane patterns and single or double linear polarization patterns are some of the important research topics nowadays. Monopole disc antennas, with circular, elliptical and trapezoidal shapes, have simpler two-dimensional geometries and are easier to fabricate compared to the traditional UWB monopole antennas with three-dimensional geometries such as spheroidal, conical and teardrop antennas. These disc monopole antennas can be designed to cover existing and upcoming UWB communication applications, (Honda et al., 1992) & (Hammoud & Colomel, 1993).

In this study, different square, circular and elliptical disc monopole antenna geometries are designed and analysed for both omnidirectional and directional applications. The feeding structure is optimized to have a maximum impedance bandwidth starting at 3 GHz. One of the general principles of small-element antenna design is the outline design equivalence one. It states that an outline of a planar antenna element performs approximately like the original planar one, (Mohamed & Shafai, 2007) and (Schantz, 2005). In this chapter, a study is made on the gradual removal of metal from the interior of all studied antennas while keeping the impedance and radiation characteristics unchanged. The minimum metal width that could be achieved is about 50% from the total radiator area. The effect of implementing a notch close to the feeding structure on impedance bandwidth is also studied. It is found that implementing notches close to the trident-feeding strip structure did not increase the impedance bandwidth of circular and elliptical antennas. Further, implementing a notch decreased the impedance bandwidth of the square monopole antenna. On the other hand, removing metal from the interior structure of the square, circular and elliptical monopoles gives the same impedance bandwidth for square and circular monopole but increased the bandwidth of the elliptical one. The circular and elliptical monopole antennas with metal removed showed better omnidirectional behaviour at higher frequencies.

The performance of a UWB quasi-circular monopole, with rectangular and trapezoidal ground planes was studied, (Wu et al., 2010). It was shown that antenna with trapezoidal

ground plane has significantly improved radiation performance, compared with the one with rectangular ground plane. The second part of this study investigates the effect of different ground plane sizes on the performance of these antennas. This includes the effect on impedance bandwidth and radiation pattern curves.

In the last part of this study, a UWB Yagi monopole antenna over a ground plane is designed and analyzed to work over the whole UWB communication band. The antenna is relatively small in size and the driven element is based on a square or circular radiator shape with some modifications, (Wong et al., 2005).

This study will help to characterize UWB monopole antennas with better performance to be used in the existing and upcoming UWB communication applications that need both omnidirectional and directional monopole type antennas.

2. UWB Monopole antennas

Spheroidal, conical and teardrop monopole antennas are some of the traditional UWB antennas with excellent electrical characteristics. However, they are three-dimensional structures, and difficult to fabricate. Monopole disc antennas, with circular, elliptical and trapezoidal shapes, can also provide UWB impedance bandwidths, but have simpler two-dimensional geometries and are easier to fabricate. In 1992, Honda and others proposed a circular monopole TV antenna operating at 90-770 MHz, (Honda et al., 1992). These antennas can be designed to cover both existing and upcoming UWB communication applications, and have omnidirectional radiation patterns over the entire frequency of operation, (Hammoud & Colomel, 1993). In 2010, both simulated annealing algorithm and the finite element method were used for profile optimization in planar UWB monopole antennas for minimum return losses, (Martinez-Fernandez et al., 2010).

In this chapter, square, circular and elliptical monopole antennas with trident feeding strip based on the square plate monopole antenna first introduced by Wong, (Wong et al., 2005) are designed and analyzed. The proposed designs cover the frequency band between 3 to 19 GHz. The effect of metal removal from the interior structure of the radiator and implementing notch in the bottom end on the impedance bandwidth and radiation pattern of these antennas are also studied.

2.1 Impedance bandwidth and radiation pattern

Impedance bandwidth is that characteristic that distinguishes a UWB antenna from a narrow band one. The lower and upper frequencies are determined based on the 10 dB return loss bandwidth criterion. An antenna is considered well matched when its return loss is greater than or equal to 10 dB. This return loss represents the impedance mismatch level of this antenna. Techniques to increase the bandwidth and control the lowest frequency of operation have been used including geometry changes, loading effects, using shorting post or feeding the antenna with different feeding schemes. A physical interpretation of the bandwidth increase of these antennas using the theory of characteristic modes was given by Ferrando-Bataller et al., 2006. The idea is to enhance the modes that give the current distributions that support the radiation. In the case of monopole antennas, it was found that the first three modes J1, J2 and J3 are enough to characterize the antenna behaviour. J1 mode supports the radiation in the lower frequency band while J3 supports radiation in the upper band. When the monopole antenna is placed vertically over a horizontal ground plane,

modes J1 and J3 will give vertical current distributions on the antenna surface, while mode J2 will give horizontal currents parallel to the ground plane. In this case, it will be useful to suppress mode J2 to reduce cross polarization component. Monopole antennas have an omnidirectional radiation pattern in the H-Plane and monopole-like radiation pattern in the E-plane. This makes monopole antennas good candidates for communication applications. There are some shortcomings with existing UWB antenna designs which include high cross polarization components especially at higher frequencies, angular dependence of the E-plane patterns and deterioration in the H-plane patterns.

2.2 Square monopole antennas

Square monopole antennas are simple antennas to be built and have radiation characteristics that are suitable for certain UWB applications. It is an omnidirectional antenna with impedance bandwidth, which depends on the antenna design parameters. These design parameters include height, width and distance from the ground plane. To increase the bandwidth of this square monopole antenna, Wong introduced the trident-shaped feeding strip to feed the square monopole, (Wong et al., 2005). Wong's optimum design parameters for the trident-shaped feeding strip gave a 10 dB bandwidth of 10 GHz with the lower frequency of 1.376 GHz. Wong used a square monopole of 40x40 mm^2 over a 150x150 mm^2 ground plane, all strip widths used were 2mm. Based on this idea, a square monopole antenna with trident-shaped feeding strip is designed to work over the frequency band starting from 3GHz. The square monopole side is scaled down to 16 mm over a 120x120 mm^2 ground plane. The optimum strip dimensions for this antenna are t = 7 mm, d = 1 mm, h = 3 mm and all strip widths are 1.5 mm. Simulation results of this antenna show an omnidirectional radiation pattern over the frequency band from 3GHz to 19.5 GHz. The optimized feeding structure resulted in a well matched traveling mode by enhancing modes J1 and J3 which support vertical currents on the radiator surface. To study the effect of implementing a notch close to the feeding structure, a rectangular notch of height 2mm and width 3.75mm is implemented at each lower side of the square monopole. Fig. 1 shows different configurations for the square monopole antenna along with the return loss curves. It was expected that implementing such a notch in the feeding region would increase the bandwidth of the antenna. But as can be seen from Fig. 1d, the 10dB higher frequency edge of the impedance bandwidth was decreased from 19.5 GHz to 15 GHz. This is due to the fact that implementing a notch along with the feeding type did not help in supporting current mode J3 at higher frequencies. Radiation patterns at different frequencies show no significant effect of implementing such a notch.

To further study the performance of this antenna, gradual metal removal was done from the interior monopole area. It was proven that by removing the metal from the interior radiator of an ultra wideband circular monopole antenna with a single feeding strip, a loop ultra wideband monopole antenna is achieved keeping the radiation characteristics of the antenna unchanged, (Mohamed & Shafai, 2007). With this square monopole design, 8x8 mm^2 metal area was removed from the radiator as shown in Fig. 1c. The impedance bandwidth of the resulting antenna gives the same impedance bandwidth from 3 to 19.5 GHz with omnidirectional radiation pattern over the entire frequency bandwidth. Fig. 2 shows its E-plane and H-plane at different frequencies and different planes. It is clear that this antenna keeps its radiation characteristics at higher frequencies.

a) Square monopole, S1

c) Square monopole with metal removal, S3

b) Square monopole with notch, S2

d) Return loss curves for square
monopole antennas S1, S2 and *S3*
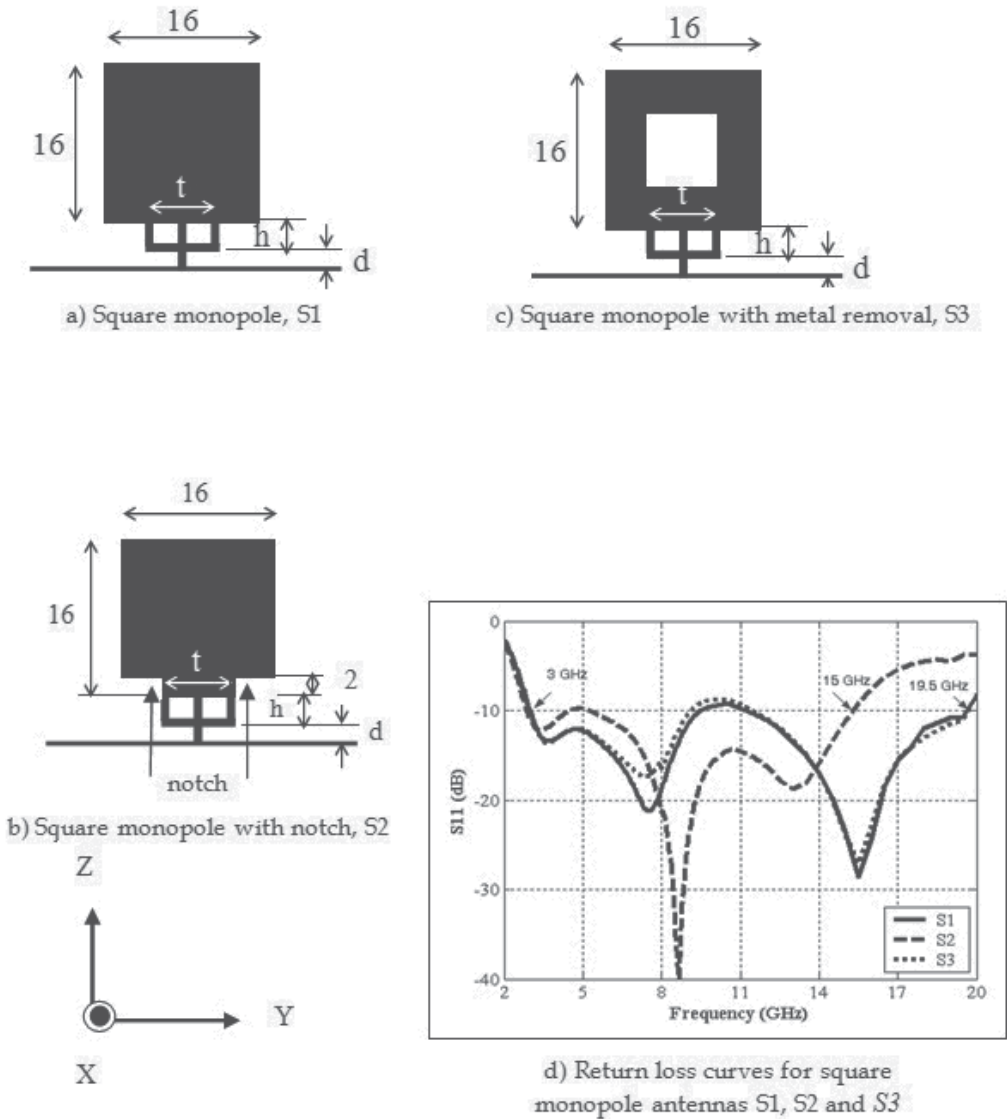
Fig. 1. Square monopole antenna with trident-feeding strip and different configurations
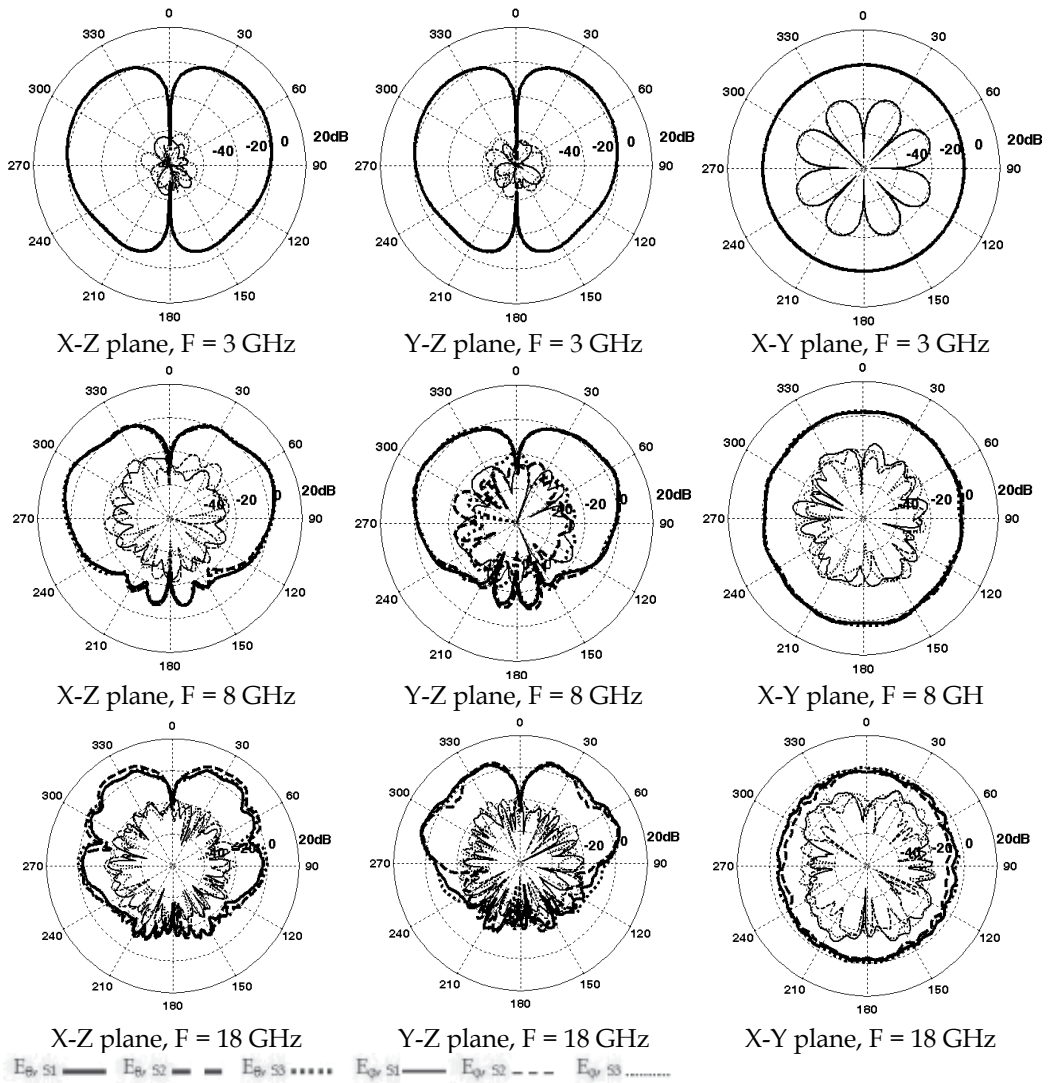
Fig. 2. Radiation patterns for three square monopole antennas S1, S2 and S3 at different frequencies

2.3 Circular monopole antennas

The second antenna to be studied is the circular monopole antenna known by its gradual bevelling near the feeding area. For the sake of comparison between this antenna and the square one, the height of the antenna, the trident-feeding strip configuration and the ground plane dimensions are kept the same. Antenna dimensions are given in Fig. 3 where t, h, and d are the same as those in the square monopole one. Fig. 3a, b and c show different circular

monopole configurations. In Fig. 3b and 3c, the same notch and metal removal approach used with the square monopole antenna design are implemented. The metal removed here is a circle of radius 4 mm. It is noted from the return loss curves shown in Fig 3d that the notch has a negligible effect on the circular monopole antenna. Similarly, the metal removal effect which made a circular loop monopole, gives almost the same impedance bandwidth of 130.58%, as the circular monopole.
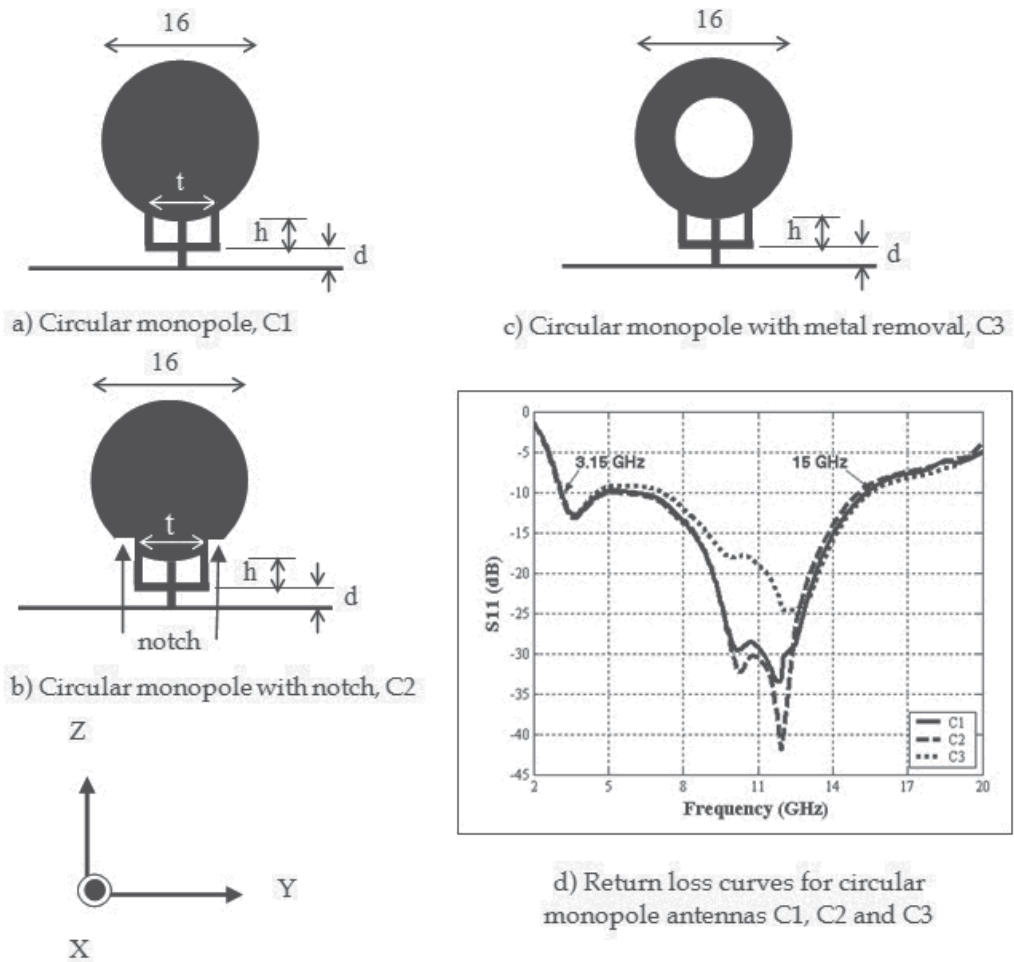
a) Circular monopole, C1

c) Circular monopole with metal removal, C3

b) Circular monopole with notch, C2

d) Return loss curves for circular monopole antennas C1, C2 and C3

Fig. 3. Circular monopole antenna with trident-feeding strip and different configurations

X-Z plane, F = 3 GHz   Y-Z plane, F = 3 GHz   X-Y plane, F = 3 GHz

X-Z plane, F = 8 GHz   Y-Z plane, F = 8 GHz   X-Y plane, F = 8 GHz

X-Z plane, F = 18 GHz   Y-Z plane, F = 18 GHz   X-Y plane, F = 18 GHz

$E_{\theta, C1}$ —— $E_{\theta, C2}$ — — $E_{\theta, C3}$ .... $E_{\varphi, C1}$ —— $E_{\varphi, C2}$ _ _ $E_{\varphi, C3}$ ....
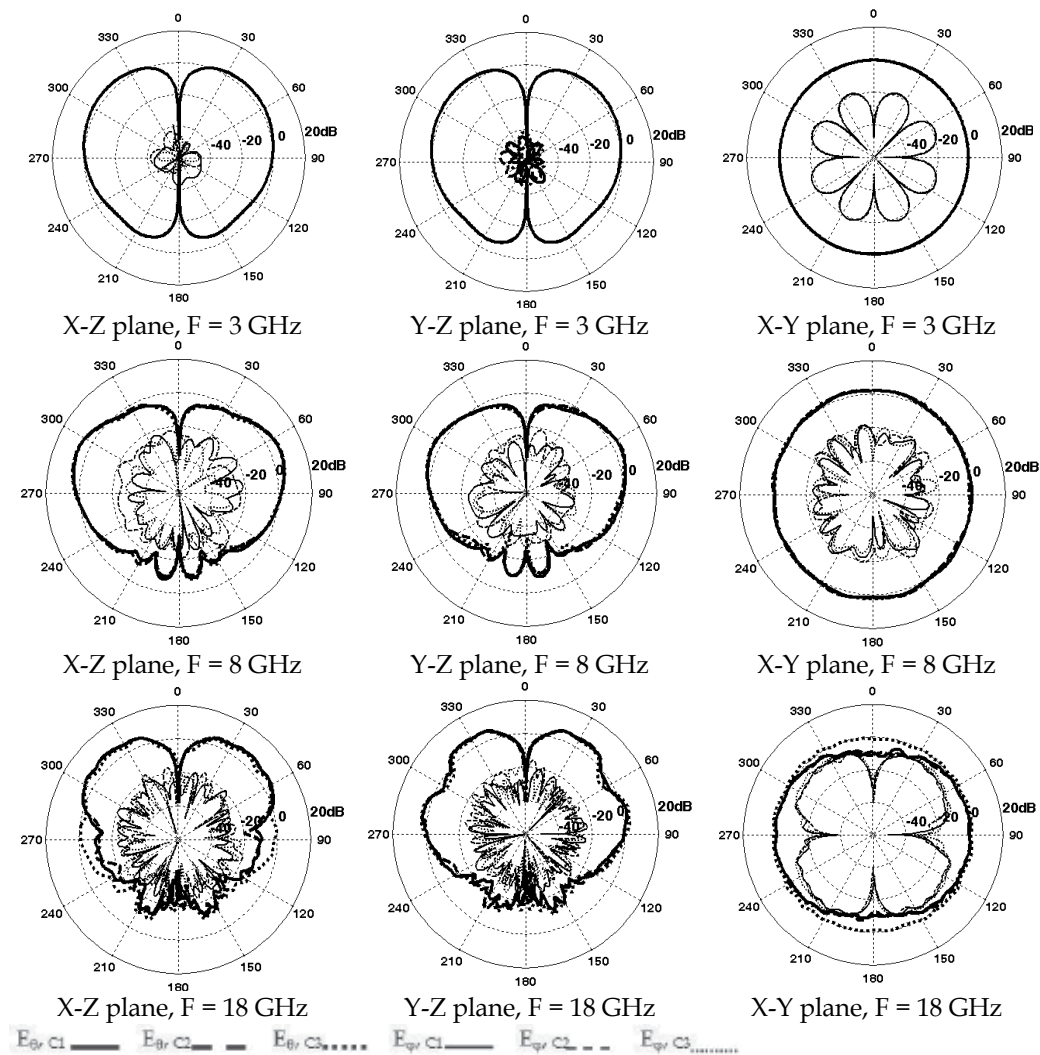
Fig. 4. Radiation patterns for three circular monopole antennas C1, C2 and C3 at different frequencies

The E and H-plane curves are shown in Fig 4. The circular monopole antenna with different configurations shows an omnidirectional radiation pattern over the frequency band of operation. The circular loop monopole antenna shows a better omnidirectional behaviour at higher frequencies. While implementing notches near the feeding region does not have a significant effect on the radiation patterns curves of these antennas.

2.4 Elliptical monopole antennas
The third antenna to be studied is the elliptical monopole antenna with trident-feeding strip. The same feeding structure and ground plane used for square and circular monopole are used here. The height of the elliptical monopole, which is the minor diameter, is 16 mm and the major diameter is 20 mm, as seen in Fig. 5. The notch implemented at the lower edge

reduced the upper frequency limit from 16.5 to 15.5 GHz. On the other hand, removing metal from the elliptical monopole by cutting an ellipse of minor 8mm and major 10 mm has increased the upper frequency limit to 17 GHz.

a) Elliptical monopole, E1

c) Elliptical monopole with metal removal, E3

b) Elliptical monopole with notch, E2

d) Return loss for elliptical monopole antennas E1, E2 and E3
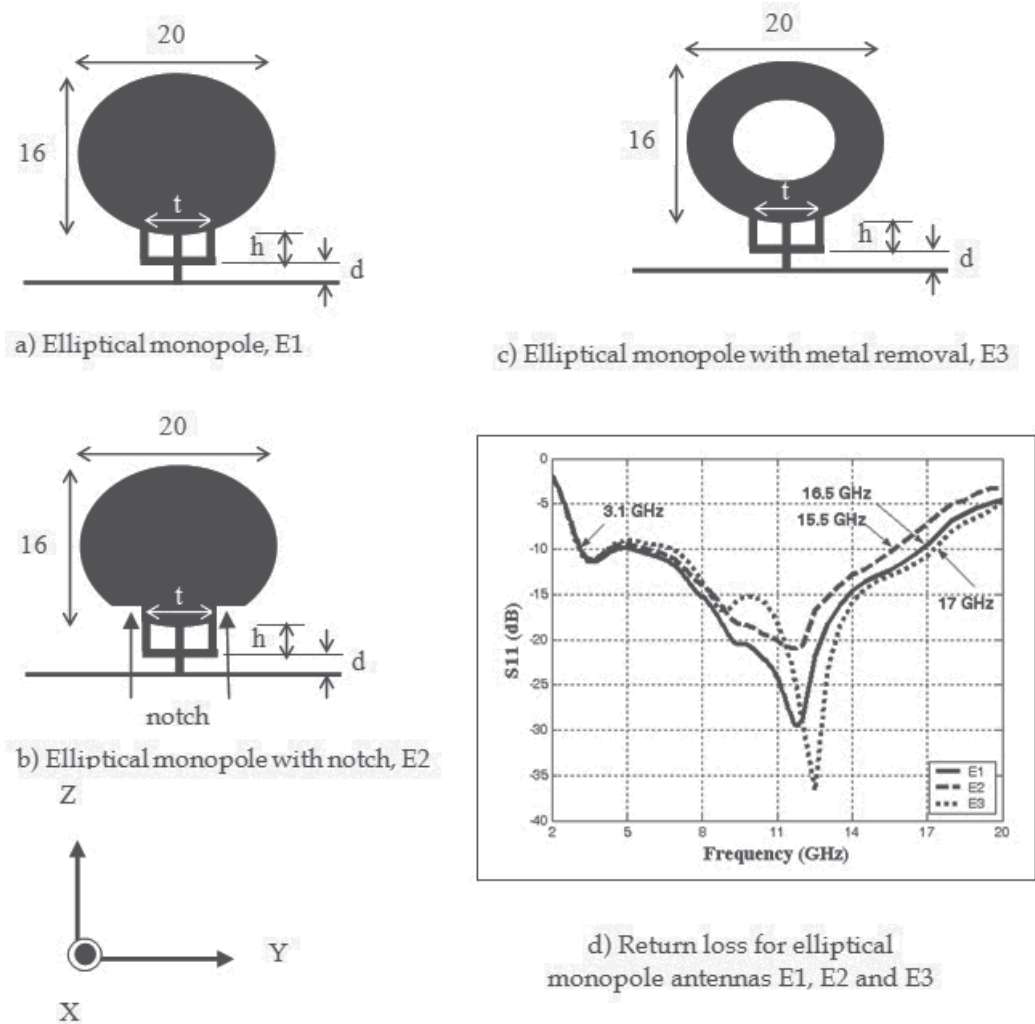
Fig. 5. Elliptical monopole antenna with trident-feeding strip and different configurations

Radiation patterns for the elliptical monopole antenna with different configurations at different frequencies and different planes are shown in Fig. 6. All the elliptical antenna configurations show omnidirectional pattern with low cross polarization. There is no effect of the notches or the metal removal on the radiation patterns at lower frequencies. While at higher frequencies, the elliptical monopole with metal removal has a better omnidirectional behaviour.
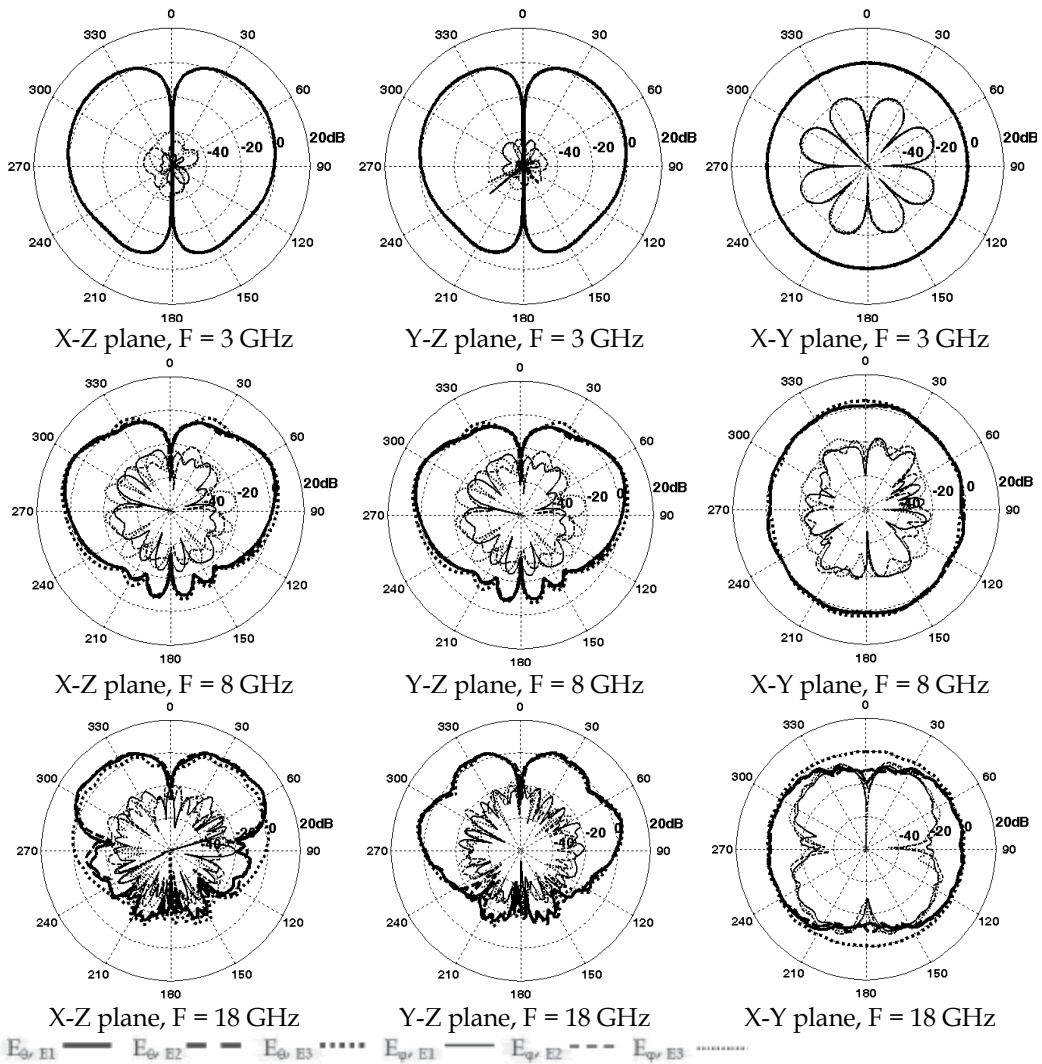
Fig. 6. Radiation patterns for three elliptical monopole antennas E1, E2 and E3 at different frequencies

3. Ground plane effect on the performance of UWB monopole antennas

Throughout the study done in section 2 of this chapter, the ground plane chosen for all monopole antennas was a square metal plate with area of 120x120 mm². The effect of a ground plane with this size appears in the results of the square, circular and elliptical monopole antennas. Using monopole antenna with height 16 mm and trident feeding strip over the ground plane and different geometries gave 10-dB impedance bandwidth with lower frequency of 3 GHz and upper frequency between 15 and 19.5 GHz. The radiation pattern curves of these antennas are monopole-like patterns with maximum radiation at the

E-plane around θ=60º and omnidirectional radiation pattern at the H-plane. Although the studied antennas so far satisfied the UWB communication applications regarding the impedance bandwidth and radiation pattern curves, the small height of the antenna over the ground plane affects the lower frequency band of operation. Also, the size of the ground plane was fixed throughout the study with total area of 120x120 mm². To further investigate the performance of such monopole antennas, the size of the ground plane is modified and different slots are implemented to study their effects on the antennas performance. The square monopole antenna with trident feeding strip designed in section 2, is used to illustrate the effect of the ground plane size on its performance. Antenna parameters of interest in this study are the return loss curves and radiation pattern curves. Simulation results indicate that by optimizing the ground plane size of UWB monopole antennas, the lower frequency edge of the impedance bandwidth can be reduced from 3 GHz to 2.1 GHz. On the other hand, this reduction in ground plane size will have an effect on the radiation pattern of the antenna. It is found that, by implementing a square slot in the original size of the ground plane, the frequency reduction in the lower edge of the impedance bandwidth can be maintained as well as the wanted radiation patterns. The radiation pattern is a monopole like pattern with the peak gain shifted to around θ = 60° above the horizon, because of the existence of the finite ground plane. The effect of the ground plane size on the peak gain angle θ is also investigated. Fig. 7 shows the square monopole antenna used in this study, while Fig. 8 shows the return loss curves for this antenna with different ground plane sizes.

As can be seen from Fig. 8, the square monopole antenna with 20x20mm² square ground plane has a UWB impedance bandwidth that starts at 2.1 GHz. This reduction of the lower edge of the bandwidth from 3 to 2.1 GHz is acheived without increasing the monopole height. The higher edge of the impedance bandwidth extends to almost 20 GHz for all cases.
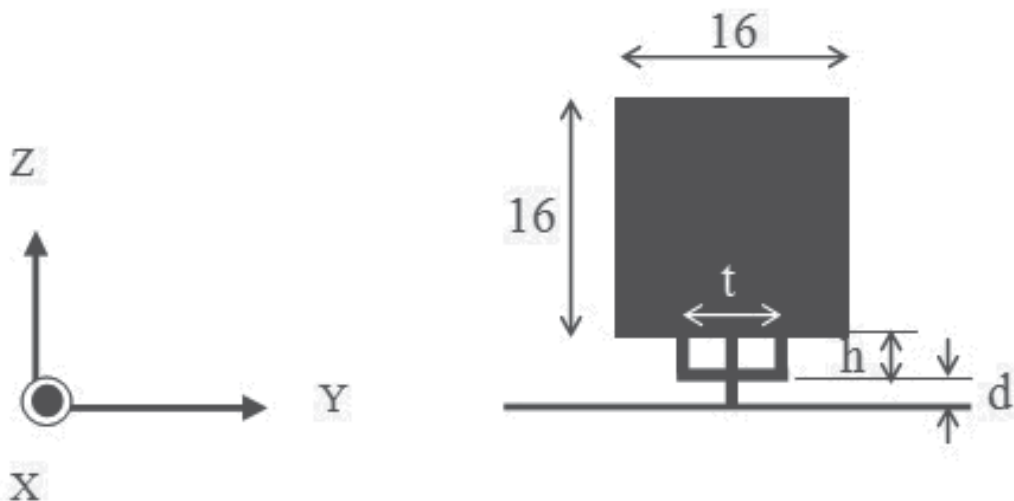
Fig. 7. Square monopole antenna with trident-feeding strip and different ground plane sizes. Optimized parameters values are: t=7mm, h=3mm, d=1mm, and all strip widths = 1.5mm
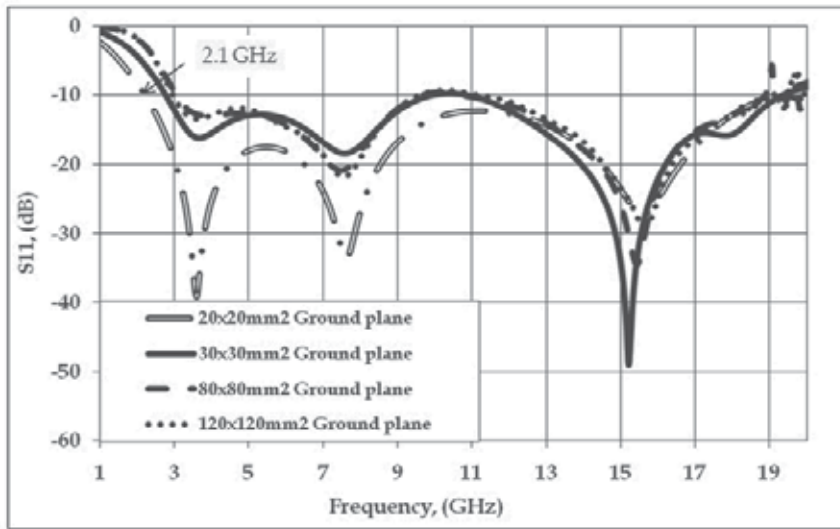
Fig. 8. Return loss curves for the square monopole antenna in Fig. 7 with different ground plane sizes.

f=3GHz: X-Z   Y-Z   X-Y

f=8GHz: X-Z   Y-Z   X-Y

| f=13GHz: X-Z | Y-Z | X-Y |
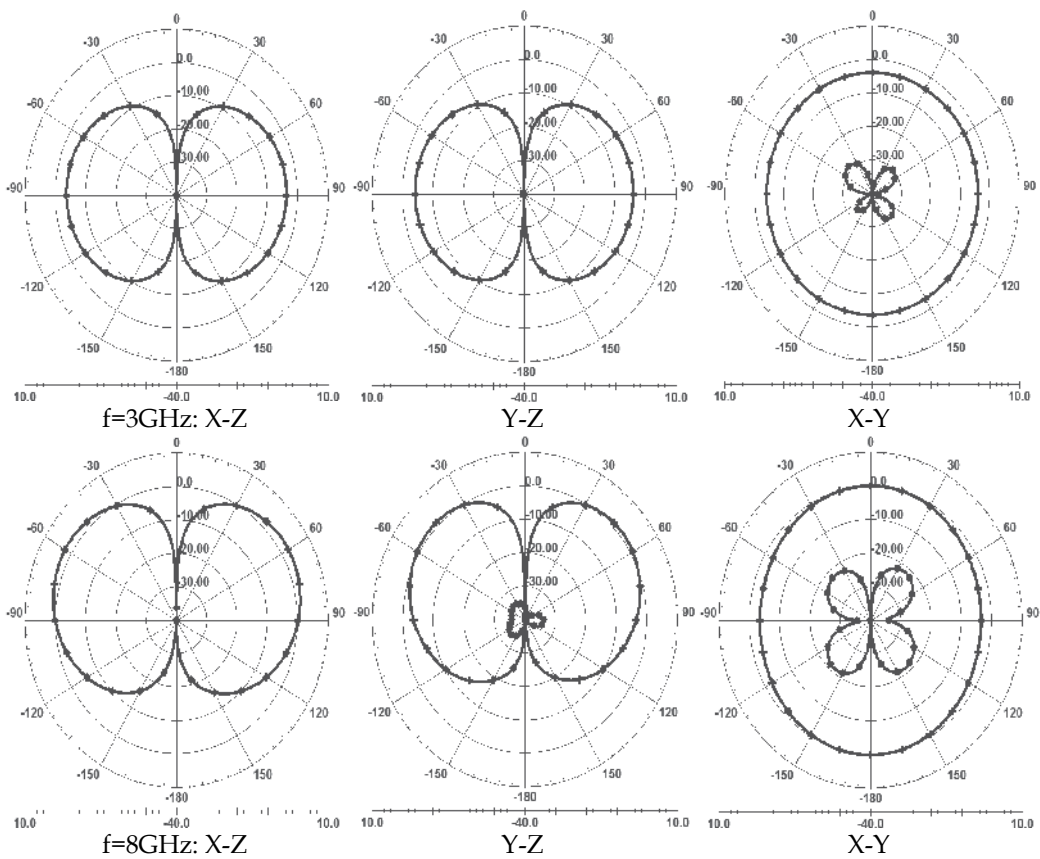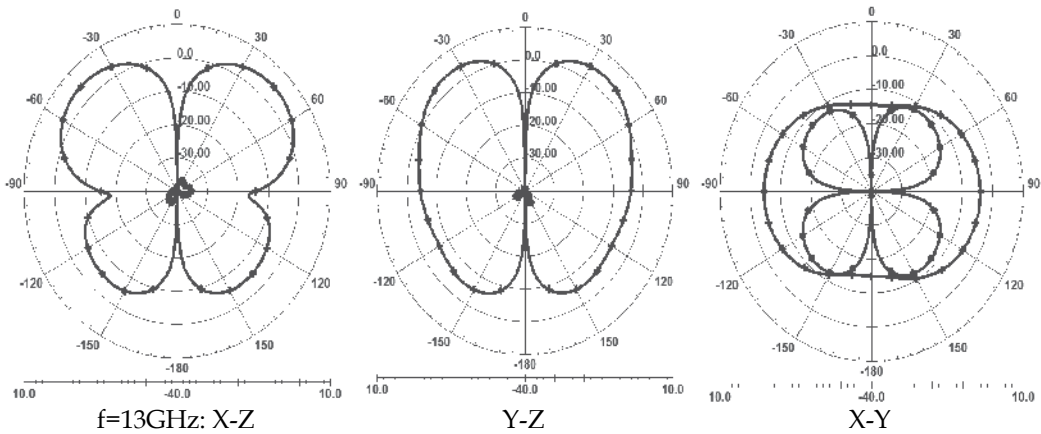
Fig. 9. Radiation patterns for the antenna shown in Fig. 7 with 20x20 mm² ground plane

To show the effect of the ground plane size on the radiation pattern curves, radiation pattern curves at different frequences are discussed. Fig. 9 shows E and H-plane curves at different planes and frequencies of 3, 8 and 13 GHz with 20x20mm² ground plane. While in section 2, Fig. 2 shows E and H-plane curves for the same antenna and same planes but with 120x120mm² ground plane size. As can be seen from Fig. 9, Fig. 2 and other simulated results, the effect of the small ground plane size is realized at lower frequencies. The gain is reduced at the maximum angle of radiation. Another attempt is done to further decrease the ground plane size and compensate for the effect of its small size on the radiation pattern. Square slots of different widths and at different distances from the origin are introduced within the ground plane. The study showed no significant effect on the radiation pattern curves of the antenna. However by having a 20x20mm² small ground plane and increasing the height of the antenna to only 30 mm, the lower frequency edge was reduced from 2.1 to 1.4 GHz and the gain was increased at the direction of maximum radiation. Fig. 10 shows the return loss curve for the antenna in Fig. 7 but with height of 30 mm, while Fig. 11 shows E and H-plane curves for the antenna in Fig. 7 with a height of 30 mm at different frequencies and different planes.
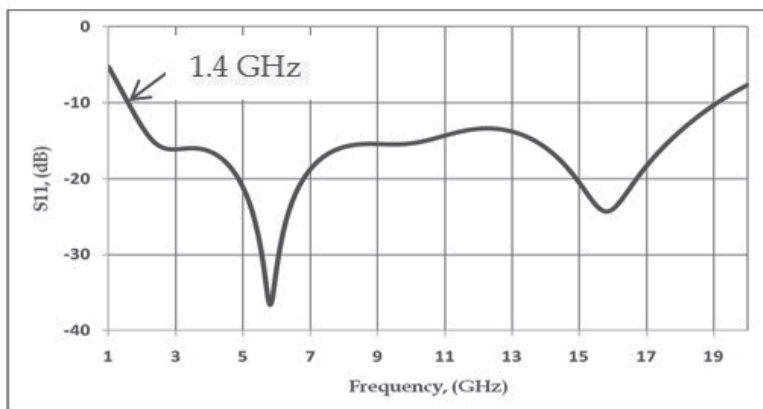
Fig. 10. Return loss curve for antenna in Fig. 7 with total height of 30mm instead of 20mm

f=8GHz: X-Z   Y-Z   X-Y

f=13GHz: X-Z   Y-Z   X-Y
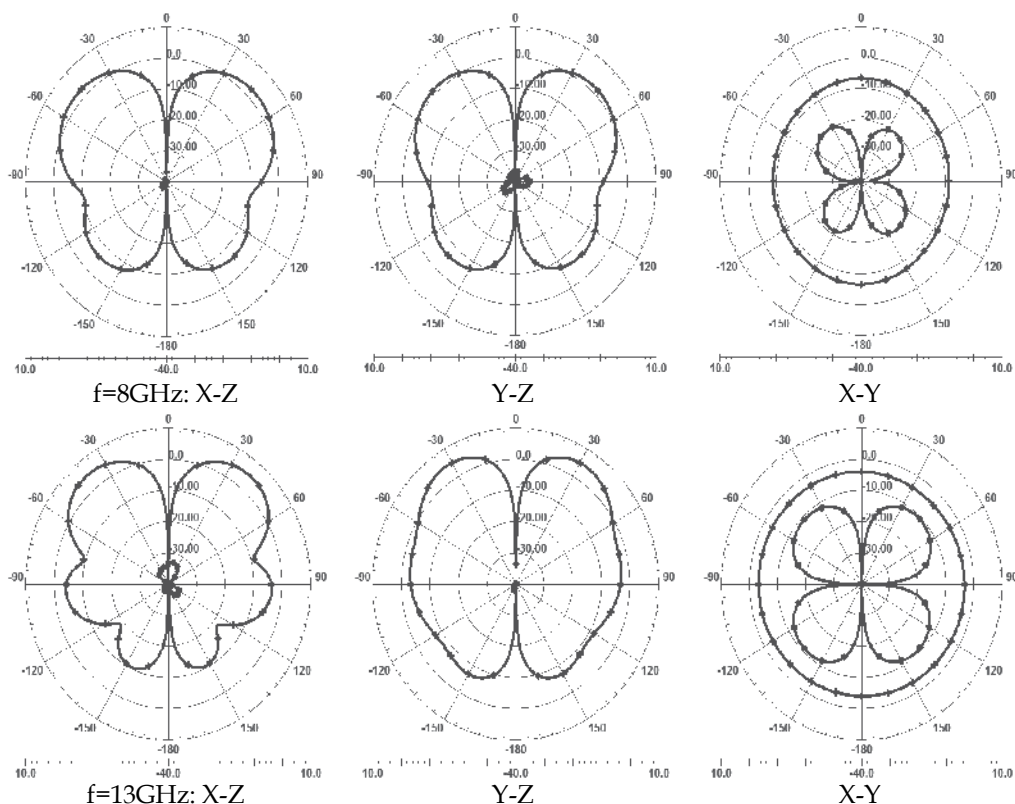
Fig. 11. Radiation Patterns for the antenna with return loss curve shown in Fig. 10

The study in section 3 showed that, the ground plane size can be reduced to 20x20 mm² to have a lower frequency edge of 2.1 GHz with some deterioration in the radiation pattern curves of the antenna. Also the total height of the antenna can be increased from 20mm to 30 mm to compensate for the change in the radiation pattern and to further reduce the lower frequency edge to 1.5 GHz. In section 4, this square monopole antenna with the trident feeding strip will be used to design a UWB Yagi monopole antenna over aground plane.

4. UWB Yagi monopole antenna

In the last part of this study, a UWB Yagi monopole antenna over a ground plane is designed and analyzed to work over the UWB communication band. The antenna is relatively small in size and the driven element is based on the square monopole antenna with trident feeding strip designed in section 2. The first step in designing such a Yagi monopole is by having a driven element and one reflector, possibly of the same shape as the driven element, and at different distances on The Y-axis from it. The second step is to optimize the ground plane size for the best impedance bandwidth. The third step is to design a slot in the square ground plane to isolate the effect of the reflector on the impedance bandwidth. Fig. 12 shows Yagi monopole antenna with a 1 mm wide square slot at 10mm distance from the centre of the ground plane. The distance between the driven element and the reflector is d, while the ground plane size is GxG mm². Simulation results

show better performance of such antenna with the slot in the ground plane, between the radiator and the reflector. Then the reflector is moved on the Y-axis behind the driven element to optimize the maximum impedance bandwidth. It is clear from Fig. 13 that the antenna has the maximum impedance bandwidth with lower frequency of about 3GH when the reflector is at a distance d=20mm from the driven element. Fig. 14 shows some of the radiation pattern curves of this antenna for illustration purpose. Simulation results indicate a good performance of this Yagi monopole antenna with only one reflector and no directors as a directional UWB monopole antenna for communication applications.
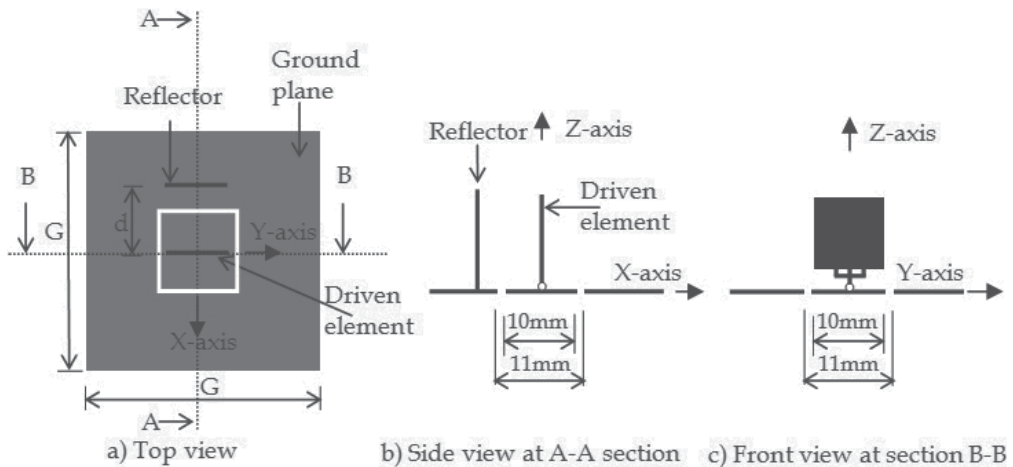
Fig. 12. Yagi monopole antenna with GxGmm² ground plane. One driven element and one reflector at distance d from the driven element . Driven elemnt has same parameters as those in Fig. 7. 1mm slot at distance 10mm from the ground plane centre.

Directors can be used in front of the radiators to further increase the directive gain of this antenna. It is found that by using only one director of the same shape as the driven element with 4mm reduction in height and at 20mm distance, directive gain increased. However, this antenna needs more investigation for minimizing the back lobe level.
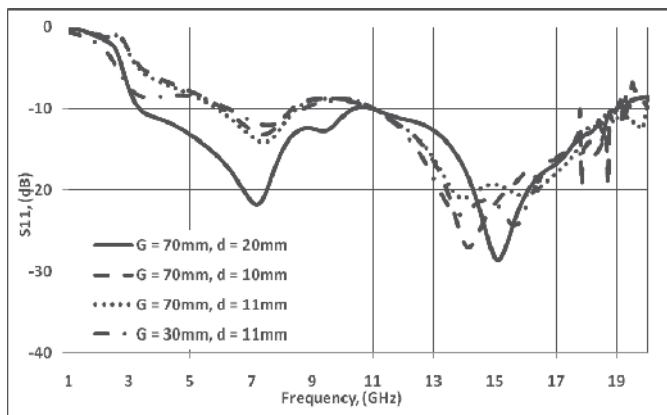
Fig. 13. Return loss curve for Yagi monopole antennas in Fig. 12

f=3GHz: X-Z   Y-Z   X-Y

f=8GHz: X-Z   Y-Z   X-Y
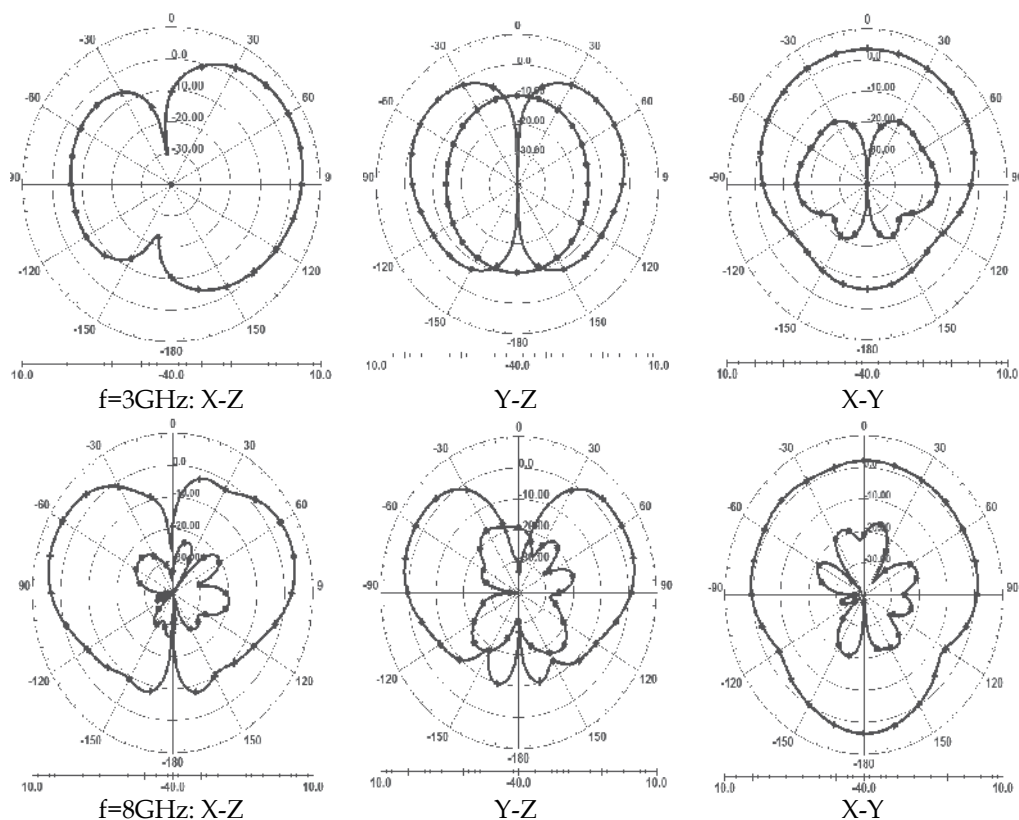
Fig. 14. Radiation patterns for the antenna shown in Fig. 12, G= 70mm, d=20mm

Note also that, the trident feeding was used for the single element to improve its impedance bandwidth. This is not necessary for all elements of the Yagi antenna. The reflector and the directors, could have other shapes, such as a simple square monopole of proper size. More research is needed to determine the optimum parameters for satisfactory front to back ratios over the entire band. The example given here was to show the possibility of beam shaping using additional elements, while keeping the wide impedance bandwidth of the antenna.

5. Building and testing some of the studied monopole antennas

To verify the performance of the antennas studied in section 2 through section 4, some of those antennas have been built and tested at The University of Manitoba Antenna Lab. All antennas modelled so far were considered as metal plates mounted vertically over a horizontal ground plane. Metal was considered perfect conductor during simulation processes using Ansoft-HFSS software, a finite element method full wave solver, (Ansoft, 2011). However to overcome the problem of deformation in the planar shape of the metal plates when mounted on the ground plane, each antenna was etched on a 22 x 22 mm² substrate with 0.8mm thickness and permittivity ε_r = 2.5. This configuration also solved the problem of soldering the metal plate to the connector without damaging it. Ground plane used in the measurements was a sheet of Aluminium because of its light weight and capability of keeping its flatness. Fig. 15 shows one of the designed antennas after being

mounted on the Aluminium ground plane and connected to The Vector Network Analyzer for return losses measurements.
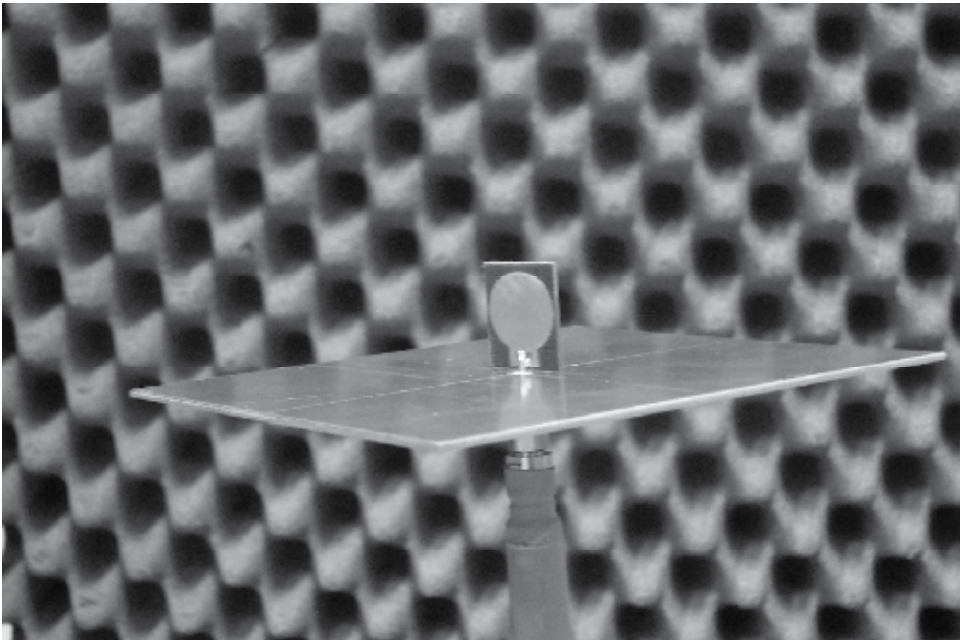
Fig. 15. Circular monopole antenna mounted on a 120x120mm² Aluminium ground plane and ready to be tested at University of Manitoba Antenna Lab using Anritsu 37397C Vector Network Analyzer
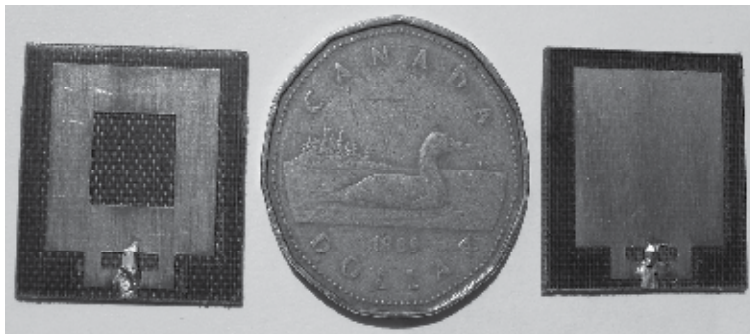
Fig. 16. Square monopole antennas of Fig. 1a and Fig. 1c etched each on a 22x22mm² substrate with ε_r=2.5, height=0.8mm. Antennas are compared to the Canadian Dollar Coin before being mounted on the Aluminium ground plane

Fig. 16 shows the square monopole antenna with trident feeding strip with and without central metal removal, studied in Section 2.2. Metal plates are etched on a 22x22mm² single sided metal. Fig. 17 shows the return loss curves of both antennas after being mounted on a 120x120mm² Aluminium ground plane. Measured results are compared to simulated ones. As can be seen, there is a good agreement between measured and simulated return loss

curves regarding lower frequency edge and resonance frequencies. There is a shift in some resonance frequencies and the upper frequency edge. Same notations can be seen also in the circular monopole antenna with and without central metal removal shown in Fig. 18 and their return loss curves shown in Fig. 19. Elliptical monopole antennas with and without central metal removal are shown in Fig. 20 and compared to the Canadian Dollar Coin to show their sizes. The Return loss curves of the two elliptical monopole antennas are shown in Fig. 21.
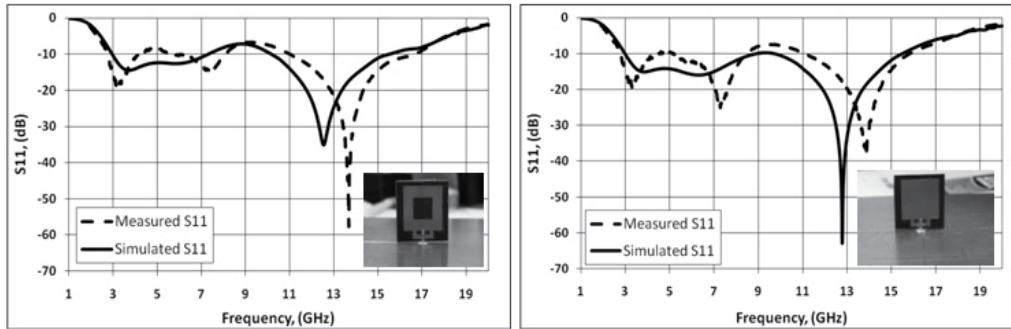
Fig. 17. Return loss curves for the square monopole antennas shown in Fig. 16

Fig. 18. Circular monopole antennas of Fig. 3a and Fig. 3c etched each on a 22x22mm² substrate with ε_r=2.5, height=0.8mm. Antennas are compared to the Canadian Dollar Coin before being mounted on the Aluminium ground plane
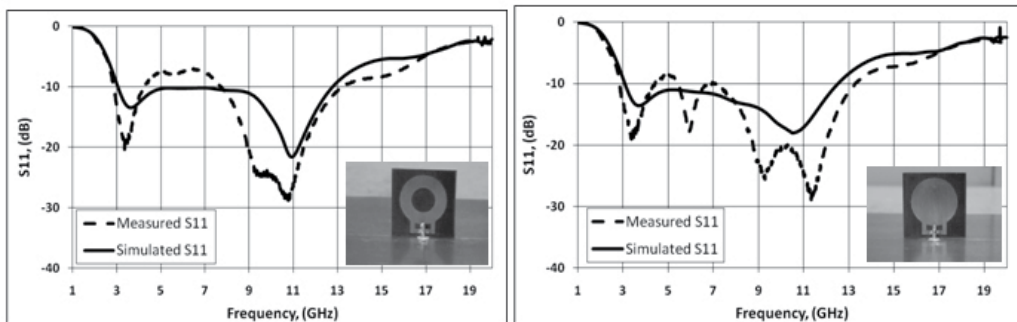
Fig. 19. Return loss curves for the circular monopole antennas shown in Fig. 18
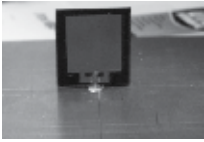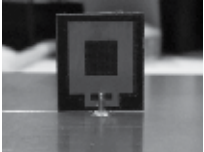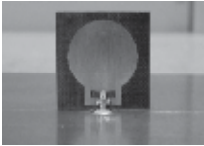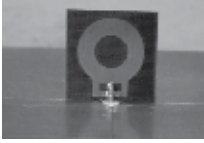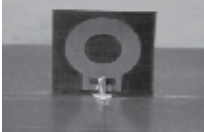
Maximum group delay (ns) measured over the entire frequency band, 3 to 20 GHz	
Square monopole antenna 	0.2325 ns
Square monopole with central metal removal 	0.2406 ns
Circular monopole antenna 	0.3154 ns
Circular monopole with central metal removal 	0.2811 ns
Elliptical monopole antenna 	0.2377 ns
Elliptical monopole with central metal removal 	0.2703 ns

Table 1. Maximum group delays measured over the frequency band, 3-20 GHz
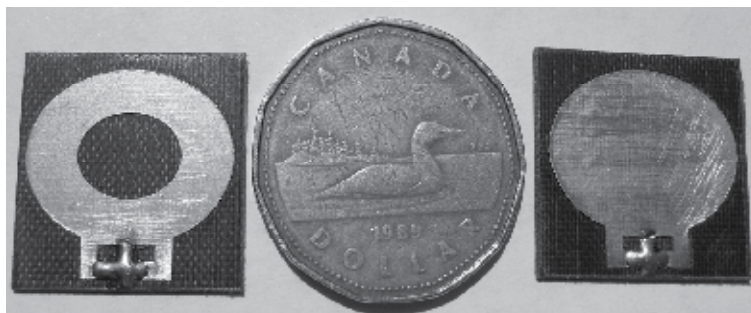
Fig. 20. Elliptical monopole antennas of Fig. 5a and Fig. 5c etched each on a 22x22mm² substrate with ε_r=2.5, height=0.8mm. Antennas are compared to the Canadian Dollar Coin before being mounted on the Aluminium ground plane
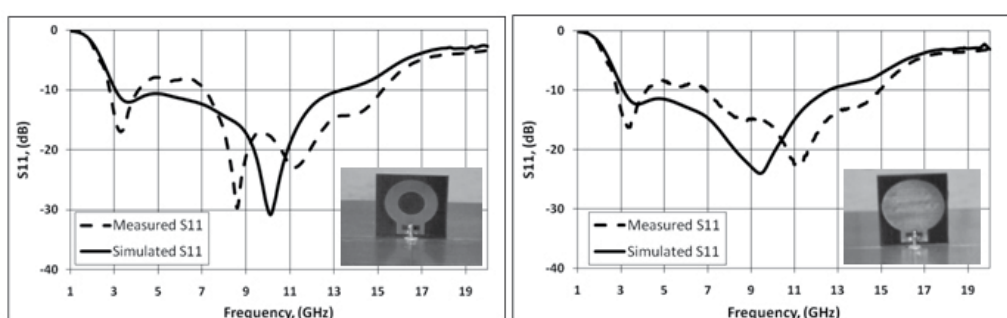
Fig. 21. Return loss curves for the elliptical monopole antennas shown in Fig. 20

To further understand how the signal transmitted or received from these antennas will be distorted; the group delay curves of the tested antennas are measured. Table 1 shows the maximum group delay of each antenna over the entire frequency band of operation, from 3 to 20 GHz. As can be seen from Table 1, all monopole antennas tested have group delay less than 0.5 ns which is less than that of the circular disc monopole with single strip feed, (Gue et al., 2007).

6. Conclusion

In this chapter, different UWB monopole antennas were studied. Square, circular and elliptical monopole antennas showed UWB impedance bandwidth that covered the existing defined ultra wideband communication band 3.1 to 10.6 GHz, and extended beyond that to 19.5 GHz for future applications. It was found that implementing notches close to the trident-feeding strip structure did not increase the impedance bandwidth of circular and elliptical antennas. Further, implementing a notch decreased the impedance bandwidth of the square monopole antenna. On the other hand, removing metal from the interior structure of the square, circular and elliptical monopoles gave the same impedance bandwidth for square and circular monopole and increased the bandwidth of the elliptical one. The circular and elliptical monopole antennas with metal removed showed better omnidirectional behaviour at higher frequencies. Some of the studied monopole antennas were built and tested. Antennas were etched on a substrate to keep their planar shape and

then mounted on an Aluminium ground plane. Return loss curves showed good agreement between measured and simulated ones. Radiation pattern measurements will also be done to confirm simulation results. The size of the ground plane was optimized to decrease the lower edge of the impedance bandwidth and slots were implemented to isolate the effect of this small ground plane on the radiation pattern of the antenna. Also, a UWB Yagi monopole antenna over a 70x70mm² ground plane was designed to cover the existing and upcoming communication applications. Both reflectors and directors were used to enhance the directivity of the antenna and decrease the back lobe levels. The future work on this UWB Yagi monopole will study how to minimize back lobe levels and determine the phase centre location at different frequencies and different planes.

7. References

Ansoft Corporation, (2011) HFSS: High Frequency Structure Simulator Based on the Finite Element Method [Online]. Available: http://www.ansoft.com/products.cfm

FCC, The Federal Communications Commission First Report and Order on Ultra-Wideband Technology, Part 15, Subpart F, Washington, D. C. 20554, Adopted: February 14, 2002, Released: April 22, 2002

Ferrando-Bataller, M. ; Cabedo-Fabres, M. ; Antonio-Daviu, E. and Valero-Nogueira, A. (2006). Overview of planar monopole antennas for UWB applications. *Proceedings EuCAP*, ISBN 92-9092-937-5, Nice, France, 6-10 Nov. 2006

Gue, L. ; Liang, J. ; Chiau, C. C. ; Chen, X. ; Parini, C. G. and Yu. J. (2007). Performances of ultra-wideband disc monopoles in time domain. *IET Microwaves, Antennas & Propagation*, vol. 1, issue 4, (2007), pp. 955-959, ISSN 1751-8725

Hammoud, P. P. and Colomel, F. (1993). Matching the input impedance of a broadband disc monopole, *Electronics Letters*, vol. 29, issue 4, (Feb. 1993), pp. 406-407, ISSN 0013-5194

Honda, S. ; Ito, M. ; Seki, H. and Jinbo, Y. (1992). A disc monopole antenna with 1:8 impedance bandwidth and omni-directional radiation pattern, *Proceedings ISAP*, Sapporo, Japan, pp. 1145-1148, Sep. 1992

Martinez-Fernandez, J. ; Gil, J. M. and Zapata J. (2010). Profile optimisation in planar ultra-wideband monopole antennas for minimum return losses. *IET Microwaves, Antennas & Propagation*, vol. 4, issue 7, (2010), pp. 881-892, ISSN 1751-8725

Mohamed, A. & Shafai, L. (2007). Ultra Wideband Loop Monopole Antennas, *Proceedings International URSI Commission B Electromagnetic Theory Symposium "EMTS"*, ISBN 978-0-9738425-3-1,Ottawa, ON, Canada, July 26-28, 2007

Schantz, Hans G., (2005). *The Art and Science of Ultra Wideband Antennas*, ARTECH HOUSE, INC., ISBN 1580538886, Boston, USA

Wong, K. ; Wu, C. and Su, S. (2005). Ultrawide-band square planar metal-plate monopole antenna with a trident-shaped feeding strip. *IEEE Trans. Antenna Propag.*, vol. 53, issue 4, (April 2005), pp. 1262-1269, ISSN 0018-926x

Wu, Q. ; Jin, R. and Geng, J. (2009). Ultra-wideband qusi-circular monopole antennas with rectangular and trapezoidal grounds. *IET Microwaves, Antennas & Propagation*, vol. 3, issue 1, (2009), pp. 55-61, ISSN 1751-8725

Ultra-Wideband Printed Antennas Design

Mohamed Nabil Srifi[1] and M. Essaaidi[2]
[1]National School of Applied Sciences, Ibn Tofail University Kenitra
[2]Abdelmalek Essaadi University
Morocco

1. Introduction

On February 14, 2002, the Federal Communications Commission (FCC) of the United States adopted the First Report and Order that permitted the commercial operation of ultra wideband (UWB) technology (FCC, 2002). The FCC allocated a bandwidth of 7.5GHz, i.e. from 3.1GHz to 10.6GHz, to unlicensed use for UWB applications. Ultra Wideband is defined as any communication technology that occupies greater than 500 MHz of bandwidth, or greater than 25% of the operating center frequency. The UWB spectral mask was defined to allow a spectral density of -41.3 dBm / MHz throughout the UWB frequency band. UWB technology has several advantages that are the reasons that make it very attractive for consumer communications applications; it has been regarded as one of the most promising wireless technologies that have a capability of revolutionizing high data rate transmission and enables the personal area networking industry leading to new innovations and greater quality of services to the end users.

Ultra wideband systems present several advantages *i*) have potentially low complexity and low cost; *ii*) have noise-like signal which makes unintended detection quite difficult, because of their low average transmission power, UWB communications systems have an inherent immunity to detection and interception; and low power consumption; *iii*) are resistant to severe multipath and jamming; and *iiii*) have very good time domain resolution allowing for location and tracking applications. Also UWB systems can penetrate effectively through different materials. The low frequencies included in the broad range of the UWB frequency band have long wavelengths, which allow UWB signals to penetrate into a variety of materials, such as walls. This advantage makes UWB technology favourable for through the wall communications, ground penetrating radar, body implant wireless communications...

Since UWB has an ultra wide frequency bandwidth, it can achieve huge capacity as high as hundreds of Mbps or even several Gbps with distances of 1 to 10 meters (Oppermann, 2004).

UWB systems operate at extremely low power transmission levels, and hence UWB signals do not cause significant interference to other wireless systems. The UWB technology is one of the viable candidates for short-range indoor radio communication systems supporting very high bit rates services and applications.

In this chapter, different aspects and challenges of UWB antennas design are discussed. And compact printed disc monopole antenna (3.5 to 31.9 GHz) for current and future ultra wideband applications will be presented.

2. Antennas for ultra wideband systems

Unlike conventional narrowband communication systems, UWB occupies a bandwidth of several GHz. Consequently, the antennas in UWB systems play a more important role than in other systems since they actually act as a band pass filter to reshape the pulse spectra so they should be carefully designed to avoid unnecessary distortions. UWB systems design are much more challenging than for conventional narrowband systems.

The systems must produce broad operating bandwidths for impedance matching, high gain transmissions in the desired direction, stable transmission patterns and gains, consistent group delays, high transmission efficiency, and low profiles. Various studies have been devoted to evaluating the performance of UWB antennas (Agrawall et al., 1998; Amman & Chen, 2003; Hertel & Smith, 2003; Klemm et al., 2005; MaTG & Jeng, 2005).

2.1 Printed monopole antennas

The huge development in communication technology and the significant demands of wireless communication systems, lead to a fast evolution in the antennas design to take up the challenges in size and performances. Antennas are considered to be the largest components of integrated wireless systems; thus antenna miniaturization is a necessary task to achieve an optimal design for integrated wireless and mobile communication systems. The microstrip antennas present good solution and play an important role in the development of the new generation of wireless and mobile communication systems.

These antennas have several advantages compared to the conventional microwave antennas. The main advantages are: lightweight, small volume, low-profile, planar configuration, compact, can be made conformal to the host surface, easy integrated with printed-circuit technology and with other MICs on the same substrate, low cost, allow both linear polarization and circular polarisation. On the other hand, theses antennas suffer from some disadvantages as compared to conventional microwave antennas, due to the fact that they have narrow bandwidth, lower gain, and Low power handling capability (Kumar & Ray, 2003).

The printed monopole antennas give very large impedance bandwidth with reasonably good radiation pattern in azumuthal plane.

2.2 UWB antenna design

As already mentioned, ultra wideband wireless communication systems are defined as any radio system that has a -10dB bandwidth larger than 25 % with respect to the center frequency. UWB is a carrier-less short range communications technology which transmits the information in the form of very short pulses.

2.2.1 UWB antennas criteria

The antenna has a greater impact in UWB than in narrower band systems because of the very large bandwidth of an UWB signal.

In the literature, several antenna types have been presented for use in UWB systems. In addition to the fundamental parameters that must be considered in designing antennas for any radio application, there are additional challenges for Ultra Wideband antennas. Antennas play a critical role in the UWB communication systems, since they act as pulse-shaping filters (Chen et al., 2004).

Based on return loss (>-10dB) or voltage standing wave ratio (VSWR<2), the impedance bandwidth can be determined. The bandwidth ΔBW is a frequency span determined by the upper frequency band limit f_2 and the lower limit f_1:

$$\Delta BW = f_2 - f_1;$$

and the center frequency f_c is defined as:

$$f_c = \frac{f_1 + f_2}{2}$$

2.2.2 UWB antennas requirements

The UWB antenna must achieve almost a decade of impedance bandwidth, spanning 7.5 GHz. The portable UWB systems are the main promising issue of UWB applications. For this, antennas must be small size, conformal design, low cost, easily integrated into other RF circuits. UWB antennas should have stable response in terms of impedance matching, gain, radiation patterns, phase, and polarization within the operating band. Moreover, the requirements for broad bandwidths are associated with other crucial constraints such as small size and low cost because most promising UWB applications will be portable devices (Arslan et al., 2006).

In addition, two essential design considerations for UWB antennas should be emphasized: 1) the power density spectrum (PDS) shaping of the radiated signals should conform to the emission limit masks for avoiding possible interference with other existing systems, and 2) the source pulses and transmit-receive antennas should be evaluated in terms of the overall system performance (minimal BER). Other crucial criterion of the UWB antennas is associated with the performance of overall transmit–receive antenna systems, due to the fact that UWB systems maintain invariable performance across a wide range of a few gigahertz, which affects the waveforms and spectra of the radiated pulses.

The design considerations of the UWB antennas and source pulses are based on investigating S parameters, transfer functions, systems efficiency, group delay and fidelity. However, in a systems point of view, the key performance parameter for wireless communications is BER, which is formulated in terms of antenna system transmission efficiency, fidelity between the received pulse and the template pulse, and incident power (Arslan et al., 2006).

In impulse radio, transient characteristics of the system are very important. In other words, the transmitted signal must be received at the receiver with minimum distortion. So, the UWB antennas must be as distortion less as possible. Also, due to power limitations specified by FCC mask for indoor UWB communications, UWB antennas must provide a good matching between radiator part and feed section.

The group delay is another consideration that must be taken into account. It will be constant for the frequency range if the phase is linear throughout the frequency range. This indicate how well a UWB pulse will be transmitted and to what degree it may be distorted or dispersed.

A nearly omnidirectional radiation pattern is desirable; this enables freedom in the receiver and transmitter location. Also, high radiation efficiency is imperative for an UWB antenna because the transmit power spectral density is excessively low. Conductor and dielectric losses should be minimized in order to maximize radiation efficiency.

With the great development on UWB technology, there is a growing demand for small and low cost UWB antennas that can provide satisfactory performances in both frequency domain and time domain.

Both transmit and receive antennas can affect the faithful transmission of UWB signal waveforms because of the effects of impedance mismatch over the operating bandwidth, pulse distortion effects, and the dispersive effects of frequency dependent antenna gains and spreading factors (Sorgel et al., 2003).

For UWB communication systems, antennas requirements differ from base station antennas to portable antennas. The base station antenna may be designed for indoor or outdoor usage, and may be either directive or omnidirectional, depending on the application (e.g. directional antennas could be used for example in radio links, whereas omnidirectional antennas would be more favourable in mobile applications). On the other part, the portable UWB antenna must be small and highly desirable to be low cost and preferably constructed on a printed circuit board. The radiation efficiency is not as critical parameter as in base station antennas, which makes it possible to use resistive loading (Oppermann et al., 2004).

The choice of antenna type differs according to the applications. For example, for radar applications a highly directive antenna is preffered, while for point-to-multipoint communications an omnidirectional antenna is desired (Telzhensky & Leviatan, 2006).

It is relatively easy to design a UWB monopole antenna when considering only the impedance bandwidth. But it is difficult to achieve the same radiation pattern bandwidth, due to the significant changes in the antenna pattern at higher frequencies (Shih et al., 2004).

An ideal wideband antenna acts like a high-pass filter, which means that the pulse waveform is differentiated when passing through the antenna. UWB antennas should be linear in phase and should have a fixed phase centre. Typical impedance circuits may not be phase linear, and the antennas should be inherently impedance matched. The UWB antenna gain should be smooth across the frequency band in order to avoid dispersion of the transmitted pulse. On the other hand, the antenna gain appears different from different angles, which lead to different pulse shapes depending on the angle to the receiver (Opperman, 2004).

The performance of a UWB antenna is required to be consistent across the entire operational band: radiation patterns, gains and impedance matching should be stable over the operational band. Sometimes, it is also demanded that the UWB antenna provides the band-rejected characteristic to coexist with other narrowband devices and services occupying the same operational band.

In several context, due to the overlap of the currently allocated UWB frequency band with other existing technologies, such as WLAN2 (5.2GHz (5150–5350 MHz) and 5.8GHz (5725–5825 MHz)), WiMAX (3400–3690 MHz) and C-band (3.7–4.2 GHz), different ways have been used: cutting a proper slot, putting parasitic elements near or rear the printed monopole (Danesfahani et al., 2009; Soltani et al., 2009), C-shaped attachment element in patch (S. Chen et al., 2007), and thus various structures with band rejection characteristic are proposed, such as U-slot, inverted U-slot (Choi et al., 2005), small strip bar (Kim & Park, 2006), H-shaped conductor-backed plane (Zaker et al., 2008), rectangle-shaped plane (W.S. Chen & Yang, 2007), arc-shaped slot (Khan et al., 2008), para- sitic coplanar elliptical patch (H.J. Chen et al., 2008), fractal tuning stub (WenJun et al., 2005), U-slotted tuning stub (S.S. Wen et al., 2005) , or fractal-shape wide slot (WenJun et al., 2006).

2.2.3 Impedance bandwidth improvement

Printed monopole antennas are largely considered for use in UWB systems, due to theirs attractive features. Circular planar monopole antennas show basic characteristics of the planar UWB antennas.

The limited impedance bandwidth of planar monopole antennas should be improved to satisfy UWB applications. Several attempts have been made to increase their operation bandwidth (Behdad & Sarabandi, 2004; H.D. Chen, 2003; Lee et al., 2002; WenJun, 2005, 2006; Sze & Wong, 2001).

Different structures with a simple bevel (Amman et al., 2001, 2003), with shorting pins (Amman & Z.N. Chen, 2003), using smooth rounded elements (Agrawall et al., 1998; Wu et al., 2007a, 2007b) and using fractal elements (Ding et al., 2007; Gianviffwb & Rahmat-Sammi, 2002) have been designed for the bandwidth enhancement, and several techniques have been proposed, such as adding steps to the lower edge of the patch Kim & Park, 2006), the insertion of additional stub to the one side of circular patch (Choi et al., 2005) and adding of the slit on one side of the radiating element (Wang et al., 2004), the use of feedgap optimization (John, 2005), bevels (Amman, 2001), groundplane shaping (Zhang & Fathy, 2007) multiple feeds (Antonino et al., 2003), and offset feeding techniques (Amman & Z.N. Chen, 2004), and introducing slit into the groundplane (Bao, 2007).

3. Printed disc monopole antenna for future UWB applications

In the last few years, circular monopole antennas have been studied extensively for UWB communications systems because of some appealing features (easy fabrication, feedgap optimization alone gives wide impedance matching and omnidirectional radiation patterns).

One of the strongest contenders in terms of good impedance bandwidth, radiation efficiencies, and omnidirectional radiation patterns are the circular disc monopole (CDM) and elliptical antennas (Abbosh & Bialkowski, 2008; Allen et al., 2007; Antonino et al., 2003, Liang et al., 2004; Powell, 2004; schartz, 2005; Srifi et al., 2009).

There is great demand for UWB antennas that offer miniaturized planar structure, so the vertical disc monopole is still not suitable for integration with a PCB. This drawback limits its practical application. For this reason, a printed structure of the UWB disc monopole is well desired, which consist on printed radiator disc on substrate. Printed CDM antennas can be fed simple microstrip line, coplanar waveguide (CPW), or slloted structures.

3.1 Geometry of the proposed antenna

The increased development on wireless technologies demands small and compact systems with high transmission speeds. This requires higher operating bandwidths for the next generation ultra wideband systems. For this reason, antennas have to be capable to provide bandwidth much larger than the currently band defined by FCC.

The proposed UWB antenna (Srifi et al, 2009) consists of a circular disc with a radius of R=7.5mm, printed in the front of dielectric substrate of 30mm x 35mm x 0.83mm dimensions and a relative permittivity of 3.38, as shown in figure 1. On the other side of the substrate, the partial ground plane with a length of 15.6mm only covers the section of the microstrip feed line. The width of the ground plane is 30mm.

For this design, it was observed that operational bandwidth of the CDM antenna is from 3.3GHz to 10.6GHz.

Fig. 1. The prototype of the proposed simple fed CDM antenna

As previously discussed, various techniques have been proposed to improve the matching over a broad bandwidth, such as: feed gap optimization, bevels, ground plane shaping, multiple feeds, and slit into the ground plane…

In this work, the bandwidth of a compact printed circular antenna is improved by introducing one and two microstrip lines between the feed line and the printed disc, which gives two design structures: antenna1 (single microstrip line transition) and antenna2 (dual microstrip line transition).

Antenna2 is modified by adding a second microstrip line between the feedline and the circular disc patch on the antenna.

Figures 2-3 show geometry of both antenna1 and antenna2.
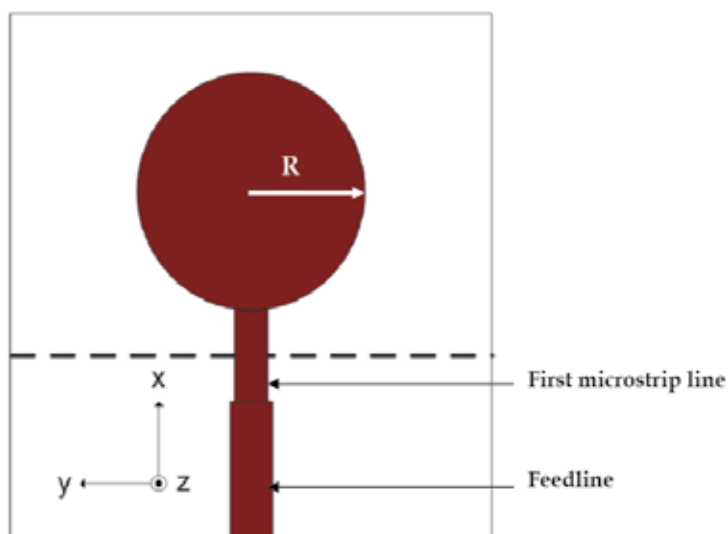
Fig. 2. Geometry fo antenna1 (single microstrip line transition)
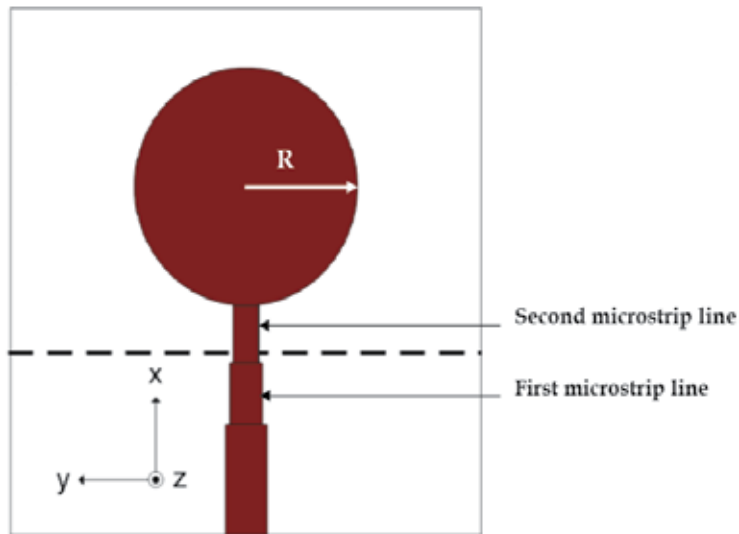
Fig. 3. Geometry fo antenna2 (dual microstrip line transition)

The following table resumes data corresponding to the proposed antenna

Width of the substrate	W	30 mm
Length of the substrate	L	35 mm
Width of the feed line	W_f	1.8 mm
Length of feed line	L_f	8 mm
Width of the first microstrip line	W_1	1.4 mm
Length of the first microstrip line	L_1	5 mm
Width of the second microstrip line	W_2	1 mm
Length of the second microstrip line	L_2	3 mm
Radius of the printed disc	R	7.5 mm
Length of the partial ground plane	L_g	15.6 mm
Dielectric permittivity	ε_r	3.38
Thickness of the substrate	H_{sub}	0.83 mm

Table 1. Dimensions of the proposed antenna

These microstrip lines, with different impedance characteristic, allow the control of the impedance bandwidth and return loss level by modifying the capacitance between the patch and the ground plane.
The proposed antennas are fabricated and tested in Royal Military College of Canada (RMC), Kingston, Ontario, Canada. Prototypes of antenna1 and antenna2 are illustrated on figure 4-5.

3.2 Experimental and simulated results
Initially reflection loss measurements of the two antennas were completed in an anechoic chamber, as shown in Figure 6.
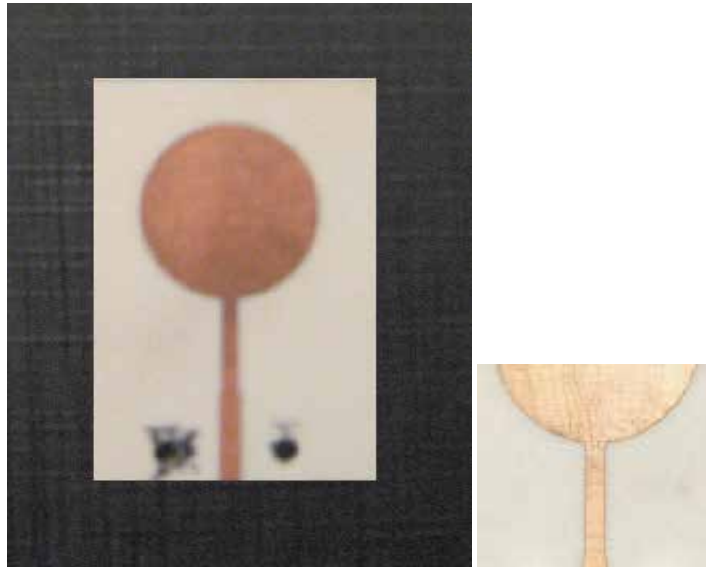
Fig. 4. Prototype of antenna1
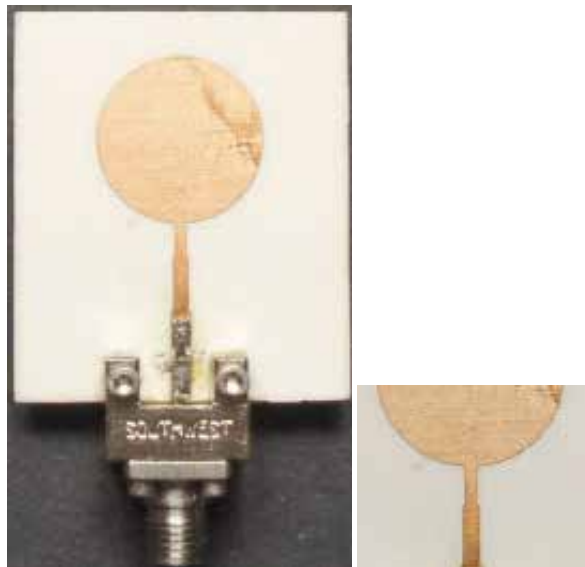
Fig. 5. Prototype of antenna2

A single S11 port calibration was completed on a Anritsu 37377C VNA from 0.2 GHz to 40 GHz with 1601 data points. The proposed antennas were connected to a SouthWest Microwave (SWM 1092-03A-5) K Connector. The end launch connector was only rated to 40 GHz (2.92 mm) and thus measurements above this frequency were not trusted.

The impedance bandwidth is improved by addition of a second microstrip line between the feed line and the printed disc (antenna2).

For the first antenna (Antenna1), return loss measurement results, as shown in Figure 7, illustrate |S11| is below -10 dB from 3.18 GHz to 11.74 GHz.

Reflection loss measurements of the second UWB antenna (Antenna2) were completed and results are shown in Figure 8. A performance increase is observed; i.e. |S11| is below -10 dB from 3.5 GHz to 31.94 GHz.
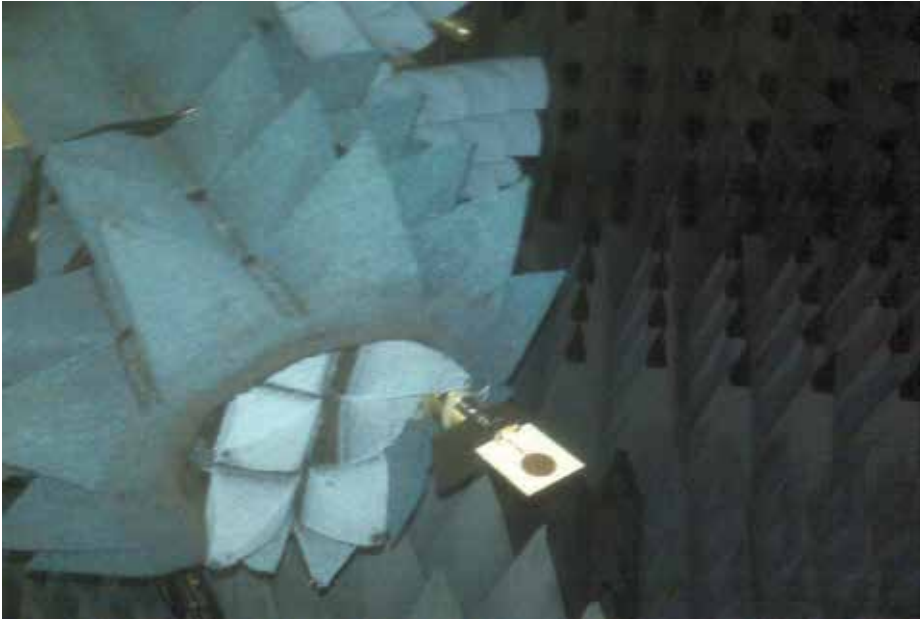
Fig. 6. Photograph of the proposed antenna in an anechoic chamber
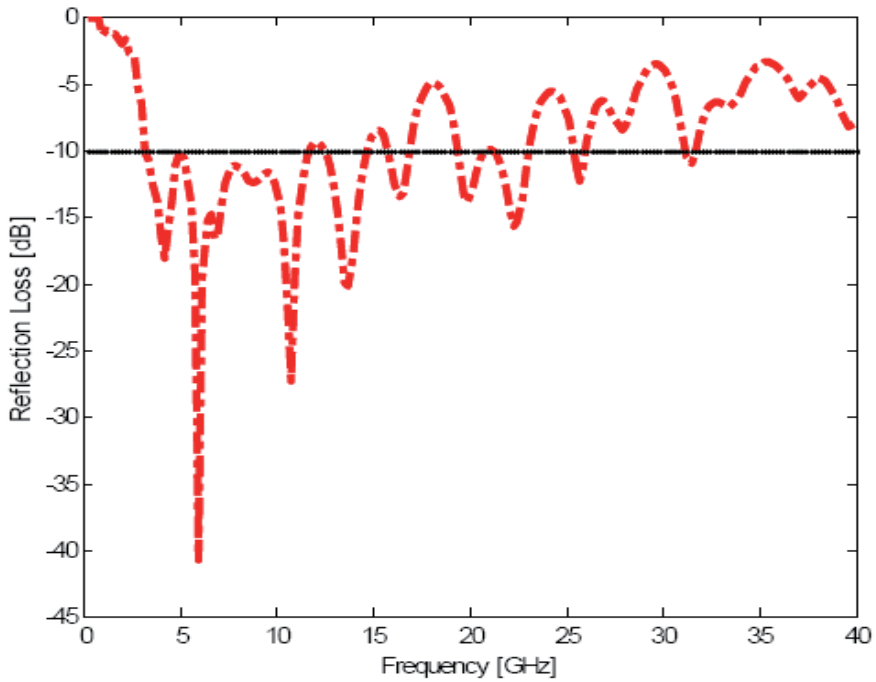
Fig. 7. Measured Return Loss of the first proposed antenna (Antenna1)
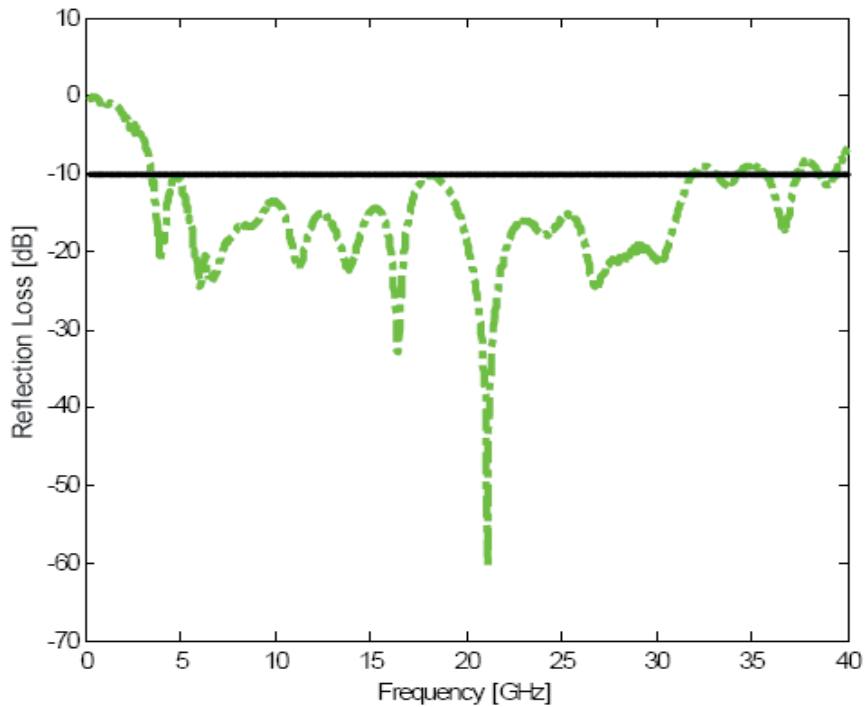
Fig. 8. Measured Return Loss of the modified antenna (Antenna2)

The measurements of Radiation pattern of the proposed antenna were completed in an anechoic chamber. Measured radiation patterns for antenna1 and antenna2, at 3.4GHz and 30.1GHz are illustrated in figures 9-10.
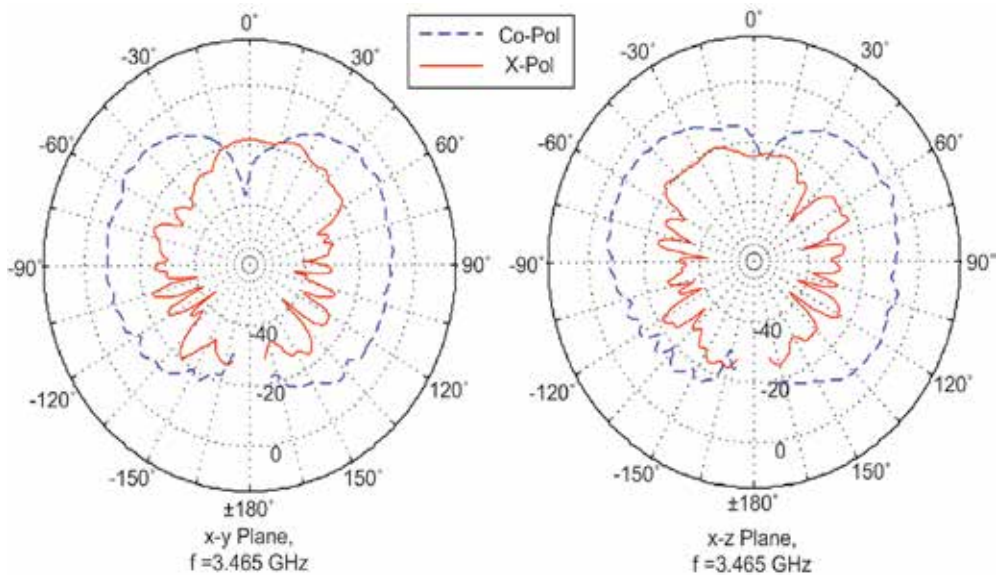
Fig. 9. Measured Return Loss of the antenna1 (single microstrip line transision)
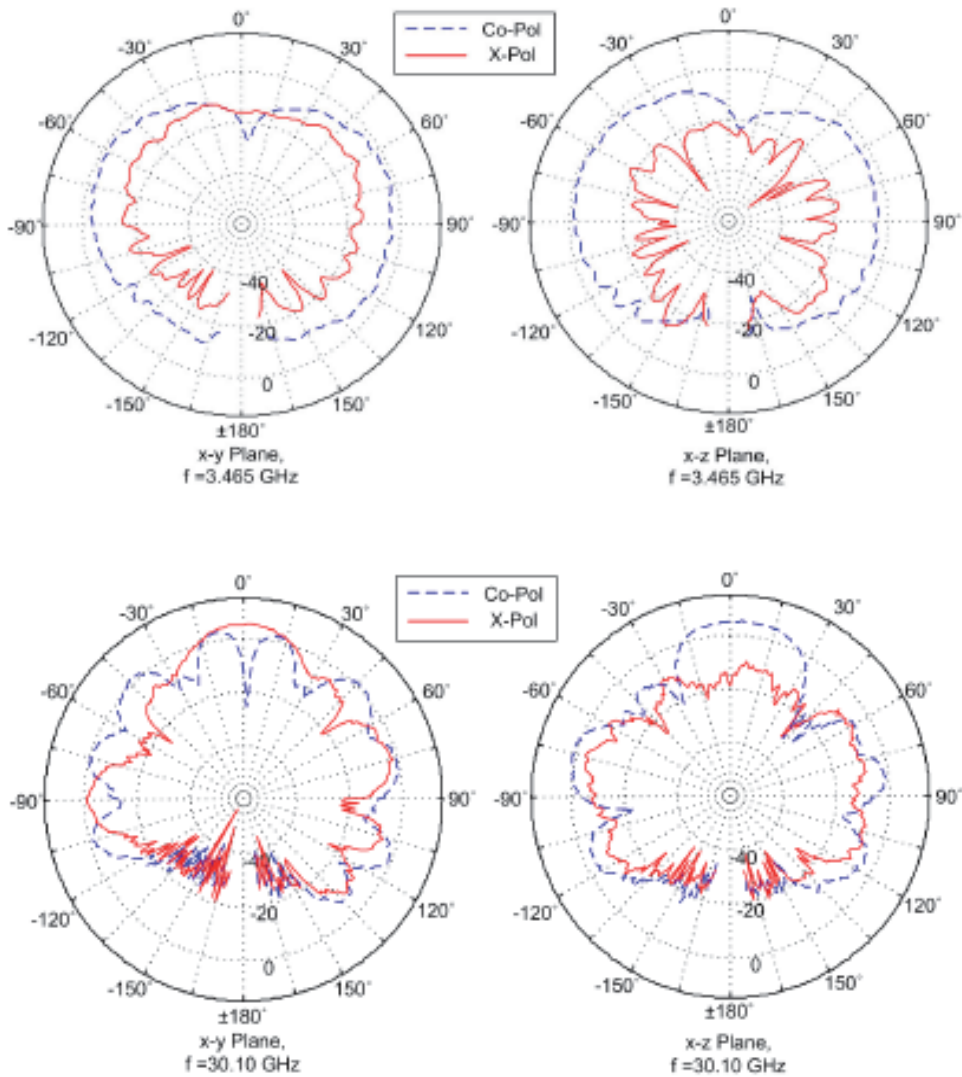
Fig. 10. Measured radiation pattern of the Antenna2 (dual microstrip line transision) at 3.4GHz and 30.10GHz

The simulated current field distributions on the antenna close to the measurement resonance frequencies (5.2GHz, 9.5GHz, and 23.5GHz) are plotted in figures 11-13.

It is observed that the current distribution is mostly concentrated near the edge of the ground plane in the closed region to the disc radiator element, while on top of the structure the current are primarily distributed along the contour of the disc (edge) and feed line on the top edge of ground plane, this leads to confirm that the performance of the antenna is almost independent of the length of the ground plane, but highly dependant to its width.
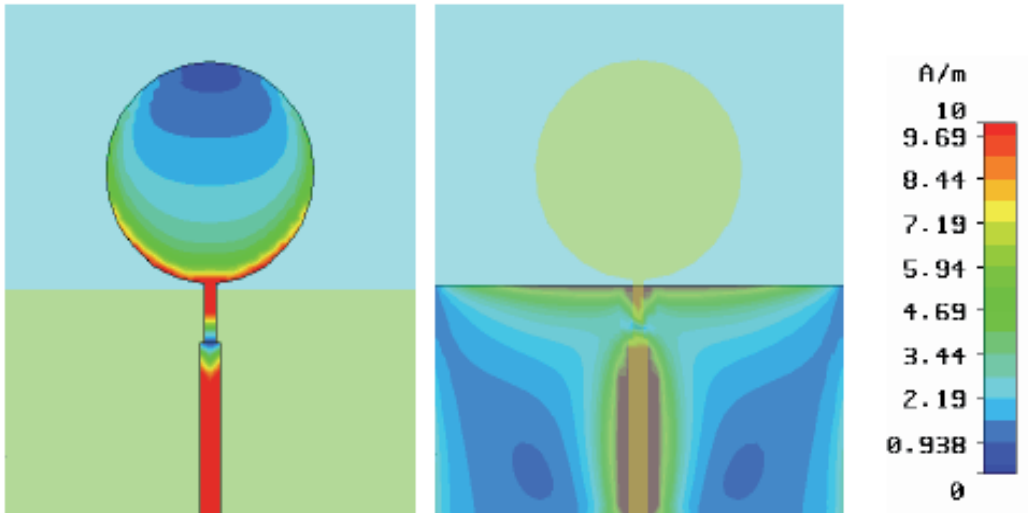
Fig. 11. Simulated current distribution on the disc monopole and ground plane at 5.2GHz
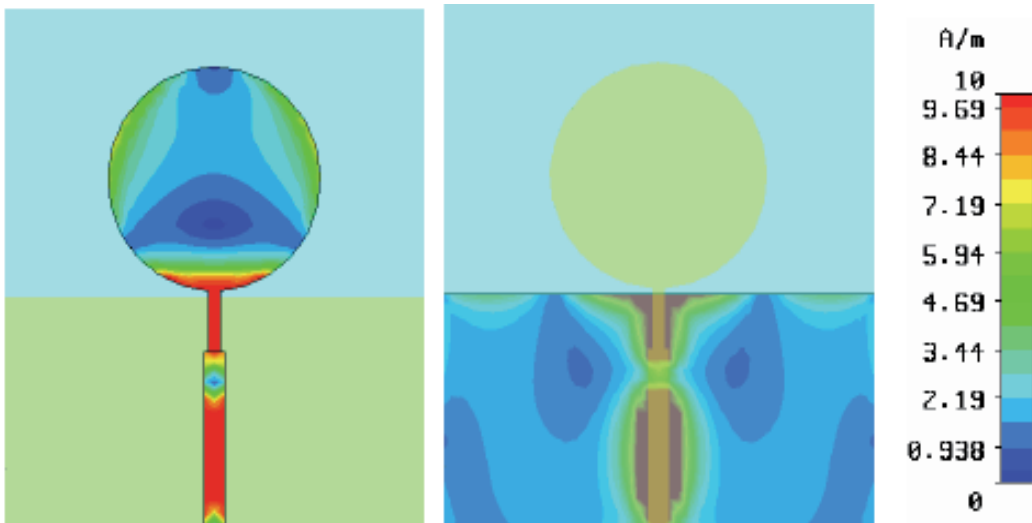
Fig. 12. Simulated current distribution on the disc monopole and ground plane at 9.5GHz
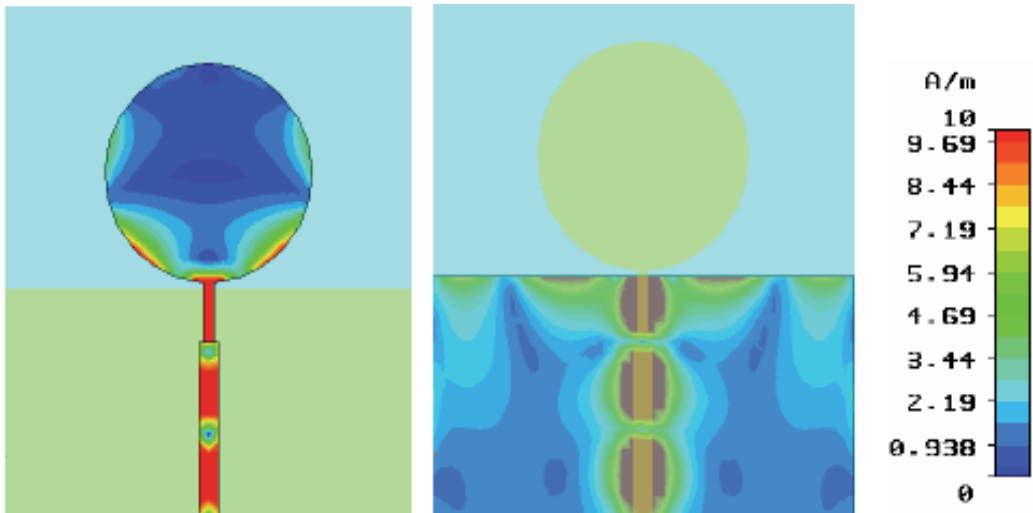
Fig. 13. Simulated current distribution on the disc monopole and ground plane at 23.5GHz

4. Printed arms monopole antenna

The design of antennas operating in multi-band (Guo et al., 2004, Lee et al., 2000, Llorens et al., 2003; Sindou et al., 1999) allows the wireless devices to be used with only a single antenna for multiple wireless applications, and thus permits to reduce the size of the space required for antenna on the wireless equipment.

In this section, we present dual band antenna designed for two promising technologies 3G and UWB wireless communication systems (srifi et al., 2009).

The geometrical configuration of this antenna, especially the size and position of the arms, and size of the slot on the partial ground plane, are the critical parameters that permit to obtain the desired operational bands, which cover several mobile and wireless communication technologies: IMT-2000, PCS (1850-1990 MHz), UMTS (1920-2170 MHz), IEEE 802.11j, a, the US-NIi, HIPERLAN2 (5.470 –5.725 GHz) frequency band, and the 5.8 GHz ISM band. The UWB frequency range for this antenna is from 5.15 to 8.22 GHz. A third frequency band, with a low level, is also observed around 3 GHz.

The antenna consists on six printed arms on the Rogers substrate (dielectric permittivity of 3.38, dielectric loss tangent of 0.0027). The substrate dimensions are of 16mm×36mm×0.83mm.

To improve the impedance matching, a rectangular slot with a size of 4mm×4mm is introduced on the partial ground plane. Figure 14 shows the prototype of the proposed antenna, a) top view, and b) bottom view.

Figure 15 plots measured return loss of the planar monopole antenna. Two frequency bands are observed: 1.8-2.3GHz, 5.16-8.12 GHz, and additionally a third band at 3.07-3.32 GHz with low reflection coefficient (-10.7 dB). The middle band is highly affected by the length of the feed line Lf, as shown in figure 5.5. By varying Lf values, the operational bands of this antenna can include other technologies such as WiMAX.

The measured radiation pattern of the proposed antenna at 2, 5.5, 5.8 and 7 GHz are illustrated in figure 16. These patterns show an omnidirectional radiation characteristic, with good gain values.

The proposed compact printed monopole antenna for ultra wideband and third generation mobile and wireless communication systems is easy to manufacture, low-cost, and can be easily integrated within the printed circuit boards (PCBs) of notebook computers, mobile terminals, and other wireless networking equipment.

By modifying antenna design parameters (mainly the size of the microstrip arms and the slot on the partial ground plane) the proposed antenna can be used also for other technologies such as WiMAX, and become thus triband antenna.
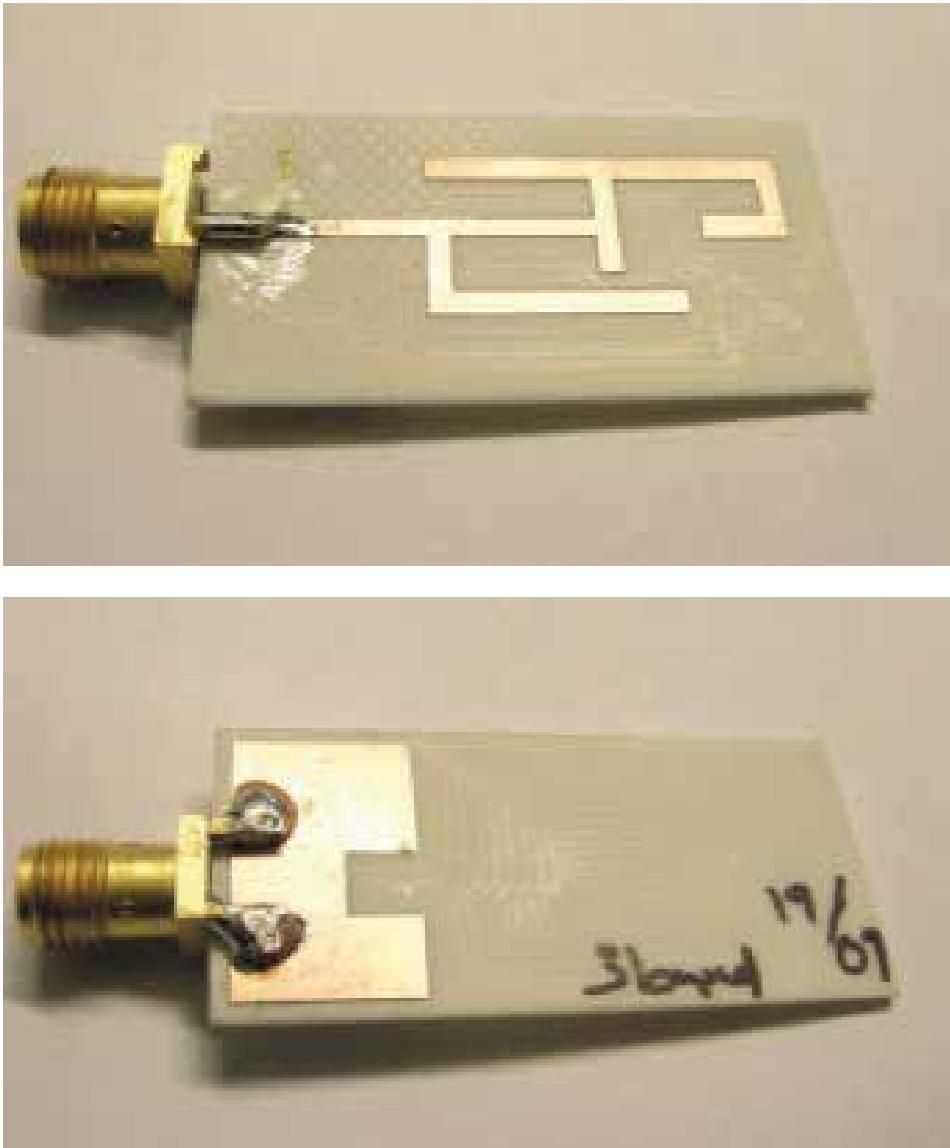
Fig. 14. Prototype of the planar monopole antenna
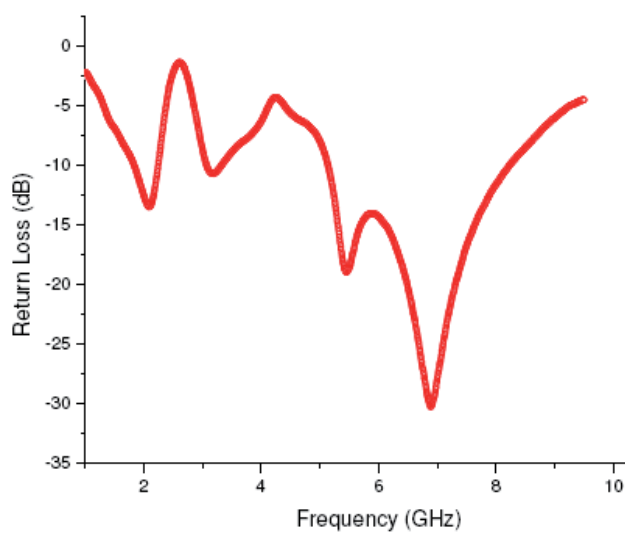
Fig. 15. Measured return loss of the proposed antenna
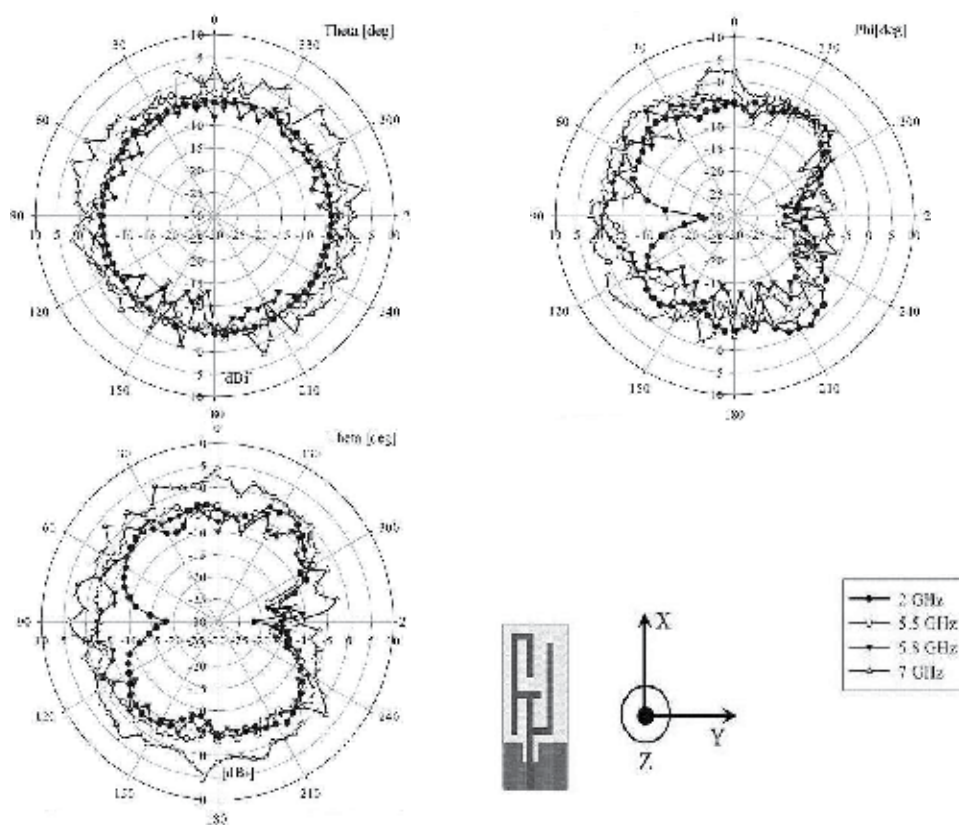
Fig. 16. Measured radiation pattern of the antenna in YZ plane, XY plane, and XZ plane, at 2, 5.5, 5.8 and 7GHz.

5. Conclusion

The UWB technology will be the key solution for the future wireless and mobile communication systems. This is due to its ability to achieve very high data rate which results from the large frequency spectrum occupied. UWB antenna is a crucial element in UWB system; it remains as a particular challenging topic because there are requirements for a suitable UWB antenna compared with a narrowband antenna.

The increasing demands for improved performances, and higher bit rate transmission speeds, gives place to the need for new and future UWB wireless schemes, in which, UWB antenna operation could be required to function beyond the 10.6 GHz upper frequency band limit currently defined by the FCC.

Therefore, it is essential to design a smooth transition between the feeding line and the radiator element for good impedance matching over the entire operational bandwidth. For this reason, a novel technique has been introduced to improve its performance, which consists on introducing two microstrip lines between the feedline and the radiator disc element. This proposed matching technique is very simple to introduce in practice and could be attractive for current and future UWB applications.

Measurements show that the operating bandwidth of the proposed antenna, after introducing the second microstrip line, increases from 3.18 GHz to 11.74 GHz (bandwidth of 8.56GHz) to 3.5 GHz to 31.94 GHz (bandwidth of 28.47GHz), so the bandwidth increase is of 232%. It's observed that the performances of the modified antenna are better compared to the first antenna.

Multiband printed arms monopole antenna is designed for 3G and UWB communications systems. Two main frequency bands 1.8-2.3GHz, 5.16-8.12 GHz are covered, and an additionally third band at 3.07-3.32 GHz is obtained and can be improved by slot size and feed line dimensions. This antenna has a good performance, thus it is more suitable for multiband systems including ultra wideband applications.

Proposed antennas in this chapter present good candidate for current and future ultra wideband applications, due to theirs attractive features (i.e. small size, low profile, low cost, impedance bandwidth, gain, nearly omnidirectional radiation).

6. Acknowledgment

7. References

FCC, First Report and Order 02-48. February 2002.

Oppermann, L.; M. Hamalainen and J. Iinatti, *UWB Theory and Applications*, John Wiley & Sons Canada Ltd, 2004.

Agrawall, N. P.; Kumar, G.; Ray K P. Wide-band planar monopole antenna. *IEEE Trans. Antennas Propag.*, 1998, 46(2): 294-295.

Ammann, M. J.; Chen, Z N. Wideband monopole antennas for multi-band wireless systems. *IEEE Antennas and Propagation Magazine*, 2003, 45(3): 146-150.

Hertel, T. W.; Smith, G. S. On the dispersive properties of the conical spiral antenna and its use for pulsed radiation. *IEEE Trans. Antennas Propag.*, 2003, 51(5): 1426-1433.

Klemm, M.; Kov'cs, I.Z; Pedersen, G. F.; Tröster G. Novel small size directional antenna for UWB WBAN/WPAN applications. *IEEE Trans. Antennas Propag.*, 2005, 53(12): 3884-3896.

Ma, T.G.; Jeng, S.K. Planar miniature tapered-slot-fed annular slot antennas for ultra-wideband radios. *IEEE Trans. Antennas Propag.*, 2005, 53(3): 1194-1202.

Kumar, G.; Ray, K.P. Broadband Microstrip Antennas, *Artech House antennas and propagation library*, 2003.

Chen, Z. N.; Wu, X. H.; Li, H. F.; N. Yang, and M. Y. W. Chia, Considerations for source pulses and antennas in UWB radio systems, *IEEE Trans. Antennas Propag.*, vol. 52, no. 7, pp. 1739–1748, Jul. 2004.

Arslan, H.; Chen, Z. N.; and Benedetto, M.G.Di, Ultra Wideband Wireless Communications, *Wiley & Sons*, Inc., Hoboken, New Jersey, USA, 2006.

Sorgel, W.; Waldschmidt, C.; and W. Wiesbeck, "Transient responses of a vivaldi antenna and a logarithmic periodic dipole array for ultrawideband communication", *IEEE Antennas and Propagation Symposium*, June, 2003.

Telzhensky, N.; and Leviatan, Y. Novel Method of UWB Antenna Optimization for Specified Input Signal Forms by Means of Genetic Algorithm", *IEEE Transactions on Antennas and Propagation*, Vol. 54, No. 8, August 2006.

Shih, T.Y.; Li, C.L.; and Lai, C.S. Design of an UWB fully planar quasi-elliptic monopole antenna, in *Proc. Int. Conf. Electromagnetic Applications and Compatibility (ICEMAC 2004)*, Taipei, Taiwan, Oct. 14–16, 2004.

Danesfahani, R.; Asadpor, L.; Soltani, S. A small UWB CPW-fed monopole antenna with variable notched bandwidth. *J Electromagn Waves* Appl 2009; 23:1067–76.

Soltani, S.; Azarmanesh, MN.; Lotfi, P. Design of band notched CPW-fed monopole antenna using two symmetric parasitic elements for UWB applications. *J Elec- tromagn Waves Appl* 2009;23:1407–16.

Chen, S.; Mulgrew, B.; Grant, PM. A planar monopole antenna design with band- notched characteristics. *IEEE Trans Antennas Propag*, 2007.

Choi, J.; Chung, K.; Roh, Y. Parametric analysis of a band- rejected antenna for uwb applications. *Microwave Opt Technol Lett* 2005;47.

Kim, K.; Park, S. Analysis of the small band-rejected antenna with the parasitic strip for uwb. *IEEE Trans Antennas Propag* 2006.

Zaker, R.; Ghobadi, C.; Nourinia, J. Novel modified uwb planar monopole antenna with variable frequency band-notched function. *IEEE Antennas Wireless Propag Lett*, 2008.

Chen, w.S.;, Yang, K.C; CPW-fed planar ultra- wideband antenna having a frequency band-rejected function. Southern Taiwan University Tainan, *2007 IEEE region 10 conference*, 2007 November 2, 2007 on page(s): 1–3.

Khan, S.; Xiong, J.; He, S. Low profile and small size frequency notched planar monopole antenna from 3.5 to 23.64GHz. *Microwave Opt Technol Lett* 2008.

Chen, HJ.; Liu, QZ., Li JF, Guo JL. A novel band-notched elliptical ring monopole antenna with a coplanar parasitic elliptical patch for uwb applications. *J ElectromagneticWaves App*l 2008.

Lu, W.j. ; Cheng, C.h. ; Cheng Y. ; et al. Frequency notched ultra-wideband microstrip slot antenna with fractal tuning stub. *Electronics Letters*, 2005,41(6): 294-296

Su, S. W.; Wong, K. L.; Chang, F. S. Compact printed ultra-wideband slot antenna with a band notched operation. *Microwave and Optical Technology Letters* 2005. 45(2): 128-130

Lu, W.J.; Cheng C.h.; Zhu H.b. Compact frequency notched ultra-wideband fractal printed slot antenna. *IEEE Microwave and Wireless Components Letters*, 2006.

Behdad, N.; Sarabandi, K. A multiresonant single-element wide slot antenna. *IEEE Antennas and Wireless Propagation Letters*, 2004, 3 (I): 5-8

Chen, H. D.. Broadband CPW-fed square slot antenna with a widened tuning stub. *IEEE Transactions on Antennas and Propagation,* 2003. 51(8): 1982-1986

Lee, H. L.; Lee H. J.; Yook, J. G., et al. Broadband planar antenna having round corner rectangular wide slot. *Proceeding of the International Symposium of IEEE Antennas and Propagation Society*, Jun 16-21, 2002, San Antonio, TX, USA. Piscataway, NJ, USA: IEEE, 2002: 460-463

Lu, W.J. ; Cheng, C.h. ; Cheng, Y. ; et al. A novel broadband multislot antenna fed by microstrip line. *Microwave and Optical Technology Letters*, 2OO5,45(1): 55-57

Lu, W.J. ; Cheng, C.H.; Cheng, Y. ; et al. A compact ultra-wideband CPW-fed slot antenna with a fork-like stub. *Microwave and Optical Technology Letters*, 2005. 46(6)

Sze, J. Y.; Wong, K. L. Bandwidth enhancement of a microstripline- fed printed wide-slot antenna. *IEEE Transactions on Antennas and Propagation*, 2001,49 (7): 1020-1024

Ammann, M. J. Control of the impedance bandwidth of wideband planar monopole antennas using a beveling technique, *Microw. Opt. Technol. Lett.*, vol. 30, no. 4, pp. 229–232, Aug. 2001.

Ammann, M. J.; and Z. N. Chen, Wideband monopole antennas for multi-band wireless systems, *IEEE Antennas Propag. Mag.*, vol. 45, no. 2, pp. 146–150, Apr. 2003.

Ammann, M. J.; and Z. N. Chen, A wideband shorted planar monopole with bevel, *IEEE Trans. Antennas Propag.*, vol. 51, no. 4, pp. 901–903, Apr. 2003.

Ding, M., R. Jin, J. Geng, and Q.Wu, Design of a CPW-fed ultrawideband fractal antenna, *Microw. Opt. Technol. Lett.*, vol. 49, no. 1, pp. 173–176, Jan. 2007.

Gianviffwb, J. P.; and Y. Rahmat-Sammi, Fractal antennas: A novel antenna miniaturization technique, and applications, *IEEE Antennas Propag. Mag.*, vol. 44, no. 1, pp. 20–36, Feb. 2002.

Wu, Q.; R. Jin, J. Geng, and M. Ding, CPW-fed quasi-circular monopole with very wide bandwidth, *Electron. Lett.*, vol. 43, no. 2, pp. 69–70, Jan. 2007.

Wu, Q.; R. Jin, J. Geng, and M. Ding, Compact CPW-fed stackedcircle monopole antenna with very wide bandwidth, *Microw. Opt. Technol. Lett.,* vol. 49, no. 5, pp. 1192–1194, May 2007.

Wang, J.; Sun X, Okada K. Uwb circular monopole omni-directional antenna with a slot for radiation pattern improvement. *IEEE conference on Ultra-Wideband* 2007; 478–82.

John, M.; and M.J. Ammann, Optimisation of impedance bandwidth for the printed rectangular monopole antenna, *Microwave Opt Technol Lett* 47 (2005), 153–154.

Zhang, C.; and A.E. Fathy, Development of an ultra-wideband elliptical disc planar monopole antenna with improved omni-directional performance using a modified ground, *IEEE Int Antennas Propag Symp Dig, Alburqueque,* NM, (2006), 1689–1692.

Antonino-Daviu, E.; Cabedo-Fabre´s, M.; Ferrando-Bataller, M. and A. Valero-Nogueira, Wideband double-fed planar monopole antennas, *Electron Lett* 39 (2003), 1635–1636.

Ammann, M.J.; and Chen, Z.N. An asymmetrical feed arrangement for improved impedance bandwidth of planar monopole antennas, *Microwave Opt Technol Lett* 40 (2004), 156–158.

Bao, X. L.; and Ammann, M. J. Investigation on UWB Printed Monopole Antenna with Rectangular Slitted Groundplane, *Microwave And Optical Technology Letters*, Vol. 49, No. 7, July 2007

Allen, B. , Dohler, M.; E. Okon, W. Malik, A. Brown, and D. Edwards, Ultra Wideband Antennas and Propagation for Communications, Radar and Imaging. *John Wiley and Sons Inc.* New Jersey: Wiley, 2007.

Abbosh, A.M.; and Bialkowski, M.E. "Design of Ultrawideband Planar Monopole Antennas of Circular and Elliptical Shape," *IEEE Trans. On Ant. and Prop.,* vol. 56, no. 1, pp. 17–23, Jan. 2008.

Liang, J.; Chiau, C. C.; X. Chen, and C. G. Parini, Printed circular disc monopole antenna for ultra-wideband applications, *Electronics Letters*, vol. 40, no. 20, pp. 1246–1248, Sep. 2004.

Powell, J. Antenna design for ultra-wideband radio, *Massachusetts institute of technology*, May 2004

Schartz, H.; The Art and Science of Ultrawideband Antennas. *Artech House*, Inc., 2005.

Srifi, M. N. ; Podilchak, S.K.; Essaaidi, M. and Y.M.M. Antar, Planar Circular Disc Monopole Antennas Using Compact Impedance Matching Networks for Ultra-Wideband (UWB) Applications, *Proc. of the IEEE Asia Pacific Microwave Conference*, pp. 782–785, Dec. 2009.

Sindou, M.; Ablart, G.; and Sourdois,C. Multiband and wideband properties of printed fractal branched antennas, *Electronic Letters,* vol. 35, no. 3, pp. 181-182, February 1999

Llorens, D.; Otero, P.; and Camacho-Penalosa, C. Dual-band, single CPW port, planar-slot antenna, *IEEE Transactions on Antennas and Propagation*, vol. 51, no. 1, pp. 137-139, January 2003.

Lee, E.; Hall, P.; and Gardner, P. Novel compact wideband or multi-band planar monopole antenna, *IEEE Antenna and Propagation Symposium*, pp. 624-627, 2000.

Guo, Y.; Chia, M.; Chen, Z. Miniature built-in multiband antennas for mobile handsets, *IEEE Transactions on Antennas and Propagation*, vol. 52, No. 8, pp. 1936-1944, August 2004.

Srifi, M. N.; Vamsi, K. P.; Essaaidi, M.; and Jantunen, H. Compact Planar Monopole Antenna for 3G and UWB applications, *Microwave and Optical Technology Letters*, Volume 51 Issue 8, Pages 1939 – 1942, 2009.

Printed Sleeve Monopole Antenna

Salman Naeem Khan and Muhammad Ashfaq Ahmed
Department of Physics
COMSATS Institute of Information Technology
Pakistan

1. Introduction

Sleeve antenna dates back to 1947 with its applications in high frequencies by [Bock 1947]. A series of consequent designs and rigorous analysis for such kind of antennas was extensively carried in the preceding years [Norgorden, 1950, King 1965, Poggio, 1966]. Furthermore, [Rispin, 1988] discussed thin-wire analysis for sleeve antennas by studying the standing wave current on the antenna surface. The impedance and pattern of the sleeve monopole antenna was studied in detail by [Wunsch 1998] with the help of Fourier series representation of its surface current. Since then, sleeves have widely been used in multiband communication systems to achieve multi-resonances, miniaturization and wide impedance bandwidth. The sleeve, when applied as extension of ground plane behaves like an additional parasitic element that generates extra resonant mode. The additional resonant mode offered by the sleeve can either be used for dualband/multiband operation or if the extra mode is in close proximity then it combines with the fundamental mode to improve overall bandwidth. On the other hand, ground shorted inset sleeve leads to formation of a virtual feed to excite low resonant mode and is simple tool for antenna miniaturization.

Although UWB antennas have been the interest of engineers over the decade but the recent attraction in the design of such antennas was initiated after the official bandwidth allocation by (FCC, 2002). In addition, after the growth of telecom industry, more and more high speed devices are emerging in the competitive telecom markets with many different built in communication systems working at different frequencies requiring more and more bandwidth to perform those operations. This requires antennas with ultra-wide impedance bandwidth. On the technical side, UWB systems provide high data rates along with large channel capacity, immunity to multipath interference, low complexity, low power consumption and coexistence with other wireless systems [Zhong, 2010]. The real efforts toward UWB antenna design started when [Honda et. al., 1992] proposed a circular disk monopole antenna for the first time to be used for indoor TV systems in Japan. After that, several novel techniques have been introduced by many researchers to achieve ultra wide-bandwidth requirement. The traditional method is to use a thicker substrate with small relative permittivity substrate. The thickness and permittivity of the substrate is comparison among its availability, usage and price. Therefore, it is not an open choice for the antenna designer. Although, the thicker substrate can improve the impedance bandwidth up to *10%*. However, the surface waves are generated for thicker substrate and degrades antenna performance. The other methods include use of different shapes of radiator, optimization of

device dimensions (e.g. ground and substrate size, substrate types etc.) and modified shape of radiator or ground. Therefore, if the ground is to be modified to achieve UWB operation, sleeves are one of the suitable alternatives. The length and distance of sleeves with respect to ground can easily be optimized to achieve ultra wide-bandwidth. However, most of the literature with reference to sleeve antenna is either focused on multiband/wide-band operation or for size miniaturization.

The use of sleeves for obtaining impedance matching up to UWB is the main focus of this chapter. The chapter is organized by studying the in-depth details how different types of parasitic element as extension of ground (ground shorted sleeve, gap sleeve and inset sleeve) can be used to tailor the impedance bandwidth with optimal performance of the radiator in the first section. Different types of sleeve UWB antenna previously found in literature will be presented in second section with quantitatively analysis in terms of impedance bandwidth and compactness. In the last section, rectangular and diamond shaped sleeve UWB antennas are proposed for UWB performance. The analysis of sleeve UWB antenna will also be explained on the basis of transmission line model of antenna and characteristics modes to get insight details of the sleeves behavior and their effect on the impedance bandwidth.

2. Sleeve antenna

Monopole antennas have widely been used in communication and are well known for their simplicity and ease of use. A simple monopole antenna with ground plane modification (ground shorted cylinder around monopole) is the simplest form of sleeve antenna (Fig. 1). Generally, a monopole of half wavelength long, the upper half (quarter wavelength) is open while the lower half is covered with ground is the fundamental known sleeve design. The sleeve basically moves the feed location up the monopole (i.e. virtual feed point) that depends on the length of sleeve. This sleeve monopole has better impedance match to transmission line as compared to the traditional monopole. Decades earlier it was mentioned in [Kraus 1988], that the ground plane degenerates into sleeve with maximum radiation perpendicular to the axis of antenna. The sleeve increases the bandwidth of the monopole due to same current at feed point over the wider range of frequencies [Milligan, T. A., 2005]. This provides an affordable control on the impedance matching over wider bandwidth range.

In order to maintain a certain level of comparison and simplicity, Fire-Resistant (*FR-4*) substrate *(ε_r = 4.5 @ 2.5GHz loss tangent 0.0018)* is used in all the simulations and fabricated prototypes. The total antenna size is also fixed to *35×35×1.6mm³*. A coplanar transmission line is designed to excite all the antennas and consists of a central conducting strip *(13mm×4mm)*. The two symmetrical grounds around the strip have dimension of *15×13mm²* with coplanar gap of 0.5mm between ground and central conducting strip to provide *50Ω* impedance match. The reader should consider the same values otherwise specified wherever necessary to avoid redundancy.

A conventional coplanar monopole antenna and its return loss is presented in Fig. 2. The properties of such monopoles are mainly the function of their ground dimensions, type and size of monopole. However, the size of monopole determines the lower frequency of the bandwidth which is approximately the quarter wavelength.

A simple coplanar monopole with two symmetric sleeves as extension of ground is shown in Fig. 3 [Chen 2007]. In comparison to the return loss with coplanar monopole without

sleeves, it is evident that an additional resonant mode at *4.95GHz* above the fundamental mode 3.15*GHz* is also excited. The excited mode resonance frequency corresponds to the length of sleeve. Therefore, the length of sleeve can also be adjusted to achieve dual/multiband operation instead of wide-bandwidth operation. Like in this case, the bandwidth of the sleeve mode is adjusted to add up with the bandwidth of fundamental mode and wider bandwidth is achieved. The offset of sleeve from the radiator and the width of sleeve are also very important and can be adjusted to control the impedance match and bandwidth of the sleeve mode.
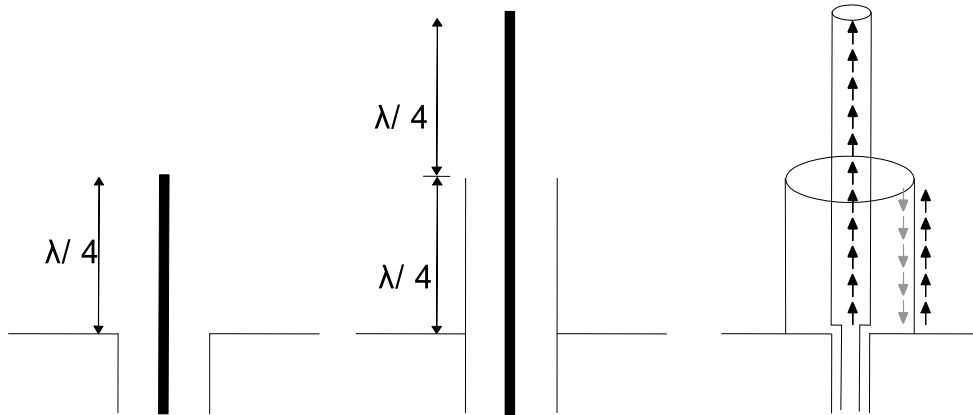
Fig. 1. Traditional monopole over the ground *(left)*, Sleeve antenna *(middle)* and 3D-view *(right)*
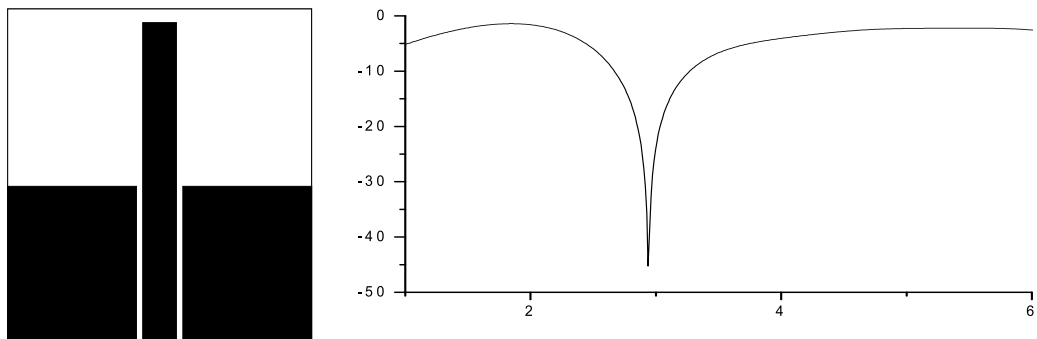
Fig. 2. Schematics *(left)* and return loss of traditional coplanar monopole antenna. The monopole has length of *21mm* and width of *4mm.*

An insight analysis is further carried out by studying and comparing the surface current distribution of standard monopole and sleeve monopole antenna (see Fig. 4). The surface current distribution of fundamental mode for simple monopole and monopole with ground connected sleeve is quite similar. However, the surface current distribution in the ground plane for the sleeve monopole has secured a longer path as compared to conventional monopole design. The surface current distribution of sleeve mode (additional resonance mode *4.95GHz* in Fig. 3.) at electrical length of sleeve is also excited. The fundamental mode of both of designs has surface current in the same direction (i.e. upward direction). The

surface current of sleeve mode is opposite to fundamental mode as evident. Moreover, the sleeve surface currents on the side toward monopole are out of phase to the monopole current same as presented in Fig. 1.
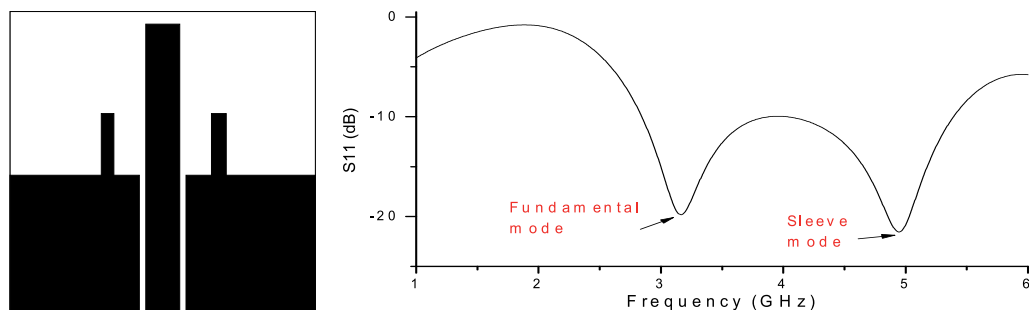
Fig. 3. Schematics of ground connected sleeve antenna and its return loss. The sleeve has length of *7.5mm* and width *3mm*. The offset of sleeve from the monopole is *2.5mm.*
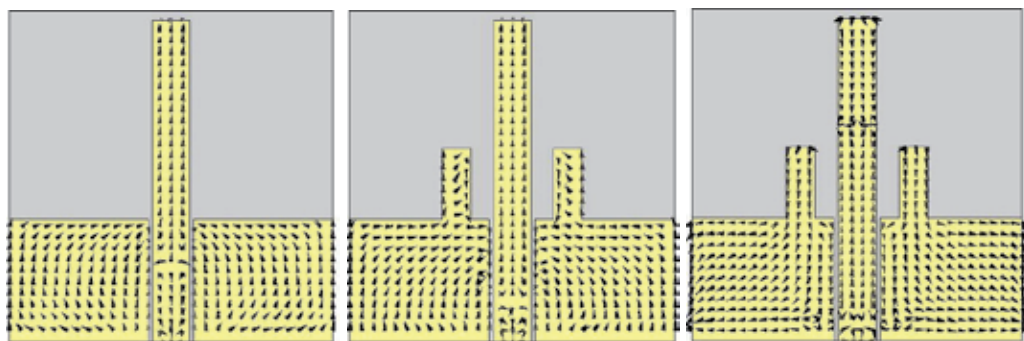
Fig. 4. Comparison of surface current distribution between simple coplanar monopole *(2.8GHz left)*, fundamental mode of ground shorted sleeve *(3.2GHz middle)* and sleeve mode *(4.8GHz right)*

Some different kinds of sleeve antenna found in literature are presented in Fig. 5. The conventional monopole design of Fig. 3 can be modified by adding multiple sleeves (Fig. 5 (*a*)) such that the additional modes (i.e. fundamental mode due to monopole and sleeve modes) coincide with each other to addup the impedance matching. In another type of sleeve, (Fig. 5 (*b*) gap sleeve) in which the sleeves are not connected to the ground rather have small gap between the sleeve and ground. This gap creates an additional parasitic element between the ground and sleeve. A similar design presented in Fig. 5 (c) utilizes combination of two sleeves. This adds an additional parameter to exploit the impedance matching of the extra resonant mode of the sleeve. Finally, inset sleeves are etched on ground opposed to traditional strip sleeves (extension of ground) are also presented. The inset sleeve moves the feed location to a virtual point that depends on the length of sleeve also shown in the figure. This leads to excitation of an additional resonant mode with electrical length (quarter wavelength) corresponding to sum of length of monopole and length of inset sleeve. Therefore, this additional resonant mode is excited before lower resonance and therefore inset sleeves can miniaturize antenna size.
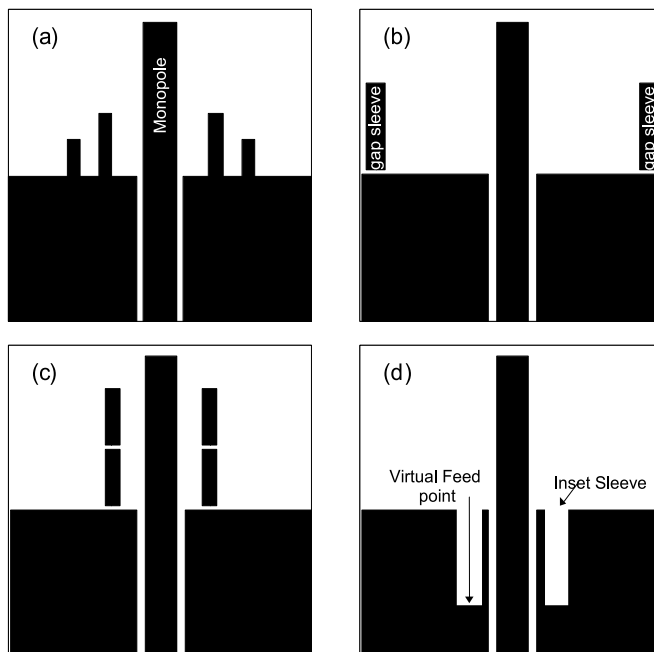
Fig. 5. Different coplanar monopole sleeve antennas. (a) double ground shorted sleeve[Dong 2009], (b) gap sleeve [Cheng 2004], (c) double gap sleeve [Yacouba 2006], and (d) inset sleeve [Baik 2008]

Before moving to sleeve UWB antennas, the reader is suggested to study the two novel design of Fig. 6 [Wu et. al., 2005, Hsiao et. al. 2006] where combination of modified monopole (T-shaped and Y-shaped) and sleeve is used to achieve desired bandwidth. Some novel applications of sleeve are also presented and to get idea of sleeves in non coplanar technology [kunda 2003, Thomas 2007].
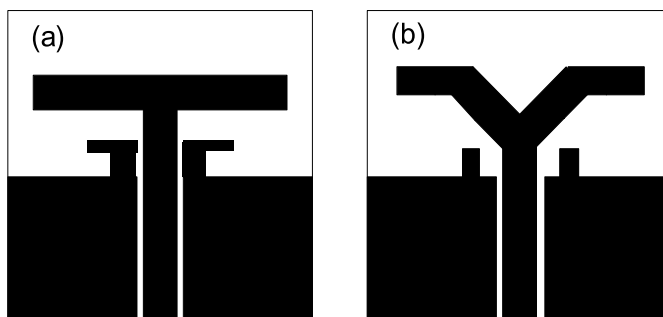
Fig. 6. T-Shaped monopole with L-shpaed sleeve (a) and Y-shaped monopole with ground connected sleeve (b)

3. UWB antenna design

In the recent years, sleeves have been successfully been utilized for UWB operation. Increase of several order of bandwidth is found in the literature. In general, beside some specific

requirements for a particular application (e.g. omni-directionality for mobile terminal antenna), finalizing an antenna is on the disposal of the choice of antenna designer that depends on many factors like the requirement and time of launch of the product. This leads to limited number of research articles where the detail description of antenna designs is presented. Therefore, before jumping to the sleeve's analysis on the impedance bandwidth of an antenna, we will slightly discuss the transmission line model of antenna and theory of characteristics mode of antenna design. It will help the reader to understand the behavior of the sleeve.

4. Transmission line model of antenna

It becomes easy to understand and analyze the impedance behavior of antenna with the help of transmission line modeling [Ray et. al., 2001, Valderas et. al. 2006]. If we consider an antenna equivalent to a transmission line, the width of bottom profile near the ground is equivalent to the length of the transmission line. Similarly, the combination of feed gap and shape of bottom profile collectively contribute to complex impedance. It is quite difficult to formulate this impedance but TLM helps to sketch an extended picture to visualize the collective behavior the antenna. Therefore, the increase in the width of monopole antenna is same as increase in the length of transmission line that in turn increases the impedance to a higher value. The length of feed gap is an inductive parameter that shift smith chart accordingly. The large bandwidth of circular disk and elliptical monopole is understandable due to the impedance varying function away from the radiator (*i.e.* lateral direction). Furthermore, it is obvious to use beveling or step generated base with structures that are small bandwidth (e.g. square, rectangle etc.) to provide linearly varying characteristics impedance function of distance from feed probe. On the basis of transmission line modeling, it is understandable to use parasitic element by either modifying the radiator or ground to countermarch the radiator bandwidth deficiencies. It will be described shortly that slits and slot can be added to the monopole radiator to force the surface currents to follow a guided path for impedance matching at desired frequency or to excite extra mode for bandwidth enhancement. On the other hand, if the ground plane is to be modified for improved impedance behavior, sleeves are among the suitable candidates. Keeping in view the transmission line model of antenna, sleeves are additional parasitic elements (e.g. ground connected, gap and inset sleeve) that can be added to modify the original design to enhance the matching over the desired bandwidth.

5. Theory of characteristics modes

In early 1971, Garbaz et. al. formulated the theory of characteristics modes for radiated and scattered fields, refined by [Harrington et al. 1971] and finally revisited by [Valencia et. al. 2005] as a design guideline for modern antenna. Characteristics modes of antenna are the real currents on the surface of antenna, extracted from generalized impedance matrix, characterized by the shape and size of the radiator and independent of the feed location. In this modern era, simulated current help us to understand the resonance behavior of the antenna and can be re-routed to achieve desired performance. We shall discuss sleeve UWB antennas proposed in the next section on the basis of theory of characteristics modes.
Now we shift our attention on the discussion of different UWB antennas utilizing sleeves previously found in literature. The designs of such sleeve antennas are listed in Fig. 7.

Square monopole with ground connected symmetrical sleeves initially presented by [Chen 2005] and it was proved that such antennas have improved impedance bandwidth as compared to square monopole. Square antenna with *L-shaped* sleeve and *T-shaped* slot is used to excite upto fifth resonance to obtain ultra wide bandwidth. The *L-shaped* sleeve enhances the electromagnetic coupling between the radiator and ground that creates broadening and electrically couples the ground with monopole. Further improvement in the design is possible with help of two *T-shaped* slots etched on the patch to re-route the surface current that can be used for impedance matching or excite additional modes at a desired frequency. This also improves the radiation efficiency but the resonant resistance is decreased. Recently, [Ojaroudi, 2010] proposed an antenna with stepped patch and truncated ground based on the Babinet's Equivalence Principle. The slot and slits placed one half is inverted at the other half. The sleeves manipulate the impedance bandwidth by modifying the capacitance between the modified patch and ground. The slits are used to force the surface current to follow the path which produces additional mode. Beveling square and rectangular monopoles is famous method of improving the impedance bandwidth as explained earlier in the beginning of this chapter on the basis of transmission line modeling of antenna. Impedance bandwidth is function of flare angle [*Ch*-8 Kraus, 1988] which in combination with feed gap in such shapes (e.g. triangle, diamond, rhombic) plays a vital role to overcome impedance mismatch and must be considered for optimization. The sleeve with beveled rectangle and truncated ground is studied [Yoon, 2010].
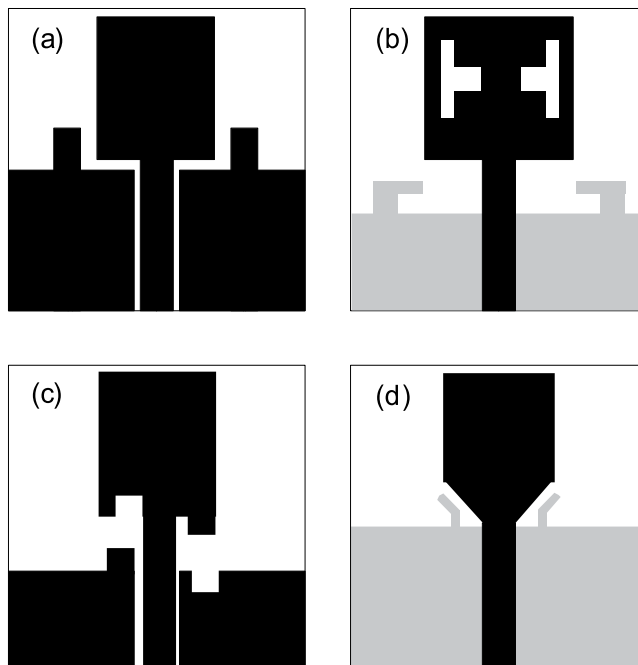
Fig. 7. Different sleeve monopole designs. *(a)* coplanar square monopole with ground connected sleeve [Chen, 2005], *(b)* microstrip square monopole with *L-shaped* sleeve and *T-Shaped* slot [Ebrahimian, 2010], *(c)* modified square monopole with slit and slot based on Babinet's principle [Ojaroudi, 2010], *(d)* Bevelled rectangular sleeve antenna with tilted sleeves [Yoon, 2010]

In Fig. 8, two triangular monopoles with sleeve modification are shown. Tilted sleeves slightly offset from the radiator are applied to triangular shaped antenna, sleeves secures current path to excite resonant modes to improve the impedance bandwidth. The same shape is further studied and improved with hillside shaped corrugation and trapezoid ridged ground. The ridged ground is in form of two symmetrical corrugations extended from the top edge of flat ground plane. These modified grounds provides a smooth transitions between transmission line and free space compared to conventional design to provide the flat response of S-parameters over the wide frequency range. The author claimed to get a significant improved of 4:1 in impedance bandwidth.
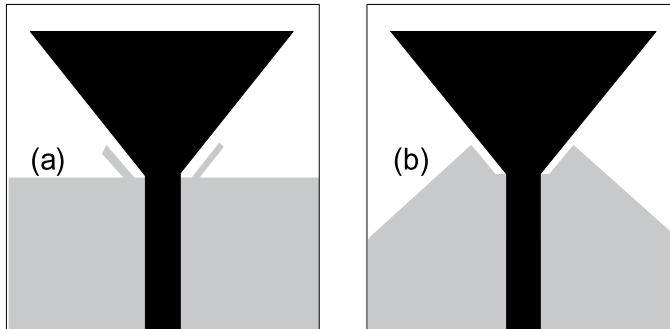
Fig. 8. Microstrip modified triangular monopole. (a) tilted offset sleeve [Lin 2008] and (b) hillside shaped corrugation and trapezoid ridged ground [Lin 2007]

Now we shift our attention towards the novel sleeve antennas (i) rectangular sleeve and (ii) diamond sleeve antenna that are presented in this chapter with special emphasis on impedance enhancement due to sleeves. Coplanar transmission line is used for the proposed antennas mainly due to their easy integration with RF-devices. However, the same treatment can also be utilized for microstrip based technology. As already discussed, several radiator designs have been implemented on microstrip and coplanar technology to study their impedance matching behavior. Among those geometries, square and rectangular monopoles are known to be of less bandwidth [Ammann et. el., 2000, Evans et. al., 1999]. Therefore, we selected rectangular and diamond shaped monopole in this chapter along with integration of different sleeve for UWB operation.

6. Rectangular monopole with double gap sleeves

To start with, the schematics and return loss of simple rectangle monopole is presented in Fig. 9 for different values of feed gap (*i. e.* distance between patch and ground). From return loss it is evident that impedance matching is not of the order of *10dB* and feed gap is always very important optimization parameter for such shapes and should always be considered for impedance matching. As the feed gap increases, the impedance matching improves at lower order of bandwidth and degrades at higher frequency. On the other hand, the lower resonance shifts to lower frequency due to increase in the overall dimension of the antenna. A novel UWB antenna utilizing combination of two gap sleeves is presented in Fig. 10. Compared to the previous design [Chen 2005], the gap sleeve (instead of ground connected) near the ground are utilized. This adds a parasitic element near the ground in addition to coupling between the antenna and sleeve. The impedance bandwidth is further exploited by

adding an extra gap sleeve. Therefore, the coupling between the sleeve and monopole is divided further with another coupling element between the two sleeves. Based on the design principle, the optimization can easily be performed through simulation. The design principle is to first get optimal width of rectangle monopole as discussed in TLM method and then optimize the feed gap. Finally, use two symmetric sleeves of same length to get UWB coverage. The return loss covers the whole UWB frequency range with *10dB* reference. Further improvement like the mismatch around *12GHz* is proposed by using the sleeves of different length. The normalized radiation pattern in the azimuth plane has good omni-directive coverage and is presented in Fig. 11.
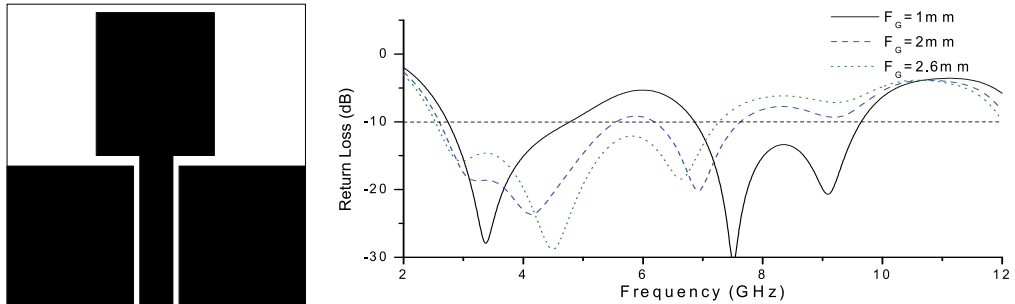
Fig. 9. The schematics of coplanar antenna with rectangle patch *(20mm×15mm)*. The return loss for different values of feed gap on the right side.
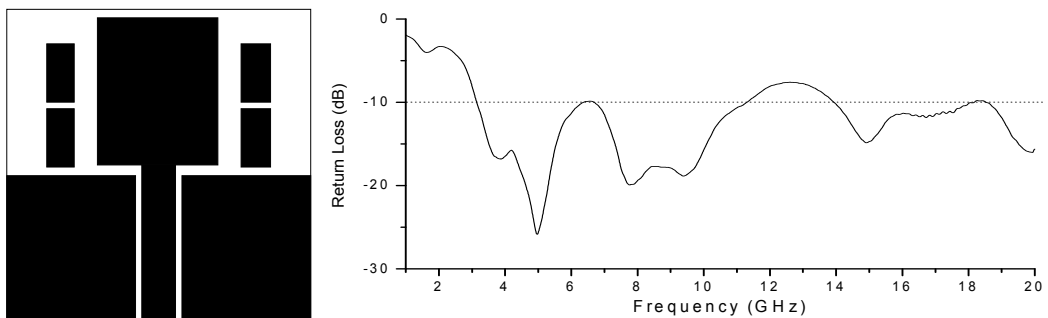
Fig. 10. Modified rectangle monopole antenna having combination of symmetric gap sleeves above the ground. Sleeves have dimension of (*6mm×3mm*) and *4mm* offset from the edge of the ground. Lower sleeves have gap of *0.1mm* from the coplanar ground and gap between the two sleeves is *0.4mm (left)*. Return loss measurements *(right)*

To study modal characteristics of the antennas, the surface current distribution is presented for different frequencies. The fundamental mode has similar current distribution like wire monopole of quarter wavelength. The direction of current is vertically up the monopole with no null. At higher mode *(4.8GHz)*, current appears to move at the edge of the monopole towards the bottom with a null appears at the gap between the two sleeves and the currents are in opposite direction. This also suggests changing the length of sleeve to vary the frequency of resonance of sleeve modes. The mode at *(7.1GHz)* is appears to be out of phase replica of *4.8GHz's* mode. At even higher frequencies (*i.e. 10GHz*), the number of nulls increases and variation of surface current in the coplanar ground is evident. The poor

radiation performance of antenna at high frequency (e.g. pattern at *9GHz* in Fig. 11) can also be considered as direct consequence of degraded surface current. The modal behavior of monopole with sleeves is slightly different from the simple monopole designs (Fabrés et. al., 2002, Lu et. al., 2009).
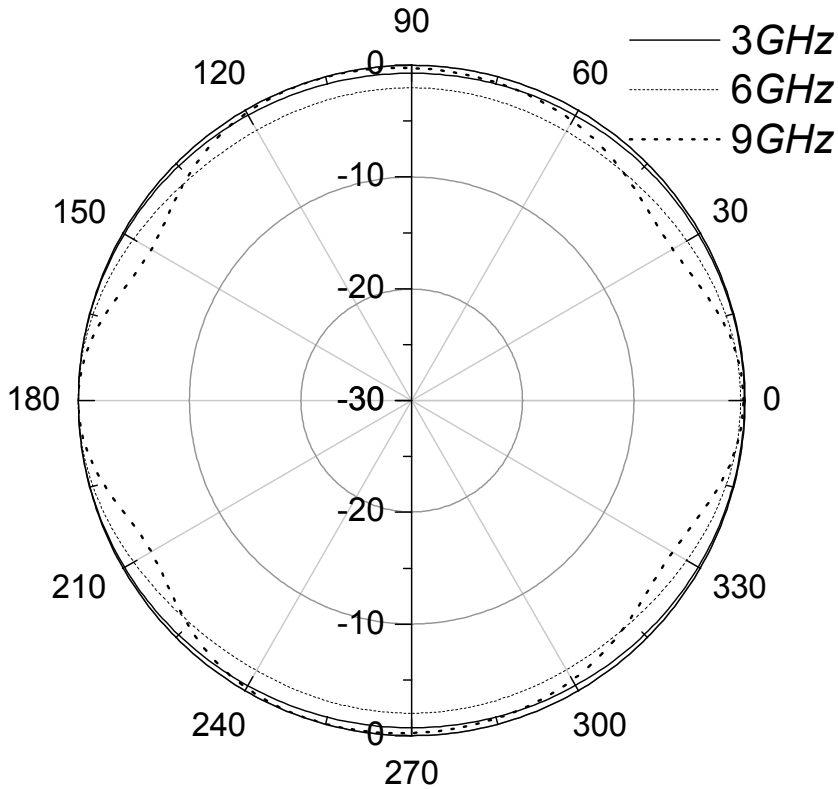
Fig. 11. Azimuth (H-Field) plane normalized pattern of the proposed design.

7. Diamond monopole with tilted gap sleeves

The bandwidth of square/rectangle monopole can be improved by modifying it to diamond shaped radiator. The diamond shape of the proposed antenna is obtained by cutting the lower and the upper vertex of a square rotated to 45⁰ (see the shaded area on the left side of Fig. 13). The height of bottom cut *(H_L)* forces the concentration of current distribution near the bottom edge of the diamond monopole that improves impedance bandwidth. The height of upper cut can be optimized either for compactness or further impedance match at high frequencies. The return loss of diamond monopole with different value of H_L is presented in Fig. 14. The impedance matching becomes better for *H_L=3mm*. On the basis of transmission line model, the height of lower cut in conjunction with feed gap counter matches the increase in the impedance of transmission line due to increase in size of monopole in the lateral direction compared to the rectangular monopole. However, the higher values of *H_L* shift the lower frequency of impedance bandwidth to higher value due to overall decrease in the size of antenna.
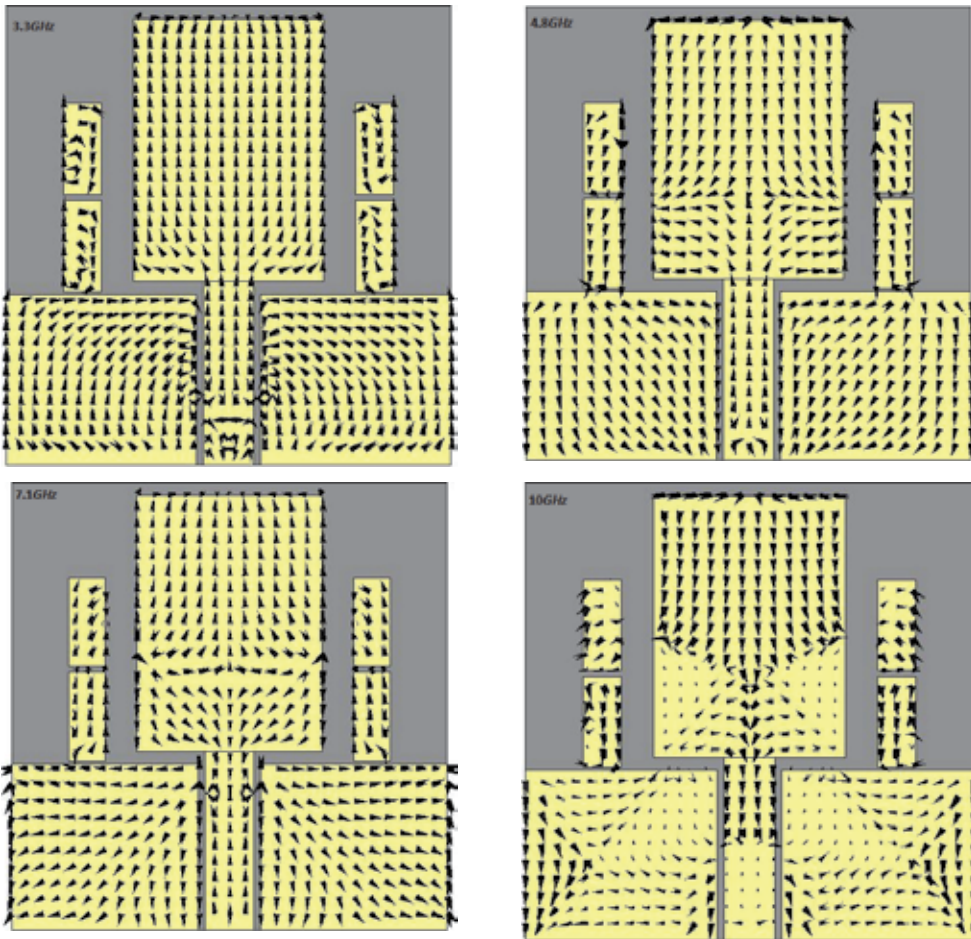
Fig. 12. Surface current distribution of square monopole with two gap strips above each of coplanar ground.
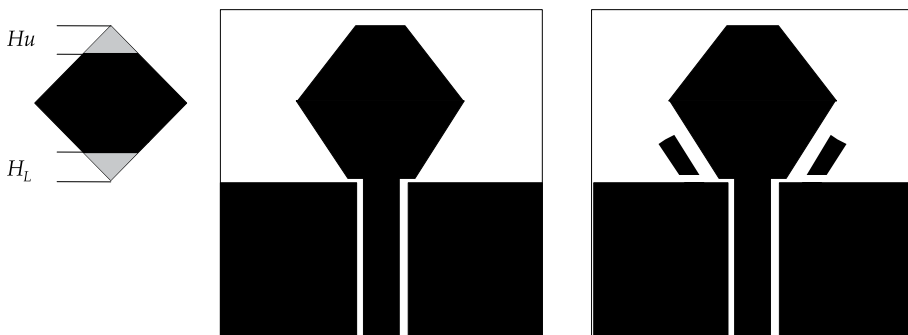
Fig. 13. Schematics of diamond shaped monopole with symmetrical tilted gap sleeves. The tilted gap sleeve has length of *7mm*. Sleeve offset from ground and diamond monopole is *0.5mm* and *0.75mm*
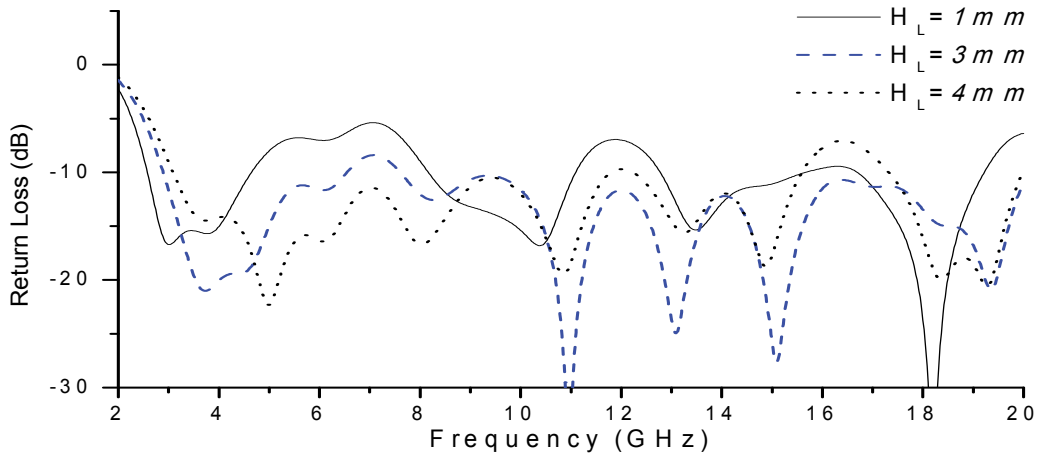
Fig. 14. Return loss for different values of H_L. The value of H_U is fixed to *4mm*.
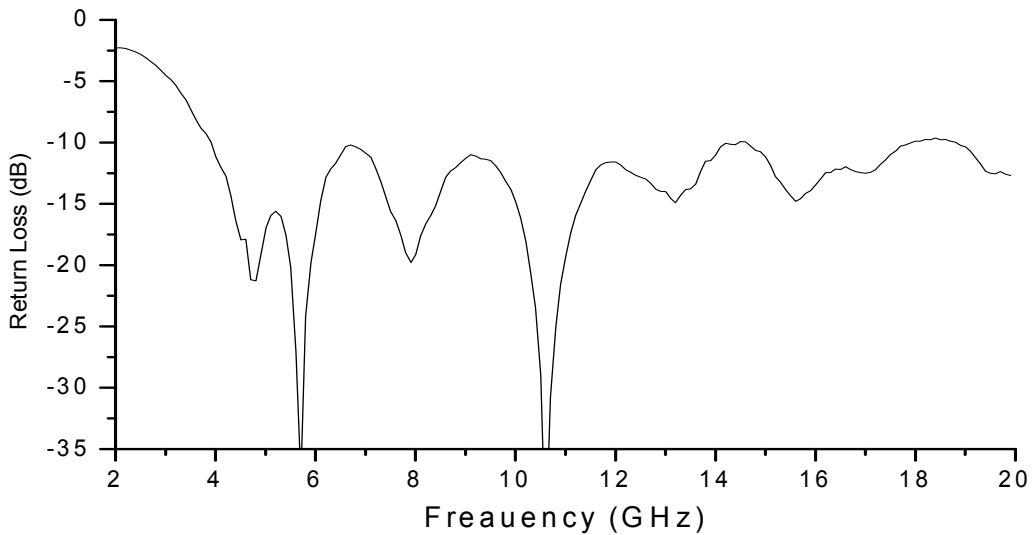
Fig. 15. Return loss of proposed diamond shaped monopole with tilted gap sleeves.

For a square like design, impedance matching upto *20GHz* represents good improvement over the conventional small bandwidth square designs (Fig. 15). The values of H_L and H_U are *3mm* and *4mm* respectively for rectangle of *(20mm×15mm)*. Coplanar transmission line of *50Ω* is design with central conducting strip of dimension *(19.5mm×2mm)* and a gap of *0.25mm* between the central conducting strip and ground. Tilted gap sleeves have dimension of *(7mm×2mm)* with gap of *2mm* from the ground. Finally, the radiation pattern in the azimuth plane presented in Fig. 16 shows typical omni-directional radiation performance usually required for general UWB communication systems. Both of the designs discussed here have typical butterfly like pattern in the Elevation plane and therefore not shown.
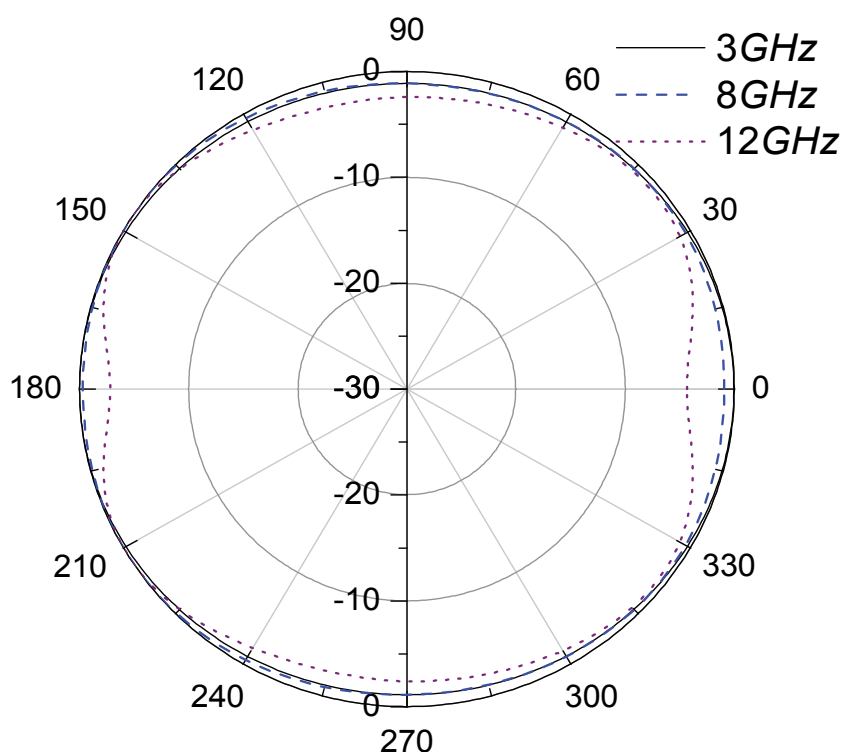
Fig. 16. Azimuth radiating pattern (H-plane) of the proposed diamond shaped coplanar antenna with tilted shapes normalized to *0dB*.

8. Conclusion

Sleeves have been considered a step head than their traditional role in the antenna design. Novel rectangle and diamond shaped monopoles with sleeves are presented with in-depth analysis based on modal and transmission line model.

9. Acknowledgment

10. Reference

Ammann M. J., (2000), "Impedance bandwidth of the square planar monopole", *Microwave and Optical Technology Letters*, Vol. 24, No. 3, pp. 183–187, ISSN: 1098-2760.

Baik J. W. & Kim Y. S., (2008), "Printed Inset Sleeve Monopole Antennas for Dual-Band Applications," *Microwave and Optical Technology Letters*, Vol. 50, No. 8, pp. 1995-1997, ISSN: 1098-2760.

Bock, E. L., Nelson, J. A., & Dorne, A., (1947), Chapter 5, "*Sleeve antennas, in Very High Frequency Techniques*", McGraw Hill, pp. 119–137, New York.

Chen, H. D. & Chen, W. S., (2007), "Ultra-Wideband Design of Sleeve Monopole Antenna", *IEEE Transactions on Antennas and Propagation*, Vol. 54, No. 3, pp. 1034-1037, ISSN: 0018-926X.

Chen S. B., Jiao Y. C., Wang W., & Liu Q.Z., (2005), "Wideband Cpw-Fed Uniplanar Sleeve-Shaped Monopole Antenna", *Microwave and Optical Technology Letters*, Vol. 47, No. 3, (November), pp. 245-247. ISSN: 1098-2760.

Cheng C. H., Lu W. J., Chen Y., & Zhu H. B., (2004) "A Dual-Band Strip-Sleeve Monopole Antenna Fed By Cpw", *Microwave and Optical Technology Letters*, Vol. 42, No. 1, (July), pp. 70-72, ISSN: 1098-2760.

Dong T., Chen Y.-P., (2009) "Novel Design of UWB Printed Double Sleeve Monopole Antenna", *Progress in Electromagnetics Research Letters*, Vol. 9, pp. 165-173, ISSN: 1937-6480.

Ebrahimian H. & Ojaroudi M., (2010), "Design Of A Novel Ultra-Wideband Printed Monopole Antenna For Use In A Circular Cylindrival Microwave Imaging Syetem", *6th International Workshop On Biological Effects Of Electromagnetic Fields Kefaluka Resort*, Turkey, (October).

Evans, J. A. & Ammann, M. J., (1999), "Trapezoidal and pentagonal monopoles with impedance bandwidths in excess of 10:1", *IEEE Antennas Propagation Society International Symposium*, Vol. 3, pp. 1558–1561, ISBN: 0-7803-5639-x.

Federal Communications Commission (2002), *Revision of Part 15 of the Commission's Rules Regarding Ultra-Wideband Transmission Systems*, First Report and Order, FCC 02-48.

Garbacz, R. J., & Turpin, R. H. (1971), "A generalized expansion for radiated and scattered fields", *IEEE transactions on Antennas and Propagation*, Vol. AP-19, pp. 348-358, ISSN: 0018-926X.

Guo, J., Ji, Y. & Liu, Q., (2003), "Sleeve monopole antennas at the center of a circular ground plane", *Microwave and Optical Technology Letters*, Vol. 38, No. 4, (August), pp. 341-343, ISSN: 1098-2760.

Harrington, R. F., & Mautz, J. R., (1997), "Theory of characteristics modes for conducting bodies", *IEEE transactions on Antenna and Propagation*, Vol. 19, pp. 622-628, ISSN 0018-926X.

Hsiao H. M.,Lu J. H, Wu J. W., (2006), "Y-shaped monopole antenna with dual-broadband operation for WLAN", *Microwave and Optical Technology Letters*, Vol. 48, No. 8, (August), pp. 1476-1480, ISSN: 1098-2760.

Fabrés M. C., Daviu E. A., Norueira A. V. & Bataller M. F., (2005), "The theory of characteristic modes revisited: A contribution to the design of antennas for modern applications", *IEEE antenna and propagation magazine*, Vol. 49, No. 5, (October), pp. 52-66, ISSN 1045-9243, OCLC: 20287815.

Fabrés M. C., Daviu E. A., Norueira A. V. & Bataller M. F., (2002), "Systematic study of elliptical loop antennas using characteristics modes", *Antennas and Propagation Society International Symposium*, Vol. 1, pp. 156-159, ISBN: 0-7803-7330-8.

Honda, S., Ito, M. & Jinbo, Y., (1992), "A Disk Monopole Antenna with 1:8 Impedance Bandwidth and Omni-directional radiation pattern", *Proceedings of International Symposium Antennas Propagation, Sapporo,* pp. 1145-1148, Japan.

King, R. W. P., and Wu, T. T., (1965), "The cylindrical antenna with arbitrary driving point," *IEEE Transactions on Antennas Propagation*, Vol. AP-13, (September), pp. 710–718, ISSN: 0018-926X.

Kraus J. D. (1988), *"Antenna theory"*, (second edition), McGraw Hill International Edition, (ISBN 0-07035422-7), New York.

Kunda V. K., Ali M., Hwang H. S., & Sittironnarit T., (2003), "Study of a dual-band packaged Patch antenna on a pc card for 5–6 GHz wireless LAN applications", Microwave and Optical Technology Letters, Vol. 37, No. 6, (June),pp. 423-428, ISSN: 1098-2760.

Li J.-Y. & Gan Y.-B., (2006), "Multi-Band Characteristic of Open Sleeve Antenna", *Progress in Electromagnetics Research*, PIER 58, pp. 135–148, ISSN: 1070-4698.

Lin C. C. & Chuang H. R., (2008), "A 3–12GHz UWB Planar Triangular Monopole Antenna With Ridged Ground-Plane", *Progress in Electromagnetics Research,* PIER 83, pp. 307–321, ISSN: 1070-4698.

Lin C. C., Kan K. Y., & Chuang H. R., (2007), "A 3-8 GHz Broadband Planar Triangular Sleeve Monopole Antenna for UWB Communication", *Antennas and Propagation Society International Symposium*, pp. 4741-4744, Honolulu, ISBN: 978-1-4244-0877-1.

Lu, Y., Huang, Y. C., & Chattha, H. T., (2009), "A further study of plnanar monopole antennas", *Antennas & Propagation Conference,* Loughborough, pp. 353-356, ISBN: 978-1-4244-2720-8.

Milligan, T. A., (2005), *"Modern antenna design",* (Second Edition), A John Wiley & Sons, INC., Publication, (ISBN-13 978-0-471-45776-3), America.

Norgorden, O. & Walters, W., (1950), "Experimentally determined characteristics of cylindrical sleeve antennas", *Journal of the American Society for Naval Engineers*, Vol.62, No. 2, (May), pp. 365–382.

Ojaroudi M., Ebrahimian H., Ghobadi Ch., & Nourinia J., (2010), "Small Microstrip-Fed Printed Monopole Antenna For UWB Application", *Microwave and Optical Technology Letters*, Vol. 52, No. 8, (August), pp. 1756-1761, ISSN: 1098-2760.

Poggio, A. J. & Mayes, P. E., (1966), "Pattern bandwidth optimization of the sleeve monopole antenna," *IEEE Transactions on Antennas Propagation*, Vol. AP-14, No. 5, (September), pp. 643–645, , ISSN: 0018-926X.

Qiao W., Chen Z. N., & Wu K., (2006), "UWB monopole antenna with a top-hat sleeve", *International Journal of Microwave and Optical Technology*, Vol. 1, No. 1, pp. 17-27, ISSN: 1098-2760.

Rispin I. W., & Chang D. C., (1998), "Wire and loop antennas in antenna handbook", pp. 723–736, New York.

Ray K. P., Anob P. V., Kapur R., & Kumar G., (2000) "Broadband Planar Rectangular Monopole Antennas", *Microwave and Optical Technology Letters,* Vol. 28, No. 1, (January), pp. 55-59, ISSN: 1098-2760.

Shen Z., (2001), "Theoretical Modeling of Multi-Sleeve Monopole Antennas", *Progress in Electromagnetics Research*, PIER 31, pp. 31–54. ISSN: 1070-4698.

Thomas K. G & Lenin N., (2007), "Ultra wideband folded rectangular monopole", *Microwave and Optical Technology Letters,* Vol. 49, No. 6, (June), pp. 1497-1500, ISSN: 1098-2760.

Valderas D. (2006), "Design of UWB folded plate monopole antennas based on TLM", *IEEE transactions on Antenna and propagation*, Vol. 54, No. 6. pp. 1676 – 1687, ISSN: 0018-926X.

Wu J. W.,Wang W. D.,Hsiao H. M. & Lu J. H.,(2005) , "T-shaped monopole antenna with shorted L-shaped strip-sleeves for WLAN 2.4/5.8-GHz operation", *Microwave and Optical Technology Letters*, Vol. 46, No. 1, (July),pp. 65-69, ISSN: 1098-2760

Wunsch, A. D., (1988), "Fourier series treatment of the sleeve monopole antenna", *Proceedings of International Electrical Engineering*, Vol. 135, No. 4, (August), pp. 217–225.

Yacouba C., Tayeb A. D., & Larbi T. (2006), "Broadband Coplanar Waveguide-Fed Printed Monopole Antenna with Strip-Sleeves", *Microwave and Optical Technology Letters,* Vol. 48, No. 2, pp. 209-212, ISSN: 1098-2760.

Yoon H. K., Park J. A., Lim Y., Yoon Y. J., & Lee C. H., (2010), "miniaturization of a ultra wide band antenna", *PIERS Proceedings, Cambridge*, USA, (July), ISSN1931-7360

Zachou V., Christodoulou C. G., Chryssomallis M. T., Anagnostou D., & Barbin S. (2006), "Planar monopole antenna with attached sleeves", *IEEE Antennas and Wireless Propagation Letters*, Vol. 5, pp. 286-289, ISBN 1536-1225

Zhong S. S., (2010), Ch. 3., "Microwave and Millimeter wave technologies: Modern UWB antenna and equipment", *In-Tech*, pp. 63-82, ISBN 978-953-7619-34-3, Vienna, Austria.

Zuo S., Zhang Z., & Yin Y., (2006), "Bandwidth enhancement of a planar sleeve monopole antenn for wireless communication applications", *Microwave and Optical Technology Letters,* Vol. 52, No. 10, (October), pp. 2235-2238, ISSN: 1098-2760.

Design and Implementation of UWB CPW-Fed Planar Monopole Antenna with Dual Band Rejection Characteristics

Woo Chan Kim and Woon Geun Yang
University of Incheon
Republic of Korea

1. Introduction

With the development of high-speed switching technology, ultra-wideband (UWB) systems in high-performance wireless technology is receiving more attention. In February 2002, the Federal Communications Commission (FCC) issued a ruling that UWB systems could use an unlicensed frequency band ranging from 3.1 GHz to 10.6 GHz for data commutations, radar, and other applications so long as their radio signals satisfy a set of spectral masks for indoor and outdoor environments (Nie & Chen, 2008; Maeng et al., 2009).

However, the design of antennas for UWB applications faces many challenges. Interference is a serious problem for UWB application systems. The rejection of interference with some existing narrowband wireless services, such as IEEE 802.11a (5.15~5.825GHz) wireless local area network (WLAN) systems and IEEE 802.16 (3.3~3.8GHz) World Interoperability for Microwave Access (WiMAX) systems are necessary for UWB application systems. One way to suppress these interfering signals is to use a spatial filter such as a frequency selective surface above the antenna. However, this approach requires too much space.

Recently, many UWB antennas have been proposed in an attempt to overcome the interference problem using frequency band rejection design. The most popular approaches for an antenna design with frequency band rejection are embedding slots (Jyoti et al., 2010; Su et al., 2010; Zhang et al., 2010). However, most of these designs have single band-notched characteristics for the rejection of the WLAN band or WiMAX band. Only a few articles addressed the dual or multi-band rejection designs (Abdollahvand et al., 2010; Hassani et al., 2011; Mei et al., 2010; Wei et al., 2011).

Obtaining highly efficient band-notch characteristics is a challenging issue. The main problem of the frequency band rejection design is the difficulty of controlling the bandwidth of the notch band in a limited space. Furthermore, strong coupling between two adjacent notch bands is obstacle to achieve efficient dual band-notched UWB antennas. Therefore, an efficient frequency bands rejection of the WLAN band and WiMAX band is difficult to implement for UWB applications.

In this chapter, we propose an ultra-wideband coplanar waveguide (CPW)-fed planar monopole antenna with dual band rejection characteristics. The proposed antenna consists of a microstrip patch with U-n slot (Yang, 1999, 2002). It can achieve a wide bandwidth of 3.0~11.0GHz for voltage standing wave ratio (VSWR) of less than 2, with dual band rejection

of 3.15~3.79GHz and 5.13~5.85GHz. Firstly, we present the basic structure for the proposed antenna in section 2. The simulation and measurement results will be presented in section 3 and the conclusion follows in section 4.

2. Proposed antenna

Fig. 1 shows the geometry of the proposed CPW-fed monopole antenna with dual band rejection characteristics, and the parameters of the proposed antenna are presented in Table 1. The antenna is fabricated on an inexpensive FR4 substrate with a dielectric constant of 4.4 and a thickness of 1.60 mm. A CPW transmission line with W_{10} = 3.00 mm and a gap distance of W_{11} = 1.00 mm between the single strip and two planar ground planes are used for feeding the antenna. Two ground planes, which have the same size of W_9 = 17.50 mm × L_{10} = 29.00 mm are symmetrically placed on each side of the CPW line. The proposed antenna has an U-n slot; a n-shaped slot for band rejection with L_5 = 1.2 mm, L_8 = 6.0 mm, W_3 = 18.0 mm, W_4 = 16.0 mm and U-shaped slot with L_6 = 1.2 mm, L_7 = 5.0 mm, W_5 = 12.0 mm, W_6 = 8.0 mm.

The proposed CPW-fed antenna structure is easy to implement with a printed circuit board. The CPW-feeding for the antenna in Fig. 1 is designed for 50 Ω input impedance. The use of U-n slot can lead to produce an additional surface current path and thus we obtain ultra-wideband operations with dual band rejection characteristics.
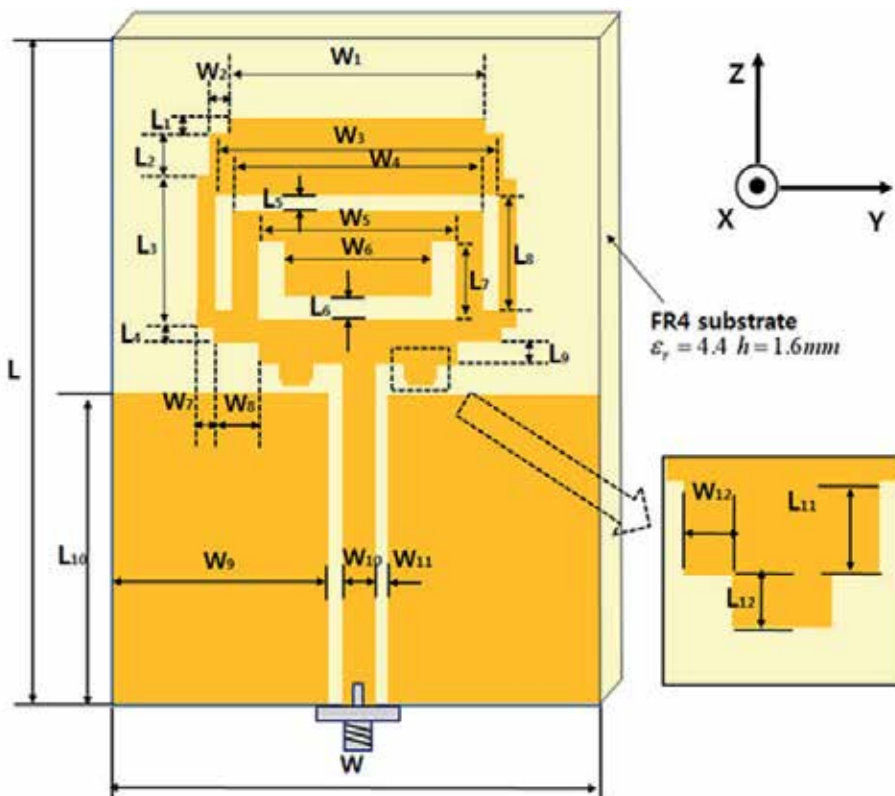
Fig. 1. Geometry of the proposed antenna.

Parameter	Length(mm)	Parameter	Length(mm)
W	40.0	L	52.0
W_1	16.0	L_1	1.0
W_2	1.0	L_2	4.0
W_3	18.0	L_3	9.9
W_4	16.0	L_4	1.0
W_5	12.0	L_5	1.2
W_6	8.0	L_6	2.0
W_7	1.0	L_7	5.0
W_8	3.0	L_8	6.0
W_9	17.5	L_9	1.8
W_{10}	3.0	L_{10}	29.0
W_{11}	1.0	L_{11}	0.8
W_{12}	0.2	L_{12}	0.2

Table 1. Design parameters of the proposed antenna.

3. Simulation and measurement results

The electrical characteristics of the proposed antenna were simulated using the High Frequency Structure Simulator (HFSS) of Ansoft. The implementation of the CPW-fed monopole antenna with dual band rejection characteristics is shown in Fig. 2.

Fig. 2. Photograph of the implemented antenna.

The measurements of the electrical characteristics, such as the radiation patterns, VSWR and return loss, of the implemented antenna were conducted in an anechoic chamber equipped with an HP 8510C network analyzer and a far field measurement system. Fig. 3 shows the S_{11} and VSWR characteristics. The S_{11} of the design example is shown in Fig. 3(a), which demonstrates that the proposed antenna covers the frequency band of 3.0 ~ 11.0 GHz for VSWR<2, except for its dual rejection bands ranging 3.15~3.79GHz and 5.13~5.85GHz. Fig. 3(b) shows the VSWR of the design example.

(a)

(b)
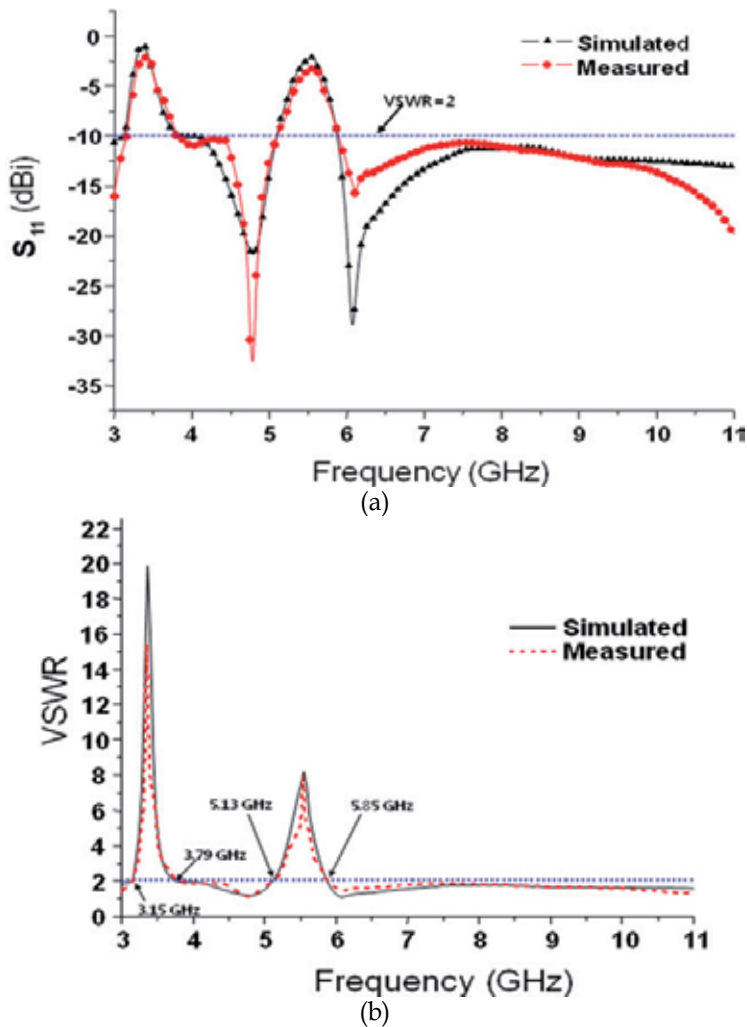
Fig. 3. Simulated and measured electrical characteristics. (a) S_{11}, (b) VSWR.

Fig. 4 shows the measured antenna gain. The maximum measured gain of the design example is about 6.13 dBi at 10.6 GHz. The measured co-polarization and cross-polarization radiation patterns of the implemented antenna in the xy-plane and xz-plane at four different frequencies are illustrated in Fig. 5. The radiation patterns show that the antenna has omnidirectional radiation characteristics.
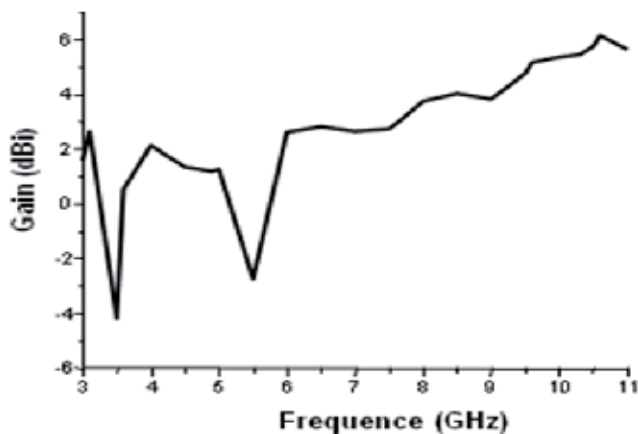
Fig. 4. Measured results for antenna gain of the design example.

xy-plane   xz-plane

(a)

xy-plane   xz-plane

(b)

xy-plane   xz-plane

(c)

xy-plane   xz-plane

(d)
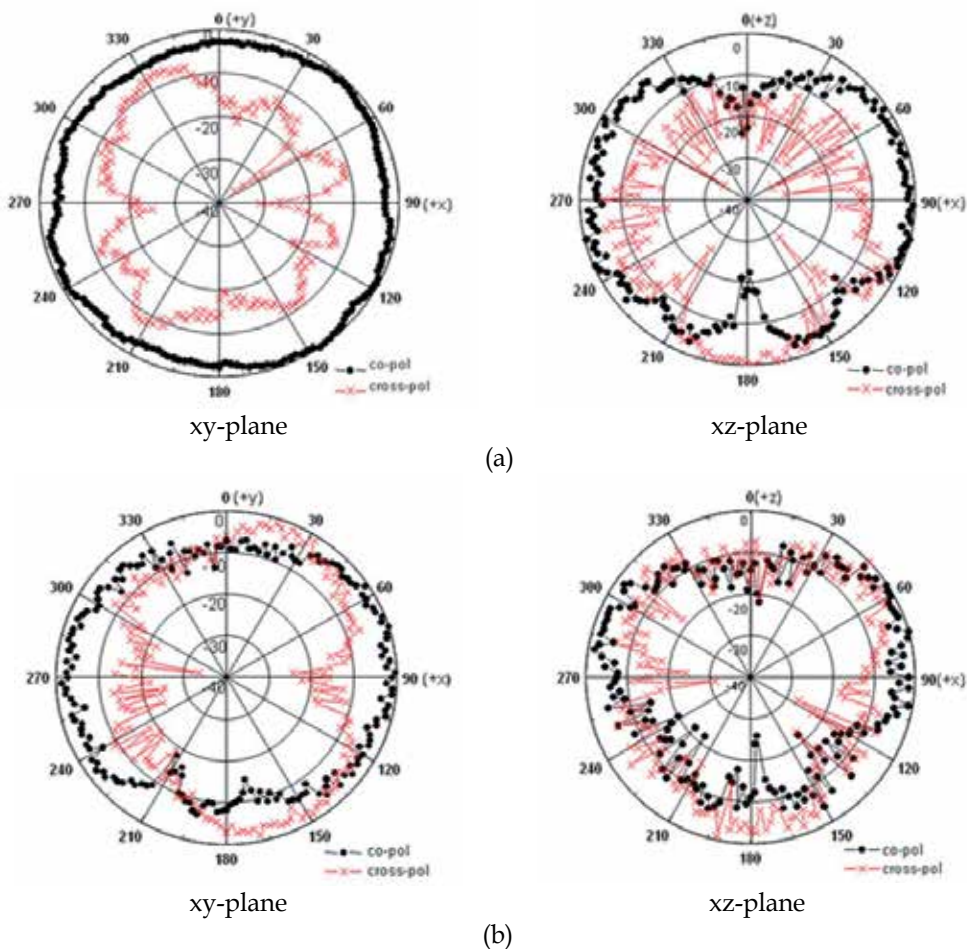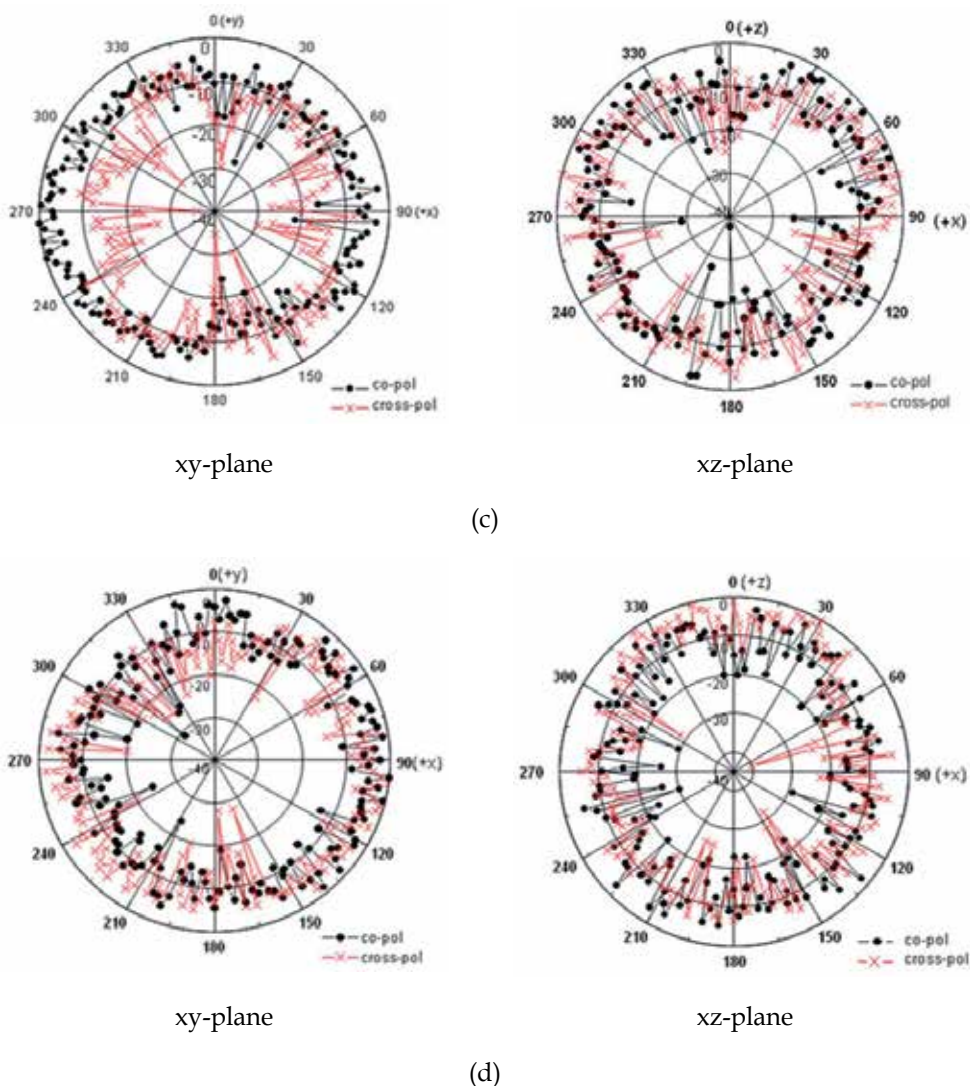
Fig. 5. Measured co-polarization and cross-polarization radiation patterns. (a) at 3 GHz , (b) at 6 GHz, (c) at 8 GHz, (d) at 11 GHz

4. Conclusion

We proposed an ultra-wideband CPW-fed planar monopole antenna with dual band rejection consisting of U-n slot. The CPW-fed planar monopole antenna provides extremely broadband characteristics with a planar compact structure, and the U-n slot has an effect on its band rejection characteristics. The measured results for the proposed antenna show that the frequency band of 3.0~ 11.0GHz is covered for VSWR<2, except for its dual rejection band ranging 3.15~3.79GHz and 5.13~5.85GHz, which is sufficient for UWB communication. The broadband antenna design is simplified by employing a CPW feeding structure and

good omnidirectional radiation patterns are obtained. The proposed antenna is suitable for use in UWB systems.

5. Acknowledgement

6. References

Abdollahvand, M., Dadashzadeh, G., & Mostafa, D. (2010). Compact Dual Band-Notched Printed Monopole Antenna for UWB Application, Antennas and Wireless Propagation Letters IEEE, Vol.9, (November 2010), pp. 1148 -1151, ISSN 1536-1225

Hassani, H., Samadi, T. M., & Mohammad, A. S. (2011). UWB Printed Slot Antenna with Bluetooth and Dual Notch Bands, Antennas and Wireless Propagation Letters IEEE, Issue 99, (February 2011), pp. 1-4, ISSN 1536-1225

Jyoti, R. P., Aditya S, R., & Rakhesh, S. K. (2010). A Compact 3.4/5.5 GHz Dual Band-Notched UWB Monopole Antenna With Nested U-Shaped Slot, Proceedings of 2010 Second International conference on Computing Communication and Networking Technologies, pp. 1-6, ISBN 978-1-4244-6591-0, Karur, July 29-30, 2010

Maeng, J. H., Lee, Y. J., & Yang, W. G. (2009). Design and Implementation of UWB CPW-Fed Plannar monopole Antenna, Microwave and Optical Technology Letters, Vol.51, No.19, (July 2009), pp. 650-653, ISSN 0895-2477

Mei, Z., Fu, G., & Gong, J. G., & Li, Q., & Wang, J. (2010). Printed monopole UWB antenna with dual band-notched characteristics, Proceedings of Ultra-Wideband (ICUWB) 2010 IEEE International Conference, Vol.2, pp. 1-4, ISBN 978-1-4244-5306-1, Nanjing, September 20-23, 2010

Nie, H., Chen, Z. Z. (2008). Transceiver Technologies for Impulse Radio Ultra Wideband (IR UWB) Wireless Systems, Proceedings of Communication Networks and Services Research Conference, pp. 3-4, ISBN 978-0-7695-3135-9, May 5-8, 2008

Su, M., Liu, Y. A., & Li, S. L., & Yu, C. P. (2010). A Compact Open Slot Antenna with Dual Notched Bands for UWB Application, Proceedings of Multimedia Communications (Mediacom) 2010 International Conference, pp. 139-140, ISBN 978-0-7695-4136-5, Hong Kong, August 7-8, 2010

Wei, F., Wu, Q. Y., & Shi X. Wei., & Chen, L. (2011). Compact UWB Bandpass Filter With Dual Notched Bands Based on SCRLH Resonator, Microwave and Wireless Components Letters IEEE, Vol.21, No.1, (January 2011), pp. 28-30, ISSN 1531-1309

Yang, W. G. (1999). Wideband Planar Antenna with U-n slot, Research Institute for Engineering and Technology, Vol.14, No.1,(1999), pp. 83-100, ISSN 1225-4509

Yang, W. G. (2002). Broadband Patch Antenna With U-n slot, Repulic of Korea Patent, No.1003207130000, January 2002

Zhang, M., Yin, Y. Z., & Wen, L. H., & Xiao, W. C., & Wang, Y. (2010). A slot antenna with band coupling strips for UWB application, Proceedings of Signals Systems and Electronics (ISSSE) 2010 International Symposium, Vol.1, p. 1, ISBN 978-1-4244-6352-7, Nanjing, September 17-20, 2010

Design of a CPW-Fed Dual Band-Notched Planar Wideband Antenna for UWB Applications

Fei Yu and Chunhua Wang
Hunan University
People's Republic of China

1. Introduction

Since the first Report and Order by the Federal Communications Commission (FCC) authorized the unlicensed use of ultra wideband (UWB) which must meet the emission masks on February 14, 2002 [1], both industry and academia have paid much attention to R&D of commercial UWB systems. Among UWB system design, the UWB antenna is the key component. Recently, a considerable amount of researches have been devoted to the development of the UWB antenna for its enabling high data transmission rates, low power consumption and simple hardware configuration in communication applications such as radio frequency identification devices, sensor networks, radar, location tracking, etc. Nowadays, the planar printed antenna fed with a microstrip line or a coplanar waveguide (CPW) has received much attention due to its high radiation efficiency and compact size and can be easily integrated with the other circuit. However, compared to the microstrip-fed antennas, the CPW-fed antennas are very good candidates since the feed line and slots are on one side of the substrate [2]. In order to obtain ultra wideband, the different optimum metal radiation patch geometries have been developed, like fork shape [3], elliptical shape [4], square shape [5], spade shape [6], circle shape [7], or made some modifications about the radiation patch [8]. Besides, over the designated frequency band, there exist some narrow bands for other communication systems, such as WiMAX operating in the 3.3 to 3.6 GHz band, and WLAN operating in the 5.15 to 5.825 GHz. They may cause communication interference with the UWB system. To solve this problem, it is desirable to design antennas with band notched characteristics to minimise potential interference. Several UWB antennas with frequency band notched function have been reported recently. The reported antennas are generally embedded with a half-wavelength structure such as a ω-shaped slot [2], a U-shaped slot [4], a C-shaped slot [8], or a V-shaped slot [9]. But most reported antennas were designed with only one notched band, mainly discussed on WLAN frequency band 5.15 to 5.825 GHz. UWB antennas with dual notched band were recently reported. In [10], the dual notched bands were formed by two nested C-shaped slots embedded in the bevelled patch. A pair of asymmetrical spurlines on the feedline was used to achieve dual notched band in [11]. A recently reported antenna has been designed by making use of two split resonant rings (SRR) to obtain dual band-notched characteristics [12]. Nevertheless, the geometry of the SRR structure is relatively complex.

In this paper, a CPW-fed novel planar ultra-wideband antenna with dual band-notched characteristics is introduced. In order to obtain ultra wideband, some modifications about

the antenna are introduced. Simply by etching a U-shaped slot in the radiating element, single band-notched characteristic from 5 to 6 GHz can be easily obtained. By etching two nested U-shaped slots in the radiating patch, dual band-notched characteristics for the proposed UWB antenna can be created to reduce the potential interferences between UWB system and narrowband systems. Details of the antenna design and simulation are presented in order to demonstrate the performance of the proposed antennas. Sec. 2 presents the details of the antenna structure and the design procedure. The antennas with single and dual band-notched characteristics were designed in Sec. 3. Sec. 4 analyses the radiation patterns and makes a comparison between recently proposed antennas and this antenna. Finally, the conclusion is presented in Sec. 5.

2. UWB antenna design

It is well known that the rectangular patch antenna has a narrow-band characteristic. To improve its operating bandwidth, we shape the bottom of the patch into an arc. In practical applications, the size of ground plane is finite and the direction of maximum radiation tilts somewhat upwards from the horizontal plane. To reduce this beam tilting, the ground plane of the proposed antenna is designed to have not rectangular but rounded shape. The arc-shaped patch and tapered ground plane make good broadband impedance matching of the antenna possible. To further expand the impedance bandwidth, a right-angle triangle on the upper corners of the patch and a small fan angle on each side of the ground plane near the feeding line are removed respectively. The improvement process steps are shown in Fig. 1.
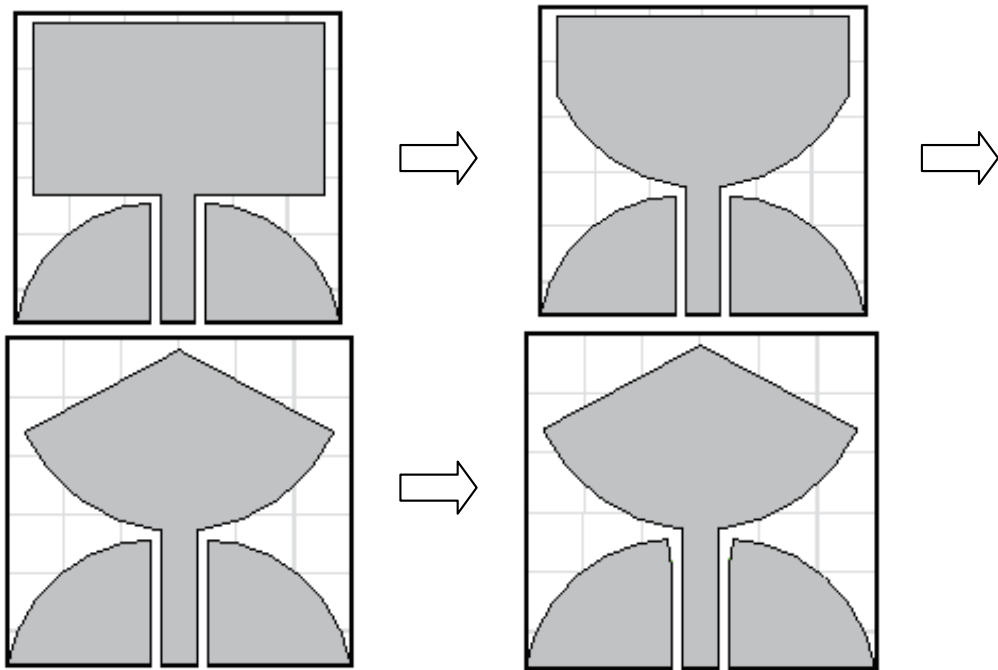
Fig. 1. The improvement process of the antenna

A comparison of the simulated reflection coefficient (S11) of the antenna with a full rectangular radiating patch, with the modification of the bottom side, with the cuts on the upper corners, and with the small angle on each side of the ground plane is plotted in Fig. 2 when all the dimensions are the same. It can be seen that the first line demonstrates the rectangular patch antenna has a narrow-band characteristic. The second line shows the impedance bandwidth is broadened when the bottom of the patch is shaped into an arc. On the basis of this, the third line about the upper corners modification indicates the bandwidth is further expanded compared with the second line (the main advantages that this modification is reducing the lowest frequency). The fourth line demonstrates the small angle on each side of the ground plane near the feeding line will affect the characteristic impedance of the CPW line and also explains the proposed antenna has a very wide impedance bandwidth.

1. —◆— with a full rectangular radiating patch
2. ····△···· with the modification of the bottom side
3. ····⊠···· with the cuts on the upper corners
4. – ·○·· with the small angle on each side of the ground plane
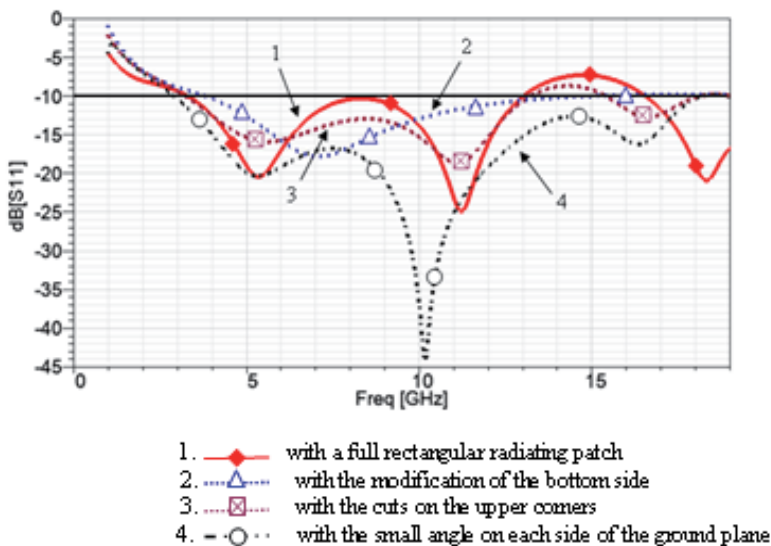
Fig. 2. Simulated reflection coefficient for different shapes of the radiation patch and the ground plane

The final geometry of the proposed compact band-notched antenna is depicted in Fig. 3. The antenna (referred to as antenna A) is printed on a FR4 substrate with size 28 mm × 30 mm, thickness of 1.6 mm, relative permittivity of 4.4 and loss tangent tan δ = 0.02. The proposed antenna is located in x-y plane and the normal direction is parallel to z-axis. The center strip and gap of the CPW line are 3.6 mm and 0.3 mm to achieve 50-Ω port characteristic impedance. By the improvement steps mentioned above the second paragraph, good impedance matching can be achieved across a wide bandwidth. We optimize the antenna geometrical parameters for S11 < -10 dB over the entire frequency range (3.1-10.6 GHz). The optimisation procedure is done by using Ansoft HFSS software. The final antenna geometry parameters are obtained as L1 = 28 mm, L2 = 30 mm, L3 = 13.5 mm, L4 = 5 mm, L5 = 1.5 mm, L6 = 10.8 mm, L7 = 5.4 mm, L8 = 12.9 mm, R = 15 mm, g = 0.7 mm, f = 3.6 mm, c = 0.3 mm, t = 0.3 mm, H = 1.6 mm. By selecting the optimal parameters, the proposed antenna can be tuned to operate within the UWB band.
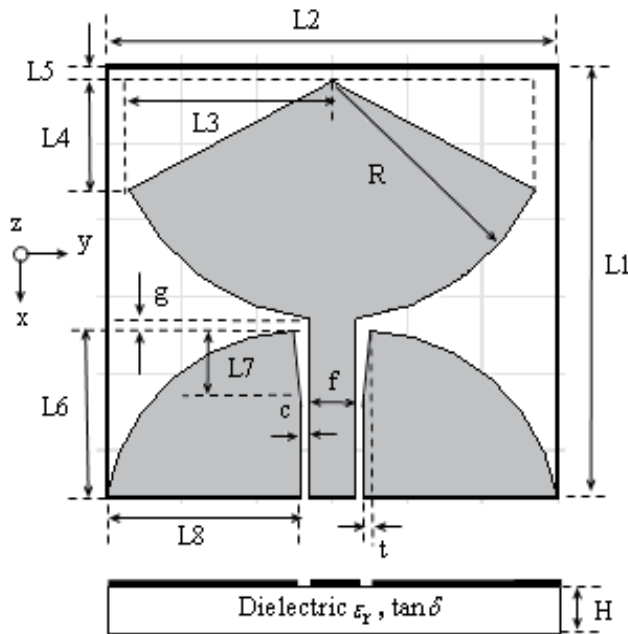
Fig. 3. Configuration of the proposed antenna A

3. Band-notched UWB antenna design

3.1 Single band-notched UWB antenna design

Interference between the existing narrow band wireless systems and UWB systems has been a concern due to the inherently ultra-wide operating frequency range for UWB communication. Such as IEEE 802.11a in U.S.A (5.15 GHz to 5.35 GHz, 5.725 GHz to 5.825 GHz) and HIPERLAN/2 in Europe (5.15 GHz to 5.35 GHz, 5.47 GHz to 5.725 GHz). To overcome this problem, various UWB antennas with a band-notched function have been developed not only to mitigate the potential interference but also to remove the requirement of an extra bandstop filter in the system. The simple and commonly used approach is to incorporate slots into the antennas' main radiator. Fig. 4 shows a schematic diagram of the UWB planar antenna (referred to as antenna B) with filtering property operating in the 5 to 6 GHz band.

The band-notched operation is achieved by using a U-shaped slot in the radiating patch of antenna A. Note that when the band-notched design applied to antenna A, there is no retuning work required for the previously determined dimensions. The notch frequency given the dimensions of the bandnotched feature can be given as

$$f_{notch} = \frac{c}{2L\sqrt{\varepsilon_{eff}}} \tag{1}$$

Where L is the total length of the U-shaped slot, ε_{eff} is the effective dielectric constant, and c is the speed of the light. We can take (1) into account in obtaining the total length of the U-shaped slot at the very beginning of the design and then adjust the geometry for the final
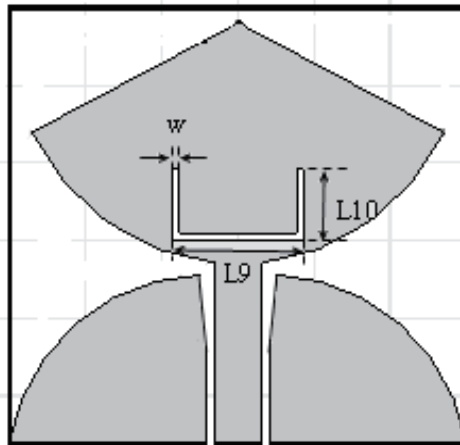
Fig. 4. Configuration of the proposed antenna B

design. From (1), we can known the length of the U-shaped slot (L = L9 + 2L10) is a crucial parameter to determine the center frequency of the stop band. In this design, the U-shaped slot was chosen to be nonresponsive close to about 0.33λ at the center frequency of the desired notched-band, where λ is the wavelength at the center frequency of the rejection band, the final design parameters of the U-shaped slot are L9 = 8.6 mm, L10 = 4.6 mm, w = 0.2 mm.

The impedance performance of the designed antenna was simulated using electromagnetic software Ansoft HFSS 11 which is based on finite element analysis. The simulated VSWR is shown in Fig. 5. The result demonstrates that a stop-band can be obtained by inserting a U-shaped slot in radiating patch. Compared to antenna A design, the single band-notched UWB antenna successfully blocks out the 5 to 6 GHz band and still performs good impedance-matching at other frequencies in the UWB band. Fig. 6 shows the simulated current distributions at specific frequencies. In Fig. 6(a) and (c), at frequencies 3.5 and 7.5 GHz, the current distributions mainly flow along the transmission line; while around the U-shaped slot the current is small. The simulated current distribution at 5.5 GHz is shown in
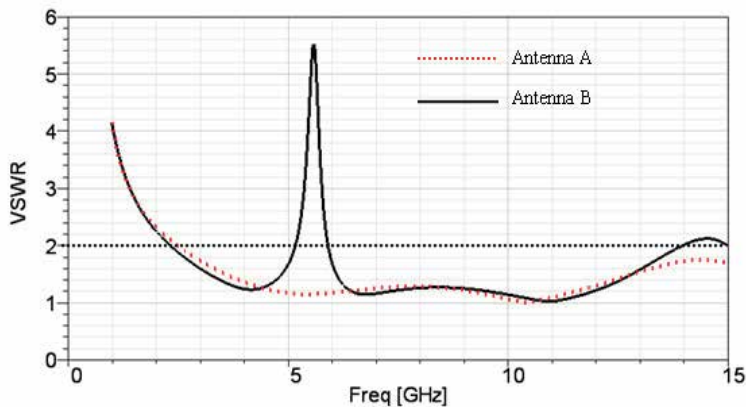
Fig. 5. Simulated VSWR of antenna B compared to antenna A
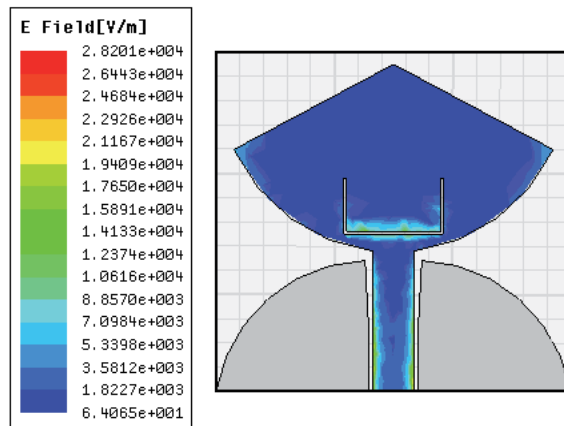
(a) 3.5 GHz
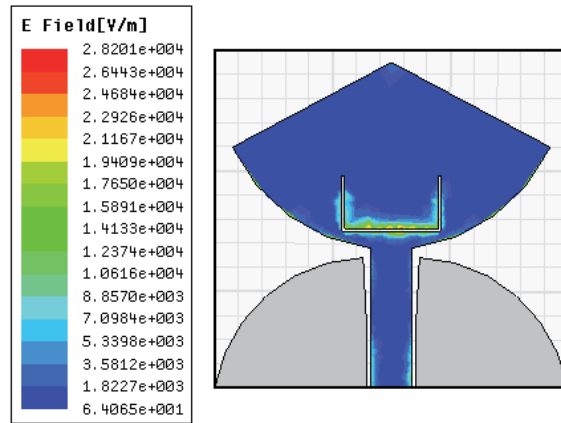
(b) 5.5 GHz
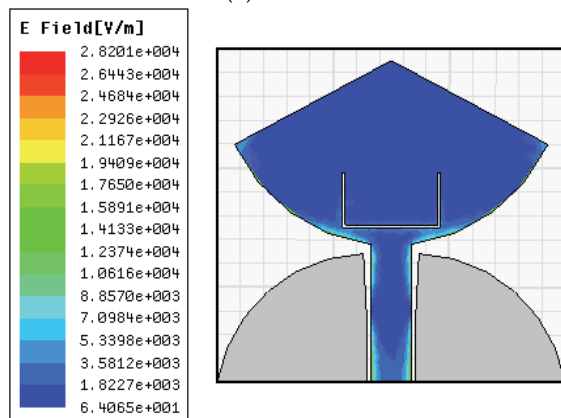
(c) 7.5 GHz

Fig. 6. Simulated current distribution of antenna B at specific frequencies

Fig. 6(b). It reveals that the currents mainly concentrate over the area of the slot in the radiation patch. The impedance nearby the feed-point changes acutely making large

reflection at the desired notched frequency. Fig. 7 also shows the surface current around the slot of antenna B at the notch frequency at 5.5 GHz. At 5.5 GHz, current is around the U-shaped slot. The impedance is nearly zero at the top of slot and the impedance is very high nearby the antenna feeding. In this case, the high impedance at the feeding point leads to the desired impedance mismatching near the notch frequency at 5.5 GHz [10].
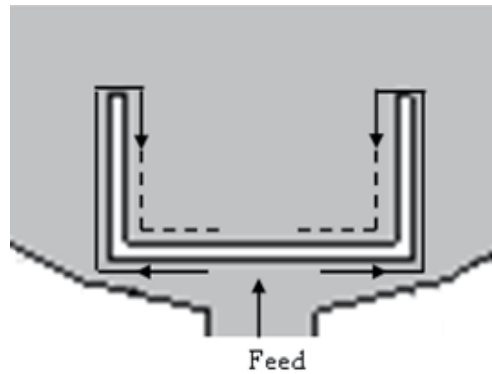
Fig. 7. Surface current around the slot of antenna B at the notch frequency at 5.5 GHz

By tuning various parameters, we can control the resonance frequency and quality factor to confirm the stop band. L9, L10 and w are key parameters to tune when the others are fixed. The effects of the lengths (L19, L10) and width (w) of the U-shaped slot on band-notched performance of the antenna are analyzed below. Fig. 8 illustrates the VSWR for different values of L9, It is obvious that when L9 becomes larger, the central frequency is reduced, and the edge of low frequency and the bandwidth are nearly unchanged. Fig. 9 shows the band-notch characteristics with different L10, the behavior is similar to changing L9. When L10 is increasing from 4.1 mm to 5.1 mm, the edge of low frequency and the bandwidth is nearly unchanged. However, the central frequency of the notched band is decreased. In Fig. 10, the central frequency increases as w increases. The bandwidth is shortened when the width (w) of the slot decreases from 0.3 mm to 0.1 mm. The antenna gain of the antenna B is shown in Fig. 11. The figure indicates that, the proposed antenna has good gain flatness except for in the stop-band. The antenna gain variations are less than 4 dB throughout the desired UWB frequency band, and a sharp gain drop of about 7 dB occurs at 5.5 GHz.
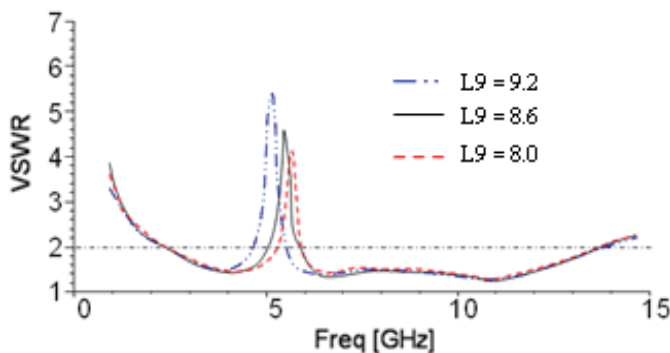
Fig. 8. Simulated VSWR for various L9 when L10 = 4.6 mm and w = 0.2 mm
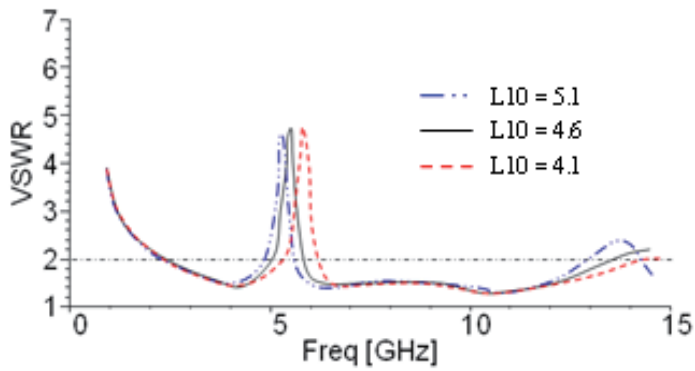
Fig. 9. Simulated VSWR for various L10 when L9 = 8.6 mm and w = 0.2 mm
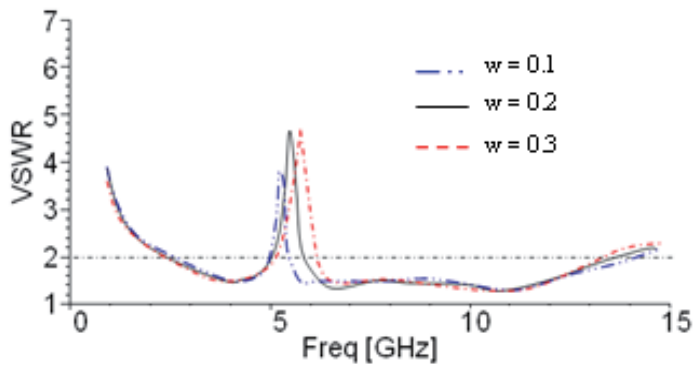
Fig. 10. Simulated VSWR for various w when L9 = 8.6 mm and L10 = 4.6 mm
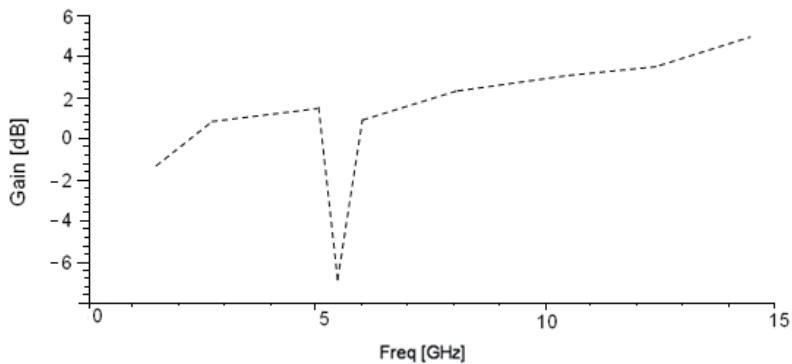
Fig. 11. Simulated gain of antenna B

To further explain the principle of the band-notched structures and how the center frequencies and bandwidths can be controlled an LC circuit model has been extracted for the proposed antenna A as shown in Fig. 12. Approximately, the radiating element of UWB antenna can be seen as several RLC parallel cells in series. The equivalent circuit input impedance can be expressed as

$$Z_R = \sum_{k=1}^{n} \frac{j\omega R_k L_k}{R_k \left(1 - \omega^2 C_k L_k\right) + j\omega L_k} \tag{2}$$

To simplify the calculation, only the real part is considered to determine the values of components with the formula

$$R_R = \sum_{k=1}^{n} \frac{R_k}{1 + R_k \left(\dfrac{1}{2\pi f L_k} - 2\pi f C_k\right)^2} \tag{3}$$
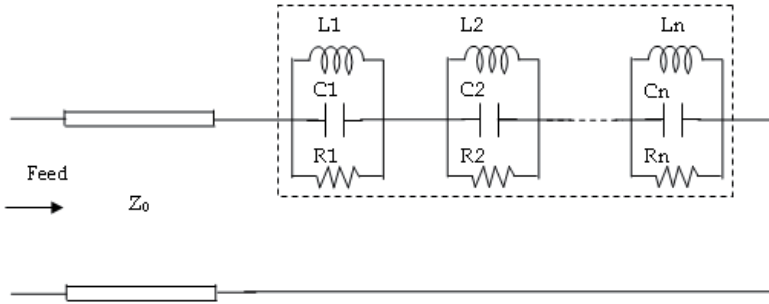
Fig. 12. Impedance model for radiating element of UWB antenna A

Fig. 13 shows the equivalent circuit model for radiating element of UWB antenna B. Le and Ce indicate the inductor and capacitor values of the slot resonator. When the current propagates along the edge of the slot, an inductance should be introduced to the model. The narrow slot is equivalent to a capacitor. Increasing the length of the slot or decreasing the slot width is similar to increasing the capacitor value in the parallel LC circuit. On the other hand, increasing the length of slot will also lead to the increase of the inductor value [13]. Next we discuss bandwidth adjustment. For the parallel RLC resonator circuit as shown in Fig. 13, the input admittance is given by

$$Y_{in} = \frac{1}{R_R} + j\omega C_e + \frac{1}{j\omega L_e} \tag{4}$$

Where R_R represents the radiation resistance of the monopole element of antenna A. For a frequency near the resonant frequency [13]

$$\omega = \omega_0 + \Delta\omega, \; \omega_0 = \frac{1}{L_e C_e}$$

$$\begin{aligned} Y_{in} &= \frac{1}{R_R} + j\omega C_e + \frac{1}{j\omega L_e} \\ &= \frac{1}{R_R} + \frac{j}{\omega L_e}\left(\omega^2 L_e C_e - 1\right) \\ &= \frac{1}{R_R} + \frac{j}{\omega L_e}\left(2\omega_0 \Delta\omega + \Delta\omega^2\right) L_e C_e \\ &\approx \frac{1}{R_R} + j2C_e \Delta\omega \end{aligned} \tag{5}$$

In this case it is obvious that Y_{in} is similar to the input admittance of a parallel R and 2C circuit near 0 GHz. Then the -3dB bandwidth (BW) of the parallel RLC resonant circuit approximately equals twice the -3dB bandwidth of the parallel R and 2C circuit as shown in below [13]

$$BW = \frac{2}{R_R \times 2C_e} = \frac{1}{R_R C_e} \tag{6}$$

$$FBW = \frac{BW}{\omega_0} = \frac{1}{\omega_0 R_R C_e} \tag{7}$$

Where FBW represents the fractional bandwidth. Based on the above analysis we have a clear method for controlling the centre frequency and bandwidth of the notch. Increasing the length of the slots, which is similar to increasing the inductor value and the capacitor value, has the effect of decreasing the centre frequency and bandwidth [13]. Simulated results shown in Figs. 8 and 9 prove this conclusion. Fig. 10 shows the simulated VSWR for various width of the slot. It can be seen that, increasing the slot width is equivalent to decreasing the capacitor value, which ultimately leads to the rise of centre frequency and bandwidth of the notch band.
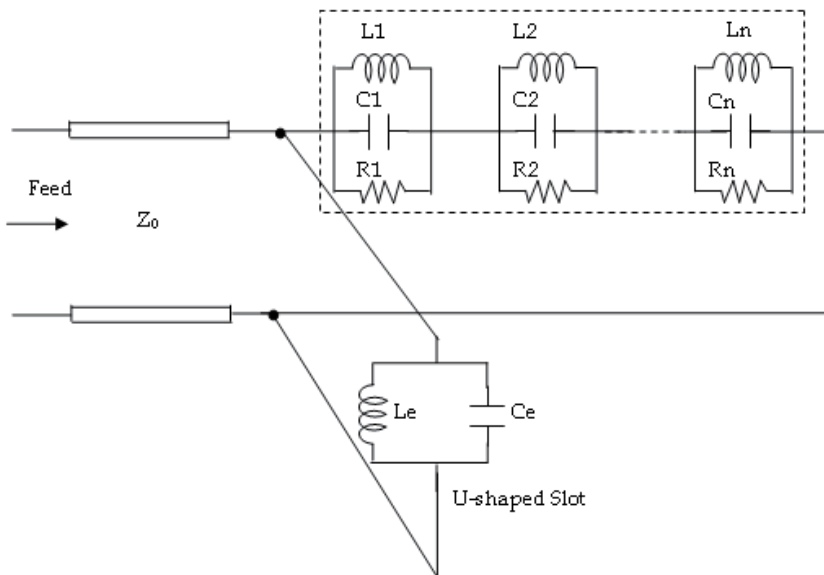
Fig. 13. Impedance model for radiating element of UWB antenna B

3.2 Dual band-notched UWB antenna design

Besides WLAN systems, IEEE 802.16 WiMAX from 3.3 to 3.6 GHz also operates in the UWB band. Dual notched bands are realized by using two nested U-shaped slots in the radiating patch (antenna A), which can yield band-notched characteristics centered at 3.4 GHz and 5.5 GHz. Fig. 14 shows the geometry and configuration of the UWB antenna (referred to as antenna C) with dual band-notched characteristics. It is note that, since the mutual coupling

exists between the exterior and interior U-shaped slots, the simulation values are not exactly equal to the prediction ones [10]. The optimized design parameters are L11 = 5 mm, L12 = 11 mm, L13 = 5.1 mm, L14 = 10 mm, w1 = 0.3 mm.
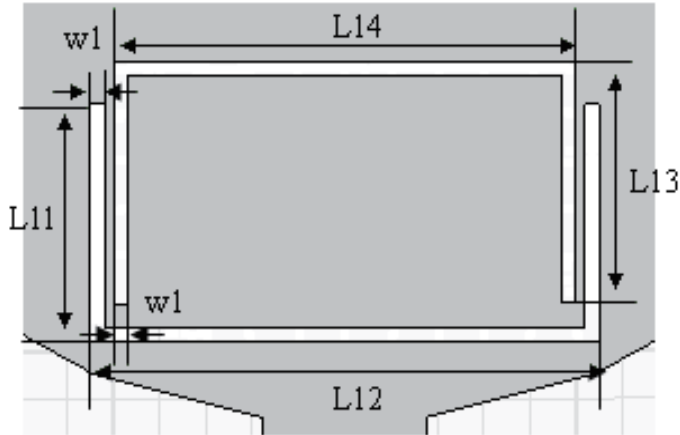
Fig. 14. Configuration of the proposed antenna C

Fig. 15 shows the simulated VSWR against frequency for the proposed antenna C. Results of the reference antennas without band-notched characteristics and with single band-notched characteristic are also shown for comparison. It is seen that the proposed antenna exhibits two notched bands of 3.3 to 3.5 and 5 to 6 GHz, while maintaining wideband performance from 1.8 to 15 GHz for VSWR < 2, covering the entire UWB frequency band. It is concluded that the notch bands for antenna C are indeed created by the two nested U-shaped slots. The simulated gain is shown in Fig. 16 and indicates a gain variation from 0.5 to 4.2 dB in the frequency range of 1.8 to 15 GHz. As can be expected, Sharp gain decreases occur both in 3.3 to 3.5 and 5 to 6 GHz bands. However, for other frequencies outside the rejected bands, the antenna gain is nearly constant in the entire UWB band. Fig. 17 shows the axial ratio against theta (spherical coordinate) for the proposed antenna C. It is observed that the whole axial ratio is greater than 3 dB, so the proposed antenna C is a linearly polarized antenna.
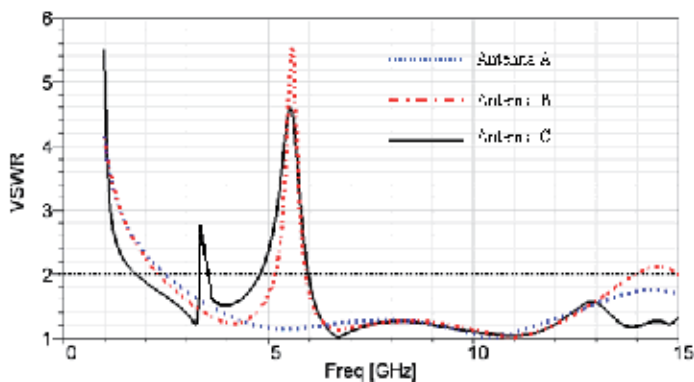
Fig. 15. Simulated VSWR of antenna C compared to antenna A and B
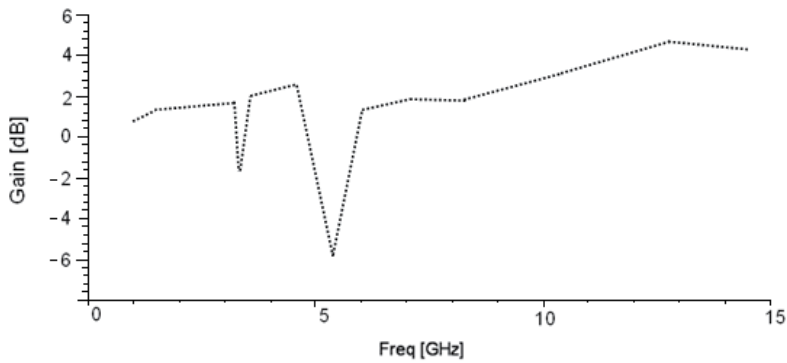
Fig. 16. Simulated gain of antenna C
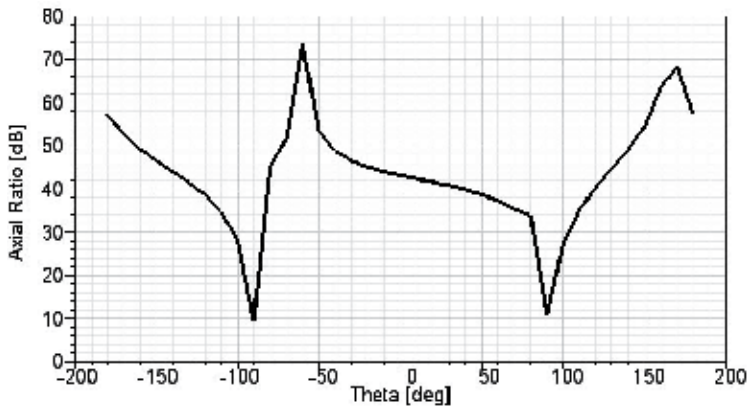
Fig. 17. Simulated axial ratio of antenna C

4. Radiation patterns and comparison

From the UWB applications point of view, the UWB antennas are usually required to have an omnidirectional radiation in the plane orthogonal to the radiating element. The radiation patterns at specific frequencies 3.2 GHz, 6 GHz, 9 GHz, 10.6 GHz and 13.5 GHz are simulated and illustrated in Fig. 18. The quasi-omnidirectional and symmetrical patterns in H plane in the whole band are obtained, which are necessary in a UWB communication system. The interference of high modes in high frequency is reduced. As a result, the proposed antenna can be used in several applications to compensate the drawback of the antennas at the whole frequency band from 3.1 to 10.6 GHz.

It is note that, the radiation patterns of antenna A and antenna B are not depicted. From the analysis by the Reference [10], the proposed band-notched structures including the single band-notched and dual band-notched ones have little influence on the radiation patterns of the UWB antenna. Tab. 1 summarizes the performances and compares this design to recently published UWB antennas with stop-band characterization. From Tab. 1, we can see that some of the antennas have only one notched band; others which have two notched bands, but the operation frequency band is not wide. When comparing the results to the

performance of some UWB antennas presented in Tab. 1, the following features of the implemented antenna can be highlighted: wide impedance bandwidth, good band-notch characteristic, compact in size and good gain flatness.

(a) 3.2 GHz

(b) 6 GHz

(c) 9 GHz

(d) 10.6 GHz

(e) 13.5 GHz
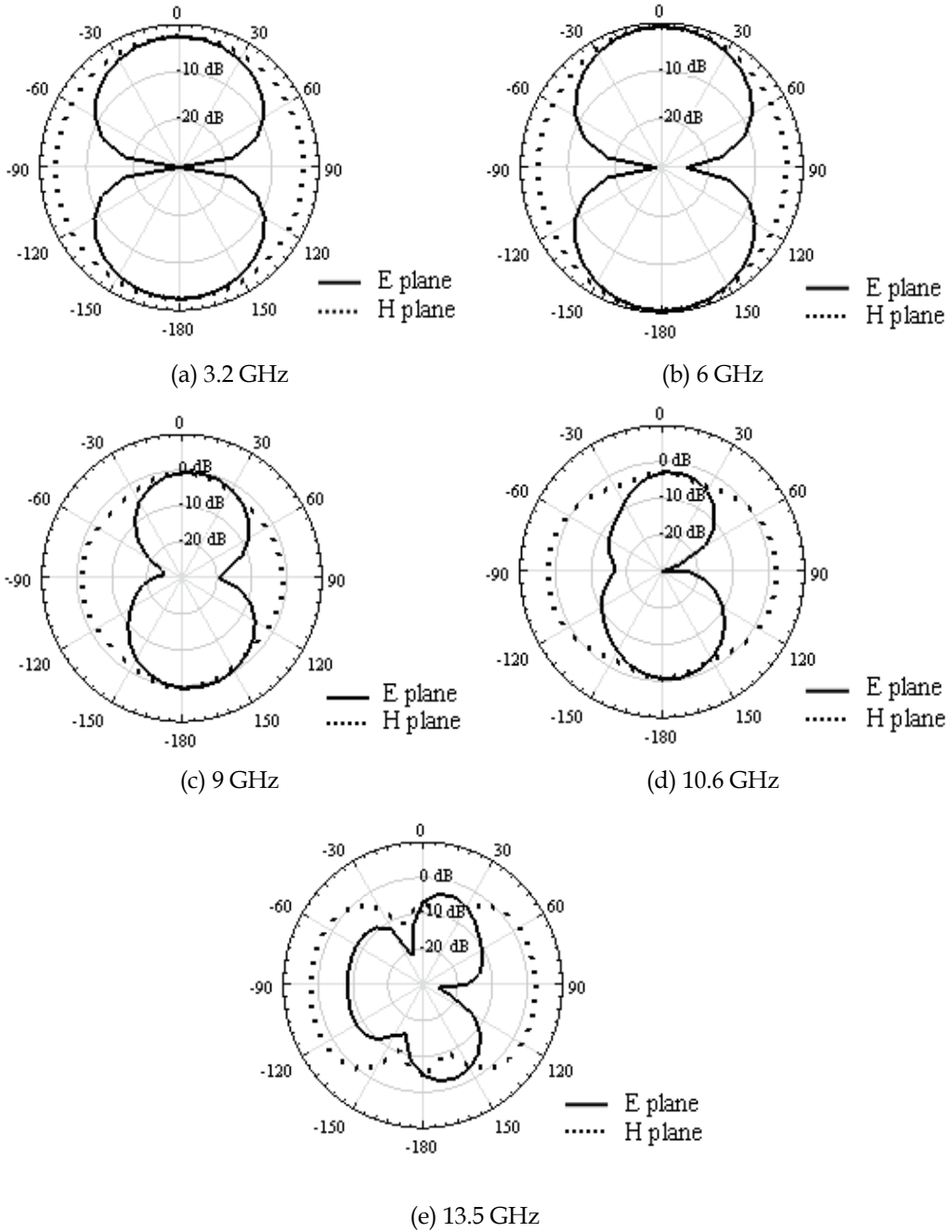
Fig. 18. Simulated radiation patterns at specific frequencies

Authors	Substrate material	Method of achieve stop-band	Operating bandwidth (GHz)	Relative bandwidth	Stop-band bandwidth (GHz)	Antenna size (mm²)	Gain (dB)
Mehdipour, A. *et al*	Rogers RT Duroid 3003	embedding a ω-shaped slot	3.0 - 11	114 %	5.4 - 5.95	35 × 35	---
Nikolaou, S. *et al*	liquid crystal polymer	inserting a U-shaped slot	3.0 - 12	120 %	5.0 - 6.0	38.7 × 26.88	< 4.2
Yu, F. *et al*	FR4	embedding a C- shaped slot	3.0 - 23	153.8 %	5.0 - 6.0	28 × 30	0.2 - 3.9
Kim, Y. *et al*	FR4	inserting a V-shaped slot	2.8 - 10.6	116.4 %	f_c = 5.25	22 × 31	0.8 - 5.0
Chu, Q.-X. *et al*	FR4	embedding two nested C-shaped slots	3.1 - 10.6	> 91.3 %	f_{c1} = 3.4 f_{c2} = 5.5	26 × 30	2 - 5
Luo, J. *et al*	FR4	embedding an E-shaped slot in the patch and a U-shaped slot in the ground	2.87 - 10.91	116.6 %	3.49 - 4.12 5.66 - 6.43	35 × 14	----
This work	FR4	embedding two nested U-shaped slots	1.8 - 15	> 157.1 %	f_{c1} = 3.4 f_{c2} = 5.5	28 × 30	0.5 - 4.2

Table 1. Comparison between recently proposed antennas and this antenna

5. Conclusion

In this paper, a CPW-fed novel planar ultra-wideband antenna with dual band-notch characteristics was presented. One right-angle triangle was simulation removed from both two upper corners of the rectangular UWB antenna combined with an arc-shaped bottom and with a tapered arc-shaped ground plane. The simulation result of the VSWR demonstrates that the antenna has very broadband impedance which covers the frequency range of 1.8 to over 15 GHz. By embedding two nested U-shaped slot in the radiating patch, two frequency band notches between the bandwidth of 3.3 to 3.5 GHz and 5 to 6 GHz for WiMAX and WLAN have been obtained. Stable radiation patterns and constant gain in the UWB band are also obtained. Simulated and analyzed in detail in this paper, the proposed antenna could be a good candidate for UWB communication applications.

6. Acknowledgment

7. References

First Report and Order. (2002). Revision of Part 15 of the Commission's Rule Regarding Ultra-Wideband Transmission System FCC 02-48. Federal Communications Commission

Mehdipour, A.; Parsa, A.; Sebak, A.-R. & Trueman, C. W. (2009). Miniaturised coplanar waveguide-fed antenna and band-notched design for ultra-wideband applications. *IET Microwave Antennas and Propagation,* Vol. 3, No. 6, pp. 974-986, ISSN 1751-8725

Ryu, K. S. & Kishk, A. A. (2009). UWB Antenna With Single or Dual Band-Notches for Lower WLAN Band and Upper WLAN Band. *IEEE Transactions on Antennas and Propagation,* Vol. 57, No. 12, pp. 3942-3950, ISSN 0018-926X

Nikolaou, S.; Kingsley, N. D.; Ponchak, G. E.; Papapolymerou, J. & Tentzeris, M. M. (2009). UWB Elliptical Monopoles With a Reconfigurable Band Notch Using MEMS Switches Actuated Without Bias Lines. *IEEE Transactions on Antennas and Propagation,* Vol. 57, No. 8, pp. 2242-2251, ISSN 0018-926X

Ojaroudi, M.; Ghobadi, C. & Nourinia, J. (2009). Small Square Monopole Antenna With Inverted T-Shaped Notch in the Ground Plane for UWB Application. *IEEE Antennas and Wireless Propagation Letters,* Vol. 8, pp. 728-731, ISSN 1536-1225

Li, W.-T.; Shi, X.-W. & Hei, Y.-Q. (2009). Novel Planar UWB Monopole Antenna With Triple Band-Notched Characteristics. *IEEE Antennas and Wireless Propagation Letters,* Vol. 8, pp. 1094-1098, ISSN 1536-1225

Dong, Y.-J.; Hong, W.; Kuai, Z.-Q. & Chen, J.-X. (2009). Analysis of Planar Ultrawideband Antennas With On-Ground Slot Band-Notched Structures. *IEEE Transactions on Antennas and Propagation,* Vol. 57, No. 7, pp. 1886-1893, ISSN 0018-926X

Yu, F. & WANG, C. (2009). A CPW-Fed Novel Planar Ultra-Wideband Antenna with a Band-Notch Characteristic. *Radioengineering,* Vol. 18, No. 4, pp. 551-555, ISSN 1210-2512.

Kim, Y. & Kwon, D.-H. (2004). CPW-fed planar ultra wideband antenna having a frequency band notch function. *Electronics Letters,* Vol. 40, No. 7, pp. 403-405, ISSN 0013-5194

Chu, Q.-X. & Yang, Y.-Y. (2008). A Compact Ultrawideband Antenna With 3.4/5.5 GHz Dual Band-Notched Characteristics. *IEEE Transactions on Antennas and Propagation,* Vol. 56, No. 12, pp. 3637-3644, ISSN 0018-926X

Zhao, Y. H.; Xu, J. P. & Yin, K. (2008). Dual band-notched ultra-wideband microstrip antenna using asymmetrical spurlines. *Electronics Letters,* Vol. 44, No. 18, pp. 1051-1052, ISSN 0013-5194

Luo, J.; Cui, Z.; Xiong, J.-P.; Zhang, X.-M. & Jiao Y.-C. (2008). Compact printed ultra-wideband monopole antenna with dual band-notched characteristics. *Electronics Letters,* Vol. 44, No. 19, pp. 1106-1107, ISSN 0013-5194

Dong, Y. D.; Hong, W.; Kuai Z. Q. & Chen J. X. (2009). Analysis of Planar Ultrawideband
Antennas With On-Ground Slot Band-Notched Structures. *IEEE Transactions on
Antennas and Propagation,* Vol. 57, No. 7, pp. 1886-1893, ISSN 0018-926X

Coplanar-Microstrip Transitions for Ultra-Wideband Communications

Mohammed El-Gibari, Dominique Averty, Cyril Lupi,
Yann Mahé Hongwu Li and Serge Toutain
Institut de Recherche en Electrotechnique et Electronique de Nantes Atlantique
University of Nantes, Faculté des Sciences et Techniques
France

1. Introduction

Nowadays optics is penetrating into the broadband access networks, so the data transmission bit-rate can be guaranteed regardless the distance between the subscriber and the central office. Many laboratories are working on the radio over fiber technology in the home networks. For home network applications, one must use low-cost and broadband modulators to transcribe the electrical signal into optical signal. The electro-optic polymers on which very active research is being carried out have the required properties for realizing this kind of modulators. Their realization needs a certain number of delicate manufacturing steps, therefore, a rigorous study of the component must be made before the realization of the modulators. The optimization of the modulator optical structure must be made first, from the properties of polymers at one's disposal and the technological constraints, in order to obtain a single mode guide with minimum losses. Then, optimization of the driving electrode, inseparable step from the optical study, should be carried out. In electro-optic modulators based on polymer, the chromophore molecules responsible for the electro-optic effect are oriented perpendicularly to the substrate as they are generally poled by Corona effect or with contact electrodes. Consequently, a microstrip line is suitable to apply the driving signal to induce the electro-optic effect. Before packaging the final component, it is necessary to assess its performances directly on wafer by use of a probe station, usually equipped with probes compatible with coplanar lines GSG (Ground-Signal-Ground) insuring an easy electrical contact. So, a transition between coplanar and microstrip lines (CPW-MS) is indispensable to characterize the components on wafer. This transition must satisfy at least these three criteria: ultra-wideband, easy to realize and low-cost. One solution is to physically connect the coplanar ground planes to the bottom ground plane of the microstrip line through a via-hole, which would make the component more expensive without eliminating all parasitic resonance (Haydl, 2002). It is in this context that we conducted a comprehensive study of via-free transitions between coplanar and microstrip lines, in order to make easy and simple the characterization of components driven by microstrip line with CPW (Coplanar waveguide) probes. These transitions may be also employed in all microwave circuits driven by microstrip lines.

2. Constraints related to modulator packaging

The electro-optical (EO) polymers are expected to allow realizing cheaper modulators with much better performances than those based on inorganic crystals such as $LiNbO_3$ (Courjal et al., 2002) and semiconductors such as GaAs (Kim et al., 1990). Among the advantages of polymers, we can quote the very broad bandwidth thanks to a good optical-microwave phase matching (Chen et al., 1997), low driving voltage due to high electro-optic coefficient (>100 pm/V) (Dalton et al., 1999), low cost and compatibility of integration with semiconductor materials (Faderl et al., 1995).

The realization of modulators on EO polymer entails the following manufacturing stages. The first stage is to deposit a thin films polymer by spin-coating in order to realize a Mach-Zehnder interferometer structure with two buried rectangular single-mode waveguide arms. In our case, this constraint dictates the choice of the cladding polymers which confines the optical wave in the electro-optical polymer. Once the single-mode optical waveguide is made, the second step consists in realizing the driving electrode which apply the control voltage and thus modulate the light. The overlap between the optical and microwave waves and the impedance matching are two important elements to take into account to determine the dimensions of this electrode. These dimensions affect also the Y junctions of the Mach-Zehnder electro-optical modulator. Figure 1 shows the structure of a modulator based on EO polymer.
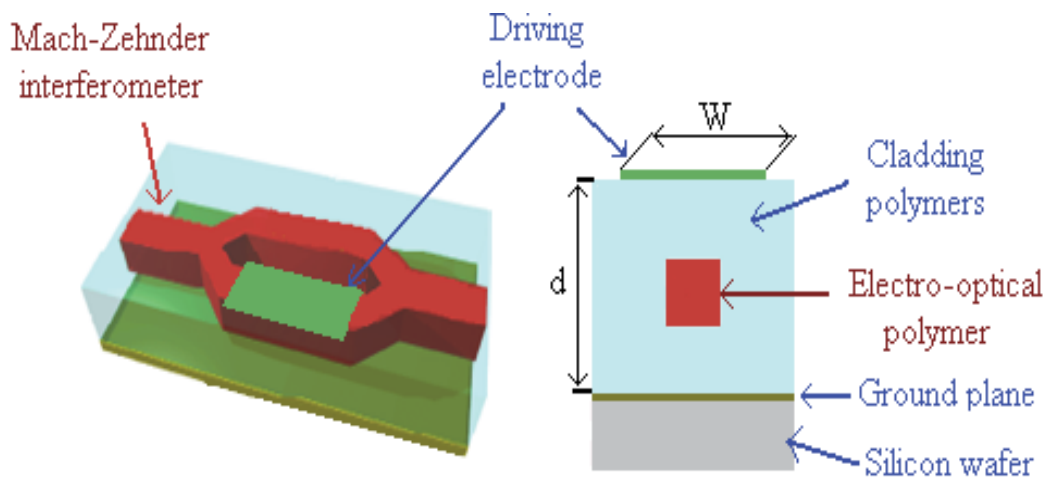
Fig. 1. Overview of the structure of an electro-optical modulator based on polymer

Optimization of modulator design consists in an optimal trade-off between the following main characteristics: high electro-optical bandwidth, low driven voltage, low optical insertion loss and high modulation ratio. The driving voltage V_π is a key parameter in the optical optimization of the component. It is defined as the voltage introducing a phase shift of π between the two arms of the Mach-Zehnder interferometer. This voltage depends on the light wavelength (λ), the refractive index (n), the gap distance (d) between signal and ground electrodes, the interaction length (L) between the optical and electrical waves, the overlap integral between them (Γ) and the electro-optical coefficient (r). This voltage is given when ignoring the microwave signal attenuation:

$$V_\pi = \frac{\lambda d}{n^3 r L \Gamma} \tag{1}$$

The major challenge is to minimize this voltage while keeping the optical insertion loss as low as possible. But these constraints are often contradictory. On one hand, an increase of the interaction length (L) minimizes certainly the driving voltage. But, the electrical losses will increase which limits the bandwidth of the component. On the other hand, the decrease of the gap distance between signal and ground electrodes reduces the optical wave confinement and results in larger absorption of evanescent wave by the electrode. The compromise to be found between a low driving voltage and a high bandwidth is a crucial point when designing electro-optical modulators.

Taking into account the characteristics and properties of polymers employed and in order to optimize the modulator driving voltage, the thickness of polymers (d) is usually fixed between 8 and 10 µm (Michalak, et al., 2006). Once the dimensions of the optical structure are fixed, it is then necessary to optimize the driving electrode in order to maximize the electro-optical effect of the modulator. Indeed, the bandwidth of the component depends on the type and the characteristics of the microwave electrode. In the case of electro-optical modulators based on polymer, the chromophores responsible for the electro-optic effect are oriented perpendicularly to the substrate as they are generally poled by Corona effect or with contact electrodes. So, in order to obtain maximum electro-optic effect, the driving electric field must be oriented as the chromophores. Consequently, a microstrip line is suitable to apply the driving signal. It is therefore necessary to optimize this microstrip line to maximize the overlap factor between optical and electrical waves and maintain its characteristic impedance around 50 Ω to avoid any reflection of the signal. Figure 2 shows the variation of the characteristic impedance of a microstrip line according to the ratio of width (W) / thickness (d) and for different relative permittivities according to the analytical equations of Wheeler and Hammerstad (Wheeler, 1977 & Hammerstad, 1975):

$$Z_c = \frac{Z_0}{2\pi\sqrt{\varepsilon_r}} \ln\left[C \frac{d}{W} + \sqrt{1 + \left(\frac{2d}{W}\right)^2} \right] \tag{2}$$

$$C = 6 + (2\pi - 6)\exp\left(-\left(30.666\frac{d}{W}\right)^{0.7528}\right) \tag{3}$$

Z_0 = characteristic impedance of vacuum

Taking into account the low relative permittivity of polymer between 2.5 and 4 (Algani, et al., 2005), a ratio (W/d) between 2 and 3 is required to have the impedance of microstrip line around 50 Ω, that's to say an electrode width W ranging between 16 µm and 30 µm.

Once the dimensions of the optical guides and microwave driving electrode are optimized, the next step is to make this modulator usable for industrial customers. Thus, for the component packaging, in addition to the dimensions, it is also necessary to take into account the inputs and outputs of the component: one optical input and one optical output via optical fiber pigtails, a microwave connector that gives access to the driving electrode and DC connectors which make possible to bring some functionalities, bias and chirping for example.
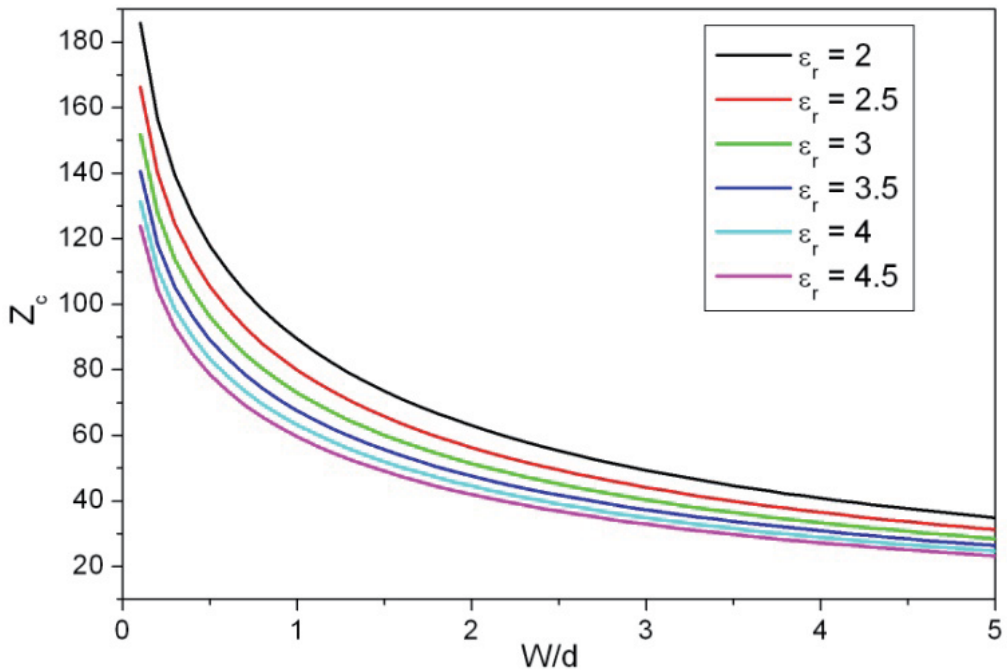
Fig. 2. Variation of characteristic impedance of a microstrip line according to the ratio W/d and for different relative permittivities.
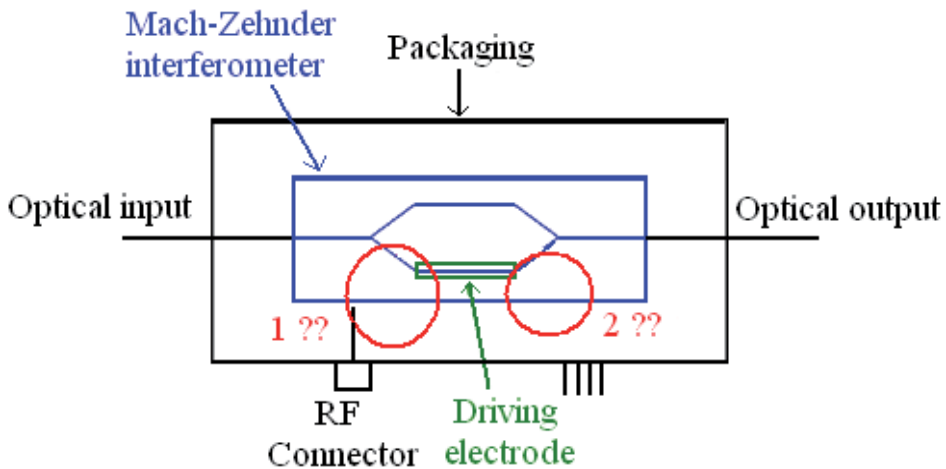
Fig. 3. Packaging of an electro-optical modulator based on polymer

Figure 3 shows a complete diagram of a modulator packaging (in black on the figure) in which we depict the structure of Mach-Zehnder interferometer in blue and the microstrip driving electrode in green. In this type of components, optical accesses will be privileged because of the strong constraints related to their dimensions. In general, the optical coupling

is made by lensed fiber allowing the injection of the light in the optical guide and collecting it at the output of the Mach-Zehnder interferometer. After a dynamic alignment, these last can be fixed at the package by using an epoxy adhesive or by brazing of a metallic coating deposited on the optical fiber by using a laser source. As to the microwave accesses, it will be necessary to connect the driving electrode to a connector whose axis is perpendicular to this microstrip line (cf. red section (1) in figure 3) and to connect the other end of the microstrip line (cf. red section (2) in figure 3) to a 50 Ω load in order to avoid signal reflection. Usually, in planar technology, broadband 50 Ω load is realized with a thin resistive film deposited on an alumina substrate and etched by laser ablation with the necessary dimensions. But that requires the realization of metalized holes, which is very difficult in our case (cf. figure 4).
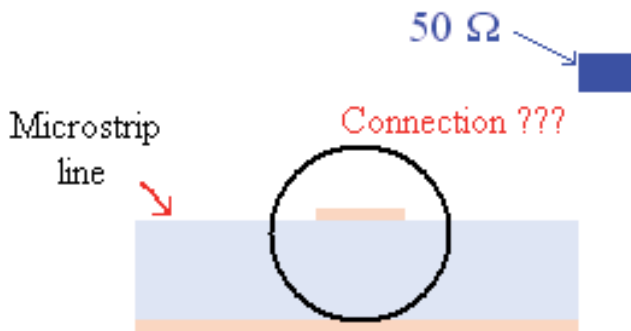
Fig. 4. Difficulty related to the interconnection of a load on a microstrip line

An easy way is to put two 100 Ω loads on a coplanar structure. They are in parallel and thus make it possible to load the microstrip line by a 50 Ω impedance (cf. Figure 5). In this case, the problem then is to realize a connection between the coplanar line and the microstrip line (red section in figure 5).
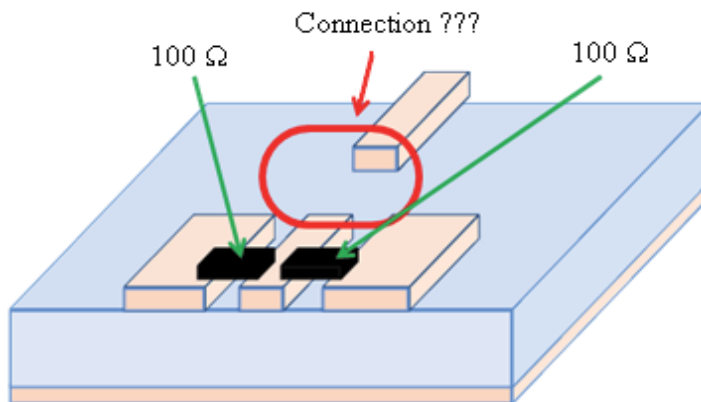
Fig. 5. Connection of a 50 Ω load realized with two 100 Ω loads connected in parallel on a coplanar line.

To launch a microwave signal from a generator to the component driving electrode (cf. red section (1) in figure 3), appropriate connectors are necessary. Indeed, with a coaxial cable,

the interior radius of its outer conductor should be approximately equal to the substrate thickness. In the case of a thin substrate, as shown in figure 6, the most of energy is reflected because of the dimensional difference between the substrate thickness and the connector contact. This mismatch can cause difficulties for electrical contact during microwave packaging and seriously degrade device performance.
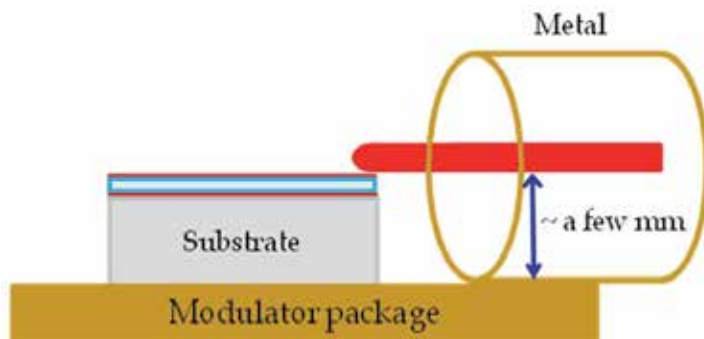
Fig. 6. Constraint related to the excitation of a structure in thin layer by a coaxial connector

Thus, to avoid mismatch problems, it is preferable to use a coplanar connector like the end launch coplanar connector, Model #1492-04A-5 of SouthWest Microwave (Figure 7). In this case, the impedance matching between the connector and the driving electrode is realized by a transition between the quasi-TEM mode of the coplanar line and that of the microstrip line.
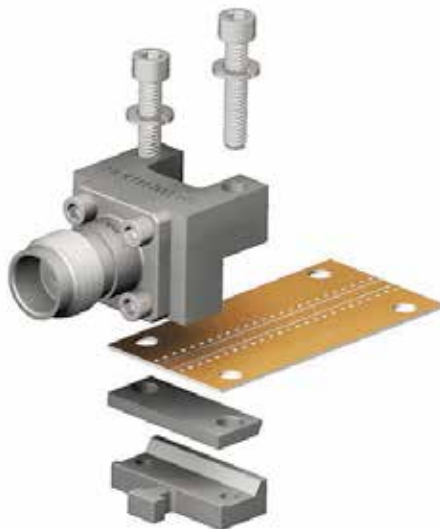
Fig. 7. The end launch coplanar connector, Model #1492-04A-5 of SouthWest Microwave [DC - 50 GHz]

So, due to the low thickness of polymer substrate, a coplanar to microstrip transition is needed for both modulator packaging and on-wafer measurement of the electro-optic

modulator before the packaging steps. As a result, we will attach ourselves to study ultra-broad bandwidth vialess coplanar-microstrip-coplanar (CPW-CPW-MS) transition on thin polymer substrate.

First, we will optimize back-to-back GCPW-MS-GCPW (Grounded Coplanar Waveguide-Microstrip lines) transitions without via-hole in the substrate to connect upper and lower ground plane and without patterning the bottom ground plane. These transitions use the electromagnetic coupling between the bottom and top ground planes. In the second part, we study the transitions for component connectorization using coplanar connectors. At this stage, patterning of the bottom ground plane is necessary to maintain the characteristic impedance to 50 Ω. So, an optimization of the dimensions of these transitions is essential for easy installation of the coplanar connectors and packaging component.

3. Coplanar-microstrip (GCPW-MS) transitions

3.1 GCPW-MS-GCPW transitions on the thick substrate

In the literature, several structures have been proposed to realize vialess CPW-MS transitions according to the intended application and the desired bandwidth (Zheng, et al., 2003 & Safwat, et al., 2002 & Lee, et al., 2006 & Gauthier, et al., 1998). Most of these vialess transitions are realized on standard commercial 635-µm substrates. With this thickness, coplanar-microstrip transitions are generally "easier" to realize, in terms of etching, that those on thin films. We essentially focus our attention on the transitions proposed by Strauss (Straub, et al., 1996) and Zhu (Zhu & Melde, 2006). The structures 1 and 2, shown in figure 8, have the advantage of a homogeneous lower ground plane. Their coplanar section is so grounded coplanar waveguide (GCPW). The first proposed structure with coplanar pads has limited bandwidth when it is realized with thick substrates. The bandwidth extension can be then obtained by using the second transition with radial stubs. The structure 3 proposed by Zhu gives promising bandwidth. However, this transition requires patterning the bottom ground plane which complicates the manufacturing process. To compare the performances of these transitions in the same configuration, we have calculated their performances, by numerical simulation with the help of HFSS, in back to back configuration on the commercial PTFE/glass/ceramic NH9338 substrate with a thickness of 254 µm (ε_r = 3.41 and Tanδ = 0.0047). This substrate is chosen because of its low relative permittivity near to that of polymers. For our simulations, we took a standard thickness of the copper of 18 µm.

In order to maintain the characteristic impedance matching to 50 Ω, the dimensions of each transition were first calculated using Linecalc software of Agilent Advanced Design System. The optimal dimensions of each transition are listed in Table 1.

Structure 1	Structure 2	Structure 3
L = 2 cm, L1 = 2 mm, G = 150 µm, W = 1.4 mm and S = 2 mm	L = 2 cm, R = 1.5 mm, G = 150 µm, W = 1.4 mm, S = 0.5 mm Stub angle = 30°	W1 = 1 mm, W2 = 1.2 mm, W3 = 1.4 mm, G1 = 125 µm, G2 = 140 µm, G3 = 1 mm Lg1 = Lg2 = Lg3 = 0.75 mm, L = 2 mm, S1 = 1.5 mm and S2 = 0.5 mm

Table 1. Dimensions of the studied transition structures in figure 8
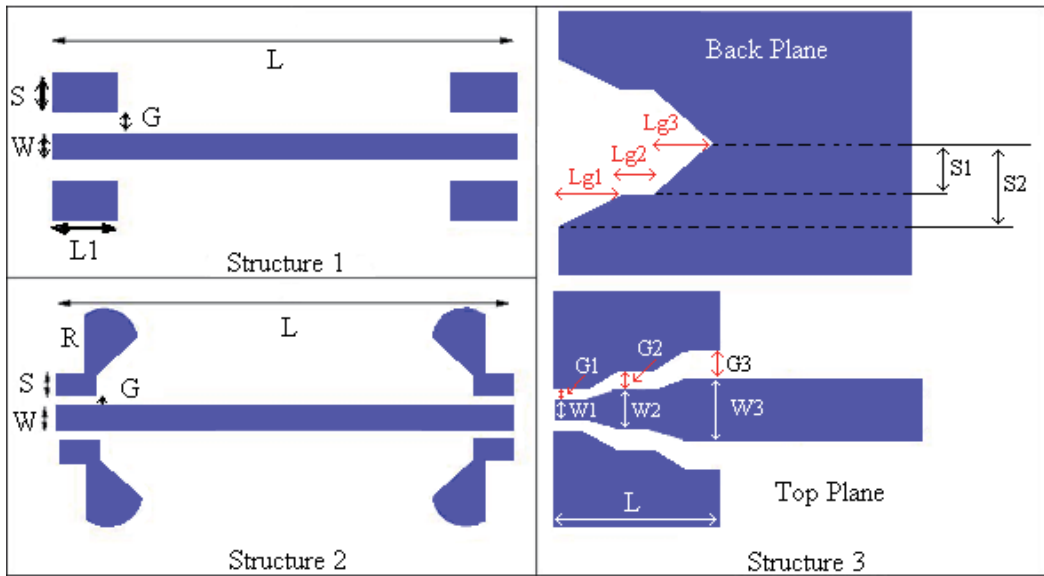
Fig. 8. Back-to-back coplanar to microstrip transition structures studied
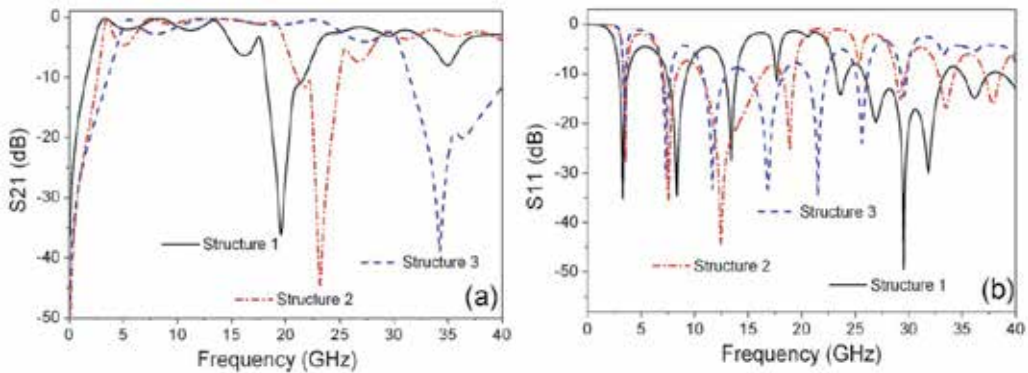
Fig. 9. HFSS simulations results of different GCPW-MS-GCPW transitions studied; (a) Transmission coefficient S21; (b) Reflection coefficient S11

Figure 9 shows the simulations results of these GCPW-MS-GCPW transitions. As expected, the widest bandwidth is obtained with the structure 3 proposed by Zhu (Zhu & Melde, 2006). However, this transition requires etching the back ground plane, so an additional fabrication step is necessary with careful alignment of the patterns on both sides of the substrate, which complicates the manufacturing process. For the other structures without patterned ground plane, we note that the radial stubs allow to broaden the bandwidth of the structure 2 compared to the structure 1. Nevertheless, the best lower frequency limit of the bandwidth is obtained with the structure 1 because of the large surface of the coplanar pads. Consequently, we chose the structure 1 for our study of vialess GCPW-MS transitions on thin polymer substrates.

Moreover, in the structure 1 the propagating mode in the grounded coplanar line is a quasi-TEM mode. As presented in figure 10, the field chart varies to satisfy the continuity
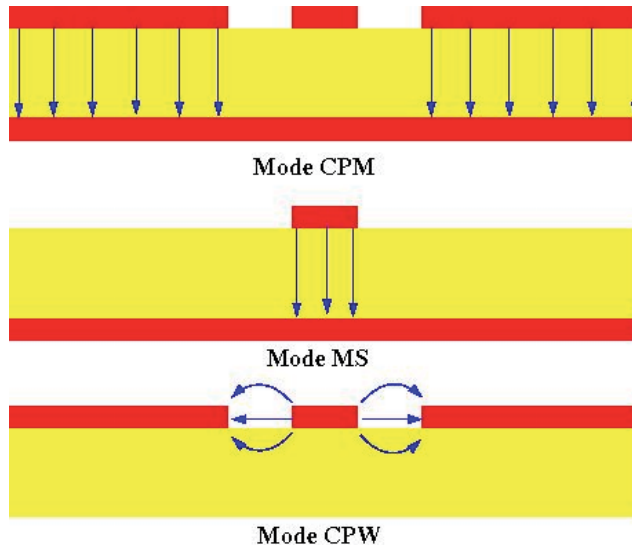
Fig. 10. Electrical field distribution in the GCPW-MS-GCPW transition structure 1

relations. As Raskin proposed in (Raskin et al., 2006), such a structure can propagate three mode configurations: the classical microstrip mode (MS) and coplanar mode (CPW), but also the coplanar microstrip mode (CPM) which diverts incident signal from propagating along the transmission line, resulting in parasitic resonance which limits the transition bandwidth. The transition should be optimized so the applied electrical signal converts rapidly from coplanar mode into microstrip mode on one hand and the excitation of the CPM mode is pushed far in frequency. We will therefore study the influence of the substrate thickness, its relative permittivity and also the surface of the coplanar ground plane the excitation of the CPM mode, both theoretically and experimentally.

3.1.1 Influence of the substrate thickness

To show the influence of the substrate thickness on the bandwidth, we have studied the GCPW-MS-GCPW transition of the structure 1 with three standard thickness of commercial substrate (635 µm, 254 µm and 127 µm). For the electrode, we took a standard copper thickness of 18 µm. And for each thickness, the coplanar width (W) and the coplanar gap (G) of the simulated transition were adjusted to ensure always a characteristic impedance of 50 Ω. And finally, the total length (L) of the back-to-back coplanar microstrip transition was fixed to 2 cm. This value is typically the optimal interaction length between the lightwave and electrical signal in order to minimize the driving voltage of an electro-optical modulator. However, for polymer with high loss tangent and high electro-optical coefficient, this length can be reduced to 1 cm (Gorman, et al., 2009 & Min-Cheol, et al., 2001) while maintaining a low driving voltage. The simulated S-parameters of these three structures are shown in figure 11.

The CPM mode excitation is the origin of the resonance peak at 20 GHz with the 635-µm thick substrate. This resonance peak is rejected to 37 GHz with the 254-µm thick substrate and up to 40 GHz with the 127-µm thick substrate. According to this result, the bandwidth can be increased by decreasing the substrate thickness. So, coplanar to microstrip transitions on thin polymer substrate are expected to have an ultra-wide bandwidth.
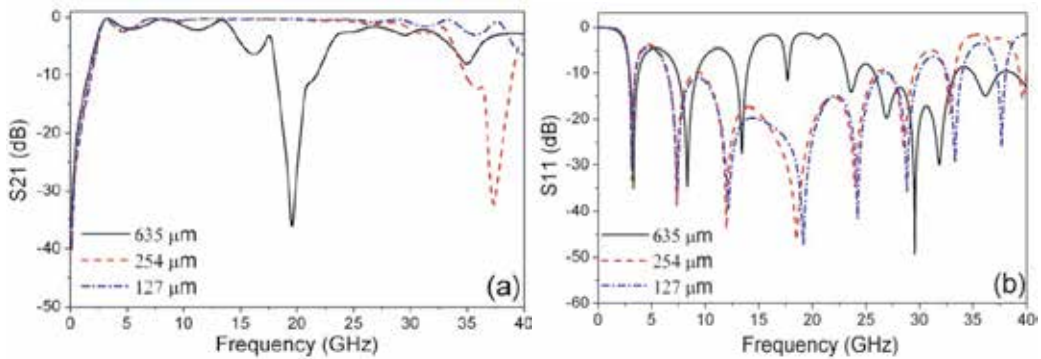
Fig. 11. HFSS simulation results of the GCPW-MS-GCPW transition for different thicknesses; (a) Transmission coefficient S21; (b) Reflection coefficient S11

3.1.2 Influence of geometric parameters

To demonstrate the influence of the geometric parameters of the coplanar to microstrip transition on its bandwidth, figure 12 shows the measured and simulated results of back-to-back coplanar microstrip transitions with two coplanar lengths (L1 = 1 mm and L1 = 5 mm). These transitions are realized on the 254-μm thick NH9338 substrate (ε_r = 3.41 and Tanδ = 0.0047). The other parameters of the transition are fixed to have an impedance matching close to 50 Ω while remaining compatible with the dimensions of the GSG probes we use: the SuSSMicrotec 50A3N500GSG probes (40-GHz bandwidth, 500-μm pitch and 30-μm wide contact pad). Taking into account these constraints, we fixed the following dimensions to realize the transitions: coplanar width W = 530 μm and coplanar gap G = 200 μm.

As shown in figure 12, we obtain, experimentally, a very wide bandwidth with these simple GCPW-MS-GCPW transitions. Indeed, with the coplanar length L1 of 1 mm (figure 12 (a)), the measured (-3 dB) bandwidth extends from 5.5 GHz to 33 GHz. And in the second case, the coplanar length is 5 mm (figure 12 (c)), the transition bandwidth is limited to 12.7 GHz because of the excitation of the CPM mode related to this bigger coplanar length (L1). However, in turn, the lower cutoff frequency is 1.7 GHz whereas this frequency is 5.5 GHz for L1 = 1 mm, because the longer are the coplanar pads, the higher is the capacity between the coplanar ground plane and the bottom ground plane, the better is the electromagnetic coupling between them. However the increase of the coplanar pad surface has drawbacks at high frequencies. Indeed, resonant modes appear at frequencies inversely proportional to their maximum size. So, this parameter is to be optimized according to the desired application. Regarding the reflection coefficient S11, we have experimentally obtained a reflection below -10 dB from 7 GHz and from 1.9 GHz respectively in the case where L1 = 1 mm and L1 = 5 mm (figure 12 (b) and figure 11 (d)). Indeed, a good matching is necessary to ensure optimal power transfer.

We also note a perfect agreement between experimental and simulation results. To obtain this good agreement, the excitation must be modeled exactly as the probes are used to characterize the back-to-back GCPW-MS-GCPW transitions. In HFSS software, we used the lumped port with the exact parameters of our coplanar probes. The skin effect must also be taken into account.
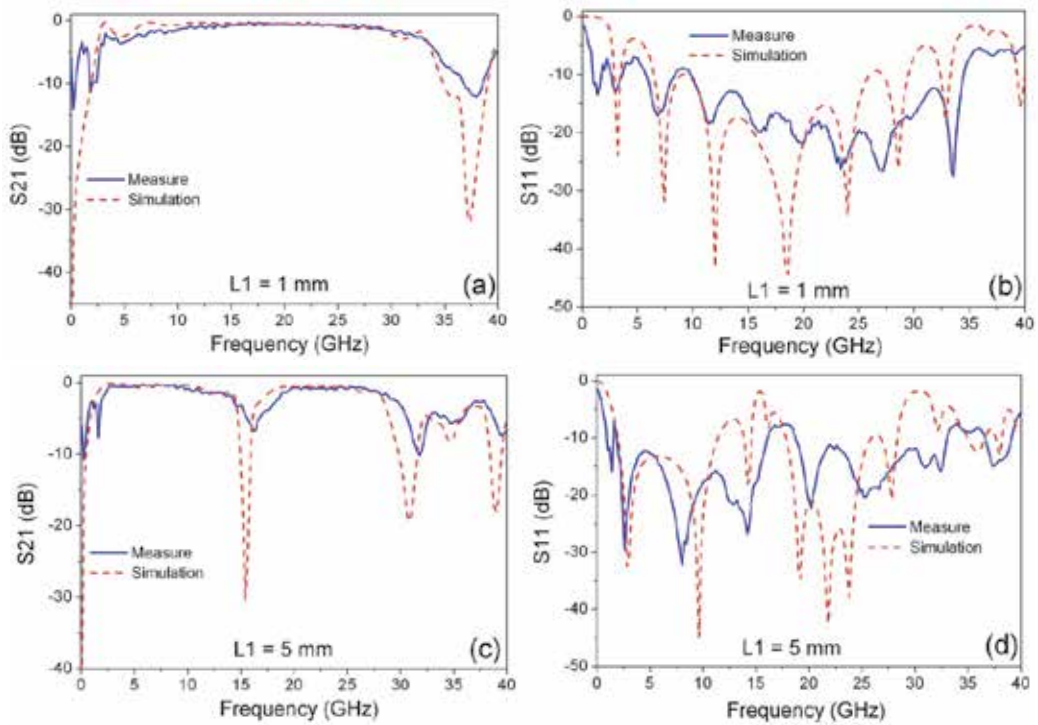
Fig. 12. Measurement and simulation results of the GCPW-MS-GCPW transitions on NH9338 commercial substrate for two coplanar lengths L1; (a) S21 for L1 = 1 mm; (b) S11 for L1 = 1 mm; (c) S21 for L1 = 5 mm; S11 for L1 = 5 mm

3.1.3 Influence of the substrate permittivity

To verify the influence of the substrate permittivity on the bandwidth, the transitions studied are realized with h=254-μm thick standard commercial substrates which have three different permittivities for comparison, RO3003 (ε_r=3, tanδ=0.0013 @ 10 GHz), RO3006 (ε_r=6.15, tanδ=0.0025) and RO3010 (ε_r=10.2, tanδ=0.0035). They are metallized on both sides with 17-μm copper. The dimensions of the transitions are determined in order to maintain a characteristic impedance of 50 Ω for both the microstrip and the grounded coplanar sections. For example, with the substrate RO3003, the width W of the center strip is 615 μm and the coplanar gap G is 185 μm. The length L of the microstrip line is 2 cm. The CPW pads are S=1 mm wide and L1=1 mm long. The measurements and simulations results of these transitions according to the different permittivities (Figure 13) show that when the relative permittivity is low, the resonance peak appears at higher frequencies. Thus, the high cut-off frequency of the transitions due to the first parasitic resonance is respectively 20.6, 25 and 33.4 GHz for substrates of permittivities of 10.2, 6.15 and 3. Due to the electromagnetic coupling between the backside conductor and the coplanar ground strips, the low cut-off frequency increases with decreasing permittivity, respectively to 1.7, 2.4 and 4 GHz. Indeed, low permittivity obtained by micromachining substrates allows to get low-dispersive waveguides (quasi TEM approximation) and to realize coplanar transmission lines with very high bandwidth without excessive dispersion and loss (Newham, 2006). The main

reason for the high cut-off frequency improvement of GCPW-MS-GCPW transitions is that the guided wavelength is bigger in low-k substrate for a given frequency, so the parasitic resonance between the backside conductor and the coplanar ground strips takes place at higher frequency (El-Gibari, et al., 2010a). In addition, as for low effective permittivities a large part of the energy is propagating in air medium, so losses can be minimized.
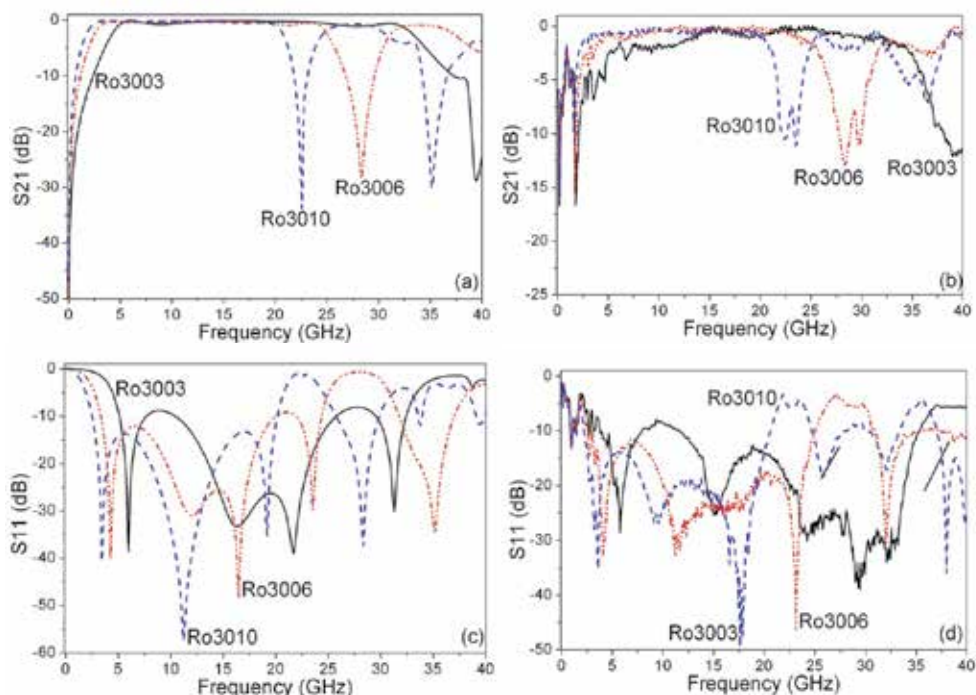
Fig. 13. Calculated and measured S-parameters of back-to-back GCPW-MS-GCPW transition on 254-µm substrates with different permittivities; (a) S21 simulated; (b) S21 Measured; (c) S11 simulated; (d) S11 Measured;

3.2 GCPW-MS-GCPW transitions on thin polymer substrate

For our study of GCPW-MS-GCPW transitions on thin film substrate, we have chosen the commercial benzocyclobutene polymer (BCB), often used in microelectronic packaging and interconnection applications, it is an excellent candidate as substrate in thin film for GCPW-MS-GCPW transitions, with its remarkable features: low-permittivity (ε_r=2.65), low loss tangent (tanδ=0.0025), simple and cost-effective to deposit, varying thickness through the spinning-curing process, resistant to some chemical agents, etc.. In order to reduce the driven voltage of the modulator, the thickness of thin film polymer is fixed usually between 8 µm (El-Gibari, et al., 2010b) and 10 µm (Michalak, et al., 2006). So, our transitions are realized on 10-µm BCB polymer. The first study in thin film consists to determine the influence of the coplanar length (L1). Our study consists to fix the coplanar width S at 1 mm and varying its length L1 (1, 2 and 3 mm). For the metal electrode, we used aluminum which can be deposited in our laboratory. The width of the central strip W = 20 µm, the coplanar gap G = 13 µm and the length (L) of the back-to-back transition is fixed at 1 cm.

3.2.1 Influence of the coplanar length L1

Figure 14 (a) presents the evolution of the transmission coefficient S21 of the back-to-back transition according to the coplanar length (L1) for a fixed coplanar width (S) at 1 mm. This study was realized without taking into account the loss tangent of the BCB polymer. As in the case of the thick substrate, the appearance of the resonance frequency due to the excitation of the CPM mode depends on the coplanar length (L1). When this length is short, this resonance peak is rejected at high frequencies. For example, when L1 = 1 mm, the first resonance peak appears around the frequency of 78 GHz, whereas it appears around 29 GHz with L1 = 3 mm. Moreover, the lower cut-off frequency of the bandwidth depends on the total surface of the coplanar pads (S.L1). The larger is this surface, the greater is the capacitive effect between the ground plane of the microstrip line and the top ground plane of the coplanar line, the more the lower limit of the bandwidth decreases. Thus, this lower cut-off frequency is at 230 MHz with L1 = 3 mm and at 670 MHz with L1 = 1 mm. Regarding the reflection, figure 14 (b) shows a good matching with a reflection coefficient S11 less than - 10 dB from 460 MHz.
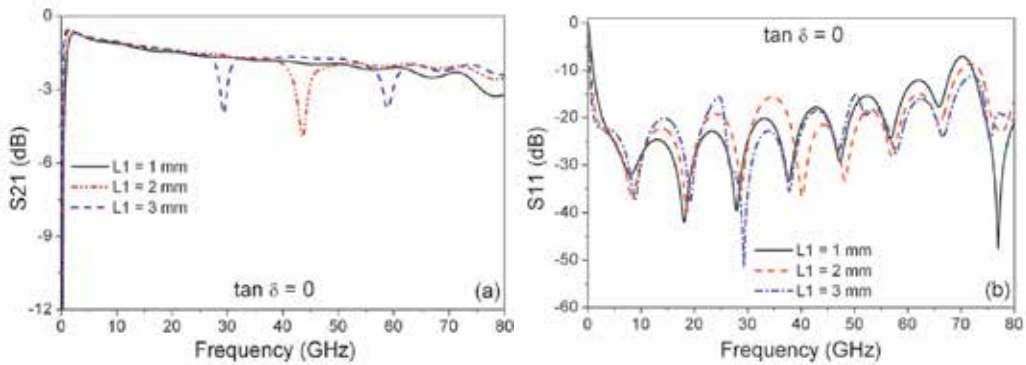
Fig. 14. S-parameters of the back-to-back transition according to the coplanar length (L1); (a) Transmission coefficient S21; (b) Reflection coefficient S11

Table 2 contains the GCPW-MS-GCPW transition bandwidth higher and lower limits. One can extend the transition bandwidth to higher frequency be decreasing the length of the coplanar pads or on the contrary push its lower limit towards DC component by increasing the length of the coplanar pads.

L1 (mm)	Tanδ	Lower cut-off frequency (MHz)	High frequency (GHz)	-3 dB bandwidth (GHz)
1		670	75,8	≈ 75
2	0	340	42,2	≈ 43
3		230	28,6	≈ 28,5

Table 2. The transition bandwidth depending on the length of the coplanar pads L1 with the width S fixed at 1 mm.

To understand the physical phenomenon underlying microwave properties of the studied transitions, we present in figure 15 the evolution of the electric field propagating along the transition at 1 GHz. The small thickness of the BCB polymer presents a double advantage for a good via-less transition. On one hand, it can easily create an electromagnetic coupling between the bottom ground plane of the microstrip line and the coplanar pads by capacitive effect. On the other hand, the low ratio of the thickness and the coplanar gap allows a fast conversion of the field between the coplanar mode and microstrip mode. This is well illustrated by figure 15 (a) showing the electric field at the input of the first transition in plane 1. The energy propagates in coplanar and microstrip modes. These two modes are coupled (figure 16) and the coupling is all the stronger as the capacity between the coplanar pad and the bottom ground plane is large. Thus, the energy is quickly confined under the central strip. In our case, the coplanar gap (G = 13 µm) is greater than the thickness of the BCB polymer (h = 10 µm). The mode "sees" first the ground plane of the microstrip line which facilitates the fast conversion between the coplanar mode and the microstrip mode. This remark seems to be justified by observing the electric field at the output of the first transition in Figure 15 (b). We note that the mode installed is of microstrip type: the maximum of energy is confined under the central strip. Thus on figure 15 (c), we have a quasi-TEM mode which corresponds to the mode propagating along the microstrip line. In figure 15 (d) which presents the electric field in the input of the second transition, we find the phenomenon of the first plane, where the propagating mode is a hybrid mode between the coplanar and the microstrip modes with a maximum of energy confined under the central strip thanks to the low thickness of the substrate.
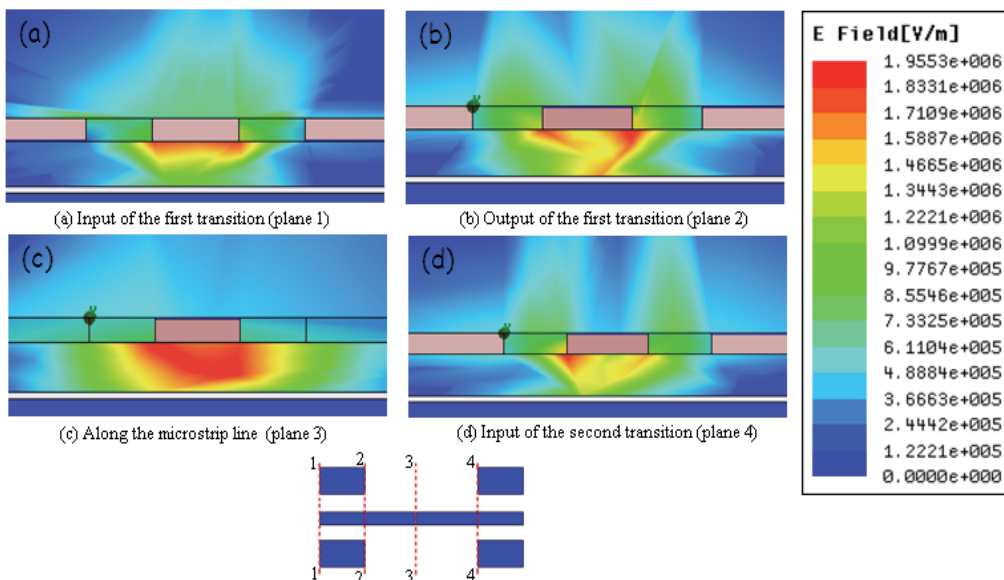
Fig. 15. Representation of the electric field at 1 GHz in several transverse planes of the GCPW-MS-GCPW transition

The physical phenomenon which we explained in the previous paragraph remains valid whatever the frequency of the wave propagating in the structure, except for those frequencies at which the CPM mode is excited. In the structure studied, the excitation of this
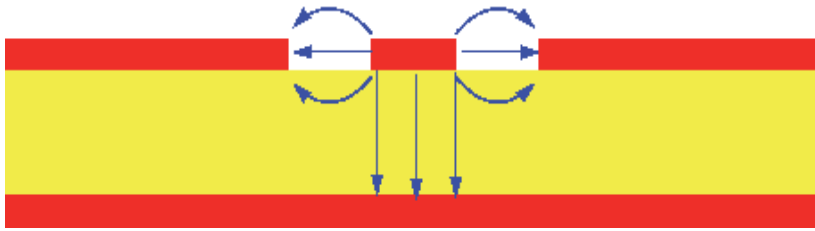
Fig. 16. Distribution of the field at the input of the GCPW-MS-GCPW transition (plane 1)

CPM mode takes place around a frequency of 43 GHz (figure 14). Figure 17 shows the cartography of the electric field at the frequency corresponding to this resonance peak. The energy is clearly directed towards between the coplanar ground plane and the microstrip ground plane instead of propagating along the center strip, resulting in a drop of the S21 parameter hence bandwidth limitation.
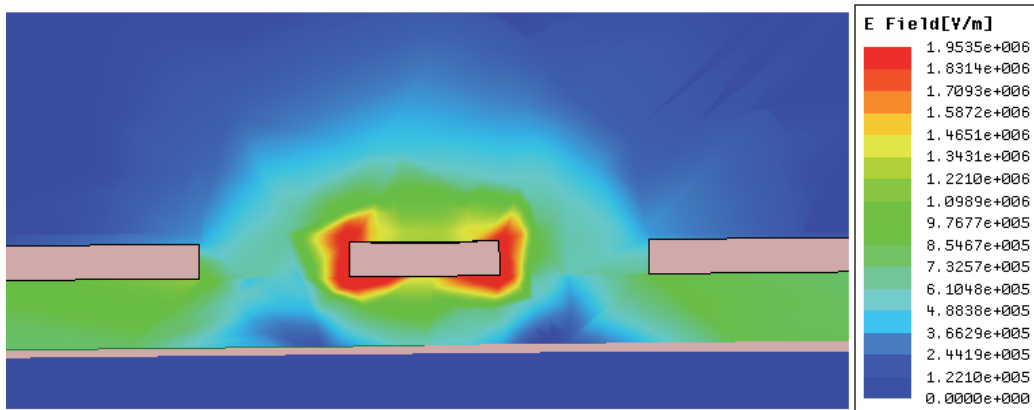
Fig. 17. Representation of the electric field at 43 GHz in the input of the GCPW-MS-GCPW transition (plane 1)

3.2.2 Realization of the GCPW-MS-GCPW transitions on BCB polymer

For experimental characterization of our structures on polymer thin film, we used a network analyzer Agilent E8364B whose bandwidth covers the frequency range from 10 MHz to 50 GHz, using the LRM (Line-Reflect-Match) calibration technique. The system is controlled by the Wincal Cascade software. For the GSG coplanar probes, we used the Cascade I40AGSG250 probes (40 GHz bandwidth, 250 µm pitch and 12 µm pad). Finally, the probes are calibrated using a calibration substrate referenced by Cascade AE-101-190.

We present in figure 18 the measurement and simulation results obtained with 10-µm BCB polymer substrate, deposited by spin-coating on a 380 µm thick metallized silicon wafer. We have realized two transitions with different aluminum thicknesses in order to show its influence. So, Figure 18 (a) presents the measurement and simulation results of the GCPW-MS-GCPW transition realized with 0.4 µm of aluminum thickness. We can notice that the insertion loss of the transition is as high as 3 dB due to the ohmic effect of the thin metal layer. In figure 18 (b) the aluminum thickness deposited and measured with a profilometer

is 1.4 µm, in this case we experimentally obtained a very large (-3 dB) bandwidth from 700 MHz to 22.5 GHz. We also note that S21-parameter curve has a very low slope thanks to the very low loss tangent of the BCB polymer and the use of a metallized silicon wafer. A good impedance matching can be also observed in figure 18 (b). Similarly, a very good agreement between the experimental and simulation results is obtained.
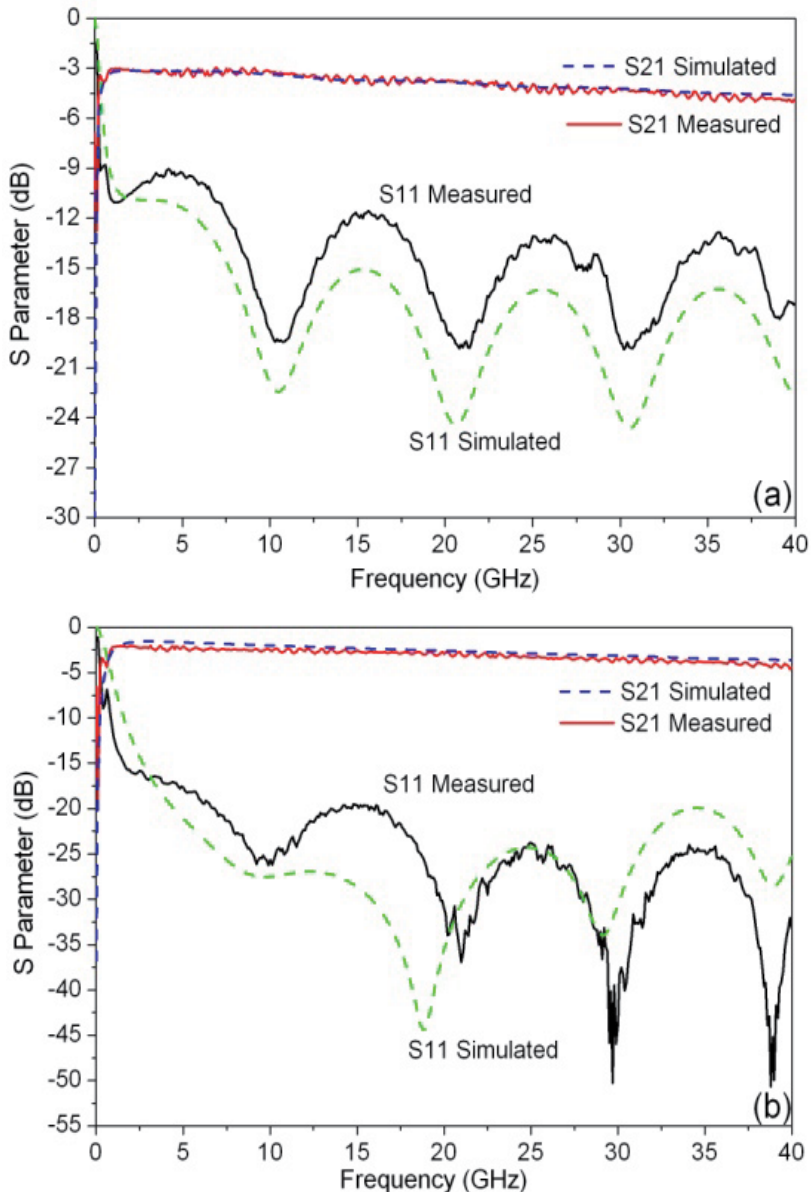
Fig. 18. Measured and simulated S-parameters of a back-to-back GCPW-MS-GCPW transition on BCB polymer substrate; (a) with 0.4 µm aluminum metallization, (b) with 1.4 µm aluminum metallization.

The low metallization thickness is one the main contributor for the losses observed in the GCPW-MS-GCPW transitions presented previously. The simulations results on BCB polymer, presented in figure 19 (a), show that an ultra-wide bandwidth (72 GHz) could be obtained by increasing the metal thickness up to 4 µm. The other conditions of simulations in this study are: W = 20 µm, G = 13µm, S = 1 mm and L1 = 1mm.

Another manner to increase the bandwidth of the GCPW-MS-GCPW transitions is to choose a metal with a higher conductivity. Figure 19 (b) shows the simulation results of the transition on BCB polymer with different metals. The bandwidth can be increased by 4 GHz if aluminum is replaced by silver.
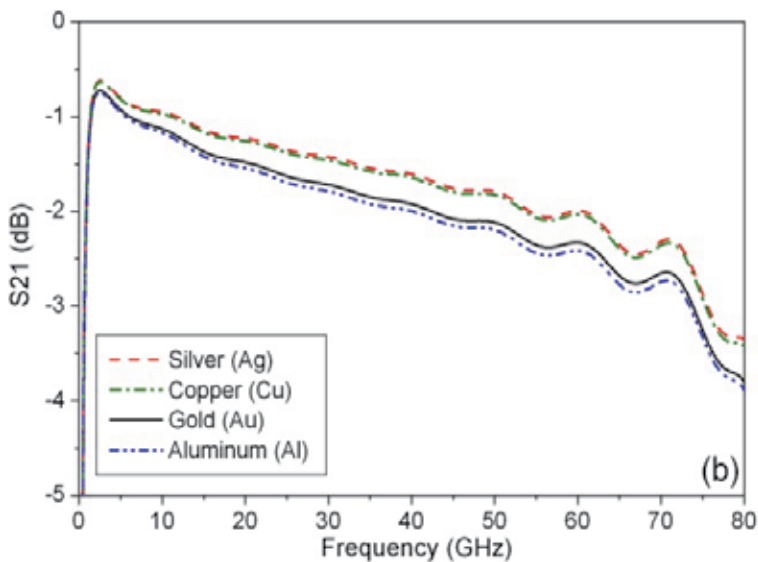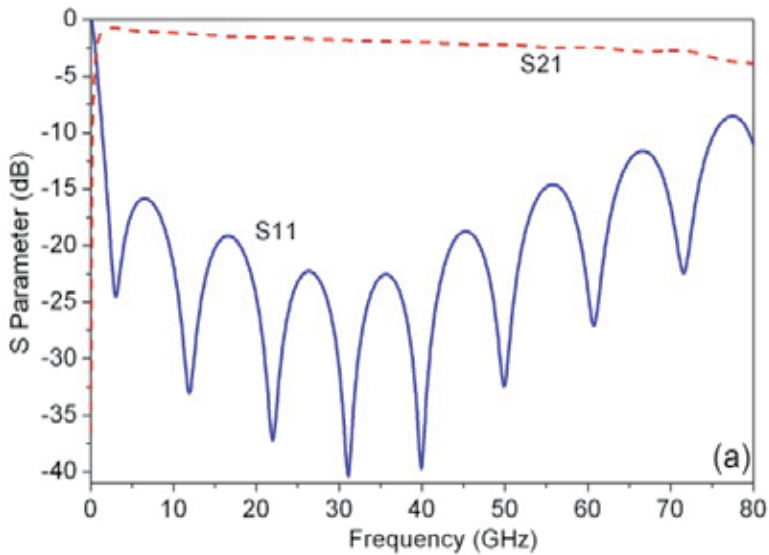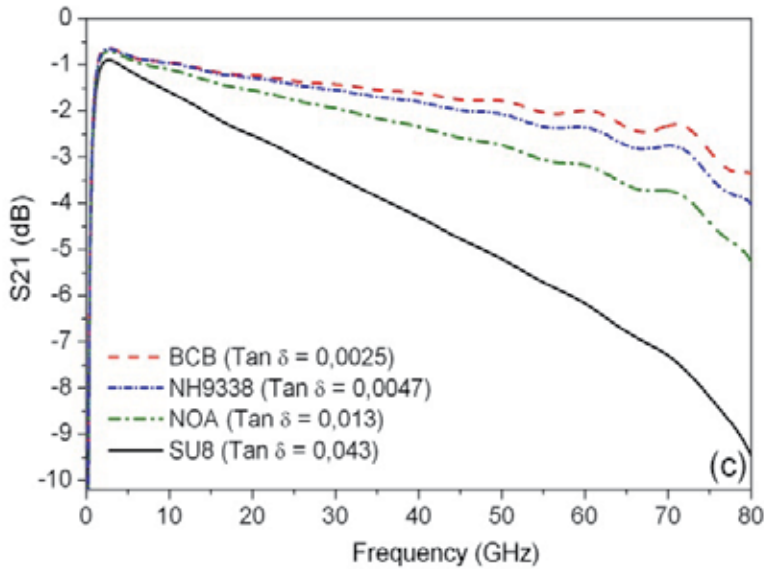
Fig. 19. S-parameters of a back-to-back GCPW-MS-GCPW transition on 10-μm thick BCB polymer substrate; (a) with 4 μm thick aluminum metallization, (b) different electrode metals (c) different substrate materials.

Another way to increase the transitions bandwidth is to use materials with low loss tangent. For example, figure 19 (c) presents the simulation results of the transition with different loss tangent of materials. For all transitions whose S-parameters are shown in figure 19, 4 μm thick metallization was assumed. The dielectric loss and metal conductivity modifies differently the transition bandwidth, the first impacts the S21 parameter slope and the second influences the insertion losses.

3.3 Transitions for connectorizing the component

For the packaging of component driven by microstrip line on thin substrate, a GCPW-MS-GCPW transition is necessary for connectorizing with a coplanar connector. For this, we chose the end launch coplanar connector, Model #1492-04A-5 of SouthWest Microwave. The diameter of its center contact is 127 μm and its coplanar gap is 254 μm. So, the center conductor width and the coplanar gap of the transition must be sufficiently large to easily install the connector.

To reduce the driving voltage of the modulator, the thickness of BCB polymer having been fixed at 10 μm, a segmentation of the bottom ground plane is needed to maintain the impedance matching when the width of the center conductor increases. Most of the transitions used in the literature are based on a smooth transformation of the field by gradually changing the physical boundary conditions (Zhu & Melde, 2006), so the characteristic impedance is maintained at 50 Ω in all sections of the transition.

The proposed transition for connectorization with the coplanar connector is shown in figure 20. In this transition, W_1, W_2 and W_3 indicate the different widths of the signal conductor in different sections, G_1, G_2 and G_3 indicate the different values of the coplanar gap, L1 the length of the coplanar line and the L2 the length of the grounded coplanar line. For each

section, the width of the signal conductor on the top plane gradually decreases from the width needed for the coplanar connector to the final width of the microstrip line optimized to have a characteristic impedance of 50 Ω. At the beginning of the transition, the bottom ground is designed to have a tapered slot. This is necessary to facilitate the excitation of the coplanar fundamental mode and a gradual installation of the microstrip fundamental mode at the grounded coplanar line. This is possible thanks to the thinness of the BCB polymer lower than the coplanar gap.
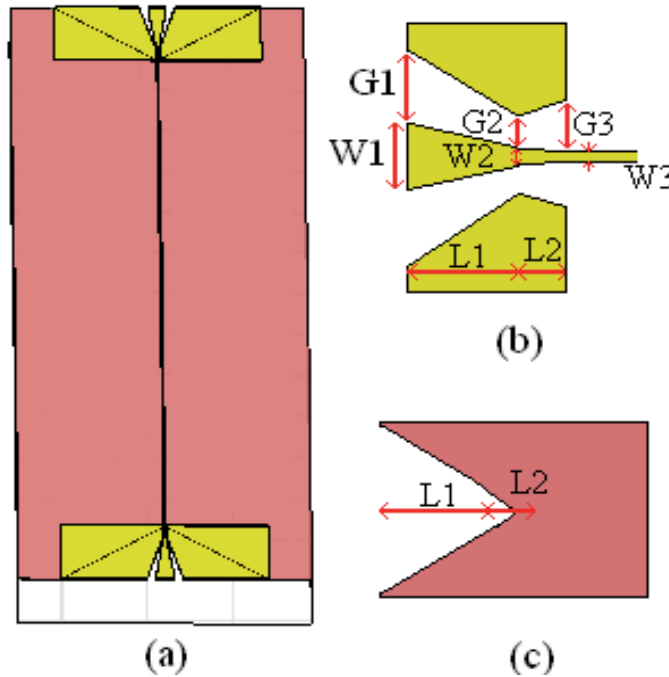
Fig. 20. Structure of the GCPW-MS-GCPW transition for connectorizing with coplanar connectors. (a) Global view of the transition studied. (b) View of the top metallization pattern of the taper. (c) View of the bottom ground plane

For mechanical fixing on the substrate, the end launch connector is equipped with screws in its corners. So, for our application we take advantage of these holes in order to obtain the DC contact. We used the RT/Duroid 6010 substrate which has a permittivity similar to that of silicon wafer, with which we studiez transitions. So, the transition was designed on BCB polymer (10 μm of thickness, ε_r=2.65 and tanδ= 0.0025) deposed on RT/Duroid 6010 substrate (635 μm of thickness, ε_r=10.2 and tanδ= 0.0035). The signal line widths were determined first. The value of W_3 was determined to have a microstrip characteristic impedance of 50 Ω. This width depends essentially on the thickness of BCB polymer deposed (10 μm) and its permittivity (2.65). So, W_3 is fixed at 20 μm. Secondly, to simplify the installation of the coplanar connector, we fixed the value of W_1 at 220 μm. We design a smooth transition by gradually changing the physical boundary conditions, so insertion losses are minimized. Simulations were realized for several different cases, the parameters of the most efficient transition are as follows: W_1 = 220 μm, G_1 = 110 μm, W_2 = 30 μm, G_2 = 8 μm. The coplanar gap becomes critical to maintain the characteristic impedance at 50 Ω.

Starting from W_2 we consider the area of grounded coplanar line, W_3 = 20 µm, G_3 = 13 µm. In order to achieve a progressive transition, the coplanar lengths L1 and L2 are chosen to minimize the losses due to the fast change of the widths of the coplanar line (from 220 µm to 20 µm). According to the various simulations realized, we took 1 mm and 300 µm respectively for L1 and L2. The total length (L) of the back-to-back transition is 15 mm in order to facilitate the placement of the coplanar connector. Figure 21 shows that a very broad bandwidth from 700 MHz to 32 GHz is achieved with the station system equipped with GSG probes, and for the coplanar connector we are working to realize this transition.
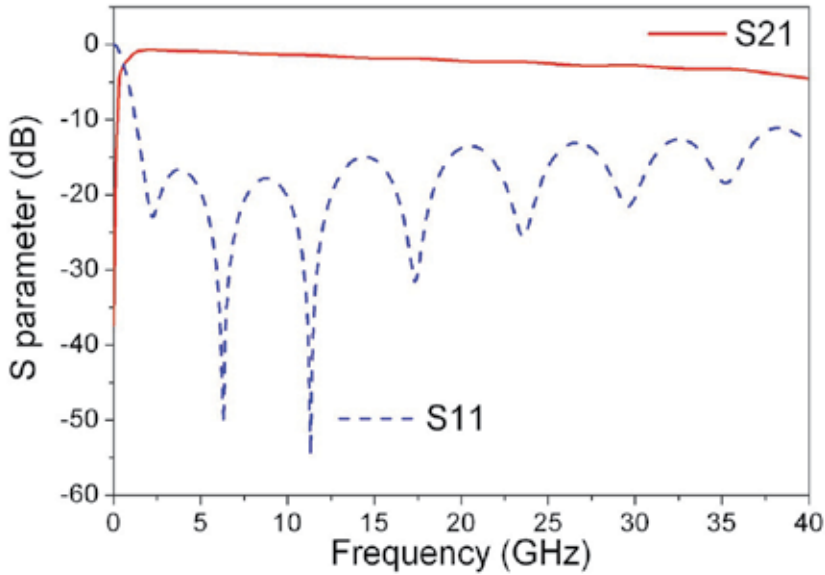
Fig. 21. Calculated S-parameters of back-to-back GCPW-MS-GCPW transition on BCB polymer deposed on RT/Duroid 6010 substrate

4. Conclusion

We present an ultra-wide bandwidth back-to-back GCPW-MS-GCPW transition without making via-hole in the substrate or patterning the bottom ground plane. These transitions, using the electromagnetic coupling between the bottom and top ground planes, simplifies the manufacturing and facilitates the on-wafer characterization with GSG probe station. These transitions are widely requested in packages, on-wafer measurements of microstrip based MMICs, and also in the interconnections in hybrid circuit including both microstrip and coplanar lines.

Low permittivity and thin substrates permit rejecting of the CPM mode resulting from parasitic resonance between backside conductor and planar ground strips, so enlarging the bandwidth of back-to-back GCPW-MS-GCPW transitions. As is shown by the measurements and simulations results, we have obtained a very wide bandwidth exceeding 30 GHz with the NH9338 substrate (ε_r = 3.41, Tanδ = 0.0047 and thick = 254 µm) and with the BCB polymer (ε_r = 2.65, Tanδ = 0.0025 and thick = 10 µm), and a bandwidth from 700 MHz to 22.5 GHz.

Simulation results with the BCB polymer show that the bandwidth could go beyond 76 GHz, which opens the perspectives of cost-effective electro-optical modulator based on polymer. This last has an enormous potential bandwidth thanks to a good optical-microwave phase match in polymers over 100 GHz, while that of their counterparts made of $LiNbO_3$ is limited to about 40 GHz. They need absolutely an electrode with a very wide bandwidth.

5. Acknowledgment

6. References

Algani, C.; Belhadj-Tahar, N. E.; Deshours, F.; Montmagnon, J. L.; Roduit, P.; Alquié, G.; Fortin, C. & Kazmierski, C. (2005). Optimization of the electrode dimensions of an electro-optic organic modulator based on polymers microwave dielectric characterization and electromagnetic simulations. *European Microwave Conference*, Vol. 2, 4 pp. (4-6 October 2005), ISBN 2-9600551-2-8

Chen, D.; Fetterman, H. R.; Chen, A.; Steier, W.H.; Dalton, L. R.; Wang, W. & Shi, Y. (1997). Demonstration of 110 GHz electro-optic polymer modulators. Appl. Phys. Lett., Vol.70, No.25, (June 1997), pp. 3335-3337

Courjal, N.; Porte, H.; Martinez, A. & Goedgebuer, J.P. (2002). $LiNbO_3$ Mach-Zehnder modulator with chirp adjusted by ferroelectric domain inversion. *IEEE Photonics Technology Letters*, Vol.14, No.11, (November 2002), pp. 1509, ISSN 1041-1135

Dalton, L. R.; Harper, A.; Ren, A.; Wang. F. F.; Todorova, G.; Chen, J.; Zhang, C. & Lee, M. (1999). Polymeric electro-optic modulators : From chromophore design to integration with semiconductor very large scale integration electronics and silica fiber optics. *Industrial & Engineering Chemistry Research*, Vol.38, No.1, (January 1999), pp. 8-33

El-Gibari, M.; Averty, D.; Lupi, C.; Brunet, M.; Li H. W.; & Toutain, S. (2010a). Ultra-broad bandwidth and low-loss GCPW-MS transitions on low-k substrates. *Electronics Letters*, Vol.46, No.13, (June 2010), pp. 931, ISSN 0013-5194

El-Gibari, M.; Averty, D.; Lupi, C.; Li H. W. & Toutain, S. (2010b). Ultra-wideband GCPW-MS-GCPW driven electrode for low-cost and wide range application electro-optic modulators. *Microwave and Optical Technology Letters,* Vol.52, No.5, (May 2010), pp. 1078-1082

Faderl, L. ; Labeye, P. ; Gidon, P. & Mottier, P. (1995). Integration of an electrooptic polymer in an integrated optics circuit on silicon. IEEE *Journal of Lightwave Technology*, Vol.13, No.10, (October 1995), pp. 2020, ISSN 0733-8724

Gauthier, G. P.; Katehi, L. P. & Rebeiz, G. M. (1998). W-Band finite ground coplanar waveguide (FGGPW) to microstrip line transition. *IEEE MTT-S International Microwave Symposium Digest*, Vol. 1, pp. 107-109 (7-12 June 1998), ISBN: 0-7803-4471-5

Gorman, T.; Haxha, S. & Ju, J. J. (2009). Ultra-High-Speed Deeply Etched Electrooptic Polymer Modulator With Profiled Cross Section. *IEEE Journal of Lightwave Technology*, Vol.27, No.1, (January 2009), pp. 68, ISSN 0733-8724

Hammerstad, E. O. (1975). Equations for Microstrip Circuit Design. *European Microwave Conference*, pp. 268-272, (1-4 September 1975)

Haydl, W.H. (2002). On the use of vias in conductor-backed coplanar circuits. *IEEE Transactions on Microwave Theory and Techniques*, Vol.50, No.6, (June 2002), pp. 1571, ISSN 0018-9480

Kim, I.; Tan, M.R.T. & Wang, S.-Y. (1990). Analysis of a new microwave low-loss and velocity-matched III-V transmission line for traveling-wave electrooptic modulators. *IEEE Journal of Lightwave Technology*, Vol.8, No.5, (May 1990), pp. 728, ISSN 0733-8724

Lee, Y. C. & Park, C. S. (2006). Vialess Coplanar Probe Pad-to-Microstrip Transitions for 60 GHz-band LTCC Applications. *European Microwave Conference*, pp. 1354, (10-15 September 2006), ISBN 2-9600551-6-0

Michalak, R.J. ; Ying-Hao Kuo ; Nash, F.D. ; Szep, A. ; Caffey, J.R. ; Payson, P.M. ; Haas, F. ; McKeon, B.F. ; Cook, P.R. ; Brost, G.A. ; Jingdong Luo ; Jen, A.K.-Y. ; Dalton, L.R. ; Steier, W.H. (2006). High-speed AJL8/APC polymer modulator. *IEEE Photonics Technology Letters*, Vol.18, No.11, (June 2006), pp. 1207, ISSN 1041-1135

Min-Cheol, O; Zhang, H.; Zhang, C.; Erlig, H.; Chang, Y.; Tsap, B.; Chang, D.; Szep, A.; Steier, W. H.; Fetterman, H. R. & Dalton, L. R. (2001). Recent advances in electrooptic polymer modulators incorporating highly nonlinear chromophore", *IEEE Journal of Selected Topics in Quantum Electronics*, Vol.7, No.5, (September 2001), pp. 826, ISSN 1077-260X

Newham, P. (2006). Coupling across gap in thick microstrip line. *IEE Proceedings H, Microwaves, Antennas and Propagation*, Vol.136, No.1, (May 2005), pp. 64, ISSN 0950-107X

Raskin, J. P.; Gautier, G.; Katheli, L. P. & Rebeiz, G. M. (2000). Mode conversion at GCPW-to-microstrip-line transitions. *IEEE Transactions on Microwave Theory and Techniques*, Vol.48, No.1, (January 2006), pp. 158, ISSN 0018-9480

Safwat, M. E.; Zaki, K. A.; Johnson, W. & Lee, C. H. (2002). Novel Transition Between Different Configurations of Planar Transmission Lines", *IEEE Microwave and Wireless Components Letters*, Vol.12, No.4, (April 2006), pp. 128-130

Straub, G.; Ehret P. & W. Menzel. (1996). On-wafer measurement of microstrip-based MIMICs without via holes. *IEEE MTT-S International Microwave Symposium Digest*, Vol. 3, pp. 1399 (17-21 June 1996), ISBN: 0-7803-3246-6

Wheeler, H.A. (1977). Transmission-Line Properties of a Strip on a Dielectric Sheet on a Plane. *IEEE Journal of Lightwave Technology*, Vol.25, No.8, (August 1977), pp. 631, ISSN 0018-9480

Zheng, G.; Papapolymerou, J. & Tentzeris, M. M. (2003). Wideband coplanar waveguide RF probe pad to microstrip transitions without via holes. *IEEE Microwave and Wireless Components Letters*, Vol.13, No.12, (December 2006), pp. 544-546, ISSN 1531-1309

Zhu, L. & Melde, K. L. (2006). On-Wafer Measurement of Microstrip-Based Circuits With a Broadband Vialess Transition. *IEEE Transactions on Advanced Packaging*, Vol.29, No.3, (August 2006), pp. 654, ISSN 1521-3323

Ultra Wideband Antennas for High Pulsed Power Applications

Baptiste Cadilhon[1], Bruno Cassany[1], Patrick Modin[1],
Jean-Christophe Diot[2], Valérie Bertrand[3]
and Laurent Pécastaing[4]
[1]CEA, avenue des Sablières, Le Barp,
[2]CEA, Gramat,
[3]CISTEME, ESTER Technopole, Limoges,
[4]LGE, SIAME Laboratory, Pau University, Pau,
France

1. Introduction

1.1 UWB antennas in the field of high pulsed power

For the last few years, the generation of high-power electromagnetic waves has been one of the major applications of high pulsed power (HPP). It has aroused great interest in the scientific community since it is at the origin of several technological advances. Several kinds of high power radiation sources have been created. There currently appears to be a strong inclination towards compact and autonomous sources of high power microwaves (HPM) (Cadilhon et al., 2010; Pécastaing et al., 2009).

The systems discussed here always consist of an electrical high pulsed power generator combined with an antenna. The HPP generator consists of a primary energy source, a power-amplification system and a pulse forming stage. It sends the energy to a suitable antenna. When this radiating element has good electromagnetic characteristics over a wide band of frequency and high dielectric strength, it is possible to generate high power electromagnetic waves in the form of pulses. The frequency band of the wave that is radiated can cover a very broad spectrum of over one decade in frequency. In this case, the technique is of undoubted interest for a wide variety of civil and military applications. Such applications can include, for example, ultra-wideband (UWB) pulse radars to detect buried mines or to rescue buried people, the production of nuclear electromagnetic pulse (NEMP) simulators for electromagnetic compatibility and vulnerability tests on electronic and IT equipment, and UWB communications systems and electromagnetic jamming, the principle of which consists of focusing high-power electromagnetic waves on an identified target to compromise the target's mission by disrupting or destroying its electronic components.

Over the years, the evolution of the R&D program for the development of HPM sources has evidenced the technological difficulties intrinsic to each elementary unit and to each of the physical parameters considered. Depending on the wave form chosen, there is in fact a very wide range of possibilities for the generation of microwave power. The only real question is

not "what power can be reached" but rather what power with what repetition rate, with what duration of transmission, with what width of spectrum and with what agility?

Putting each of these parameters on the same level in isolation is meaningless. On the other hand, ranking the impact of each parameter on the opportunity of developing a system makes it possible to outline the avenues of research.

The impact of the antenna unit is a major factor in the sizing of this so-called "system'". In fact, the limitations in terms of transmission power of the existing devices restrict the possibilities of the system. Moreover, the impact of the radiation lobes on the system itself or on the operators is a further limitation to the powers that can actually be reached.

The technological progress achieved on this elementary unit is an immediate point of entry for the sizing of the systems, on a par with other parameters such as the repetition frequency or the duration of operation with impact the energy storage and power amplification means.

1.2 Brief recapitulation of the state-of-the art in high power UWB antennas

The classic broad-band antennas available are used in the harmonic mode and do not offer the characteristics expected for experimentations in the transient domain. To be usable, the antennas have to be sufficiently broad band in order to cover the ultra short pulse spectrum generated. The first step is the choice of type of antenna matching the application.

There is a great variety of antennas that can be used for UWB applications, requiring some optimization to meet the requirements, including:

- frequency independent antennas,
- aperture antennas,
- reflector antennas,
- travelling wave antennas.

For most UWB applications, the radiating elements are specifically designed as a part of the complete system for the project in question. We are looking here for an antenna with good directivity, a broad band (to be compatible with the frequency spectrum of the pulse to radiate) and capable of withstanding high voltages (over a several dozen kilovolts). The criterion of dispersion (i.e. the spreading effect of the pulse resulting from a shifting phase center of the antenna) can be an important parameter depending on the application (as in UWB radar or measurement applications). Compactness and integration constraints are becoming increasingly topical and must be taken into account from the outset of the antenna design.

1.2.1 Frequency independent antennas

1.2.1.1 Log-periodic antennas

Log-periodic antennas consist of several elementary dipoles mounted in parallel on a two strand armature such that two consecutive dipoles are in phase opposition when the antenna is powered. Each dipole radiates independently with maximum efficacy when its length corresponds to the half wavelength of the power frequency. The low frequency is thus determined by the size of the largest dipole and the high frequency by the size of the smallest dipole.

The antennas available off the shelf generally present an input impedance of 50Ω over a relatively wide frequency band (approximately one decade). The effective structures in low

frequency are naturally cumbersome (a low frequency of 200MHz corresponds to a dipole 75cm long). Certain devices combine a biconical antenna with this structure for a trade-off between bulk and bandwidth. The classic structure withstands power levels of no more than few kilowatts for a gain of around 6dB over one decade. A major modification of the structure must therefore be envisaged in order to radiate high powers.

1.2.1.2 Monopole and dipole

Outside of their resonance ranges, monopoles and dipoles can be seen as elementary UWB structures. Their gain levels are, however, extremely poor, their radiation patterns are not directional and their input impedances are generally high.

1.2.2 Horn antennas

TEM horns are also frequently used for the radiation of ultra short pulse. They have a pyramidal flared or conical shape. In the high frequencies of their use spectrum they are powered more often than not by a wave guide. For the lowest frequencies, the power system generally consists of a coaxial cable ending in a quarter wave strand. That makes it difficult to send high level and especially repetitive signals. This type of wide band antenna is not suitable for operational in a transient regime. Each spectral component is transmitted from a phase center which moves inside thus causing a spread of the signal transmitted. Moreover, performance at low frequencies (< 1GHz) can only be obtained within very large structures. They are very often equipped with a polyethylene lens positioned at the opening of the horn (figure 1) which provides a flat wave at the exit from the antenna, thus reducing spatial scattering. Depending of the level of performance required, however, the lens rapidly becomes cumbersome and considerably increases the size and weight of the antenna as whole.

Addition of a pair of arches the shape of which is exponential to the structure of the horn gives a ridged horn. This modification makes it possible to widen the operational band while keeping within relatively modest dimensions. The problems of high voltage power still remain, however, especially if a balun has to be used to adapt the input impedance of the radiating element (Bigelow et al., 2004).
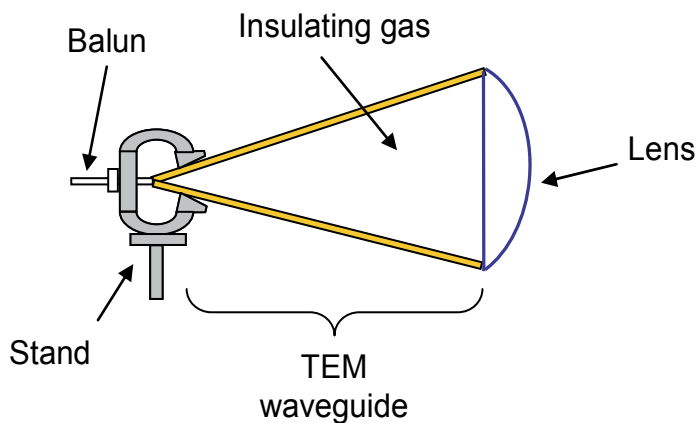
Fig. 1. Schematic cut-away of a TEM horn

Their combination with a parabolic reflector with the right specifications is easier to install.

1.2.3 Reflector antennas

The combination of a parabolic reflector with a UWB source of radiation (typically a horn) makes it possible to reach directivities much greater than those of the antennas presented before.

The radiation source, positioned at the focal point of the reflector (or offset in certain cases) must be adjusted so as not to upset the radiation patterns of the transmission as a whole.
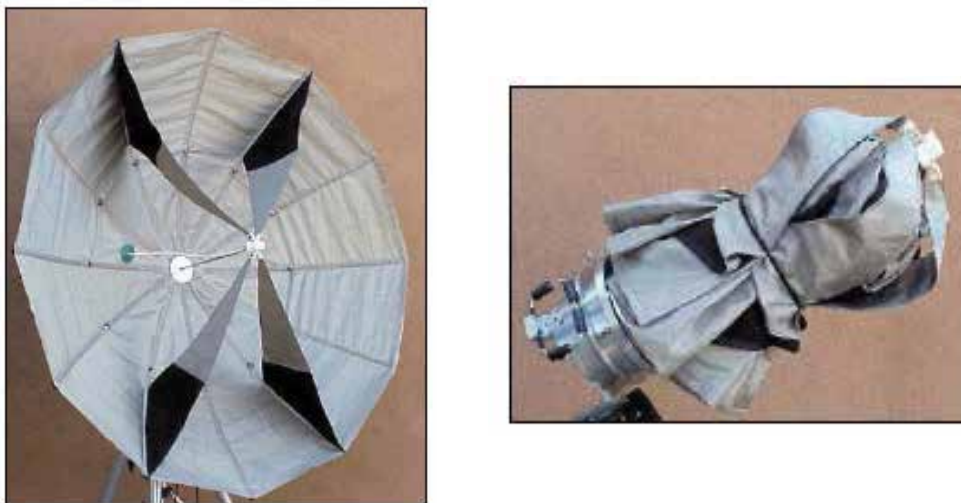
Fig. 2. U-CIRA1 antenna developed by Farr Research (USA)

The Farr Research company excels in this field. The U-CIRA1 antenna shown in Figure 2 (Farr, 2004) is a derivative of the IRA model (Baum & Farr, 1993), developed by C. Baum. It operates in the 250MHz-12GHz range and presents a relatively constant gain of round 20dB as from 2GHz. Its extremely small size (a diameter of 1.42m once deployed) makes it one of the best performance antennas in its class.

1.2.4 Travelling wave antennas

These antennas are characterized by their specific mode of operation. The radiation element must be extremely large given the wavelength of the signal to be transmitted so that when an excitation current is propagated along the metal structure it is totally radiated before reaching the end. This excludes any phenomenon of resonance or standing waves. In practice, this antenna is difficult to make because the structural dimensions remain in the order of the greatest wavelength to be transmitted. There are various designs aimed at reducing the unwanted reflections at the end and the resulting oscillations. The adaptation of these antennas on 50Ω is easy over a wide frequency band and effective directional structures can be made. These aerials are the most widely used in impulse UWB applications.

1.2.4.1 Biconical antennas, discone and conical skirt monopole

When they are large enough, these antennas can also be included in the family of travelling wave antennas. The biconical antenna consists of two cones facing each other by their

summits (or by their bases in the case of the discone). The cones can be made from rolled sheet metal or a set of metal rods. Power is injected at the summit of the cones. The cone corresponds to a biconical half-antenna placed on a ground plane.

The frequency domain of these antennas ranges from 300MHz to 18GHz. Their adaptation on 50Ω is obtained by adjusting the half-angle at the summit of the cone(s). The high cut-off frequency is determined essentially by the quality of the electrical continuity between the power line and the summit of the cable. These antennas are very poorly directional and therefore have low gains of less than 4dB. Their radiation pattern is very similar to that of the dipoles. These aerials are omnidirectional in the H plane (rectilinear polarization).

1.2.4.2 Specially designed antennas

Several travelling wave antennas can be found in the literature, each designed for a very specific project. The High Current Electronics Institute – HCEI – in Tomsk in Russia has developed an antenna (Koshelev et al., 2001; Efremov et al., 2006; Koshelev et al., 2006) which combines several radiating elements (figure 3): an electric monopole 1, two magnetic dipoles, 5 and 7 and a TEM horn, 6. The size of the loop, 5, is adjustable by the plate, 4. This antenna can be assimilated with a travelling wave antenna to which a magnetic loop has been added making it possible to increase the width of the spectrum in the low frequencies.
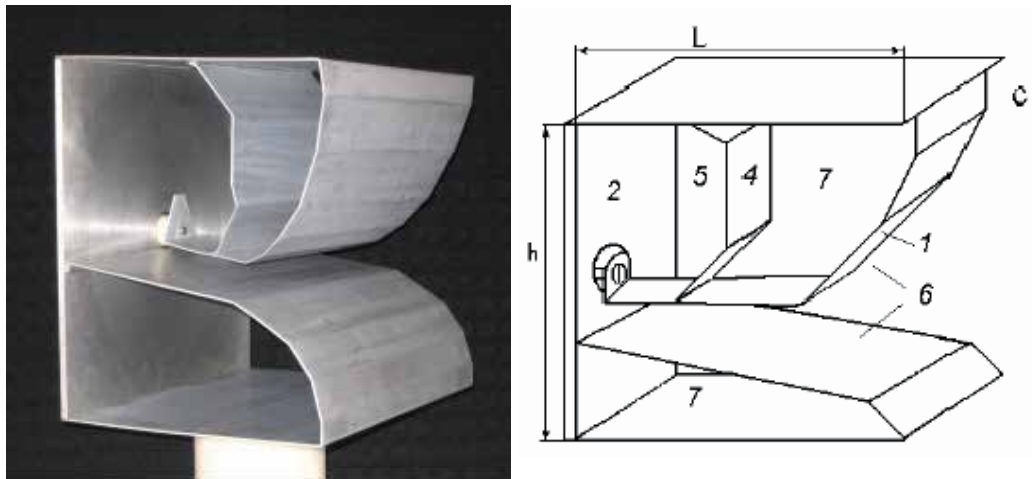
Fig. 3. Combined antenna developed by HCEI (L=385mm ; h=450mm)

Maintained in an atmosphere of SF6, the aerial is capable of withstanding bipolar voltage peak to peak amplitudes of 460kV for a few nanoseconds (τ). The length of the antenna, L, is defined by the maximum pulse width to be radiated: $L \approx \tau \cdot c / 2$ (where c is the speed of light). The TOS of the antenna is under 3 in the 200MHz-1.5GHz bandwidth. The gain achieved in the axis is constant between 6 and 8dB for a field radiated in vertical rectilinear polarization.

Over the last few years in France, the RUGBI project (the French acronym for "Instantaneous Ultra Wideband Radar") (Diot, 2006) has resulted in the construction of two travelling wave antennas. The aim of this project, pursued by the XLIM laboratory of Limoges University, was to design and produce a multi-source pulsed UWB radar system

demonstrator based on the use of optoelectronic switches to extend the limits of pulsed UWB radars in terms of range, resolution and acquisition. The antennas developed in the project are based on the Vivaldi type profile, the Valentine antenna (Diot et al., 2007) being used for the construction of the transmission array and the Libellule antenna (Delmote et al., 2004) being used for the reception of the UWB radar signals formed.

These two antennas (figure 4) are made according to the same principle but their geometry is different. The low frequency pulse components propagated on the strands are radiated at the point of the greatest opening of the antenna whereas the high frequency components are transmitted at its entrance. These antennas therefore present a slight distortion of the signal. For the frequencies between 500MHz and 3GHz, the gain of the Valentine antenna is relatively constant around 10dB with 12dB between 500MHz and 4GHz for the Libellule antenna.

a- Libellule antenna   b- Valentine antenna

Fig. 4. Travelling wave antennas developed by XLIM

1.3 Basic principles

Within the complete device, the antenna ensures the transmission of energy between the pulsed source and the free space in which it will be propagated. Depending on the quality of the radiating elements, the transmission will be made with varying input losses, the directivity of the radiation and the deformation of the pulse transmitted will both vary.

The design of very wide band antennas in the pulsed regime is more difficult than in the narrow band for many reasons related to the laws of electromagnetism. All transmission antennas are characterized by their transfer function on transmission.

This transfer function H_T links the electric field of the wave $E(r,t)$ to the complex amplitude of the incident wave V_i on the antenna input port by the relationship of temporal convolution (1):

$$E(r,t) = \frac{1}{r}\sqrt{\frac{\eta_0}{4\pi}}\left[H_T(t) \otimes \delta(t) \otimes V_i(t)\right] \tag{1}$$

where η_0 represent the characteristic impedance of the free space, r the distance as from the center of the phase on which the field E is measured and $\delta(t)$ is the Dirac pulse. This evidences that the temporal shape of the pulse transmitted results from the convolution of the excitation pulse and from pulse response of the antenna. If the latter is not a pure Dirac, it can be seen that the antenna distorts the pulse.

Moreover, within the transmission device, the antenna can be seen generally to be a kind of end dipole which must absorb all the incident energy (V_i wave) to radiate it. That implies that the reflected wave V_r must be negligible. The reflection coefficient S_{11} describes the impedance adaptation by linking V_i and V_r and the impedance of the antenna Z_A and to the impedance of the excitation source Z_G by (2):

$$S_{11} = 20 \cdot \log\left(\frac{V_r}{V_i}\right) = 20 \cdot \log\left(\frac{Z_A - Z_G}{Z_A + Z_G}\right) \tag{2}$$

It can therefore be seen that total absorption of the excitation wave implies wideband impedance matching, which is a naturally difficult problem. The usual frequency dependency of the behavior of antennas tends to make them more directional in the high frequencies than in the low frequencies. In fact, the antenna radiation patterns depend on the frequency. Naturally, there will be a situation where the vectorial transfer function will depend on the direction aimed at. Another way of addressing the problem consists of saying that a UWB antenna is « small » for the low frequencies and "big" for the high frequencies. The frequency stability of the radiation pattern is therefore a fundamental problem, which means that the shape of the pulse transmitted is unstable from an angular point of view.

One final limitation on the widening of the bandwidth lies in the size of the antenna. That can be understood as follows: the electromagnetic radiation of the antenna can be broken down into a base of spherical modes. When the currents transiting on the antenna are coupled to those modes, there is radiation. For a small antenna, only the modes in the lowest orders are likely to be coupled. The low frequency of an antenna is often inversely proportional to the greatest size of the antenna. Any attempt to extend the bandwidth towards the low frequencies of less than a hundred megahertz or so comes up against large size antennas.

As pulsed operation of antennas is little used, the prior design of an antenna using a digital design tool is essential.

Various characteristics must therefore be observed simultaneously for an aerial to match a UWB application. The parameters enabling the frequency and temporal definition of the antenna are, essentially, its input impedance, its gain, its radiation patterns and the resultant bandwidth.

The power holding of the antenna is linked to its voltage strength. The pulses radiated are very short. The energy absorbed by the antenna is therefore very low. Even in the case of high repetition rates, generally speaking there is no danger of overheating of the antenna. However, the constraints related to the dielectric strength of the radiating element very often means that its geometric dimensions must be modified or dielectric materials added (liquid, gas or solid) to withstand the high voltages applied, ranging from a few dozen kilovolts to several hundred kilovolts as the case may be. Modification of the element must

not adversely affect its electromagnetic performance. These aspects of voltage strength must therefore be taken into conditions in the design of the antenna.

2. Valentine antenna: high power design for transient applications

2.1 Principle of a travelling wave antenna

The radiation principle of the Valentine antenna is that of a travelling wave antenna.

Instead of standing waves or resonant antennas which exhibit current and voltage standing wave patterns formed by reflections from the open part of their structure, travelling wave antennas are designed to form travelling wave (uniform) patterns in current and voltage by properly terminating the end of the structure so that reflections are minimized if not completely eliminated (Balanis, 2005).

In practice, the Valentine antenna was designed to guide the electrical field from the antenna input to its end. The radiation is built up during the propagation of the transient current on the antenna from the input impedance (50Ω) to the plane wave impedance in air (120πΩ). Figure 5 illustrates the radiation principle of the Valentine antenna.
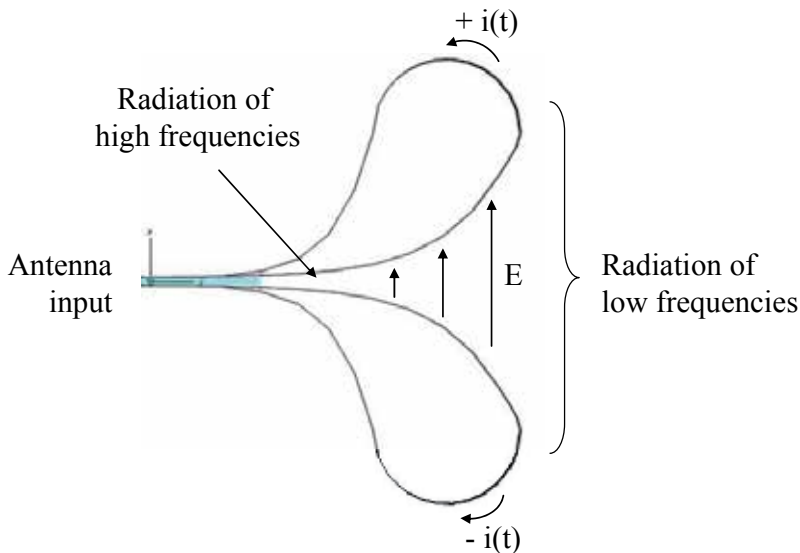
Fig. 5. Radiation principle of the Valentine antenna

This antenna consists of two brass strips curved along a specific profile. The input of the antenna is a symmetrical 50Ω double strip transmission line. A dielectric part between the two strips ensures a dielectric strength for a short pulse width (in the order of a few nanoseconds). After this line section, the two strips spread symmetrically according to an exponential profile and return back to the input within a circular form. The width of the strips is not constant and increases as the strips move away. The diameter of the rounded part has been increased in order to minimize the current reflections from the end of the antenna and to improve the radiation of low frequencies. This structure is reinforced by a dielectric material which has a dielectric permittivity close to one so as to minimize the perturbations of the high frequency radiation.
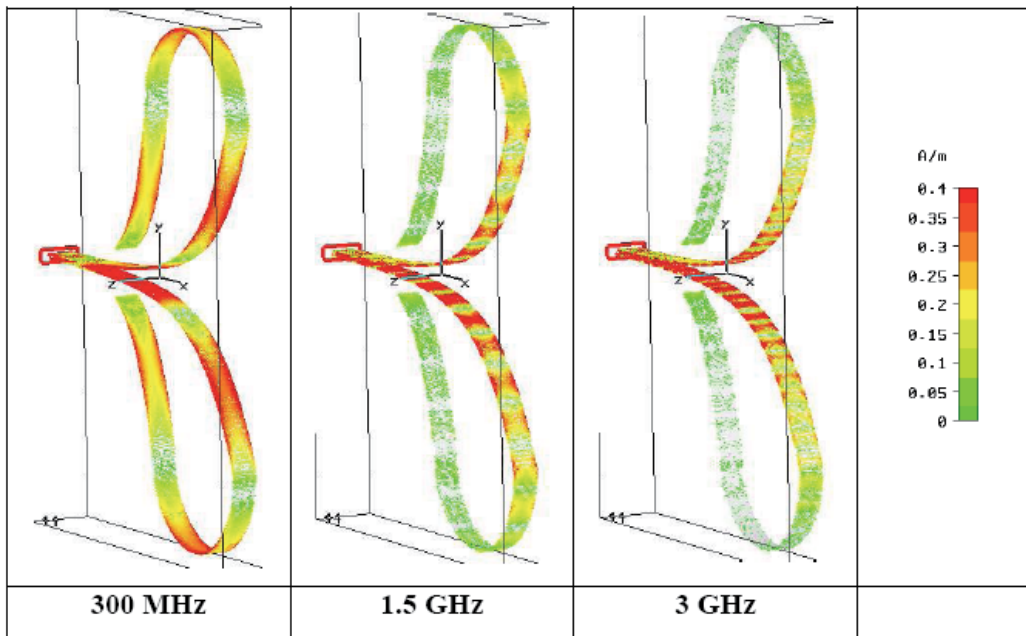
Fig. 6. Surface current distribution on the Valentine antenna

Radiation starts when the pulses reach the zone where the double-strip flares at the beginning of the exponential profile. High frequencies are radiated first and the low frequencies towards the end of the antenna. Part of the low frequencies is not radiated and returns to the generator. Polarization of the radiated electric field is mainly rectilinear and vertical for a vertical position of the antenna (as it can be seen in figure 5).

Figure 6 illustrates the current distribution (which is the origin of the radiation) on the antenna for 300MHz, 1.5GHz and 3GHz. At 300MHz, currents flow over the whole structure. The antenna aperture used to calculate the far-field zone (Fraunhoffer zone) corresponds to its higher dimension, which is 110cm. At 1.5GHz, currents fade away as they reach the rounded part. The antenna aperture is then equivalent to around 85cm. At 3GHz, the surface covered by the currents is still reduced. The antenna aperture becomes 63cm. Consequently, the far-field area depends on the frequency for travelling wave antennas. Here, the far-field zone, from which the wave can be considered as a spherical wave (centered on the antenna phase center), is calculated for the highest frequency and is equal to 9m.

2.2 The "Tulipe": impedance and geometrical matching

The structure of the Valentine requires a 50Ω double strip feeding section. For the antenna to be associated with the 50Ω coaxial output of the HPP generator, a "Tulipe" transition has been designed. This transition provides both a geometrical transformation between those two line types and ensures a good impedance matching around the characteristic impedance (50Ω). It has the advantage of enabling characterization of the antenna with classic measurement devices, such as a spectrum analyser, which have 50Ω coaxial test interfaces.

High voltage considerations must be taken into account for HPP applications. To ensure good dielectric insulation, many materials can be considered such as oil, gas and solid dielectrics. For each material, the dielectric strength of a homogenous gap structure is generally given in dc operation or for a normalized pulse voltage (Malik, 1998). However, these values are not directly available in our application. They are in fact typically used for pulse durations longer than those of interest here (less than 1ns) and for slow rise times. Their extrapolation to faster rise times and shorter pulse widths is not therefore clearly defined. Moreover, these values are often deduced for single-shot operations, whilst the interest here is in repetitive operations (as fast as hundreds of hertz). Finally, these values have been established for homogenous spark gap purposes and not for a large panel of structures which may entail certain field reinforcements. The use of a solid dielectric for the initial experimental tests was excluded because of the difficulty of its maintenance in the event of a failure. Oil is commonly preferred to gas to obtain a high dielectric strength with a relatively simple mechanical implementation.

However, there are many simple calculations to design the transition. To estimate the transition dielectric strength, it is possible, in an initial approach, to use the formula (3) written by Adler (Adler, 1991) for short pulse operation where $t_{63}^{1/3}$ is the pulse duration at 63% of the peak voltage applied to the line:

$$E_{\max} = \frac{0.48}{t_{63}^{1/3} \cdot A^{0.075}} \tag{3}$$

E_{max} is the maximum electric field in MV/cm and A is the inner conductor area of the coaxial line in cm² ($A = \pi d/l$, where d is the inner conductor radius and l the transition length. The above rule applies to the case where the inner conductor is positive. For repetitive pulses, Farr (Farr, 1994) recommends the use of the standard formula (1) and that the maximum field $E_{\max}$ be reduced by a factor of four in order to estimate the dielectric strength at a repetition rate close to 1 kHz. Moreover, for the transition design, it is essential to take the bandwidth into account. While dielectric strength considerations push the design towards large dimensions, bandwidth considerations push the design towards minimizing the dimensions in order to transit short pulses without damaging the rise time. A trade-off has to be found.

According to Foster (Foster & Tun, 1995), the length of such a transition must be a one quarter of the lowest frequency wavelength. Farr gives also a simple formula (4) concerning the rise time which can be preserved in such a transition as a function of the numerous transition dimensions:

$$t_r = \frac{\pi^2}{2} \frac{\sqrt{\varepsilon_r} R^2}{l \cdot c} \tag{4}$$

ε_r is the relative dielectric permittivity of the insulating material, R is the output conductor inner radius of the transition coaxial part, l is the transition length and c is the speed of light. Figure 7 is a 3D illustration of a longitudinal section of an arbitrary designed Tulipe transition. The design and electromagnetic simulation of the transition and antennas presented in this paper have been performed with the transient solver of Microwave Studio, the 3D electromagnetic software of the CST Company.
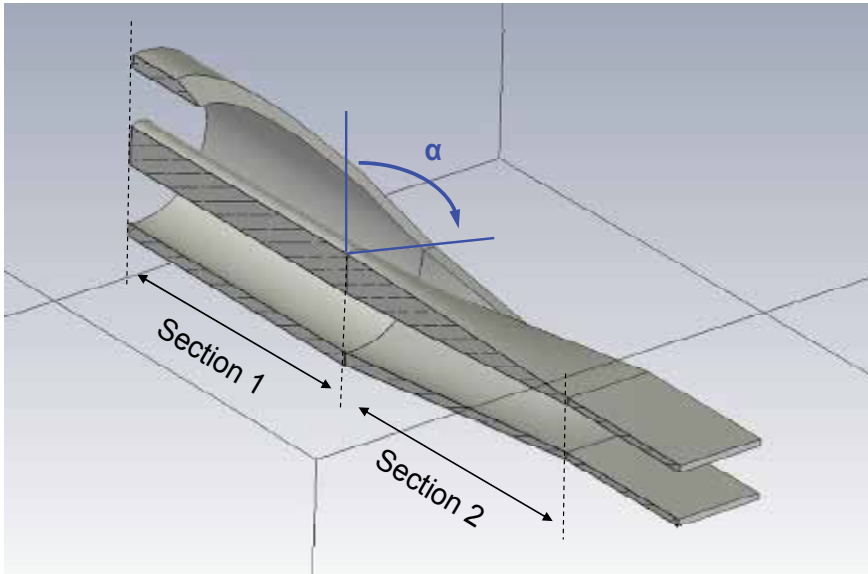
Fig. 7. 3D schematic diagram of the Tulipe transition

The length and radial dimensions of the transition are of great importance to transform a coaxial TEM field into a double-strip TEM field in the frequency spectrum concerned. Figure 8 shows the evolution of the electric field lines in the transition for several cut-away views along the z-axis (a, b, c and d).

In the first section of the transition (see section 1 in figure 7), the outer conductor of the coaxial line is opened up to a semi-angle $\alpha = 90°$ and the inner conductor diameter remain unchanged. The characteristic impedance in this section 1 increases as the semi-angle α increases. In the second section (see section 2 on figure 7), the outer conductor changes into a rectangular shape which will become the lower conductor of the double-strip line. The inner conductor of the coaxial line becomes, by a series of elliptical profiles, the upper conductor of the double-strip line.

Electric and magnetic lines remain in a TEM mode. Figure 8 shows the electric field lines arrangement for different abscissa along the transition. This analysis shows that some poor electric field reinforcements could appear in the transition. These reinforcements could cause dielectric breakdown in the case of high voltage applications.

The impedance along the Tulipe is evaluated by the mean of TDR (Time Domain Reflectometry) analysis. In order to keep it constant, dielectric materials with the same dielectric permittivity in the upstream coaxial line, the Tulipe and the downstream double-strip line must be used as soon as possible.

2.3 Design for an ultra compact high power broadband source
2.3.1 The deployed Valentine antenna
The project required the development of a new UWB antenna which is small with respect to the overall dimensions of the system and able to radiate with high gain, high voltage transient monopolar and bipolar pulses at high repetition rates. Dimensioning of this antenna was performed with the help of CISTEME and the XLIM laboratory (Limoges University, France).

z=0   z=a>0

z=b>a   z=c>b
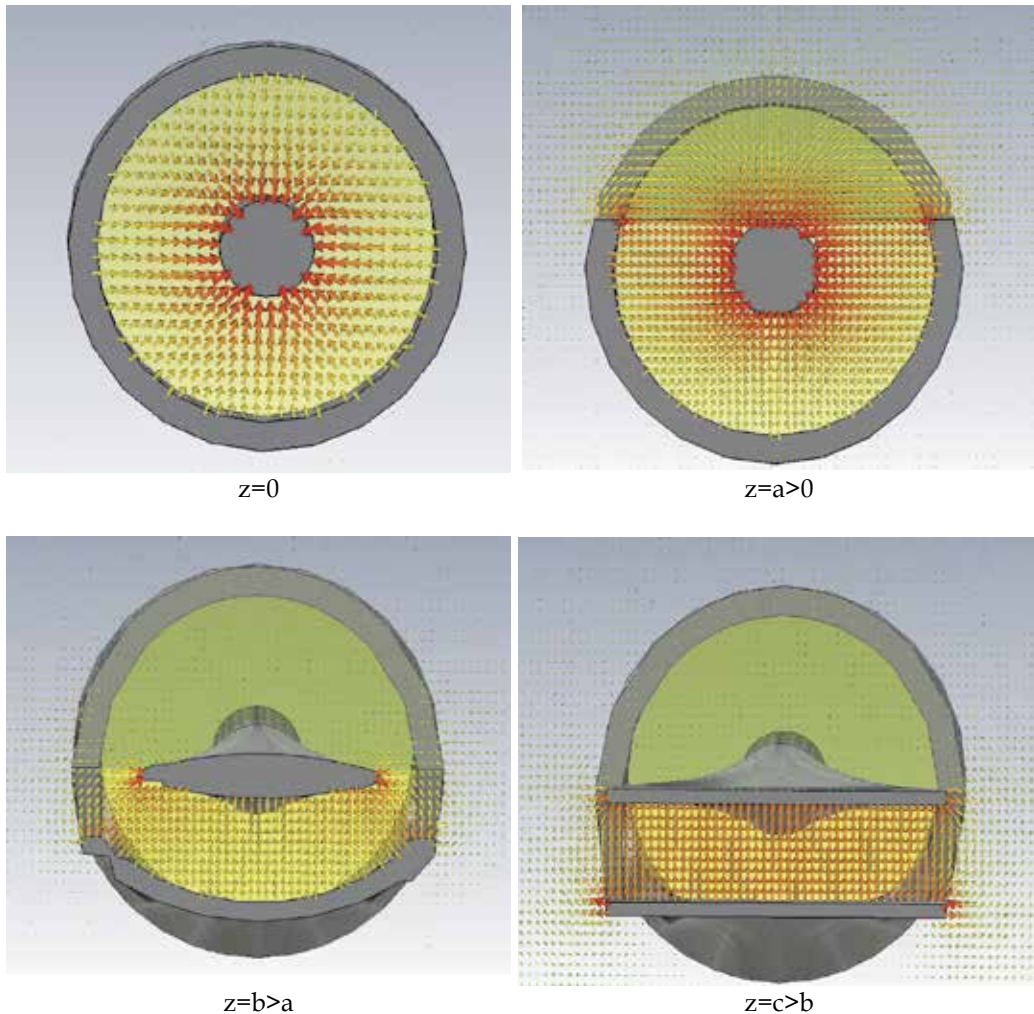
Fig. 8. TEM field evolution in the Tulipe transition

Inspiration for the design presented here came from the existing Valentine antenna. The basic principle to reach a high degree of compactness is to deploy the antenna when it is used and fold it away when the system is off. For reasons of confidentiality, the overall dimensions cannot be given in this paper.

Just as the Valentine presented in section 2.1, the deployed Valentine antenna consists of a coaxial-to-double strip transition and two metal strips curved along a specific profile separated by an insulating plate. The input transition transforms the 50Ω coaxial geometry of the generator output into a 50Ω stripline geometry. The two strips of the line then flare symmetrically according to an exponential profile and return back to the ground linearly. The strip widths are not constant and increase as the strips move away. The transition is filled with oil (ε_r = 2.3) to ensure good dielectric strength. The space in the stripline is filled with an insulating plate which has the same dielectric permittivity. A 3D schematic diagram of the antenna is presented in figure 9.
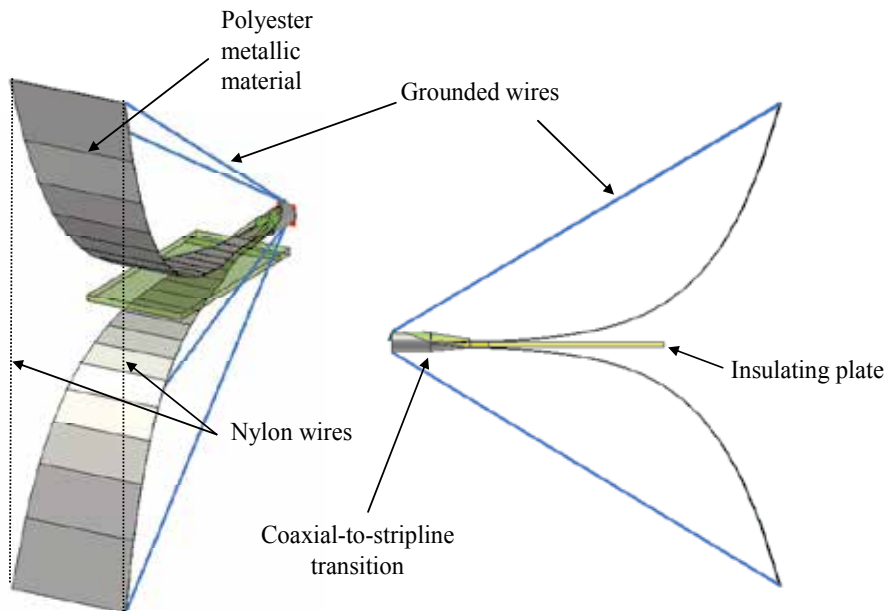
Fig. 9. Deployed Valentine antenna
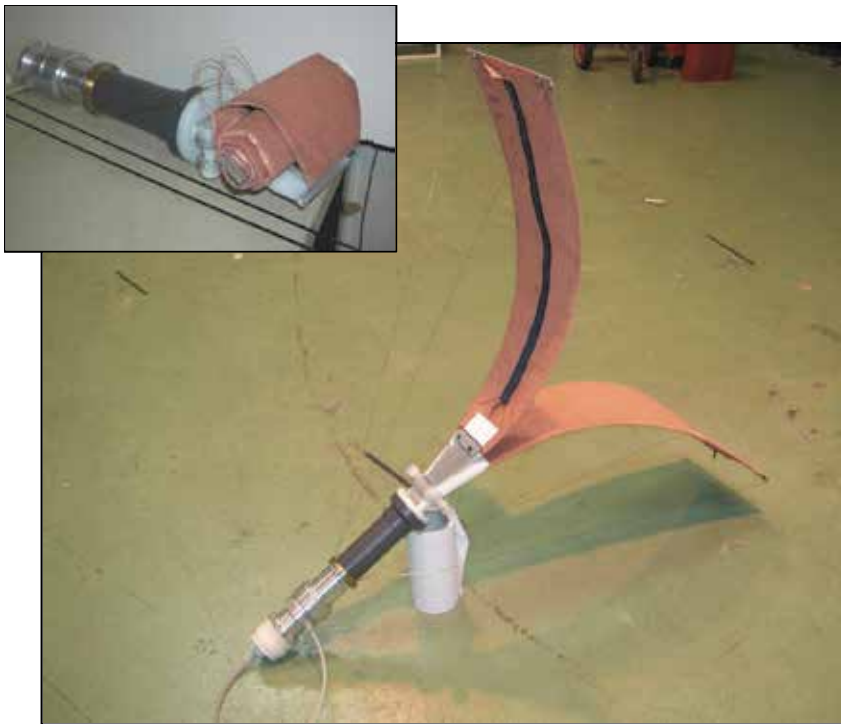
Fig. 10. Photographs of the deployed Valentine antenna

Figure 10 shows photographs of the deployed Valentine antenna (connected to a section of an HPP generator). The Tulipe transition is inserted into a cylindrical PVC tight container. A polyester metal coated material was chosen to make the two strips. The specific profile of a strip is maintained by stretching a set of two carbon shafts with two nylon wires and two copper grounded wires. These two copper wires, directly linked to the ground, avoid the electric charge of the antenna for repetitive tests and improve roughly the electromagnetic performance (especially the radiation patterns for lower frequencies). They highly contribute to the mechanical support of the antenna when it is deployed.

The two strips are fastened to the transition by means of a mechanical clamp to ensure an excellent surface continuity between the "solid" part of the strips and the "supple" part.

Assembly and disassembly can be performed in three minutes using the zip mounted on each strip.

By mean of a TDR study, the shapes of the transition and its dielectric material have been improved. The impedance variation is small over 50 Ω. Its value varies between 42.5 Ω and 58 Ω.

The calculated impedance along the Tulipe transition is shown in figure 11.
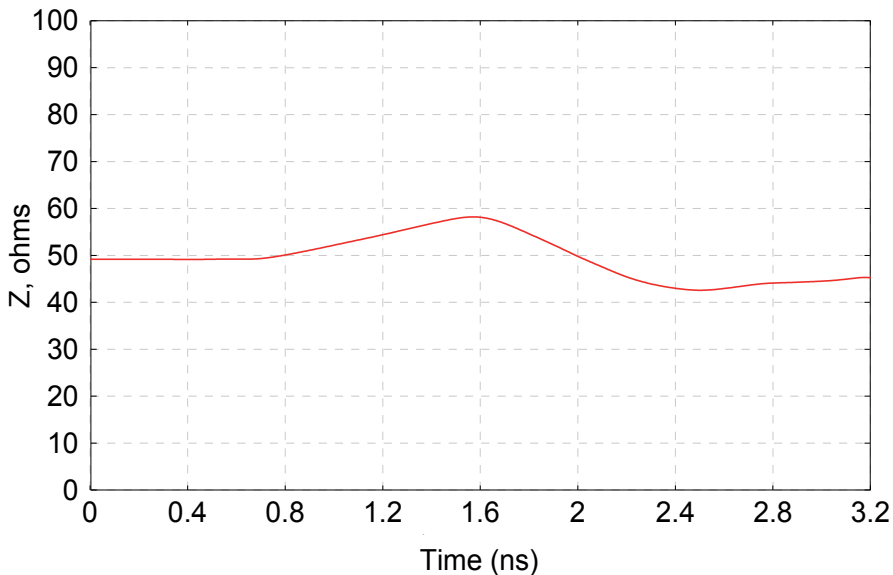
Fig. 11. Impedance variation along the Tulipe transition

2.3.2 Electromagnetic characteristics

The radiation principle of this antenna is that of the classic Valentine antenna. The electromagnetic energy is guided in a Transverse Electro-Magnetic mode from the coaxial input to the stripline section before being radiated. Radiation starts when the pulse reaches the zone where the two sides of the stripline flare and continues during the propagation of the transient currents along the surface of these two strips. The high frequency part of the spectrum is radiated first and the low frequency part more at the end of the antenna. The fact that the two strips are shortened is a compromise between the size, the ease of assembly and the electromagnetic performance of the antenna.
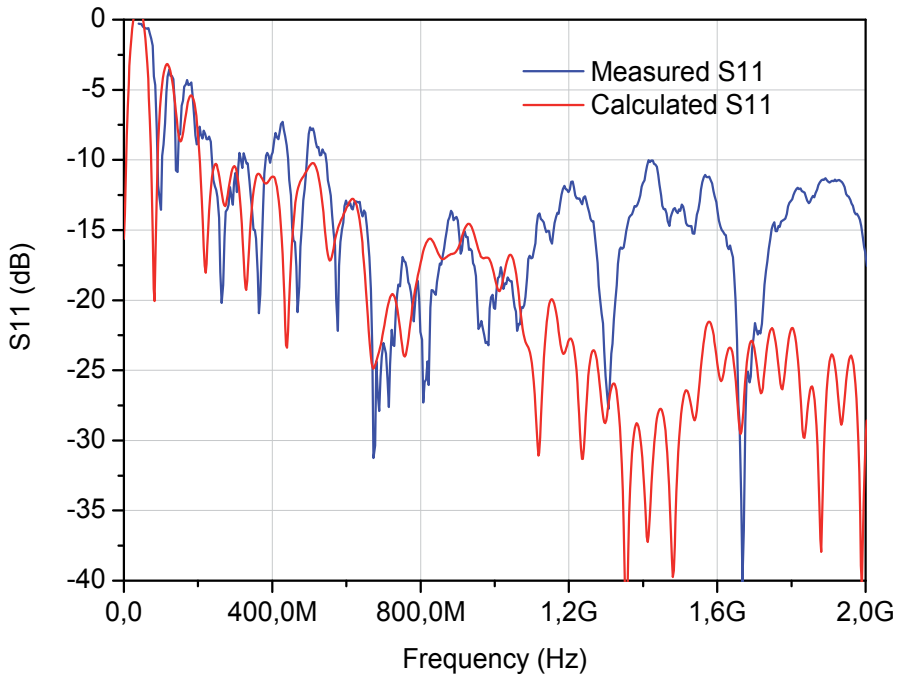
Fig. 12. S_{11} parameter
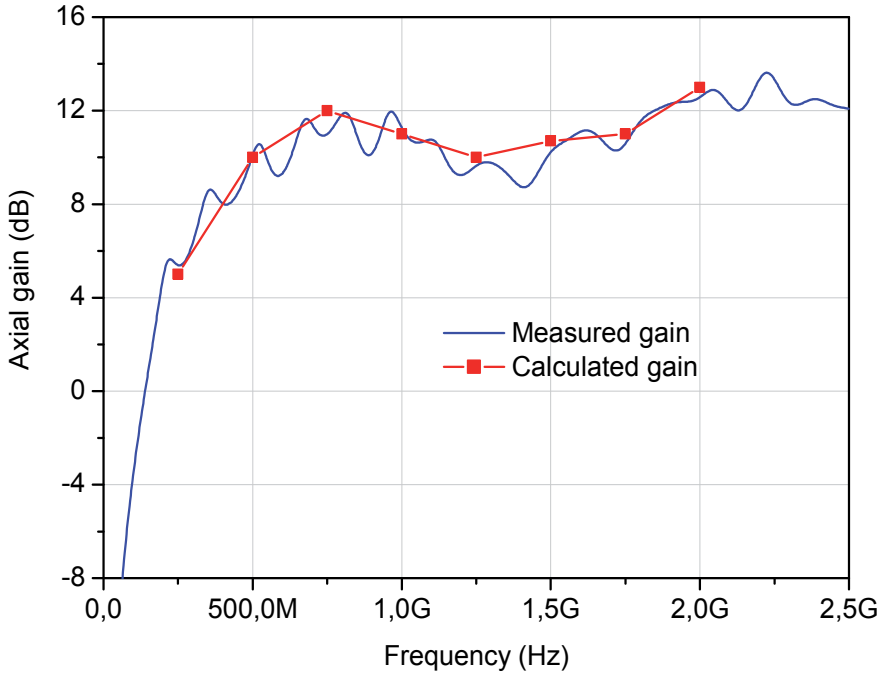
Fig. 13. Axial gain obtained

Polarization of the radiated electric field is mainly rectilinear and vertical for a vertical position of the antenna (see the position in figure 9).

Figure 12 shows the measured and calculated S_{11} reflection parameter of the antenna in the frequency range of 300kHz – 2GHz. Calculations for the design of this antenna were made using the transient solver of the CST Microwave Studio time-domain electromagnetic software.

The results are relatively similar from the low frequencies up to 1GHz. A S_{11} maximum level of -10dB is obtained in the frequency band of 250MHz – 2GHz except at frequencies between 400MHz and 550MHz where the measured S_{11} oscillates with a maximum of -7.5dB.

(a) f = 250MHz   (b) f = 500MHz

(c) f = 750MHz   (d) f = 1GHz

(e) f = 1.25GHz   (f) f = 1.5GHz
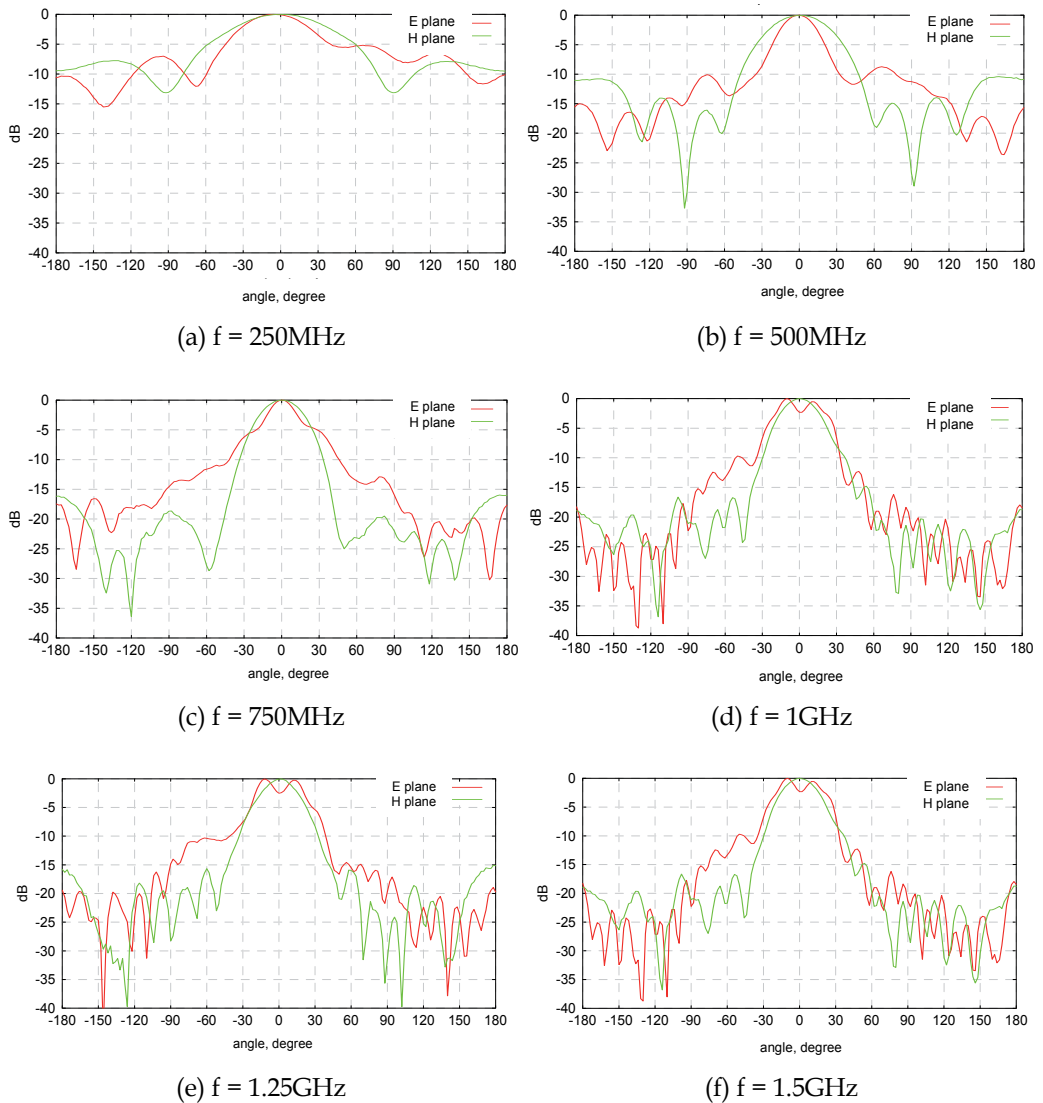
Fig. 14. Radiation patterns in E and H planes between 250 MHz and 1.5 GHz

To analyze its transient performance levels, the antenna was used as a transmitting antenna and powered by a pulse generator (Kentech APG1). The characteristics of the pulse with a 50Ω load are: an output voltage of 220V, a rise time of 116ps and a FWHM of 147ps. A well-known UWB receiving antenna is placed in front of the deployed Valentine antenna and connected to a 8GHz real time oscilloscope (Tecktronix TDS 6804 B). Antennas are positioned facing each other at a distance of 7.85m at a height of 2.75m.

The axial gain, shown in figure 13, is deduced from these transient measurements for a frequency range of 300kHz – 2.5GHz. It is compared to the calculated gain of a classic Valentine antenna with the same a, b and c dimensions.

Good agreement can be seen between these results showing that the new deployed structure of this new Valentine antenna does not degrade the electromagnetic spectrum of the source. The gain is more than 8dB in the frequency range of 330MHz – 2.5GHz.

Radiation patterns were also determined using transient measurements for each direction (10° steps from 0° to 360°). The radiation patterns measured in the E-plane and the H-plane at 250MHz, 500MHz, 750MHz, 1GHz, 1.25GHz and 1.5GHz are shown in Figure 14 (a)-(f). The main lobe is narrower in the H plane than in the E plane and in the H-plane becomes narrower with the increase in frequency. The shape of the radiation pattern in the E-plane depends on the profile followed by the metallic strips. It can prove the dissymmetrical form of the pattern in this plane, perhaps due to an incorrect shape of the antenna during the test. Back radiation is close to -20dB for the higher frequencies.

3. Optimized ultra-wideband array design

3.1 Introduction

Usually, the radiation pattern of a single antenna is relatively wide (especially for broadband antennas) and each element provides low values of directivity. Enlarging the dimensions of the antenna often leads to more directive characteristics. Another way to enlarge the dimensions of the antenna, without necessarily increasing the size of the individual element, is to form an assembly of radiating elements in an electrical and geometrical configuration.

The total field of the array is determined by the vector addition of the fields radiated by the individual elements. The theoretical array gain then depends directly on the number of antennas as in the expression 5.

$$G_R = G_A + 10 \cdot \log(N) \qquad (5)$$

G_R and G_A are respectively the gain of the full array and the gain of a unit antenna (in dB).

In this way, when the number of antennas is doubled, the gain increases by 3dB. That assumes that the current in each element is the same as that of the isolated element (neglecting coupling). This is usually not the case and depends on the separation between the elements. To provide very directional patterns, the fields from the elements of the array must interfere constructively in the desired directions and interfere destructively in the remaining space. Ideally, this can be accomplished, but in practice it is still being examined. In an array of identical elements, many parameters can be used to shape the overall pattern of the antenna. Among them, the most important are:

- the geometric configuration of the overall array
- the relative distance between individual elements
- the excitation amplitude and phase of the individual elements

- the relative pattern of the individual elements.

The influence that each of the above has on the overall radiation characteristics may be significant to the extent that the design of such an array is always a compromise between each one of them.

It must also be stressed that for high power applications, a unique antenna system needs a means to reduce high dielectric strength constraints. On the other hand, the use of an N antennas array makes it possible to divide the power into the N antennas.

3.2 Size optimization of the single element: the K antenna

The antenna array presented in this third part consists of K type antennas, the concept of which was defined by the HCEI team in Tomsk (Koshelev et al., 2001) already presented in section 1.2.4.2 of this paper. This antenna was designed to be integrated into a high power electromagnetic wave radiating system.

The antenna was purchased and optimization work performed in particular to reduce its dimensions and to centre its operational band on the required frequency band. The optimization work was performed in simulation using CST Microwave Studio software following a preliminary characterization study of the original antenna carried out by the XLIM laboratory of Limoges University. Figure 15 shows a 3D view of the CST optimized antenna and a photograph of the antenna actually made.
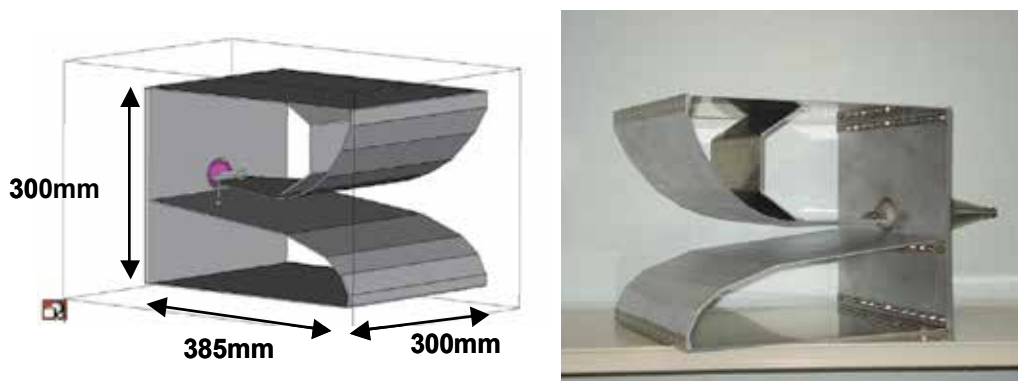
Fig. 15. Optimized K antenna

Optimization of the basic antenna made it possible to widen its frequency band and thereby to make it more compact. The reflection coefficient is shown in Figure 16. A measurement is compared to the network analyzer and the simulation. The frequency band for which a good adaptation of the antenna was obtained ($S_{11} \leq$ -10dB) is between 320MHz and 1,16GHz. The adaptation is not as good as in theory: 320MHz – 1,75GHz. The difference is due to the modeling which fails to take account of the conical part ensuring the coaxial transition N. Moreover, the characteristics of the coaxial connections are different in simulation. The low frequency of the antenna was therefore reduced from 450MHz (original antenna) to 320 MHz, and the high frequency was boosted beyond 1GHz.

To analyse its transient performance levels, the antenna is used as a transmitting antenna and powered by a pulse generator (Kentech APG1). The characteristics of the pulse at a 50Ω load are: an output voltage of 220V, a rise-time of 116ps and a FWHM of 147ps. Measurement of the E field along the main axis is compared in figure 17 to a simulation

where the antenna is fed with the same voltage signal. The antenna factor *AF* (corresponding to the ratio of the electric field peak magnitude *E* at the distance *r* by the input voltage peak magnitude *V*: $AF = \frac{1}{r}\frac{E}{V}$) obtained in this case is 1.2.
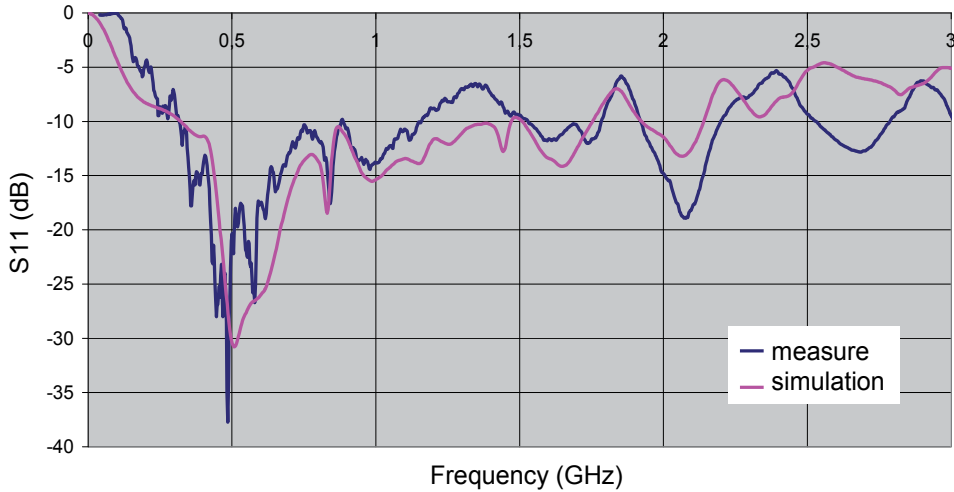
Fig. 16. S_{11} parameter of the optimized K antenna
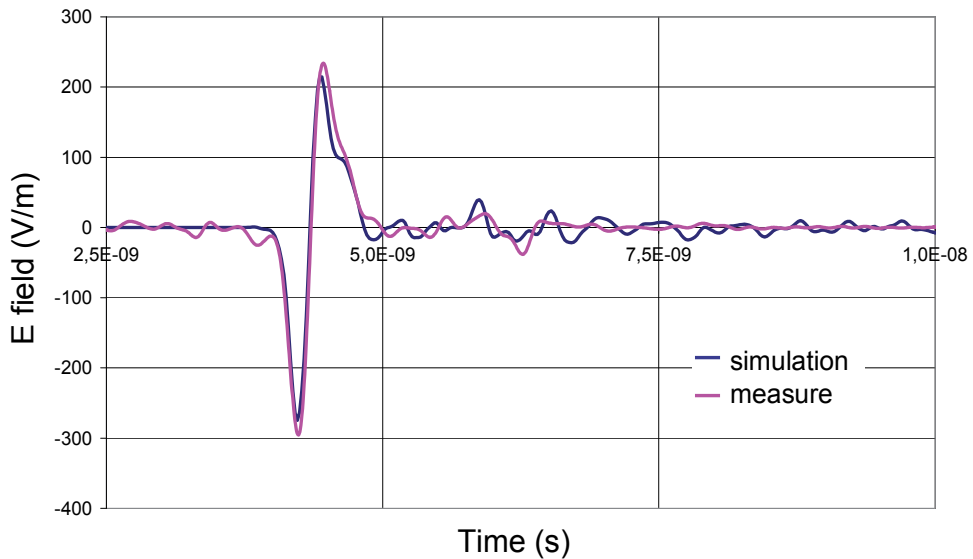
Fig. 17. E-field along the main axis at 1m

The axial gain is deduced from these transient measurements for a frequency range of 300kHz - 3GHz. It is compared, in figure 18, to the calculated range.
Radiation patterns were also determined using transient measurements for each direction (10° steps from 0° to 360°). The radiation patterns measured in the E-plane and the H-plane are shown in figure 19 as intensity graphs.
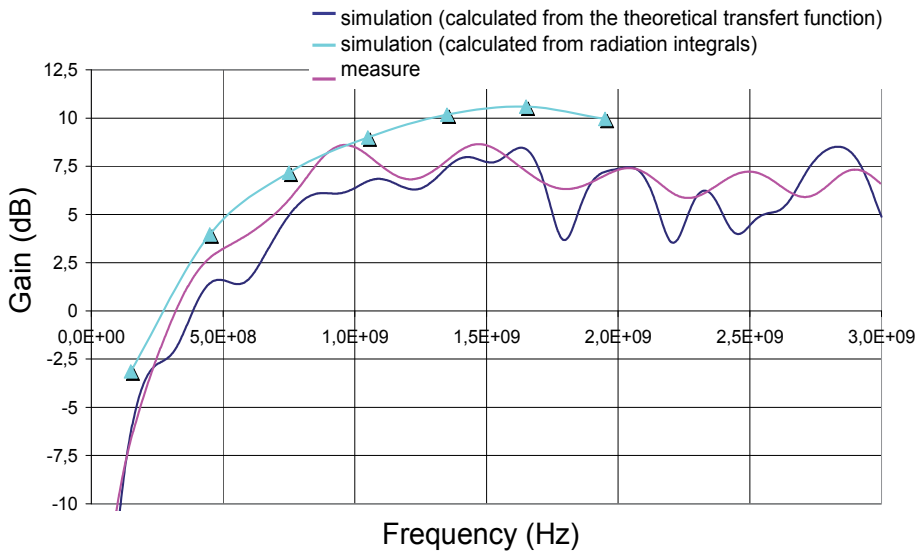
Fig. 18. Gain of the optimized K antenna obtained
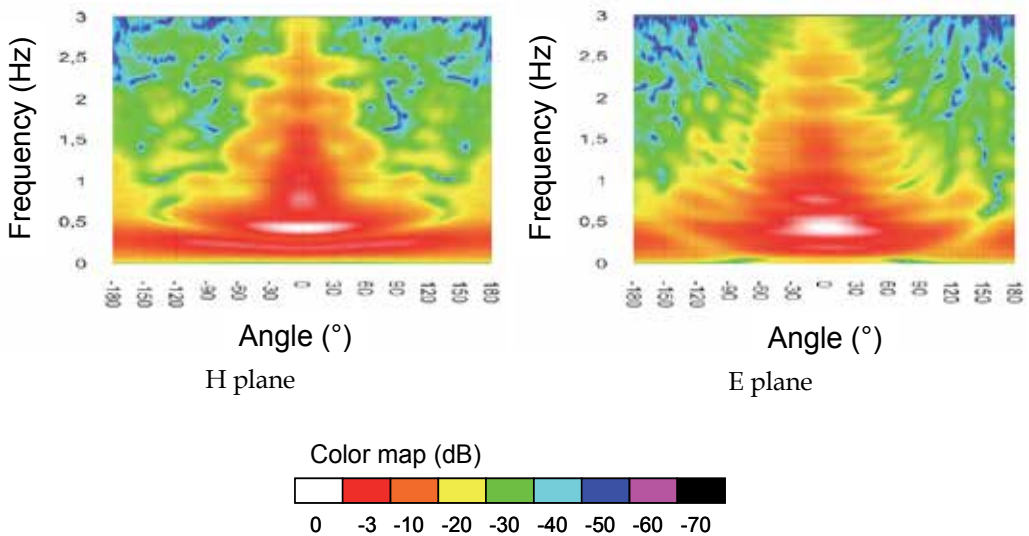
Fig. 19. Radiation patterns in the E and H planes

As for the most part of travelling wave antenna, the main lobe of the pattern is narrower in the H plane than in the E plane. In each plane, this lobe becomes narrower with the increase in frequency. Back radiation level is less than -10dB from 320MHz to 750MHz and less than -15dB from 750MHz to upper frequencies.

3.3 Electromagnetic characteristics of the optimized UWB array.
Figure 20 is a photograph of the K antennas array. It consists of 16 optimized K antennas in contact.

Fig. 20. 16 optimized K antennas array

3.3.1 Numerical justification of the array arrangement

Not all the results which contributed to the sizing of the array will be detailed here but only the most representative, in particular those concerning the choice of the vertical spacing (d_v) and horizontal spacing (d_h) between the antennas.

The study was performed on two vertical and horizontal single dimensional arrays with three and four antennas respectively so as to decouple the induced effects. The study was performed vertically on three distances, of 0, 25mm and 50 mm.

Figure 21 presents the figure-of-merit (the maximum value of the far-field peak electric field multiplied by the distance) in the axis of the E plane for the different vertical differences between the antennas when they are powered simultaneously by a 200ps rise time, 1V peak, bi-exponential pulse. The figure-of-merit (FOM) in the main axis is identical for the three array configurations. On the other hand, this representation shows the increase in the back radiation with the increase of the distance between the antennas. The variation in the peak level of the field appears as from ±135°. For that reason, it was decided to perform a maximum reduction of the distance d_v down to the vertical contact between antennas.
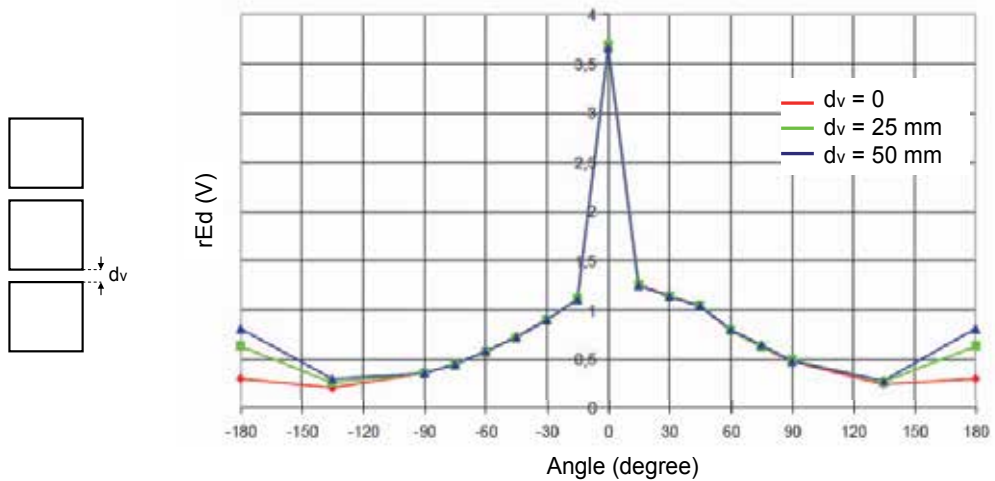
Fig. 21. FOM as a function of the incident angle (for 1V antenna feed voltage) - E-plane

The same simple study was performed with a horizontal array of four optimized K antennas. The distance adopts successively the three values of 20mm, 80mm and 160mm.
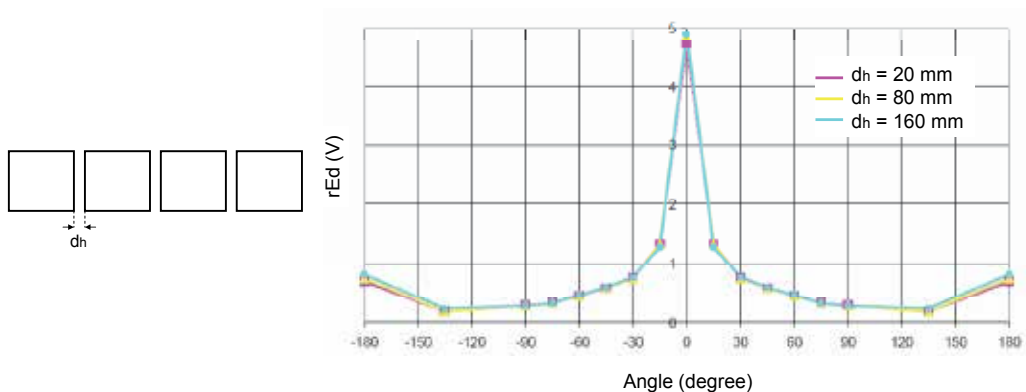
Fig. 22. FOM as a function of the incident angle (for 1V antenna feed voltage) - H-plane

The variation in the peak amplitude of the field, according to the angle of observation (shown in Figure 22), evidences that the array makes it possible to focus the radiation. The front/back radiation ratio remains constant irrespective of the spacing between the antennas. The transient radiation does not appear to be degraded although the coupling between the antennas increases with the reduction in the space between the antennas.

Moreover, at the frequencies considered, the spacing of the antennas tends to increase the lobes of the arrays. From the radiation viewpoint, the antennas can therefore be positioned very close to each other.

Given the previous results and then following a modeling study of the various array solutions, the choice was made, in order to observe a certain trade-off between the size and the radiated field level, to reduce the distance between the antennas to the extent that they were in contact with each other.

To study the influence of the antennas being placed in contact on their adaptation, power was supplied to the port N° 6 (Figure 23). Given the symmetry used to reduce the necessary computer resources, the symmetrical port was also powered. Consequently, the coefficients calculated are not « true » reflection and coupling parameters. That nonetheless makes it possible to have a general idea of the coupling between the antennas.

The « reflection » coefficient S_{66} is greater than –10dB over practically the entire frequency band (Figure 23). When the antennas are in contact, the reflections at the low frequencies (< 500MHz) increase. As far as the port n°2 situated next to the port n°6 is concerned, the coupling on this port is high and increases all the more when the antennas are in contact. The ports 1, 3 and 5 are better insulated in the event of the antennas touching.
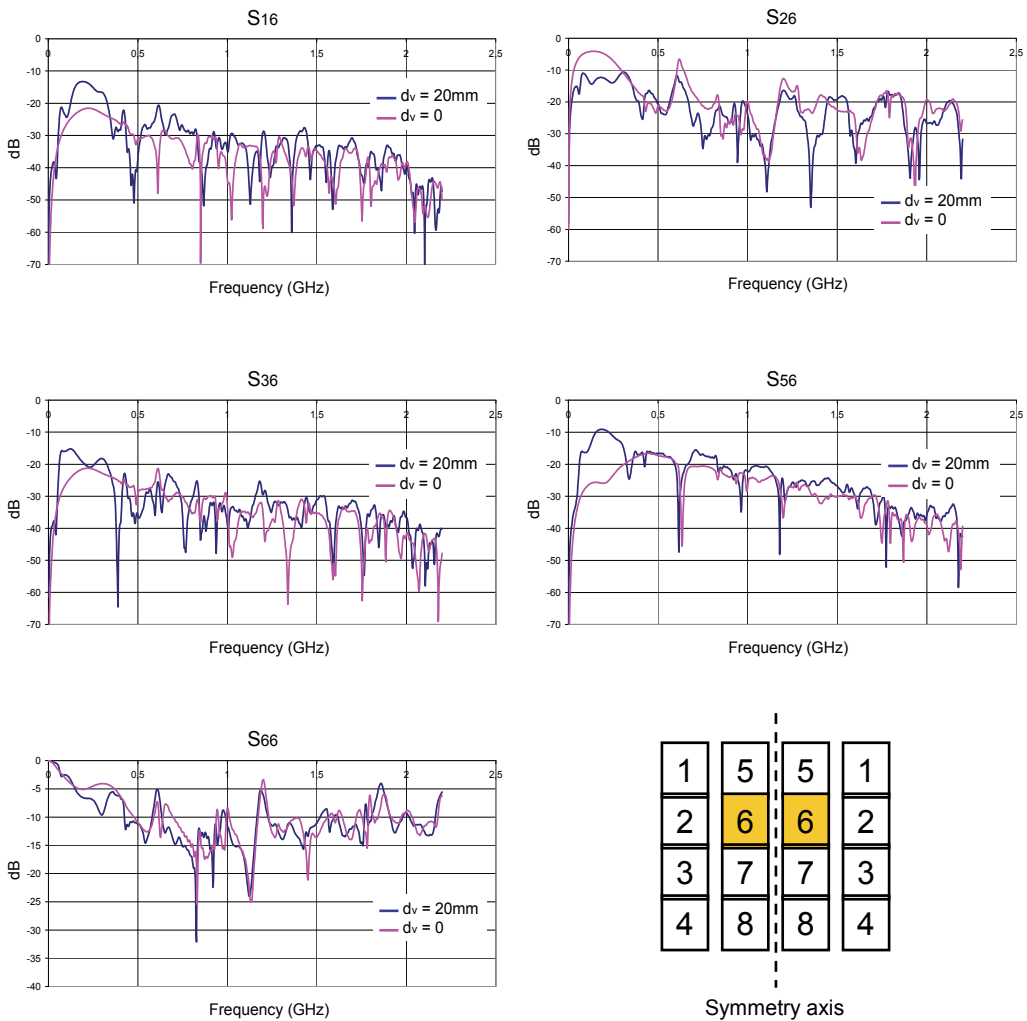
Fig. 23. S_{ij} coupling parameters

E-plane   H-plane
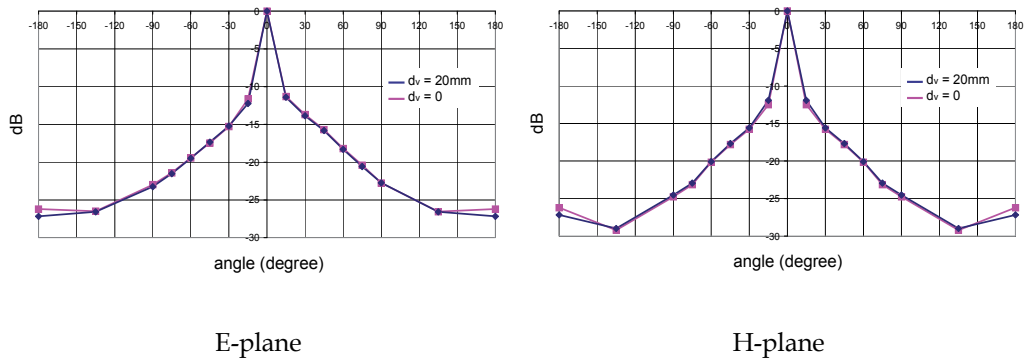
Fig. 24. FOM as a function of the incident angle (for 1V antenna feed voltage)

The diagrams in Figure 24 representing the amplitude of the radiated field according to the angle of observation are identical from –135° to +135°. As previously recorded, the back radiation is lower when the antennas are in contact. These results confirm the possibility of making an antenna array with all the radiating components in contact.

3.3.2 Experimental investigation on the array produced
An initial test was run to verify the operating of each pathway of the array and the summation of the fields in the axis. A reception antenna was placed facing the array. A *Picosecond Pulse Labs* pulse generator, which enables the generation of a subnanosecond step (level 10V, rise time 150ps, duration 40ns), powered the array through a distributor 1 to 16. A reception antenna coupled to a singe stroke 20Gech/s - 5GHz oscilloscope ensured the acquisition of the signals transmitted.

The antennas was first placed in a short circuit situation and then activated one after the other, the aim being to verify the increase of the field with the increase in the number of active antennas. It should be noted here that the far field condition was not perfectly respected (distance between the reception and the array in the order of 10m).

Figure 25 shows the evolution of the field (in proportion to the voltage received) according to the number of antennas activated. A mean increase of 20mV can be seen when an additional antenna is activated. The level recorded for the complete array was 340mV, i.e. approximately 16 times the amplitude of the field radiated by a single antenna. This test therefore enabled an initial validation of the operation of this array.
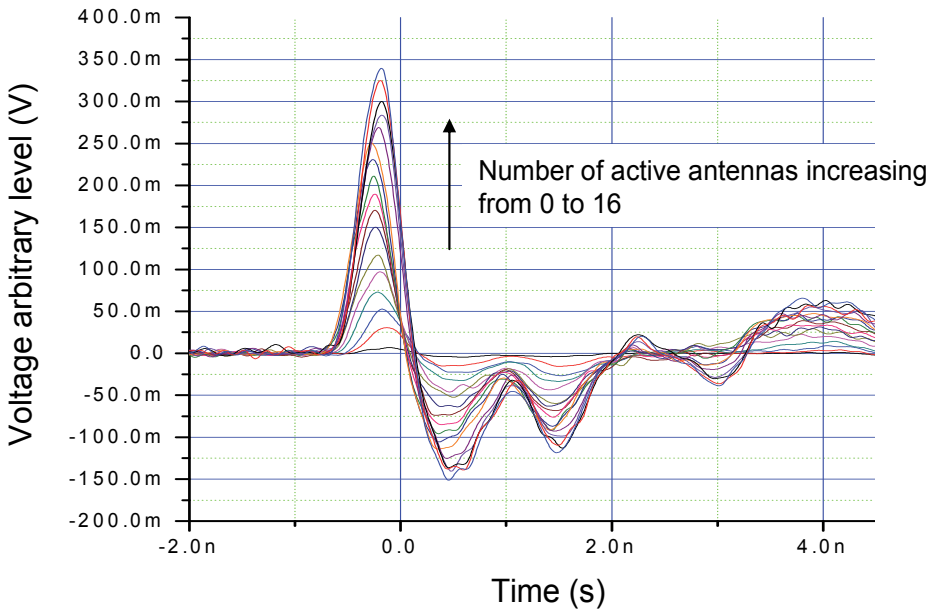
Fig. 25. Experimental field measurement on the array

3.3.3 Back radiation reducing using quarter wavelength corrugations

As shown in the previous sections, the back radiation level is under -25dB from -120° to +120° around the main axis. This back radiation level can be improved by adding quarter wavelength metal corrugations on the array.

Other solutions, such as the use of a metal ground plane, a ferromagnetic absorbent plane or the use of high impedance surfaces, can be implemented to reduce this back radiation. The choice of the solution is essentially dictated by the size, the weight and the ease of use as each of these different techniques offers similar results.

Figure 26 shows the array fitted with its metal corrugations. These rest on a metal plane the dimensions of which are identical to the preceding plate, namely 80cm×186cm. The length L of the corrugations is 50cm, namely a quarter wave at 150MHz and the gap e between each metal plate is 7.5cm.

Corrugations have no effect on the electric field level in the main axis.

The temporal waveform of the electric field back radiated is shown in Figure 27. The array is fed by a bi-exponential pulse with a 200ps rise-time (which matches the frequency spectrum of the array). It is compared to calculated results of the array with no corrugation and the array with only a ground plane mounted just behind antennas. It can be seen that the magnitude of the electric field is greatly reduced and that the temporal form of the field has changed.

Radiation patterns in the E and H planes are shown in figure 28. The main radiation lobe remains unchanged and the radiation in the back half space is greatly reduced. The frequencies considered for the radiation patterns are 150MHz harmonics. That corresponds to the frequencies which are most sensitive to the corrugations. The behavior of the corrugations is similar to that of a simple metal plated for the frequencies far from 150MHz and the low frequency harmonics.
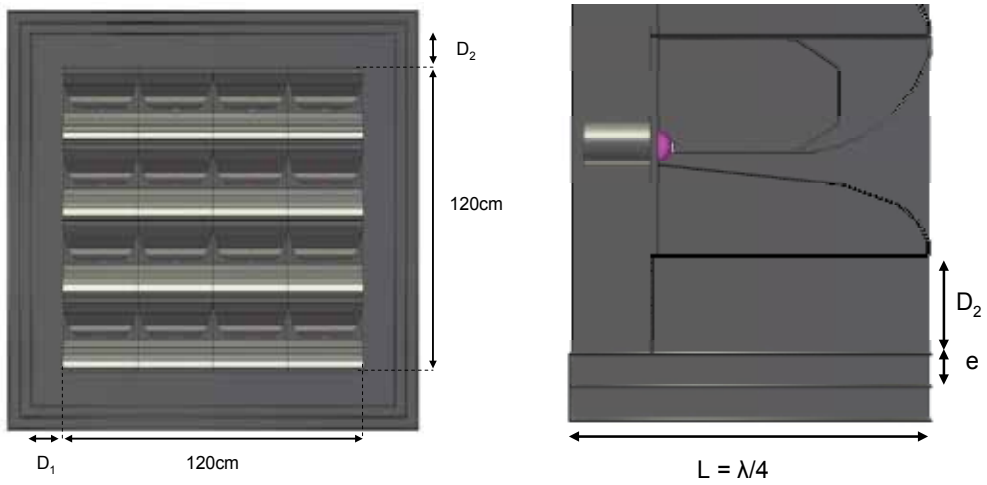
Fig. 26. Design and dimensions of corrugations
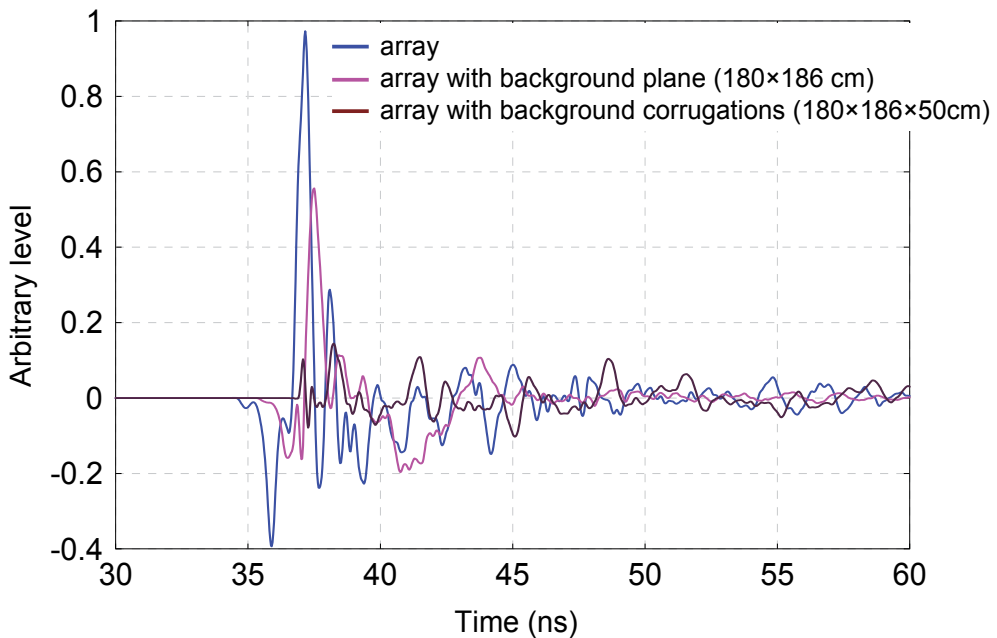
Fig. 27. Back radiation electric field level calculated for an input pulsed voltage (200ps rise-time)

However, for the higher frequencies of the spectrum considered (> 1GHz) the input of the corrugations remains undeniable.

In an angle of approximately 90° around the 180° angle, the level of back radiation remains under -30dB over the frequency band of 200MHz - 1GHz and under -40dB beyond that and around the harmonics of the 150MHz frequency (150MHz, 300MHz, 450MHz, 600MHz,…etc).

E-plane

H-plane

f = 450MHz

f = 750MHz

f = 1050MHz

f = 1350MHz
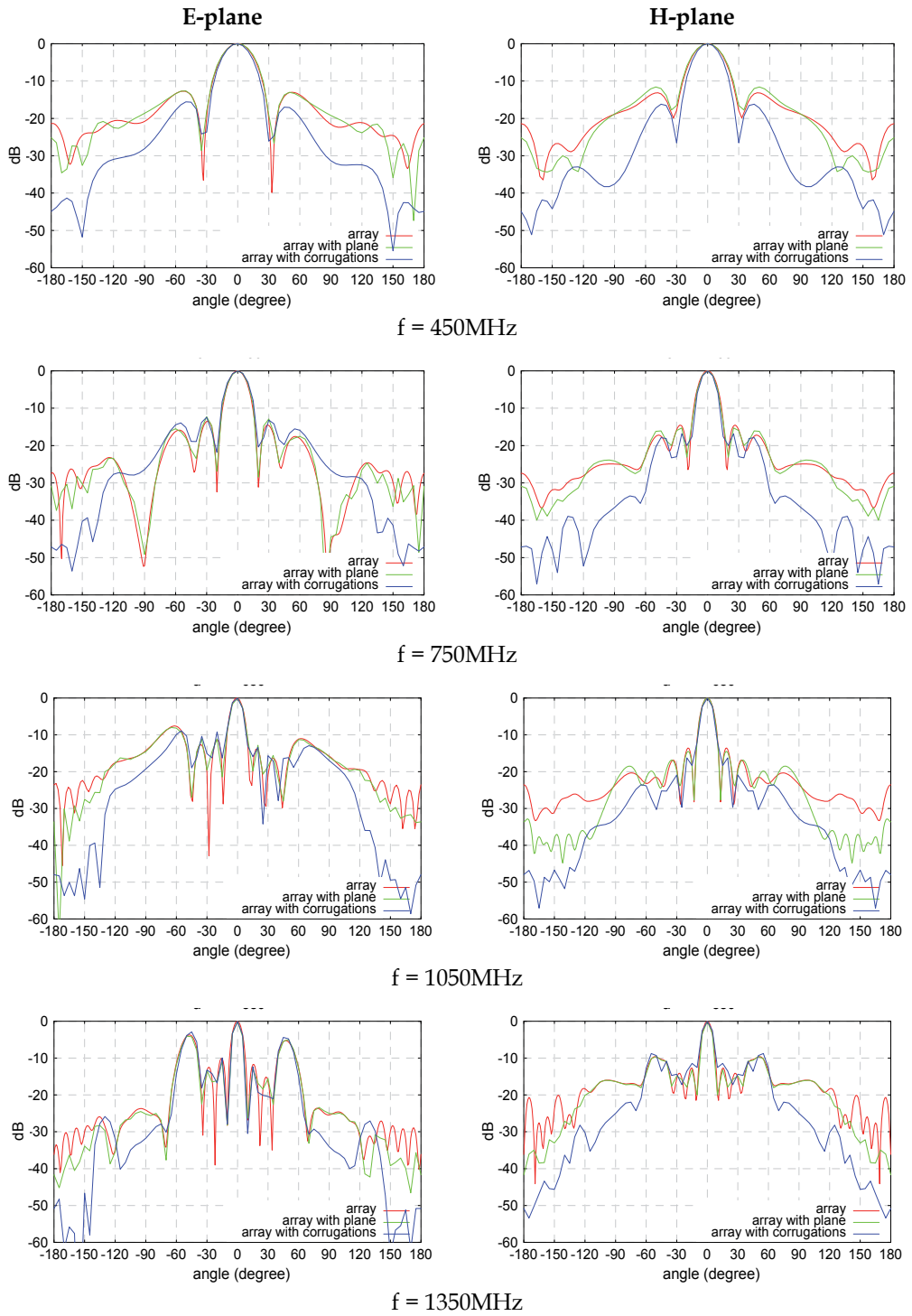
Fig. 28. Radiation patterns in the E and H planes – Benefits of the corrugations

4. Conclusion

The choice and the design of the radiating component of a high power microwave source are vital as they determine the choice of all or part of the complete system.

The choice of antennas available for high voltage ultra wide band applications is relatively limited. It has been shown here that progressive wave antennas behave extremely well in those operational ranges.

Upstream work on the Valentine and K antennas made it possible to benefit from a definite feedback of experience with those antennas in order to redesign them into new radiating devices specifically adapted to our constraints of compactness. 3D simulations coupled with experimental tests on prototypes made it possible to refine the various geometrical parameters of the components to obtain the best possible levels of electromagnetic performance in small volumes.

The work presented on the Valentine antenna made it possible to validate the concept of deployment of the antenna. It is still a prototype that could be further improved. However, its adaptation at –10dB is between 550MHz and 3GHz. It is slightly degraded at -7dB between 240MHz and 550MHz (probably because of fabrication defects). The gain and factor of merit obtained are in good agreement with the theoretic results. Development of an antenna of this type makes it possible to obtain a compact and lightweight antenna system. More intensive industrialization would make it possible to increase the capacities of this antenna (weight, rapidity of assembly, better observance of the exponential profile, compactness once folded away, etc.).

The theoretic study of the sizing of the K antenna made it possible to reduce its volume by a factor of 2.3 (antenna dimensions 300×300×385mm). An array of 16 of these antennas offers the best size/performance trade-off. Were this array to be combined with a pulsed source, it would make it possible to obtain a factor of merit of 1MV for a bi-exponential power signal with a rise time in the order of 200ps and a peak level per antenna of approximately 50kV.

The influence of the distance between the antennas on radiation was studied. All the antennas can be placed in contact both in the horizontal and in the vertical plane. The production of a single block array would however result in the loss of the modular aspect of the system. For example, it is possible to obtain radiation in the two polarizations by arranging half of the antennas in horizontal polarization.

A certain number of solutions to reduce the transient back radiation were also studied. The simplest solution is the combination of a ground plane placed behind the array. This is linked to the plane surface and to the power signal of the antennas (a spectrum covered by the pulse). The addition of quarter wave corrugations is the most effective solution for the field peak level. This method has the disadvantage of offering very high performance at special frequencies but it is not homogenous over the entire spectrum. To lower the radiation further, it would be possible to contemplate longer corrugations. For example, 75cm long corrugations would give rise to an initial hole at 150MHz and then at the higher harmonics and therefore a greater number of holes, but at the expense of size.

5. Acknowledgments

6. References

Adler, R.J. (1991). Pulse power formulary, North Star Research Corp.,

Balanis, C. A. (2005), Antenna theory: analysis and design, Third edition by J. Wiley & Sons, ISBN 0-471-66782-X

Baum, C. E., & Farr, E. G. (1993). Impulse Radiating Antenna, *Ultra-wideband, Short Pulse Electromagnetic*, ed. Bertoni, New York, Plenum, pp. 139-147, available from http:\\www.farr-research.com

Bigelow, W. S., Farr, E. G., Bowen, L. H., Ellibee, D. E., & Lawry, D. I., (2004). Design and Characterization of lens TEM Horn, *Sensor and Simulation Notes*, Note 490, available from http:\\www.farr-research.com

Cadilhon, B., Pécastaing, L., Reess, T., Silvestre De Ferron, A., Pignolet, P., Vauchamp, S., Andrieu, J., & Lalande M., (2010). High Pulsed Power Sources for Broadband Radiation, *IEEE Transactions on Plasma Science*, Vol. 38, n° 10, pp. 2593-2601, ISSN: 0093-3813

Delmote, P., Dubois, C., Andrieu, J., Lalande, M., Bertrand, V., Beillard, B., Jecko, B., Largeau, T., Guillerey, R., & Colson S., (2004). Two original UWB antennas: the Dragonfly antenna and the Valentine antenna, *Proceedings of Radar 2004 Symposium*, Toulouse

Diot, J.C., (2006). Design and realization of an impulse optoelectronic Ultra Wide Band radar, Ph. D. dissertation, University of Limoges, n°502006

Diot, J.C., Delmote, P., Andrieu, J., Lalande, M., Bertrand, V., Jecko, B., Colson, S., Guillerey, R., & Brishoual, M., (2007). A novel antenna for transient applications in the frequency band 300MHz-3GHz: the Valentine antenna, *IEEE Transactions on Antennas and Propagation*, vol. 55, n°3, pp 987-990, ISSN: 0018-926X

Efremov, A. M., Koshelev, V. I., Kovalshuk, B. M., Plisko, V. V., & Sukhushin, K. N., (2006). High-power sources of ultrawideband radiation with subnanosecond pulse length, *Proceedings of the 2nd International Congress on radiation physics, high current electronics and modification of materials*, pp. 446-449, Tomsk

Farr, E.G., Sower, G.D., & Buchenauer C. J., (1994). Design considerations for ultra-wideband, high-voltage baluns, *Sensor and Simulations Notes*, n° 371, available from http:\\www.farr-research.com

Farr, E. G., Bowen, L. H., Lawry, D. I., & Tyo J. S., (2004). An ultra compact impulse radiating antenna, *Sensor and Simulation Notes*, n°494, available from http:\\www.farr-research.com

Foster, P.R., & Tun, S.M., (1995). A wideband balun from coaxial line to TEM line, *Proceedings of the IET Conference on Antennas and Propagation*, pp. 286–290, Eindhoven, ISBN: 0-85296-637-7

Koshelev, V. I., Buyanov, Y. I., Andreev, Y. A., Plisko, V. V., & Sukhushin K. N., (2001). Ultrawideband radiators of high-power pulses, *Proceedings of the IEEE Pulsed Power Conference*, Vol. 2, pp. 1661-1667, Tomsk, ISBN: 0-7803-7120-8

Koshelev, V. I., Gubanov, V. P., Efremov, A. M., Korovin, S. D., Kovalshuk, B. M., Plisko, V. V., Stepchenko, A. S., & Sukhushin K. N., (2006). High-power ultrawideband radiation source with multielement array antenna, *Proceedings of the 2nd*

International Congress on radiation physics, high current electronics and modification of materials, pp. 258-261, Tomsk

Malik, N.H., Al-Arainy, A.A., & Qureshi, M.I., (1998). Electrical insulation in power systems, In: *Power engineering,* H. Lee Willis, (Ed.):, Marcel Dekker Inc., ISBN: 0-8247-0106-2

Pécastaing, L., Cadilhon, B., Reess, T., Silvestre De Ferron, A., Pignolet, P., Vauchamp, S., Andrieu, J., Lalande M., & Brasile J.P., (2009). A 250kV, 300ps, 350Hz Marx generator as source for an UWB radiation system, *Proceedings of the IEEE Pulsed Power Conference*, Washington, p. 51-56, ISBN: 978-1-4244-4064-1

UWB Multifunction Antennas

Paolo Baldonero, Roberto Flamini,
Antonio Manna and Fabrizio Trotta
Antenna Dept. Elettronica S.p.A. - Via Tiburtina Valeria
Italy

1. Introduction

In the last years Ultra-Wide Band technology has known an enormous success, both in military and civilian applications thanks to its undeniable advantages over standard systems.

Nowadays the three main types of UWB applications are the following:

1. Applications involving radar, in which the signal penetrates nearby surfaces, allowing objects to be detected behind walls or other coverings.
2. Applications of communication: voice and data transmission using digital pulses, allowing a very low powered and relatively low cost signal to carry information at very high data rates within a restricted range.
3. Military applications, which comprehend the control of the e.m. scenario, preserving the use of electromagnetic spectrum for friendly use while denying its use to the enemy (that is the aim of the Electronic Warfare, EW[1]).

The use of large bandwidths offers multiple benefits including high date rates, robustness to propagation fading, accurate ranging and geolocation, superior obstacle penetration, resistance to jamming, interference rejection, and coexistence with narrow bandwidth systems.

For the commercial systems, the Federal Communications Commission (FCC) in the United States established the rules for the operation of UWB devices.

An UWB antenna is defined as a radiating element having a fractional bandwidth greater than 0.2 and a minimum bandwidth of 500 MHz.

$$BW = 2\frac{f_H - f_L}{f_H + f_L} \geq 0.2 \qquad \text{and} \qquad f_H - f_L \geq 500 Mhz \tag{1}$$

---

[1] Electronic warfare is defined as the art and the science of preserving the use of the electromagnetic spectrum for friendly use while denying its use to enemy (David Adamy). Electronic warfare has classically been divided into: (a) Electromagnetic Support Measures (ESM) – the receiving part of EW; (b) Electromagnetic Countermeasures (ECM) – jamming, chaff, and flares used to interfere with the operation of radars, military communication, and heat-seeking weapons; (c) Electromagnetic Counter-Countermeasures (ECCM) – measures taken in the design or operation of radars or communication systems to counter the effects of ECM.

where f_L and f_H are the frequencies defining the antenna's operating band (10dB below the highest radiated emission).

Moreover the FCC allocated the 3.1-10.6GHz spectrum for unlicensed commercial applications of UWB technology.

For military applications the definition of UWB technology does not fully agree with the commercial approach proposed by the FCC.

Currently, EW Antenna research and development is pushed by the demand for new, high performing electronic systems for electronic support (ES) as well as electronic counter-measures (ECM) in both communication and radar frequency bands. To meet this demand, R&D teams are focused on antenna systems working over frequency range of 1.5 MHz up to 40 GHz (Misra, 2009).

Therefore, for military applications an UWB antenna has to cover a frequency band of several octaves (some examples are 2-6GHz, 6-18GHz, 0.5-18GHz, 18-40GHz) maintaining the same electric and radiating characteristics throughout the whole operating spectrum.

In conclusion, an UWB system requires electromagnetic sensors capable of receiving over each frequency of its operating band at the same time. For this reason, antenna behaviour and performance must be consistent and predictable, i.e. radiation patterns, gain and matching should be stable across the operating band.

The aim of this chapter is to provide an introduction about UWB multifunctional antennas, pointing out all the main features, advantages and drawbacks, in a quick and easy-to-understand way. The chapter will start presenting a brief history of UWB radiating elements; it will continue explaining the theory behind the frequency independent antennas and the feeding techniques. After that an introduction to the impulse response of UWB antennas will follow and finally, the last part of the chapter will suggest a complete design of UWB multifunctional phased array.

2. History of UWB antennas

Ironically, the patent which inaugurated the concept of narrowband frequency domain radio also disclosed some of the first ultra-wideband antennas. In 1898, Oliver Lodge introduced the concept of "syntony," the idea that a transmitter and a receiver should be tuned to the same frequency so as to maximize the received signal (Lodge, 1898). In this same patent, Lodge discussed a variety of "capacity areas," or antennas, that will be quite familiar to modern eyes:

"As charged surfaces or capacity areas, spheres or square plates or any other metal surfaces may be employed; but I prefer, for the purpose of combining low resistance with great electrostatic capacity, cones or triangles or other such diverging surfaces with the vertices adjoining and their larger areas spreading out into space; or a single insulated surface may be used in conjunction with the earth, the earth or conductors embedded in the earth constituting the other oppositely-charged surface"

In what is likely the most profound and sweeping sentence in the history of antenna technology, Lodge disclosed spherical dipoles, square plate dipoles, biconical dipoles, and triangular or "bow-tie" dipoles. He also introduced the concept of a monopole antenna using the earth as a ground. In fact, Lodge's patent drawings make very clear his preferred embodiments. Figure 1 shows Lodge's patent pictures in which triangular or bow-tie elements are clearly indicated and in which biconical antennas are unmistakably used in a transmit-receive link.
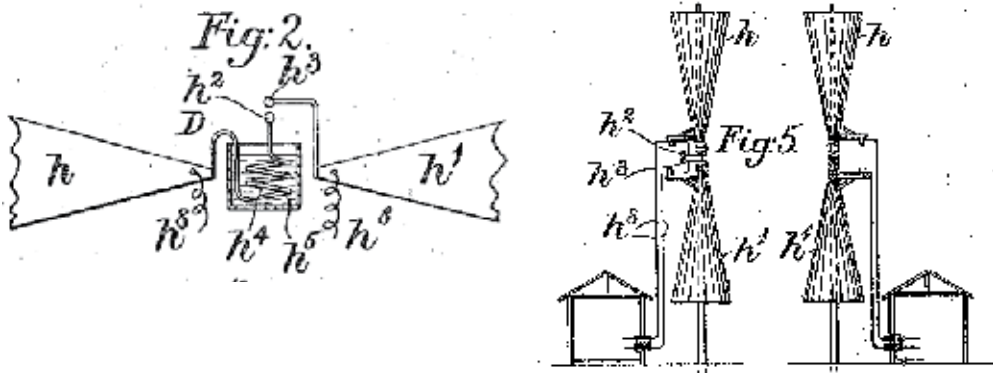
Fig. 1. (left) Lodge preferred antennas consisting of triangular "capacity areas," precursor of the "bow tie" antenna (right) Lodge's biconical antennas

Around 1940, with the advent of research into television, interest in antennas that could handle the wider bandwidths associated with video signals increased.
This renewed interest in wideband antennas led to the rediscovery of the biconical antenna and conical monopole by Carter in 1939 (see figure 2) (Carter, 1939).
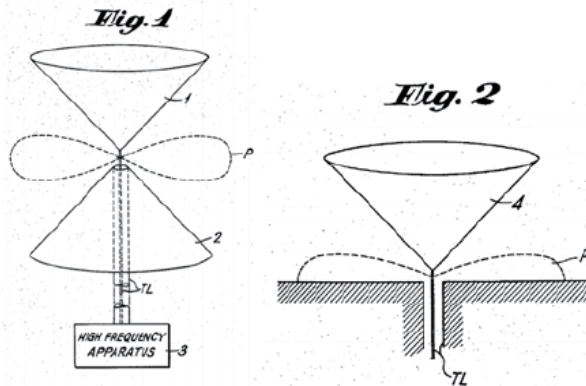

Fig. 2. Carter's biconical antenna (left) and conical monopole (right)

Carter improved Lodge's original design by incorporating a tapered feed. Carter was among the first to take the key step of incorporating a broadband transition between feed line and radiating element.
Perhaps the most prominent UWB antenna of the period was Lindenblad's coaxial horn element (Lindenblad, 1939-1941). Lindenblad improved on the idea of a sleeve dipole element, adding a gradual impedance transformation to make it more broad banded. RCA chose Lindenblad's element (figure 3 left) for experimental use in television transmission. RCA envisioned multiple channels being broadcast from the same central location, thus a wideband antenna was essential. For several years during the 1930's, a turnstile array of Lindenblad's coaxial horn elements graced the top of the Empire State Building in New York City where RCA located its experimental television transmitter. The figure 3 right displays a patent drawing of this array. The antennas at the top of the tower in this figure are folded dipoles used to transmit the audio portion of the television signal.
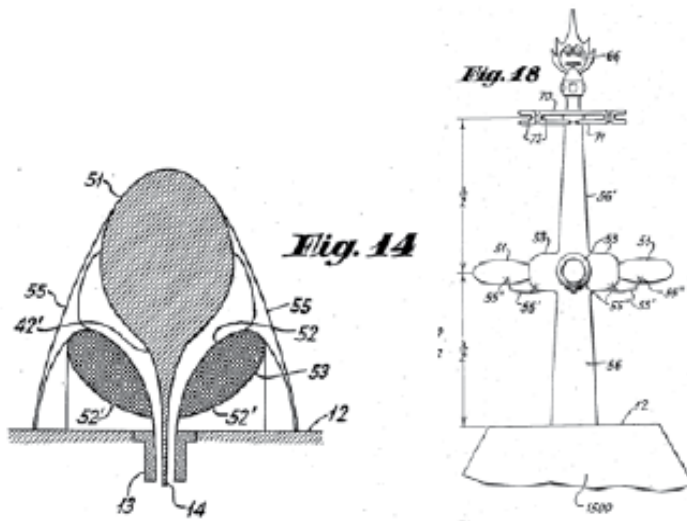
Fig. 3. Lindenblad's element cross-section (left) and turnstile array for television transmission (right)

Other researchers pursued the idea of constructing antennas from coaxial transitions. Brillouin introduced coaxial horns, both omni-directional and directional (figure 4) (Brillouin, 1948).
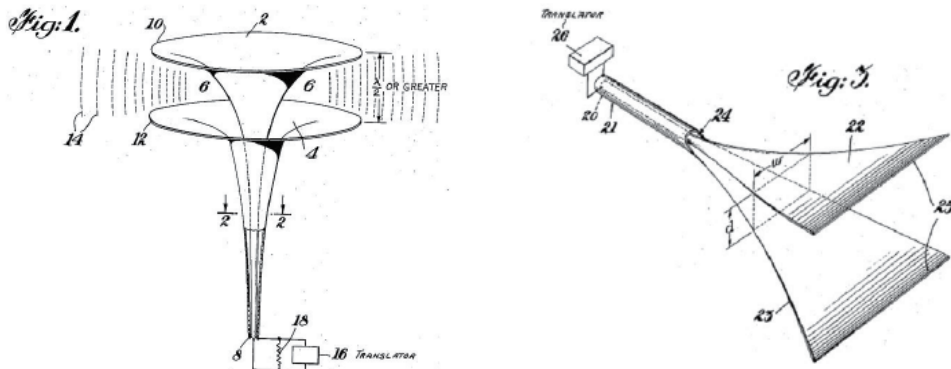
Fig. 4. (left) omni-directional coaxial horn, (right) directional coaxial horn

By the year of 2000, an innovative UWB slot antenna was proposed by Barnes, as illustrated in figure 5. This slot antenna maintains a continuous taper design, therefore, with a suitable design of the slot taper, outstanding bandwidth and performance can be achieved. This UWB antenna was employed by The Time Domain Corporation as their first generation through-wall radar (Schantz & Barnes, 2001).

From 1992, several microstrip, slot and planar monopole antennas with simple structure such as circular, elliptical or trapezoidal shapes have been proposed (Liang, et al., 2004; Lui, et al., 2005; Kim & Known, 2004; Seok,, et al., 2004; Ying & Zhang, 2004). Today the state of the art of UWB antennas focuses in these microstrip, slot and planar monopole antennas

with different matching techniques to improve the bandwidth ratio without loss of its radiation pattern properties.
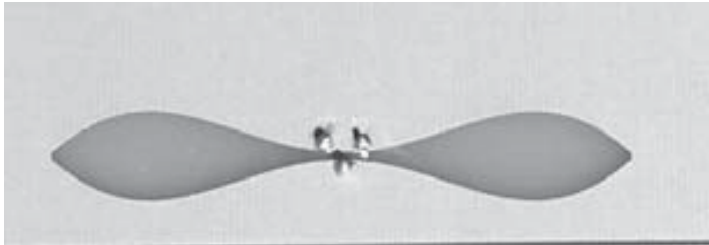
Fig. 5. Barnes's UWB slot antenna

Recent work had been focused on Vivaldi antennas (Gibson, 1979). The Vivaldi antennas (see figure 6), also known as "tapered slot" or "notch" antennas, can operate as end-fire, traveling wave antennas producing somewhat directive radiation. As a traveling wave antenna, the impedance and pattern bandwidths are moderately wide. Printed Vivaldi antennas are easy to fabricate, having no highly sensitive dimensional tolerances. Theoretically, the Vivaldi antenna has an infinite bandwidth and the only limitation is its physical size and fabrication capabilities. In practice, one of the main bandwidth limitations is the microstrip-to-slotline transition.
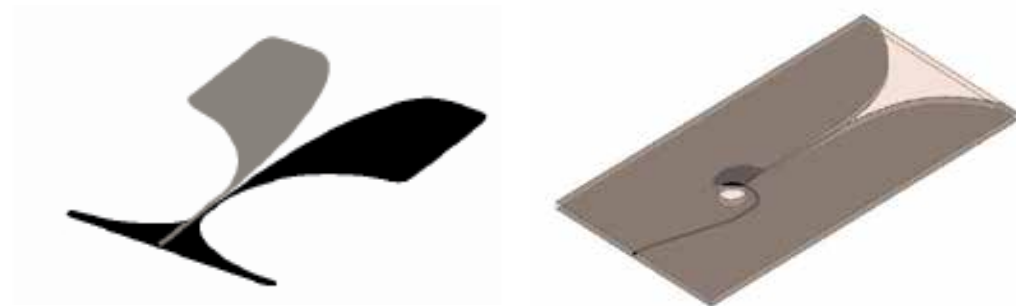
Fig. 6. (left) Antipodal Vivaldi antenna (Guillanton 1998), (right) Vivaldi with stripline feeder

3. Frequency independent antennas

From an ideal point of view the "perfect" UWB antenna covers instantaneously an infinite frequency band (the entire electromagnetic spectrum). The only class of antennas that theoretically can manage the infinite frequency spectrum is represented by "frequency independent antennas".

By definition a frequency independent antenna is a radiating element whose electromagnetic properties (like characteristic impedance, radiation pattern, directivity) are constant along frequency.

From a practical point of view also this kind of antenna operates over a finite band: the low-frequency limit is set by the maximum dimension, and the high-frequency limit is set by how precisely the input terminal region can be realised (Rumsey, 1966).

All the studies made on this topic established that there are some principles to follow when designing a frequency independent antenna:
1. The scalability principle
2. The truncation principle
3. The self complementarity principle

3.1 Scalability principle

This principle can be summarized as follows: an antenna can be defined as "scalable" if the current distribution on it does not change if antenna dimensions and operating wavelength change with the same ratio. In other words, decreasing the wavelength (increasing frequency), the model size decreases in the same proportion, and vice versa.

Through this principle we can assure that a geometric structure, invariant to scaling changes, will be a frequency independent antenna.

Structures that obey to this principle are called "auto-scaling" structures or continuously-scaled structures.

V.H. Rumsey in 1966 looked for these particular configurations with the possibility to spatially fix the feeding terminals in order to keep them locked during the scale changes. In this way, a scale change of the geometric structure corresponds to its rotation.

Putting these words in a mathematical language, we need to consider a polar coordinate system (r, θ, φ) and each structure within this system is identified by $r(\theta, \varphi)$.

The auto-scalability condition is expressed by the following expression:

$$K * r(\vartheta, \varphi) = r(\vartheta, \varphi + C) \qquad (2)$$

Where K is the scaling factor and C is the rotation angle.

This method leads to continuously scaled structures which satisfy the scalability principle. The equiangular spiral shape is a typical example of perfectly scaled structure (Dyson, 1959).

A second class of antenna shapes satisfies this principle only at *discrete frequency intervals*. Such antennas are called "quasi frequency independent" and include "log-periodic" structures (the scaling law is logarithmic). This class of radiating elements shows a certain ripple on electrical performances between the frequency points of scaling. Sinuous and log-periodic dipoles belong to this latter class.

A third class satisfies a different version of auto-scalability condition called "translation principle" that comes from a work by B. Stockbroeckx (Stockbroeckx , 2005). He tried to verify if the scalability principle could be satisfied also by structures not fully described by angles. In his work he looked for geometric shapes for which a scale variation does not imply a change in dimensions but a translation of the structure.

Considering a rectangular coordinate system, for generic 3D structure we can describe the width as a function of height and length: $x=x(y,z)$.

The auto-scalability condition can be expressed as follows:

$$K \cdot x(y, z) = x(y + C, z + D) \qquad (3)$$

and it is satisfied by all the structures that if scaled of a factor K, remain congruent to themselves translated of C respect to y and of D respect to z.

It has been demonstrated that a geometrical structure with an **exponential profile** results independent from a geometrical scaling. Thus an antenna with an exponential shape (i.e. Vivaldi antenna) will show a frequency independent behaviour.

3.2 Truncation principle

The discovery of structures invariant to changes in scale brings with it the assumption that these structures have infinite dimensions.

Obviously this assumption makes not feasible the realization of such structures.

Therefore, in order to obtain a realizable antenna, we need to truncate its geometry trying to maintain the same radiating and electric characteristics of the infinite structure.

So, following this approach, the radiating element has to satisfy the scalability principle and the truncation principle.

There is an implicit fact included into the truncation principle: going away from the excitation source up to the end of the antenna, the current flowing through the structure has to decay up to nullify itself just before the end of the antenna. In other words, the travelling wave needs to be attenuated after the radiating active region and before the end of the structure. This attenuation should preferably be due to the radiation phenomenon, in fact, in this way good efficiency and input impedance constant in frequency are assured.

This is a direct consequence of the fact that if the energy is mostly radiated, from a certain point of the structure, the presence or absence of conductor is irrelevant.

Concluding we can say that constant radiating properties are obtained only if the active-region dimension scale with wavelength and so, if the truncation effects are negligible, a finite part of the auto-scaling antenna could yield a very wide operating band.

For the biconical antenna the angles' principle is satisfied while the truncation one is not: the total current along the infinite structure does not decrease with the distance from the excitation point, so the truncation operation causes an important effect on radiating characteristics. This happens because any finite portion, however large, will show end-effects (like reflections from the ends) that produce variations of the radiation pattern. Therefore the bandwidth cannot be increased at will by increasing the size.

3.3 Self-complementarity principle

An additional characteristic that could be very helpful in the design of frequency independent antennas is the self-complementarity feature. In more details, the self-complementarity principle (Booker, 1946) affirms that for a planar self-complementary structure (i.e. a planar shape identical to its own planar complement except for a rotation or a mirroring) the input impedance is the real constant $\eta^2/4$, where η is the intrinsic impedance.

Then, it is clear that this principle could be satisfied also by non frequency independent shapes and that a frequency independent structure could not be a self complementary shape.

However the possibility to design a circuit that belongs to frequency independent antenna family and at same time satisfies the self complementarity principle is of great interest. In this way such radiator will have input impedance purely real and constant along the whole frequency band. Consequently, the design of the feeding system will certainly require lower effort respect to classic case of an UWB antenna with complex frequency dependent input impedance.

For this reason this useful principle is widely applied with spiral and sinuous radiating elements. However, in general, we need to keep in mind that self-complementary structures only guarantee constant input impedance, but not necessarily constant radiation characteristics.

4. Feeding systems for UWB antennas

Most of UWB antennas have a balanced topology, i.e. they need a balanced feeding structure to properly excite the fundamental radiating mode. The previously cited UWB antennas such as spiral, sinuous and Vivaldi belong to balanced radiating element class and thus they need differential feeding currents (i.e. equal in magnitude and with 180° differential phase) to radiate the fundamental mode.

Usually, to carry high-frequency signals, asymmetric guiding structures are commonly employed. Coaxial cables and microstrip lines are two examples of the so called unbalanced guiding structures. These structures present a strong asymmetry between the internal metallic conductor or strip and the reference conductor. Thus, from a physical point of view, the current densities are strongly different and then they are not in differential form.

Such unbalanced structures must be transformed in balanced ones to correctly feed balanced radiating elements. The two-wire transmission line or the broadside coupled stripline are examples of balanced, symmetric structures. The *bal - un* represents the hardware realization of such RF function (i.e. the transformation of a balanced structure into an unbalanced one and vice versa).

From a circuital point of view, the balun could be represented by the equivalent circuit shown in figure 7.
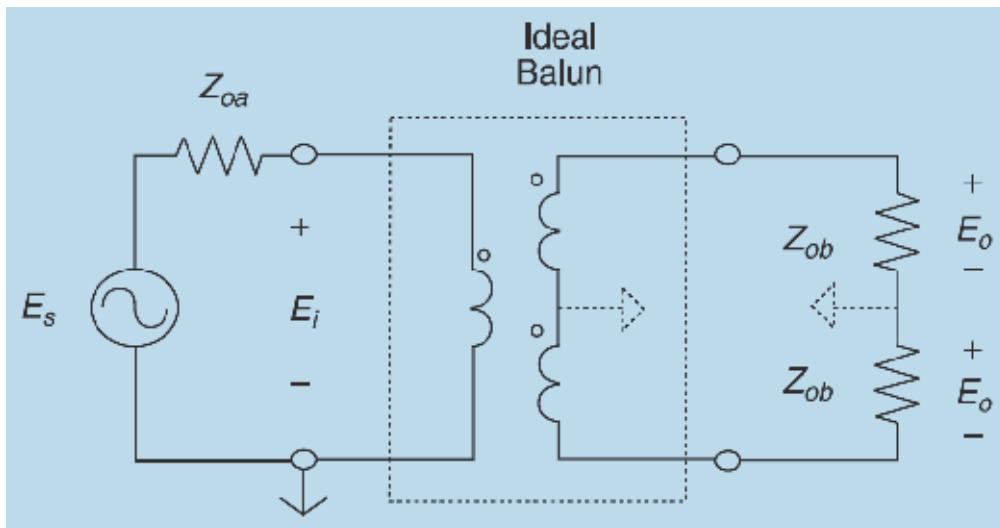
Fig. 7. Balun circuital model

Usually an additional function addressed to balun structure is to realize also an impedance transformation in order to match the input unbalanced impedance (commonly the coaxial 50 Ohm, in figure Zoa), to the input antenna impedance (2Zob).

In the following sub paragraph the mainly used multioctave baluns will be described.

4.1 Tapered balun

The tapered balun was introduced by Duncan and Minerva (Duncan & Minerva, 1960) and it is one of the most popular balun typology, widely employed in its coax version and microstrip version as shown in figure 8.
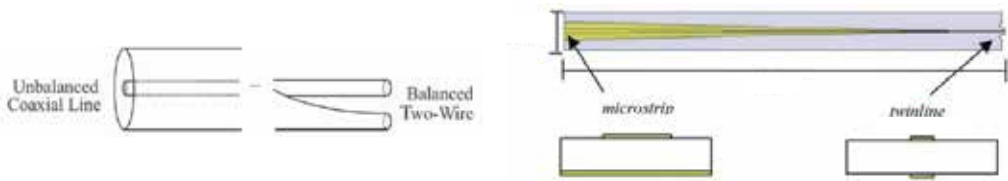
Fig. 8. Duncan and Minerva Balun; coaxial version (left) and microstrip version (right)

This kind of balun realizes its function by means of physical tapering of unbalanced structure (i.e. peeling of outer conductor for the coaxial and tapering of metallic ground of microstrip version). The shape and length of peeling and tapering affect respectively the Return Loss and the operating frequency band of such structure. The balun minimum operating frequency is strictly related to the total length of the transition i.e. $\lambda_{max}/4$.
Hereafter, in figure 9, a typical S-parameter response of the aforementioned balun is shown.
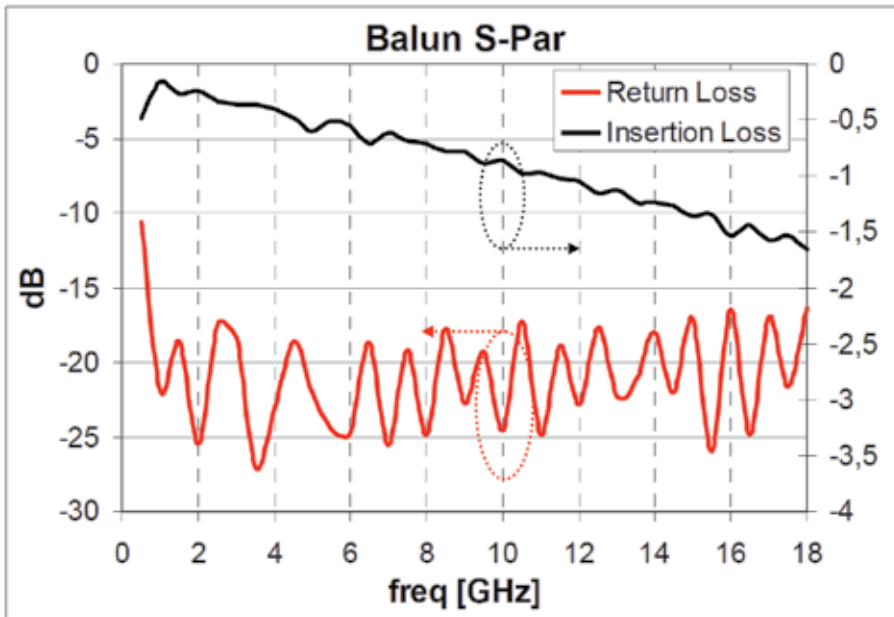
Fig. 9. Typical tapered balun S-par performances.

For the microstrip balun it is possible also to perform an impedance transformation by tapering both the ground reference and the microstrip trace.

4.2 Marchand balun: microstrip/stripline to slot line transitions

The Marchand balun (Marchand, 1944) is another typology of UWB balun. In figure 10 (left) such structure is shown in its coaxial configuration. The basic operating principle consists into force a differential signal across a gap on the outer conductor. By means of a proper length of central conductor open stub (i.e. $\lambda/4$ after the outer conductor cut) it is possible to force and collect the differential signals between the gaps ends.
Obviously such balun typology could be physically implemented also with printed technology such as microstrip and slot line.

In figure 10 (right), the microstrip line is ended with a wideband open termination (metallic fan) and the high frequency signal is enforced to flow along the slot realized into the reference metallic plate. Furthermore, the presence of UWB slot short circuit at one end of the slotline conveys the RF energy to flow only towards the other end.
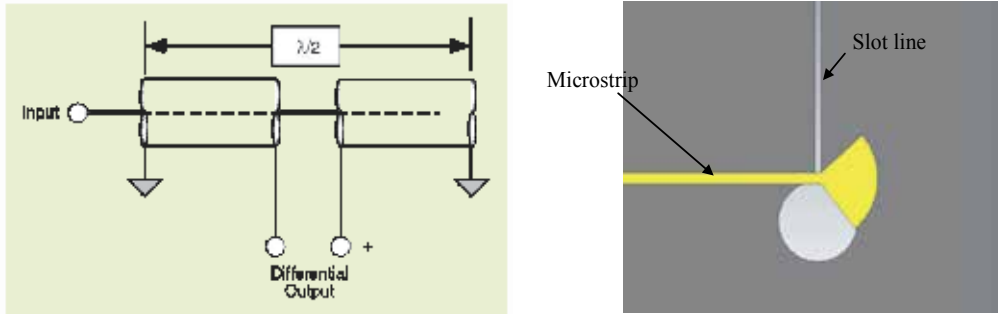
Fig. 10. (left) Marchand balun in coaxial configuration (right) UWB Marchand balun in printed circuit configuration

Due to its popularity, different versions of the above mentioned transition have been developed. For example the most commonly one used to properly feed a Vivaldi antenna is the stripline to double slot line transition (see figure 6 right). The difference respect to the previously described version regards the presence of a stripline instead of a microstrip and the balanced structure is realized with a double slot on the two external metallic plates of the stripline.
Such structure could be designed to operate over multi octave band. In the following figure 11 a 4-18 GHz stripline to double slot transition Return Loss is reported.
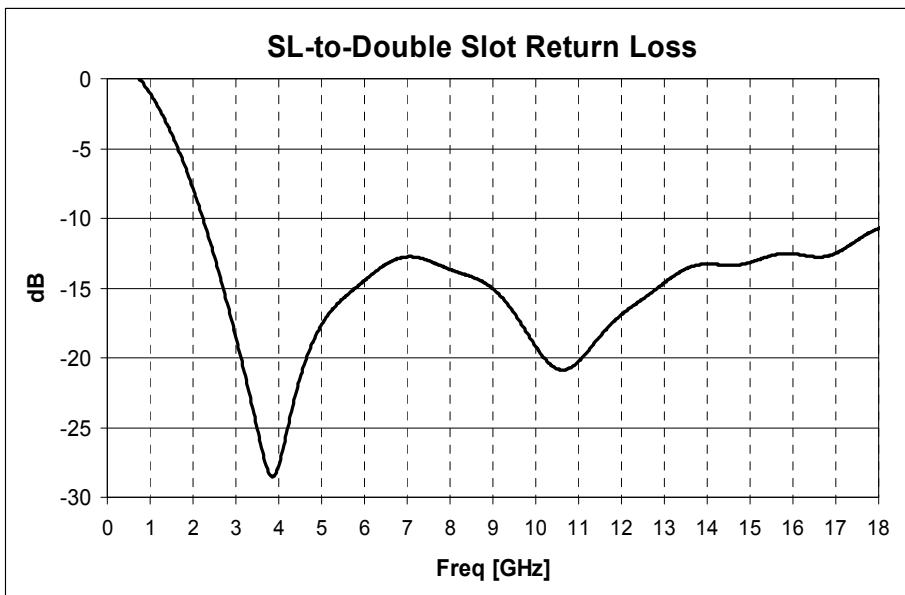
Fig. 11. StripLine to Double Slot line RL

4.3 Phelan Balun

The balun introduced by H. R. Phelan (Phelan, 1969) is a particular realization of generalized Marchand balun also called "parallel-connected balun". A parallel connected balun employs a two-wire or coaxial section of line in parallel with the balun junction to achieve a balanced output (see figure 12).
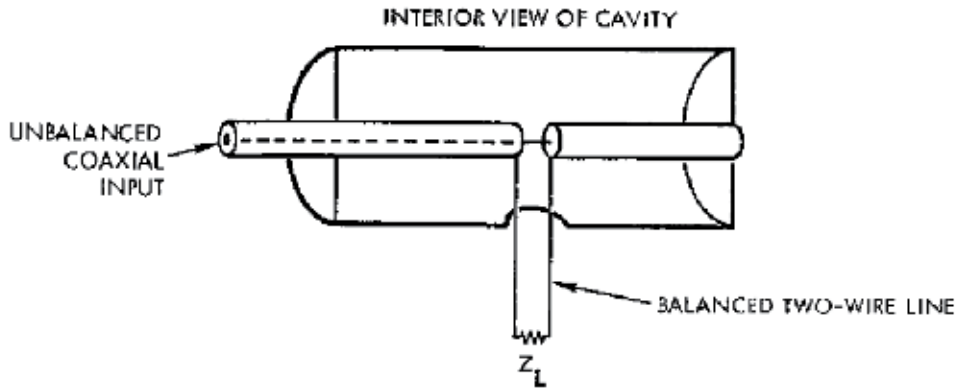
Fig. 12. Marchand balun

Here these structures will be referred to as resonant baluns due to the resonant line which is inherent to their operation. The proposed Phelan balun is depicted in figure 13.
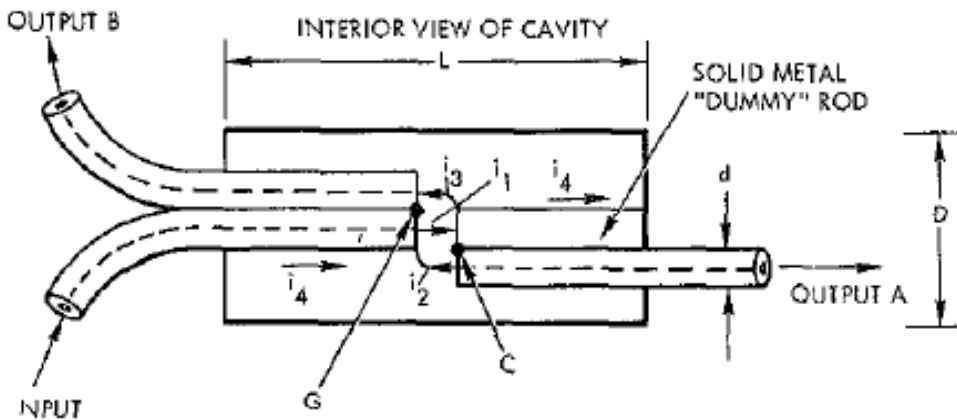
Fig. 13. Phelan balun

The central conductor of the coaxial input is connected to a solid "dummy" rod which maintains symmetry. The outer shield of output B is attached to the outer shield of the input cable, and the central conductor of output B is connected to the dummy rod. The outer shield of output A is soldered to the dummy rod and its central conductor is connected to the shield of the input cable. The balun junction is enclosed by a cavity which may be round or square. Note that this construction maintains symmetry both in the two ends of the cavity and at the feed point. In most applications, the outputs would be bent together to form a balanced double coaxial line.

With such kind of structure it is possible to cover a 25:1 frequency band. Hereafter a 3D cad of a realized balun and its simulated performances in terms of S-parameters are shown (figure 14 and figure 15).
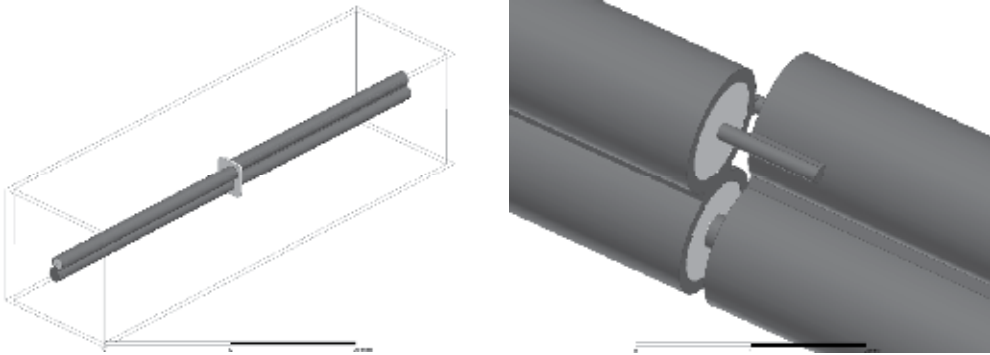
Fig. 14. 3D cad of realized balun
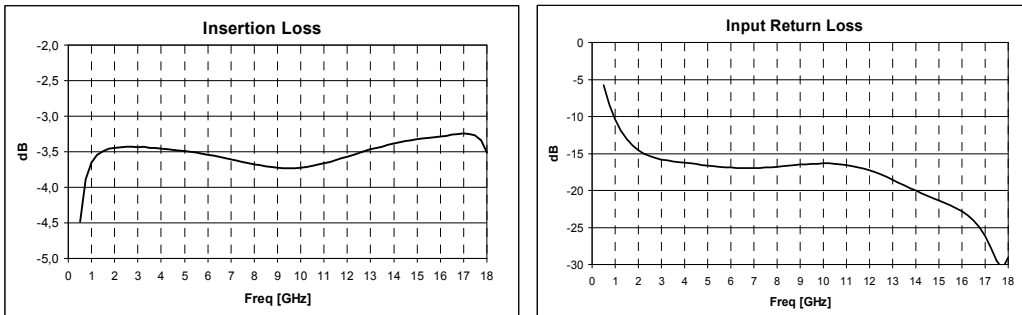
Fig. 15. Simulated Insertion Loss (left) and Return Loss (right) of the designed balun

Such structure is widely used to feed a four arms sinuous antenna as described in DuHamel patent (i.e. Sinuous antenna inventor).

5. Impulse response of UWB antennas

In UWB communications the RF systems perform voice and data transmission using digital pulses rather than employing a continuous wave carrier to convey information.
As a matter of fact another name for UWB wireless applications is "short-pulse radio" since the signalling pulses are of extremely short duration – often less than one nanosecond.
For this first reason the effect of the antenna on the transmitted pulse becomes a crucial issue, so a UWB antenna is required to achieve good time domain characteristics (Licul, et al., 2003).
On the other hand it is well known that the traditional approach to evaluate and design antennas is focused only on few basic parameters like gain, return loss, HPBW in the whole operating frequency band. This approach is meaningful and suitable for narrowband antennas because all these parameters can be considered and treated as constants over a few percent bandwidth (in fact for typical narrow band antennas these parameters show a very slight variation within their operating frequency band) (Schantz, 2004).

Since gain, return loss and HPBW generally vary with frequency, the previous assumption is obviously not more valid for UWB systems where a huge bandwidth is occupied (Licul, et al., 2003), therefore the frequency dependent characteristics of the antennas must be considered.

Bearing in mind these two main reasons we can state that there is a demand for both frequency-domain and time-domain representations of the antenna behaviour. Through this section we will focus on time-domain representation, underlining that it is extremely interlaced with frequency-domain one.

As a first consequence of the frequency dependent characteristics, an UWB antenna has to behave as a band-pass filter (over a very broad frequency spectrum) instead of a spot-filter as in narrow-band communications.

Since the antenna behaves like a band-pass filter, its effect is to reshape the spectra of the pulses (Ma & Jeng, 2005). This implies that the signal waveforms arriving at the receiver usually do not look like the waveforms of the source pulses at the transmitter. The antenna, hence, should be designed with care in order to avoid undesired distortions.

As a direct result, a good time domain performance, i.e. minimum pulse distortion in the received waveform, is a primary concern of a suitable UWB antenna (Licul, et al., 2003) because the signal is the carrier of useful information.

Furthermore, a UWB antenna should be a non-dispersive radiating element, having a fixed phase centre[2], in order to obtain a radiated waveform as identical as possible to the input one.

Indeed, even if an antenna shows a good gain over its operating band, it could be possible that its phase centre moves as a function of frequency or as a function of look angle; in this case the result would be an altered and dispersed radiated waveform (Schantz, 2004).

Two examples of dispersive antennas are the log-periodic antenna and the log conical spiral antenna. These radiating elements use their small-scale parts to receive high frequencies and their large-scale parts to receive the low frequency range. This behaviour causes a double effect: the received signal will have a temporal extent longer than the transmitted one and will show an appreciable chirp. The earlier part of the signal exhibits relatively high frequency content whilst the later part of the received signal exhibits relatively low frequency content. Also, since the phase centre moves, the temporal extent and chirp-like effect of the received signal will vary as a function of look angle (Schantz, 2003, 2004).

Besides it has been confirmed in a further study (Wiesbeck, 2009) that a non-distorted structure is characterized by linear phase in the whole operating frequency range that is a constant group delay τ_g:

$$\tau_g(\omega) = -\frac{d\varphi(\omega)}{d\omega} = -\frac{d\varphi(f)}{2\pi df} \qquad (4)$$

The nonlinearities of a group delay indicate the resonant behaviour of the device, which involves the ability of the structure to store the energy causing ringing and oscillations of the antenna impulse response.

Concluding we can stand that, for all these reasons, an UWB antenna:

---

[2] In antenna design theory, the phase centre is the point from which the electromagnetic radiation spreads spherically outward, with the phase of the signal being equal at any point on the sphere.

1. shall behave as a band-pass filter (instead of a spot-filter as in narrow-band systems)
2. shall not impact on the input signal shape
3. shall be a non-dispersive radiating element
4. shall show a fixed phase centre and a constant group delay.
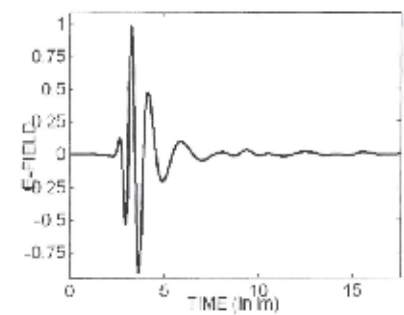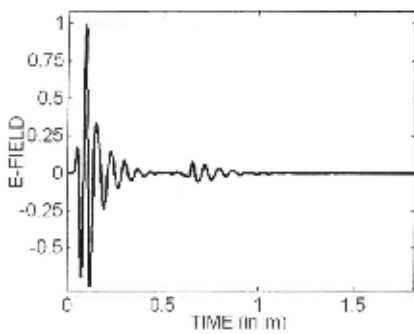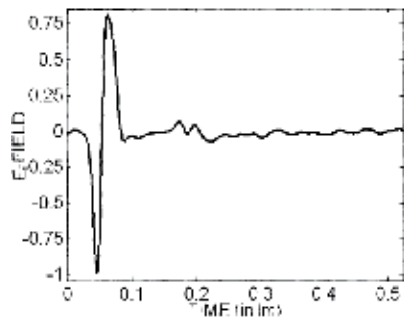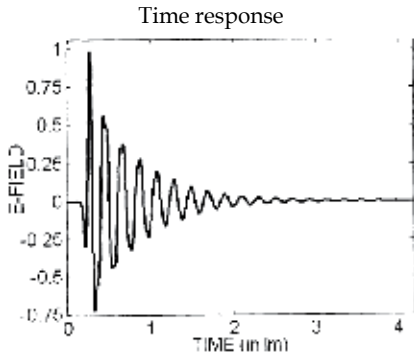
Time response   Antenna
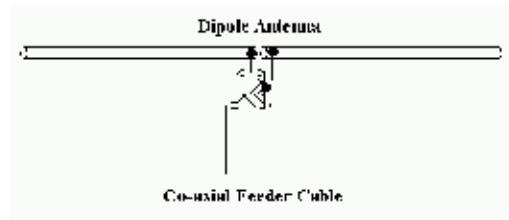
Dipole

spherically capped Biconical
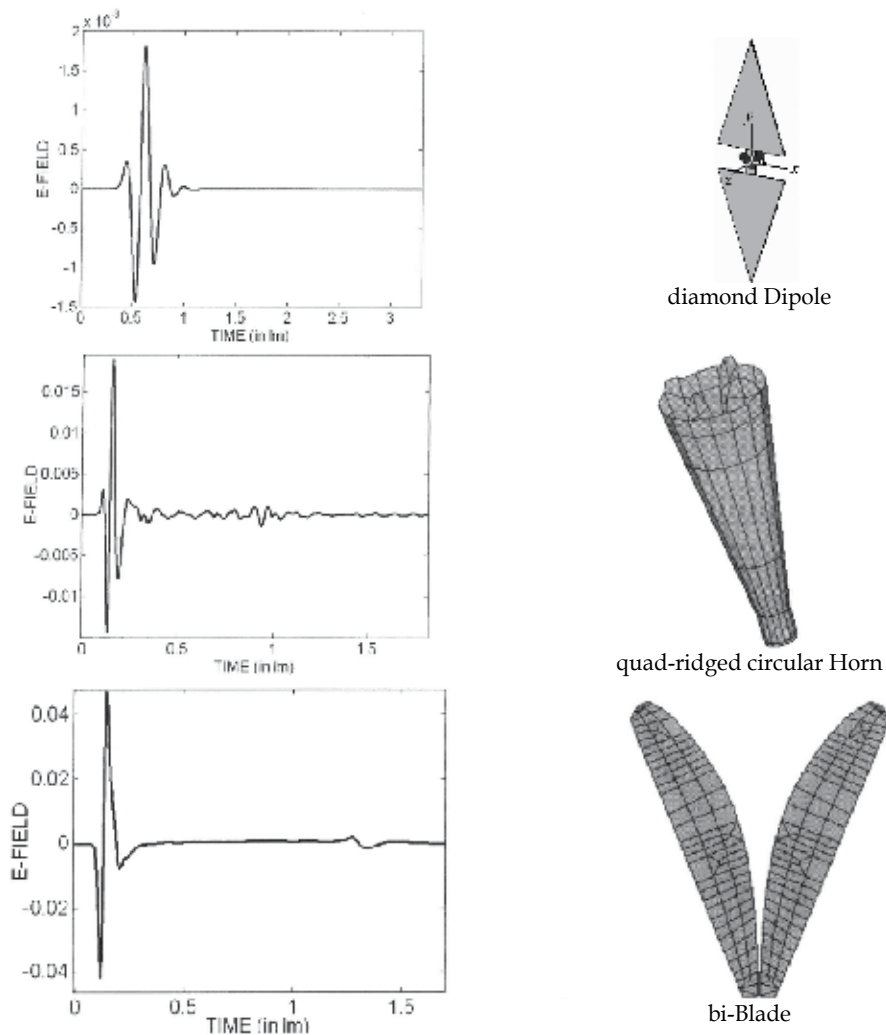

Log-periodic Dipole

equiangular Spiral

diamond Dipole

quad-ridged circular Horn

bi-Blade

Table 1. Time response of different antennas
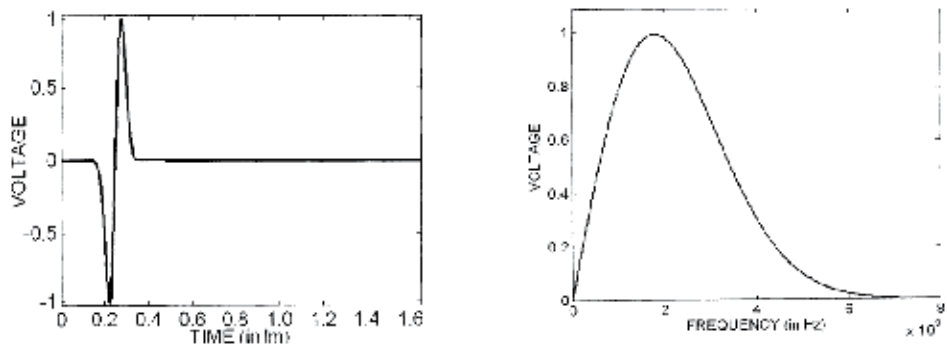
Fig. 16. Time behaviour and spectral content of the monocycle Gaussian pulse

In a very interesting article (Ghosh, 2006) the authors analyzed the transient response of several well-known UWB antennas, and in Table 1 we list some of those results.

Each antenna was fed by a monocycle Gaussian pulse and the unit of time was a light meter (lm), that is the time required by light to travel 1m ($1lm = c^{-1} = 3.333 \cdot 10^{-9} s$)

In figure 16, the time behaviour and the spectral content of the monocycle pulse are shown.

6. UWB phased array

When the requirements about antenna gain, radiation pattern control and ERP (Effective Radiated Power) are very demanding, it is not possible to choose a single element antenna strategy. In this case an array approach is mandatory. Furthermore, in order to achieve the array pattern control, the phase of the excitation signal of each single element must be independently controllable. This is the so-called "phased array antenna strategy".

If the operating bandwidth of the involved applications is extremely wide, UWB elements are needed for populating the selected array lattice. Clearly, depending on the application (i.e. communications, radars or EW), the antenna specifications could be extremely different. In this paragraph we will present the design of an UWB phased array suitable for EW applications.

In figure 17 the design flow chart of the adopted approach is shown. Obviously the first step consists in the definition of requirements (e.g. Operating Bandwidth, Gain, HPBW, Polarisation, mechanical constraints, etc...). Then the second phase concerns the element selection. For our design we have employed the AHP (Analytical Hierarchy Process) methodology to select the best antenna candidate (Saaty, 1980). Then a first optimization loop occurs in order to improve the single radiating element performances in free space. In the following step the optimized element is merged in the selected array lattice and simulated in infinite array structure. This latter approach allows us to reduce the simulation time and memory requirements exploiting the so called *unit cell* strategy (Pantano, et al., 2007). The unit cell consists in the single element of the array with suitable

 periodic boundary conditions that replicate an infinite array structure. Obviously such approach does not take into account edge and corner effects and will be meaningful for "electrically" small array. Due to mutual coupling phenomena, the antenna performances change. Therefore, a second optimization loop is needed to take into account the presence of surrounding elements. At the last point, depending on time and HW resources, the analysis of the finite array is performed and the truncation and corner effects are then considered.

Hereafter, the UWB double polarised planar phased array (DPPPA) design specifications are listed:

- Operating Bandwidth 4-18GHz (goal 2-18 GHz)
- Required scan angle ± 60° in both Azimuth and Elevation plane;
- Typical radiating element HPBW 90° in both E and H plane;
- VSWR less than 2.5:1 in the frequency band;
- Grating lobes free @ 10.5 GHz;
- Double linear polarisation;

Two different radiating elements have been selected: the Vivaldi notch element, fed by strip-line, and the four arms Sinuous element, fed by ultra wide band double printed balun.

According to the aforementioned design-flow chart, the design of the DPPPA has been divided into two phases:
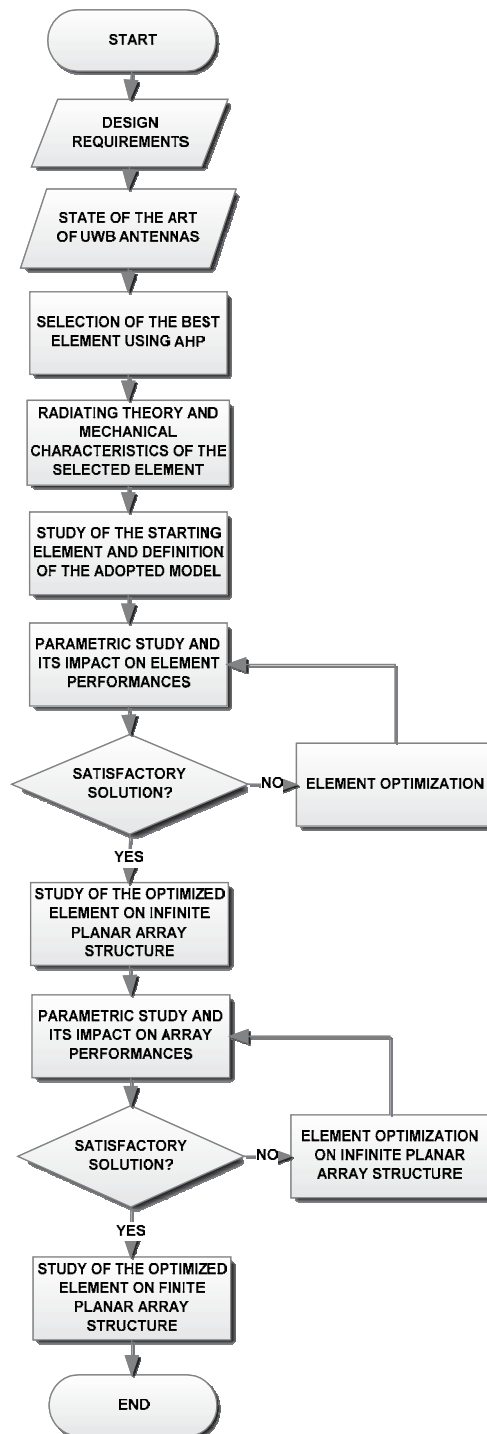
Fig. 17. Design flow chart

1. the design and optimisation of the "isolated" element starting from the array specifications;
2. a further step of optimisation considering the "isolated" optimum element in infinite array configuration.

6.1 Vivaldi DPPPA

Starting from the grating lobes free requirements, the selected array lattice is a regular square grid with 14.28 mm side (i.e. $\lambda_0/2$ @ 10.5GHz). Consequently, the area dedicated to each single element is 14.28 mm x 14.28 mm.

In addition, due to the double linear polarization requirements each single array element consists of two orthogonal Vivaldi antennas as depicted in figure 18. The selected Vivaldi structure has been shown in figure 6 right (i.e. double Vivaldi with stripline feed).
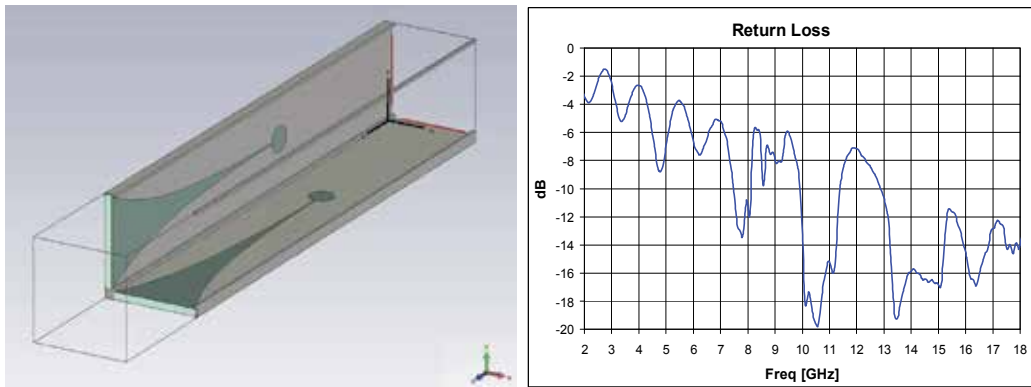
Fig. 18. Array double circuit model and free space simulated Return Loss

It is noteworthy that in this way the two polarizations phase centre are not coincident and their different location could be a disadvantage when a circular or slant 45° polarisation must be realized.

According to the aforementioned design flow, the single Vivaldi couple has been optimised in free space and then merged in the selected lattice to populate an infinite array.

In the following figures the simulation results after the infinite array optimisation loop are reported. In particular, in figure 19 the 2D contour-plots of active Return Loss vs. Azimuth and Elevation scan angle are respectively shown.

The active reflection coefficient is defined as the reflection seen in the antenna elements when all elements are transmitting (active). If the antenna aperture scattering matrix is denoted [S], the active reflections coefficients Γ_i are then defined as

$$\begin{bmatrix} \Gamma_1 \\ \Gamma_2 \\ ... \\ \Gamma_N \end{bmatrix} = \begin{bmatrix} S_{11} & S_{12} & ... & S_{1N} \\ S_{21} & S_{22} & ... & ... \\ ... & ... & ... & ... \\ S_{N1} & ... & ... & S_{NN} \end{bmatrix} \cdot \begin{bmatrix} e^{j\psi 1} \\ e^{j\psi 2} \\ ... \\ e^{j\psi N} \end{bmatrix} \tag{5}$$

where N is the number of antenna elements and Ψ_i is a scan dependent phase angle.

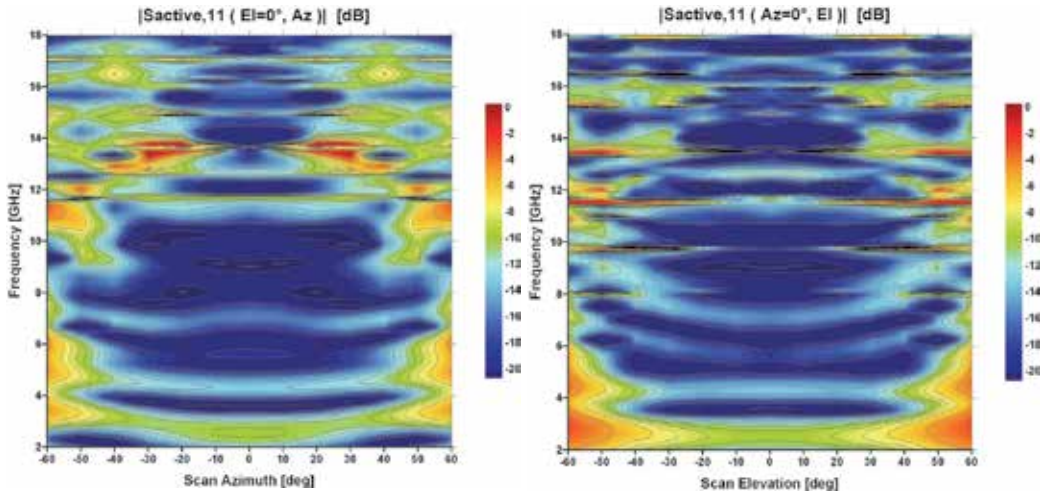From the shown results, two main characteristics could be highlighted:

Fig. 19. (left) Active Return Loss @ Az-Plane when El = 0° (right) Active Return Loss @ El-Plane when Az = 0°

- Due to the small single element dedicated area it is impossible to avoid mutual coupling between surrounding elements. Then the adopted strategy during the optimisation phase has been to exploit mutual coupling phenomena in order to properly "load" the electrically small single element (especially in the lower part of the operating frequency band). The trick consists into short circuit the metallic edges of all Vivaldi elements to avoid discontinuities for the radiating currents (Chio & Schaubert, 2000).
- From figure 19 it could be seen that at 13.5 GHz at steering point Az = 25° and El = 0° an active return loss of about 0 dB is revealed. It is than obvious that for the infinite array structure it represents the so called "blind spot". Different strategy could be adopted to mitigate such undesired phenomena (Ellgardt, 2008).

In figure 20 left, the layout of the finite 8x8 sub-array antenna model is depicted.
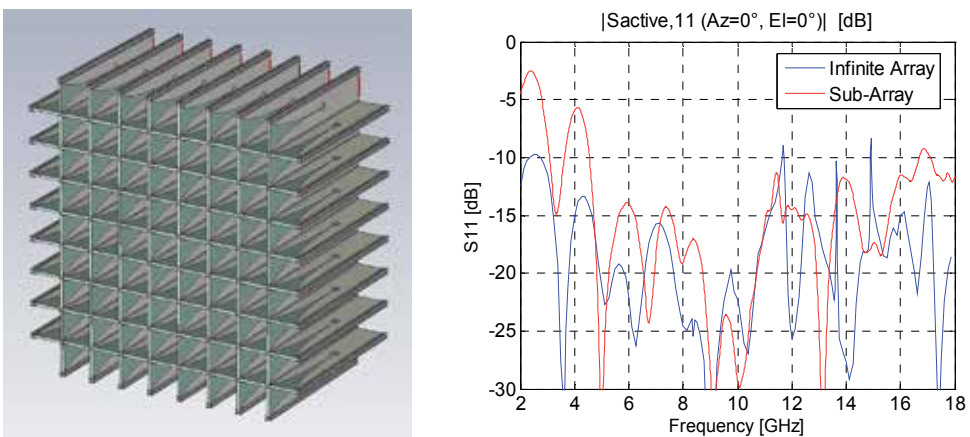
Fig. 20. (left) Sub-array model for double circuit with metallic post (right) return loss comparison between finite and infinite array model

In figure 20 right, the comparison of active Return Loss at boresight between 'Infinite' Array and 'Finite' Sub-Array simulation model is shown.

The main differences are due to the limited sub array size dimensions (impact on the e.m. performances at lower frequency) and geometrical mesh (impact on the e.m. performances at higher frequency) of the simulated models.

As last step, a small 8x8 sub array has been realised and fully characterised by means of a new spherical near field test range (i.e. Starlab by Satimo). In figure 21 left, the realised sub-array is shown. Each single Vivaldi couple is connected to surrounding elements by means of metallic rods.
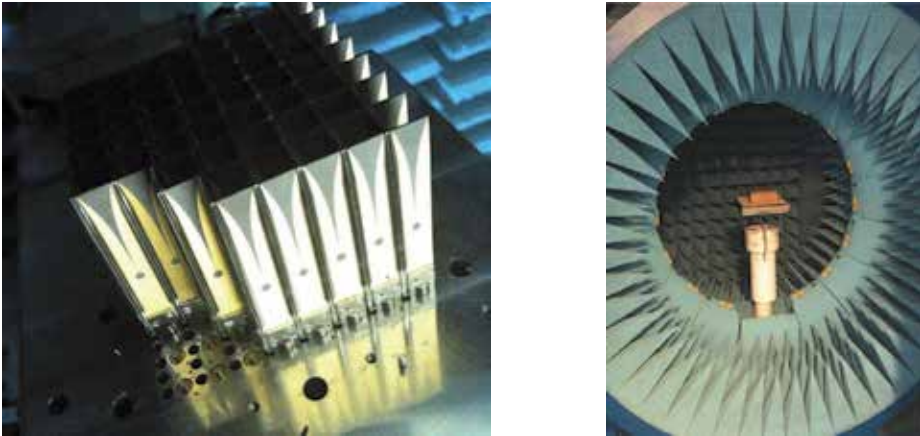
Fig. 21. (left) realized sub array, (right) sub array in the test range

Hereafter in figure 22 the calculated sub array active return loss, from reflection coefficients measures, is presented. From the reported results it is clear that:

- in the low part of operating frequency band, very high RL level have been measured according to finite array simulations due to sub-array electrically small size;
- the presence of blind spot has been confirmed although its level is lower because the array is finite.
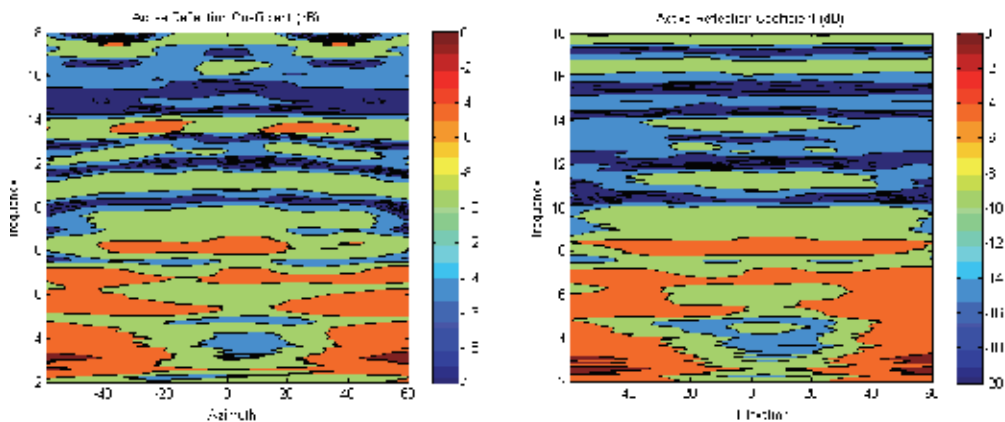

Fig. 22. (left) calculated active Return Loss @ Az-Plane when El = 0° (right) calculated active Return Loss @ El-Plane when Az = 0°
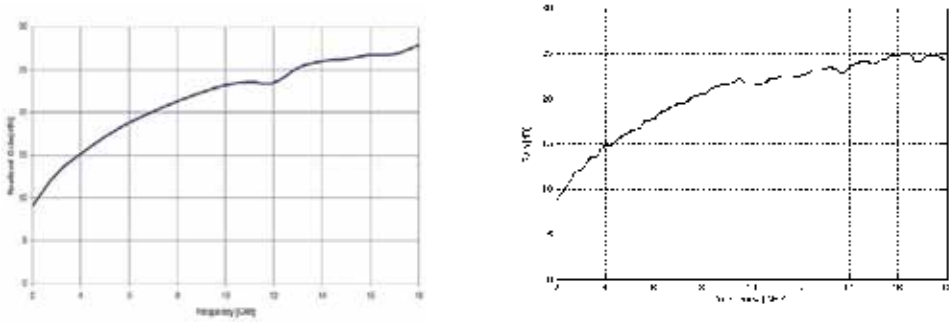
Fig. 23. (left) simulated Sub-Array boresight gain (right) measured Sub-Array boresight gain
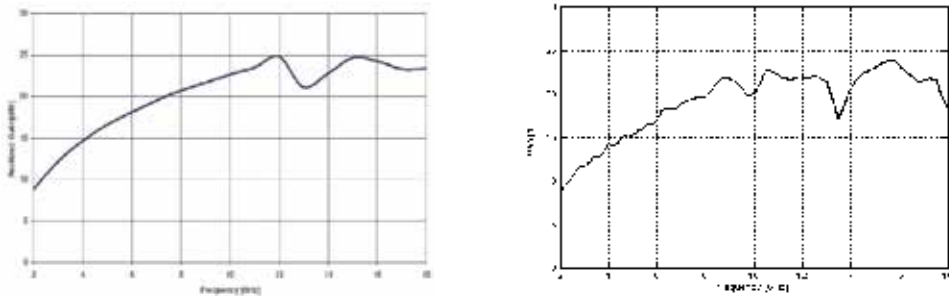

Fig. 24. (left) simulated Sub-Array gain for azimuth beam steering of +25° (right) measured Sub-Array gain for azimuth beam steering of +25°
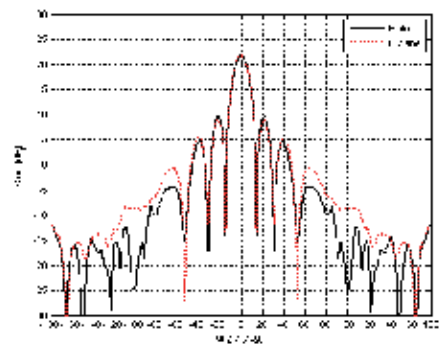
In the previous figures the simulated and measured Far Field array performances at different steering point are shown. The figure 23 shows the gain at boresight, while the figure 24 shows the measured gain when the array steering point is 25° in the azimuth plane for elevation 0°.

As it is possible to see, there is a good agreement between simulated and measured values.

In figure 24 it is also noticeable that a gain drop occurs in correspondence of 13.5 GHz and 25° azimuth scan angle. Such behavior is in agreement with previous blind spot analysis. Indeed, if we go back to figure 19 and figure 22, we can retrieve that at the same frequency and scan angle the presence of a blind spot was detected.
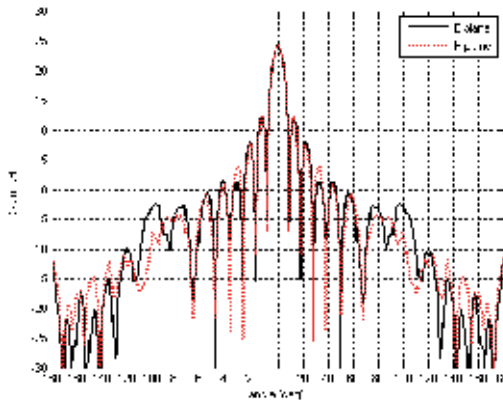
The following figure 25, figure 26 and figure 27, show the results of some measured pattern cuts at different frequencies and beam steering.
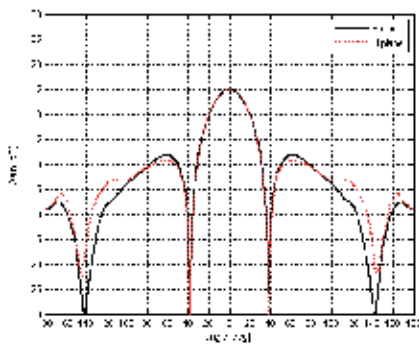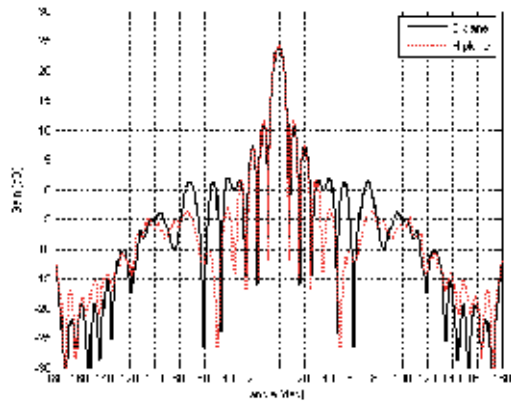

Sub-Array pattern @ 4 GHz   Sub-Array pattern @ 10 GHz
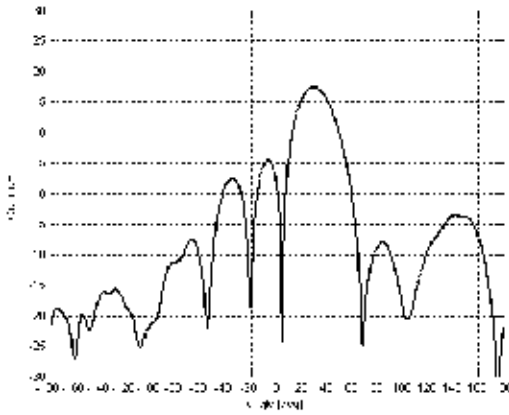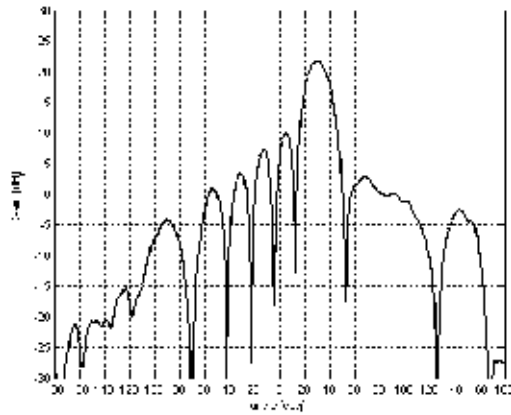
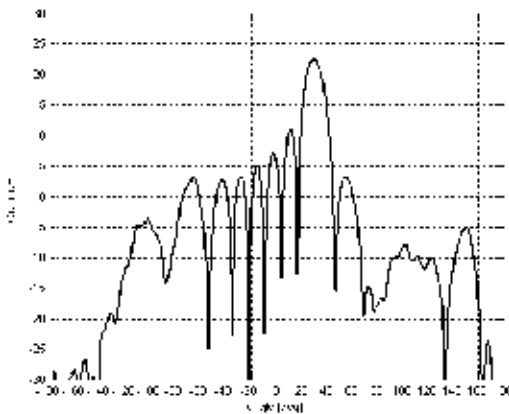Sub-Array pattern @ 17 GHz   Sub-Array pattern @ 18 GHz

Fig. 25. Boresight Sub-Array patterns
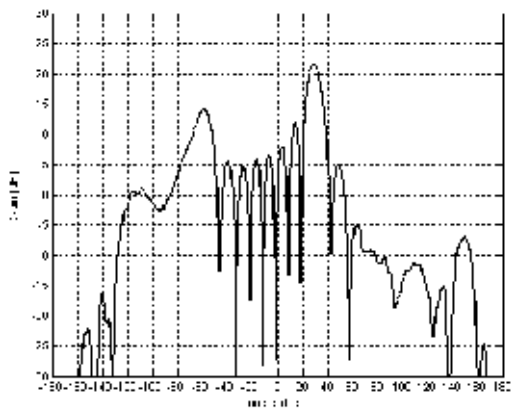

Sub-Array pattern @ 6 GHz scan 30°   Sub-Array pattern @ 9 GHz scan 30°
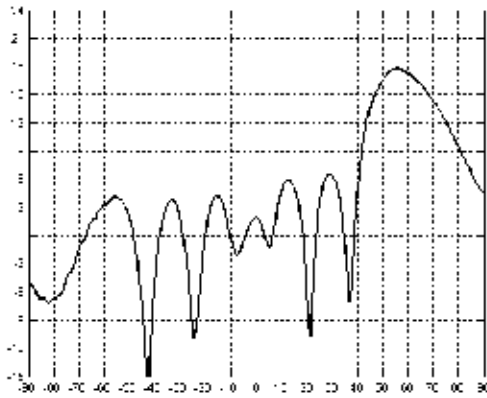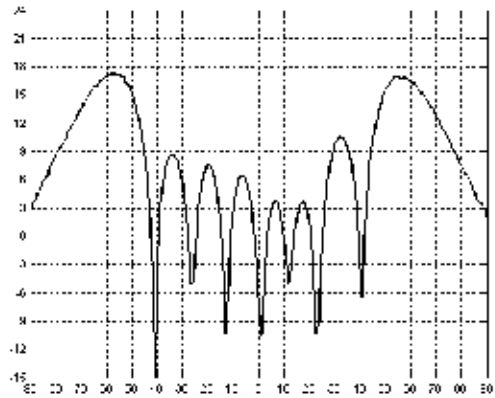

Sub-Array pattern @ 12 GHz scan 30°   Sub-Array pattern @ 15 GHz scan 30°

Fig. 26. 30° beam steering Sub-Array patterns (azimuth cut @ elevation 0°)

Sub-Array pattern @ 10 GHz scan 60°   Sub-Array pattern @ 12 GHz scan 60°

Fig. 27. 60° beam steering Sub-Array pattern (azimuth cut @ elevation 0°)
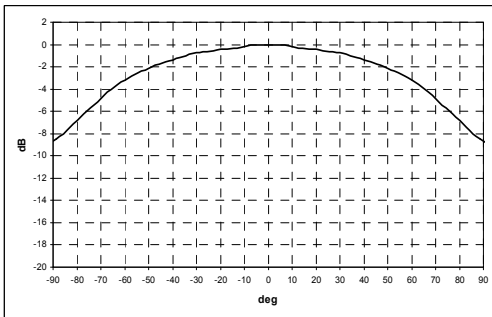
average element pattern @ 6 GHz   average element pattern @ 10 GHz
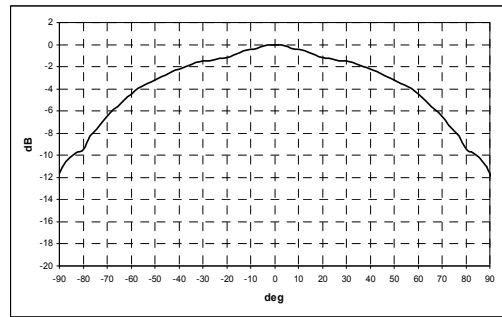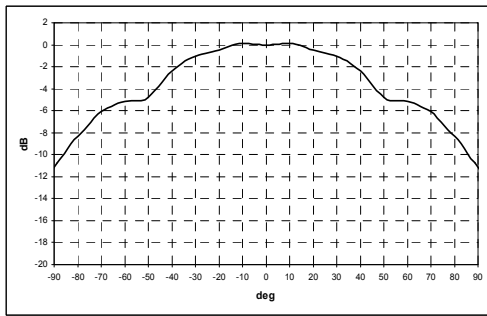
average element pattern @ 12 GHz   average element pattern @ 15 GHz
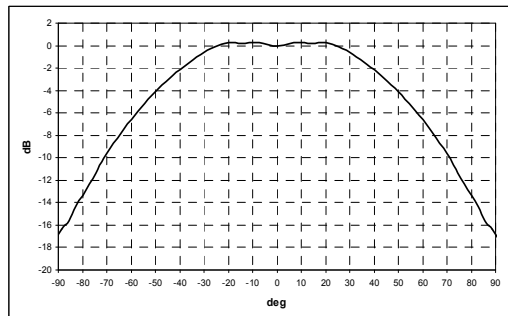
Fig. 28. Sub-Array element, average pattern

Starting from the selected array lattice (14.28mm x 14.28mm) it is interesting to point out that for 60° scan angle no grating lobe arises up to 10GHz as confirmed in figure 27 left. Conversely in figure 27 right, where the azimuth cut of Sub-Array pattern @ 12 GHz is shown, it is possible to see the presence of grating lobe.

In figure 28 the average patterns of Sub-Array element are shown. These values have been calculated by measuring and averaging the element's patterns in the array structure. In this

figure the patterns are normalized to the boresight value and represent the "so-called" element factor of the array that represents its scanning losses.

6.2 Sinuous DPPPA

The second UWB element selected to populate the array grid is a double polarised sinuous antenna (DuHamel, 1987). This element is a broad-side radiator (the Vivaldi is an end fire antenna) and it is an "intrinsic" double polarised element, i.e. the two polarisation arms lay on the same area and have an identical position of the phase centre.

The design of this element followed the same procedure described for the DPPPA Vivaldi case.

Due to the small electrical area dedicated to each single element the main problem with sinuous antenna consists in its minimum operating frequency. From theoretical point of view, for a sinuous antenna physical area and effective area are strictly related. It is simple to realize that for such radiating structure a pitch of 14.28 x 14.28 mm is a very small area to efficiently radiate in the 2-6 GHz band.

In order to extend the minimum operating frequency down to 4 GHz (as requested in specs), two tricks have been exploited:

1. the selection of a higher permittivity (ε_r) dielectric substrate. It is noteworthy that if we increase the ε_r indiscriminately the feeding structure becomes "electrically too large" in order to correctly operate at higher frequencies (Thus a good trade off for this design is an ε_r=6.15)

2. the meandering of the sinuous antenna shape. In figure 29 an example of sinuous shape respectively without and with meandering of its arms is shown.
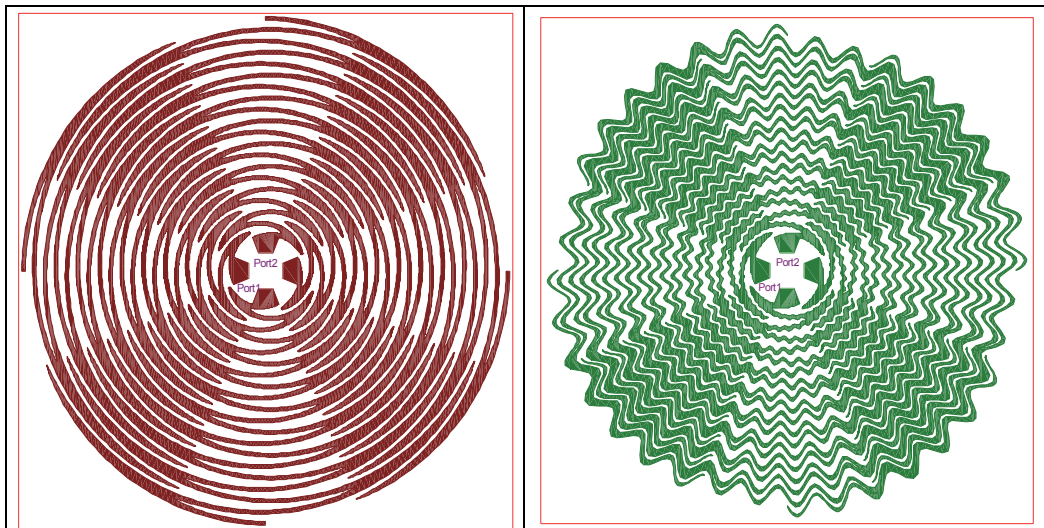
Fig. 29. (left) classic sinuous shape with linear growing rate τ (right) sinuous shape with meandering (informally called zigzag sinuous)

Regarding the meandering strategy, in figure 30 the RL comparison between sinuous without and with meandering with a fixed outer diameter is shown. It is clear that for the zigzag sinuous, the minimum operative frequency (fmin with RL = -10dB) is about 30% lower than the case of classic sinuous shape.
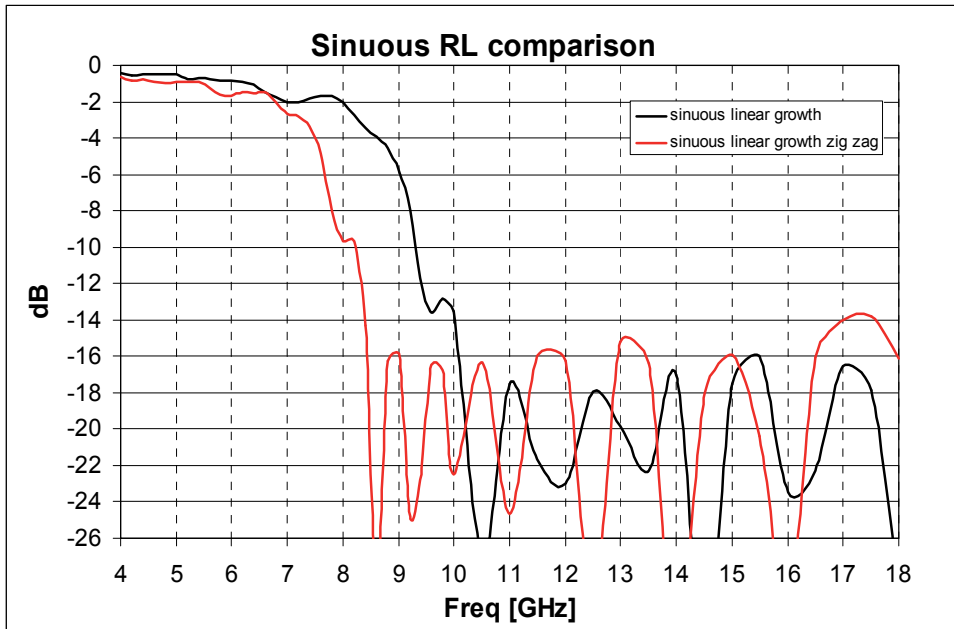
Fig. 30. RL comparison between normal and zigzag sinuous with fixed outer radius

Furthermore, from figure 30 it is also possible to see that inside the operating band the RL peaks are higher than for the normal case. Thus, it is important to be careful when using these techniques because the higher the meandering amplitude, the higher the RL peak values.
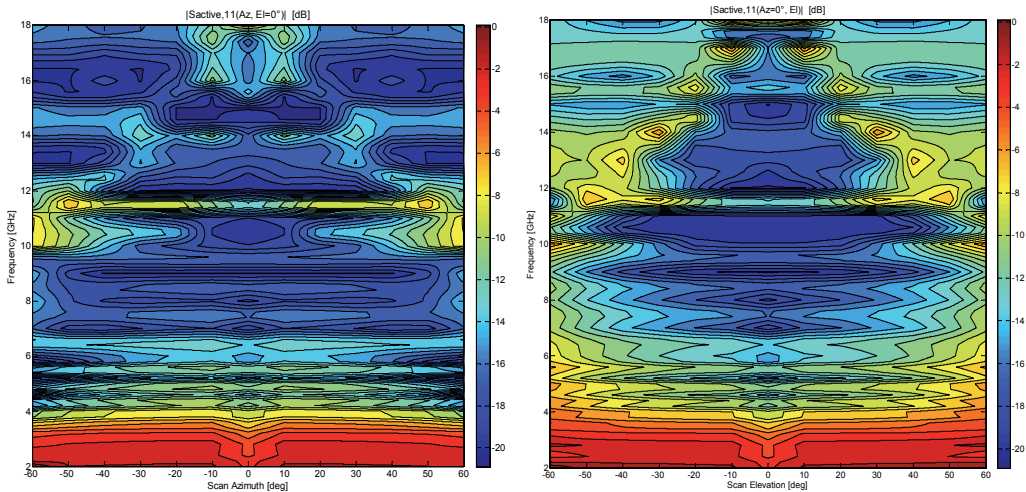
Fig. 31. (left) calculated active Return Loss @ Az-Plane when El = 0° (right) calculated active Return Loss @ El-Plane when Az = 0°

In figure 31 the 2D contour-plots of active Return Loss vs. Azimuth and Elevation scan angle are respectively shown.

In conclusion the developed solution fits the design requirements similarly to Vivaldi case. The further benefit consists in the absence of blind spot phenomenon in the spatial coverage.

6.3 Conclusions

The two designs have demonstrated that the proposed array design flow is successful. Vivaldi and Sinuous elements are good choices for populating UWB antenna phased array.

A key point for UWB array design is the mutual coupling phenomenon. Indeed, due to the small electrical distance among the array elements it is impossible to neglect this aspect. Thus, the winning strategy consists into exploit the mutual coupling in order to fit the electromagnetic UWB requirements especially for the low part of the frequency band.

The next step will be the design of an array that covers several octaves without the presence of grating lobes.

These presented elements are suitable for multifunction systems applications i.e., a single aperture that can manage communication, radar and EW functionalities.

7. References

Adamy, D. *A first course in Electronic warfare*, Artech House

Brillouin, L.N. (November 1948). Broad Band Antenna. U.S. Patent 2,454,766

Carter, P.S. (October 1939). *Short Wave Antenna.* U.S. Patent 2,175,252

Booker, H. G. (1946). Slot aerials and their relation to complementary wire aerials (Babinet's principle). *J. Inst. Elect. Eng., pp. 620–627*

Carter, P.S. (December 1939). *Wide Band, Short Wave Antenna and Transmission Line System.* U.S. Patent 2,181,870

Chio, T.H., Schaubert, D.H. (June 2000). Parameter Study and Design of Wide-Band Widescan Dual-Polarized Tapered Slot Antenna Arrays. *IEEE Transaction on Antennas and Propagation, Vol. 48, No. 6, pp 879-886*

Choi Seok, H., et al. (2004). A new Ultra-Wideband Antenna for UWB Applications. *Microwave and Optical Technology Letters, Vol. 40, pp. 399-401*

DuHamel, R.H. (April 1987). *Dual Polarized Sinuous Antennas*. U.S. Patent 4,658,262

Duncan, J. W. & Minerva, V. P. (1960). 100:1Bandwidth balun transformer. *Proc. IRE, vol. 48, pp. 156-164*

Dyson, J. D. (April 1959). The Equiangular Spiral Antenna. *IRE Transaction on Antennas Propagation, Vol. AP-7, pp. 181-187*

Ellgardt, A. (September 2008). A Scan Blindness Model for Single-Polarized Tapered-Slot Arrays in Triangular Grids. *IEEE Transaction on Antennas and Propagation, Vol. 56, No. 9, pp 2937-2942*

Gibson, P.J. (June 1979). The Vivaldi Aerial. *Proc.9th European Microwave Conference, UK, pp.101-105*

Ghosh, D., et al. (October 2006). Transmission and Reception by Ultra-Wideband (UWB) Antennas. *IEEE Antennas and Propagation Magazine, Vol. 48, No. 5, pp. 67-99*

Guillanton, E., et al. (1998). A new design tapered slot antenna for ultra-wideband applications. *Microwave and Optical Technology Letters Vol. 19., pp. 286-289*

Kim, Y., Kwon D.H. (April 2004). CPW-fed planar ultra wideband antenna having a frequency band notch function. *Electronics Letters Vol. 40 No. 7, pp. 403 - 405*

Liang, J., et al. (September 2004). Printed circular disc monopole antenna for ultra-wideband applications. *Electronics Letters, Vol. 40 No. 20. 30, pp. 1246 – 1247*

Licul, S., et al. (October 2003). A parametric study of time-domain characteristics of possible UWB antenna architectures. *IEEE 58th Vehicular Technology Conference, VTC 2003-Fall, vol. 5, pp. 3110-3114*

Lindenblad, N.E., el al. (April 1939). RCA Review

Lindenblad, N.E. (April 1941). *Wide Band Antenna.* U.S. Patent 2,239,724

Lodge, O. (August 1898). *Electric Telegraphy.* U.S. Patent 609,154

Lui, W.J., et al. (March 2005). Frequency notched ultra-wideband microstrip slot antenna with fractal tuning stub. *Electronics Letters, Vol. 41 No. 6, 17 March 2005, pp. 9 – 10*

Ma, T.G. & Jeng S.K. (Mrch 2005). Planar Miniature Tapered-Slot-Fed Annular Slot Antennas for Ultrawide-Band Radios. *IEEE Transactions on Antennas and Propagation, vol.53, no.3, pp. 1194-12021*

Manna, A., et al. (July 2008). Design, Simulation and Measure of Broadband Cavity Backed Combined Spiral Antenna. *Int Journal of Microwave and Optical Tech (IJMOT), vol. 3, No. 3, pp. 311-317*

Marchand, N. (December 1944). Transmission line conversion transformers. *Electronics, vol. 17, pp. 142–145*

McFadden, M., Scott, W. R. Jr (November 2007). Analysis of the Equiangular Spiral Antenna on a Dielectric Substrate. I*EEE Trans. Antennas and Propag., vol. AP-55, pp. 3163-3171*

Milligan, T.A. (2005). *Modern Antenna Design.* John Wiley & Sons, Inc, Second Edition.

Misra, V.C. (March 2009). Recent Trends in Antennas for Electronic Warfare Applications. *DRDO Science Spectrum, pp. 114-119*

Pantano, A., et al. (December, 2007). Optimization of a UWB Vivaldi antenna array and measurements with a near field Starlab system and farfield anechoic chamber. *11th International Symposium on Microwave and Optical Technology*

Phelan, H.R. (May 1970). A Wide-Band Parallel-Connected Balun. *IEEE Transaction on Microwave Theory and Techniques, vol. MTT-18, no. 5, pp. 259-263*

Rumsey, V. H. (1966). *Frequency Independent Antennas.* Academic Press, New York

Saaty, T.L. (1980). *The Analytic Hierarchy Process: Planning, Priority Setting, Resource Allocation.* McGraw-Hill, New York

Schantz, H.G., Barnes M. (July 2001). The COTAB UWB Magnetic Slot Antenna. IEEE APS

Schantz, H.G. (2003). Introduction to ultra-wideband antennas. *IEEE Conference on Ultra Wideband Systems and Technologies, pp. 1-9*

Schantz, H.G. (2004). Dispersion and UWB Antennas. *Proc. Conf. Ultrawideband Systems and Technologies, pp. 161-165*

Stockbroeckx, B. (1998). Space wave and surface wave radiation in the Vivaldi Antenna. *Ph. D. dissertation, Catholic University of Louvain., Louvain-la Neuve*

Wiesbeck, W., et al. (February 2009). Basic Properties and Design Principles of UWB Antennas. *Proceedings of the IEEE | Vol. 97,No. 2, pp. 372-385*

Ying, C., Zhang, Y.P. (May 2004). Integration of ultra-wideband slot antenna on LTCC substrate. *Electronics Letters, Vol. 40, No. 11, 27, pp. 645 – 646*

Reconfigurable Antennas of Wide Tuning Ranges and Controllable Selectivity Using Matching Networks

Chin-Lung Yang and Chieh-Sen Li

Department of Electrical Engineering, National Cheng Kung University
Taiwan

1. Introduction

In this chapter, a novel design method was proposed for reconfigurable antennas, independent of the geometries and the dimensions of the antennas, providing wide tuning ranges and controllable selectivity. A simple, unspecified S-UWB antenna can be attached to a feeding network to form one integrated selective and reconfigurable antenna. Through the design of tunable wideband matching network, a simple modified ultra-wide band (UWB) antenna can be reconfigurable and re-operated in different bands over a wide of ranges. Based on UWB antennas with proper T- or π-shaped matching network designed in frequency domain, the receiving antennas can be switched to specific bands or even multiple bands continuously. Most of the multiband antennas need complicated approaches to control bandwidths and lack of tuning flexibility. However, the design principles and the controlling mechanism based on microwave circuit theorems are relatively simple, so different fractional bandwidths from 5% to 20% can be feasibly implemented in our proposed architecture. Therefore, the parameters for the antenna operation bands and bandwidths can be calculated and estimated in a straight forward manner.

The L-, T- and π-network are chosen for examples to demonstrate the performance in simulation and in implementation. The simulation results show that the proposed antenna can cover from 1.8 GHz to 11.5 GHz with bandwidth ~300 MHz. Replacing the L- type with a T-type or π-type network which gives one more variable freedom to achieve high selective reconfigurable antenna of 80 MHz bandwidth. By utilizing special designed tuning inductors, the antenna bandwidth can be further controllable. The simulation results show that this proposed antenna can switch to 1.8, 2.45, and 3.5 GHz with bandwidths from 80 to 400 MHz.

The proposed antenna architecture provides a reconfigurable RF front end for transmission and reception. Such high flexibility can enable antennas to operate in varying environments for biomedical applications and different bands and thereby, make antennas applicable to wireless body area network (WBAN) as well as multi-mode/multi-band commercial applications. The novel circuitry antenna (modified UWB antenna combining with feed matching components) approach expands the flexibility and the bandwidth for multiband communication systems in a simple implementation.

Reconfigurable multi-band antennas have drawn attentions for modern heterogeneous communication systems, such as antennas for quad-band cellphones, Software-defined

radio (SDR), and Cognitive Radio (CR) which even requires antennas to cover multiple bands or operate at flexible frequency ranges. New technologies, such as micro-electromechanical systems (MEMS), expand the reconfigurable design varieties [Weedon 1999]. In this chapter, a novel concept of 'impedance matching in frequency domain' (as Figure 1) is proposed to make the design of reconfigurable antenna straight forward and can be implemented in low cost, simple circuits. This method is different from other methods based on the geometric modification which is developed to induce multiple resonant radiating frequencies. For example, the tri-band antenna in constructed based on a patch antenna design [Guo 2008][Sheta 2008] which peels off some slots or connect some discrete patches to create other effective current path and enable higher/lower radiation frequencies. Most of the designs modify the geometries and the dimensions of the antennas for multiband antennas. Moreover, this seems similar to but is totally different from filter-based reconfiguration. The most obvious feature is that it is not easy for tunable filters to design and implement, nor is its bandwidth tuning easily. In our proposed architecture, merely three components can fulfill reconfigurable antennas of wide tuning ranges and controllable selectivity by using matching networks.

A tunable filter provides an excellent selection to implement tunable bands, but tunable filter are usually difficult to design and control. The comparison is listed in Table 1. To achieve tunable capability, our proposed architecture has advantage of very wide tuning range, flexible control, and easy analysis. There are currently many fabrication technologies [Hoarau 2008]. Hybrid circuits using discrete components such as diodes and SMD components are easier to make and design for prototypes in commercial bands to verify concepts, and these components may be further integrated in compact size in the future. The main design issues of tunable matching network include applicable frequency ranges, impedance tuner dynamic range, control methods, linearity, size and losses. Concerning the tunable frequency range, a high selectivity usually comes along with a limited tunable range. However, this problem can be easily overcome in our proposed architecture. The four main investigative objectives in this chapter are operating frequency ranges, other undesired bands suppression, the use of one single component to fulfill the tunable function, and energy loss reduction.
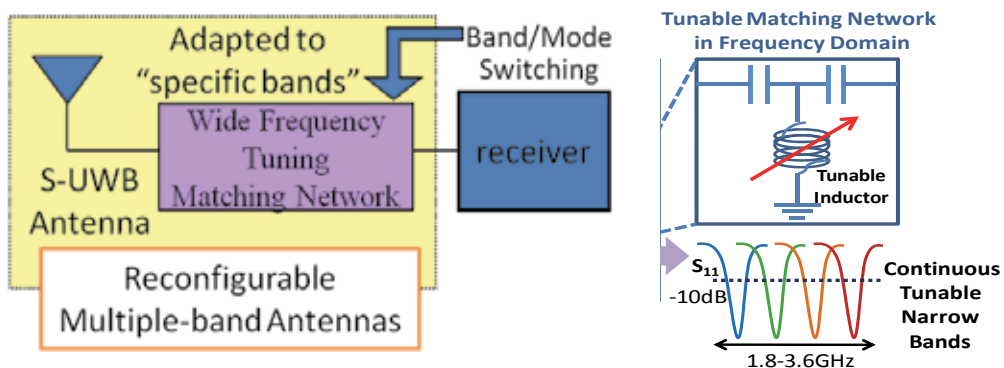

Fig. 1. The architecture of the reconfigurable multiband antennas.

In this chapter, by expanding the concept of "analog antenna" and 'impedance matching in frequency domain' [Yang 2009], the design of reconfigurable multimode and multiband

antennas is developed in a straight forward manner and also implemented in low cost, simple circuits. The "analog antenna" in this chapter means that one un-designed antenna combined with a small circuitry to enhance or expand the original function or specification. For this proposed antenna, a frequency-tuning matching network which may have different architectures is added. The illustration of the reconfigurable multiband analog antenna is shown in Figure 1. The matching networks may have traditional structures, such as L/T/π-shaped matching network and cascaded/mixed matching network with RF switches or varactors to tune the impedance of the semi-ultra wide band (S-UWB) antennas in specific bands, which are easy to design and implement instead of using wide-band reconfigurable and sharp filters. Therefore, multiband can be achieved while covered range is still wide.

Tuning Types	Tuning		Analysis	Impedance Matching	Antenna Patterns
	Range	Control			
Modified Geometry	Broad	+++	Middle	Yes	Yes
Tunable Filter	Narrow	+	Hard	No	No
This Design	**VeryWide**	**++++**	**Easy**	**Yes**	**No**

Table 1. Typical Comparison for Frequency Tuning Functions

Moreover, to add on extra specific bands needs not to re-design the whole antenna, but to modify the matching network parameters. In this chapter, we demonstrate this concept in tri-band using lump elements for the prototypes. ADS simulations are performed to predict those multiple bands and procedures of tuning these practical lumped component values are also developed and will be addressed later. The proposed switchable multi-band antennas have the features of utilizing semi-UWB antennas, operating at multiple bands, re-configuration, and controllable bandwidth. However, these multiple bands will not occur at the sample time, each one will function as the communication system switches to their mode and frequency.

2. System description and design principles

This system includes three parts: a semi-UWB antenna, frequency-tuning matching network, and the controlling unit. The system block is shown in Figure. 2. From this figure, not only the components are variable, but also some switches are placed at the joins of the matching network to modify its own architectures. Two major steps for such proposed multiband antennas include S-UWB antenna design and matching network design. The controlling unit is assumed to be pre-assigned to turn on different modes. Each step is easy and quick, so the development and optimization process can and be improved significantly. In this chapter, a tri-band system will be demonstrated and operated at 1.8 GHz, 2.45 GHz, and 3.5 GHz, which are common for cellphone frequency band (GSM), ISM/WLAN band, and WiMAX band in some countries, respectively.

Taking loss and design complexity into consideration, we use as few components as possible to simplify mathematical analysis and induce less loss. In contrast to L-type network which has limited impedance dynamic ranges to match and lack of freedom for controllable Q value, T-type and π-type networks are commonly confined to carry out high selectivity and

a wide scope of tunable impedance network due to that the extra degree of freedom can further be used to control the bandwidth. We chose a T-type (C-L-C) network that includes two serial capacitors and a parallel inductor between them shown as Figure 3. The central shunt part is the variable inductor L, implemented by a fixed L and a varactor.
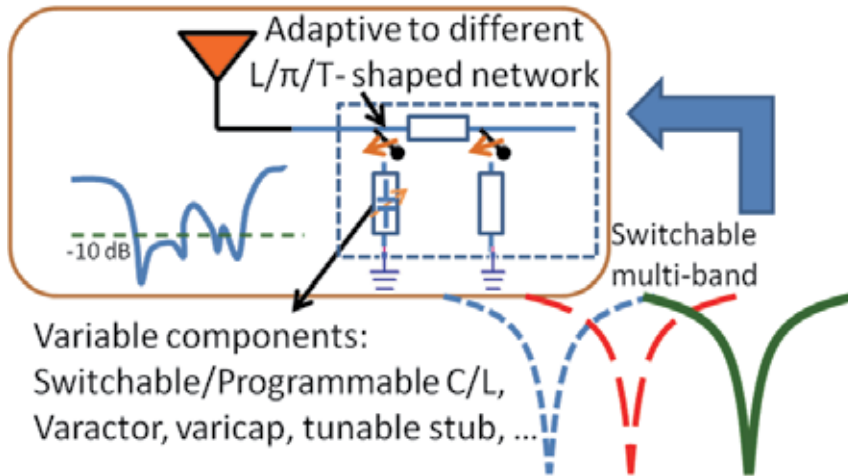

Fig. 2. System diagram of the band-switchable antennas.
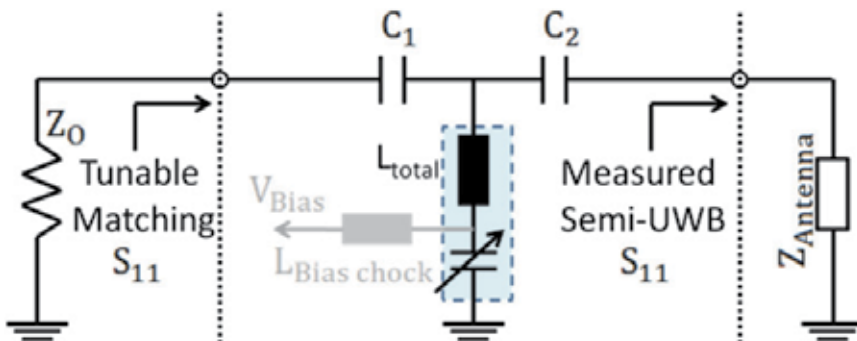
Fig. 3. Equivalent circuit of the tunable matching network and S-UWB antenna with control bias voltages V_{BIAS}, series capacitor shunt inductor L and varactor

There are two major steps to design the proposed reconfigurable antenna, including S-UWB antenna design and tunable matching network design. Each step is quite straight forward and thereby improves significantly the development and optimization process.

2.1 Design for semi-UWB antenna
Instead of designing a tri-band antenna directly to cover these bands simultaneously, a semi-UWB antenna is desired to cover these bands. A semi-UWB antenna means similar to UWB antenna, but it does not guarantee all the return loss below -10 dB over its operation bandwidth. Popular or compact UWB antenna designs can be referred and guided [Wong 2005] [Peyrot-Solis 2005]; however, it is not necessary to optimize all the dimensions to have

ultra wide band response, like one real UWB antenna does (so we called such antennas as S-UWB antennas). On the contrary, radiating over semi-wide bands is sufficient. Therefore, antenna design and procedure for tradeoff between the bandwidth, gain, and efficiency can be reduced substantially.

We randomly pick up two kinds of antennas to demonstrate our concepts and design. One is circle-shaped, and the other is beveled-shaped. A circle-shaped antenna on a 1.6-mm FR4 (ε_r = 4.3, loss tangent δ = 0.015) substrate is chosen as one of the options for demonstration in this chapter. Its dimension is determined from HFSS simulations. The relevant dimensions of circular-shape antennas are [r/d/g/w_f] = 21.3/1/10/2.7 mm; [L_1/L_2/W] = 62/19/64 mm. The dimension of the beveled-shaped one is determined from HFSS simulations and listed in below. The geometry and dimension is shown in Figure 4 and 5. Surely other shapes and UWB-like antennas can be possible to apply following the same design principles. The return loss is measured and shown in Figure 4 and 5. From the result of the measured S_{11}, we found this S-UWB antenna performs relatively poorly at 4-5 GHz, but we need not to tune its dimensions and feeding structure to optimize this antenna. These performances at desired bands will be considered with matching network altogether.

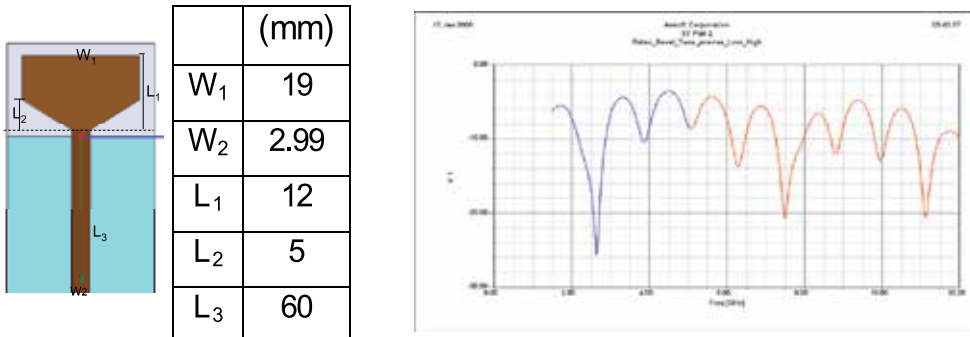|	(mm)
W_1	19
W_2	2.99
L_1	12
L_2	5
L_3	60

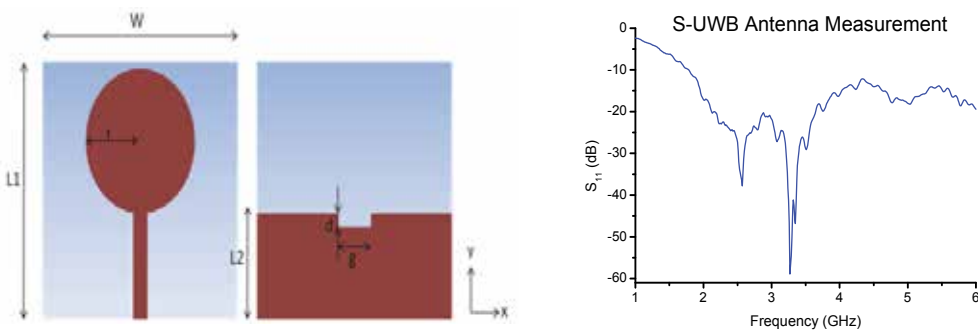Fig. 4. Beveled-shaped S-UWB antenna and S_{11} plot from the HFSS simulation.

Fig. 5. The circle-shaped S-UWB antenna and S_{11} plot from the HFSS simulation.

2.2 Design for frequency-tuning matching network

The L-C type matching network, which is optional, is chosen to adapt the impedance to match at the desired frequency. Therefore, the overall antenna with the matching network

becomes narrowband band implying high selectivity. This is reasonable due to the semi-UWB antenna has low-Q and overall the response is dominated by the matching network as well. The S_{11} parameters are estimated from HFSS simulations and output as a file to ADS (Advance Design System), so ADS can do the matching network corresponding to the specific S_{11} at target frequencies as shown in Figure 6. After matching network, the S_{11} is re-shaped and a specific frequency can be well-matched as Figure 7(b) shows.
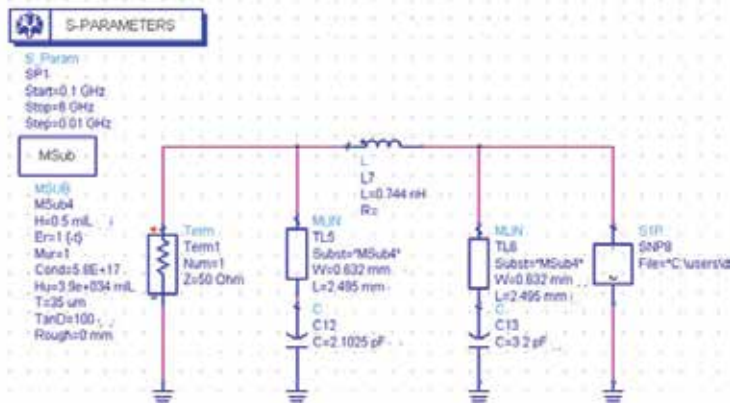
Fig. 6. ADS simulation combined tunable matching network and an S-UWB antenna (S1P).

The π-shaped matching network, which is optional, is chosen to adapt the S-UWB antenna impedance to match at the desired bands. As parts of the L/C components are tunable, this combined analog antenna becomes switchable to specific bands. This is desirable, so the bottleneck of the design of such analog antennas is the tuning and implementation of the matching network circuits which is relative low cost and technically feasible without the modification of the antenna itself. The development starts from the theoretical prediction of the proper L/C component values by feeding the measured S_{11} parameters estimated from HFSS simulations as a load file to Advance Design System (ADS) in Figure 6.

freq (1.500GHz to 12.00GHz)   freq (1.500GHz to 12.00GHz)
(a)   (b)

Fig. 7. S_{11} of Bevelled antenna (a) without and (b) with a matching network.

The procedure of determining the component values is shown as below. This is well-established and makes the development of the multiband based on our proposed architecture relatively easy. We further apply a practical C model (S parameters are measured) into the ADS for a fine tuning in the frequency band to reduce the errors 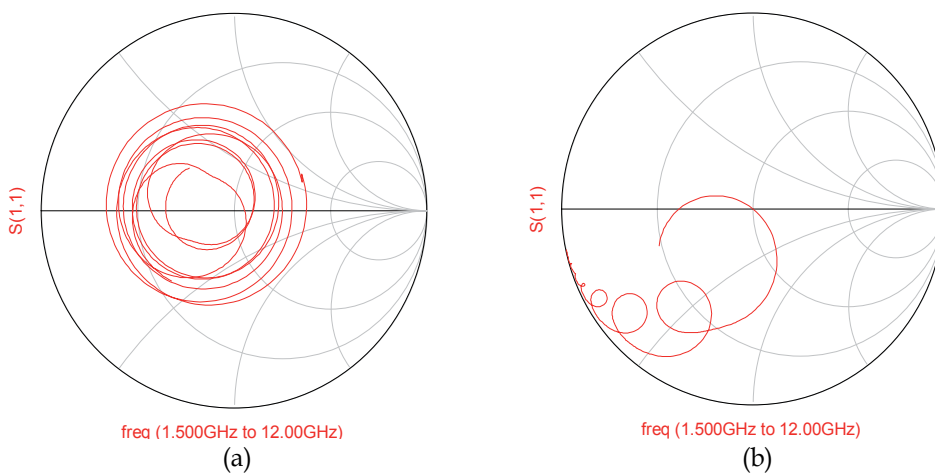of the implementation. Our goal is to set the S-UWB antenna to have good matching (Z_{in} (ω_c) = R_s) at the operation band centered at ω_c, which means Γ_{in} (ω_c) = 0; meanwhile we also estimate the bandwidth by circuit Q values. We set a redundant resistance (R_V) as the mediate step to calculate matching as two cascaded L-shaped networks (shown in Figure 8).

$$Q_1 = \sqrt{\frac{R_s}{R_v} - 1} \tag{1}$$

$$Q_2 = \sqrt{\frac{1}{R_v \cdot G_L} - 1} \tag{2}$$

The unloaded Q of the cascaded network Q =max ($|Q_1|$, $|Q_1|$), and the bandwidth can be determined by 2/$|Q|$. Applying (1) and (2) into ADS, Table 2 lists the component values of the matching network for this proposed tri-band antenna.
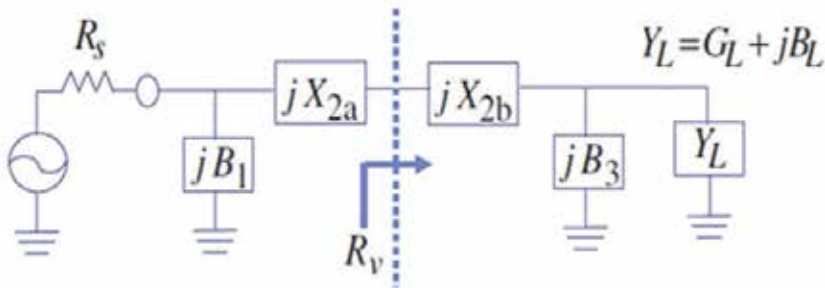
Fig. 8. The mediate step reconfigurable multiband analog antennas.

Frequency (GHz)		C_1 (pF)	L_2 (nH)	C_3 (pF)
Band I	1.8	3.858	2.590	6.545
Band II	2.4	3.760	2.972	5.250
Band III	3.5	2.490	1.150	5.800

Table 2. L-C values of the matching network for tri-band.

According to those desired L/C values based on specific Q values, ADS can fulfill the simulations of this analog antenna at target bands. After π-shaped matching network, the simulated S_{11} of this circular S-UWB antenna is re-shaped to a narrow band antenna and in this specific band, S_{11} can be well-matched as Figure 9 shows. The original S-UWB antenna covers from 2 to 4.5 GHz well. Using the band II parameters, the 2.45 GHz band is will matched, while others are rejected and this proposed antenna functions as a high selective antenna. After the proper L/C values are found, we need further to calibrate the practical values and the influences of the switches (GaAs SPDT, model no. SKY13306-313LF) on the

matching performance for the implementation which will be discussed in the later section. The switches are modeled as loss transmission lines unless they are RF-MEMS switches which provide extremely low loss and huge isolation.

a)   b)

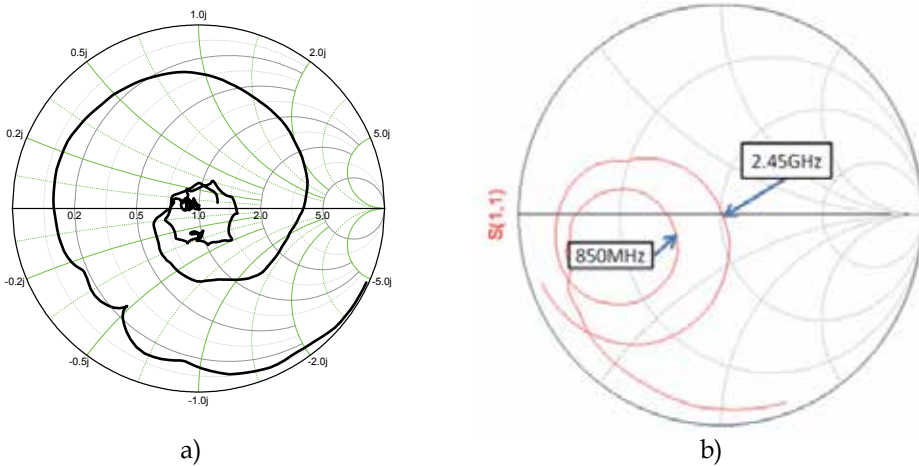Fig. 9. Measured S_{11} smith chart of circular S-UWB antenna: (a) without and (b) with a matching network tuned to 2.45 GHz.

3. Analysis and simulations for matching network

A complete impedance matching theory and numerical analysis are well-established [Thompson 1996][Schmidt 2007]. However, there exists a high complexity and practical performance loss after considering the parasitic effects, fabrication errors and self-resonant frequency from components in realistic operation. The traditional matching network encounters unavoidable tolerance errors from capacitance and inductance resulting in a frequency deviation away from desired frequency. In this chapter, not only do we have to solve the matching problem, but furthermore, we also eliminate the frequency deviation due to the drifting of capacitance and inductance components.

The π- and T-type networks themselves can be designed with a desired Q value. However, one common problem for the wideband matching is that uniqueness of the matched bands, which means other undesired bands might happen to be matched unintentionally. Moreover, an unfavorable drawback occurs when using a varactor which needs an additional biased from microstrip line, resulting in discontinuity and parasitic effects. All of these factors above shall be taken into consideration seriously to increase the selectivity and performance. These issues will be addressed in following sections to further improve a highly selective matching network with high Q value and with a continuously smooth tuning effect. These practical factors are also taken into account for simulation, especially for the models of precise values in high frequency.

3.1 Analysis for High-Q tunable S-UWB antennas
One of the unique merits for UWB antennas to design such tunable matching network is that its input impedance already resembles 50 Ω ($Z_{ANT} \cong Z_o$) within a very broad bandwidth. Based on this characteristic, 50 Ω terminals are used at both ports of the matching network as the preliminary design to determine the appropriate values of C_1, C_2, and L, and to

reduce the number of variables from antenna impedances. We chose two fixed similar low-value capacitors C_1 and C_2 for two serial components of T-type network in Figure 3. The simulation and implementation has proved that this nearly 50 Ω assumption does not affect the accuracy of performance evaluation.

The high selectivity can be explained by tracing the trajectory of the impedance. By using the first series low-value capacitor C_2, original antenna impedance, Z_{ANT}, will be moved to the right half of Smith chart (Z_2, high capacitive reactance) along the unit circuit, and the end point intersects with high Q circle (as shown in Figure 10). The target matching frequency is set through a 'single' variable inductor L and the impedance becomes Z_1. Then, by applying the up-down symmetrical nature of Smith chart, a second series capacitor C_1 of the same value, $C_1=C_2=C$, pulls back from impedance Z_1 to the center point $Z_o = 50$ Ω and completes the impedance matching at the desired frequency. The tuning antenna is operated at this band thereby. As the large C_1 and C_2 are applied, a low selectivity can be fulfilled theoretically as shown in the right part of Figure 10(b).
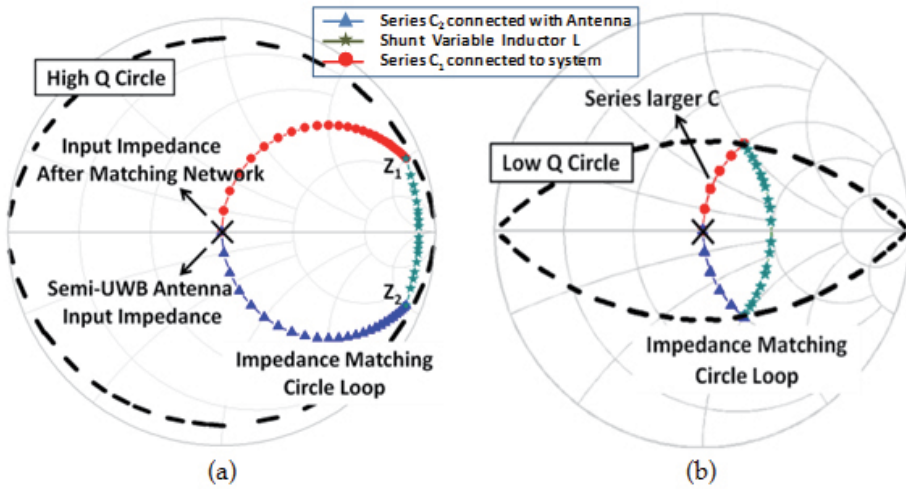
Fig. 10. Matching analysis on Smith chart with (a) High Q; (b) Low Q value.

An analytic formula for calculating the unknown inductance can be obtained as below, so the unknown inductance value *L* can be determined according to tunable matching frequency. T-type network impedance matching function can be observed from Figure 3 and is given as equation (3).

$$Z_0 = \left(\left(Z_{Ant} - \frac{j}{\omega C_2} \right)^{-1} - \frac{j}{\omega L_{total}} \right)^{-1} - \frac{j}{\omega C_1} \tag{3}$$

Applying the conditions of $Z_{ANT} \cong Z_o$, $C_1 = C_2 = C$ (constant), and the target frequency ω_{target}, and simplifying the equation, we get the equation (4) to obtain the inductor L_{total}.

$$L_{total} \approx \frac{1}{2} \left(C Z_0^2 + \frac{1}{\left(\omega_{taget}{}^2 C \right)} \right) \tag{4}$$

where L_{total} is controlled by a vacator series with a fixed L to achieve well-matched at the frequency ω_{target}, and continuous tuning can be fulfilled by using a varactor, instead of discrete switching. We must apply the actual component values before it can comply with the predicted target frequency and find the precise frequency tuning ranges. Through basic thru-reflect-line (TRL) calibration technique, the values of the capacitance, the inductance and the parasitic impedance can be obtained precisely.

After we calculated the theoretical matching inductance, L_{total}, and the corresponding cascaded capacitance, $C_{varactor}$, the bias voltage value for the required capacitance can be determined from the varactor C-V curve we measured. Therefore, the variable inductor can be modeled with a proper varactor model which can be referenced in [Stauffer 2003]. The varying range of inductance is dominated by the varactor. This factor has thus determined the tunable ranges. In this chapter, a preliminary validation around 3 GHz is verified. The components are not optimized intentionally yet. Due to SMD component tolerance errors, the actual implemented operation frequency might be deviated. From the deviation status, the inductance differences are calibrated, and then the frequency deviation is compensated by correcting the bias voltage slightly to achieve the precise target frequency.

4. Implementation and experiment setup

To implement the proposed wide tuning antenna, three major parts are fabricated including an S-UWB antenna, a tunable matching network, and a controlling circuit. S-UWB antenna is fabricated without optimized fully-qualified performance. A circular-shaped antenna on FR4 (ε_r = 4.3 and loss tangent δ=0.015) substrate of 1.6 mm thickness is chosen and fabricated for demonstration as a simple design with an available wideband. Of course, other wideband antennas in different shapes are possible options. The relevant dimensions of S-UWB antenna are [r/d/g/w_f] = 21.3/1/10/2.7 mm and [L_1/L_2/W] = 62/19/64 mm. Those long transmission lines are extended for measurement and can be removed. The 'π'-shaped matching network is very small and attached at the interface of the antenna and RF front end. The frequency-tuning matching network is separated for the test purpose and it is feasible to fabricate nearly the antenna. The whole band-switchable tri-band antenna (analog antenna) and the transmission test is shown in Figure 11. Tri-band operation will be validated using Agilent NWA 8753E. Furthermore, we setup a UWB ridged horn to test path loss S_{21} using the proposed antenna. The orientation setup is based on the original the directivity of the S-UWB antenna.

The whole integrated reconfigurable antenna is shown in Figure 11, including the fabricated tunable matching network on Roger substrate (R04003C, ε_r = 3.55, loss tanδ= 0.0021) of 32 mil (0.81 mm) thickness. The component values are C_1 =C_2 = 0.6 pF, L_2 = 4.7 nH, and L_{choke} = 7.8 nH (for bias voltage input). The model number of GaAs hyperabrupt tuning varactor is MGV-125-23-E28, with a useable capacitance from 0.3 pF to 4 pF. The Q factor of the varactor is 3000, and its series resistance is about 1 Ω. The controlled circuitry is made by the micro-processor 89C51 to set a proper bias voltage on varactor through a DAC and an OP-Amplifier. The controlling module can be miniature using ASIC technologies in the future. The S_{11} of the reconfigurable antenna can be measured with the network analyzer Agilent N9020A. One double ridged UWB horn antenna (1 GHz ~ 18 GHz) is placed at a distance of 60 cm as the far field region to test the reception performance (S_{21}) of the tunable antenna.
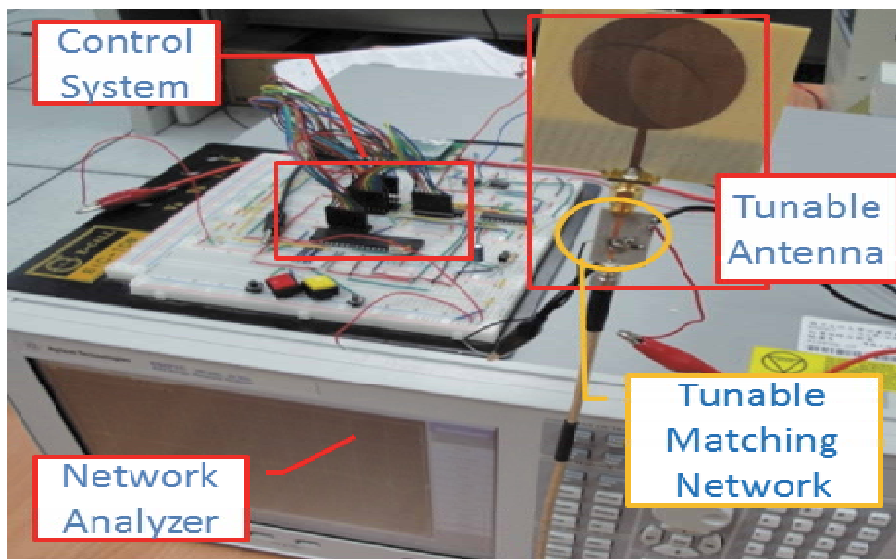
Fig. 11. The implemented reconfigurable S-UWB antenna attached with matching network.

5. Results and discussion

5.1 Simulation results of wide range for reconfigurable antennas

Table 3 shows the simulation results of antenna impedances; therefore, series inductor L and parallel inductor C is chosen correspondingly. Then, the W-USB antenna becomes a narrowband one and selects at frequencies 1.8, 2.4, 3.5, 5.8, 9, and 11.5 GHz as shown in Figure 12. This implies the proposed techniques can provide a very broad tunable range, which is very significant. The ratio is 11.5/1.8 (~640%). In practice, the loss of the realistic matching network should be taken into account, so this is one of the reasons why S-UWB antennas are chosen so that the matching component can be realistic. For example, an antenna whose impedance contains a low resistive part and very high reactance is not good for matching implementation. Of course, while considering the practical parasitic effects, the tuning ratio will reduce, but it is still wide enough and will be shown in measurement.

Frequency(GHz)	1.8	2.4	3.5	5.8	9	11.5
$Z_{antenna}(\Omega)$	15.678 + j0.93	39.05 + j13.52	17.12 + j21.11	15.03 + j13.63	33.87 – j30.55	26.43 – j7.95
Parallel Cap, C_1 (pF)	1.969	0.474	0.119	0.255	0.953	0.145
Series Ind, L_2 (nH)	2.617	0.702	1.261	0.837	0.244	0.228

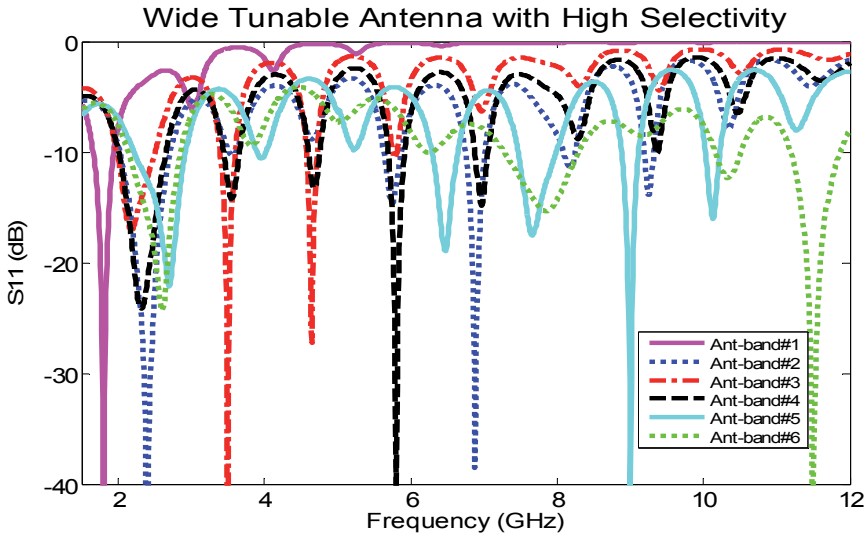Table 3. Designing L-C values for specific frequencies.

Fig. 12. The reconfigurable antenna can cover range from 1.8GHz – 11.5GHz.

5.2 Simulation results of high selectivity for reconfigurable antennas

Though at the desired frequency, the antenna can achieve high Q and good selectivity, however, from the Figure 13, there are some ripples falling into other bands which mean at these bands, the unwanted signals will leak into the receivers. Take 3.5 GHz-band as example, at 4.65GHz, S_{11} is also down to -25 dB, implying that the antenna can perform relatively well in transmitting and receiving at 4.65 GHz, which is not our design 3.5 GHz. This can be improved by changing the matching network from L-shaped to 'π'-shaped or 'T'-shaped. There will be one additional freedom to determine the Q factor, thereby other wanted parts can be eliminated. Figure 13 shows after applying $Cp_2/L/Cp_1$ of 7.958 pF / 0.448 nH / 5.85 pF values, the antenna again becomes very selective. Our proposed antennas do not have complicated design themselves but cooperate with the following matching network; multi-band reconfigurable antennas can be designed.
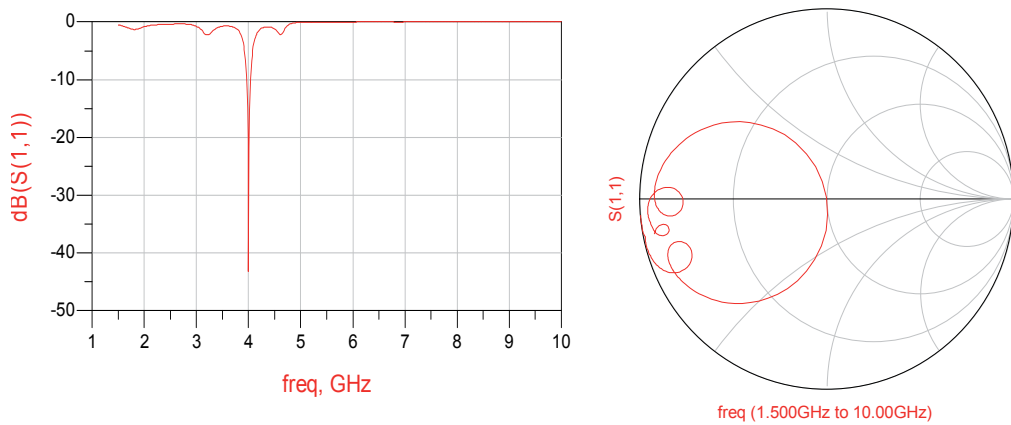

Fig. 13. Performance (S_{11} and the smith chart) using π-network at 4 GHz.

5.3 Measurement of fabricat ed tri-band antennas

Due to the manufacture variation of the lump elements, those calculated L/C values are tested separately to obtain its practical S-parameter model (S1P). After re-tuning according to these manufactured parameters and considering those transmission and switch influences carefully, the performance of the proposed tri-band antenna is shown in Figure 14. The dashed, solid, and dotted lines correspond to the ADS simulated results in different bands. Furthermore, this antenna keeps the flexibility of the tuning to the three bands without replacement of the S-UWB but the matching network components. Furthermore, if we add one set of the $C_1/L_2/C_3$ (=5.06pF/ 0.397nH/ 4.11pF) lump element values, we can expand this antenna into a quad-band antenna. This implies this fabricated antenna can be extended to a multiband antenna (more than four bands) easily with extremely low cost. However, close bands need extremely high-Q and precise components to isolate and it is not fulfilled in this work.
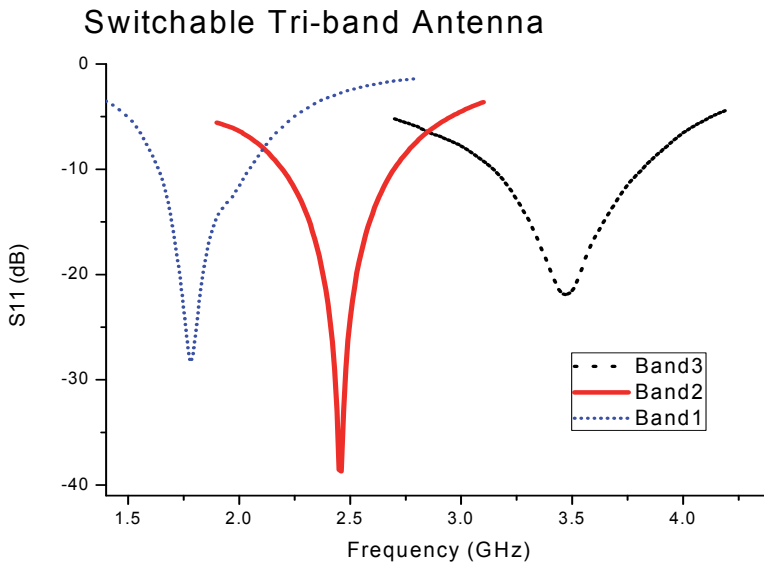
Fig. 14. S_{11} of the measured tri-band antenna.

5.4 Measurement of controllable bandwidth

As we mention in introduction, most of the multiband antenna is fixed and can be optimized the performance for their specific bands; however, it is relatively complicated to control the bandwidth. This may be useful for the adaptively date rate system for SDR or CR to minimize the noise floor power yet keep the SNR as large as possible. In our proposed architecture, we may use the frequency-tuning network in the traditional aspect; in other word, the frequency is fixed (for example, at f_c = 2.45GHz). Therefore, we may switch different L/C values in the π-shaped matching network to control its bandwidth. A fabricated circular S-UWB antenna is applied into the ADS simulations to obtain the L/C component values. The three cases of the bandwidths are demonstrated in Figure 15 using the values in Table 4. These results show the fractal bandwidths of 11%, 22%, and 33%.

f_c = 2.45GHz	C_1(pF)	L_2 (nH)	C_3(pF)
Small Q	0.75	2.6	1
Big Q	2	2.9	2.4
Extreme Q	5	1.5	5.6

Table 4. The matching network to various antenna bandwidths.

Fig. 15. A sample line graph using colors which contrast well both on screen and on a black-and-white hardcopy.

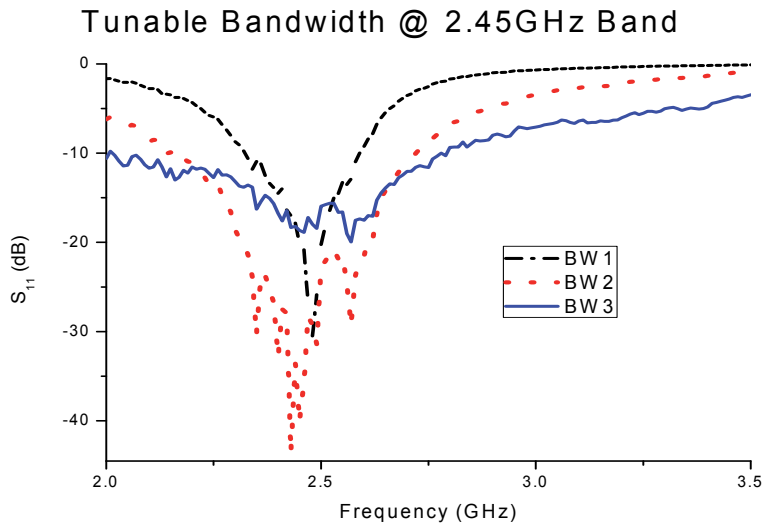### 5.5 Measurement of continuously tuning for the reconfigurable antennas

An UWB horn antenna was used to compare S_{21} towards the S-UWB antenna itself with and without the frequency tunable matching network as the wideband and narrowband reception comparisons. First, the frequency tuning capability of the proposed antenna is verified and only a single controlling voltage is applied. The S_{11} measured results are shown in Figure 16. The components in the matching network are C_1=C_2=0.6 pF with two different series inductance (a) 4.7 nH and (b) 2 nH. The varactor is biased from 0 ~ 23 V. These tunable bands cover two different ranges, 1.8 GHz - 2.8 GHz (155%) and 2.19 GHz – 3.86 GHz (176%), respectively.

The matching network can change the original UWB frequency response to the narrowband operation at the desired frequency, so this S-UWB antenna is validated as the novel reconfigurable antenna. Moreover, our results show that only one desired band can be matched without other undesired matched bands and that ensures quality selectivity. The performance of the reconfigurable antenna can be listed in Table 5. This table shows the tunable range from 2.19 GHz to 3.86 GHz. The gain can be as low as -0.58 (up to -0.94 dB), which implies very low insertion loss.
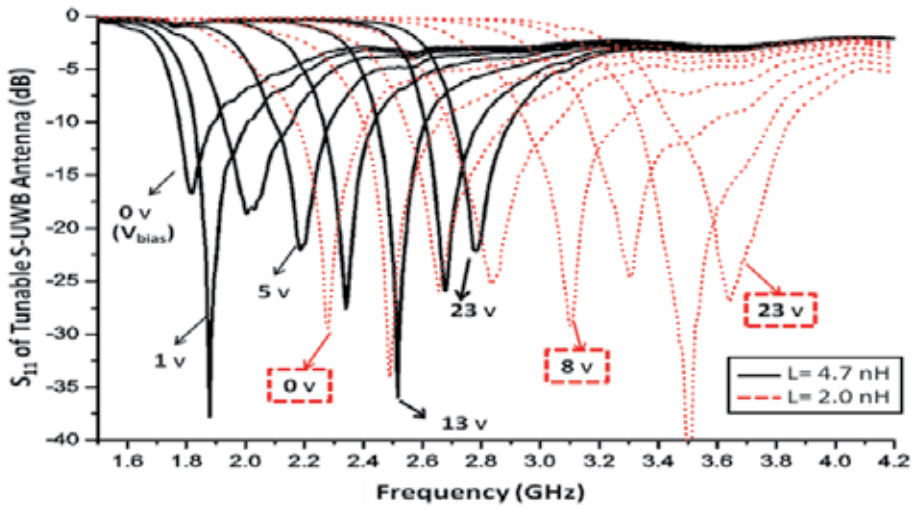
Fig. 16. Measured results of reconfigurable antenna S_{11} with biased voltage from 0 ~ 23 V; $C_1 = C_2 = 0.6$ pF. L= 4.7 nH (solid line) or 2 nH (dashed line).

V_{bias} (volts)	0	1	2	5	10	15	23
Frequency (GHz)	2.19	2.31	2.78	2.97	3.44	3.73	3.86
Return Loss (dB)	-21.9	-30.3	-34.9	-38.2	-42.3	-20.7	-23
Gain (dB)	-0.94	-0.93	-0.89	-0.82	-0.7	-0.61	-0.58
BW (MHz)	288	240	239	300	432	324	222

Table 5. Performance of the reconfigurable antenna with $C_1/L/C_2 = 0.6$ pF/2 nH/0.6 pF.

6. Conclusion

A novel band-switchable multi-band antenna is proposed by integrating a reconfigurable frequency-tuning matching network with an S-UWB antenna. Therefore, a tri-band (1.8/2.45/3.5 GHz) antenna is demonstrated. Moreover, the proposed multiband antenna not only has the features of switchable multiple bands and easy re-configuration, but also tunable bandwidth. 11% ~ 33% bandwidths are shown at 2.45 GHz. By using ideal components without parasitic effects, high selective antennas which cover ultra wide ranges from 1.8 GHz to 11.5GHz are achieved in simulation.

A procedure of handling practical lump components tolerate error is developed and calibrated to implement a tested prototype which is shown to match the predicted performance at operation frequencies. The measurement results show that the matching network features an average transducer power gain of -0.58~ -0.94 dB, which enables the antenna capable of tunable ratio of 163%, controlled by only one single bias voltage, and an average bandwidth of 300 MHz (from 2.5% to 9.6%). We have also investigated into the continuous controllable mechanism and overall improvement of Q value.

This chapter provides a wide and feasible method to apply the matching network as part of the reconfigurable antennas to expand their functions, to ease the design flow, and to reduce the implementation cost. Modifying the matching network can further tune to extra bands and different bandwidths and improves the flexibility of traditional multiband antennas. All these results recommend that this design concept is able to lower the process, time and analytical difficulty of the tunable antenna design significantly. The general analytical principle and design equations can be applied in any kind of wideband antennas. In the future, this design concept can be applied in designing and controlling multi-band tunable antennas as well.

7. References

Guo, Y. X.; Chia, M. Y. W. & Chen, Z. N.(2004) Miniature Built-in Multiband Antennas for Mobile Handsets. *IEEE Transactions on Antennas and Propagation*.

Hoarau, C.; Corrao, N. ; Arnould, J.-D.; Ferrari, P. & Xavier, P. (2008). Complete Design and Measurement Methodology for a Tunable RF Impedance-matching Network. *IEEE Trans. on Microwave Theory and Techniques*, vol.56, no. 11, (Nov 2008), pp. 2620 - 2627.

Peyrot-Solis, M. A.; Galvan-Tejada, G. M. & Jardon-Aguilar, H. (2005). State of the Art in Ultra-wideband Antennas. 2005 *International Conference on Electrical and Electronics Engineering*, (Sept. 2005), pp. 101- 105.

Schmidt, M.; Lourandakis, E.; Leidl, A. Seitz S. & Weigel, R. (2007). A Comparison of Tunable Ferroelectric PI and T-matching Networks. *Proceedings of the 37th European Microwave Conference*, (2007), pp. 98 – 101.

Sheta, A.-F. & Mahmoud, S. F. (2008). A Widely Tunable Compact Patch Antenna. *IEEE Antennas Wireless Propagat. Lett.*, vol. 7, (2008), pp .40-42.

Stauffer, G. H. (2003). Finding the Lumped Element Varactor Diode Model. *High Frequency Electronics*, Technical Media, 2003.

Thompson M. & Fidler, J. K. (1996). Determination of the Impedance Matching Domain of Passive LC Ladder Networks: Theory and Implementation. *J. Franklin Institute*, v. 333(B), n. 2, (1996), pp. 141-155.

Weedon, W. H.; Payne, W. J.; Rebeiz, G. M.; Herd, J. S. & Champion, M. (1999). MEMS-Switched Reconfigurable Multi-Band Antenna: Design and Modeling. *Proceedings for the 1999 Antenna Applications Symposium*, IL, (Sep. 1999).

Wong, K.-L.; Wu, C.-H.; Su, S.-W. (2005). Ultrawide-Band Square Planar Metal-Plate Monopole Antenna with a Trident-Shaped Feeding Strip. *IEEE Transactions on Antennas and Propagation*, v. 53, i. 4, (Apr. 2005), pp. 1262- 1269.

Yang, C.-L. (2009). Novel High Selective Band-Reconfigurable Antennas over Ultra-wide Ranges Using Reconfigurable Matching Network. *IEEE Antennas and Propagation Society International Symposium* (July 2009).

A Novel Directive, Dispersion-Free UWB Radiator with Superb EM-Characteristics for Multiband/Multifunction Radar Applications

D. Tran[1], N. Haider[1], P. Aubry[1], A. Szilagyi[2],
I.E. Lager[1], A. Yarovoy[1] and L.P. Ligthart[1]

*[1]International Research Centre for Telecommunication and
Radar (IRCTR), Delft University of Technology
[2]Military Equipment and Technologies
Research Agency (METRA)
[1]Netherlands
[2]Romania*

1. Introduction

The number of topside shipboard antennas doubled every decade; in 1990s they were close to 200 and have no sight of stop growing (Tavik, 2005). The over-crowded present of such many topside antennas in a limited-space of littoral warfare ship has created/caused many critical, unavoidable problem like antenna blockage, electromagnetic interference, increase RCS, worsen the effective stealthy signature of combatant ships, which is stealthy-intended designed, and most of all is the maintenance costs of multiple systems, huge numbers of repair-personnel and operators (Tibbitts & Baron, 1999). As modern warfare ships continue to require higher levels of functionality, performance and interoperability, these problems became so bad and unresolvable and gradually as severe as unacceptable. Much efforts around the globe are concurrently conducting research works on shaping their warfare sensors/systems to form network centric warfare (NCW) ready for network centric operations (NCO). As part of the NCW, combatant ships (LCS, DDX, CGX etc.) are moving towards the governing of their integrated and centralised sensor systems, in which both ITD (integrated-topside-design of radars, and electronic warfare), and TSDC (Top Side Design Communications of civil/military communications) are being seriously investigated.

The frequency occupation on board of a warship is extremely wide, from several Hz to hundreds of GHz. To reduce the topside antenna problem, with restriction to the RF sensors only, it may better to divide the occupied frequency spectrum into a number of spectra based on their related tasks. The number of spectra can be roughly divided in four main spectra: 1) VHF-UHF-L band, 2) S-band, 3) X-Ku band, and 4) K-Ka-Q band.

The ITD and TSDC conclusively assert several key demands, to name but a few:

a. Reduction of the number of topside antennas: this can be done by application active electronically scanned array (AESA) for the three last spectra previously discussed.

b. Effectively treating all the problems of topside antennas: this can be done by moving all the AESA systems to an optimized position on the desk (Tibbitts, et.al., ibid).

c. Combatting all the single-function systems: by increasing/combining the number of functions/tasks of the sensor systems, the number of topside antennas will be drastically reduced, and by doing so multi-spectrum/multifunction AESA systems will be formed.

d. Combining/integrating both ITD and TSDC as much as possible: that is collocating/grouping/aperture sharing/integrating of systems with same/close spectrum, by doing this one can reduce both space and volume and as well as the number of top-side antennas and help the NCO moves towards the governing of integrated and centralized sensor systems.

e. Choosing correct technological/functional devices/sensors with highly compact, modular, easy to install, operate, maintain, use less power, less intensive man-power for operation and services, and jointly interoperable as well. For ship-borne AESA systems, the most appropriate choice is technological tile (Lamanna & Huizing, 2006).

In the context of multiband-multifunction AESA sensor, assessments *a* to *e* all together put several stringent demands that the applied antenna must be dealed with: to be array-applicable, antenna must be 1) *unidirectional;* to prevent grating lobes the radiator must be 2) *small*, 3); to ensure stable tracking performance, preventing lost of tracking of the desired signal, reducing miss detections and false alarms, etc., the radiator must have 4) *low cross-polarization*; for accurate determination of scatter's 3D information the radiator's patterns must be: 4) *non-squint, accurate heading*; further demands are: 5) *Linear phase, negligible group delay, etc.*; to enhance resolution, smearing the multipath-lobing-dips (van Genderen, 2003), as well as supporting multiband-multifunction operation the radiator must be: 6) *wideband*; other criteria are: 7) Planar, low profiles, symmetrical pattern, etc. are crucial design issue that the radiator must comply with.

Two dominant planar antenna technologies concurrently exists, brick radiators are mostly of end-fire class, while tile radiators are plainly broadside, the choice for airborne is the first, whilst the second is favourite in littoral AESA systems. The state-of-the-art in multiband-multi-function AESA is dominant by activities in X-Ku bands. This report also focuses to technological-tile radiators and restricts to these spectra only.

Multiband-Multifunction system: perhaps the most active R&D activity in radar technology in recent years is the shift from AESA to wide-multiband-multifunction AESA radar, or sensor systems that can perform a variety of tasks/applications in different spectra within the same system. The move to active solid-state radar is possibly the only option for performing several applications with the same radar system. Numerous studies have conducted concurrently, to name but a few, for airborne systems: AN/APG-series, MP-RTIP, CAPTOR, AMSAR, Vixen-500E, Elta EL/M-2052, FSX; for ground and sea-based systems: APAR, AN/SPY-series, XBR, CVN-21, Selex, EMPAR, SAMPSON, MESAR, ATNAVICS, CEAFAR, OPS-24, MEADS, THAAD, Elta EL/M-2248, RIAS, etc. (wikipeadia, 2011)

Multiband-multifunction system requires its components must also sustain and support the functional actions that the system wants it to be executed either *sequentially* (type I) and/or *simultaneously* (type II). The problem at hand lies on how to get away from the top-side

problem and looking for as much functionalities/spectra as possible for reconfigurable/switchable/tuneable radiators either type I or II.

Based on presumable key EM-characteristics, planar radiators candidate for mutiband-multifunction AESA are roughly taxonomized in table 1.

EM-characteristics	MPA	Stacked MPA	UWBA	DUWB
Linear phase	+++	+	- -	+ + +
Phase delay	++	+	-	+ + +
Group delay	++	+	-	+ + +
UWB	- - -	-	+ + +	+ +
Flat response	+	+	- -	+ + +
Uni-directional	+ + +	+ + +	- - -	+ + +
Patterns in xoy-plane	+	-	-	+
Size	- -	- -	- -	+ +
Cost	+ +	- - -	+ + +	++
Form factor	- -	-	++	+ +

Table 1. Taxonomy of candidate radiators for UWB multiband-multifunction radar applications; The plus and minus signs roughly indicate the suitable/applicable degrees of radiator for wideband multiband-multifunction AESA applications.

Basic design considerations: Size, form factor, cost, bandwidth, gain, radiation patterns and dispersions characteristics (phase centre included) for wideband-multiband-multifunction AESA are more stringent than the short range UWB and or narrowband phase array applications. The multi-wideband-multifunction long/medium range UWB array/phased array applications (especially, when high/super fine resolution is required) place requirements on device's EM-characteristics, in particularly on a) dispersion, b) the impedance bandwidth and c) radiation patterns, and d) transmission efficiency, which is directly related to the dispersive attribute of the radiator, this will be detailed in section 6.

Dispersions is the main and most severe cause of performance deterioration in EM-devices/systems; as natural inheritabilities, it always exists in EM-devices, especially in multi-resonant structures and wideband devices. Non-dispersion is undoubtedly the most critical requirement, total elimination of dispersions from EM-devices is, however, impossible; the only possibility is partly reducing them to an acceptable limit. To realize this, the radiator must have a linear phase, has as small as possible phase delay, and possess no aberration (i.e., dispersion-free/constant group delay). Our proposed radiator advocates a unidirectional UWB radiator with extremely low transmission dispersion level, nearly dispersion-free.

Impedance bandwidth: wideband transmission capability/high-resolution relates to short pulse; to convey such pulse the necessary condition is UWB; however, a more stringent requirement is the constant characteristic of power transmission w.r.t. frequency. To fulfil this, the impedance bandwidth must be equally balance-matched over the whole interested band. The proposed directional ultra wideband (DUWB) radiator is concurrently designed so that it is not only ultra wideband but also the power are equally distributed over the possessed band, this radiator also proved that it is flexible enough in managing to have such unique property of equal-power-distribution.

Radiation characteristics: Radiators used in arrays/phased arrays must: electrically have unidirectional radiation patterns, and equally gain patterns in the array plane (XOY), and be geometrically small enough to fit in the array to prevent grating lobes, low profiles for dealing with issue related to blind angles, scan loss, etc.

Close to 60 years of development, planar microstrip patch antennas (MPA) and their variants stacked microstrip patch antennas (SMPA), and ultra-wideband antenna (UWB) have reached maturity. Numerous ground-based, space-borne, air-borne, ship-borne phased array applications are realized with these types of planar antennas with varieties of architectures.

Obviously, as previously discussed, a radiator that is suitable for multi wideband-multifunction array/phased array applications must keep the good (unidirectional pattern, linear phase of the MPA, SMPA, and ultra-wide band characteristics of the UWBA, and eliminate the bad properties of them as well. One of the challenges in the realization of wide multiband-multifunction AESA systems is the development of suitable radiators that sustain their agile wide multi-band and waveforms.

MPAs are unidirectional but they are *narrowband*. SMPAs are complicated, costly and furthermore not wideband enough. All UWBAs can not be used in planar or conformal arrays because they are mostly not compact, dispersive and their radiation's patterns are *bidirectional*. The merits and demerits of MPA, SMPA and UWBA as candidates for wideband multiband-multifunction AESA applications are generally listed in table. 1.

Directional antennas and bandwidth broadening techniques:

MPAs are inherently narrowband (<5%). Either or both increasing the substrate's height and lowering the permittivity of the dielectric slab doesn't help much, but creating other unwanted side effects such as loss in surface wave and increase cross-polarization. Application of different slot architectures (square, circular, finger, and U slot, etc.) could broaden the BW up to 50% but with the penalty of distortion in pattern symmetry and increasing of cross -polarization etc. (Lee & Luk, 2011)

SMPAs could increase the BW up to 100%, but the stacked height also increases the mutual coupling (caused by surface-wave), higher cross-polarization, higher loss, and higher thermal heat (dissipated inside the many layers), which is severe and difficult to treat in high power phased array, particularly in pulse doppler radar.

UWB antennas are inherently wideband but have not unidirectional pattern, several techniques for converting bi-directional pattern into unidirectional one are introduced such as using either earthed and floating backing/reflecting plane, cavity backed, high-impedance surface, artificial magnetic plane, quasi magnetic plane, meta-material, etc. However, by doing so the resulting radiator lost it compactness, higher profile, and the non-linearity of the associated phase, which is already a headachy problem, gets double worse due to the extraneous interference/reflection (beside its natural multiple resonances) between the top-patch and the reflecting plane underneath.

End-fire radiators (Chen & Quing, 2005) such as Vivaldi, TSA, LTSA and planar dipole are super wideband, high gain, and having directive radiation pattern ideal for airborne applications, but not for AESA applications in littoral combat systems which demands stringent requirements that end-fire radiators are not sufficient for, such as wide-scan, stable phase, low mutual coupling and stable phase centre, the last is critical for coherent radar.

UWB techniques: Investigations of all UWB directional radiators in both open and close literature, we learned: To obtain wider bandwidth, several bandwidth enhancement techniques have been studied such as: using log periodic arrays in which the different

elements are deduced from an homothetic ratio (Rahim & Gardner, 2004), introducing a capacitive coupling between the radiating element and the ground plane (Rmili & Floc'h, 2008), using microstrip-line feed and notching the ground plane (Tourette et al., 2006), using symmetrical notch in the CPW-feeding (Zhang et al., 2009), asymmetrical feeding by microstrip line together with reduced ground plane and appropriate gap-patch distance (Karoui et al., 2010), adding T-slots for both patch and feeding strip (Rahayu et al., 2008), using cross-lot in the truncated circular patch with tapered microstrip feed line (Kshetrimayum et al., 2008). All these techniques are based on the modification of the surface current distribution to broaden the antenna's impedance bandwidth.

Unidirectional techniques: to reverse the bidirectional radiation patterns into unidirectional, several method and techniques have been introduce to design radiator(s), which are both ultra-wideband and unidirectional, by: introducing a PEC-plane under an UWB ring-slot antenna, which is matched by a balanced stub (Rao & Denini, 2006). Designing of an electromagnetic bandgap (EBG) under a ring slot radiator (Elek, et al., 2005); Using high profile foam with low dielectric constant (Suh et al.,2004); using a composite corrugated reflector under printed plannar dipole (Wu & Jin, 2010); using fractal clover leaf (FCL) as radiation patch and fed by L-probe (Tayefeh, et al.,2004); use of artificial magnetic conducting plane(AMC)(Tanyer et al,2009b).

Studying of these works, we observed that the invented radiators are i) high profile (5-66 mm), ii) using floating reflecting plane, iii) using different dielectrics in vertical stacked profiles, iv) having complicated backing topologies AMC, EBG, FCL, FSS, meta-materials, etc. These radiator are indeed UWB and unidirectional, however there are till profound issues which are not suitable for multiband-multifunction AESA applications.

We report here a compact, directional ultra-wideband antenna (DUWB) with simple grounded coplanar waveguide (CPWG) topology and special architecture which could eliminate all the unwanted effects and integrate all the merits of other candidates for multiband-multifunction AESA applications. The proposed prototype reports in this chapter belongs to the tile-class type II, it is a quasi-electric-magnetic (QEM) unidirectional planar broadside UWB antennas. The advantages of the proposed DUWB antennas with respect to other possible candidates (MPA, SMPA, UWBA) for multiband-multifunction AESA applications are roughly indicated and tabled in table 1

This chapter is organized as follow: In section 2 the definition of bandwidth is reviewed, then subsequently the concepts of quasi-electric antenna (quasi-E), quasi-magnetic antenna (quasi-M), and quasi-electric-magnetic antenna (quasi-EM) are introduced based on the basic concept of electric- and magnetic antenna. Definition and concept which is wire-version antennas that all planar antennas were derived thereof, the concepts of quasi-electric and quasi-magnetic for planar antennas are typically discussed, also definitions pertaining to qualitatively expressing the antenna's impedance bandwidth were considered. The EM-duality, Babinet's principle, Booker's impedance formula and Mushiake's relationship are discussed, which formed the main driven impetus to the design of the proposed DUWB prototype. In section 3 the topology and architecture of the DUWB antenna are described, RF-considerations on design material, PCB technology and detailed architecture and its associated parametric functions are reported. In section 4: detail works on parameter identification, investigation and optimization are discussed. As a "proof of concept", we examine the performances of the proposed radiator, and provide a methodological procedure for simplifying the multivariate optimization process, which were intensively used in previous work (Tran, et al., 2009), also parametric investigations and numerical

simulations of the proposed DUWB radiator are also reported in this section. In section 5: we report of how the implication of UWB transmission formula is simplified into the narrowband one and made it applicable to the proposed DUWB. The prototype are fabricated, tested and evaluated in both frequency- and time–domain. The measured results of reflection coefficients, co-polar and cross-polar radiation patterns are carried out and evaluated in frequency domain, whilst the transmission coefficients are measured and evaluated in time domain, the transmission's characteristics are derived and reported also section 6. Acknowledgement is expressed in section 7. Conclusions are summarized in section 8, the chapter is concluded with key references which support the arguments and assessments proliferated in this works.

2. Fundamentals and concepts

This section recapitulates and discusses the basic definitions, concepts and their corollaries, which are frequently used in this work. Section 2.1 discusses the basic definitions of impedance bandwidth, points out their defects and mistakes in usage. Section 2.2 recapitulated the concept of electric and magnetic antennas. Section 2.3 introduces the concepts of quasi electric (quasi-E) antenna, quasi-magnetic (quasi-M) antenna together with the introduction of an additional quasi-electric-magnetic concept, our proposed prototype antenna representing for this offshoot will be termed as quasi-electric-magnetic (quasi-EM) antenna. In section 2.4 the principle of EM-duality, Babinet principle together with Booker's relation and Mushiake's relationship will be wrapped-up. These fundamental principles formed the main impetuses driving to the design of the proposed quasi-EM DUWB prototype.

2.1 Bandwidth definitions

Traditional communications systems typically used signals having a percent bandwidth of less than 1%, while standard CDMA has an approximately of 2%. Early definition in the radar and communications fields considered signals with percent bandwidth of 25% or greater (measured at the *-3 dB points*) to be ultra-wideband. The recent FCC regulations (IEEE Std, 2004), which will be used as a standard throughout this text, defined UWB devices/signals as having an nominal bandwidth which exceeds 500 MHz or percent bandwidth of over 20%, measured at *-10 dB points*.

The term super wide-band (SWB) has been often used to indicate bandwidth, which is greater than a decade bandwidth. Since the percent bandwidth confused and failed to envision the SWB property adequately. The "ratio bandwidth" is exceptionally suitable and often be used for describing bandwidth of decade bandwidth or more.

There are several definitions of bandwidth circulated among our antennas and propagation society; those frequently met are octave-, decade-, fractional-, percent-, and ratio-bandwidths. The two definitions, that most frequently used, are the percent bandwidth and the ratio bandwidth. They are defined respectively as follows:

$$BW_P = 100\% \times BW / f_C \qquad (1)$$

$$BW_R = BW / f_L \qquad (2)$$

Where:

f_H and f_L are respectively the maximum and minimum frequency, which are mostly defined at reflection coefficient at level of -10 dB.

BW is the *nominal bandwidth* defined by $BW = f_H - f_L$

f_C is the central frequency defined by $f_C = (f_H + f_L)/2$

BW_P is the percent bandwidth and,

BW_R is the ratio bandwidth, commonly denoted as $B_R = R$-over-1, where R is the normalized ratio of the highest frequency to the lowest frequency defined as $R = f_H/f_L$.

Formulae in Eq.1, 2 and 3 are three common bandwidth definitions, often named as the *percent bandwidth*, the *ratio bandwidth* and the *UWB-bandwidth*, respectively.

$$BW_{UWB} = BW_P \geq \left\{ \begin{array}{ll} 25\% & DARPA \\ 20\% & FCC \end{array} \right. \qquad (3)$$

The UWB bandwidth definition, which is based on the percent bandwidth, acquired the percent bandwidth with two different norms; the $BW_P \geq 25\%$ is the acquired norm defined by the defense research projects agency (DARPA) and the $BW_P \geq 20\%$ is for the federal communications commission (FCC).

The *percent bandwidth* (1) has originally been used to describe the narrow-bandwidth of conventional antennas and microwave-devices. Its usage is quite popular and often considered as a standard in many textbooks, nevertheless, it is mathematically not a solid definition because it possesses a defect when f_L approaching zero. For example, suppose that the nominal bandwidth of antennas #1 is 2GHz (0-2GHz), and antenna #2 is 20GHz (0-20GHz). It is clearly that the nominal bandwidth BW of the second antenna is 10 times wider than the first one; however, formula (1) indicates that both antennas have the same percent bandwidth. Another weak point is the percent bandwidth of formula (1) is always less than or equal to 200% irrespective of how wide the antenna's nominal bandwidth was. Note also that formula (1) is often mistakenly called as *fractional bandwidth*, indeed the formula (1) consolidates its meaning "fractional bandwidth" only when the factor 100% is removed.

Alternatively, the *ratio bandwidth* (2) can also be used for expressing the bandwidth of UWB or SWB antennas and devices. The defect at zero-frequency point still lurks there but the 200%-limit is lifted. The use of the ratio bandwidth is more adequate to envision the wideband characteristics of devices under investigation.

How to choose between the two formulas, although no official consent, however, the first formula (Eq.1) is often used for cases that the bandwidths are less than 100%, whilst the second (Eq.2) is for both UWB and SWB antennas/devices. It is noted that for bandwidth greater that 100%, it is better to use second formula since it reflects more correctly, especially when the impedance bandwidth of device to be investigated is super wideband.

2.2 Electric and magnetic antennas

Inspection of open and protected literature, the readers may obviously observe that planar UWB antennas, at present day, have come with a countless varieties of antennas. Almost there is a new type of antenna created for every dedicated application. These antennas vary not only in topology and architecture but also in technology and the spectra they served. It is impossible to classified or group them base on their size, shape, structure or architecture.

Planar UWB and SWB antennas which geometrically resemble its counterpart (wire)-monopole antennas are widely called monopole. However, this topological naming for the planar radiators is incorrect and confused, because the radiation pattern of all the so-called

(planar)-monopole antennas have not the shaped of the monopole but of the dipole antenna i.e., having the shape of the full-doughnut.

The term "magnetic antenna" has been occasionally employed in (IEEE STD 145, 1983) and by (Schantz & Bames, 2001) to describe antennas with radiation properties closely resembling those of a thin wire loop (Balanis, 2005). The term "electric antenna" was also mentioned in (IEEE Std, op. cit.; Schantz et al., 2001, 2003, 2004; and Baum, 2005). Formal definition, however, is still lacked. To keep this chapter self-content and avoid cross-reference, and to avoid ambiguities, formal definitions for planar antennas are summarized and given hereafter:

As a first step, let the *base plane B*, be the plane comprises the antenna's effective radiating/ receiving aperture, and let *n* be the unit normal vector to this plane, with reference to Fig.3, *B* can be assimilated into *xOy*, while $\mathbf{n} = \mathbf{i}_z$.

Assume that the field has a transverse electromagnetic (TEM) distribution propagating along the base plane. Then the following cases can be distinguished:

- The case when the base plane *magnetic field* $\mathbf{H}(\mathbf{r})$, with $\mathbf{r} \in B$, is directed along n, the radiator is referred as *magnetic antenna*.
- In the case when the base plane *electric field* $\mathbf{E}(\mathbf{r})$, with $\mathbf{r} \in B$, is directed along $\mathbf{n}$,the radiator is referred as *electric antenna*.
- *Corollary*: If there exists a structure which sustains both $\mathbf{E}(\mathbf{r})$ and $\mathbf{H}(\mathbf{r})$, with $\mathbf{r} \in B$, is directed along $\mathbf{n}$, then the radiator is referred as electric-magnetic antenna.

The above definitions are strictly applied to structures that support propagating-and-non-rezo TEM- field distributions only, so that the waveguide case is automatically excluded by this TEM regard. We note here that the above definition have not taken in to account the diffraction effects at the edges/vertexes/corners of the metallic/dielectric material that constituent the transmitting/receiving aperture.

2.3 Quasi-electric, quasi-magnetic and quasi-electric-magnetic antenna

Quasi-E and Quasi-M antennas: In general, as discussed in previous section, planar antennas can either be assimilated into the class of electric antenna or magnetic antenna. However, most of the cases, particularly in planar antenna configuration, the topology of the radiating apertures may prevent the above-indicated conditions from being rigorously satisfied. Even in such cases, either one or the other of the two situations may prevail, thus correctly determine the type of the antenna. For instant, a radiator for which the magnetic field strength $\mathbf{H}(r)$ or the electric field strength $\mathbf{E}(r)$ is parallel to $\mathbf{n}$ over most of the effective aperture will be denoted as quasi-magnetic antenna, or quasi-electric antenna, respectively.

Obviously, planar antennas fed by microstrip-line or co-planar-waveguide can be classified as quasi-electric or quasi-magnetic antennas, respectively. For example, the RAD-NAV antenna (Tran, et al., 2010) and (Tran, et al., 2007) are quasi-E and quasi-M antenna, respectively.

E-M antenna and Quasi E-M antenna: Now that if there exists antenna which simultaneously support and has both electric and magnetic field perpendicular to the base plane *B*, **r**egarding to the concept outlined in the section 2.2, such an antenna should corollary be *EM-antenna*.

In practice, there could have antenna that itself possesses topology and architecture that only partially gratifies both of conditions asserted in section 2.2, obviously such antenna

should be classified as *quasi-EM antenna*. As will be demonstrated hereby, our proposed prototype falls in the class of quasi-electric magnetic (quasi-EM) antenna.

2.4 Babinet's principle, Booker's formular and Mushiake's relationship

Babinet principle can be used to find complementary impedances (Mushiake, 1996). Babinet's principle states geometrical-optically that when a field behind an infinite screen with an transparent opening is added to the field of a opaque complementary structure, then the sum is equal to the field where there is no screen. Rigorous proof can be found in standard optics or antenna textbooks (Hecht, 2001; Balanis 2005; Stutzman & Thiel, 1997).

Booker extended the Babinet principle to vector electromagnetic fields, with polarization taken into account and derived a useful formula of practical interest for antenna engineers and designers.

$$Z_s Z_d = Z_0^2 / 4 \qquad (4)$$

Where,

- Z_s is impedance of the slot antenna, the magnetic impedance.
- Z_d is the impedance of the electric antenna, i.e the complementary antenna of the corresponding magnetic antenna.
- $Z_0 = 120\pi$ Ohm is the free-space impedance.

Mushiake investigated Booker's formula relation and applied to a class of Self-Complementary Antennas, and found that the antenna's optimum impedance bandwidth is determined by (Mushiake, 1996)

$$Z_{in} = Z_0 / 2 \approx 60\pi\Omega \approx 180\Omega \qquad (5)$$

Where Z_d and Z_S are input impedances of the metal part (electric source) and slot radiating part (magnetic source), and Z_0 is the intrinsic impedance of the media in which the structure is immersed. In practice, Z_s is not only the impedance of the slot, but can be viewed as the complementary impedance (a dipole or loop). A more general definition of intrinsic impedance $Z_0 = \sqrt{(\mu / \varepsilon)}$.

A strip dipole and a slot can be considered as complementary radiators. Booker had shown (Booker, 1946), that the electromagnetic fields of a slot and its complementary dipole are identical excepts that the vibration directions of the electric and magnetic field are interchanged. Both impedance and patterns can be found in the same manner in accordance with the duality property of Maxwell's equation (i.e., interchange E with H, H with -E, ε with μ, and μ with ε)

3. Antenna topology and architecture

The conceptual idea: starts form the Booker's impedance relation between the complementary sources. The starting point in the design of the antenna advocated in this work is the logical selection of the correct topology that could possibly support the requirements discussed in previous section. The topology of the proposed radiator is depicted in Fig.1a. The developed radiator anticipated several advantages of grounded coplanar waveguide (CPWG) topology to create an antenna structure which is capable of either supporting both quasi-E and quasi-M to form a quasi-EM antenna.

3.1 Antenna topology

Topological choice: investigation of Booker's formula and Mushisake's relation, we anticipated that impedance bandwidth of the antenna can be improved by creating a structural topology, which possesses design parameter(s) which can be used to balance the impedances of both of its electric-part and magnetic part. To have that, one has to create or take a topology that inherently posses both electric and magnetic part in the same structure i.e. creating a quasi-EM antenna.

The CPWG is quite suitable for that purpose, as seen in Fig.1, the internal copper part of the CPWG's upper-side-ground can be etched away to form a closed a loop this will function as the magnetic loop antenna (which is *current-driven* by the current along the edge of the loop), while the central signal line is protruded further into the loop to form the electric antenna (which is *voltage-driven* by the applied potential between the stub and the lower ground plane).

The stub is expanded in width and length to form a patch as show in Fig.2. The patch's width and length will be chosen to match the Mushiake's impedance value, as will be detailed in the next section. The CPWG under ground plane form a grounded reflecting plane to make the radiator unidirectional. Another distinct feature of CPWG is that it inherently possesses a mechanism for to prevent mutual coupling, because there is artificial electric conducting plane (AEC) at the edge of the radiator since both ground planes (under and upper) have the same grounded potential when the SMA is connected.

Fig. 1. CPWG topology comprises both electric-source and magnetic-source.

3.2 Antenna architecture

The starting point in the design of the SWB antenna reports in this section is mainly credited to the original radiator (Tran et al.,2009), whose topology is planar, as sketched in Fig.2, with structural topology comprised of following stack-ups:

- Single dielectric layer to provide structural rigidity.
- CPWG topology is chosen as single feeding structure which supports both electric and magnetic radiating part.
- The quasi-M radiating section is formed by etching a slot as show in Fig.1.

- The quasi-E radiating section is formed by modifying the stub (Fig.1) to form a patch as show in Fig.2, The antenna patch is directly connected to the CPW-feeding, together with the ring both magnetic and electric radiating part form a single planar pattern run on top of the structure.

The CPW feeding structure has been chosen because of it well-behaved properties: such as negligible radiation, low loss, the effective dielectric is constant over a sustained wide frequency range, where the later property is more suitable for super-wide-band feeding a SWB-radiator than the micro-strip line (Simons, 2001).
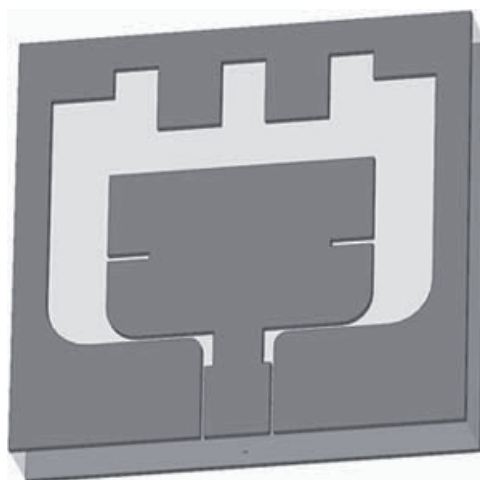
Fig. 2. The proposed architecture based on CPWG Topology

As discussed in pervious section, we strived to create an architecture such that the radiator comprises of both electric and its complementary part to improve the impedance bandwidth. The architecture of Fig.2 advocates the following features: compactness, simplicity, unidirectional, low-dispersion, and ultra-wideband.

Compactness: The antenna is designed in such a way that its outer dimension must comply with the AESA dimensional constraint requirement on grating lobe up to certain degree of steering angle.

Unidirectional radiator: the CPWG topology itself has the base (under) ground plane, this automatically supports and functions as grounded reflecting plane for both of the quasi-electric source (the stub/patch) and quasi-magnetic source (slot inside the ring).

Dispersion control: the right side of Booker's equality (Eq.4) is real, this implies that when perfect complementary takes place the inherent reactance and susceptance (in the left-side of Eq.4) of the quasi-EM radiator must be vanished. This can only be satisfied (up to some degrees of satisfaction) if we could created some parameters to control the current flows on the quasi-E radiator and the slot area of the quasi-M counterpart.

Ultra-wideband: by appropriate balancing the impedances of electric and magnetic part in accordance with the Mushiake's optimum values (Eq.5), wideband matching is feasible.

The proposed radiator's architecture, which is based on the CPWG topology (Fig.1), is shown in Fig.2. Perfect electric conductors (PEC) are situated on both side of the electric slab, the underneath PEC functions as ground plane, while the upper ring side serves two functions both ground and matching. With the different stubs that are visible in Fig.2 being

electrically connected to the waveguide's grounded ring, the employed top centre-signal stubs are extruded down to control (enhance) the current flows along the quasi-E patch antenna, this makes the quasi-E radiator electromagnetic-virtually longer in length, which effectuates the resonance and shifts it to lower frequency.

The structure is kept small for allowing for susceptance matching in the higher segment of the operational frequency band. The notches in the patch physically and electromagnetically force the currents to flow along longer paths, making the patch (virtually) extra longer; this makes it possible to neutralize the reactance in the lower end of the frequency bandwidth. The stubs at the upper-side of the ring are extruded down to form capacitive gaps that provide paths for the flow of the displacement currents. In this manner, more degrees of freedom are created for tuning the antenna at lower frequencies. To manage the match between the patch and feeding section, the carves at the feeding point (the 'neck') of the patch allow a smooth transiston from CPWG to both of the patch and the loop. More details on the design and working principles of this radiator can be found in the original article which discussed the first version of the quasi-EM antenna (Tran et al., 2010)

3.3 Design and material consideration

The propose prototype with topology and architecture depicted in fig.1 and 2. with design dimensions listed in table.1, have been fabricated on Duroid RT 5880 high frequency laminate with substrate height h=5.375 mm, copper cladding thickness t=17µm, relative dielectric constant εr=2.2, electric and magnetic loss tangents are given by tan δ$_E$=0.0009 and tan δ$_H$=0, respectively. The foremost reason of choosing this material is that it could relatively afford SWB frequency range up to 77 GHz (Huang et al., 2008, p.64). Other reasons are assessments related to temperature, moisture, corrosion, stability and missile-proof applications, which were investigated in details and reported by (Brown et al., 1980).
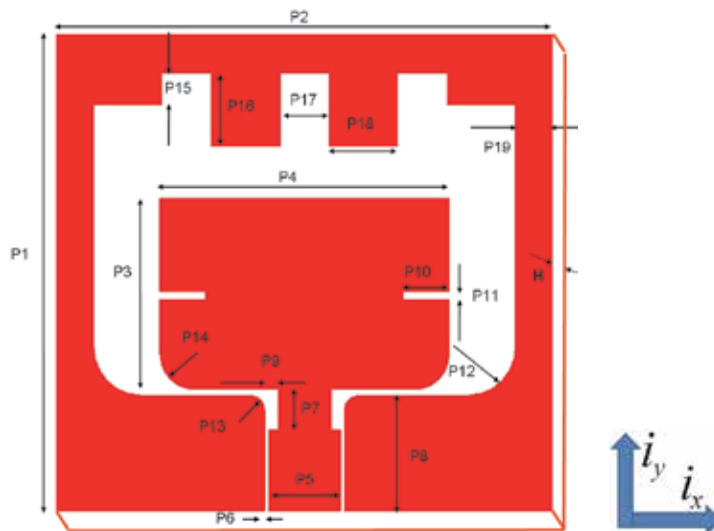
3.4 Antenna design parameters

Fig. 3. The quasi-electric-magnetic antenna: design parameters.

All the cryptic design parameters are shown in Fig.3, Their dimensions (in mm) and their design-functionalities are listed together in table 2.

The antenna is designed to cover both of the X & Ku bands, emphasized on wideband multispectrum-multifunction AESA X-band applications (8-12GHz) and satellite communication (10.95-14.5GHz). The central frequency is taken at centre of the X-band f_C =10 GHz, the maximal dimension is limited to $d_{max} < (1+\sin\theta)^{-1}$, where θ is 60^0, the scanned angle required.

In order to accelerate the optimization process, several parameters are kept fixed, as well as empirically chosen as follows:

a. Antenna-boundary constraint parameters: square radiator is chosen in accordance with technological-tile applied to phased array with dense grid. The nominal values are P1 = P2 = 13.4 mm which is 0.45 λ_C and 0.54 λ_H at 10GHz and 12GHz, respectively.

b. Feeding parameters: the topology of the feeding structure is CWPG, where the interdependent parameters signal width P5 and gap P6 are chosen such that the feeding line is 50 Ω, their nominal dimension are given in table 2. Note: use has been made of the CPWG-feeding-parameters, this interdependent parameter pair (P5, P6) provides a flexibility for controlling the separation of oscillation positions at the transition between the feed and the patch, note that the two oscillation points are chosen wide enough to dispread the currents flow on the electric-patch and are attracted by the two inner stubs on the upper side of the ring.

Par	Dim.	Description	Define/ Create/ Control
P1	13.4	ant. length	Fund. resonance / modif
P2	13.4	ant. Width	Shifting/moving the resonance
P3	4.95	patch length	Shifting/matching the resonance
P4	7.81	patch width	Matching/balancing the resonance
P5	1.94	sig. width	Impedance paired with P6
P6	.102	gap width	Fixed, Impedance paired with P5
P7	.9	carve length	Transformer length
P8	3	feed length	n.a.
P9	.25	carve depth	Transformer match
P10	1.86	notch length	Shifting BW
P11	.21	notch width	Match BW L/R
P12	1	slot mitered	Field matching / shaping
P13	.5	CPWG mitered	Imp. transform / match
P14	1	stub mitered	field matching / shaping
P15	.84	stub length	Ind. tuning /match
P16	1.9	stub length	Cap. tuning /match
P17	1.33	Separation	Adjusting /shifting resonace
P18	1.86	stub width	Cap./ Ind. balance
P19	1	ring width	Mutual coupling
H	5.537	Substrate height	RT5880, ε_r=2.2; tanδ=0.0009, cladding ½ oz

Table 2. Design parameters (in mm) and their functions

c. The ring width P19 plays an important role in preventing coupling effect causes by lateral wave and space wave, in general the wider the ring the lower (i.e better) the mutual coupling. However, we are limited by the size constraint in scanned array (as discussed in a), also we can not extend the width of the ring inwards because that will decrease the magnetic area and disturb the balance between the electric and magnetic impedance balance. 1mm is the widest we are tolerated to have in this design.

d. The carving parameter P9 add an extra parameter mechanism for fine tuning the mating between the feeding line to the electric patch, the boundary for this parameter is from 0 to 0.25% of P5's nominal value.

e. Blending edge parameters P12 & P14: these have negligible on impedance bandwidth but smoothing them will prevent the cross-polarization due to the diffraction of the two perpendicular edges both on the ring and the patch, we took an empirical value of 1mm.

f. The fixed inner width of the slot (P2 - 2xP19), on this upper ring we place four stubs with equally width P18, their inter distance is balanced by same distance P17.

g. Outer stubs are implemented to control the area of the quasi-M radiator, whilst the two inner-stubs are for controlling the electrical length of the quasi-E radiator. The idea of introducing the outer stubs with protruding parameter P15 on the top corners of the ring are not only for balanced matching the impedance of the quasi-E (patch) to that of the quasi-M (slot), but "also" for controlling the radiation patterns of the slot.

h. Patch: the patch is a rectangular patch with under-corners blended (see *e*), the patch width P4 and length P3 will determine the resonances of the quasi-E radiator, in order to shift the resonance to the lower frequency region (and also keeping the balance between the E and the M-radiator) the two inner stubs are extruded downward to provide a GND potential close to the top of the patch which attracts the currents on flowing upward instead of sideward, this virtual extends as of the patch is electromagnetically longer. The two side notches of the patch are introduced to push the current flows more parallel along the resonance length of the electric radiator.

Optimized values are listed in table 2, all the dimension are in mm, also short description of their functions are included in the same table. Since the proposed radiator comprised of two quasi actuators (E,M), which share the same compact structure all the parameters influence both of the radiators, however depending on their position their influences will be predominant to E or M radiators.

4. Parameter identification, investigation and optimization

With the many design parameters possessed by our proposed prototype, global multivariate-optimization is possibly impossible. In dealing with structure with such many parameters, all the design parameters of the proposed architecture, each indeed has different influential magnitude on certain aspects of the radiator's overall performance. *Optimization*: in dealing with the many parameters as this architecture exhibited, We strived to reduce them by singling out the critical design parameters, by closely inspection of the parameters, they can be gratified into two groups based on their main functional-effect, that are resonance-matching parameters and resonance-shifting parameters
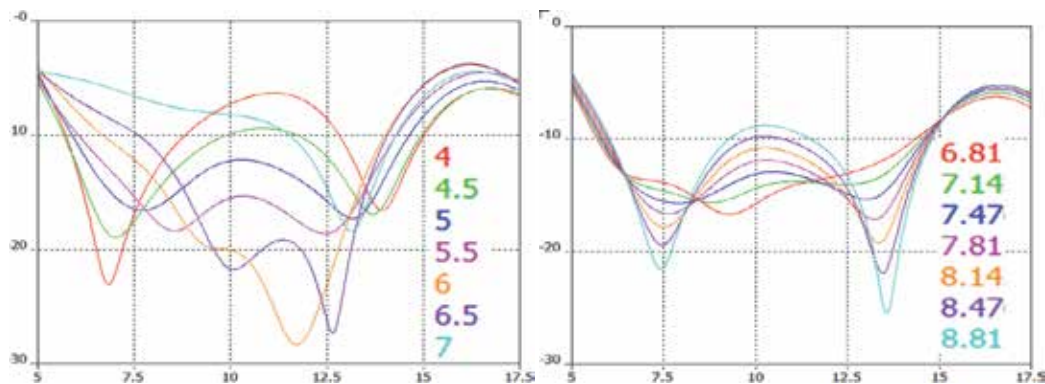
Fig. 4. Parametric investigation: a) effects of the path length P3; b) effects of the patch width P4

The microstrip patch antenna inside the slot, functionally acts as an embedded quasi-E antenna. Conventional design rules for MPA is exploited and used as start values for both parameter sweeping and optimization process. As usual the length P3 of the patch set the resonance frequency (the longer the patch the lower the resonance frequency), It is noted that the length of the patch is extended by the inner stubs, this effects is used to control/create the lower resonance, these effects are plotted in Fig.4a. The patch width P4 provide the balance-match the impedance bandwidth, the effect of P4 is clearly seen in Fig.4b. Since the right hand side of the Babinet-Booker impedance relation is a constant, and a optimum value of 180 Ohm was found by Mushiake (Eq.5), we need to control only one impedance (either electric or magnetic part), the other will result automatically. Since Z_D can be decreased by increasing the width P4 of the patch, this is acceptable as far as the ratio of P4/P3 does not exceed 2.
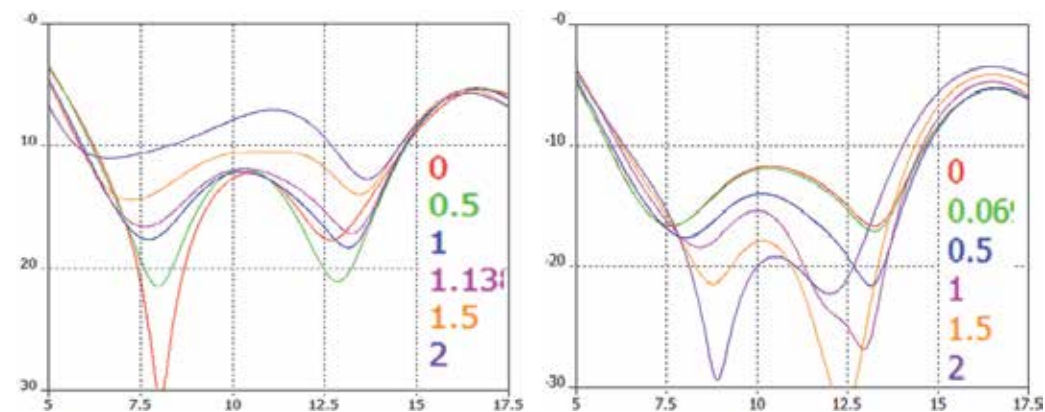
Fig. 5. Parametric investigation: a) effects of the inner-stub P16; b) effects of the outer-stub P15

In our architecture, we are not allowed to vary the width P4 freely because that will disturb the impedance balance between the magnetic and the electric parts, the only way to set the resonance is, first, to sweep the length parameter P3, we see that in contrast with traditional design, the length (instead of the width) is used to set the resonances, the low-resonance is

controlled by shortening the length P3, whilst high-resonance is by lengthening it (as shown in Fig.4a). The impedance bandwidth is balanced by limitedly sweeping the width parameter P4, we saw that P4 has no shifting-function on both low and high resonances but only just balancing them.

Fig.5a and 5b showed the effects of virtually varying the electrical length of the quasi-E, and the magnetic-area of the quasi-M by varying the two inner-stubs P16 and outer-stubs P15, respectively. The electric-effects of the inner stubs P16 are anticipated to control the low resonance (Fig.5a) while the magnetic-effects of the outer stubs P17 are for the higher resonance (Fig.5b). P16 and P15 demonstrated strong influences both on matching the resonances and balancing them as well but with marginal shifting-functionality.
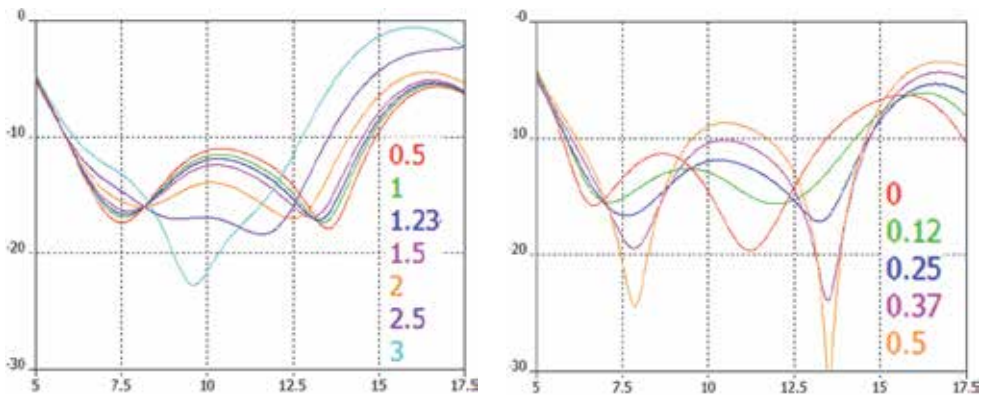
Fig. 6. Parametric investigation: a) effects of the notch length P10; b) effects of the carving P9.

The notch length P10 is another parameter which can be used to control the electrical path length of the quasi-E radiator, and to pull down the hump at mid-band, balancing the resonance, and widening/narrowing the bandwidth as clearly shown in Fig.6a. The carving parameter P9 can be utilized to enhance the resonance matching, to widen the bandwidth, the effectuated usages of this parameter is not totally exploited but clearly displayed in Fig.6b. Note that this parameter also demonstrated its potential of creating multiband radiator, which can be seen by closely inspection of Fig.6b.
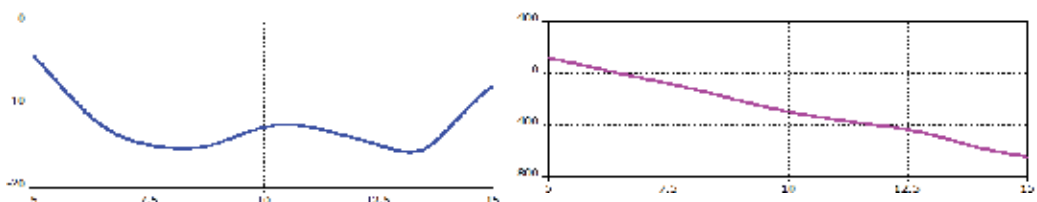

Fig. 7. a) balanced reflection coefficient; b) perfect linear phase of reflection spectrum

Fig.7a shows the reflection coefficient (S11). It is optimized such that all strong and deep resonances are merged or faded out, in this manner, as a result, we have

- Obtained a unidirectional-radiator with the widest impedance bandwidth ever recorded on a single substrate layer (over 100% percent BW), as shown in Fig.7a.

- Obtained an equally-flat power delivery to the radiator in the dedicated band.
- Achieved a nearly perfect linear phase, Fig.7 b demonstrated an excellent linear phase which covers the whole designated X to Ku bandwidth
- Limited the dispersive of the group delay to the lowest level ever designed (Fig.8a), this figure displayed a smooth and negligible group delay of sub-nanosecond level as shown in the plot with magnified scale of Fig.8b.
- The X-band transmission efficiency of the radiator is over 94%, with constant, flat power-delivery and low inband-deviation of only 0.1dB (Fig. 9).
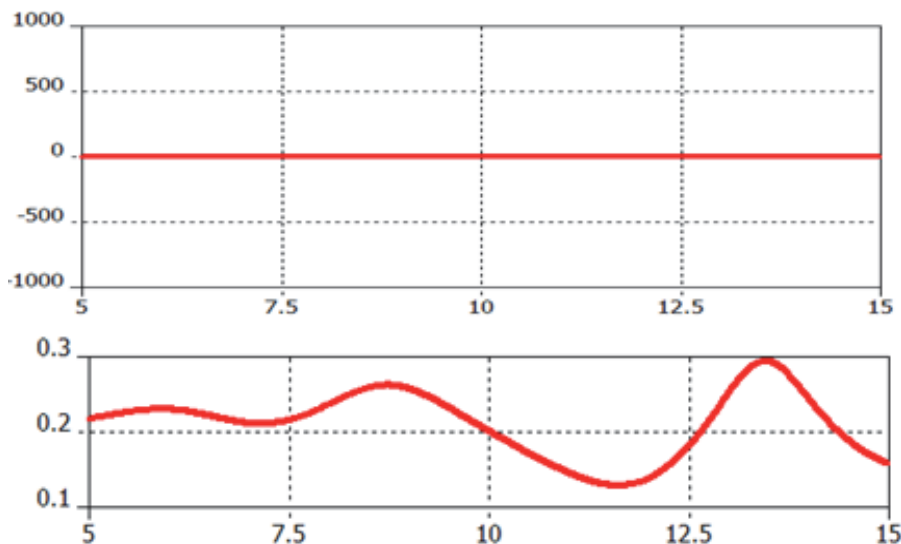
Fig. 8. a) Perfect group delay, b) magnification in sub-nanosecond scale
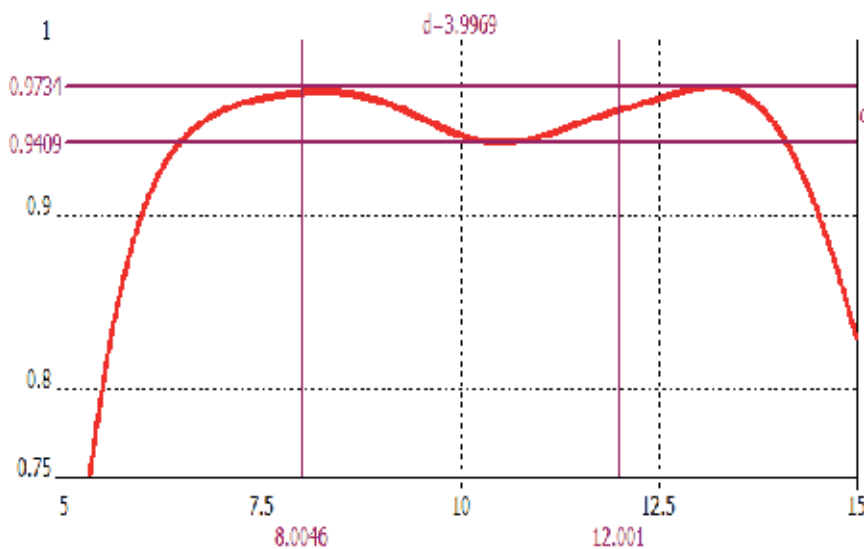
Fig. 9. Constant and high transmission power effciency; inband-deviation only 0.1dB

5. Transmission efficiency

In system point of view, regardless of narrowband or ultra-wideband, the antenna's transmission efficiency η_{TRAN} is the *most* vital parameter for gauging the effectiveness of the radiator (Wu et al., 2003). Taking the *transmitting mode* as investigation case (the *receiving mode* is equally valid by reciprocity theorem).

$$\eta_{trans,NB} = 1 - |S_{11}|^2 \tag{6}$$

$$\eta_{trans,UBW} = \frac{\int_0^\infty P_{in}(f)(1-|S_{11}(f)|^2)\,df}{\int_0^\infty P_{in}(f)\,df} \tag{7}$$

For narrowband Eq.6 is the standard norm for gratifying the performance of the applied radiators/devices/systems. This equation is valid by assuming that $|S_{11}|$ is constant over the designed signal bandwidth, and as was discussed and shown in table.1, MSAs have all criteria for the equation to be applied. For UWBAs however, the return loss $|S_{11}(f)|$ is naturally a function of frequency, for accurate determination of the transmission efficiency, one have to integrate over the frequency band to account for all the dispersion variation in the designed band in accordance with Eq. 7.

The proposed DUWB radiator is ultra-wideband, however, because its return-loss $|S_{11}|$ is nearly constant over the designated band, as discussed in previous section, without loss of generation the term $(1-|S_{11}|^2)$ can be take out of the integration sign, and as a result the UWB transmission efficiency formula (Eq.7) is reduced to narrowband one (Eq.6); In other words the narrowband transmission efficiency equation (Eq.6) is exceptionally applicable to our proposed radiator despite the contrary fact that our proposed radiator is an UWB radiator. the transmission efficiency of the proposed DUWB radiator is calculated and shown in Fig.9.

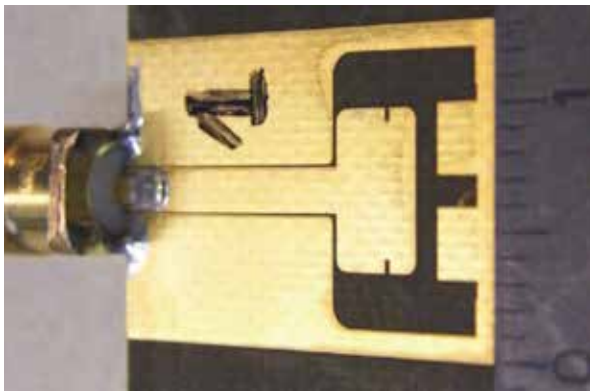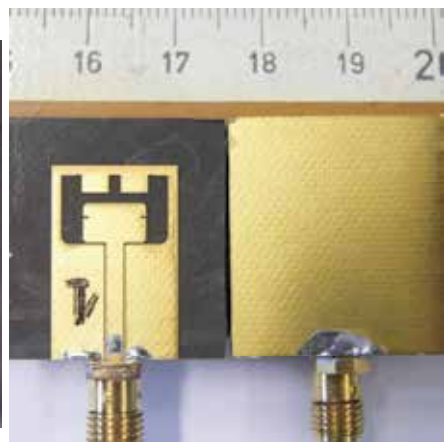## 6. Physical implementation of the prototype

Fig. 10. Prototype with TAB-SMA connector.   b) Front and back, dimensions in mm

The optimized design discussed in Section 3 was designed and based on CPWG topology
and to be realized in PCB technology. In an initial phase, the optimum physical
implementation replicated the configuration resulting from the optimization process (see
table 2). However, for feeding the antenna in practice, a sub-miniature SMA connector was
used. We experienced that (Tanyer et al. 2009): 1) the close proximity of the comparatively
large connector as well as 2) the alteration of the coplanar waveguide's profile due to the
soldering had a detrimental impact on the reflection-coefficient performance and on the
radiation patterns. As concerns the radiation patterns, experiments (Tanyer, ibid.) have
shown strong perturbations due to the diffraction and the scattering from the standard SMA
connector, which had dimensions that were comparable with the antenna itself. To
counteract these adverse features, the coplanar-waveguide line was extended by an
additional 10mm-long section. This resulted in a twofold beneficial effects: i) making it
possible to perform a time-domain de-embedding in the reflection coefficient
measurements, and ii) creating the possibility to cover the SMA connector with an absorber
during the pattern measurements, without affecting the antenna itself. The total coplanar
waveguide length then became LF = 13 +10 =23 mm. This choice was made by assuming
that the additional transmission line did not result in a noticeable increase in the feed-line
losses (Tran et al., 2011), while allowing the feeding section to be covered by absorbing
material during the radiation-pattern measurements. Eccosorb HR (from Emerson &
Cuming microwave products) was used for this purpose. From the data sheet, the
maximum reflectivity of the material was -20 dB.

The proposed DUWB radiator is a quasi-EM antenna, its topology and architecture are
created on a *planar-basis* (the base plane *B* defined in section 2.2) with mutual impedance
balanced between the quasi-E and the quasi-M counterpart. Now by attaching the SMA to it,
the SMA's flange (which is perpendicular to *B*) will immediately disturb the E-M balance of
the radiator, because the flange of the SMA-connector acts as an erected reflecting plane
which reflects the field of the magnetic part of the quasi-em radiator. The practical prototype
of the proposed quasi-EM DUWB has been redesigned, where the effect of the SMA's flange
is also taken into account, as shown in Fig.10a.

6.1 Impedance bandwidth simulation and measurement results

To include the disturb contribution of the SMA-connector and the elongation of the CPWG-
feed, the prototype are re-optimized and modified as shown by the photograph in Fig.10a.
Front ground plane (ring) and back ground plane is made equi-potential via the SMA
common-ground as shown by photograph in fig.10b.

Fig.11a compared the calculated and the measured results of the reflection coefficients in
full-spectrum of our equipment's capability, good agreement between the calculated and
measured result is obtained.

Inspection of the zoom-in plot (Fig. 11b) we see that the prototype measured result covered
an impedance bandwidth larger than 100 percent, to our knowledge this is the widest
impedance bandwidth ever recorded for a planar, single layer, unidirectional broadside
microstrip patch antenna, further more the structure also possessed several usable spectra
with deep match at Ka and Q-band.

The measured results have, as a proof-of-concept, demonstrated the feasibility of the
introduced concept and technique for bandwidth enhancement as well as controlling other
EM-characteristics of the radiator. Nevertheless, the investigation of the proposed prototype

is by no means exhausted the potential of this radiator, inspection of figure 11.a, we anticipate that by careful design and re-optimization of the architecture it is possible to have a unidirectional UWB broadside antenna which could match more closely to the frequency independent impedance bandwidth as predicted 65 years ago by Babinet-Booker formula (Eq.4).
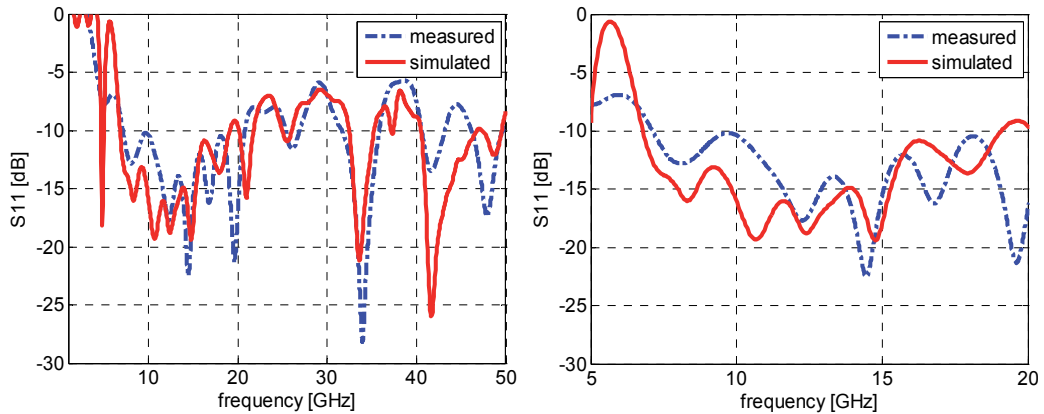

Fig. 11. a) S11 computed vs. measured in full spectrum, b) S11: complete X and Ku coverage
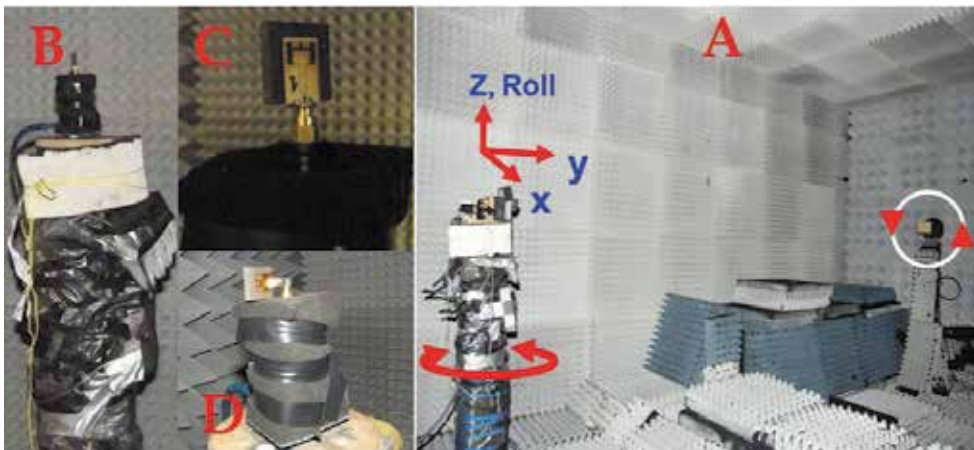
6.2 Farfield measurement set up

Fig. 12. Patterns measurement set up: a) anechoic chamber DUCAT, b) AUT on the rotatable column, c) Vertical configuration and, d) Horizontal configuration.

Anechoic chamber:
the far field radiation patterns are measured in the Delft University Chamber for Antenna Test (DUCAT); the anechoic chamber DUCAT (Fig.12a) is fully screened, its walls, floor and ceiling are shielded with quality copper plate of 0.4 mm thick. All these aimed to create a Faraday cage of internal dimension of 6 x 3.5 x 3.5 m³, which will prevent any external signal from entering the chamber and interfering with the measurements. The shielding of the chamber is for frequencies above 2 GHz up to 18 GHz at least 120 dB all around

A Novel Directive, Dispersion-Free UWB Radiator with Superb
EM-Characteristics for Multiband/Multifunction Radar Applications

371

(Ligthart, 2006). All sides are covered with Pressey PFT-18 and PFT-6 absorbers for the small walls and long walls, respectively. It is found that one side reflects less than -36 dB. All these measures were taken together in order to provide sufficient shielding from other radiation coming from high power marine radars in the nearby areas.

TX:

Single polarization standard horn is used as transmitter (Fig.12a), which can rotate in yaw-y-direction to provide V, H polarizations and all possible slant polarizations. The choice of the single polarization horn above the dual polarization one as calibrator is two-folds: 1) keeps the unwanted cross-polarization to the lowest possible level, 2) and also voids the phase center interference and keeps the phase center deviation to the lowest level.

RX:

Prototype is put as antenna under test (AUT) on the roll-z-rotatable column (Fig.12b). For the measurements of polarimetric components (VV, HV, VH, HH, the first letter denotes transmission's polarization state, the second is for the reception).

Calibration:

The HF-ranges of the Sucoflex-cable, T-adapters and connectors used in this measurement set up all catalogued as 18GHz max, owing to this limitation, we calibrated the PNA with Agilent N4691B cal-kit (1-26GHz).

Configuration setup:

*T*wo measurement setups are configured: i) the vertical reception setup (VRS, Fig.12c) for the receptions of co and cross polarization patterns VV and VH, respectively; ii) the horizontal reception setup (HRS, Fig.12d) for co and cross polarization patterns HH and HV, respectively. Combination of the two spatial reception states (VRS and HRS) with the two polarization states (V,H) is sufficient in providing full polarimetric characterization for the DUT.

6.3 Co-polar radiation patterns (VV) measured with VRS-configuration set-up

The co-polar pattern measurements are carried in the anechoic-chamber DUCAT, Full calibrated spectrum is plotted in Fig.13, typical zoom-in spectra are plotted in Fig.14.
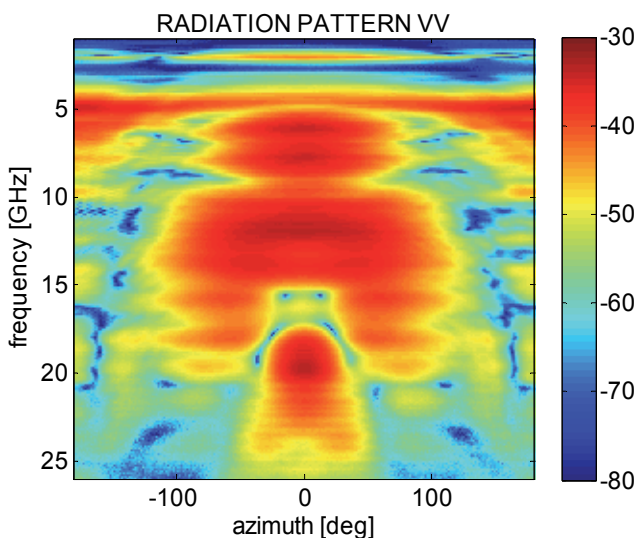

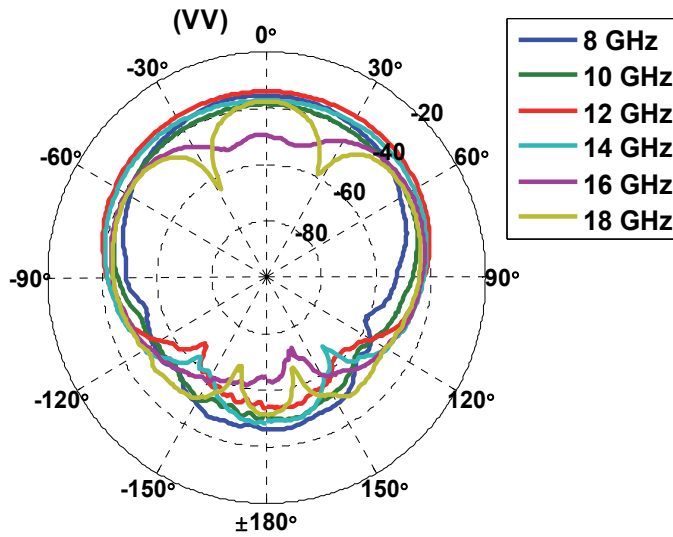Fig. 13. Measured results: full spectrum Co-polar (VV) radiation patterns

Fig. 14. in-band spectra: stable, symmetrical and repeatable co-polar (VV) uni-directional radiation patterns

As show in both plots, the measured in-band co-polar radiation patterns pertain a perfect symmetry and repeatable in the designated spectrum, this suggests the wideband utilization of this antenna (a UWB antenna is usable if and only if both of its impedance bandwidth and patterns are usable).

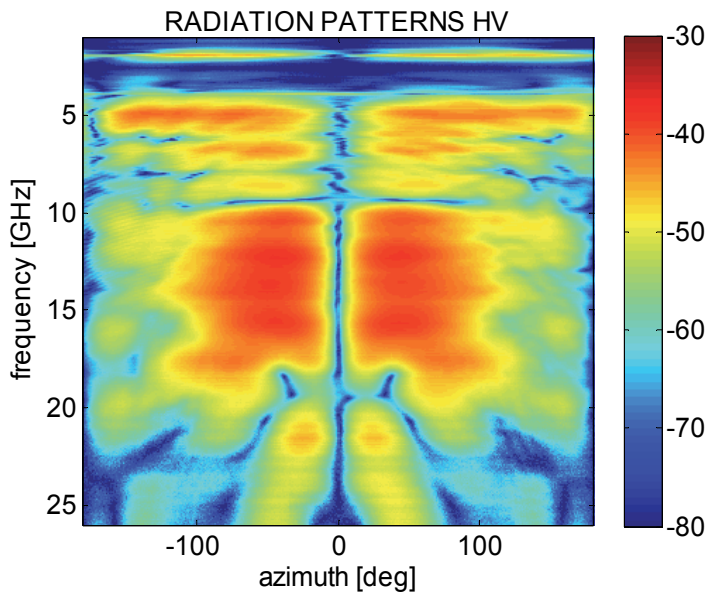## 6.4 Cross polar radiation patterns (HV) measured with VRS-configuration set-up

Fig. 15. Measured results: full spectrum Co-polar (HV) radiation patterns
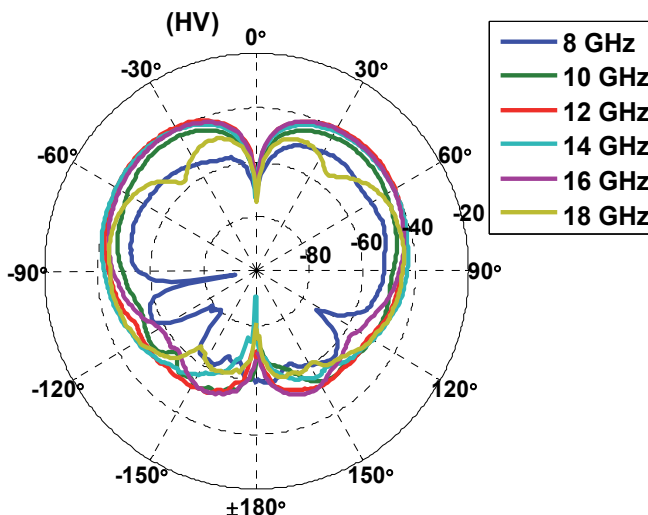
Fig. 16. in-band spectra: stable, symmetrical and repeatable Butterfly–shape of cx-polar(HV) patterns.

The cross-polar patterns measured with VRS configuration. Full spectrum results are plotted in Fig.15, typical zoom-in spectra are plotted in Fig.16. Typical symmetrical butterfly shape of cross polar patterns with exact deep centre as low as -75 dB are measured.

6.5 Co and cross polarization patterns measured with HRS-configuration set-up
For the HRS configuration, the co-polar and cross-polar patterns are measured and plotted in Fig.17a and 17b, respectively. The symmetry is lost in this HRS configuration (Fig.12d) due to the connector, the radiator's ground plane and the mounting column's back-cable (Fig.12b). Nevertheless, the measured patterns are repeatable, and usable as shown.
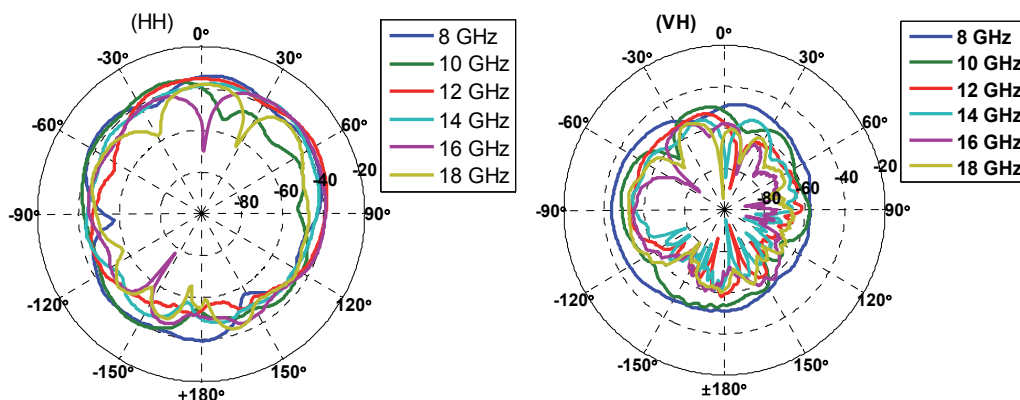

Fig. 17. in-band radiation patterns, a) Co-polar (HH) patterns, b) Cx-patterns (HV)

6.6 In-band co- and cross-polar radiation patterns discussions
The measures co-polar and the cross-polar plotted of the VRS are plotted in rectangular coordinated (Fig.18a &b), which reveal more excellent details which are not observable in
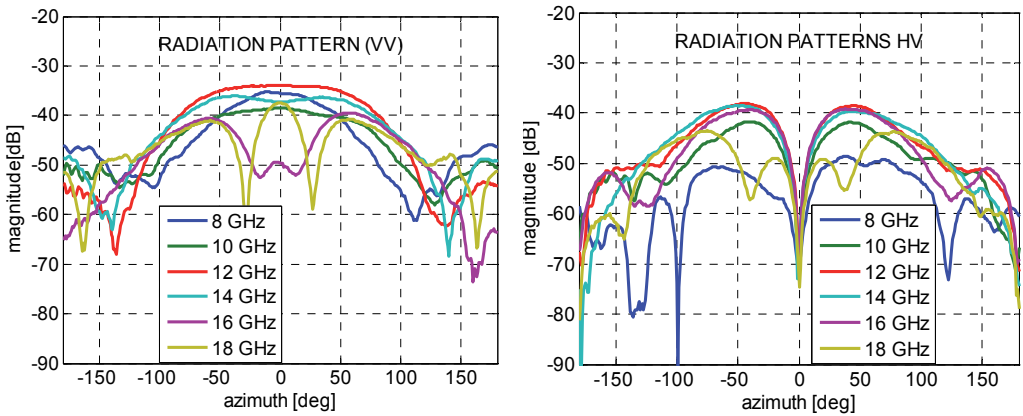
Fig. 18. Constant gain, non-squint co-polar pattern in designed band, VV-case

Constant, extremely low cx-polarization (HV) in the designed band
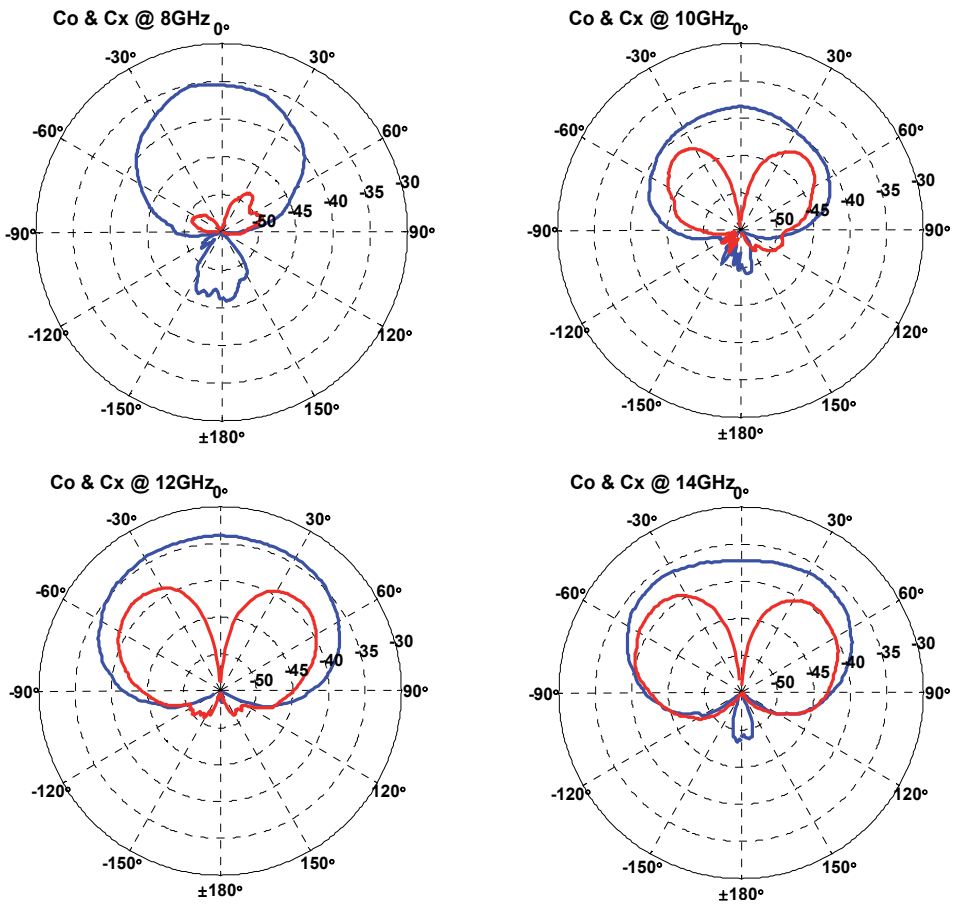

Fig. 19. Typical zoom-in Co-polar (VV) and cx-polar (HV) radiation patterns in the designed band

polar coordinated. This plots displayed: 1) repeatable patterns, 2) minimum front-to-back ratio in all case is >16dB , this value is remarkable for this small size antenna, 3) the patterns come closely to the ideal Silver's theoretical radiator, which guaranties having effectively coverage over the upper hemisphere. 4) the cross-polarization patterns were perfectly symmetric and all have an extremely deep about -75db exactly pointed at broadside of the radiator, this distinct property is possibly the most important requirement for all applications which require extremely high sensitive, accurate sensing and truly 4D space-time information of scatterers, (distance, angle , height, DOA and Doppler).

The measured in-band radiation patterns for 8, 10, 12, 14 GHZ are plotted in Fig.19 a, b, c and d, respectively. The data plotted were raw-power data which are intentionally not normalized. Inspection of the plots, we learn following distinct features of the proposed prototype:

- The radiator is undoubtedly a broadside unidirectional radiator.
- The gain is stable and constant over the designated band.
- The patterns are stable and come very close to the ideal Silver's $\cos \theta^n$ which is very difficult realized in practice.
- The radiator has practically negligible back-lobes, the plots realistically showed very high front to back ratio (FBR), remarkably at 12GHz (where no back-lobe is observed) the FBR at this frequency interpreted a surreal high FBR number, however, it is de facto true measured results.
- The cross-polarization patterns were also very low and exhibit a clear deepest patterns exactly at the pointing direction of the co-polar pattern, this indicated that the polarization purity of this radiator is extremely high, again with number close-to 40dB of cross-polar discrimination (XPD) realized with patch antenna, and in such a UWB bandwidth, is quite unique and unparalleled results. This remarkable property proved that the radiator is very suitable for applications which require extremely high accuracy in sensing, screening or ranging.
- The non-quint radiation patterns over and UWB bandwidth indicated that this prototype will provide accurate bearing resolution and DOA in both short range and long range radar applications.

6.7 Time domain measurements

Fig. 20 shows time-domain setup for measurement and evaluation of: 1) pulse deformation, 2) the semi-omni-radiation characteristics of the AUT. The same prototype is used for TX (left) and RX (right), they both stood on a horizontal foam bar which situated 1.20m above the floor.

6.7.1 Pulse transmission measurements in time domain

Pulse spreading and deformation: Fig.21 showed the time-synchronization between the measured receive pulses (MRP) at three representative angles, qualitative inspection showed that the synchronization-timing the received pulses is very good, there is no pulse spreading took place, these measured features proved that the device is suitable for accurate ranging/ sensing-applications, the small deviation at the beginning of the received pulse is due to RF-leakage (Agilent, AN1287-12, p.38), and at the end of the received pulse are from environments and late-time returns (Agilent, ibid., p.38), Note that the measurements are carried out in true EM-polluted environment as shows in Fig.20, and no gating applied.
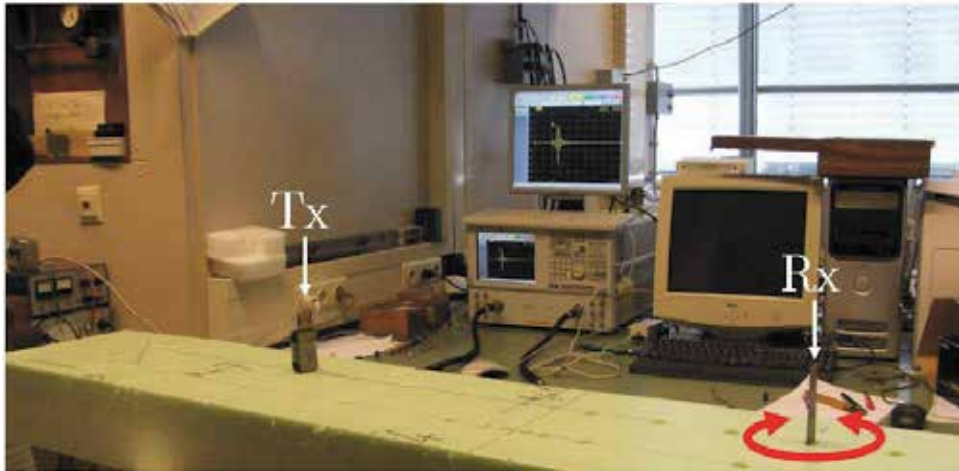
Fig. 20. Time domain measurement setups for co-polar (VV); equipment: Agilent VNA, E8364B; Calibration kit: Agilent N4691B, calibrated method: 2-port 3.5 mm, TRL (SOLT), 300 KHz – 26 GHz.

Uni-directional radiation characteristics: to correctly evaluate the directional property of the AUT, both quantitative characteristics (spatial) and qualitative characteristics (temporal) are carried out, the spatial-properties of prototype are already tested and evaluated in frequency-domain (depicted in Fig.12), and only the temporal-characteristic is left to be evaluated. To evaluated temporal-radiation characteristics, three principal cuts are sufficiently represent the temporal-radiation characteristics of the AUT in the time domain. Due to the editorial limitation, we report here only the most representative case (uni-directional in the azimuthal plane, i.e. co-polar VRS, which represents the most of all realistic reception scenarios, as shown in Fig.20). Fig.21 shows three MRPs of the measurement configuration pictured in Fig.20 with RX 0^0, 45^0, and 90^0 rotated. The results show a perfectly identical in timing, there is no time–deviation or spreading detected between the three cases. Furthermore, although the radiator is planar and unidirectional, it still exhibits a remarkable azimuthal independent property of 3D-symmetric radiators (for the 90^0 configuration, the projection of the receiving aperture vanished, however the prototype still able to receive 60% power as compare to the face-to-face case), this TD-measure results pertained the $\cos \theta$-directional property of the radiator, and this is also in agreement with, and as well consolidate the validity of the measured results carried out in the FD-measurement setup.

6.7.2 Transmission dispersion characterization
To evaluate the amplitude spectral dispersion of the prototype, the measured time-domain transmission scattering coefficients of the three co-polar configurations (0^0, 45^0, and 90^0 configurations displayed in Fig.21) were Fourier-transformed in to frequency domain. The measured magnitudes are plotted in Fig.22a, the measured results show a smooth and flat amplitude distribution in the designated band, and all are lower than -42dBm.
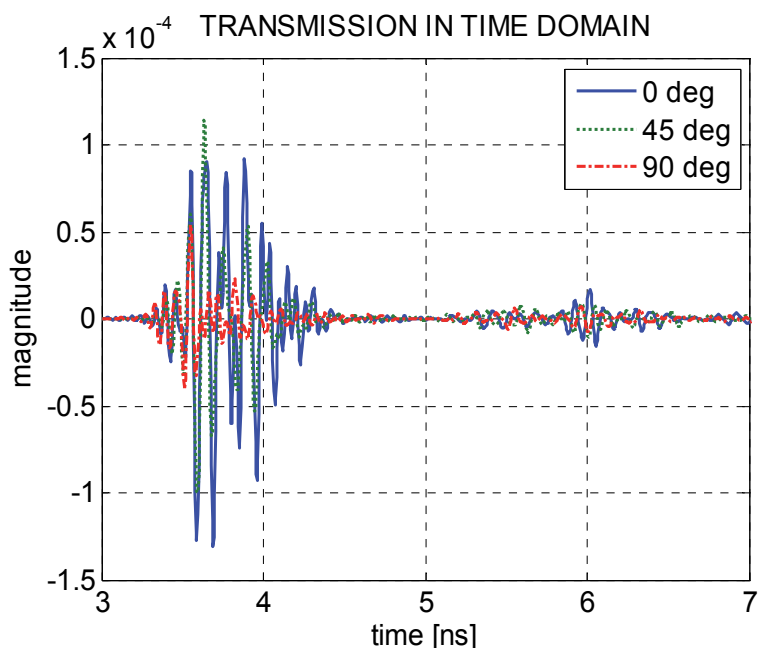
Fig. 21. Time domain measurement setups, equipment: Agilent VNA E8364B; Calibration
kit: Agilent N4691B, calibrated method: 2-port 3.5 mm, TRL (SOLT)

6.7.3 Transmission phase delay and group delay

Group-delay is an important gauge by which the highest sensitivity/accuracy of sensors are
judged, particularly for sensors/systems which implements phase referencing
mode/coherent detection for applications in space geodesy, absolute astronomy (Petrov et
al., 2010) and in sensors with independent beam steering for multiple beam applications
(Yaron et al., 2010). Low group delay is critical for quint-free operations of the beam-former,
preventing lost of tracking and miss-hit, etc.

The measured phase responses of the transmission parameter S_{21} for the three co-polar
configurations are plotted in Fig. 22. In narrowband technology, the metric for judging the
quality of transmission is the phase-delay, define as $\tau_P = -\theta/\omega$, which is the phase delay
between the input and output signals of the system at a given frequency. In wideband
technology, however, group delay is a more precise and useful measure of phase linearity of
the phase response (Chen, 2007). The transmission group delays for the three above-
mentioned configurations are plotted in Fig. 22c. The plots show a flat, stable and negligible
variation in group delays in order of sub-nanosecond. The group delays in broadside
direction, representative here with RX 0^0, 45^0 rotated, shown almost *identical group delays*
(this guaranties for quint-free wide-scan operations of the designate band; this is no surprise
because the phase responses of the prototype are almost linear (Fig.22b), thus the group
delay, which is defined as the slope of the phase with respect to frequency $\tau_G = -d\theta/d\omega$,
resulted accordingly. Note: although the group delay (Fig.22c) is mathematically defined as

a constituent directly related to the phase, but it was impossible to visually observe directly from the phase plot (Fig.22a), but well from the magnitude plot (Fig.22a).
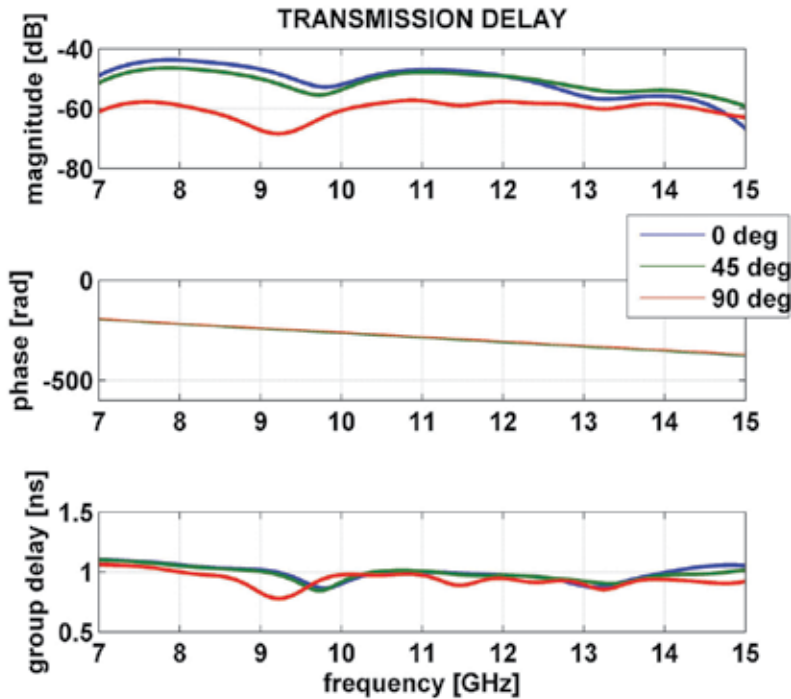

Fig. 22. Transmission dispersion characterization: a) Transmission magnitude, b) Transmission phase, c) Transmission group delay.

7. Acknowledgement

8. Conclusions

In this chapter the top side antennas dilemma and impasses are addressed, the logical solution to this problem is the shift from phased array to active electronic scanned array, key aspects relating to this shift are discussed; the state of the art, trends and activities on wideband-multiband-multifunction AESA is summarized; existing radiators and methods

as well as techniques for creating wideband and unidirectional radiators are convened and reviewed; their advantages and disadvantages are discussed and summarized.

The logical shift in phased array technology to multiband multifunction active electronic scanned array put stringent demands on the applicable radiator. The AESA-applicability implies that the radiator must be unidirectional, small size in array plane and compact in volume. The AESA functional performance required that the radiator must be wideband, linear phase, negligible group delay, low cross polar patterns, accurate pattern heading, stable phase center in the whole covering band.

To comply with these stringent demands, a novel quasi electric-magnetic ultra wideband is proposed; it is designed to comprise all the merits and to eliminate all the demerits of the MPA, SMPA and UWB antennas. The proposed DUWB pertains the linear phase, compactness, low cross-polarization of the MPA, possesses the directional property of the MPA and the SMPA, and has as ultra wideband as common UWB antennas. The prosed antenna's topological structure is simple and its architecture is easy to realize with low cost PCB technology.

Concepts and ideas

Our intent message is not the performances of the proposed prototype but heavily weights on the concepts, the design methodology, and the process of identification of the critical design parameters which are the objectives that we report in this chapter.

- The ideal electric antenna, magnetic antenna are wholly revisited, and the electric-magnetic antenna is corollary added for completeness.
- The concept of quasi electric, quasi magnetic are revisited, and their propositional concept of quasi electric-magnetic antenna is extended to complete the set.
- The main driven idea led to the design of this DUWB radiator is anticipated from the self-complementary principle stated by Babinet-Booker's principle.
- The Babinet-Booker's frequency-independent impedance relation, together with the Mushiake's optimum impedance, are ultimately and functionally applied to the design of the proposed DUWB radiator.
- Distinct concepts and definitions scattered in literature are collected, defused, arranged and systematically and correctly applied to antenna design.
- The concepts 1-4 above led to the quest for a specific topology and architecture that supports the self-complementary principle and hence the frequency-independent (wideband) property.

Methodologies and implementations

- Topology: the CPWG has been chosen for the realization of comprised quasi electric–magnetic radiator.
- Architecture: By forcing the overall dimension of the radiator fixed, the created topology and architecture kept the impedances of the magnetic and electric parts mutual related in accordance with the Babinet-Booker impedance relation. The current-driven quasi-magnetic radiator is formed by the top grounded-ring (i.e circumscribing the quasi-electric radiator also by this ring). By this doing the voltage-driven quasi-electric radiator is automatically embedded inside its complementary counter-part.
- Engineering: several design parameters are created to control the quasi electric-magnetic properties of the proposed radiator, the effects of these design parameters are characterized and analyzed.

- Parameter identification and optimization: Since the E- and M-radiator are imbedded in the same architectural radiator. We observed that any parameter varying of electric (or magnetic) will automatically effectuate it complementary magnetic (or electric) part, so the process of optimization can be reduced by optimization (sweeping) the critical design parameter in identified priority order. We identified the critical design parameters and report their priority herewith: the patch length P3, the patch width P4, the inners tubs P16, the outer stubs P15, the notch length P10, the carves P9; The investigation of other parameters is by no means exhausted, they have their own meaning and functionalities in fine-tuning the performance of the quasi-em radiator, however they effectuated only marginally as compare to the critical ones previously listed and discussed.
- Although the prototype comprised a simplest structure and shape, however superior UWB impedance bandwidth is achieved and stable UWB-patterns are uniquely preserved. This structure, although, can be modified to obtain huge frequency bandwidth, but cannot be one-size-fit-all for gain-size requirement. However, the architecture is flexible enough for scaling up/down its dimensions to match customer's gain-size requirements and applications.

Results

As a proof of concept, a quasi electric-magnetic, planar, unidirectional, broadside UWB prototype is designed, fabricated. Performance of the prototype are tested and evaluated. Good agreements between numerical predictions and measurements are obtained, we reported and demonstrated herby with following results:

- A DUWB radiator comprises all the goods but avoids the bads of the MPAs, SMPAs and the UWBAs has been realized
- The first unidirectional broadside radiator effectively comprised both electric and it complementary part in one *planar* structure, and functionally and partly proved the frequency-independent property stated by Babinet, Booker and Mushiake.
- Minaturization: single dielectric layer, compact with voluminous dimension: 13.4 x 13.4 x 5.537 mm^3. With this size the radiator is small enough for X-phased array applications; no grating lobe will theoretically appear for scanning up to 60° for the whole X-band.
- The "bandwidth and antenna size are inversely related" has been ultimately optimized, the advocated antenna is possibly the one which posses the largest "form factor" to date (BDR: BW(100%)-over-Dimension(13x13mm^2) Ratio)
- UWB: A planar low-profiles (5mm), non-floating ground radiator with performance of over 100% percent bandwidth ever designed, for full coverage of the designated X & Ku band , this being the widest ever obtained with single substrate MPA and perhaps, the widest ever published for a unidirectional broadside patch radiator.
- The prototype possessed all properties required for wide multiband multifunction AESA applications such as: unidirectional, wideband, balanced and flat complex reflection power spectrum, high efficiency, non-squint heading, phase linearity, low dispersion (negligible group delay), polarization purity, low cross polarization, stable phase center, compact and finally the planar and broadside topology make the proposed radiator very attractive for technological-tile which is a critical requirement for dense implementation and integration of radiator with T/R module together with the associated controls and calibrated circuitries.

- Pattern stability: Repeatable patterns in full X-band spectrum, nearly perfectly omni-directional pattern in the "array-plane" (X0Y),

- Time dispersive characteristics: Pulse measurement show excellent pulses synchronization, repeatable pulse patterns, non-squint, constant power over wide angle and fidelity is greater than 90% in the upper hemisphere.

- Parameter sequential order and sweeping methodology are elaborated in details, the priority and role of separable parameters are identified (table.1), and so, instead of multivariable-optimization, the optimization process can be accelerated by carry out sequence of parameter sweeping. The proposed design, optimization procedure can possibly be used as a gauging-process for designing or optimizing similar DUWB structures.

- The proposal antenna could possible be a solution for reducing/resolving the top side antennas problem and to somewhat degree will certainly be a push forwards the network the Network Concentric Operations (NCO)

- The DUWB-prototype has been designed years ago but not published elsewhere; due to editorial limits, we exclusively report here only the design methodology and conceptual approach; detailed mathematical formulation and numerical aspects related to this DUWB prototype will be published in another occurrence.

9. References

Agilent technologies (2007). Time Domain Analysis Using a Network Analyzer, Application Note 1287-12, 2007.

Balanis, C. A. (2005). Antenna theory analysis and design, Wiley & Sons 3rd, New York.

Baum, C.E. (2005), Compact Electric Antenna, Sensor and Simulation Notes, N500.

Booker, H.G. (1946). Slot Aerials and Their Relation to Complementary Wire Aerials, Proc. IEE, pt. IIIA, no. 4, pp. 620-629, April 1946.

Brown, D., Fiscus, T. E, Meierbachtol, C. J (1980). Results of a study using RT 5880 material for a missile radome, In: *Symposium on Electromagnetic Windows*, 15th, Atlanta, GA, June 18-20, Proceeding (A82-2645, 11-32), Georgia Institute of Technology, p.7-12.

Chen, Z. N. And Quing, X,(2005) Research and development of plannar UWB antennas. *Proceeding of the APMC 2005*.

Chen Z.N. (2007). Antenna Elements for Impulse Radio, In: *Ultra-wideband Antennas and Propagation for Communications, Radar and Imaging*, Allen B. (Ed.),Wiley & Sons.

Elek, F. et al. (2005), A uni-directinal ring slot antenna achieved by using Electromagnetic bandgap surface. *IEEE Trans. on AP.,* vol. 53, no. 1, Jan. 2005, pp. 181-190.

FCC (2002). Federal Communications Commission, FCC 02-48, ET-Docket 98-153, *"First Report and Order"*, Apr. 2002.

FCC (2004), Federal Communications Commission, FCC 04-285, ET-Docket 98-153, *"Second Report and Order and Second Memorandum Opinion and Order"*, Dec. 2004.

Hecht, E.,(2001), Optics, 4th edition, Addison Wesley,Aug, 2001.

Huang, Y. & Boyle, K. (2008). *Antennas from Theory to Practice*, John Willey and Sons, Singapore, 2008, pp.64.

IEEE Std 145-1983 (1983). *IEEE Standard Definitions of Terms for Antennas*, New York, IEEE Press, 1983, pp.11-16.

Karoui, M. S., Ghariani, H., Samet, M., Ramadi, M., Pedriau, R. (2010). Bandwidth Enhancement of the Square Rectangular Patch Antenna for Biotelemetry applications, *International journal of information systems and telecommunication engineering,* v.1, 2010, iss.1, pp.12-18.

Kshetrimayum, R. S., Pillalamarri, R. (2008). Novel UWB printed monopole antenna with triangular tapered feed lines, *IEICE Electronics express*, vol.5, No. 8, pp. 242-247.

Lamanna, M and Huizing, A. G.(2006), Scalable multifunction active phased array systems: from concept to implementation, *IEEE Int. Radar Conference, Verona, NY, Apr. 2006.*

Lee, F.L. & Luk, K.M (2011), Microstrip patch antennas, Imperial College Press, ICP ltd., London, 2011.

Ligthart, LP (2006). Antennas and propagation measurement techniques for UWB radio, *Wireless personal communications*, 37(3-4), pp.329-360.

Mushiake, Y.(1996), Self-Complementary Antennas: Principle of Self-Complementarity for Constant Impedance, Springer Verlag, London, 1996.

Petrov, L., Phillips, C., Bertarini, A., Murphy, T. and Sadler, E.M.,(2010). "The LBA Calibrator Survey of southern compact extragalactic radio sources — LCS1", Mon. Not. of Roy. Astron. Soc.,000,pp.1-13, Dec. 2010.

Rahayu, H., Rahman, T. A., Ngah, R., Hall, P. S. (2008). Slotted ultra wideband antenna for bandwidth enhancement, 2008, *Loughborough A&P Conference*, Loughborough, UK.

Rahim, M. K. A. & Gardner, P. (2004). The design of nine element quasi microstrip log periodic antenna, MW&RF *conference*, RFM 2004,Selangor, Malaysia, pp.132–135.

Rao Q. & Denidni T. A. (2007), Ultra-Wideband and Uni-Directional Radiation Slot Antenna for Multi-Band Wireless Communication Applications, Wireless Personal Communications v. 41, pp. 507–516, 2007.

Rmili, H. & Floc'h, J. M. (2008). Design and analysis of wideband double-sided printed spiral dipole antenna with capacitive coupling, *Microwave and optical technology letters,* Vol. 50, No.5, pp. 312-1317.

Schantz, H.G. and Bames, M., (2001),"The COTAB UWB Magnetic Slot Antenna," IEEE International Symposium on Antennas and Propagation Digest, 4, 2001, pp.104-107.

Schantz, H. G and Barnes, M. (2003). UWB magnetic antenna, *IEEE International Symposium on Antennas and Propagation Digest*, 3, 2003, pp.604-607.

Schantz, H. G. (2004). A brief history of UWB antennas, *IEEE Aerospace and Electronic Systems Magazine*, vol .19(4), pp.22-26, 2004.

Schantz, H, (2005); The Art and Science of Ultra-Wideband Antennas, Artech House Publishers Boston, MA, July, 2005.

Simons, R. N. (2001). *Coplanar Waveguide Circuits, Components, and Systems*, John Wiley & Sons, New York, 2001.

Stutzman, W.L. and Thiele, G.A.(1997), Antenna theory and design, Wiley & Sons, 1887.

Suh, S. S., et al., (2004); A novel printed dual polarized broadband antenna, the fourclover antenna; *Proceeding of the international symposyum on antenna and Progation, ISAP 2004,Sendai, Japan,* pp. 77-80.

Tanyer, F. M, Tran, D., Lager, I. E., Ligthart, L. P. (2009a). CPW-fed Quasi–Magnetic Printed Antenna for Ultra-Wideband Application, *IEEE Antennas and Propagation Magazine*, Vol.51, No.2, April 2009, 1, pp.61-70.

Tanyer, F.M; Lager, I. E., Mateos, R. M., Craeye, C(2009b).; Design of an AMC Plane for a Unidirectional, Low-profile Tulip-Loop antenna, Proceeding of the 3rd European Conference on Antennas and Propagation, EuCAP2009, Berlin, Germany.

Tavik, G. C. et al.(2005), The Advance Multifunction RF concept, IEEE Transaction on MTT, Vol.53,No.3, Mar. 2005, pp.1009-1020.

Tayefeh,M., Aligodarz, K., Rashidian, A. (2004), Wideband Miniaturized L-Probe Fed Fractal Clover Leaf Microstrip Patch Antenna, in: *Proceedings of JINA2004,* France, 2004

Tibbitts, B and Baron, N. (1999), Topside design of warships : a 100 year perspective ; Naval Engineers Journal, vol. 111, is. 2, pp. 27–44, Mar. 1999.

Tourette, S., Fortino, N., Kossiavas, G. (2006). Compact UWB printed antennas for low frequency applications matched to different transmission lines, *Microwave and optical technology letters*, Vol. 49, No.6, pp.1282-1287.

Tran, D., Tanyer-Tigrek, F. M., Vorobyov, A., Lager, I.E. & Ligthart, L.P.(2007). A Novel CPW-fed Optimized UWB printed Antenna, In: *Proceedings of the 10th European conference on wireless technology,* p.40-43, Munich, Germany, October 8-10, 2007.

Tran, D., Tanyer, F.M., Lager, I.E, Ligthart, L.P.(2009); A Novel Unidirectional Radiator with Superb UWB Characteristics for X-band Phased Array Applications; 3rd European Conference on Antennas and Propagation,EuCAP2009, Berlin, Germany, Mar. 2009.

Tran, D., Coman, C.I., Tanyer, F.M., Szilagyi, A., Simeoni, M., Lager, I. E., Ligthart, L. P. & van Genderen, P.(2010).The relativity of bandwidth – the pursuit of truly ultra wideband radiators, In: *Antennas for Ubiquitous Radio Services in a Wireless Information Society*, Lager, I. E (Ed.), pp.55-74, IOS Press, 2010, Amsterdam.

van Genderen, P. (2003), The APAR multifunction radar, system overview, Proceeding of the international symposium on Phased Array Systems and Technology, 17 Oct. 2003, pp.241-246, Boston, MA, 2003.

Wikipedia2011 ; http://en.wikipedia.org/wiki/Active_Electronically_Scanned_Array.

Wu, Q and Jin, R. (2010); On the Performance of Printed Dipole Antenna With Novel Composite Corrugated-Reflectors for Low-Profile Ultrawideband Applications; IEEE Trans. on AP. vol. 58, no. 12, dec. 2010, pp.3839-3846.

Wu, X.H, Chen, Z.N. & Chia, M.Y.W,(2003), Note on antenna design in UWB wireless communicaiton systems, IEEE conference on UWB and Technologies,p. 503–07.

Yaron, L., Rotman, R., Zach, S. & Tur, M.(2010), Photoniv beamformer receiver with multiple beam capabilities. IEEE photonic technolgy letters, vol.22, no.23, Dec.2010

Zhang, X., Wu, W., Yan, Z. H., Jiang, J. B. & Song, Y. (2009). Design of CPW-Fed monopole
      UWB antenna with a novel notched ground, *Microwave and optical technology
      letters*, Vol. 51, No.1, pp. 88-91.

Edited by Mohammad Matin

This book explores both the state-of-the-art and the latest achievements in UWB antennas and propagation. It has taken a theoretical and experimental approach to some extent, which is more useful to the reader. The book highlights the unique design issues which put the reader in good pace to be able to understand more advanced research.

IntechOpen